ATTACHMENT B
NEDC
EPRI Contract RP701-1
DRF 509DEV0023

Advanced Release by
Permission of
J.C. Danko, EPRI,
full release anticipated,
January, 1980)

EVALUATION OF NEAR-TERM BWR PIPING REMEDIES

(Research Project 701-1)

Final Report

May 1979

Prepared by

Nuclear Energy Engineering Division
General Electric Company
175 Curtner Avenue
San Jose, California 95125

Principal Investigators
A.J. Giannuzzi
Nolan R. Hughes

Prepared for
Electric Power Research Institute
3412 Hillview Avenue
Palo Alto, California 94304

Project Managers
J.C. Danko
R.E. Smith

90014054

NUCLEAR ENERGY ENGINEERING DIVISION • GENERAL ELECTRIC COMPANY
SAN JOSE, CALIFORNIA 95125

GENERAL ELECTRIC

8001100 378

LEGAL NOTICE

This report was prepared by General Electric Company as an account of work sponsored by the Electric Power Research Institute, Inc. Neither the Electric Power Research Institute, members of Electric Power Research Institute, nor General Electric Company, nor any persons acting on behalf of either:

A. Makes any warranty or representation, express or implied, with respect to the accuracy, completeness, or usefulness of the information contained in this report, or that the use of any information, apparatus, method of process disclosed in this report may not infringe on privately owned rights; or

B Assumes any liabilities with respect to the use of, or for damages resulting from the use of, any information, apparatus, method or process disclosed in this report.

ACKNOWLEDGMENTS

RP701-1 PROGRAM CONTRIBUTORS

TASK 1 — SCREENING MEASUREMENTS

D. C. Bertossa (Task Leader)

D. C. Bertossa
W. Vanderputten
P. P. Hallila
C. Schoenfeldt
A. J. Giannuzzi
T. R. Hayes
N. R. Hughes
J. D. Heald
W. L. Walker
A. E. Pickett
V. M. Romero
W. L. Clarke
J. P. Higgins
A. Chavez
J. C. Donko

TASK 2 — STATISTICAL PIPE TESTS

W. L. Walker (Task Leader)

W. L. Walker
A. J. Giannuzzi
S. A. Wilson
J. D. Heald
J. Yuen
J. C. Donko
T. L. Gerber
I. R. Coussens
D. C. Bertossa
A. E. Pickett
D. Hughes
N. R. Hughes
W. Vanderputten

TASK 3 — ELECTROCHEMICAL MEASUREMENTS

M. E. Indig (Task Leader)

A. R. McIlree
J. C. Donko
J. Weber

TASK 4 — FERRITE EFFECTS STUDIES

T. L. Devine (Task Leader)

R. E. Hanneman (Consultant)
M. G. Benz (Consultant)
D. A. Vermilyea (Consultant)
H. D. Solomon (Consultant)
B. J. Drummond
I. Mella
W. Moore
J. Hughes
T. Douglas
F. Clark
E. Nagy
R. Greening

Thanks are also expressed to the Electric Power Research Institute (EPRI) for cosponsoring the program and to R.E. Smith and J.C. Danko, Project Managers, EPRI, for their guidance and suggestions in helping to direct this program.

ABSTRACT

Full-size welded pipe screening tests have been conducted to evaluate the intergranular stress corrosion cracking susceptibility of reference Type-304 stainless steel and candidate remedies and protection methods. In addition, statistical pipe test evaluation of the most promising remedies and protection methods has been performed in the Pipe Test Laboratory. These methods include solution heat treatment after butt welding, application of a corrosion resistant cladding to the pipe inside surface, and heat sink welding. Laboratory specimen parametric studies and stress corrosion evaluations of the candidate remedies have supplemented this work. Special studies included an analysis of elastic constraint in the region of welds and an investigation of the effects of prior cold work on strain to surface fracture. Corrosion and oxidation potential electrochemical studies on Type-304 stainless steel and platinum as a function of oxygen level and temperature have been conducted both in the laboratory and in an operating BWR. Straining electrode measurements were made on reference Type-304 stainless steel and the candidate remedies. A topical report describing the effect of ferrite on the intergranular corrosion behavior of Type-308 stainless steel and presenting a model explaining the improved resistance of duplex stainless steels to intergranular stress corrosion cracking is presented in this final report.

1. SUMMARY

During this program, significant technical data have been generated and are presented in this comprehensive final report. Highlighting these results are the following:

- Laboratory full-size pipe and small specimen screening tests of reference Type-304 stainless steel and potential pipe remedies.
- Laboratory full-size pipe tests representing the statistical pipe test program for reference Type-304 stainless steel and the candidate pipe remedies.
- Laboratory stress corrosion cracking and degree of sensitization measurements on small specimens removed from welded pipe sections of reference Type-304 stainless steel and the candidate remedies.
- Elastic weld constraint computer modeling.
- Elastic weld constraint high temperature welded pipe segment tensile tests.
- Studies of the effect of surface condition on the strain to cracking of Type-304 stainless steel.
- In-reactor electrochemical potential measurements of Type-304 stainless steel.
- Laboratory electrochemical potential measurement and straining electrode measurements of Type-304 stainless steel and the candidate remedies.
- A topical report summarizing the results on the intergranular corrosion and stress corrosion cracking behavior of microduplex stainless steels.

The following subsections (1.1 through 1.4) summarize the work performed.

1.1 TASK 1 — SCREENING MEASUREMENTS

Stress corrosion tests have been conducted on full-size welded pipe sections of 10.16-cm (4-in.) diameter Schedule 80 Type-304 stainless steel and candidate remedies to evaluate their resistance to intergranular stress corrosion cracking in boiling water reactor (BWR) environments. The following remedies have been shown to considerably reduce intergranular stress corrosion cracking susceptibility. These remedies are described in Section 2.0, Program Objective.

1. Solution heat treatment of welded pipe,
2. application of corrosion-resistant cladding to pipe inner surface prior to welding, and
3. application of heat sink welding techniques during pipe welding.
4. Alternate materials (316L, CF3, 347, 304L).

A series of 11 full-size pipe tests have been performed to screen remedies. These tests have included four cyclic axial loaded pipe tests in the Large Environmental Fatigue Test Facility, two 4-point bending pipe tests in the CL-4 test facility, and six cyclic axial loaded pipe tests in the Pipe Test Laboratory. Figure 1-1 accelerated test conditions were used to reduce the required testing time to failure. These accelerants included high stress cyclic loading, high oxygen water environments, heavy grinding on the inner surface weld heat affected zones, and in some welds, high weld heat input.

Small specimen stress corrosion tests (constant load and constant extension rate) have been performed on a variety of samples machined from pipe weldments. A summary of small specimen results is as follows:

- All three heats of Type-304 stainless steel used for Task 2 of this program were susceptible to intergranular stress corrosion cracking.

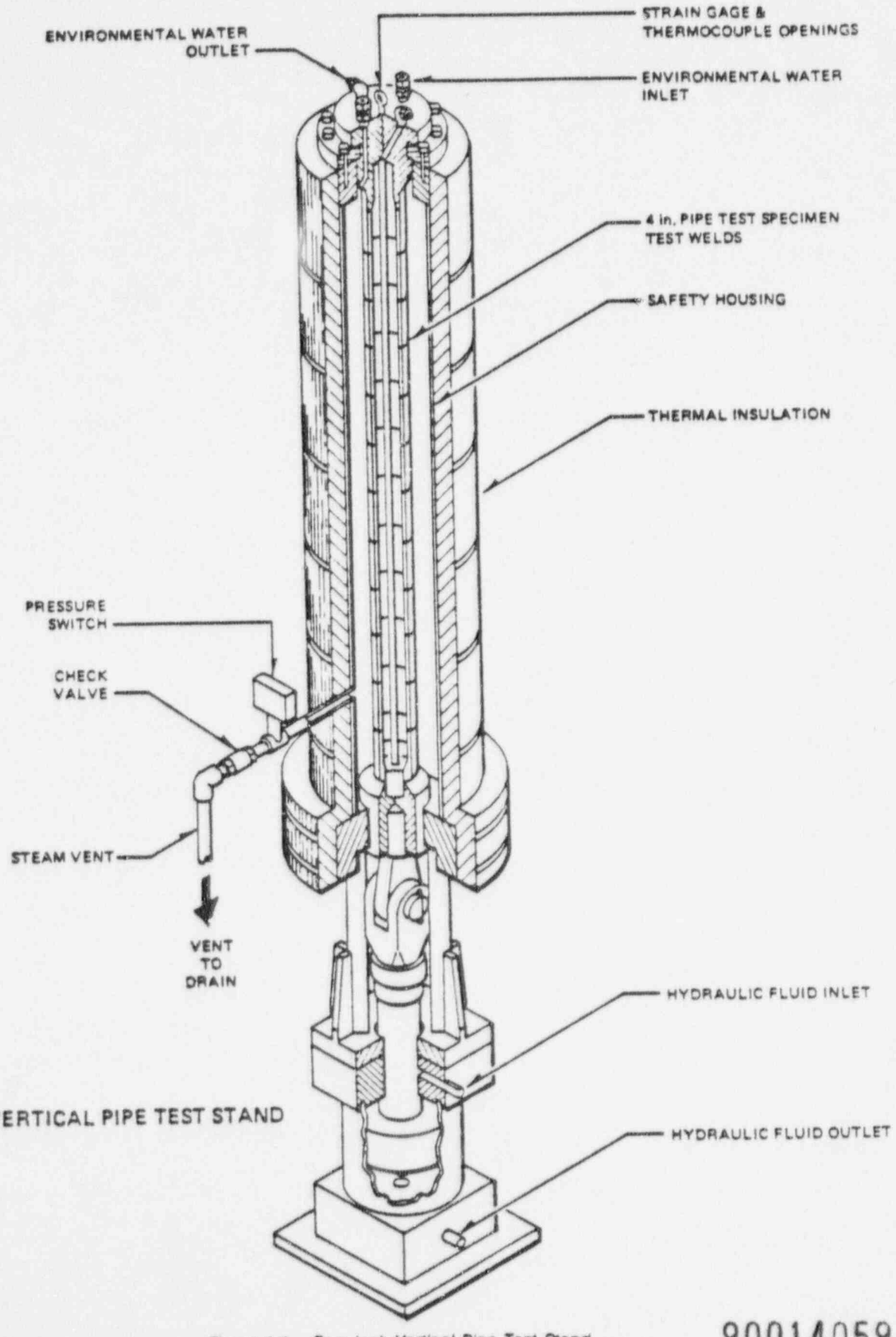

Figure 1-1. Four-inch Vertical Pipe Test Stand

90014059

- The laboratory specimen degree-of-sensitization and stress corrosion cracking tests showed no susceptibility to IGSCC for the shop corrosion-resistant cladding remedy (solution heat treatment of initial cladding deposit).

- The heat sink-welding protection method and the field (as deposited) corrosion-resistant cladding exhibited some susceptibility to IGSCC in constant extension rate tests. In constant load tests the field corrosion-resistant cladding has not failed in over 5,700 hours while reference Type-304 stainless steel of the same heat failed in 250–500 hours. Heat sink welding has shown inconsistent behavior in constant load samples; some samples failed by IGSCC, others did not.

- The CF-8 heat of material used in this investigation failed by intergranular stress corrosion cracking in the annealed and welded condition in the constant extension rate test. In addition, this heat showed transgranular stress corrosion cracking initiation in constant load tests. These failures are contrary to previous experimental results, and to the expected behavior of CF-8. The reason for this unique behavior is not fully understood.

1.2 TASK 2 — STATISTICAL PIPE TESTS AND SPECIAL STUDIES

Twelve reference and remedy pipe specimens were fabricated and tested in the Pipe Test Laboratory. A statistical basis for evaluation of results was established which allowed calculations of factors of improvement for remedies versus reference pipes. Table 1-1 the four heat sink welds fabricated at Bechtel Corporation under Task 1 were also included in the statistical studies. In addition, small laboratory welded specimens of reference Type-304 stainless steel were placed on test in the Variable Load Facility, examining the effect of stress and cyclic frequency on the IGSCC behavior of reference as-welded Type-304 stainless steel. Special studies included studies of elastic constraint and an investigation of the effects of prior cold work on the percent strain required to produce surface fissures. Highlights of these tests include the following:

1. Both the solution anneal after welding and the solution annealed corrosion-resistant clad remedies appear to offer improved resistance to stress corrosion cracking by factors of 46 or more on one heat of Type-304 stainless steel.

2. The as-deposited corrosion-resistant clad remedy appears to have demonstrated a minimum improvement factor of approximately seven, based on data obtained from the worst reference heat of material which was sensitized in the mill annealed condition.

3. Based on limited test exposures, the heat sink welding remedy has demonstrated an improvement factor of 9.7 at this time. The true factor of improvement for this remedy may be significantly greater than this value.

4. Within the range of carbon contents normally encountered in Type-304 stainless steel, the specific carbon content of a particular heat may significantly affect its resistance to stress corrosion.

5. The absolute stress level at which specimens are tested may exert a significant influence on time to initiation of stress corrosion cracking, based on evaluation of three heats of one nominal composition.

6. Cycling rate does not significantly affect times to failure of small specimens over the range of 0.67 to 3.35 cycles/hr. However, cyclic loading greatly decreases the variance in times to failure, as compared to constant loading at the same stress levels. This increased variance often results in longer mean failure times for constant load samples when compared to cyclic loading.

7. Cycle shape significantly affects the times to failure of small specimens stressd to the same maximum stress level at the same cycling frequency. The results indicate that time at maximum stress is the controlling factor in stress corrosion cracking initiation.

Table 1-1

Heat	Remedy	Factor of Improvement
M7616 (0.060% C)	Solution Heat Treatment	46.3
	Corrosion-Resistant Cladding (solution annealed)	48.2
	Corrosion-Resistant Cladding (as-deposited)	6.6*
	Heat Sink Welding	9.3*
M0063 (0.050% C)	Solution Heat Treatment	4.6
	Corrosion-Resistant Cladding (solution annealed)	6.0
	Corrosion-Resistant Cladding (as-deposited)	6.0
454570 (0.042% C)	Solution Heat Treatment	1.6
	Corrosion-Resistant Cladding (solution annealed)	1.6
	Corrosion-Resistant Cladding (as-deposited)	1.7

*Based on first failure.

1.3 TASK 3 — ELECTROCHEMICAL MEASUREMENTS

The studies described herein were aimed at providing understanding and predictability capability of the environmental aspects of intergranular stress corrosion cracking of welded Type-304 stainless steel in boiling water reactors. Electrochemical techniques were used in performing both in-reactor and laboratory experiments. In aqueous systems the effect of the environments on metals can be characterized by the electrochemical potential and pH. Because the pH was known, or in a few cases determined, the electrochemical potentials of Type-304 stainless steel were either measured or controlled. In order to accomplish this end, a silver/silver chloride reference electrode was developed that could measure potentials from room temperature to about 300°C (572°F). The potentials were then converted to a standard thermodynamic scale and this conversion allowed direct comparison of potentials regardless of whether they were determined in a nuclear reactor or the laboratory.

At the Vermont Yankee Boiling Water Reactor, corrosion potentials and supportive chemical analyses of the reactor water were determined during a reactor start-up. The corrosion potential of Type-304 stainless steel during reactor startup is shown in Figure 1-2. It was found that the potentials at low temperatures, less than about 125°C (257°F), were considerably higher than those which could be accounted for from just dissolved oxygen. A shift of potentials and water chemistry transient caused by the unexpected decomposition of ion exchange resins in the reactor during start-up were also measured.

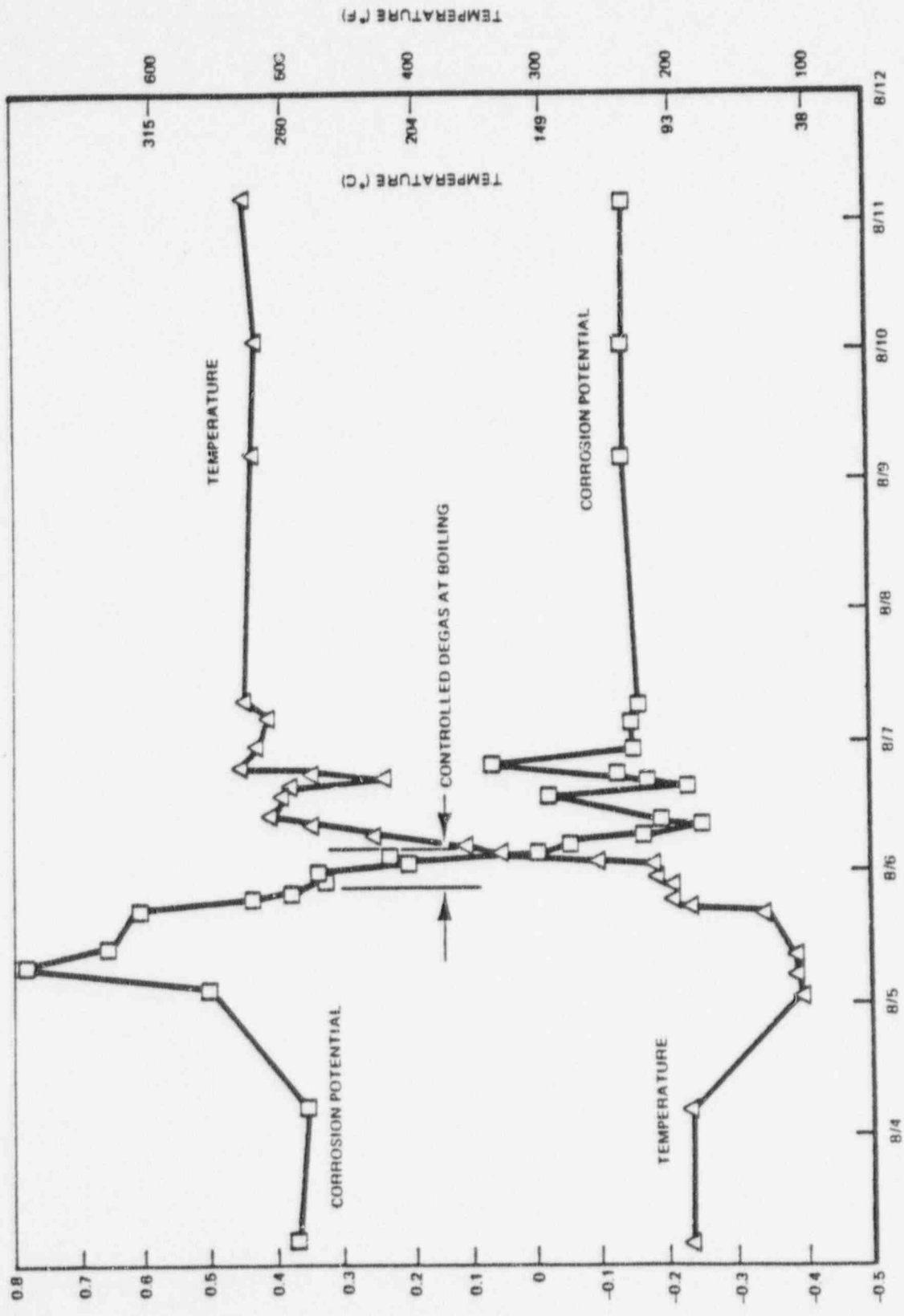

Figure 1-2. Corrosion Potential of Type-304 Stainless Steel During Reactor Startup

In the laboratory, carefully controlled experiments were performed where the dissolved oxygen was varied in water and the potential response was determined. At low temperatures the effects of combinations of H_2O_2 and O_2, which simulated reactor environments, were measured. From the laboratory and in-reactor experiments, it was found that at low temperatures the potential of Type-304 stainless steel was determined by the specific combination of H_2O_2 and O_2. Above approximately 150°C (302°F), the corrosion potentials were determined by the dissolved oxygen concentration. Dissolved hydrogen had a negligible effect on corrosion potential but an increase in hydrogen ion as caused by the resin decomposition increased the corrosion potential to a region where the susceptibility to IGSCC increased significantly.

At any temperature, an increase in oxygen concentration caused an increase in potential. The effect was most dramatic for the potential/oxygen experiments conducted at 232°C (450°F) and 274°C (525°F) where, as shown in Figure 1-3, the potential increased about 0.75 V as the dissolved oxygen was increased from 10 ppb to 8 ppm. These large differences in potentials can be used to determine potential driving forces for IGSCC and calculating concentration factors in crevices.

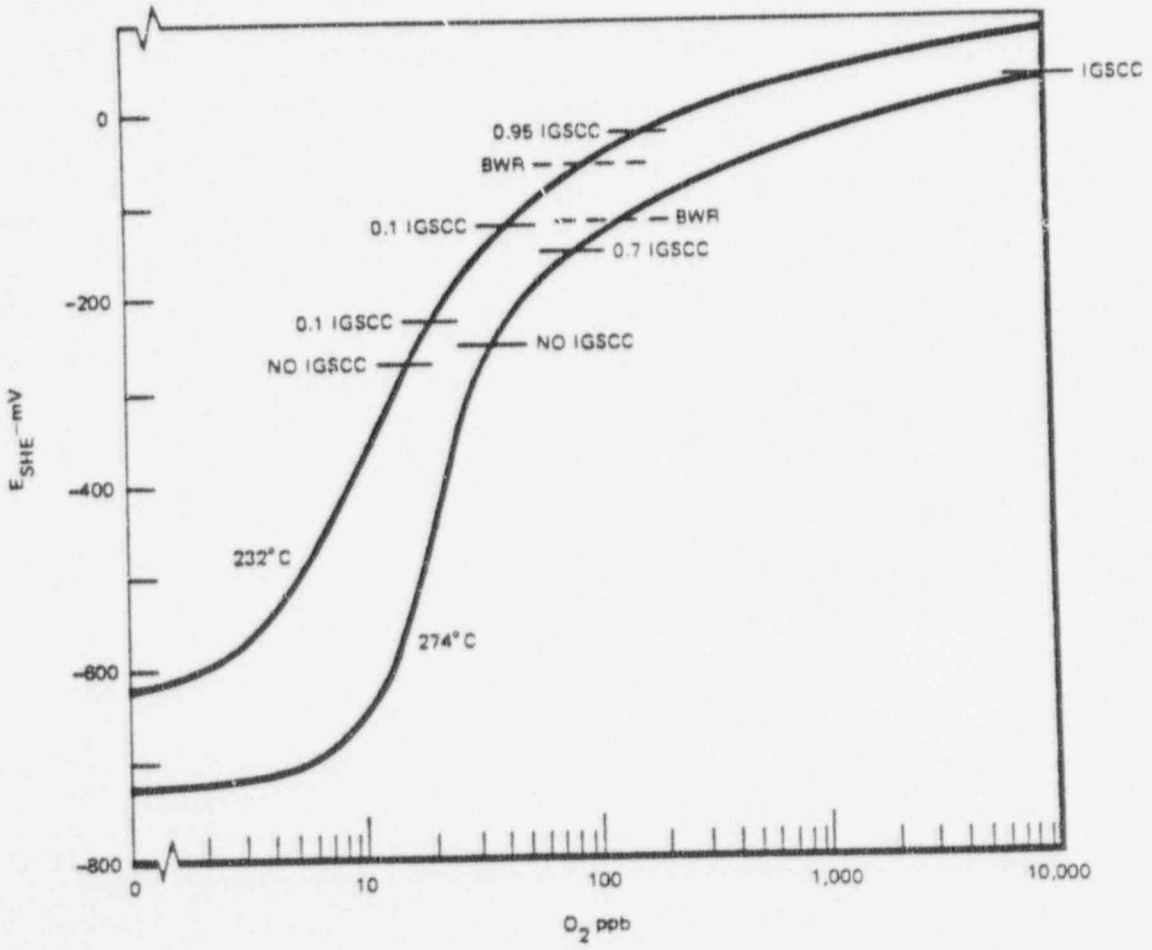

Figure 1-3. The Effect of Dissolved Oxygen on the Corrosion Potential and IGSCC of Type-304 Stainless Steel (Average Curves)

Since the range of potentials equivalent to specific oxygen concentrations and reactor environments were now known, straining electode experiments could be performed where the potential of a sample strained continuously, was controlled. For a specific heat of Type-304 stainless steel, it was found that in the as-welded condition IGSCC occurred at 274°C (525°F) at potentials equivalent to or greater than a dissolved oxygen concentration of about 50 ppb. Although this heat was known to be highly susceptible to IGSCC, it was found that with decreasing temperature the stress corrosion process for the as-welded condition became more difficult (required higher strains to initiate IGSCC). It is postulated that for alloys in a more susceptible metallurgical condition, for example, such as welding followed by a low temperature sensitization (LTS) or the furnace sensitized condition, initiation and propagation of IGSCC could proceed more easily at the lower temperatures.

Although IGSCC was the major mode of failure when stress corrosion occurred, transgranular cracking was often detected. Short transgranular cracks occurred either as a result of cold work, (cracks at the root of machine grooves) or after a significant amount of strain during the test had occurred.

In addition to determining the effect of potential (equivalent oxygen concentration) on the IGSCC susceptibility of welded stainless steel, the straining electrode test was used to evaluate proposed pipe remedies and alternate alloys. At potentials that would result in early IGSCC failures of welded Type-304 stainless steel, it was found that the corrosion-resistant clad and solution heat treat remedies as well as the as-welded Types-304L and CF3A (cast 304L) provided almost complete immunity toward IGSCC.

Potentiokinetic curves (anodic polarization curves) were performed to increase our understanding of corrosion behavior of the stainless steel and its sensitized grain boundaries. The grain boundary behavior was studied indirectly with experimental alloys whose, bulk composition approximated chromium depleted grain boundaries (contained <18% Cr) of sensitized stainless steel. From the presence or absence of the active-passive transition of the experimental alloys it was deduced that below some low temperature (~150°C) (302°F) IGSCC would be restricted to a narrow potential range. With increasing temperature, the alloy corroded actively above some minimum polarizing potential. This indicates that above some corrosion potential or minimum oxygen concentration, IGSCC would occur over a broad potential range with increasing severity.

While much of the straining electrode test data can be applied to study the effect of the reactor start-up transient on IGSCC, a more direct approach was sought. An electrochemical/constant load system was built that can directly determine the effect of the changing start-up environment on the tendency toward crack initiation. Initial studies have shown that in a simulated BWR aerated start-up, complete IGSCC can occur on furnace sensitized Type-304 stainless steel in less than six hours. The start-up tests will help determine the proper environmental control to prevent crack initiation of welded Type-304 stainless steel during real BWR start-ups.

1.4 TASK 4 — FERRITE EFFECT STUDY

In-reactor experience and numerous laboratory studies conducted in simulated boiling water reactor environments have indicated duplex stainless steels to be much more resistant to intergranular stress corrosion cracking than austenitic stainless steels. This program has sought to determine those metallurgical conditions responsible for this resistance to stress corrosion cracking in the various boiling water reactor environments. In particular, the mechanism of carbide precipitation in duplex stainless steels was determined as was the critical amount and distribution of ferrite required to inhibit intergranular stress corrosion cracking (IGSCC). To expedite testing of a large number of duplex alloys to provide foundry personnel and fabricators with an easy technique for assessing the IGSCC resistance of duplex alloys, several corrosion and electrochemical tests were examined for their ability to detect and screen out duplex alloys and/or heat treatments highly susceptible to IGSCC.

The corrosion behavior of duplex 308 stainless steel as a function of aging treatment was measured by ASTM practices A262A, A262C, and A262E, by its potentiodynamic and galvanostatic pitting behavior in 0.1N HCl and compared to the stress corrosion cracking behavior of specimens pulled at slow strain rates in air saturated water at 288°C. The corrosion behavior of 308 stainless steel in A262E and its pitting behavior determined galvanostatically in 0.1N HCl correlated extremely well with the stress corrosion cracking behavior in air saturated water at 288°C.

The mechanisms of carbide precipitation and intergranular corrosion in duplex stainless steel were determined from experiments performed on 308 stainless steel which was given four different high temperature heat treatments to introduce four different ferrite levels, 0 v/o, 1 v/o, 10 v/o and 20 v/o. Whereas $M_{23}C_6$ precipitation occurs intergranularly during aging of austenitic Type-308 stainless steel, no $M_{23}C_6$ precipitation occurs along austenite-austenite grain boundaries in duplex Type-308 stainless steel containing suitable amounts and distributions of ferrite. Instead, in duplex Type-308 stainless steel containing a critical amount and distribution of ferrite, $M_{23}C_6$ precipitation occurs exclusively along austenite-ferrite phase boundaries. This is because chromium diffusion is the rate determining step in the precipitation reaction. Since chromium diffusivity is approximately 1000 times greater in the ferrite than in the austenite at 600°C, $M_{23}C_6$ forms first along austenite-ferrite boundaries (there are no ferrite-ferrite grain boundaries, since each ferrite region is a single grain) probably by both chromium and carbon diffusing from the ferrite. The carbon in the ferrite is quickly reduced to the solubility limit and subsequent carbon comes almost exclusively from the austenite, thereby depleting the austenite grains of carbon, and preventing any carbide precipitates from forming along austenite-austenite grain boundaries. Although the chromium in the $M_{23}C_6$ precipitates is supplied principally by the ferrite phase, a small but significant amount of chromium is contributed by the austenite phase. The latter results in localized corrosion of the austenite-ferrite boundary in the A262E test. That the chromium-depleted zone lies on the austenite side of the austenite-ferrite interface is demonstrated by the fact that pits initiate there during galvanostatic pitting experiments in 0.1N HCl. The chromium-depleted zone formed in the austenite adjacent to the carbide formed along the original austenite-ferrite interface is very narrow relative to that formed adjacent to intergranular $M_{23}C_6$ in fully austenitic Type-308 stainless steel. Consequently, the chromium-depleted zone is quickly replenished by chromium diffusing from the interior of the austenite. When the chromium level has been replenished to above a critical value (occurs within 8 hr at 600°C), the material is immune to intergranular corrosion in A262E and IGSCC in air-saturated water at 288°C.

Decomposition of the ferrite phase occurs during the above healing process. After aging at 600°C for times longer than 2 hours, the ferrite phase decomposes into cellular $\gamma + M_{23}C_6$ starting at the original $\alpha-\gamma$ interface. The low chromium content of the austenite phase ($\approx$14 wt%) in the cellular $\gamma + M_{23}C_6$ zone results in localized corrosion attack of this region in the A262E test. With continued decomposition, the limited carbon supply of the ferrite phase is exhausted and the ferrite transforms solely to austenite by rejecting chromium back into the bulk ferrite. The chromium-enriched zone of ferrite at the new austenite-ferrite interface then transforms to σ. The remaining ferrite transforms to a duplex structure of austenite plus ferrite. The presence of σ phase did not result in SCC in air-saturated water at 288°C.

When duplex Type-308 stainless steel is aged at 480°C, the chromium possesses insufficient mobility for $M_{23}C_6$ to form. Instead, an extremely fine chromium-rich precipitate, α', forms throughout the ferrite. When specimens aged for 100 hours at 480°C are tested in A262E, the chromium depletion of the ferrite phase resulting from α' precipitation causes concentrated attack of the ferrite regions. However, the presence of α' did not adversely affect the SCC resistance in SERT.

Based on the above mechanism of intergranular carbide precipitation and intergranular corrosion in duplex stainless steel a model is developed which describes the intergranular corrosion behavior as a function of the carbon content and the amount of distribution of $\alpha-\gamma$ boundary area. Alloys containing a critical amount of distribution of austenite-ferrite boundary area develop a sensitized microstructure and subsequently undergo a healing phenomenon very rapidly during isothermal aging treatments (e.g., within 10 hr at 600°C). Rapid healing is essential for alloys used in components which must receive a nitriding or stress relief annealing treatment at sensitizing temperatures. The critical amount of $\alpha-\gamma$ boundary area required for rapid healing is that amount which is sufficient to tie-up all of the available carbon as $M_{23}C_6$ exclusively along $\alpha-\gamma$ boundaries. The critical distribution of $\alpha-\gamma$ boundary area required for rapid healing is that which places each carbon atom in the austenite phase within easy diffusion distance of an $\alpha-\gamma$ boundary. Both the amount and distribution of $\alpha-\gamma$ boundary area can be expressed as a function of the metallographic parameter, N_L. The latter is a measure of the number of intercepts a random test line makes with $\alpha-\gamma$ boundaries per unit length of test line. Figure 1-4 plots the variation in N_L with %C that is required to maintain a critical *amount* of $\alpha-\gamma$ boundary area (straight-line labeled S_v) as well as that which is required to provide a critical *distribution* of $\alpha-\gamma$ boundary area (curve labeled λ_γ). The value of N_L required for rapid healing is the higher of the two.

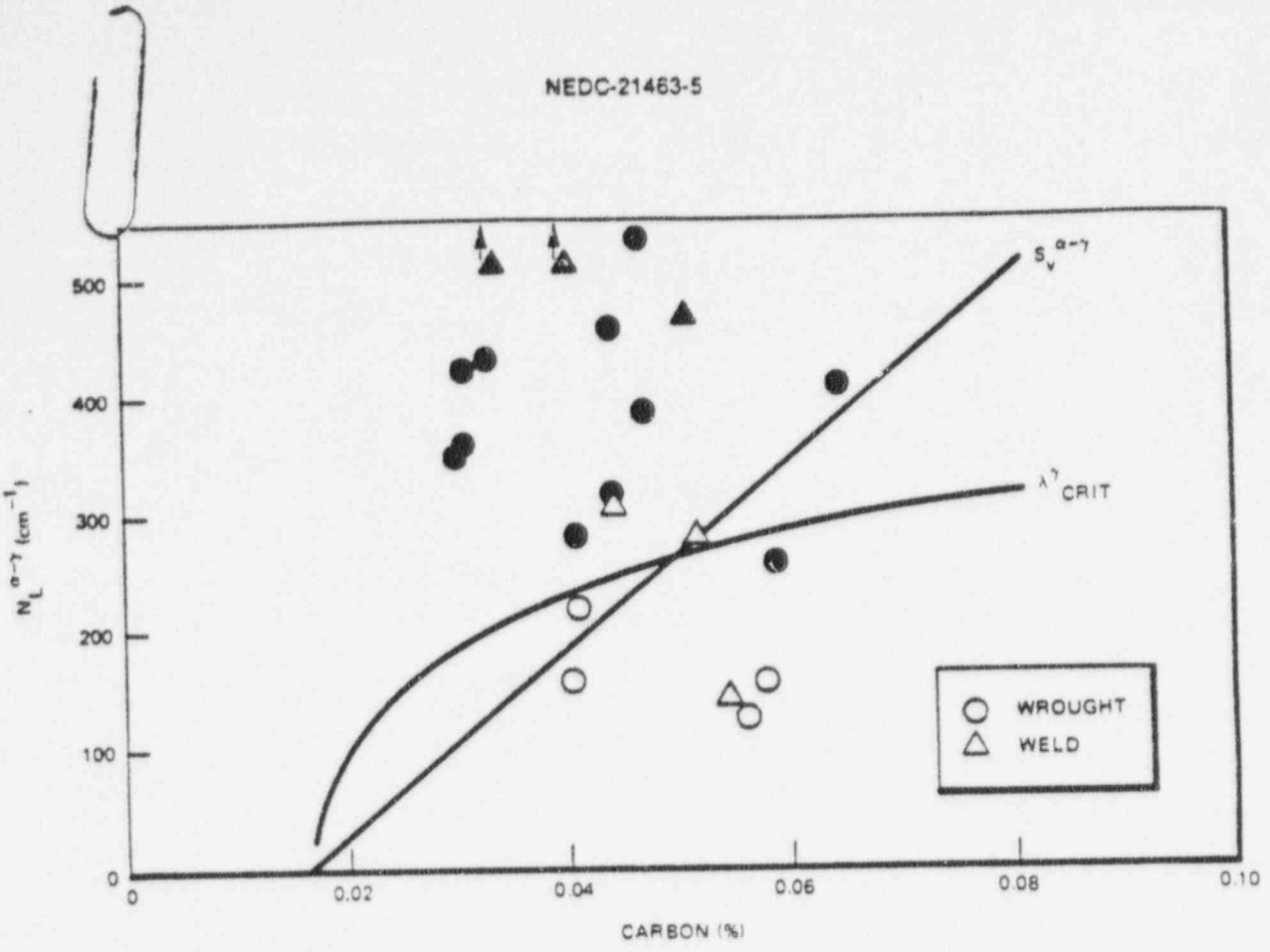

Figure 1-4. The Influence of $N_L^{\alpha-\gamma}$ on the Intergranular Corrosion Behavior of Aged Samples of Wrought and Weld-Deposited Type-308 Stainless Steel

At low carbon contents the critical *distribution* criterion is limiting and at high carbon contents the critical *amount* criterion is limiting. The circles in Figure 1-4 represent data obtained on wrought heats of Type-308 stainless steel and the triangles represent data obtained on weld deposits of 308. Closed points indicate rapid healing and open points indicate no healing within 10 hrs. at 600°C.

The model was extended to predict the amount and distribution of $\alpha-\gamma$ boundary area required to produce an alloy which is immune to sensitization. For such an alloy, no aging treatment can produce a sensitized microstructure. The critical distribution criterion is the limiting factor in the case of an immune alloy and is shown in Figure 1-5 along with the critical distribution criterion for rapid healing which was depicted in Figure 1-4. The two points represented by stars were immune to sensitization. The data are fairly well described by the theory.

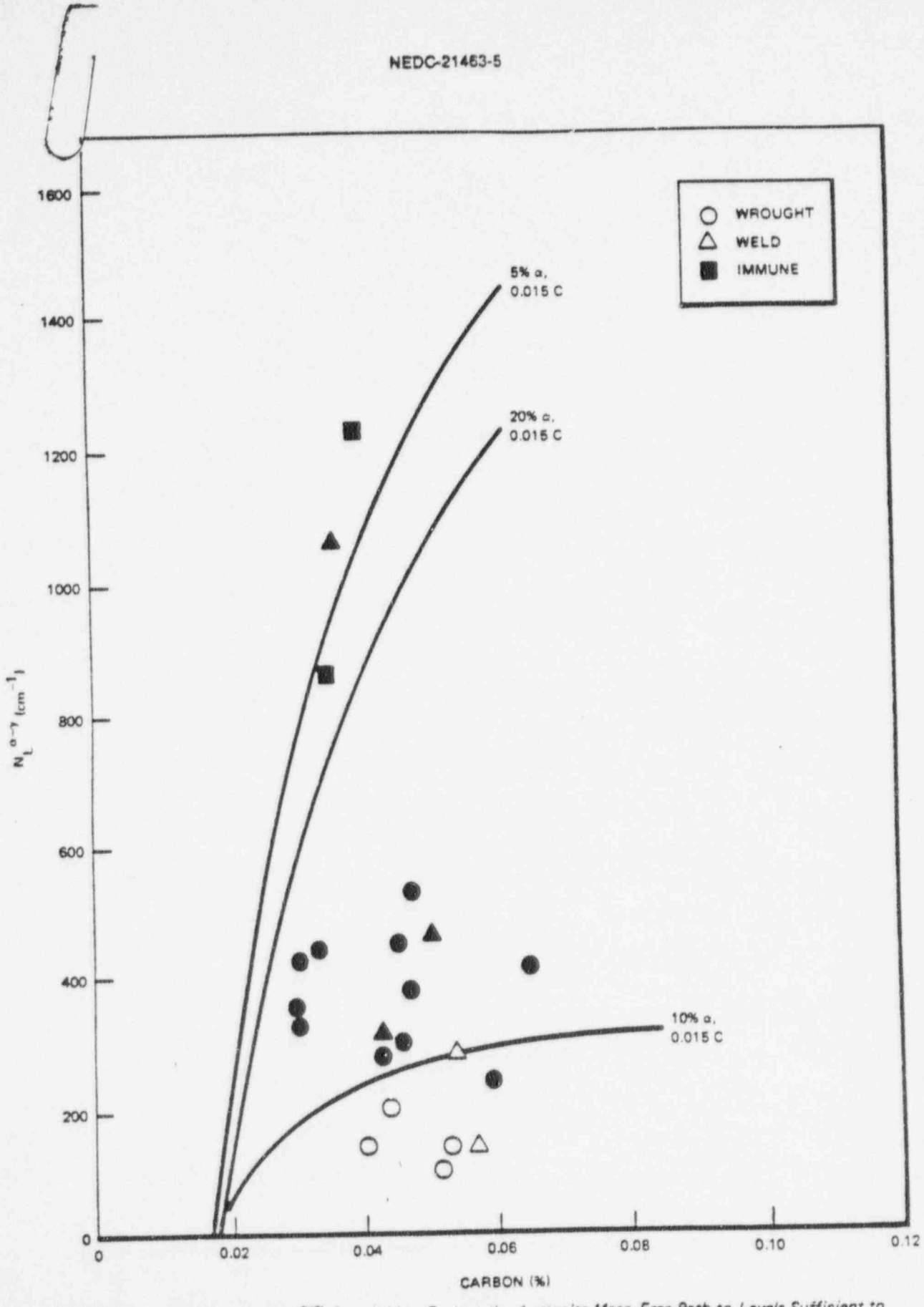

Figure 1-5. The Values of $N_L^{\alpha-\gamma}$ Required to Reduce the Austenite Mean-Free-Path to Levels Sufficient to (a) Restrict and (b) Prevent Sensitization of Type-308 Stainless Steel

2. PROGRAM OBJECTIVE

The contract RP701-1, covering an agreement between the Electric Power Research Institute and the General Electric Company, describes a two-year program to verify the reliability of one or more near-term remedies to the boiling water reactor pipe cracking problem. The aim of the program is to provide a sound statistical basis with which to demonstrate that one or more of the recommended remedies will provide immunity to intergranular stress corrosion cracking of welded piping in boiling water reactor environments.

2.1 DESCRIPTION OF NEAR-TERM BWR PIPE REMEDIES

This program investigated the intergranular stress corrosion cracking performance of reference Type-304 stainless steel and several candidate near-term piping remedies in both pipe tests and specimen tests in simulated boiling water reactor environments. The list of pipe remedies with a description of the procedure for application in welded piping and the rationale for consideration follows.

2.1.1 Solution Heat Treatment of Pipe Butt Welds

It has been demonstrated by the General Electric Company and by other organizations that weld sensitization of some heats of Type-304 stainless steel piping combined with high stress (or plastic strain) produces conditions for intergranular stress corrosion cracking in the boiling water reactor environment. Further, mill-annealed and solution-annealed Type-304 stainless steel piping is believed to be immune to intergranular stress corrosion cracking in the BWR boundaries. A prime pipe-remedy for welded Type-304 stainless steel piping systems is therefore to solution heat treat the pipe welds. Solution heat treatment of the pipe welds, in addition to eliminating weld sensitization, also relieves the weld residual stresses. Wherever possible, solution heat treatment of pipe welds in requisition plants has been performed in the pipe fabricator's shop according to procedures approved by the General Electric Company.

The procedure for applying solution heat treatment is presented in Figure 2-1. Here, the pipe is butt welded as in the case of reference Type-304 stainless steel. No unusual welding controls are employed during welding. Following the butt welding operation, the entire pipe segment is solution annealed at 1900 to 2100°F (1038 to 1148°C) for 15 minutes per inch of thickness but not less than 15 minutes nor more than 1 hour regardless of thickness, followed by quenching in circulating water to a temperature below 400°F (204°C).

2.1.2 Application of Corrosion-Resistant Cladding to Pipe Inside Surface Prior to Field Butt Weld

The intergranular stress corrosion cracking observed in the bypass, and core spray lines of operating BWR plants has been exclusively associated with weld-sensitized or furnace-sensitized components. The carbide precipitation observed in the heat affected zone inside surface is also present in the weld metal. However, the nature of the duplex (austenitic-ferritic) structure of the weld metal provides resistance to intergranular stress corrosion cracking in the BWR, although carbide precipitation is present. In fact, intergranular stress corrosion cracks propagating from the weld HAZ are blunted when they reach the weld metal. A minimum amount of ferrite must be present in the alloy to provide immunity to intergranular stress corrosion cracking in BWR water. Based on General Electric tests on duplex structures, the minimum ferrite level recommended to provide for the corrosion-resistant cladding is 8% after final processing, including field welding.

There are two variations of the proposed use of corrosion-resistant cladding (Figure 2-2):

1. Where a solution heat treatment can be performed in the shop prior to the final field weld, the cladding will consist of Type-308L stainless steel with high initial ferrite (to allow for reduction in ferrite during subsequent solution heat treatment as shown in region A of Figure 2-2). The solution heat treatment is then performed to eliminate potentially unfavorable residual stresses introduced during the cladding

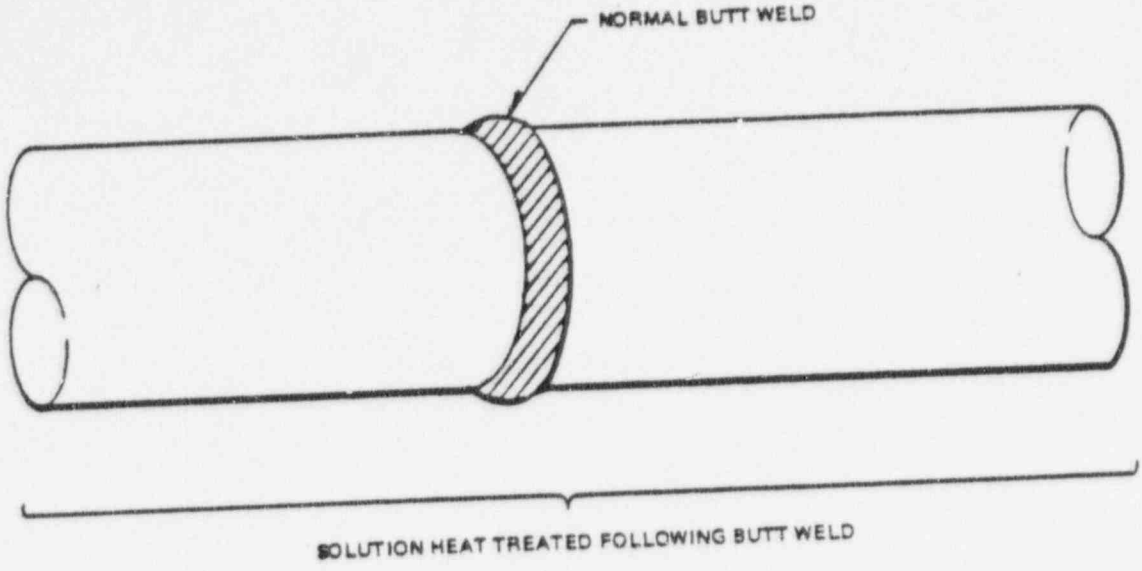

Figure 2-1. Application of Solution Heat Treatment of Type-304 Stainless Steel Pipe Welds

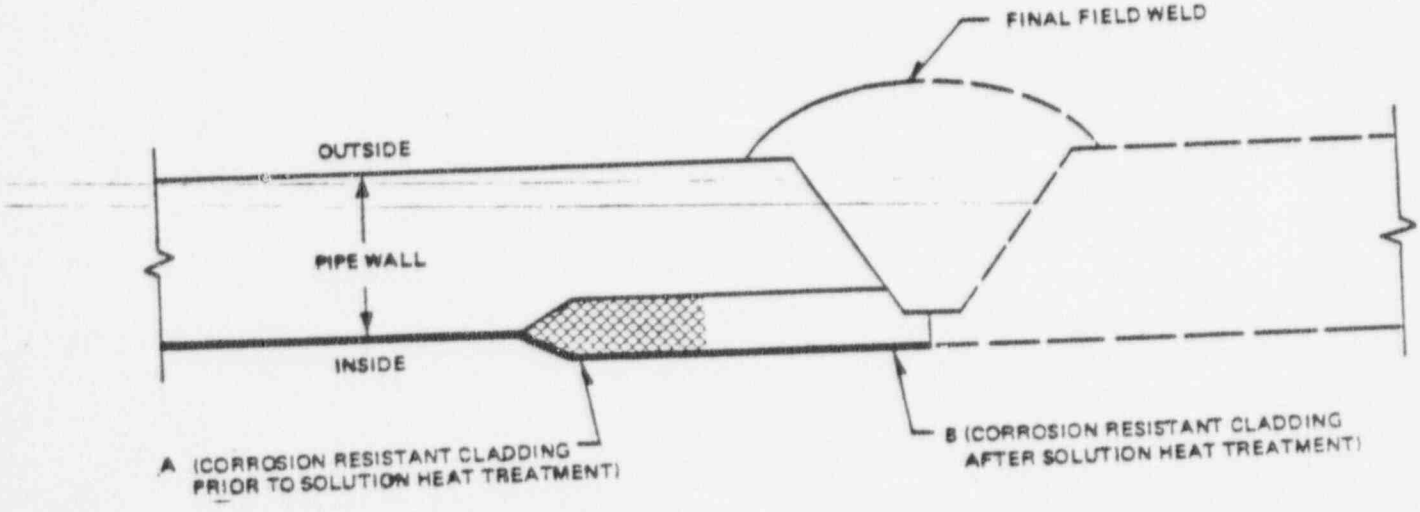

Figure 2-2. Corrosion Resistant Cladding Process for Type-304 Stainless Steel Welded Piping

operation and to eliminate the modest sensitization expected in the region of the inside surface of the Type-304 stainless steel immediately adjacent to the cladding. Following the solution heat treatment, region B is deposited using Type-308L stainless steel and the field butt weld is performed as in the reference Type-304 stainless steel butt welds.

2. Where a solution heat treatment cannot be performed (such as the final closure weld in a pipe repair of an operating reactor), the cladding material would then be Type-308L stainless steel with 0.030% carbon maximum and 8% ferrite minimum. In this case, both regions A and B in Figure 2-2 would be clad identically. In addition the base material is tested by the electrochemical potentiokinetic reactivation technique to assure that it is not sensitized prior to depositing the cladding.

2.1.3 Application of Inside Surface Heat Sink Welding Control During Welding

Field and laboratory intergranular stress corrosion cracking data reveal that high residual welding stresses coupled with the applied stresses plus weld sensitization provide conditions for intergranular stress corrosion cracking of Type-304 stainless steel in the BWR environment. If a pipe can be welded without producing a sensitized structure and high residual tensile stresses in the weld HAZ, the resultant component will be resistant to intergranular stress corrosion cracking in the BWR environment. The inside surface heat sink welding program was directed to the development and qualification of procedures that reduce the sensitization produced on the inside surface of welded pipe, and reduce or change the state of surface residual welding stresses from tension to compression. This approach can be used in shop or field applications where either the solution heat treatment or use of a corrosion-resistant cladding are not possible.

Laboratory Type-304 stainless steel butt welds have been produced by General Electric licensees evaluating the inside surface heat sink welding techniques. It has been found that inside surface tensile surface residual stress is reduced substantially or changed from tension to compression as a result of this approach.

The inside surface heat sink welding program can be performed using still water, flowing or turbulent water, or water spray cooling of the inside surface by means of a sparger arrangement Figure 2-3. In all cases, the water cooling is applied following the initial root weld layer deposit. The weld is fabricated with normal field welding practice but with the addition of the inside surface water cooling following the root pass.

2.1.4 Other Remedies

Several other remedies were developed and tested during the Screening Task of this program. These remedies were all designed to address sensitization and or stress, both of which are contributing factors to stress corrosion cracking.

Item

1. Backlay (joint reinforcement by weld deposit)
2. Polishing/Conditioning Inner Pipe Surface
3. Extended Weld Bevel Constraint
4. Reduction in Weld Heat Input
5. Pre-Weld Solution Heat Treatment of Pipe
6. Alternate Materials
7. Effect of Low Temperature Heat Treatment
8. Material Composition Factors (ASME-SA312, Type-304 pipe with varying carbon content)
9. Mill Fabrication Variations (seamless pipe vs rolled and welded)

2.2 TASK OBJECTIVES

The work under this contract is divided into four major tasks. These tasks and a brief description of the task objectives are as follows.

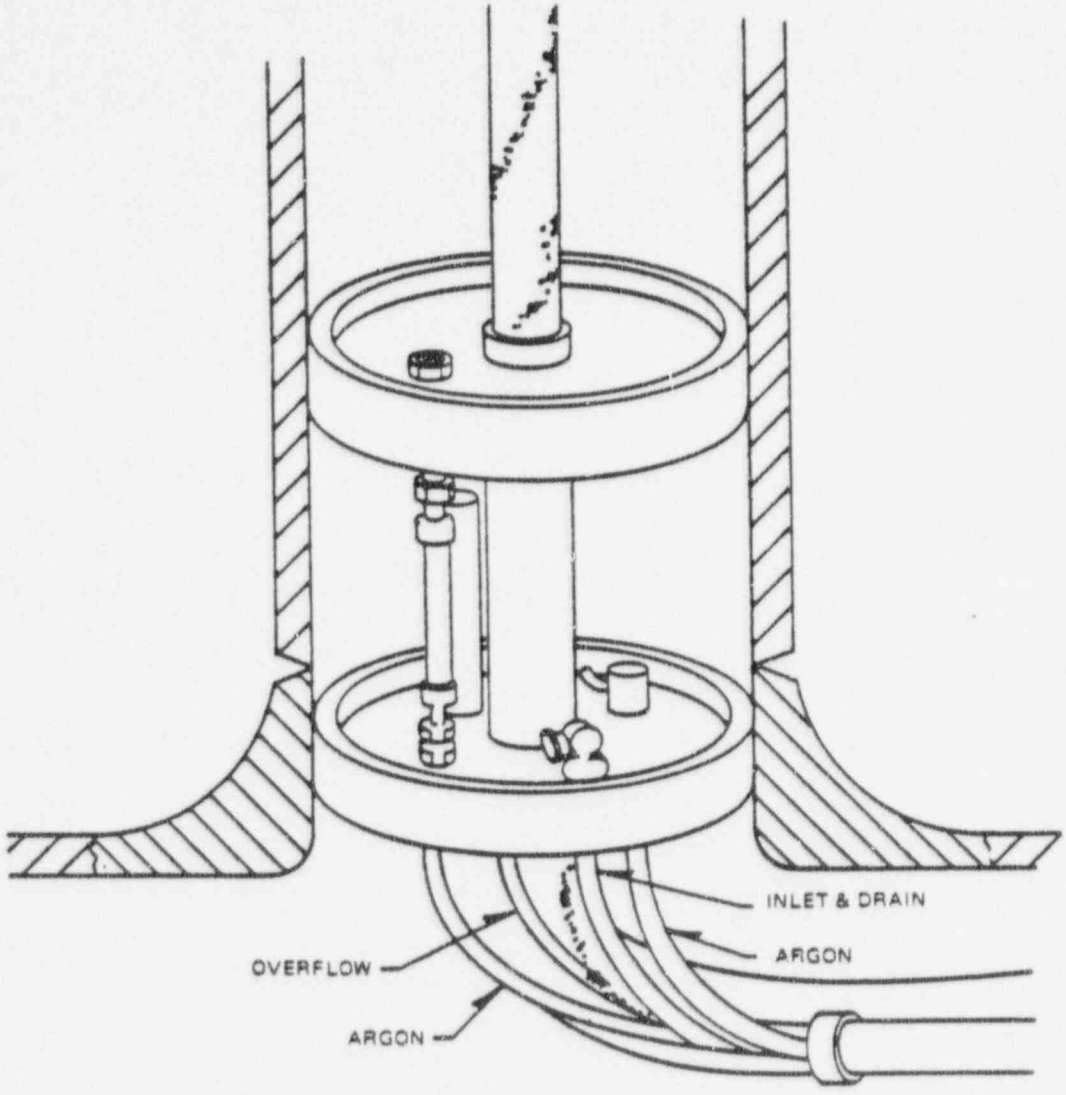

Figure 2-3. Reactor Riser Sweepolet Weld Heat Sink Welding Equipment

2.2.1 Task 1—Screening Measurements

The objective of this task was to perform full-size-pipe and laboratory specimen screening tests of several proposed pipe crack remedies to identify the most promising candidates for statistical verification in the pipe testing phase of the program. The screening tests were performed in high purity, 550°F (288°C) oxygenated water at high stress using severe fabrication, process, and mechanical loading conditions to demonstrate a clear performance improvement of the remedy as compared to the reference Type-304 stainless steel piping specimens.

2.2.2. Task 2—Statistical Pipe Tests and Special Studies

The objective of this task was to verify the reliability of one or more of the candidate pipe remedies through full-size-pipe testing of sufficient scope so as to provide a statistical demonstration of significant margin improvement of the remedy. The testing was performed in 550°F (288°C) high purity oxygenated water at sufficient stress so as to cause the reference Type-304 stainless steel welds to fail. Chemical, electrochemical, and metallurgical accelerants were used to simulate worst case conditions and to increase the speed of data gathering.

2.2.3 Task 3—Electrochemical Measurements

The objectives of this task were to: (1) determine the corrosion potential of Type-304 stainless steel and remedy materials and system oxidation potentials in BWR reactor environments; (2) determine the range of potentials for stress corrosion cracking susceptibility, and immunity in simulated BWR environment; and (3) couple the laboratory and in-reactor measurements to assure the validity of the statistical pipe verification test program (Task 2). In-reactor test data on Type-304 stainless steel during startup, operation, and shutdown conditions were used to set the minimum laboratory system potentials for Type-304 stainless steel and the remedy materials. In addition, a rugged reference electrode was developed for BWR application, which can operate for extended periods of time over the range of temperatures that exist in the BWR environment.

2.2.4 Task 4—Ferrite Studies

The objective of this task was to perform fundamental metallurgical studies to evaluate the role of ferrite on the resistance of duplex stainless steels to intergranular stress corrosion cracking in the BWR environment. The aim of this task was to identify the metallurgical conditions responsible for the increased resistance of duplex stainless steels to intergranular stress corrosion cracking in high purity oxygenated water.

3. TASK 1 — SCREENING MEASUREMENTS

3.1 INTRODUCTION

The data developed in Task 1 are based on a minimal number of test coupons and a maximum number of remedy concepts (screening function).

Essentially the screening information was developed from 4-in. "Schedule 80 pipe" (10.16 cm) weldments tested in low cycle rate, tension in excess of the pipe yield strength at the BWR service temperature and in a BWR simulated environment which added oxygen as an accelerant. The scope of full size pipe screening tests can be outlined broadly as follows:

Part 1 — Early exploratory pipe weld tests (LEFT and CL-4 Loop)

Part 2 — Four weldments (E19A, E19B, E20A and E20B) of 12 welds each fabricated to evaluate the heat sink weld concept.

Part 3 — One weldment (E21-A) of 12 test welds fabricated to evaluate the use of weld additions (corrosion-resistant clad — backlay — extended weld crowns/bevels).

Part 4 — One weldment (E21-B) of 12 test welds fabricated of alternate materials or specially heat treated materials.

The early exploratory pipe weld tests were performed initially by four point bending in an existing environmental corrosion test loop identified as CL-4. Appendix A describes the fixture and conditions of testing. These tests proved that field induced IGSCC could be duplicated in Type-304 stainless steel welds in a full-size pipe test in the laboratory. This technique was further refined and an axial tension test method was developed in a large environmental facility (LEFT). Appendix B describes the test machine and conditions of testing. Early screening tests of pipe crack remedies were conducted in the CL-4 and LEFT loops.

From this single pipe LEFT tensile test capability an entire pipe test laboratory (PTL) facility evolved capable of testing 72 weldments simultaneously. Appendix C describes the PTL facility, test fixture and test conditions. The final six screening test weldments were environmentally tested in the PTL. A drawing of a test stand is shown in Section 4 (Task 2) of this report.

3.2 DESCRIPTION OF PIPE REMEDY CONCEPTS SCREENED

The concepts for solution heat treatment, corrosion-resistant cladding and heat sink welding were described in Section 2.1. Other concepts tested are discussed in the following paragraphs.

3.2.1 Weld Overlay Reinforcement At the Pipe Joint Outside Diameter (Backlay)

The addition of weld reinforcement over the joint area after butt welding (backlay) reduces service stress at the HAZ location where stress corrosion occurs. A sketch of the concept is given in Figure 3-1. A backlay can also provide some residual inside diameter compressive stress if coupled with water cooling on the pipe inner surface during weld deposition and offer some crack arrest capability, if the weld composition produces a duplex (ferrite phase) structure in the backlay. This remedy may present ultrasonic inspection difficulties.

"Backlay" is visualized as a method for providing an added safety margin to pipe joints now in service, and it can be applied wherever access permits.

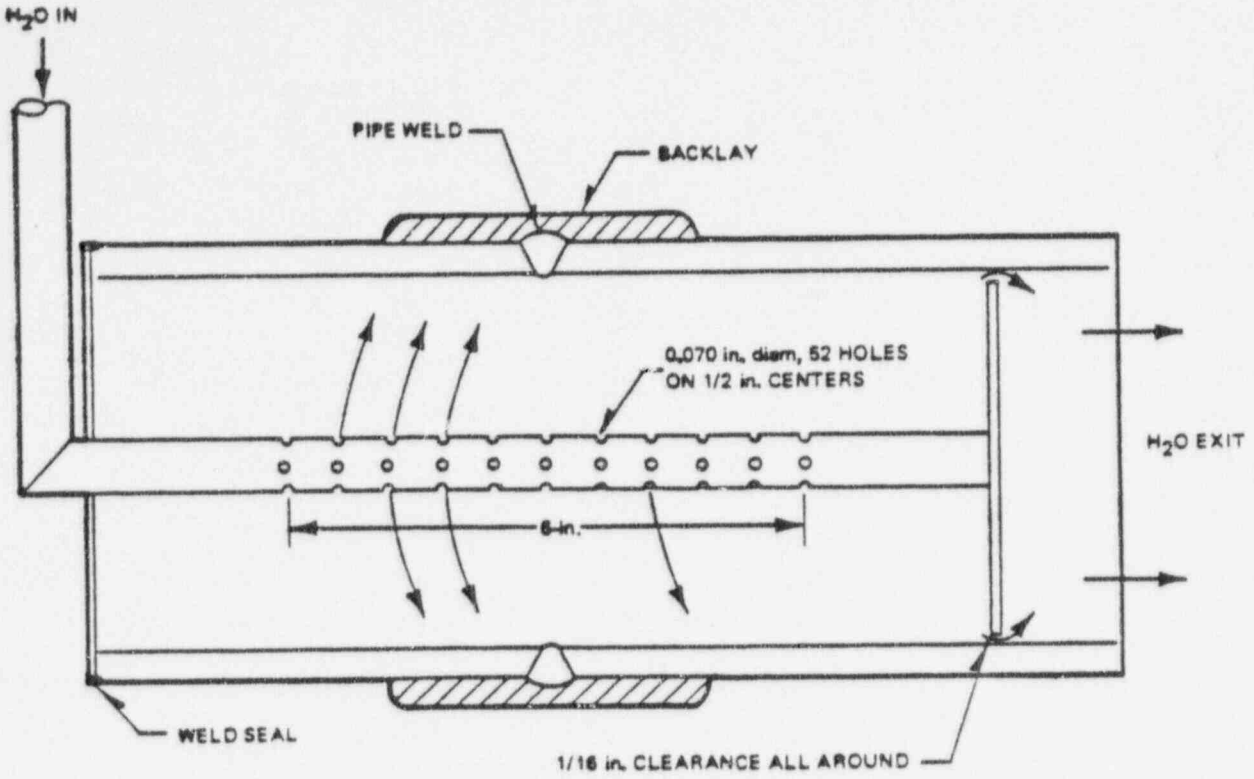

Figure 3-1. Backlay Applied with ID Water Spray Quench

3.2.2 Special I.D. Conditioning Tests

In some cases field failures at Type-304 stainless steel pipe weld HAZs were associated with a disruption and cold working of the surface by rough grinding. Tests were proposed to evaluate techniques of reconditioning ground heat affected zones and other techniques of improving the original surface condition of i.d. heat affected zones.

Among these were polishing previously rough ground surfaces, grit blasting surfaces, fine flapper sanding, and skin fusion of cold worked surfaces.

3.2.3 Extended Weld Bevel to Provide Constraint Above the Weld HAZ

By extending the outside diameter weld crown width over the inside diameter weld HAZ, a reduction in service imposed stress at the "sensitized" zone was envisioned. This constraint by the wider weld crown is due to the higher strength of weld metal compared to pipe base metal. Figure 3-2 illustrates the concept.

3.2.4 Weld Heat Input Controls

Intergranular Stress Corrosion Cracking (IGSCC) initiation has been directly related to precipitation of grain boundary carbides by weld heat. Lower heat input by weld practice control was proposed as a technique to reduce grain boundary carbides and provide added margin against IGSCC initiation.

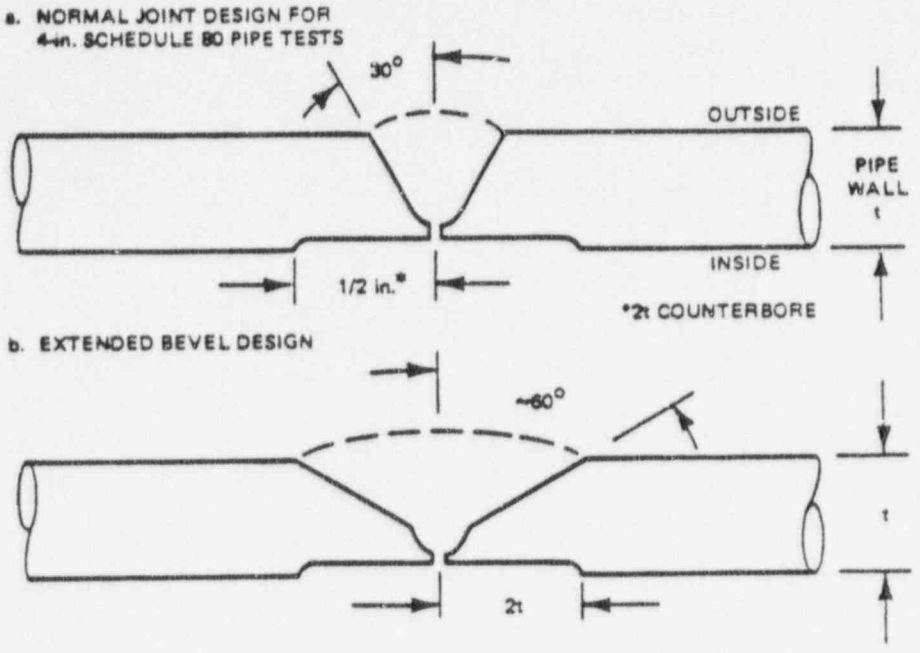

Figure 3-2. Extended Crown Weld Technique

3.2.5 Pre-Weld Solution Heat Treating

Weld heat effects superimposed upon improper mill annealing were considered a possible accelerator of IGSCC. Selected susceptible pipe sections were re-solution annealed by laboratory practices just prior to butt welding of test specimens to evaluate this concept.

3.2.6 Alternate Materials and Chemical Variations

Stress corrosion cracking in BWR service has not been a problem in as-welded austenitic stainless steels containing molybdenum, carbide stabilizers, small amounts of ferrite or reduced carbon content (carbon <0.045%).

Screening tests of these materials in the accelerated pipe test laboratory conditions were proposed in preparation for qualifying them by statistical testing. Selected alloys were:

Type-304 stainless steel — 0.08% carbon maximum

Type-316 stainless steel — 0.08% carbon maximum — (normal carbon)

Type-316L stainless steel — 0.03% carbon maximum

CF-8 stainless steel — 0.08% carbon maximum — (normal carbon), high ferrite

CF-3 A stainless steel — 0.03% carbon maximum — (low carbon), high ferrite

Type-347 stainless steel* — 0.08% carbon maximum — stabilized carbon

Type-304 L stainless steel — 0.03% carbon maximum

* Including 347 stainless steel filler metal.

3.3 EQUIPMENT AND MATERIALS

3.3.1 Materials

Materials used in individual weld joints are described in fabrication documents.

3.3.1.1 Pipe Test Materials

The basic pipe size for all environmental "full-size" screening tests was the four inch schedule 80 (10.16 cm).

The basic pipe material was ASME SA312, Type-304 stainless steel. This material was obtained in the mill annealed condition in several mill heats and from varying manufacturers. The majority of tests were performed on one heat from B&W, Tubular Products Division (Heat M7616) which was found to be particularly susceptible to intergranular stress corrosion cracking**. The reasoning for selecting the most susceptible heat of Type-304 stainless steel to perform screening tests for pipe crack remedies was to evaluate these concepts in a "worst case" condition.

The identification and certified chemical analyses of Heat M7616 and other significant pipe heats used in screening tests are given in Appendix D.

3.3.1.2 Welding Materials

The basic weld filler metal for joining Type-304 stainless steel pipes in screening tests was Type-308 stainless steel in earlier test welds and Type-308L stainless steel in more recent pipe tests. Since in no instance was there a failure in weld metal, the filler metal compositions will not be discussed in detail. The more recent Type-308 and 308L filler metals were procured to 8FN minimum ferrite content, but earlier materials were not procured to a specific ferrite content.

3.3.2 Equipment

The equipment for fabrication and testing is described in the original procedure documents. Typical equipment employed from a basic aspect include welding, weld inspection, pipe testing and metallurgical evaluation equipment.

3.3.2.1 Welding

1. Manual gas tungsten arc welding equipment for the butt weld root pass and second layer.
2. Manual shielded metal arc welding equipment for all additional butt weld layers.
3. Machine gas tungsten arc welding equipment for most heat sink weld joints.
4. Weld positioners.

3.3.2.2 Weld Inspections

1. Ultrasonic test equipment to perform "baseline" and in-service inspections.
2. Liquid dye penetrant methods for weld fabrication control.
3. Acoustic emission in selected tests.

3.3.2.3 Pipe Testing

1. Four point bend test fixture (early exploratory tests). See Appendix A.
2. Large environmental fatigue test (LEFT) facility (early exploratory tests). Appendix B.
3. Hydraulic tensile test modules specifically designed for these pipe tests in conjunction with environmental control loops (CL-4 loop and Pipe Test Laboratory loop). Appendix C.

** ASME SA312, Type-304 stainless steel heats from other venders in this same carbon content range (0.05 to 0.06%) were also found to be susceptible to IGSCC under the same test conditions.

3.3.2.4 Metallurgical:

1. Scanning electron microscope.
2. Optical microscopes.
3. Normal Miscellaneous Metallurgical Laboratory Equipment.

3.4 FABRICATION & WELDING

3.4.1 Summation of Weldments and Test Welds Fabricated in Screening Activities

For the preparation of test pieces, a detailed fabrication procedure was written for each weldment to govern the shop activities including welding. Tables 3-1 and 3-2 list 17 weldments containing a total of 136 test weld joints that were fabricated for screening and investigatory purposes. In these charts, identification is provided for each weld joint.

Table 3-1
SUMMARY OF EARLY EXPLORATORY SCREENING TESTS

Item	Identification of Weldment	No. of Test Welds	Purpose of Test
1	First LEFT (Lab No. 3)	2	• To duplicate IGSCC* in a laboratory test using a 304 pipe heat which cracked in the field.
2	Second LEFT (Lab No. 4)	7	• To test various heats of Type-304 SS • To evaluate post weld solution heat treatment (SHT) • To evaluate corrosion resistant cladding (CRC) at weld end. "Preps"
3	Third LEFT (Lab No. 23)	9	• To evaluate Type-316SS and Type-CF8 • To evaluate inside diameter (i.d.) water cooling or heat sink welding (HSW) • To evaluate Type 316SS (as welded)
4	Fourth LEFT (Lab No. 41)	9	• To evaluate Post Weld Low Temperature Sensitization • To evaluate alternate materials of Types 316 and 316L
5	First 3 point Bend Test (Lab No. 9 & No. 10)	8	• To evaluate i.d. grinding on two heats of Type-304SS in 3 Point Bend testing
6	First 4 point Bend Test (Lab No. 11 & No. 12)	6	• To evaluate weld heat input affects on three heats of Type-304SS in 4 Point Bend testing
7	Second 4 point Bend Test (Lab No. 29 A&B)	8	• To evaluate CF3 and CF8 alloys • To evaluate Post Weld SHT • To evaluate Type-309SS CRC
8	Third 4 point Bend Test (Lab No. 36)	8	• To evaluate Types-312 & 308L CRC
9	56-G	12	• To evaluate pipe i.d. conditioning
10	48C (E19B)	1	• To evaluate counterbore machining effect on IGSCC initiation
11	E19B-8	1	• To evaluate counterbore skin fusion by GTAW

* IGSCC = Intergranular Stress Corrosion in Packing
** SS = Stainless Steel
*** SHT = Solution Heat Treatment
**** CRC = Corrosion Resistant Cladding

Table 3-2
SUMMARY OF FINAL SCREENING TEST WELDMENTS

Item	Identification of Weldment	No. of Test Welds	Purpose of Test
12	E19A	11	Heat Sink and Reference Welds in Type-304SS—Maximum Test Load 1.36 x 550°F (288°C) yield strength of the 304SS pipe
13	E19B	11	Same as E19A except not polished on i.d. after root pass
14	E20A	11	Heat Sink and Reference Welds in Type 304SS—Maximum Test Load 1.10 x 288°C (550°F) yield strength of the 304SS pipe
15	E20B	11	Same as E20A except not polished on i.d. after root pass
16	E21A	12	To evaluate various corrosion resistant cladding techniques
17	E21B	12	To evaluate various alternate materials and heat treat practices

As failures occurred in the course of testing, the failed joint was weld repaired. The entire weldment was reinspected by U.T. techniques and returned for continued testing.

3.4.2 Welding Procedures and Test Pipe Configurations

A control document detailing the fabrication of welds in each weldment is available, but is not included in this final report due to the bulk and also since the procedures were previously presented in quarterly status reports. A brief description will accompany a discussion of results.

3.5 PIPE TEST PROCEDURES

Although test techniques varied in the full-size pipe program in some weld tests, a general practice was developed which was the base condition. Variations from the following described test procedure will be discussed for individual tests when test results are reviewed:

3.5.1 Four Point Bend Test (see Appendix A)

3.5.1.1 Environment Within the Pipe

- High purity water with 8 ppm oxygen
- 288°C (550°F ± 5°)
- Flow rate of 2 to 3 gpm
- 1285 psig

3.5.1.2 Imposed Mechanical Stress Cycle

- Maximum stress in excess of 288°C (550°F) yield strength
- 1 cycle in 8 hours

3.5.2 Prototype Axial Tensile Test (see Appendix B)

3.5.2.1 Environment Within the Pipe

- High purity water with 8 ppm oxygen
- 288°C (550°F) average
- Flow rate of 2 to 3 gpm
- 1235 psig

3.5.2.2 Imposed Mechanical Stress Cycle

- 0.67 cycles/hour
- 110% to 136% of 288°C (550°F) yield strength*

3.5.3 Final Axial Tensile Test Facility (see Appendix C)

3.5.3.1 Environment Within the Pipe

- High purity water with 8 ppm oxygen
- 288°C (548°F) average

3.5.3.2 Imposed Mechanical Stress Cycle

- 0.67 cycles/hour
- 110% to 136% of 288°C (550°F) yield strength*

3.6 SCREENING TEST RESULTS AND DISCUSSION

3.6.1 General

Testing in six screening weldments is still in progress at this writing. The present status of these tests is given in Table 3-3 and in more detail in Appendix E. In evaluating remedy results a breakdown will be made in terms of the principal pipe crack remedy applied to the individual weld joint, rather than by the total weldment involved. The discussion will progress in the sequence of preferred corrective measure to those of lesser preference. In the following discussion it shall be understood the pipe material is ASME SA312 Type-304 stainless steel, commercially produced, unless a different material is specifically called out. The test technique is the full-size pipe test. To establish baseline conditions, reference welds were fabricated and conditions producing IGSCC were evaluated. This baseline was used to determine the margin of improvement produced by various remedy concepts. It was found that in a susceptible Type-304 stainless steel pipe with standard fabrication practices a through wall failure can occur at approximately 100 cycles in a Pipe Test Laboratory pipe test with a stress maximum of 1.36 x 288°C (550°F) yield strength (σ_y). Refer to Appendix E.

Table 3-3
FINAL PIPE SCREENING TEST RESULTS (IGSCC REMEDIES)
Four Inch Schedule of Full Size Pipe Test

Four Inch Schedule 80 Full Size Pipe Test

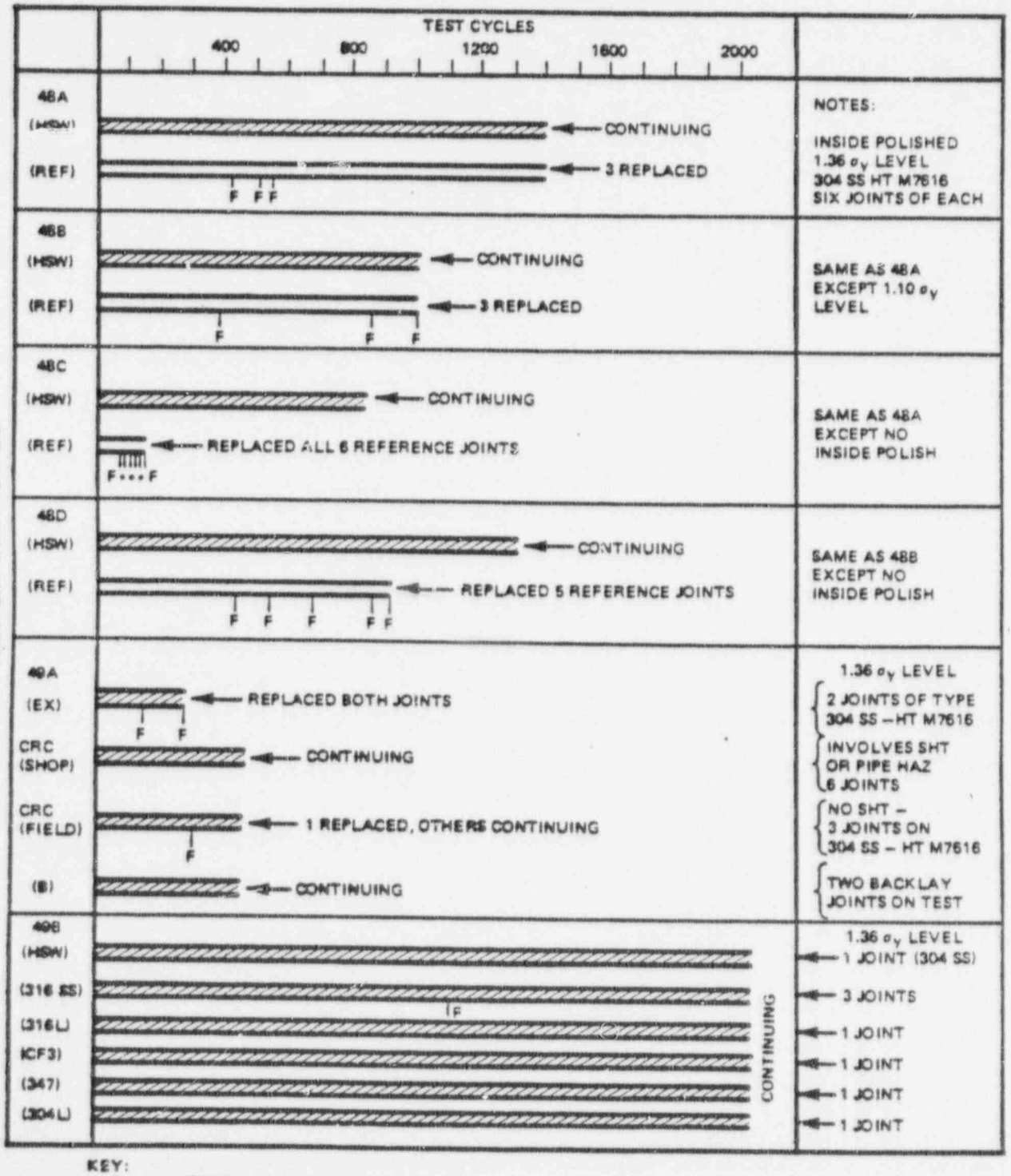

KEY:

F	– THROUGH WALL FAILURE BY IGSCC	B	– BACKLAY
HSW	– HEAT SINK WELD TECHNIQUE	REF	– UNPROTECTED TYPE 304 SS HEAT M7616
CRC	– CORROSION RESISTANT CLAD		
HAZ	– WELD HEAT AFFECTED ZONE	SHT	– SOLUTION HEAT TREATED
EX	– EXTENDED BEVEL		

3.6.2 Post Weld Solution Heat Treatment (SHT) Results

To date no failures have occurred in Type-304 stainless steel girth weld joints solution heat treated after welding (Figure 2-1). This includes pipe heats proven to be highly susceptible to IGSCC without post weld SHT. Early exploratory weld joints using this practice were Joint G, 2nd LEFT test, and Joints A-B, A-C, A-D, A-E, B-B and B-C in the second 4 Point Bend Test. These 4 inch schedule 80 pipe weld joints received the following test life before termination and inspection:

SOLUTION HEAT TREATED WELDS

Material	Test Type	Maximum Test Stress*	Cycles	Hours
	2nd LEFT Axial Tension Test			
Type-304 Stainless Steel	Joint G	1.36σ, & 1.75σ,	891	1384
	2nd 4 Point Bend Test			
Type-304 Stainless Steel	Four heats, six heat affected zones	1.36 σ,	136	2509

* Percent of 288°C (550°F) yield strength in material tested

In view of these results the post weld solution heat treat remedy was recommended as a top candidate for Task 2, the statistical proof test program.

3.6.3 Corrosion-Resistant Cladding (CRC) Results

There are two principal techniques for applying a corrosion-resistant weld deposit at the pipe i.d. adjacent to the butt weld. The two types are shown in Figure 2-2.

The first option (involving SHT) is applicable to shop fabrication. The second option is applicable to field usage where SHT after cladding is impractical. These deposits may be applied either as an overlay or an inlay.

To date, no failures have been encountered in screening tests using the "shop" CRC procedure which includes SHT at the interface of CRC and base pipe. In a screening test using "field" CRC (without the SHT option) a through wall failure occurred at the junction of base pipe and CRC deposit in one test.* These screening CRC joints received the following test life:

Shop CRC: 435 cycles—633 hours without failure in susceptible Type-304 stainless steel pipe

Field CRC: One failure at 337 cycles in susceptible Type-304 stainless steel pipe (Heat M7616).*

Additional "field" CRC weld joints (No SHT) remain on test without failure thus indicating that a significant margin of improvement is obtained for susceptible heats of pipe, but "field" CRC does not provide immunity in these severe test conditions. The CRC involving SHT has to this date provided immunity with the test conditions and test periods described.

As a result of these screening tests on two types of corrosion-resistant clad joints, it was recommended that both concepts be included in Task 2 statistical proof testing. Table 3-4 lists the present status of CRC screening welds. In evaluating these results it should be kept in mind that this is an accelerated test and Type-304 stainless steel, Heat M7616 weld heat affected zones in the absence of a protective measure, started failing by IGSCC at less than 100 test cycles in axial tension type tests.

*Weld E21A, Joint K. It should be noted that this heat (M7616) was sensitized in the mill annealed condition prior to applying the field CRC.

Table 3-4

SCREENING TEST RESULTS — CORROSION RESISTANT CLAD WELDS

Identification Pipe	HAZ*	Cyclic Test Type	Heat Number	CRC Type Description Materials	Design	Initial ¼-in. SHT	Maximum** Test Stress	Test Cycles/Hour	Status
Second LEFT	F1	Tensile	M7616	E312 SS	Overlay	No	1.75	891/1384	No Failure
Second LEFT	F2	Tensile	M7616	E312 SS	Overlay	Yes	1.75	891/1384	No Failure
Second LEFT	H1	Tensile	M7616	E312 SS	Inlay	Yes	1.75	891/1384	No Failure
29A	E2	Bend***	M7616	E309L-Mo	Inlay	Yes	1.36	328/3812	No Failure
29A	F1	Bend***	M7616	E309L-Mo	Inlay	Yes	1.36	328/3812	No Failure
29B	E2	Bend***	F50343	E312 SS	Inlay	Yes	1.36	328/3812	No Failure
29B	F1	Bend***	F50343	E312 SS	Inlay	No	1.36	328/3812	No Failure
36A	C1	Bend	Licensee	308L	Inlay	Yes	1.36	292/2683	No Failure
36A	C2	Bend	Licensee	308L	Inlay	Yes	1.36	292/2683	No Failure
36A	D1	Bend	Licensee	308L	Inlay	Yes	1.36	292/2683	No Failure
36A	D2	Bend	Licensee	308L	Inlay	Yes	1.36	292/2683	No Failure
36B	C1	Bend	M7616	312/308L	Inlay	Yes	1.36	292/2683	No Failure
36B	C2	Bend	M7616	312/308L	Inlay	Yes	1.36	292/2683	No Failure
36B	D1	Bend	M7616	308L	Inlay	Yes	1.36	292/2683	No Failure
36B	D2	Bend	M7616	308L	Inlay	Yes	1.36	292/2683	No Failure
E21A(49A)	A2	Tensile	M7616	E308L	Overlay	Yes	1.36	435/633	No Failure
E21A(49A)	B1	Tensile	M7616	E308L	Inlay	Yes	1.36	435/633	No Failure
E21A(49A)	B2	Tensile	M7616	E308L	Short Inlay	No	1.36	435/633	No Failure
E21A(49A)	E1	Tensile	Licensee	E308L	Overlay	Yes	1.36	435/633	No Failure
E21A(49A)	E2	Tensile	Licensee	E308L	Overlay	Yes	1.36	435/633	No Failure
E21A(49A)	F1	Tensile	Licensee	E308L	Overlay	Yes	1.36	435/633	No Failure
E21A(49A)	F2	Tensile	Licensee	E308L	Overlay	Yes	1.36	435/633	No Failure
E21A(49A)	I1	Tensile	M7616	E308L	Short Inlay	No	1.36	435/633	No Failure
E21A(49A)	I2	Tensile	M7616	E308L	Inlay	No	1.36	435/633	No Failure
E21A(49A)	J1	Tensile	M7616	E309L	Inlay	Yes	1.36	435/633	No Failure
E21A(49A)	J2	Tensile	M7616	E309L	Inlay	Yes	1.36	435/633	No Failure
E21A(49A)	K1	Tensile	M7616	E309L	Inlay	No	1.36	337/460	Failed
E21A(49A)	K2	Tensile	M7616	E309L	Inaly	No	1.36	435/633	No Failure
E21A(49A)	L1	TEnsile	M7616	E038L	Inlay	Yes	1.36	435/633	No Failure

* Heat affected zone

** 550°F (288°C) yield strength of base pipe multiplied by factor given.

*** Four cycles in eight hours

3.6.4 Heat Sink Welding (HSW) Results

3.6.4.1 Initial Pipe Tests (Weldment 23 — third LEFT test)

The initial exploratory heat sink weld joints caused some confusion due to post weld root grinding in two quadrants of the internal circumference. The grinding produced a "skin" tensile stress in which IGSCC initiated (Figure 3-3). Later heat sink welds without post weld root grinding have shown a significant improvement in IGSCC resistance. Table 3-5 shows that six of eight heat affected zones in heat sink welds ground after welding cracked. However, only 1 of 16 HAZs in heat sink welds not ground after welding displayed a crack, and the crack appeared to initiate in an adjacent ground area (quadrant) and was thus suspect. The details of this initial heat sink pipe test are discussed in Appendix F.

90014082

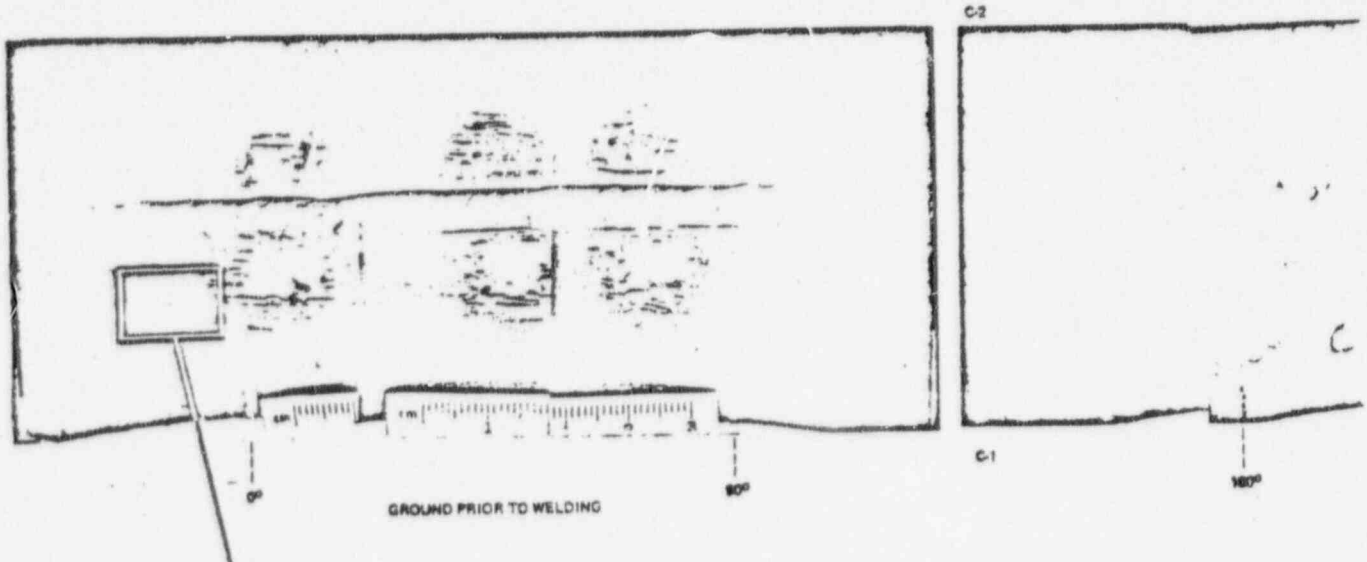

GROUND PRIOR TO WELDING

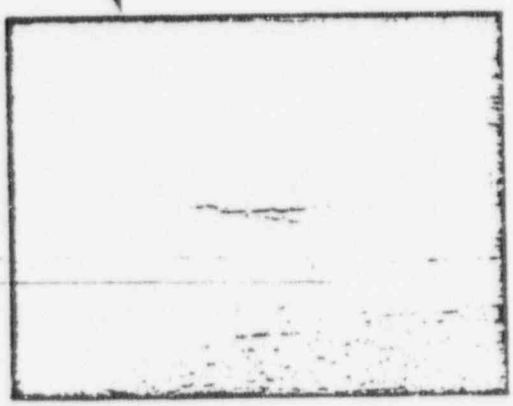

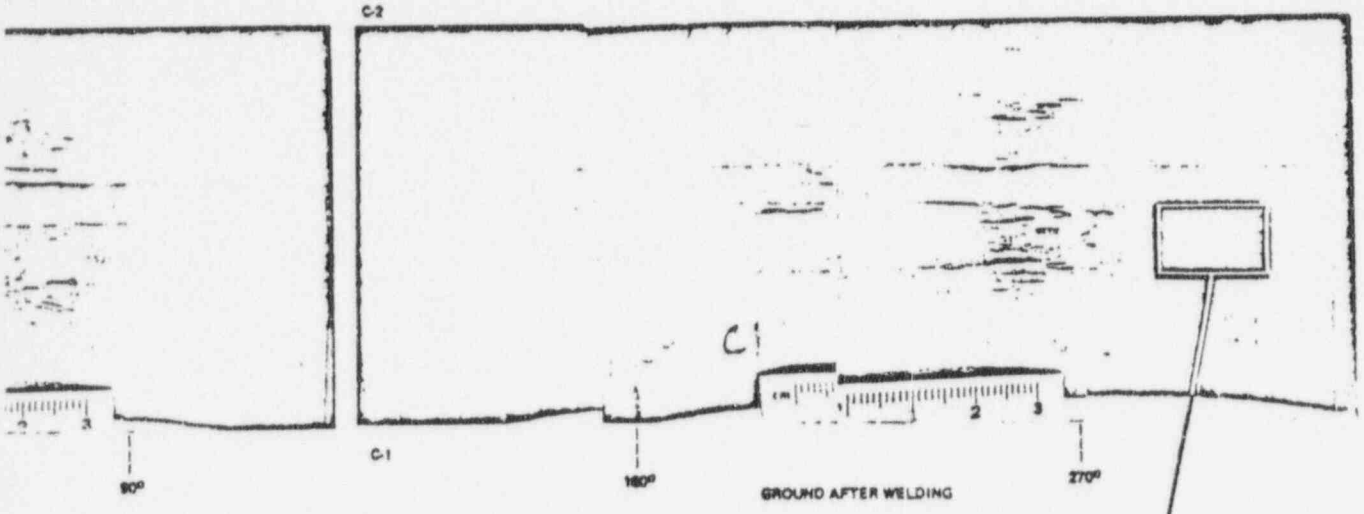

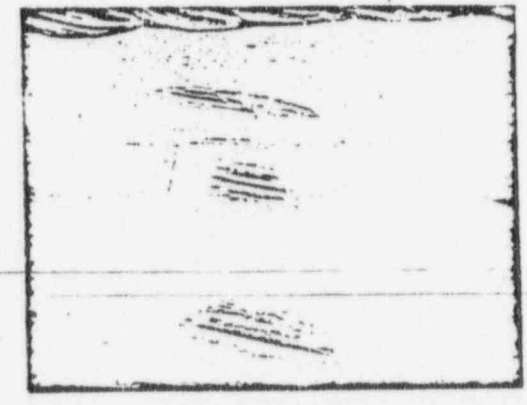

Figure 3-3. Weld C Inside Pipe Showing Cracks on C1 Side in Machined Regions, in Large Ground Areas, and in Localized Ground Spots

Table 3-5
EFFECT OF POST WELD GRINDING ON HEAT SINK WELD RESISTANCE TO IGSCC

Material or Protection Method	No. of Heats Evaluated	No. of Heats Failed	No. of Heat Affected Zones Failed/Tested***	Remarks
Unprotected welds Type-304 Stainless Steel	1	1	8/8	Post-weld grinding at weld HAZ*
Heat sink Welded Type-304 Stainless Steel	1	1	6/8	Post-weld grinding at weld HAZ*
Unprotected Welds Type-304 Stainless Steel	1	1	7/8	Pre-weld machining at weld HAZ
Heat Sink Welded Type-304 Stainless Steel	1	1	1/8	Pre-weld machining at weld HAZ**
Unprotected Welds Type-304 Stainless Steel	1	1	4/8	Pre-weld grinding at weld HAZ
Heat Sink Welded Type-304 Stainless Steel	1	0	0/8	Pre-weld grinding at weld HAZ

* Post weld grinding is known to introduce large tensile residual stresses thus neutralizing the beneficial residual stress effects of heat sink welding.
** The single heat sink failure noted may have initiated in an adjacent ground quadrant.
*** Tested for 183 hours (122 cycles) @ 1.36 × 289°C (550°F) yield strength.

3.6.4.2 Screening Heat Sink Weld Pipe Tests (weldments E19A, E19B, E20A and 520B)

After initial testing demonstrated the highly detrimental effect of post-weld grinding (disruption of residual compressive stress at the weld joint root) 24 heat sink welds were fabricated and matched against 24 reference welds which were not heat sink welded. The make-up of these test weldments is shown in Figure 3-4. Note that at each stress level one weldment was polished on the inside surface after the root pass. The other welds were machined rather than ground. Figures 3-5, 3-6 and 3-7 compare the polished and machined surfaces with a typical ground surface. Note that reference welds in the polished condition failed after longer test times than the machined welds. The 24 welds are sufficient in number for statistical data evaluation in addition to acting as a screening test. Data accumulation has been slowed by the early and frequent failure of the matching reference welds. In the same tests, no original heat sink welds have displayed IGSCC.

The details of screening heat sink weld pipe testing are discussed in Appendices F and G. In brief, the original HSW joints are continuing on test at two stress levels (1.10 x 550°F yield strength of the Type-304 stainless steel pipe and 1.36 x 550°F yield strength of the pipe) without failure.

Those at the higher stress level now have accumulated test periods ranging to 1397 cycles or 2029 hours. Those at the lower stress level now have accumulated test periods ranging to 1100 cycles or 1565 hours. For comparison, eight of twelve matching reference welds at the 1.36 stress level failed by through wall cracking starting at 68 test cycles, and the remaining reference welds show extensive crack indications in ultrasonic test (UT) inspections. The original heat sink welds do not show any significant UT indications.

Statistical calculations for Heat Sink Weldment E19B are included in Task 2 of this report.

A single heat sink screening weld in Weldment E21-B has 2013 test cycles (2869 test hours) in the PTL without failure which exceeds all other HSW joints on test. It has been on test at the high stress level (1.36) during this time. The improvement margin in this single test is high, but it is not statistically significant since it is a single weld. It does serve as a screening test to encourage continued evaluation of this pipe crack remedy.

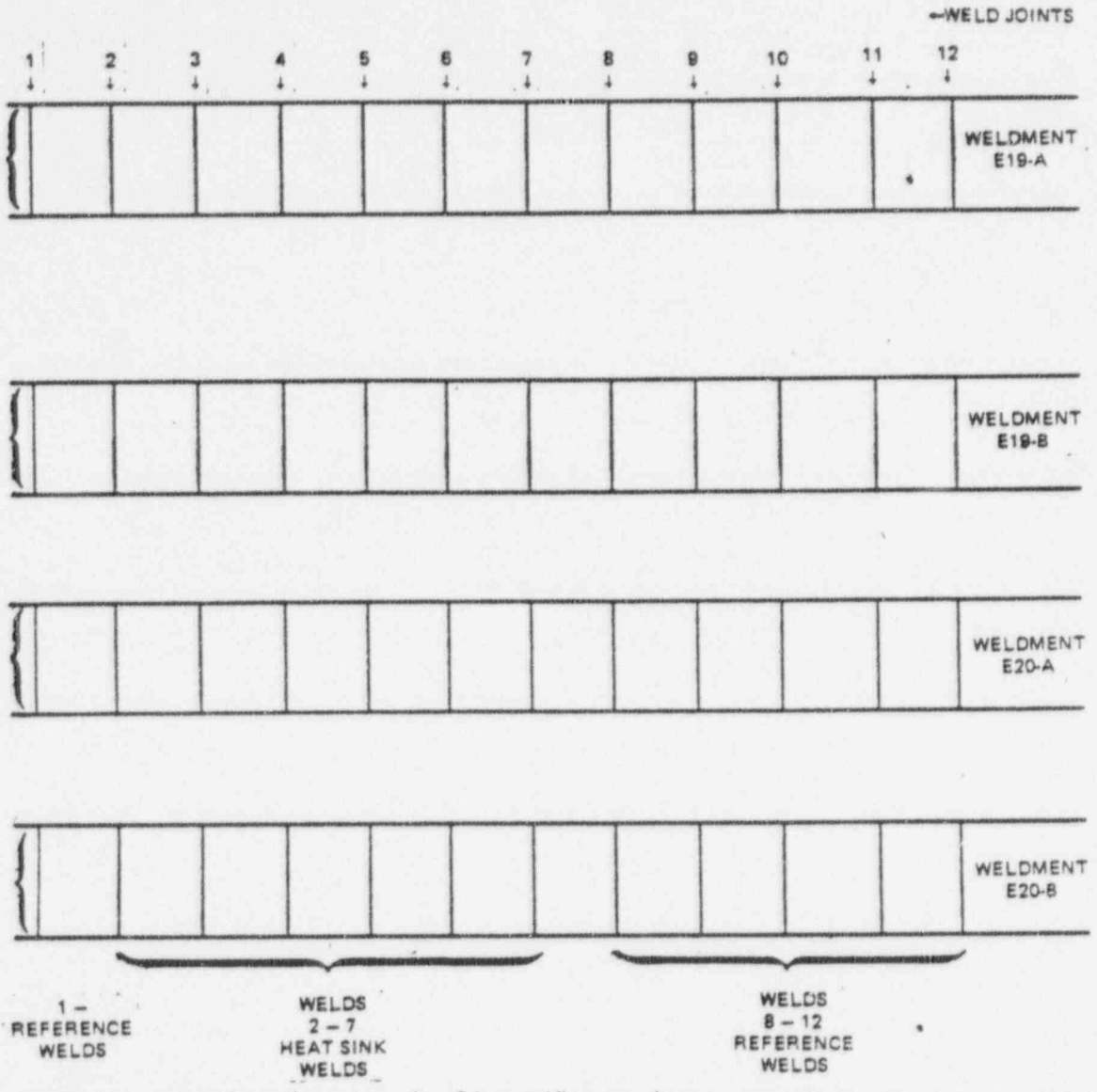

NOTES: WELDMENTS E19-A AND E20A WERE GROUND AND POLISHED ON THE INSIDE SURFACE AFTER ROOT PASS WELDING
WELDMENTS E19-B AND E20B WERE NOT GROUND AND POLISHED AFTER ROOT PASS WELDING (SEE FIGURES 3-5, 3-6, 3-7)
E19 WELDMENTS: MAXIMUM TEST LOAD STRESS – 1.36 X 288°C YIELD
E20 WELDMENTS: MAXIMUM TEST LOAD STRESS – 1.10 X 288°C YIELD

Figure 3-4. Bechtel Fabricated Heat Sink Weldments (Fully Automatic-2G Position — Type-304 Stainless Steel Pipe)

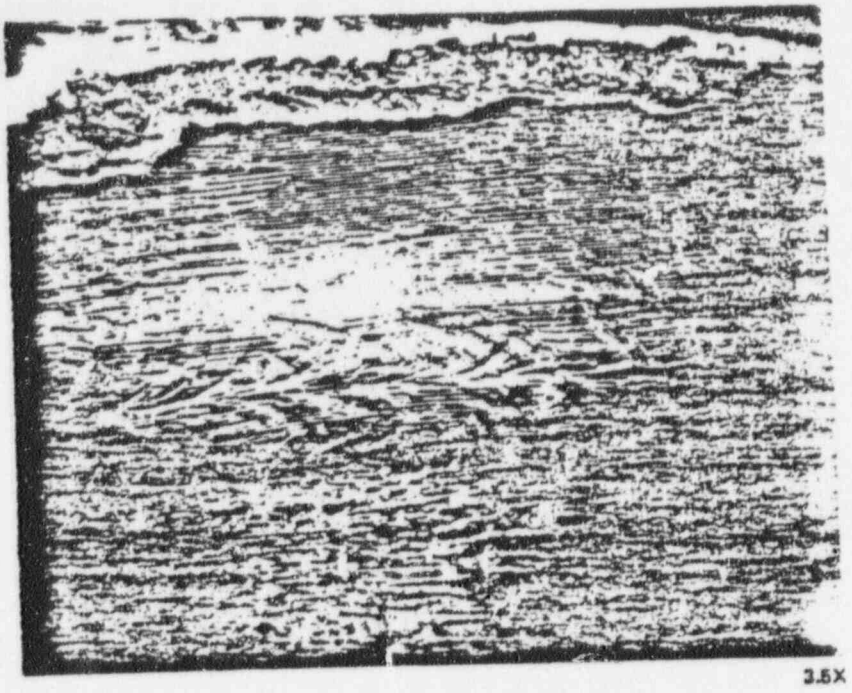

Figure 3-5. Weldment E19A Showing Gravel and Polished Inside Surface 65 RMS

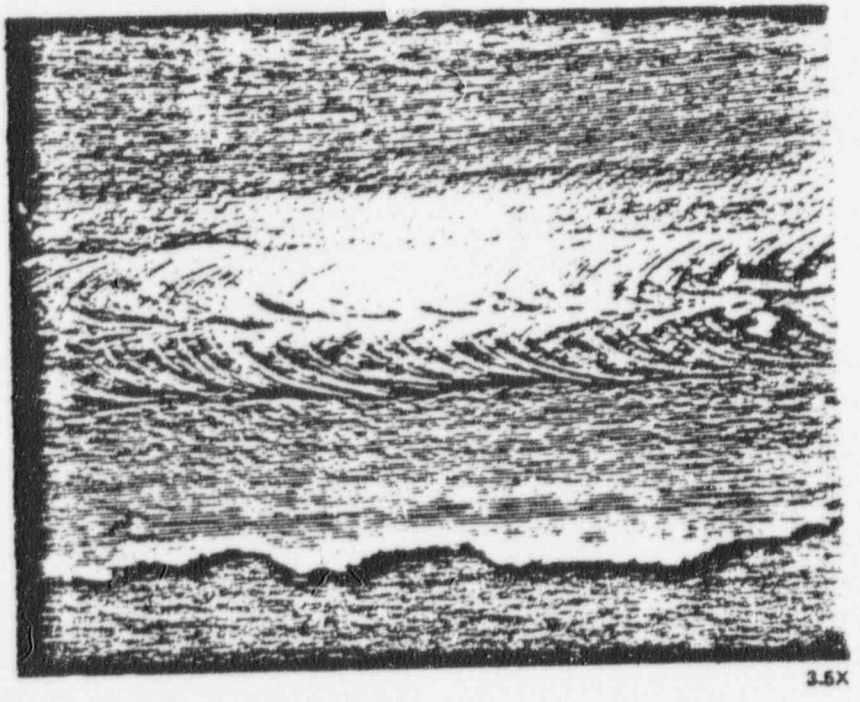

Figure 3-6. Weldment E19B Showing As Machined Surface 125 RMS

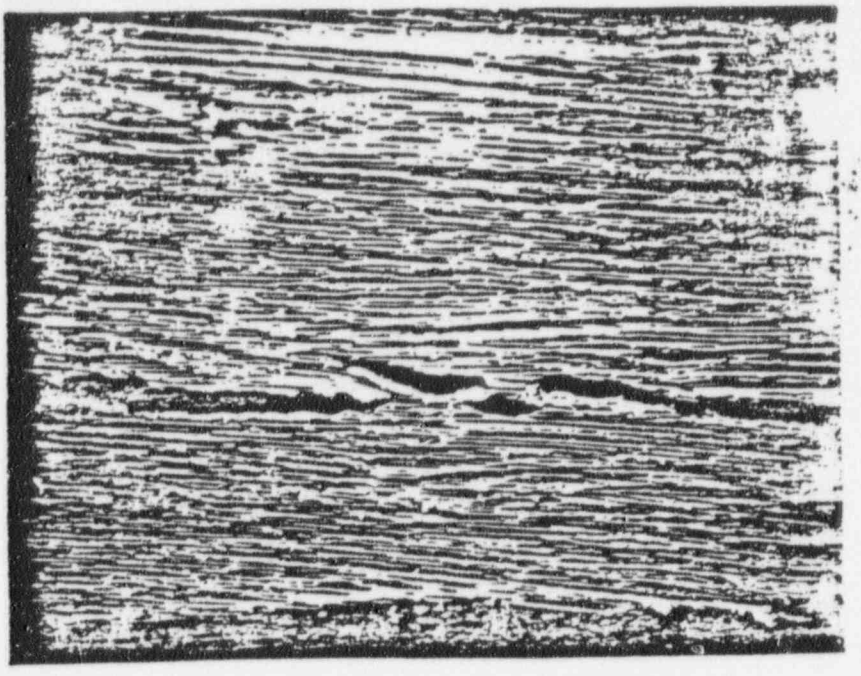

Figure 3-7. Weldment E18 — Heavily Ground Heat Affected Zone

3.6.4.3 Repair of Failed Reference Welds by Manual Heat Sink Welds

The failed reference welds were repaired to continue testing the six original heat sink welds in each weldment after reference weld failures. Repairs were principally by manual heat sink welding and, as needed, splice pieces of pipe were added to restore the test weldment to its original length for fixturing purposes. The repair HSW technique differs from the original heat sink welds continuing on test in several respects; principally in welding process i.d. cooling application and weld position. Repair heat sink welds have failed in relatively short (125–500 cycles) periods of testing in three of approximately 20 instances. The failures are recent and have not been evaluated at this date. Preliminary observations indicate failure at repair heat sink weld heat affected zones may have been caused by: (1) the proximity of two welds is often much less than the nominal 4 inches between original welds, (2) reduced wall thickness, and/or (3) yield strengths in replacement pieces below that of the original Type-304 stainless steel, Heat M7616.

It is possible that stresses well above the 1.36 x 288°C (550°F) yield strength could have occurred in replaced welds due to splice material yield strength differences. Thus, the beneficial compressive residual stresses from the HSW process would be counteracted. It is also possible that prior testing thinned the pipe wall at replaced welds, also resulting in higher stress at the heat affected zones. Shortened test life may have occurred due to repair welds placed with minimal spacing between them. In one repair HSW failure, only approximately 1-1/2 inches existed between welds. Originally, a four inch (1 x pipe diameter) spacing was required to minimize stress interaction.

All of the original heat sink welds made with 4 inch spacing except one were made by automatic welding in the 2 G position, with the heat sink applied after the root weld. The one exception is Weld H, in Screening Weldment E21B. This manual HSW* now has 2013 test cycles (2869 hours) without failure, which exceeds all other heat sink welds on test. The base pipe was ASME SA312, Type-304 stainless steel (Heat M7616) previously shown to fail in approximately 100 test cycles under these test conditions when it was not protected. The failed repair HSWs were all in Type 304 stainless steel pipe (Heat M7616). The heat sink for these repair welds was applied in the 1G weld position after the second weld layer (Manual HSW failures: E16-C/D (600 Cycles) E19B-11A, (293 Cycles) and E21A-G1 (126 Cycles). The repair HSW failures are summarized in Table 3-6.

Table 3-6
ORIGINAL VERSUS REPAIR HEAT SINK WELD TEST RESULTS

No. of Welds	Weld Identification	Stress Level	HSW Position	HSW Process (Water Cool)	Base Material (Type 304SS)	Cycles to Failure
	ORIGINAL WELDS					
6	E19A (Welds 2 to 7)	1.36	2G	Automatic GTA (at 2nd layer)	Heat M7616	No failures at 1397 cycles
6	E20A (Welds 2 to 7)	1.10	2G	Automatic GTA (at 2nd layer)	Heat M7616	No failures at 1100 cycles
6	E19B (Welds 2 to 7)	1.36	2G	Automatic GTA (at 2nd layer)	Heat M7616	No failures at 863 cycles
6	E20B (Welds 2 to 7)	1.10	2G	Automatic GTA (at 2nd layer)	Heat M7616	No failures at 1300 cycles
1	E21B (Weld G)	1.36	Vertical (3 o'clock)	Manual SMA (at 2nd layer)	Heat M7616 to Heat M0063	No failure at 2113 cycles
	REPAIR WELDS					
1	E16 (Welds C/D)	1.36	1G repair	Manual SMA (at 3rd layer)	Heat M7616	Failed at 600 cycles
1	E19B (Weld 11A)	1.36	1G repair	Manual SMA (at 3rd layer)	Heat M7616	Failed at 293 cycles
1	E21A (Weld G1)	1.36	1G repair	Manual SMA (at 3rd layer)	Heat M7616 (prior Lab. SHT)	Failed at 126 cycles

* Flowing water HSW after first pass and welding position was vertical-up at three o'clock on the horizontal pipe.

3.6.5 Weld Overlay Reinforcement Results (termed "Backlay")

A sketch of this concept is shown in Figure 3-1 and a description of fabrication practices for "backlay" weld deposition is given in Appendix H. The "backlay" technique's benefit is due to reduced stress in the HAZ which results from the increased cross-sectional area. In addition, a more favorable residual stress distribution may result on the inside surface due to the additional weld buildup and i.d. cooling during the backlay.

Two standard girth weld joints protected by a "backlay" weld build-up on the weld crown area were included in screening weldment E21-A (joints C and H) and have been on test 435 cycles/633 hours without failure. Monitoring by conventional ultrasonic inspection is not practical on backlay welds unless the deposit is machined or ground smooth. No in-test results are available. Testing is continuing on these joints to develop a larger margin of improvement over reference Type-304 stainless steel welds. In both of these original backlay welds the base pipe was the susceptible heat of Type-304 stainless steel used in reference welds (Heat M7616). The material was, however, solution heat treated prior to welding.

Two more "backlay" welds (E21A-D and E19A-11) were made to replace failed reference welds. At this date these additional "backlay" welds do not have sufficient test exposure on-test time to supply significant information although one weld has exceeded the life expectancy of unprotected pipe.

Results to date indicate the backlay concept has provided additional protection to Type-304 stainless steel weld joints which would otherwise be susceptible to IGSCC. The existing data is limited. Table 3-7 summarizes the information available at this date.

Table 3-7
FULL SIZE PIPE TEST RESULTS ON "BACKLAYED" WELDS

Weld Joint Identification	Fabrication Type	Maximum Test Stress	Cycles on Test	Hours on Test	Base Pipe Material (Type 304SS)
21A-C	Longitudinal Passes	1.36	396*	546	Heat M7616
21A-H	Longitudinal Passes	1.36	396*	546	Heat M7616
21A-D	Circumferential Passes	1.36*	219	327	Heat M7616/Japan 304
19A-11	Circumferential Passes	1.36*	29	43	Heat M7616

Notes:
1. Welds C and H were original pipe welds made by GE in the Schenectedy R & D Laboratory (see Appendix H).
2. Welds D and 11 were replacement joints at failed reference welds, and were fabricated by the GE welding laboratory in San Jose.
* The actual Backlay test stress was approximately 0.75 σ_Y 1.36 x 550°F (288°C) yield stress calculation is based upon the original wall thickness prior to backlay.

3.6.6 Inner Pipe Surface Conditioning Results

In early pipe screening tests the strong influence of grinding at inside surfaces (weld heat affected zones) on acceleration of IGSCC initiation was evident. This is shown in summary in Table 3-8.

Examinations of service failures in Type-304 stainless steel piping also identified grinding with the early onset of IGSCC. Grinding at accessible pipe joint weld root surfaces has been a common shop and field fabrication practice to improve the weld root contour for inspection purposes. For this reason numerous Type-304 stainless steel ground weld joints are in existence in various stages of nuclear plant construction and operation.

Remedial measures were examined for those pipe joints fabricated in which grinding was performed at the inner surface weld heat affected zones. The principal investigative measures were directed toward the improvement of previously ground surfaces. An entire weldment of 12 test joints was fabricated with varying surface treatments to evaluate their effects on IGSCC. The details of this test are described in Appendix I.

In this study reconditioning ground weld HAZ surfaces by post weld mechanical polishing did not prevent IGSCC. In comparison, the areas "machined before welding" were essentially free of cracking. In this time period however, the specimens polished after welding and grinding were markedly less attacked than those only ground after welding in the same test conditions and time.

Another test compared machined counterbore surfaces with original "mill" surfaces. The original mill surfaces did not crack in the same circumstances which drastically cracked machined surfaces. Additionally, the machined surface cracking appeared to be arrested by adjacent thinner wall mill annealed surfaces.

Table 3-8
SUMMATION OF EARLY SCREENING TEST RESULTS ON I.D. GRINDING

Test Identification	Premachined Counterbore Cracked/Tested	Condition of HAZ Surface Ground Before Butt Weld Cracked/Tested	Ground After Butt Weld Cracked/Tested
1. 2nd LEFT (axial tension)	4/14	3/7	4/7
2. 3rd LEFT (axial tension)	15/18*	5/8	8/8
3. 3 Point Bend	0/4	---	2/4
4. 1st Four Point Bend	0/3	1/1	4/6
5. 3rd Four Point Bend	1/2	---	2/2
Total	20/41*	9/16	20/27
Percent HAZ's cracked	(49%)*	(56%)	(74%)

1. Full size pipe test data only.
2. Test stress at 1.36 x 288°C (550°F) yield strength.
3. Weld heat affected zone (HAZ) data on the inside diameter.
4. No pipe crack remedy applied.
*The 3rd LEFT test was quadrant ground. Therefore, this value may be in error because it was difficult to tell if cracks initiated in adjacent ground quadrant.

Oxy-acetylene heating of ground surfaces was tested but was not successful, as metallography and electro-potentiokinetic-reactivation (EPR) tests for sensitization indicated increased sensitivity, which was confirmed by light microscopy inspections.

A skin fusion conditioning by the gas tungsten arc process showed considerable promise by EPR testing and light microscopy. In view of these encouraging results a pipe test reference joint has been repaired in pipe weldment E19B (Weld 8A) using this method, and is now on test in the PTL along with the other pipe crack remedies. It has not shown any signs of failure after 736 cycles and 1104 hours at a maximum stress of 1.36 x 288°C (550°F) yield strength. This is in comparison to reference welds of the same pipe material failing within 100 cycles.

Tests have also been performed to evaluate preweld grinding vs post weld grinding. Preweld grinding appears to be slightly less detrimental than post weld ground surfaces in time to failure by IGSCC (Table 3-8).

To date in the full-size pipe test no mechanical reconditioning technique has prevented IGSCC from occurring in previously ground surfaces of susceptible Type-304 stainless steel, although smoother surfaces prolong time to failure. The "skin" fusion method by GTAW has provided a significant beneficial reconditioning effect on previously ground surfaces. As a result of this screening test, an opportunity to significantly improve existing welds may be possible. Further testing would be required to verify this effect statistically.

3.6.7 Weld Heat Input Control Results

Early screening tests compared time to cracking in susceptible heats of Type-304 stainless steel which were welded with relatively high heat input (50K to 60K joules/inch, with those welded using low heat input practices (25K to 30K joules/inch). It was found that in the higher weld heat input joints, IGSCC initiation occurred in less test time than in the lower heat input welds. Table 3-9 shows these results in terms of the fraction of quadrants cracked for high and low heat input welds. Note that heat to heat variation is more significant than the effect of post weld grinding.

Table 3-9
LEFT TEST RESULTS
1.36 × Sy

Quadrants Cracked/Number Tested

Heat	High Heat Input		Low Heat Input	
	Post Weld Ground	Not Post Weld Ground	Post Weld Ground	Not Post Weld Ground
M7616	9/9	—	9/11	3/8
M7772	0/3	0/1	0/7	0/5
M7616 HSW	4/4	1/4	3/4	0/4
Total	13/16	1/5	12/22	3/17

HSW = Heat Sink Welding — early screening welds not made by Bechtel Corp.

The conclusion reached is weld heat input control within practical ranges will not prevent IGSCC from occurring in susceptible Type-304 stainless steel material, although it is an improved practice.

It was not a recommended remedy technique for Task 2 statistical tests.

3.6.8 Preweld Reannealing Results

In the most susceptible heat of Type-304 stainless steel pipe (Heat M7616) the degree of sensitization tests indicated the original mill anneal was inadequate. To test whether this material would have behaved in an acceptable manner if it had been properly heat treated in the mill, pipe sections were re-solution heat treated in our laboratory by careful practices, just prior to girth welding.

Weld joints of this type placed in the pipe test (Weldment E21-B) also failed by IGSCC within an unacceptable time span. Appendix E contains these results.

3.6.9 Extended Weld Bevel Results

It was thought that by extending the width of weld crown by means of a wider angle weld end preparation, as shown in Figure 3-2, the added constraint would provide added resistance to IGSCC at the underlying inside diameter heat affected zone.

The improvement detected in screening Weldments E21A and E21B for extended crown welds was slight. The joints failed by IGSCC in the heat affected zones.

3.3.10 Variations in Mill Practices and Heat to Heat Variations in Type-304 Stainless Steel

Initial testing was mainly performed on three mill heats of 4 inch schedule 80 ASME SA312, Type-304 stainless steel seamless pipe. Chemically they differed in percent carbon within the allowed ASME specification range. Heat 454970 was relatively low at 0.042% C. Heat M7616 was relatively high at 0.06% C. Heat M0063 at 0.05%C was the third seamless pipe heat tested. A fourth heat fabricated by rolled and welded practice was included in early tests with inconclusive comparison results.

The lower carbon Heat 454970 has not failed in screening tests, whereas Heat M7616 quickly failed. Heat M0063 of intermediate percent carbon failed only after prolonged time on test. These results were indicative of the range of IGSCC resistance possible within the chemistry limits of ASME specifications. It was recommended that three heats of widely varying carbon content be evaluated in statistical testing to obtain Type-304 stainless steel reference data.

3.6.11 Alternate Material Screening Tests

Austenitic stainless steels other than Type-304 stainless steel were included in screening tests to a limited extent. Type-316 stainless steel was tested in three mill heats (Weldment E21B), and it ultimately failed in prolonged testing. However, it showed a large margin of improvement in resisting IGSCC compared to the susceptible heat of Type-304 stainless steel. In another test, one CF8 cast pipe (Heat 98695) failed by IGSCC but only after the test maximum stress was raised from 136% to 175% of the 288°C (550°F) yield strength of Type-304 stainless steel Heat M7616.

At this date, Type-CF3, Type-316L, Type-304L and Type-347 stainless steel pipes continue on test in screening weldments without failures. Each of these were recommended for statistical evaluation. EPRI PROGRAM RP968 is evaluating alternate alloys on a statistical basis.

In all the screening tests on full-size pipes the girth weld filler metal has not developed any cracks due to stress corrosion. Initially the root welds were made with Type-ER308 metal filler ordered from manufacturers to 5% minimum ferrite. In later screening tests the filler metal was Type-ER 308L, ordered to a minimum ferrite number of 8FN.

To extend the screening function, in Weldment E21B, weld filler materials of ER 316 and ER 347 were included. No cracking has been detected in these welds after 2013 test cycles.

3.6.12 Conclusions

The screening tests served their purpose very effectively and directed proof test activities accurately to those practical crack remedy concepts and fabrication techniques which provide the highest margin of safety against future IGSCC. They also provided an accurate interim basis for guiding prevention activities in the relatively prolonged period when statistical data were being developed.

3.7 SMALL SPECIMEN TESTS

Small specimen tests were performed to compliment the full size pipe screening tests. The screening pipes tested a large number of concepts with few samples of each. The use of small specimens provided an opportunity to increase the number of samples tested for some of the promising candidates.

Three groups of small specimens were tested for stress corrosion resistance in constant load and/or constant extension rate tests. These specimen groups are discussed under the following headings:

- Bechtel Heat Sink Welding Study
- Pipe Remedy Studies
  (includes test of three reference Type-304 stainless steel heats as well as CRC welds and additional HSWs)
- Additional Pipe Remedy Studies
  (includes tests of reference Type-304 stainless steel and Type-CF-8 castings).

3.7.1 Bechtel Heat Sink Welding Study

3.7.1.1 Introduction

A study was completed to evaluate the degree of sensitization and stress corrosion cracking susceptibility in large diameter pipe weldments produced for the laboratory sample heat sink welding study. Test weldments were prepared from a 25.4-cm (10 in.) diameter schedule 80 Type-304 stainless steel pipe having the chemical composition given in Table 3-9. It was intended that both sides of each weldment be fabricated from Heat A5351; however, one side of test weld TW-4 (discussed subsequently) was inadvertently fabricated from a different heat of material (Heat 24971W). This latter heat contained a higher carbon content than Heat A5351 (0.084 w/o compared to 0.050), and was slightly sensitized in the as-received condition. The high heat input weldments are identified as follows:

1. TW-4, reference manual weld
2. TW-13, reference automatic weld
3. TW-15, manual weld, water spray inside surface cooled.

3.7.1.2 Experimental Procedure

Semi-curvalinear, uniaxial tensile samples were fabricated from each weldment for intergranular stress corrosion cracking testing. The samples contained the weld joint in the center of each gage section, and were taken such that the pipe inside surface was maintained as one side of the sample. The samples were tested under constant load in 550°F (288°C) high-purity water with 8 ppm dissolved oxygen. The applied stresses were nominally 60% of the ultimate tensile strength at 550°F (288°C) for each weldment (see Tables 3-10 and 3-11). The higher applied stress percentage for samples from TW-4 is attributed to the lower strength of the second heat of material (Heat 24971W) used to prepare this weldment.

The weld heat affected zones were evaluated for degree of sensitization using the Electrochemical Potentiokinetic Reactivation (EPR) test. A planar sample from the pipe inside surface was mounted and polished and then EPR tested in 0.5*M* H_2SO_4 + 0.01*M* KSCN at 86°F (30°C) and 6V/h reactivation rate.

3.7.1.3 Results and Discussion

The results of these stress corrosion tests are given in Table 3-11. All three weldments were susceptible to intergranular stress-corrosion cracking, but the TW-4 condition was the most susceptible, followed by TW-15 and then TW-13.

Table 3-10
TENSILE PROPERTIES OF BECHTEL WELDED SAMPLES
(Average of Two Tests)

Welding Method	Weld Identification	Test Temperature (°C)	Ultimate Tensile Strength Ksi (MPa)	Elongation (%)
Manual	TW-4	RT	97.0 (669)	28.84
		288	61.7 (426)	15.34
Automatic	TW-13	RT	103.1 (711)	28.88
		288	70.4 (486)	14.07
HSW	TW-15	RT	101.6 (701)	30.94
		288	69.3 (478)	12.80

Table 3-11
STRESS CORROSION CRACKING DATA FOR BECHTEL WELDMENT SAMPLES TESTED UNDER CONSTANT LOAD IN 550°F (288°C) WATER WITH 8 ppm DISSOLVED OXYGEN

Weldment*	Weld Metal Ferrite (%)	Pa** (C/cm²)	Applied Stress ksi (MPa)	Percent UTS (288°)	IGSCC Failure Time 1	2	Average
TW-4	1.6–3.2	34.0	40 (276)	65	44	89	67
TW-13	2.5–3.2	26.1	40 (276)	57	411	9253NF***	>4800
TW-15	1.2–4.0	7.5	40 (276)	58	969	136	553

*See Table 3-10 for welding technique.
**Degree of Sensitization after EPR Testing at 86°F (30°C) in 0.5 $M H_2SO_4$ + 0.01 M KSCN (grain boundary adjusted area). Measurements taken 50 mils (1.27 mm) from weld fusion line for Heats 24971W(TW-4) and A5351(TW-13 and 15).
***NF = No Failure in Time Tested.

The lower resistance of TW-4 is probably due to the greater relative applied stress and the sensitization noted in the as received 0.084% carbon heat (the failures occurred in this heat rather than in the A5351 heat side of the weldment). The TW-13 weldment appears to be the more resistant, which, based on degree of sensitization consideration (discussed later), is contrary to expectations. The TW-15 weldment exhibited intermediate susceptibility, but both samples failed by intergranular stress corrosion cracking in the constant load test. The appearance of the fracture surfaces showing the intergranular mode of failure for these samples are shown for TW-4, TW-13 and TW-15 in Figures 3-0 to 3-10 respectively.

The results of EPR measurements are also given in Table 3-11, where TW-4 reveals the greatest sensitization, followed by TW-13 and TW-15. The structure obtained for Heat A5351 in the as-received condition after EPR testing is shown in Figure 3-11. Although many carbide and inclusion stringers are delineated, it is apparent that the grain boundaries are denuded of carbide particles (sensitization).

The structure observed for TW-4 after EPR testing is shown in Figure 3-12, where the grain boundaries are heavily etched due to the electrolyte action on the chromium depleted grain boundaries.

Weldment TW-13 revealed a heavily banded structure (see Figures 3-13 and 3-14), which may have accounted for the superior stress corrosion resistance of this condition. The greatest degree of sensitization occurs in the fine grained structure (~ASTM 5-6) compared to the coarser grained regions (~ASTM 1-2). Conversely, stress-corrosion cracks generally propagate much faster through coarse grained regions, and, because the TW-13 sample failed in the fine grained banded portion (refer to Figure 3-9) the failure time for this sample may have been prolonged compared to the other weldments.

The TW-15 weldment after EPR testing is shown in Figure 3-15. The grain boundaries are decorated with carbides, but the extent is much less than that shown for TW-4 and 13, and this finding was substantiated by the values measured; *i.e.*, Pa = 7.5 C/cm² for TW-15 compared to 26 and 34 C/cm² for TW-13 and TW-4, respectively. Regardless, the degree of sensitization was sufficient to render the TW-15 samples susceptible to intergranular stress corrosion cracking, as given by the data in Table 3-11.

3.7.2 Pipe Remedy Studies

3.7.2.1 Introduction

Pipe sections from three heats of Type-304 stainless steel which constitute the statistical part of the program were evaluated for degree of sensitization and stress corrosion cracking susceptibility. Weld heat affected zones were tested from the outside and inside diameter regions of Heat M0063, and from the outside diameter region of Heat 454970. Also, samples were taken from a standard reference weld (E4) of Heat M7616, which was fabricated similar to

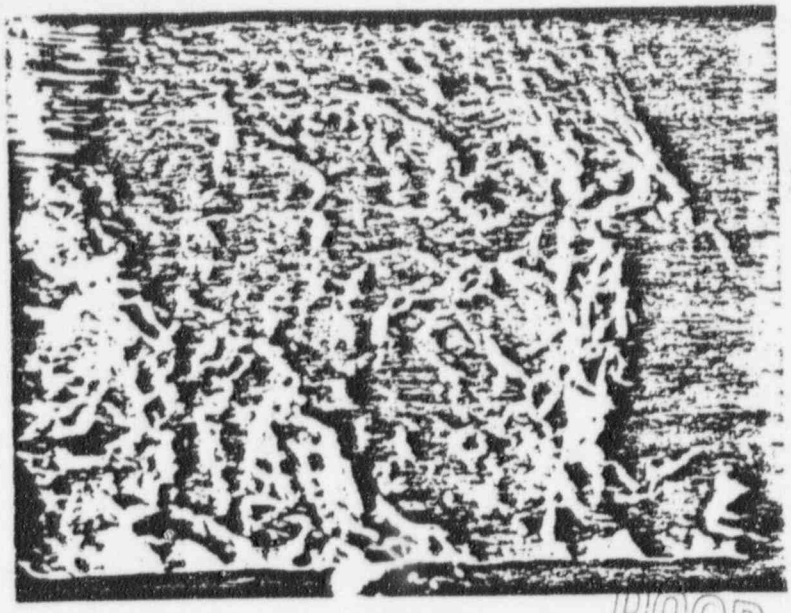

(a) 30X, SEM

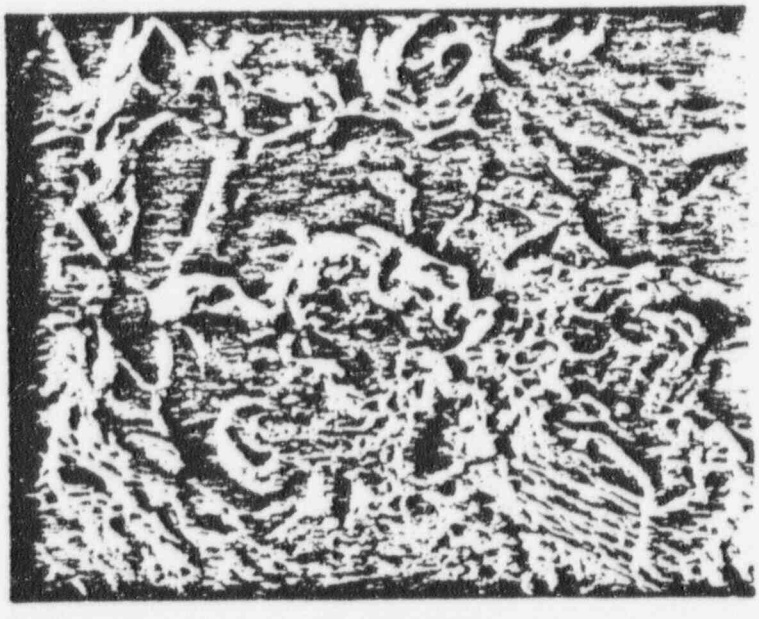

(b) 100X, SEM

Figure 3-8. As-Welded TW-4 Sample Fracture Surface After Constant Load (40 ksi) Testing in 288°C Water With 8 ppm O_2 (T_r = 44 hr)

38

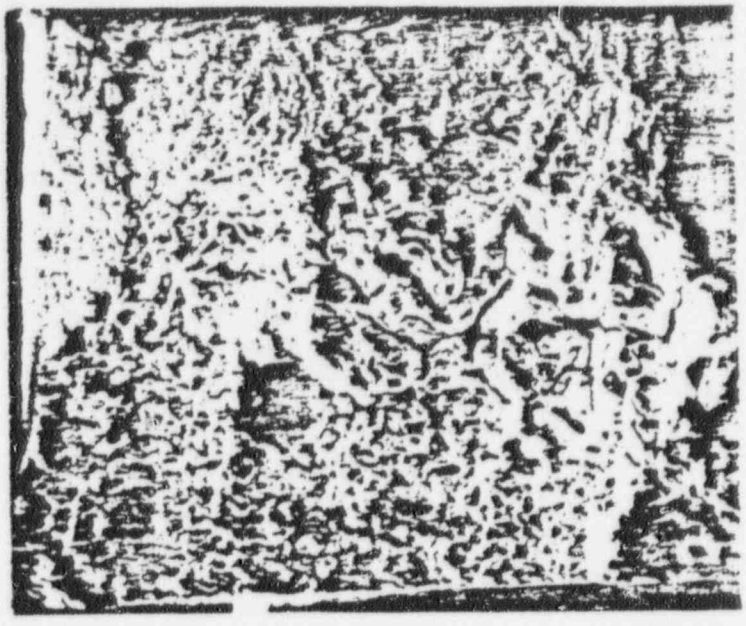

(a) 30X, SEM

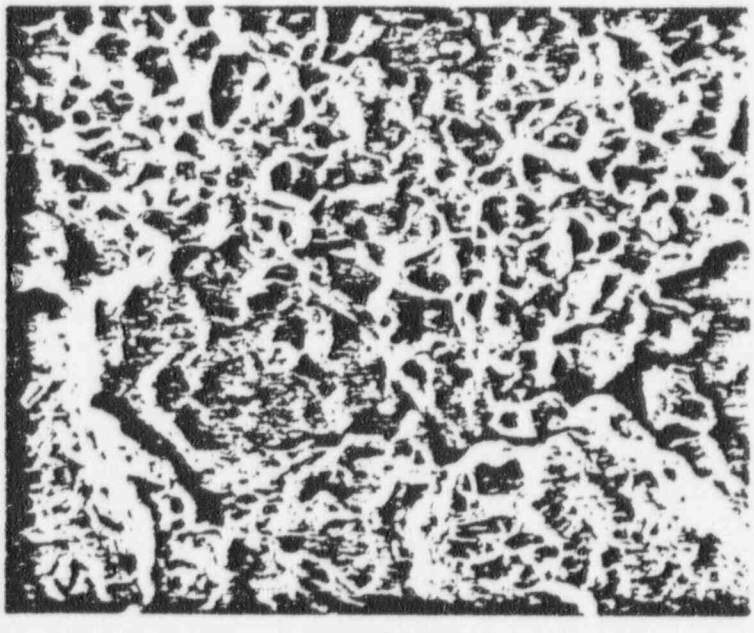

(b) 100X, SEM

Figure 3-9. As-Welded TW-13 Sample Fracture Surface After Constant Load (40 ksi) Testing in 288°C Water With 8 ppm O_2 (T_r = 411 hr)

31

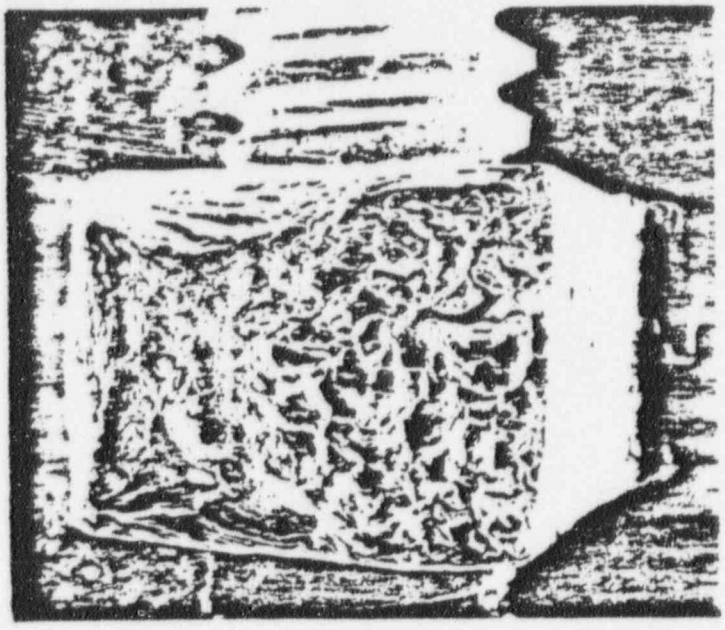

(a) 25X, SEM

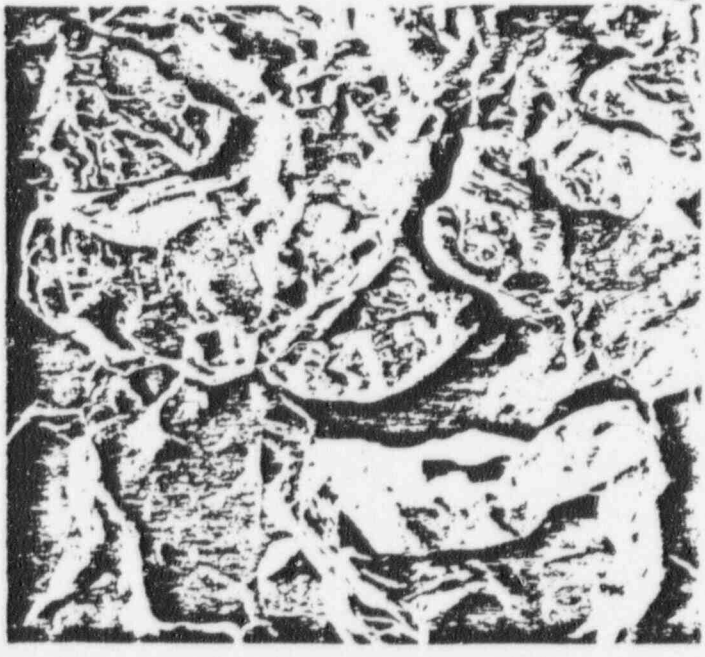

(b) 100X, SEM

Figure 3-10. As-Welded TW-15 Sample Fracture Surface After Constant Load (40 ksi) Tested in 288°C Water With 8 ppm O_2 (T_f = 136 hr)

40

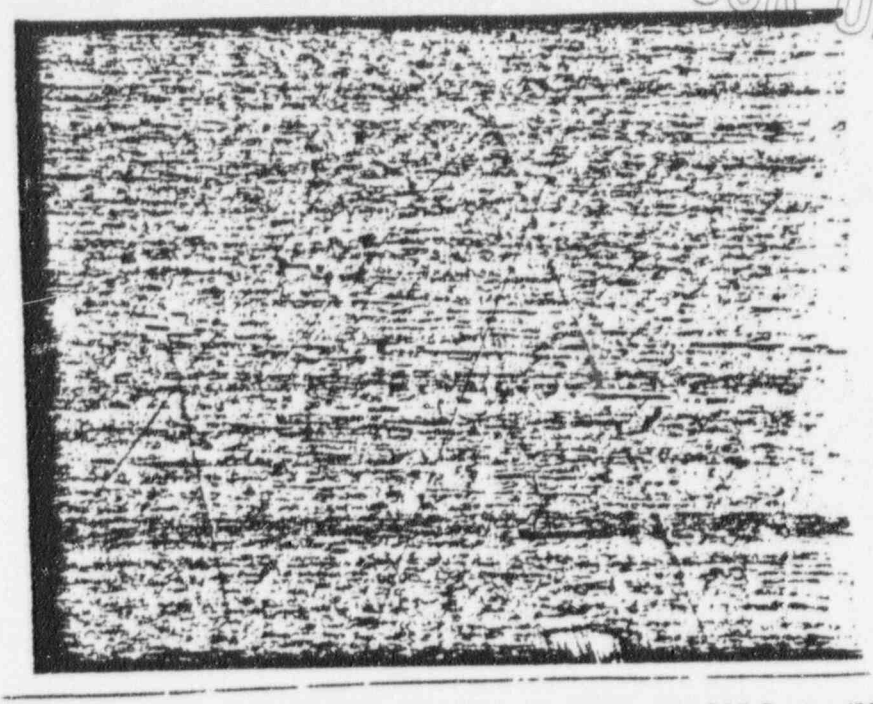

Figure 3-11. As-Received Type-304 Stainless Steel (Heat No. A5350) After EPR Testing (50X)

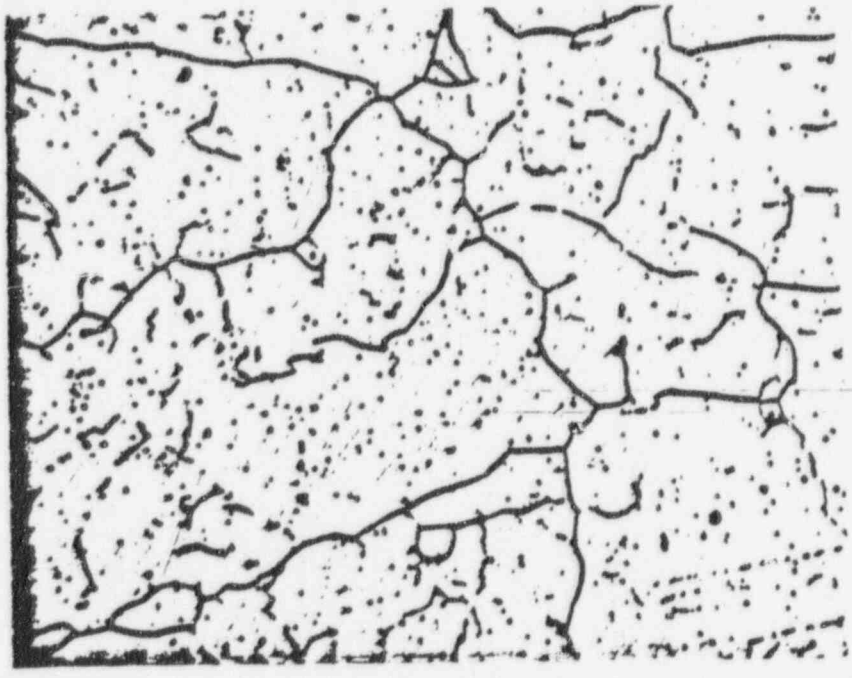

Figure 3-12. As-Welded Type-304 Stainless Steel (Heat No. 24971W) After EPR Testing, Joint TW-4, Reference Manual Weld, High Heat Input (118X)

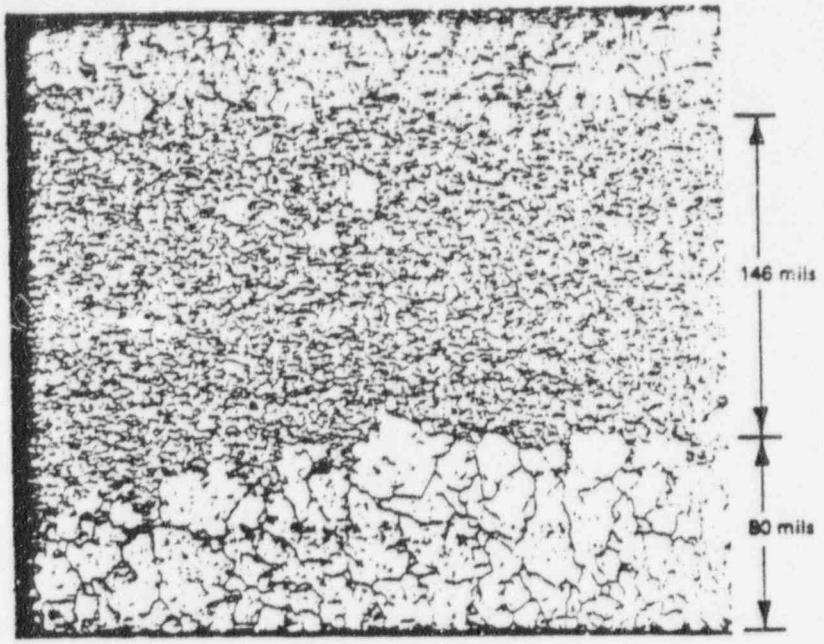

Figure 3-13. As-Welded Type-304 Stainless Steel (Heat No. A5350) After EPR Testing, Weld Joint TW-13, Reference Automatic Weld, High Heat Input (12X)

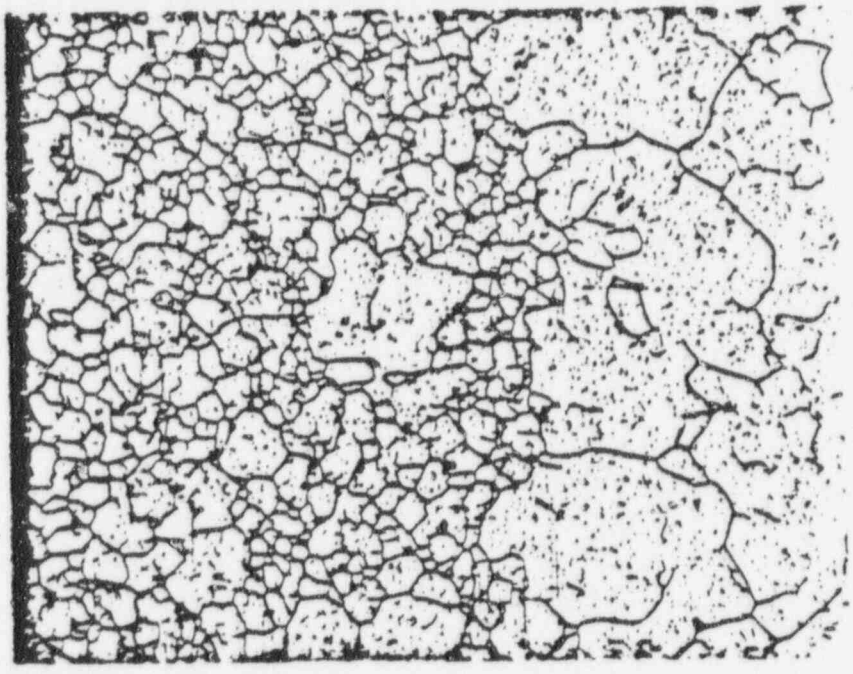

Figure 3-14. Higher Magnification View of Banded Structure Shown in Figure 3-13 (50X)

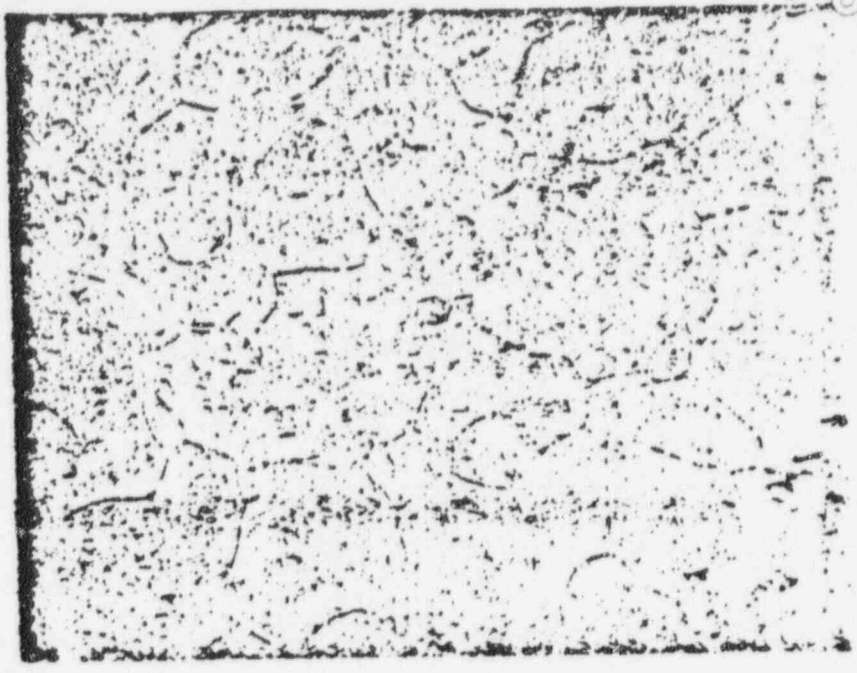

Figure 3-15. As-Welded Type-304 Stainless Steel (Heat No. A5351) After EPR Testing, Weld Joint TW-15, Manual Weld, Water Spray Inside Surface Cooled, High Heat Input (50X)

the reference welds in the heat sink welded pipes by Bechtel Corporation. A companion pipe section (E3) was also tested, which was fabricated by heat sink welding techniques by Bechtel Corporation. And finally, two segments of Heat M7616 piping, which were fabricated using corrosion-resistant cladding techniques were evaluated. One segment (26B) was tested in the as-deposited condition, the second segment (27B) was solution heat treated after the corrosion-resistant cladding process. Chemistry and Mechanical Properties of all three heats are reported in Appendix D and in Task 2 of this report.

3.7.2.2 Experimental Procedures

Uniaxial tensile samples were sectioned from each pipe segment for testing by constant extension rate and constant load techniques. The samples were removed in a manner which included the weld bead in the center of each gage section. Hence, the weld heat affected zones on both sides of the bead were under stress during each test. For the corrosion-resistant clad samples, the heat affected zones between the cladding and the base metal were located at the center of each sample gage section. For these samples, the inside pipe surface was maintained intact in each case.

The constant extension rate tests were conducted in 550°F (288°C) water containing 7–8 ppm dissolved oxygen at an extension rate of 0.0008 mm/min ($\dot{\varepsilon} = 4.4 \times 10^{-6}$/min). After testing, all samples were examined by scanning electron microscopy (SEM) to assess the mode of failure.

The constant load tests were tested in the same environment as above, except the applied loads were 60% of the weld metal ultimate tensile strength at 550°F (288°C).

Finally, specimens were removed from each sample for degree-of-sensitization measurement using the EPR technique. The specimens were removed to either evaluate the butt-weld heat affected zone or to evaluate the heat affected zone at the cladding-base metal interface (for the corrosion-resistant cladding samples).

3.7.2.3 Results and Discussion

The results of the constant extension rate (CERT) and EPR tests are given in Table 3-12. In the case of the Heat M0063 samples, the outside diameter failed by intergranular stress-corrosion cracking, but the inside diameter failed by ductile rupture (Figure 3-16). This finding was supported by the EPR data, which revealed greater degree of sensitization on the outside (Pa = 5.5 compared to 0.6 C/cm² on the inside surface) for these particular samples. This behavior is unusual, since previous testing generally indicates a reverse trend. The present tests only included single samples, however, so that the unusual behavior noted may be due to normal weld variability rather than a characteristic of this heat of material. The as-received pipe of Heat M0063 has a Pa value of 0.2 C/cm².

Both the reference (E4) and heat sink welded (E3) samples welded from Heat M7616 failed by intergranular stress-corrosion cracking in the constant extension rate test. A representative photomicrograph is shown for sample E3 in Figure 3-17. Although both samples failed by stress-corrosion, the extent of damage was much worse for the E4 sample, as indicated in Table 3-12. Additionally, the E4 sample was much more severely sensitized (Pa = 6.7 C/cm²). Heat M7616 of Type-304 stainless steel is sensitized in the as-received condition with Pa values typically greater than 3.0 C/cm².

Table 3-12
CONSTANT EXTENSION RATE TEST RESULTS
(550°F (288°C) WATER—8 ppm O_2; $\dot{\epsilon}$ = 4.5 x 10^{-5}/min)

Sample	Heat	Condition	Breaking Stress ksi	Breaking Stress MPa	Failure Time (h)	RA (%)	E (%)	IGSCC	Charge, Pa (C/cm²)
1-7M9	M0063	As-Welded (o.d.)HAZ	63.1	435	87	24.8	13.9	Yes	5.5
1-7N8	M0063	As-Welded (i.d.)HAZ	71.9	496	127	51.4	19.5	No	0.6
E3	M7616	HSW*-HAZ	77.9	537	84	16.5	13.1	Yes	2.9
E4	M7616	As-Welded HAZ	54.4	375	31	8.5	5.0	Yes	6.7
26-B	M7616	As-Deposited Corrosion Resistant Cladding-weld metal	75.8	523	78	22.5	12.0	No	9.8**
26-B	M7616	As-Deposited Cladding base metal	64.2	443	60	29.7	8.6	Yes	1.4
27-B	M7616	Solution Heat Treated Corrosion Resistant Cladding-weld metal	83.0	573	64	17.6	9.2	No	8.2**
27-B	M7616	Solution Heat Treated Cladding-base metal	75.2	519	99	41.1	14.0	No	0.5

* Heat Sink Welded
** Values taken in the pipe above the corrosion resistant clad (material machined off and not part of test specimen).

Only one of the four corrosion-resistant cladding samples failed by intergranular stress corrosion cracking in the constant extension rate tests. The as-deposited clad sample (26B) failed in the heat affected zone ~2.54 mm (0.1 in.) away from the cladding-base metal interface. The appearance of the fractured surface of this sample is shown in Figure 3-18. Why the degree-of-sensitization value (Pa = 1.4 C/cm²) obtained on the inside surface of this sample is lower than for the as-received material (Pa = 3.0C/cm²) cannot be explained at this time. Additional EPR work is necessary for resolution.

The solution heat-treated clad sample (27B) did not show any evidence of stress corrosion. A relatively low (Pa = 0.5 C/cm²) sensitization value was measured for this cladding-base metal heat affected zone sample.

45

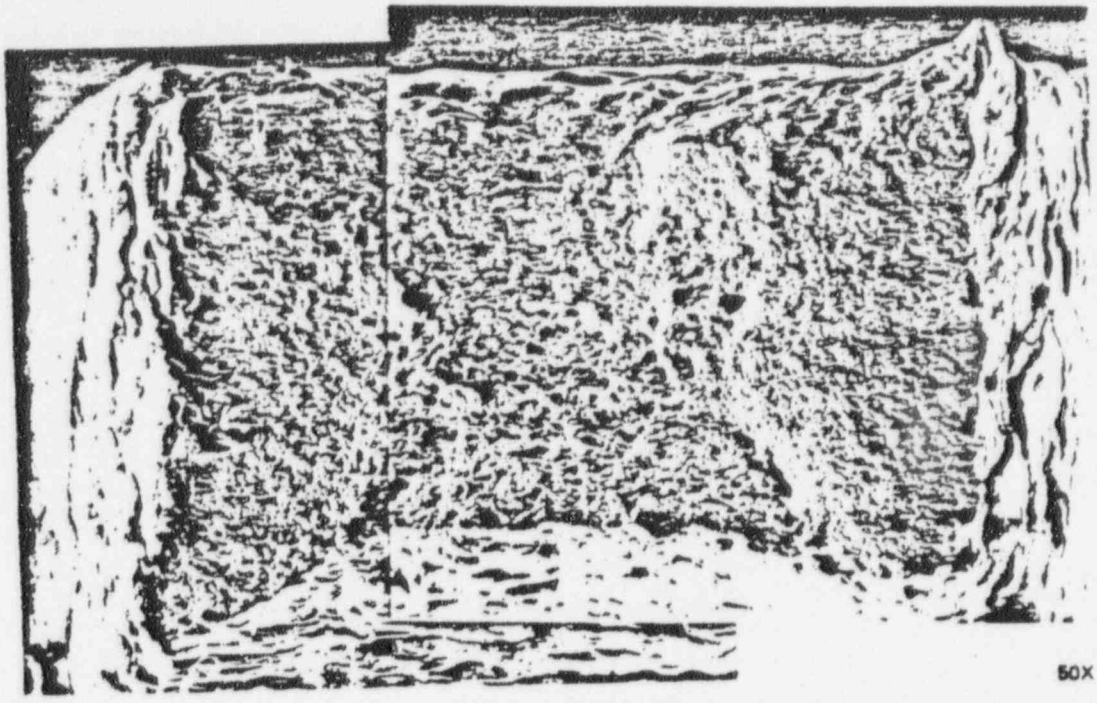

(a) INSIDE DIAMETER

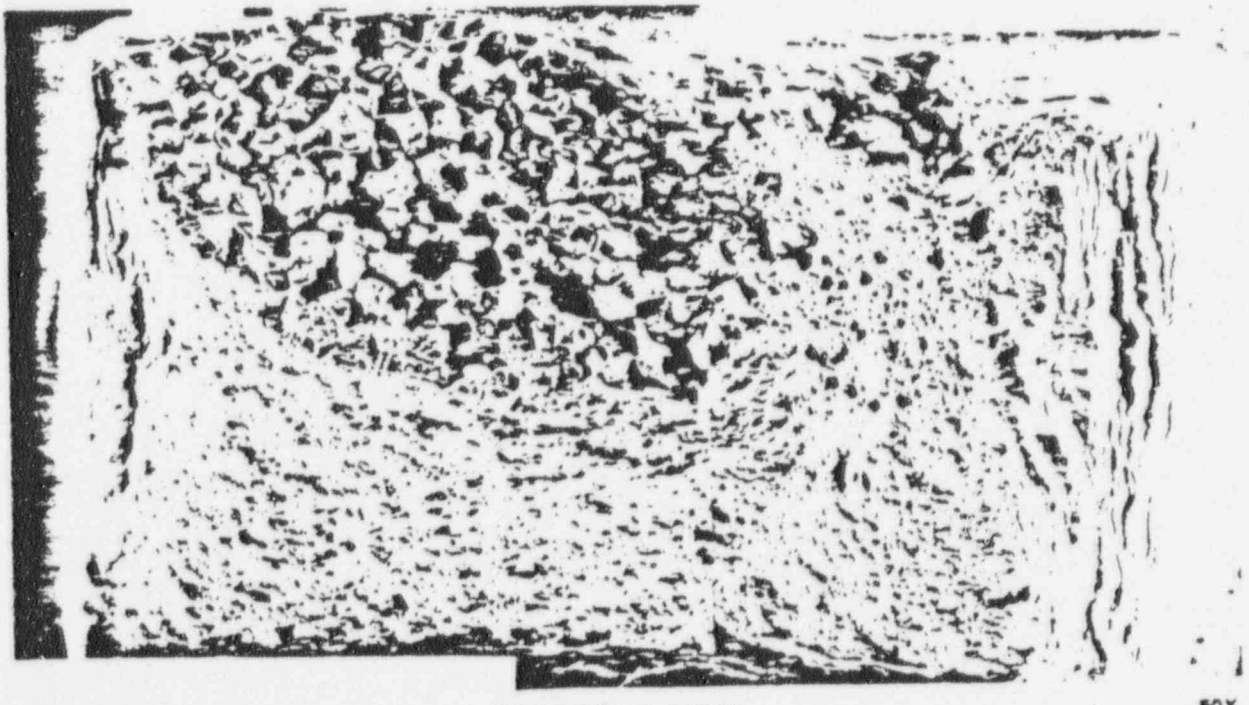

(b) OUTSIDE DIAMETER

Figure 3-16. Fracture Surface of Welded Type-304 (Heat M0063) Sample Tested by CERT in 550°F (288°C) Water With 8 ppm O_2 at $\dot{\epsilon} = 4.4 \times 10^{-6}$/min (SEM)

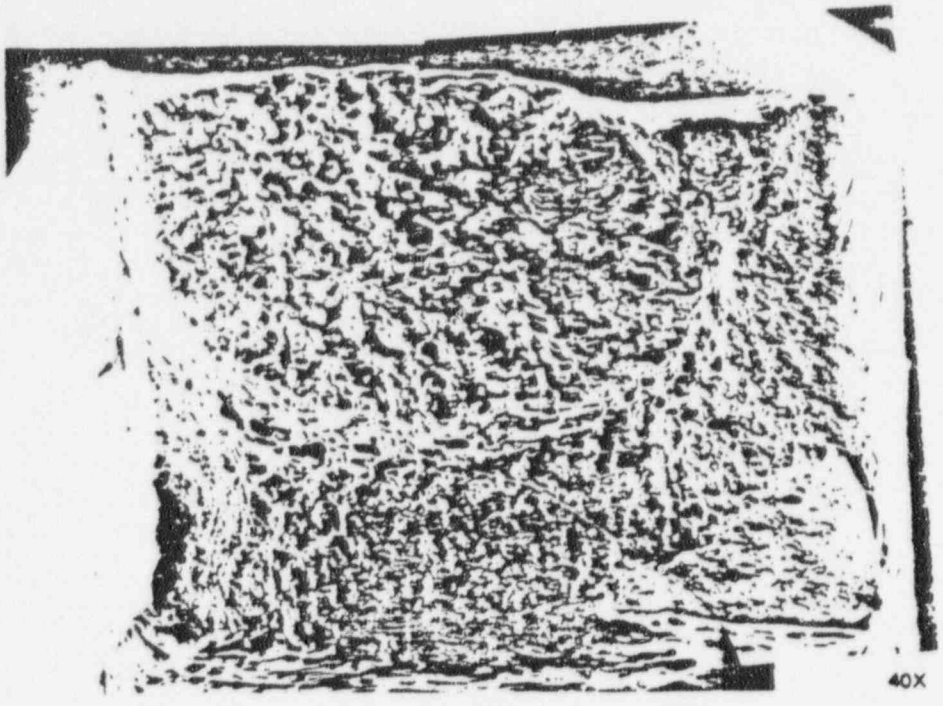

(a)

(b)

Figure 3-17. Fracture Surface of Welded E3 Sample (Heat M7616) Tested by Cert in 288°C Water With 8 ppm O_2 at $\dot{\epsilon} = 4.4 \times 10^{-4}$/min (SEM)

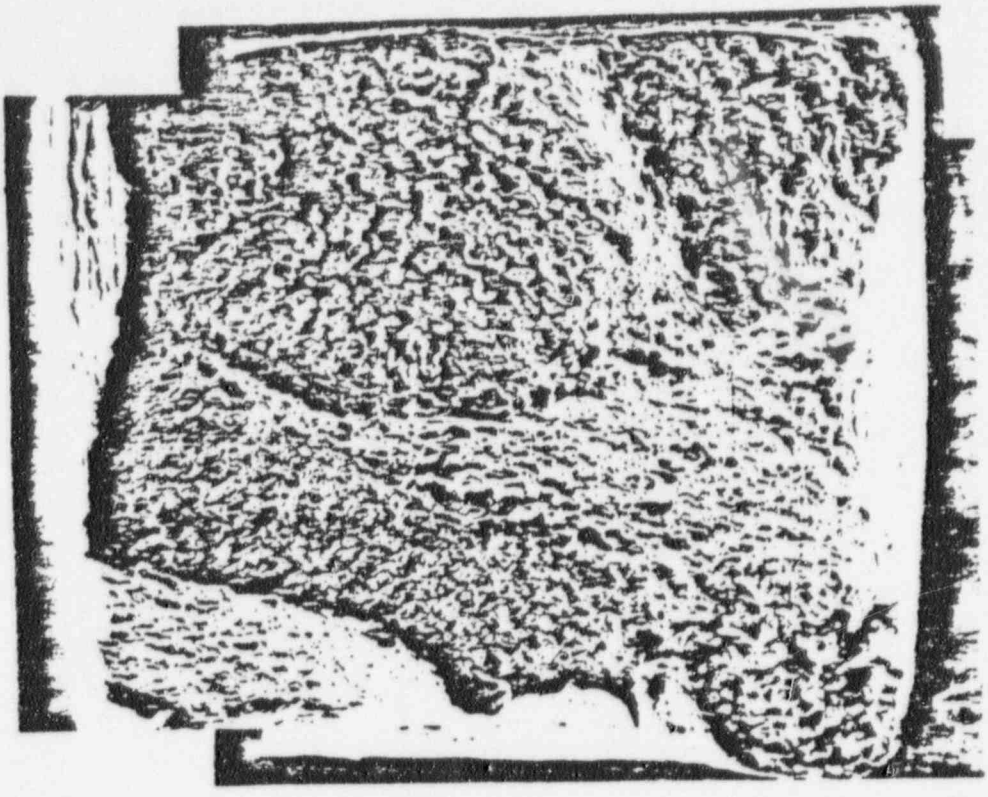

40X

(a)

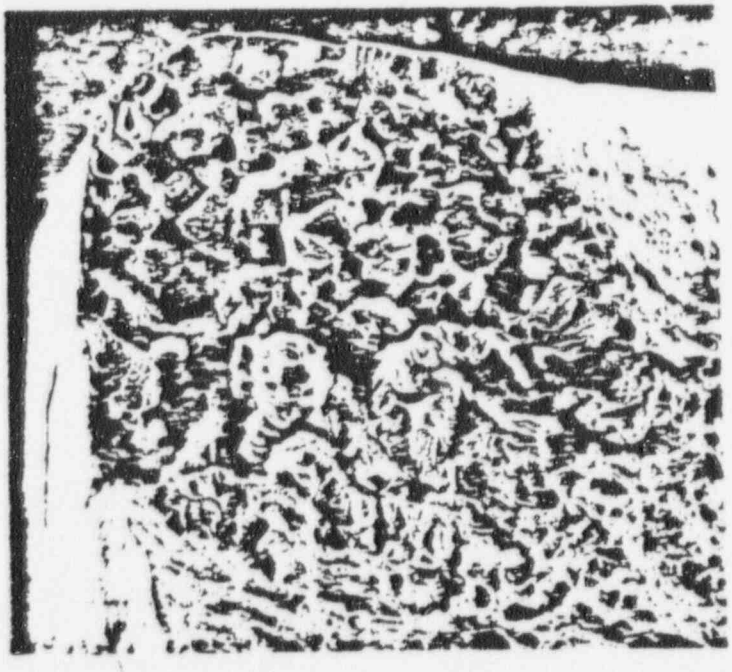

200X

(b)

Figure 3-18. Fracture Surface of Welded 26B Corrosion-Resistant Cladding Sample (Heat M7516) Tested by Cert in 288°C Water With 8 ppm O_2 at $\epsilon = 4.4 \times 10^{-4}$/min (SEM)

Neither of the corrosion resistant cladding butt-weld samples failed by stress-corrosion. The through-thickness of both the 26B and 27B samples consisted of cladding weld metal. The high Pa values obtained for this weldment (Pa = 9.8 and 8.2 C/cm²) were measured in the weld heat affected zone above the cladding (towards pipe outside diameter), which was machined off and was not part of the test sample.

The results of the constant load tests are given in Table 3-13. In these longer term and less severe tests (compared to the constant extension rate tests), intergranular stress corrosion cracking occurred in the as-welded outside diameter sample from Heat M0063, in the as-welded sample from Heat 454970, in one of two heat sink welded samples from E3 (Heat M7616), and in both as-welded E4 (Heat M7616) samples. These data compare favorably to the constant extension rate data, and provide better indicators of relative susceptibility to stress corrosion. For example, although both the control (E4) and heat sink welded (E3) samples experienced intergranular stress corrosion cracking, the failure time for E3 (4129 hours) and the fact that a second sample has not failed after 6735 hours compared to E4 (failure times of 250 and 488 hours) clearly demonstrates the superior resistance of the heat sink welding.

None of the weld overlay (26B and 27B) nor corrosion-resistant clad samples failed in the times tested (>5000 hours). The constant extension rate tests indicated that the as-welded overlay condition (26B) is susceptible to stress corrosion. However, based on the longer term constant load test results, the susceptibility is considered low.

Table 3-13
CONSTANT LOAD IGSCC TEST RESULTS
(550°F (288°C) WATER—8 ppm O_2; σ = 60% UTS 288°C)

Heat	Condition	Applied Stress ksi	Applied Stress MPa	Exposure* Time (h)
M0063	As-Welded—o.d.	40	276	3938F
M0063	As-Welded—i.d.	41	283	5785NF
M7616	As-Deposited Corrosion-Resistant Clad-weld metal 26B	41.5	287	5784NF
M7616	As-Deposited Cladding 26B-base metal	41.6	287	5841NF
M7616	Solution Heat Treated Corrosion-Resistant Clad-27B-weld metal	41.6	278	6322NF
M7616	Solution Heat Treated Cladding-27B-base metal	41.6	287	5247NF
M7616	Heat Sink Welded-E3	41.6	287	4129F
M7616	Heat Sink Welded-E3	41.6	287	6735NF
M7616	As-Welded-E4	41.6	287	250F
M7616	As-Welded-E4	41.6	287	488F
454970	As-Welded	41.6	287	3141F

* NF = No Failure; F = Failed by IGSCC

3.7.3 Additional Pipe Remedy Studies

3.7.3.1 Introduction

Testing was completed to further evaluate the beneficial effects of various pipe remedies to ameliorate intergranular stress corrosion cracking in welded Type-304 stainless steel. Four pipe weldments were investigated; these include: reference Type-304 (Heat 454659) butt welded to itself, heat sink welded Type-304 (Heat 454659) welded to itself using inside surface water cooling, cast CF-8 (Heat 98695) butt welded to itself following a solution heat treatment of the CF-8 spool pieces, and Type-304 (Heat 78500) butt welded to the cast CF-8 (Heat 98695) and then solution heat treated.

3.7.3.2 Experimental Procedures

Samples removed from the inside surfaces of these weldments were tested for stress corrosion cracking resistance by both constant load and constant extension rate methods. The tests were conducted in 550°F (288°C) water containing 8 ppm dissolved oxygen. The constant load tests were performed at applied stresses equivalent to 60% of the material ultimate tensile strength (at 288°C), and the constant extension rate tests at a 4×10^{-4}/min strain rate.

Table 3-14
COMPOSITION (MILL CERTIFICATION VALUES)

Heat	Alloy	C	Mn	S	P	Si	Cr	Ni	N
454659	304	0.043	1.22	0.010	0.018	0.59	18.40	10.00	0.029
98695	CF8	0.07	0.64	0.010	0.026	1.31	20.05	9.03	—
78500	304	0.043	1.64	0.012	0.016	0.55	19.06	8.88	0.073

3.7.3.3 Results and Discussion

The results of the constant extension rate and constant load tests are given in Tables 3-15 and 3-16, respectively. In the constant extension rate tests, only the solution annealed and welded CF-8 to CF-8 sample failed by intergranular stress corrosion cracking; the other samples all failed in a ductile mode.

Table 3-15
RESULTS OF CONSTANT EXTENSION RATE TESTS
FOR PIPE REMEDY SAMPLES

Weldment	Specimen Test Condition	Fracture Stress ksi (MPa)	Failure Time (h)	Reduction of Area (%)	Fracture Mode*
Type-304 Stainless Steel to itself	As welded	66.7 (460)	124	33.3	Ductile
Type-304 Stainless Steel to itself	Heat Sink Welded	65 (448)	107	25.0	Ductile
CF-8 Stainless Steel to itself	Solution Annealed and Welded	47 (324)	71	26.4	IGSCC
Type-304 Stainless Steel to CF-8 Stainless Steel	Welded then Solution Annealed	54.6 (376)	147	44.2	Ductile

* IGSCC — intergranular stress corrosion cracking

90014107

Table 3-16
CONSTANT LOAD TEST RESULTS FOR PIPE REMEDY SAMPLES

Weldment	Specimen Test Condition	Stress ksi (MPa)	Failure Time (h)	Fracture Mode*
Type-304 Stainless Steel to itself	As Welded	40 (276)	10,250NF	N/A
Type-304 Stainless Steel to itself	As Welded	40 (276)	1,328NF	
Type-304 Stainless Steel to itself	Heat Sink Welded	40 (276)	10,270NF	N/A
Type-304 Stainless Steel to itself	Heat Sink Welded	40 (276)	10,050NF	N/A
CF8 Stainless Steel to itself	Solution Annealed and Welded	35 (241)	9,970NF	N/A
CF8 Stainless Steel to itself	Solution Annealed and Welded	35 (241)	469	TGSCC
Type-304 Stainless Steel to CF8 Stainless Steel	Welded, then Solution Annealed	40 (276)	372	Ductile
Type-304 Stainless Steel to CF8 Stainless Steel	Welded, then Solution Annealed	40 (276)	1,263NF	N/A
Type-304 Stainless Steel to CF8 Stainless Steel	Welded, then Solution Annealed	40 (276)	299	TGSCC**

* N/A Not Applicable (samples did not fail).
** TGSCC—Transgranular Stress Corrosion Cracking.

The casting from which this sample was machined was procured with a 20.16 cm (7.94 inch) outside diameter and a 6.2 cm (2.44 inch) inside diameter. This thickness, unusual for centrifugally cast pipe, resulted in uneven ferrite distribution and large grains. The fracture surface of the CF-8 sample is shown in Figure 3-19 where the intergranular (interdendritic) nature of the fracture is clearly evident. This fracture mode was unexpected, as welded cast CF-8 has never failed intergranularly in these types of corrosion tests in previous studies (especially since the sample contained 10–15% ferrite). Further investigation revealed an irregular morphology of the ferrite phase (Figure 3-20), and profuse precipitation (presumably carbides) of a relatively continuous phase at the grain boundaries (Figure 3-21). This grain boundary phase, which appears as interconnected particles, provided the path for propagation of the interdendritic stress corrosion cracks (Figure 3-22). The cracks propagated primarily along the elongated, "stringered-type" ferrite phase aligned parallel with the applied stress (refer to Figure 3-20). The reason for the unusual extent of precipitate formation is presently unknown. However, this precipitation was unique to the solution annealed and then welded condition. The sample which was welded and then solution annealed failed the stress corrosion test in a ductile manner (Figure 3-23), and the ferrite distribution appears somewhat more uniform (Figure 3-24) than the solution annealed and then welded condition. The welded and then solution annealed CF-8 microstructure did not reveal the profuse grain boundary precipitation characteristic of the solution annealed and welded condition.

Both the Type-304 control and inside diameter cooled and welded samples fractured with ductility in the constant extension rate test. Both samples revealed "thumbnail" cleavage areas on one corner of the fracture surfaces (Figures 3-25 and 3-26). These cleavage fractures are becoming a frequent characteristic of the fractures caused by the constant high strain extension rate testing of Type-304 stainless steel, and currently have no particular significance attached to their occurrence.

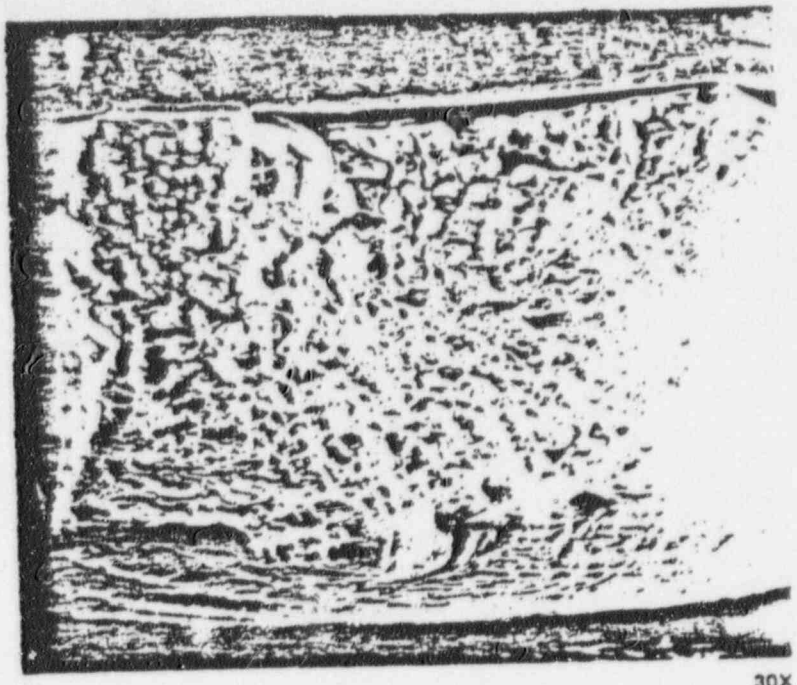

(a) 30X

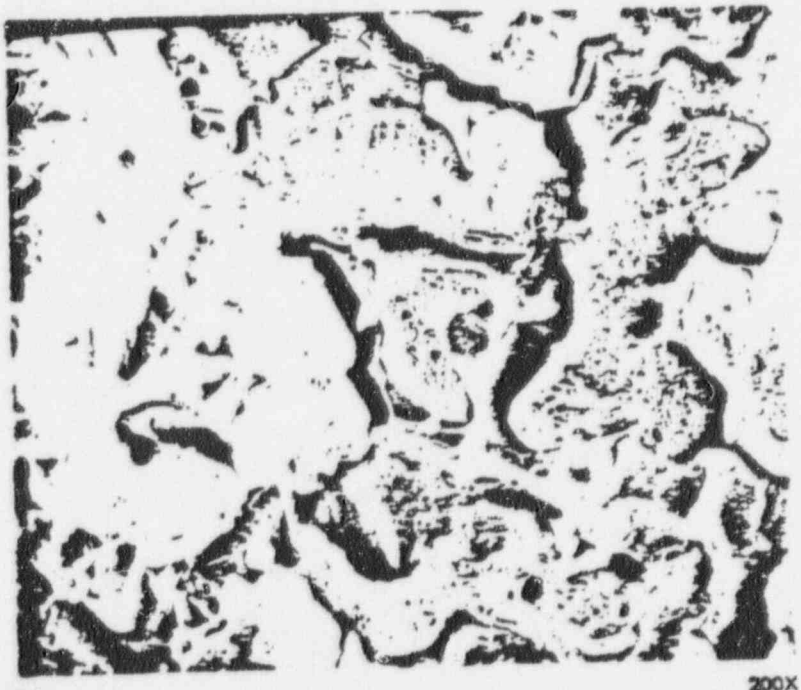

(b) 200X

Figure 3-19. IGSCC in CF-8 (Heat 98695) Annealed and Welded Sample Tested by CERT in 550°F (288°C) Water With 8 ppm O_2 (SEM)

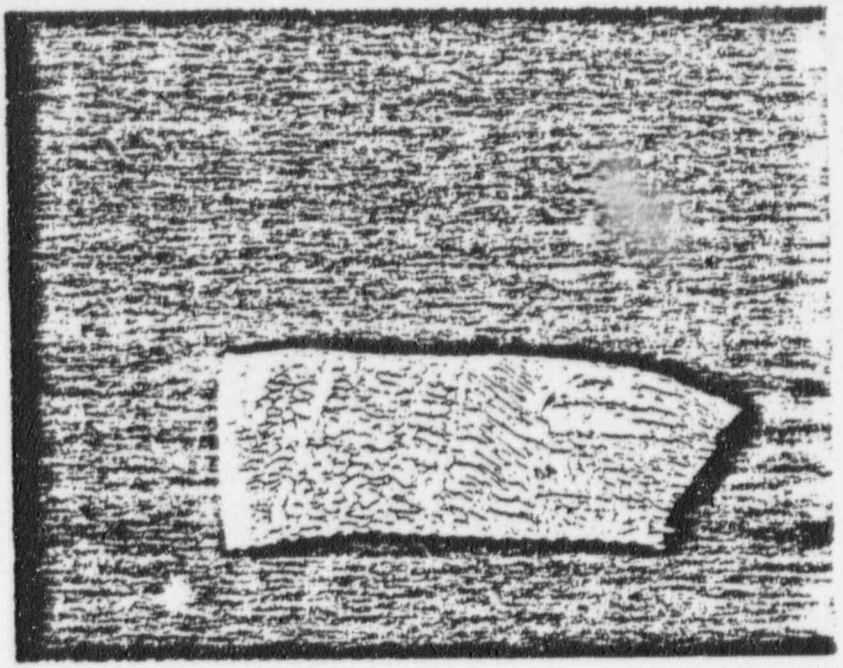

(a) 20X

(b) 100X

Figure 3-20. Ferrite Distribution in CF-8 Annealed and Welded Samples. (Oxalic Acid Etched)

(a) BRIGHT FIELD 500X

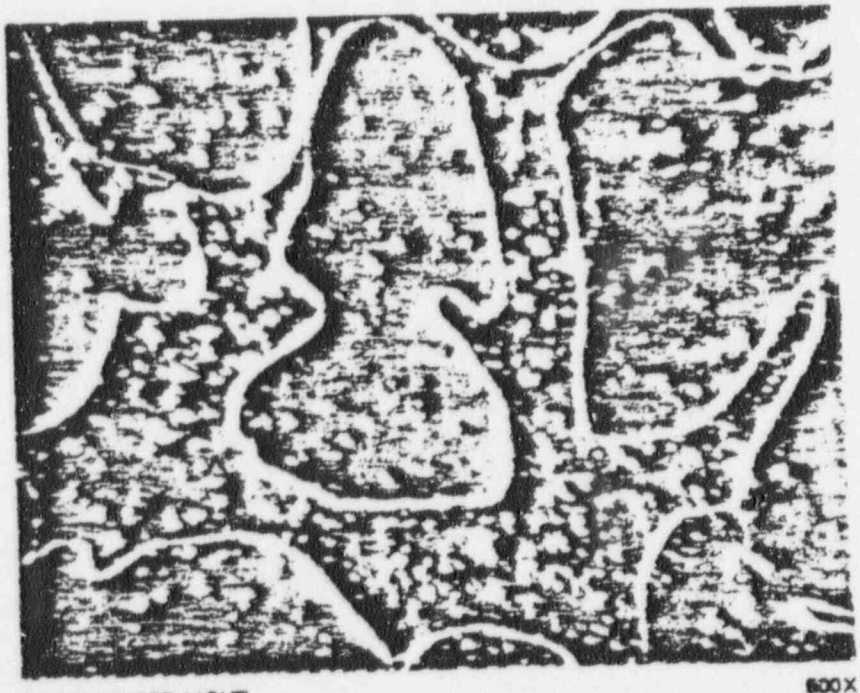

(b) POLARIZED LIGHT 500X

Figure 3-21. Appearance of Carbide Precipitates Around Ferrite Phase in CF-8 Annealed and Welded Samples. (Oxalic Acid Etched)

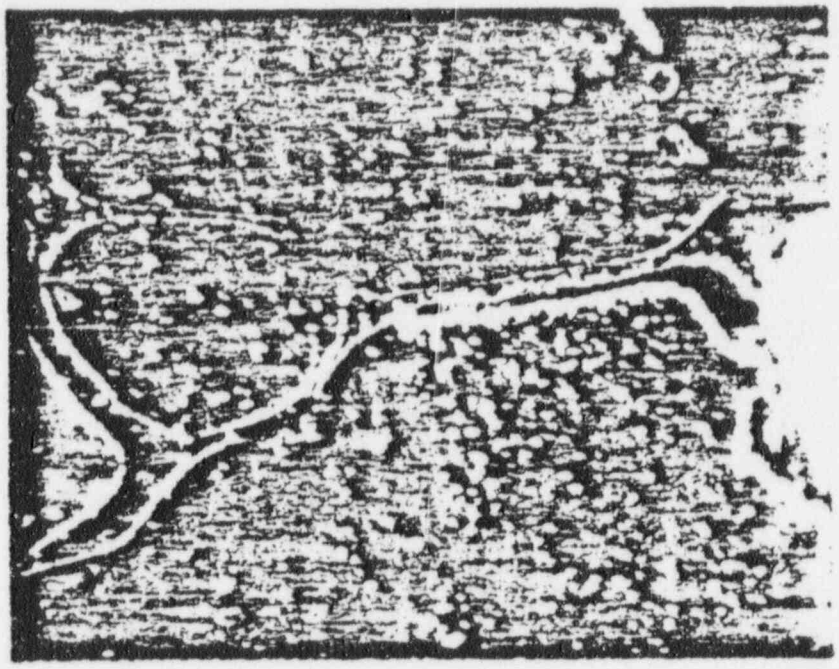

Figure 3-22. Interdendritic Stress Corrosion Crack Along Carbide Decorated Ferrite Phase in CF-8 Annealed and Welded Sample Tested by CERT in 550°F (288°C) Water With 8 ppm O_2 (Polarized Light, Oxalic Acid Etched, 500X)

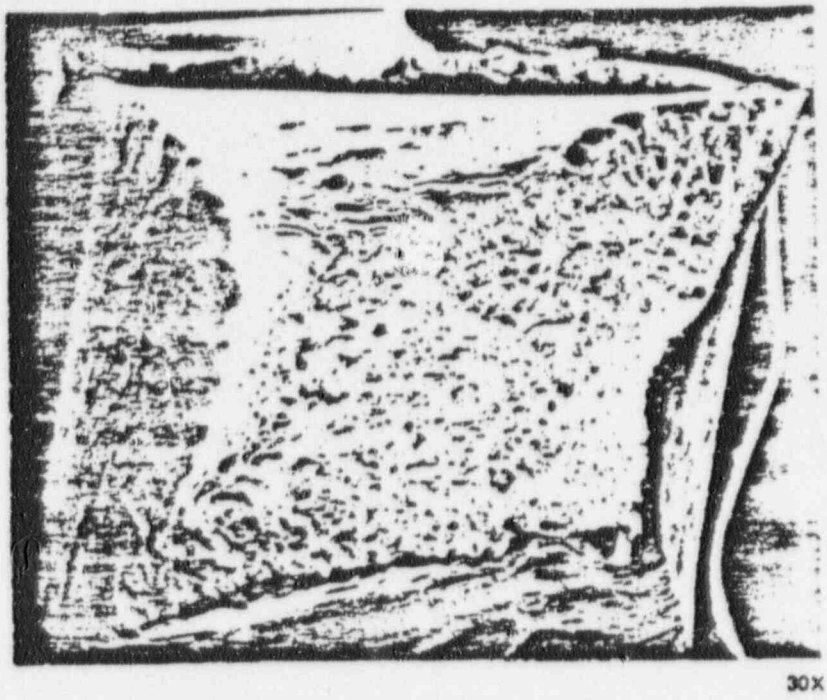

Figure 3-23. Fracture Surface of Type CF-8 (Heat 98695) Welded and Annealed Sample Tested by Constant Load in 550°F (288°C) Water With 8 ppm O_2 at σ = 40 ksi (276 MPa). (SEM, 30X)

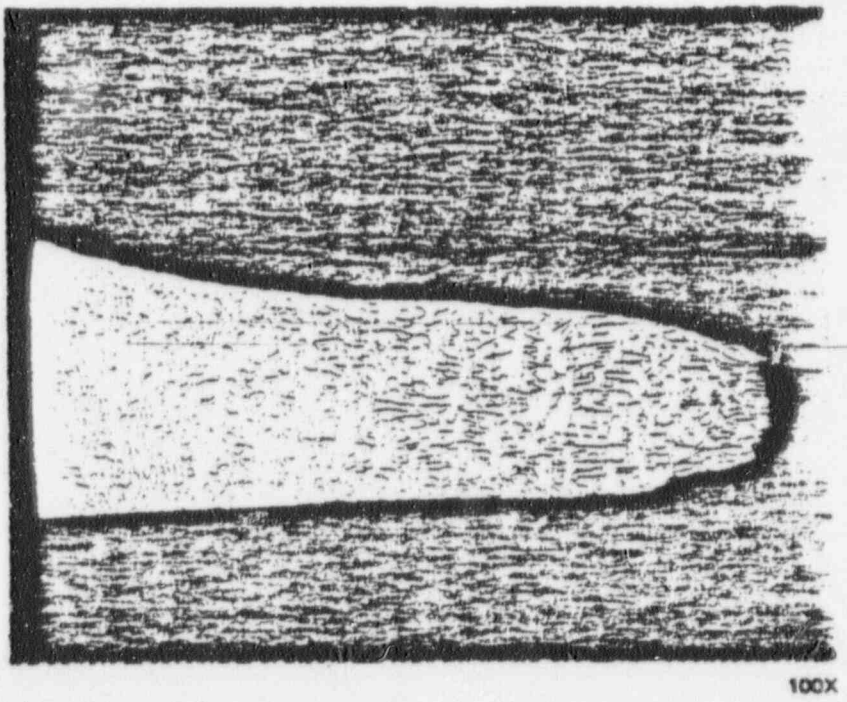

Figure 3-24. Ferrite Distribution in CF-8 Sample after Welding and Annealing. (Oxalic Acid Etch, 100X)

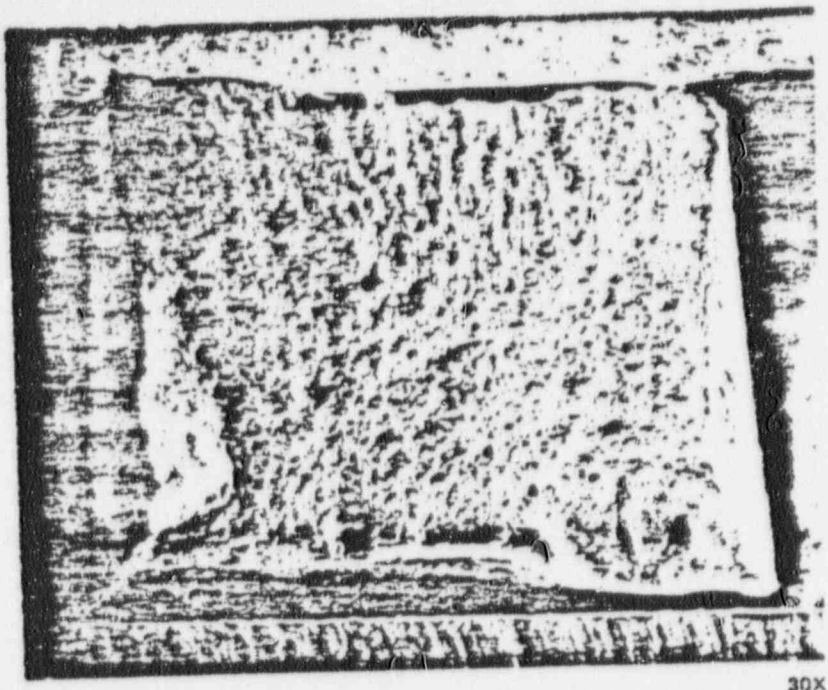

30X

(a)

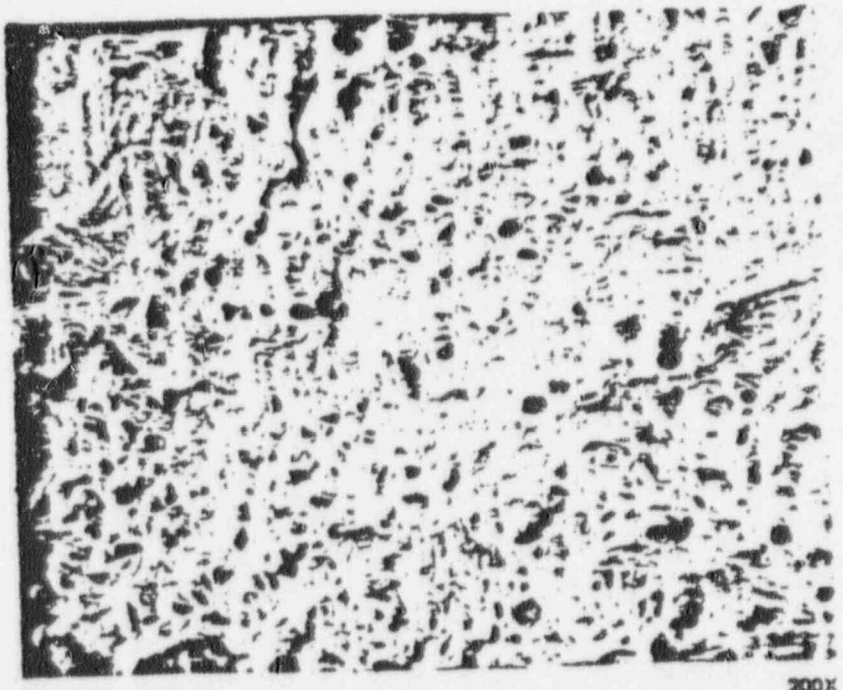

200X

(b)

Figure 3-25. Fracture Surface in Welded Type-304 (Heat 454659) Control Sample Tested by CERT in 550°F (288°C) Water with 8 ppm O_2 (SEM)

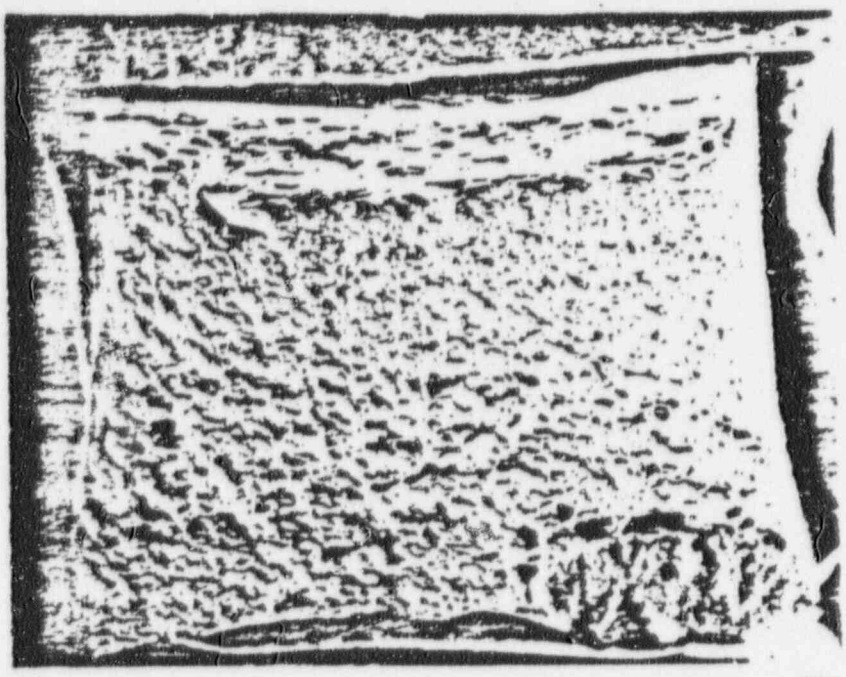

(a) 30X

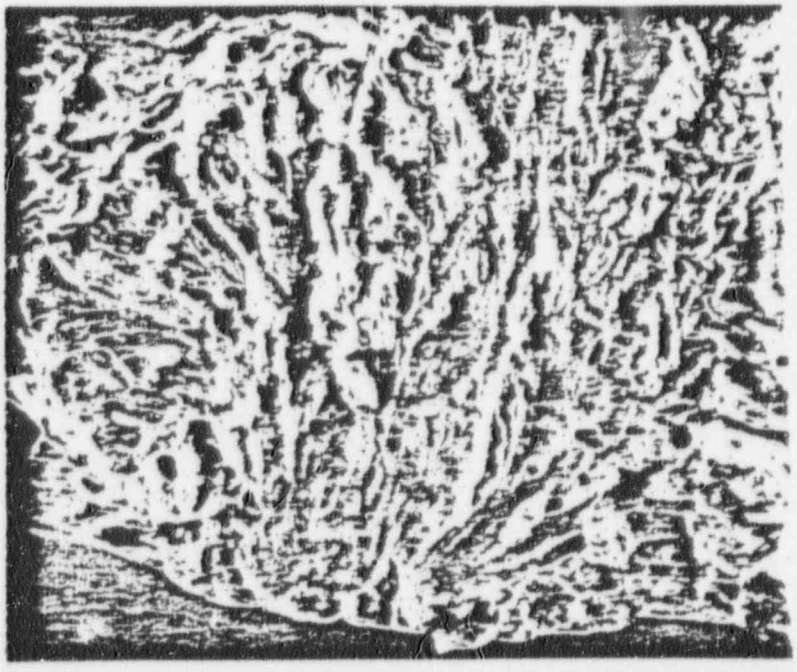

(b) 200X

Figure 3-26. Fracture Surface of Welded Type-304 (Heat 454659) Inside Surface Cooled Sample Tested by CERT in 550°F (288°C) Water with 8 ppm O_2. Note Cleavage Fracture on One Corner of Sample b. (SEM)

The constant load test results are given in Table 3-16. The Type-304 stainless steel control and inside diameter cooled samples have not failed after greater than 10,000 hours exposure. These data are consistent with the constant extension rate tests which indicate the good stress corrosion resistance of these particular Type-304 (Heat 454659) weldments.

None of the CF-8 samples failed by intergranular stress corrosion cracking in the constant load tests, although one of the solution annealed and welded samples fractured in a relatively short exposure time (469 hours). This sample failed by transgranular stress corrosion crack initiation (Figure 3-27), followed by ductile rupture of the remaining cross-section. The companion sample accumulated almost 10,000 hours test exposure without failure.

Two of three of the welded and then solution annealed samples failed during constant load testing. Both samples failed in the CF-8 side of the CF-8 to Type-304 welded samples. One sample failed ductilely in a short time (372 hours); the other sample failed by transgranular stress corrosion crack initiation in a manner similar to that shown in Figure 3-27.

The intergranular stress corrosion cracking noted after constant extension rate testing and the premature failures in the constant load tests (particularly at very low applied stresses) are both uncharacteristic of CF-8 material. It appears that there is something detrimentally unique about the heat of CF-8 used in this investigation. The reason for this uniqueness may be related to the fact that these thin samples were machined from a very thick casting with uneven ferrite distribution and large grains.

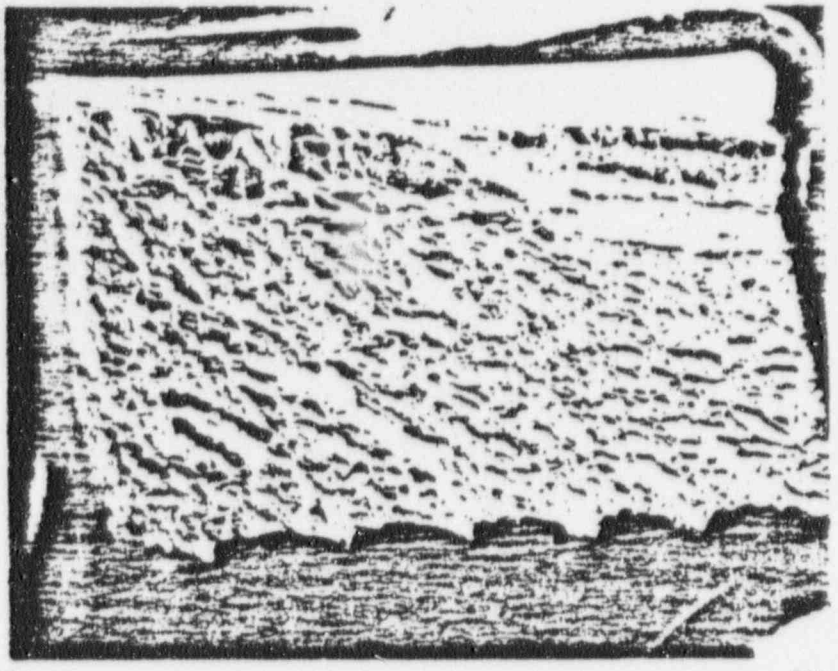

(a) 30X

(b) 200X

Figure 3-27. Fracture Surface at CF-8 (Heat 98965) Annealed and Welded Sample Tested by Constant Load in 550°F (288°C) Water with 8 ppm O_2 at σ = 35 ksi (241 MPa). Note Cleavage Fracture Along Upper Edge of Sample b. (SEM)

4. TASK 2 — STATISTICAL PIPE TESTS AND SMALL SPECIMEN SCREENING TESTS

4.1 INTRODUCTION AND TASK OBJECTIVES

A statistical approach is a requirement for analysis of stress corrosion cracking data for a number of reasons. First, a number of different sources of variability must be recognized and accounted for, such as, inter-heat and intra-heat variability in the material being investigated, variability in fabrication practices between different specimens, variability in testing procedures, and variability in the corrosion mechanism under investigation. Second, since some claim as to the improvement in stress corrosion cracking resistance will be made as a result of the investigation, an objective and rigorous test of that claim must be made and statistics is the only tool for making such a test. Third, to avoid excessively long test times, accelerated test conditions are required. However, even under these circumstances, a simple relative demonstration of a significant difference in behavior may involve very long test times. Statistics offers a means of further shortening the required test time on a rational basis.

4.1.1 Assumptions

Only two assumptions are involved in the statistical approach to be used for the demonstration of an improvement in stress corrosion cracking resistance of the desired magnitude. First, the effect in reducing specimen life of the accelerating factors chosen for these tests is proportional at all levels of all factors for both the reference material and the alternate, as illustrated by Curve A compared to curve 304 in Figure 4-1. Those two curves identify time to first failure of an alternate and of Type-304 stainless steel as the levels of various accelerants are made more severe. It is recognized that this proportional reduction in life assumption may not be exactly correct, and that either of two other relationships may exist, as also shown in Figure 4-1. If the effect of one or more accelerating factors is less for the alternate than for the reference material then the situation illustrated by curve B in Figure 4-1 would exist. The result of this would be that any predictions made regarding the alternate under service conditions would be non-conservative; that is, the alternate would not perform as well as was predicted from the accelerated test. However, if the effect of one or more of the accelerating factors is greater for the alternate than for the reference material, then a situation illustrated by curve C in Figure 4-1 would exist. In this situation, the alternate would perform better in service than predicted from accelerated tests. It is difficult to imagine a mechanism by which the situation represented by curve B might exist within the same class of materials, and the probability of its occurrence is therefore considered to be insignificant. Since the situation represented by curve C results in conservative predictions, its occurrence does not cause an error in the wrong direction and it can be ignored for the purposes of this test program.

The second assumption relates to the distributions of times to failure of Type-304 stainless steel in the reference welded conditions, and the times to failure of Type-304 stainless steel in the remedy condition. While no assumption is necessary regarding the shapes of these two distributions, it is assumed that the variances of the two distributions are not greatly different from each other. This particular assumption is not a requirement for the use of the statistical approach, however, some assumption regarding the distribution of times to failure of the remedy condition is necessary if one is to avoid very long testing times.

4.1.2 Objectives

The primary objective of this task was to demonstrate an improvement in resistance to stress corrosion cracking by at least a factor of 20 for one or more of three proposed remedies: solution annealing after welding, corrosion-resistant cladding, and solution annealed corrosion-resistant cladding. In addition, statistical evaluation of a short term remedy (heat sink welding) on a single heat of Type-304 stainless steel was also included. Finally, small specimen evaluations of several testing and fabrication variables were also to be performed. However, the results from the early stages of the latter investigation indicated that further testing would not yield useful data, for reasons to be discussed in detail later in this report.

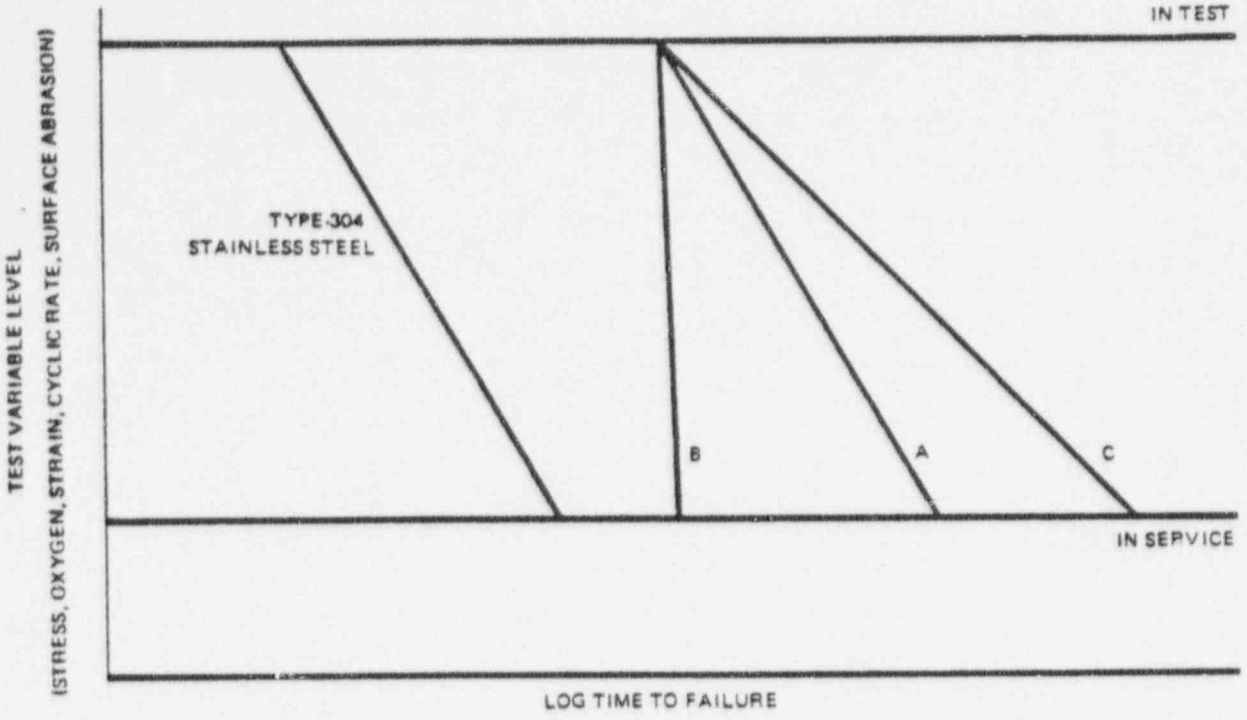

Figure 4-1. Possible Effect of Accelerants on Type-304 Stainless Steel and on an Alternate in Test and in Service

4.1.3 Criteria

Two criteria must be defined for the purposes of this investigation. The first is the criterion of a failure in the testing program, and the second is the criterion for acceptable improvement. For the purposes of this investigation, the criterion chosen for failure was complete severance of small specimens or a through-wall leaking crack in full-size pipe specimens. The criterion selected for acceptable improvement was a factor of at least 20, at the 90% confidence level. The selection of the criterion of failure was based on simple expediency; it is much easier to detect the two events chosen than any others associated with stress corrosion cracking and their detection does not involve any interpretation on the part of an inspector or operator. The basis for the selection of a factor of 20 improvement was the median time to first failure for welded Type-304 stainless steel in boiling water reactor service among plants as of 1974 (approximately 5 years). While an increase by a factor of only about 8 would appear to be adequate to meet the requirements of a 40-year design life, some failures would still be anticipated in service. It was therefore decided to build conservatism into the remedy by requiring that it exhibit at least a factor of 20 improvement in resistance to intergranular stress corrosion cracking.

4.2 TEST DESCRIPTIONS

4.2.1 Pipe Tests

Pipe testing consisted of stressing welded 10 cm (4 in.) Schedule 80 pipes in a cyclic tension mode, at a frequency of 0.7 cycles per hour. The load was increased linearly over a 5-minute period until the stress reached a value of 136% of the 288°C (550°F)-0.2% offset yield strength of the particular heat, held at that level for 75 minutes, reduced linearly to a value of approximately 10 MPa (1.5 ksi) over a time period of 0.5 minutes; and held at that level for 5 minutes, and then repeated for subsequent cycles. A limited number of tests were performed at a stress of 110% of the yield strength on a single heat (M7616). The test environment was 288°C (550°F) high purity water with 8 ppm dissolved oxygen circulated through the inside diameter of the pipes. A schematic drawing of a pipe test station is shown in Figure 4-2.

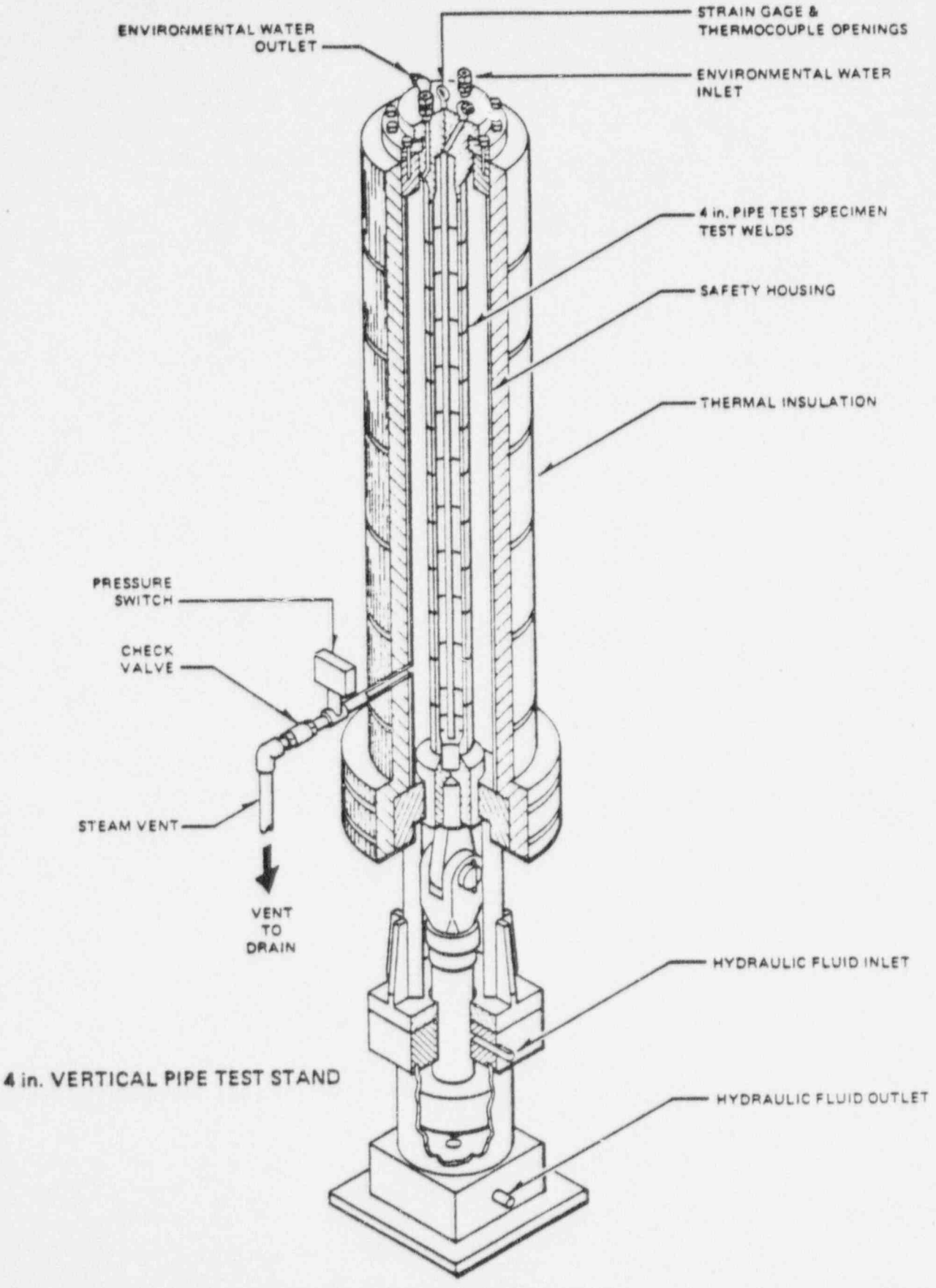

Figure 4-2. Four-Inch Vertical Pipe Test Stand

4.2.2 Small Specimen Tests

Testing of the reference condition small specimens was essentially identical to that of the full-size pipes. The nominal loading cycle was the same as that of the pipes, although linear loading and unloading was not possible in the facility in which these tests were conducted. However, this difference would not be expected to have significant effects on the results of the tests. The test environment was 288°C (550°F) high purity water with 8 ppm dissolved oxygen circulated around all surfaces of the test specimens. In addition, tests were performed at stresses of 110% and 90% of the yield strength at cycling rates of 0.67 and 3.35 cycles per hour and with a slowly rising load to the test maximum value. A schematic drawing of a variable load test station is shown in Figure 4-3.

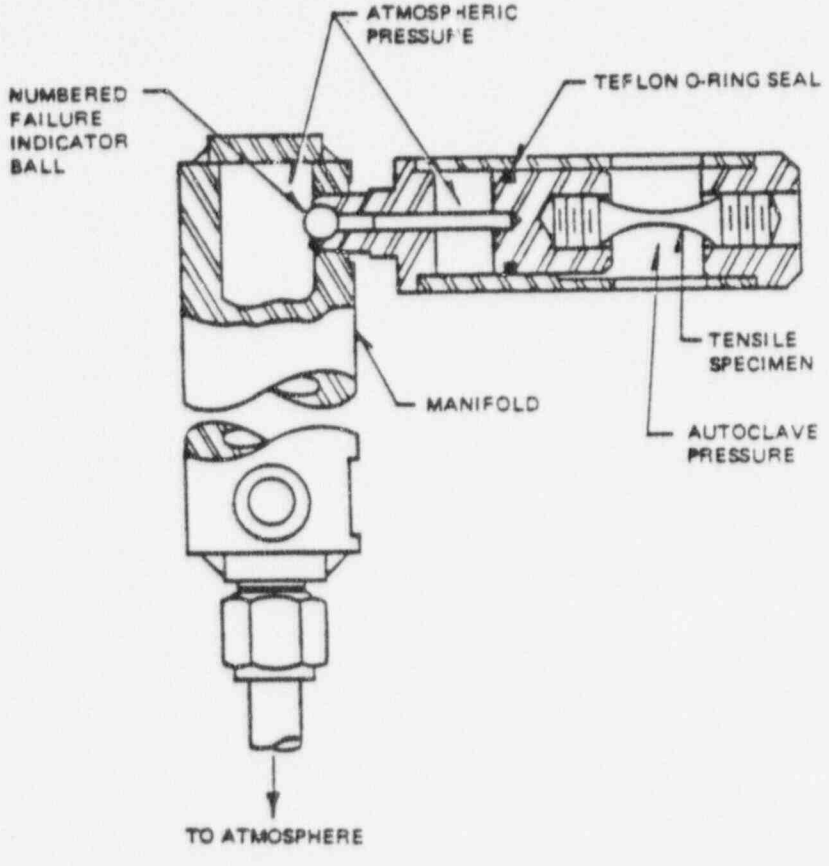

Figure 4-3. Uniaxial Tensile Specimen Loading Module

4.3 MATERIALS AND CONDITIONS

4.3.1 Pipe Tests

Three different heats of Type-304 stainless steel pipe were tested in the statistical demonstration tests in four different welded conditions; the reference case, solution annealed, corrosion-resistant clad, and solution annealed corrosion-resistant clad. The fabrication sequence and relative location of the heat-affected zones in the pipe base metal is shown schematically for each case in Figure 4-4. A total of 12 welded pipe specimens with 12 welds per specimen were fabricated; one pipe from each heat of material in each of the four conditions, as shown in Table 4-1. Chemical compositions and room temperature mechanical properties of the three heats of pipe are also shown in Table 3-1.

Table 4-1
STATISTICAL TYPE TEST FABRICATION INFORMATION

Pipe Specimen	Weldment Number	Pipe Heat Number	Remarks
Reference	E18	M7616	Ground afer welding
Reference	E12	454970	Ground after welding
Reference	E11	M0063	Ground after welding
Solution Anneal	E13	M7616	Solution anneal after welding and grinding
Solution Anneal	E14	M0063	Solution anneal after welding and grinding
Solution Anneal	E15	454970	Solution anneal after welding and grinding
As-Deposited Corrosion Resist Clad	E16	M7616	Ground after welding
As-Deposited Corrosion Resist Clad	E24	M0063	Ground after welding
As-Deposited Corrosion Resist Clad	E25	454970	Ground after welding
Solution Annealed Corrosion Resist Clad	E32[1]	M7616	Ground after welding
Solution Annealed Corrosion Resist Clad	E34[1]	M0063	Ground after welding
Solution Annealed Corrosion Resist Clad	E35[1]	454970	Ground after welding

NOTES: [1]Initial 1.25 cm (½ in) of corrosion-resistant clad was solution annealed prior to deposition of remainder.

COMPOSITION (MILL CERTIFICATION VALUES)

Heat	C	Mn	S	P	Si	Cr	Ni
M7616	0.060	1.72	0.012	0.025	0.54	18.83	10.42
M0063	0.050	1.72	0.010	0.025	0.62	18.64	10.46
454970	0.042	1.09	0.012	0.018	0.33	18.10	10.10

ROOM TEMPERATURE MECHANICAL PROPERTIES (MILL CERTIFICATION VALUES)

Heat	Yield Strength	Tensile Strength	Elongation (5.1 cm)
M7616	316 MPa (45.8 ksi)	577 MPa (83.7 ksi)	58%
M0063	268 MPa (38.9 ksi)	567 MPa (82.3 ksi)	68%
454970	259 MPa (37.6 ksi)	558 MPa (81.0 ksi)	61%

288°C (550°F) MECHANICAL PROPERTIES (MEASURED)

Heat	Yield Strength	Tensile Strength	Elongation (3.8 cm)
M7616	199 MPa (28.8 ksi)	478 MPa (69.4 ksi)	40%
M0063	148 MPa (21.4 ksi)	455 MPa (66.0 ksi)	40%
454970	157 MPa (22.8 ksi)	451 MPa (65.4 ksi)	31%

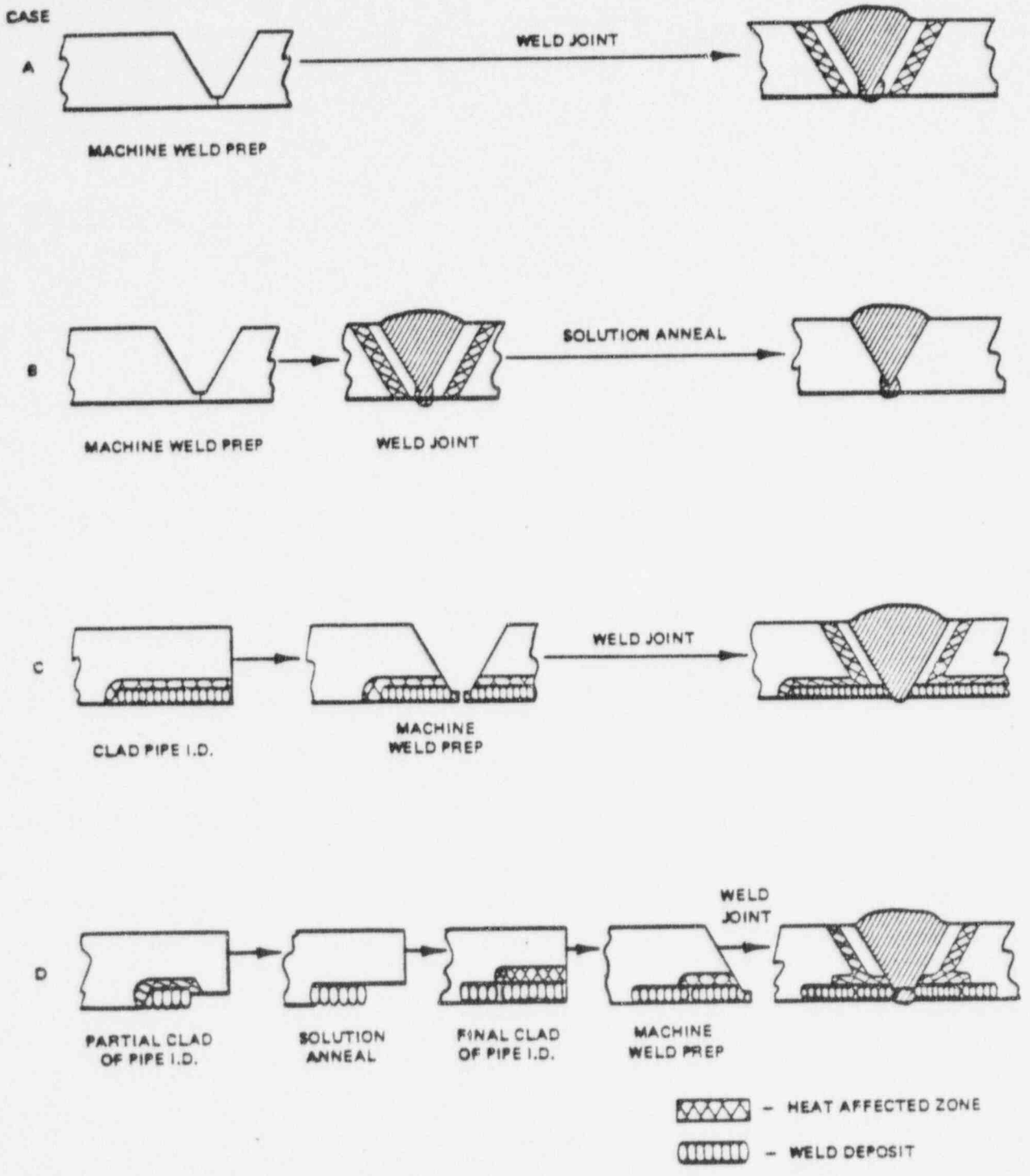

Figure 4-4. Schematic Showing Sequence of Fabrication Operations and Location of Heat-Affected Zones in Type-304 Stainless Steel Pipe Base Metal for Reference Welds (A), Solution Annealed Welds (B), Corrosion Resistant Clad Welds (C), and Annealed Corrosion Resistant Clad Welds (D)

The heat sink welds were represented by a single pipe of M7616 material with a total of 12 welds; six in the reference condition and six heat sink welded. Heat sink welding consisted of spray or flow cooling of the inside diameter surface of the pipe with water during welding and after completion of the root pass in the conventional manner. The location of the weld heat-affected zone would be nearly identical with that in a reference weld, but the degree of sensitization on the inside diameter surface should be significantly less and the residual stress level on that same surface should be significantly lower.

All specimens were prepared as consumable insert welds with an extended land configuration. The root pass and the second pass were made with the gun-tungsten arc process at a heat input of approximately 9500 joules per centimeter (23,000 joules per inch). The remaining passes were made with the shielded metal arc process at a heat input of approximately 12,200 joules per centimeter (31,000 joules per inch). All welds were ground on the inside diameter surface after the completion of welding except for the heat sink welded pipes and their reference welds. Heat input rates for weld cladding were approximately 7200 joules per centimeter (18,000 joules per inch).

4.3.2 Small Specimen Tests

The specimens utilized in this portion of the investigation were fabricated from Heat M7616. One set was prepared from a pipe weld made in the same manner as the reference condition pipe test welds; one set was prepared from a weld that was ground prior to welding; and a third set was prepared from a weld which had not been subjected to any grinding. All specimens were prepared in a manner which maintained the original pipe inside diameter surface in its original as-fabricated condition by making a deeper-than-normal counterbore in the weld preparation such that the finished weld root-side surface would represent one face of the final specimen reduced gage section. A normal reference weld was made in the pipe, and the inside diameter surfaces were ground after completion of the welding. Following this, the crown-side of the weld was machined to produce the second face of the reduced gage section in the finished specimen. Finally, longitudinal blanks were cut with the weld in the approximate center; the ends were threaded, and the reduced gage section sides were machined. The sequence of fabrication steps is shown graphically in Figure 4-5. Specimens were matched for gage section cross-sectional areas in groups of four, and were tested in high purity water at 288°C (550°F) with 8 ppm dissolved oxygen.

4.4 TEST MATRICES

4.4.1 Pipe Tests

The test conditions and number of welds tested are shown in Table 4-2. Pipe E19B is included in Table 4-2 and represents the heat sink welded tests, which were not originally part of the statistical design and for which a lower improvement factor would have been predicted. In addition, Pipe E20B is included to show the effects of test stress level.

4.4.2 Small Specimen Tests

The test conditions and numbers of small specimens tested are shown in Table 4-3. In addition, the conditions under which further tests were to be conducted under the original plan are also shown.

4.5 RESULTS

4.5.1 Pipe Tests

The results of the pipe tests are shown in Table 4-4. A number of failures occurred in Heat M7616 during the "same" loading cycle, in the most restrictive sense. That is, a failure would be observed during a given cycle and the pipe would be removed from test and repaired. The pipe would be returned to test, and another failure would be observed before another full loading cycle could be applied. Under these circumstances, the pipe would have seen only the original number of cycles but would have been exposed to the environment under some state of stress for some additional time. To assign the same times to failure to different failures under these circumstances would under-estimate the true variance of the stress corrosion cracking behavior of the material. Because of these

Table 4-2
STATISTICAL PIPE TEST MATRIX

Pipe Specimen	Pipe No.	Heat No.	Stress[1]	Welds
Reference	E18	M7616	136% (39.01 ksi)	12
Reference	E20-B	M7616	110% (31.7 ksi)	6
Reference	E12	454970	136% (29.8 ksi)	12
Reference	E11	M0063	136% (29.1 ksi)	12
Reference	E19-B	M7616	136% (39.0 ksi)	6
Heat Sink Welded	E19-B	M7616	136% (39.0 ksi)	6
Solution Anneal	E13	M7616	136%	12
Solution Anneal	E14	M0063	136%	12
Solution Anneal	E15	454970	136%	12
As-Deposited CRC[2]	E16	M7616	136%	12
As-Deposited CRC[2]	E24	M0063	136%	12
As-Deposited CRC[2]	E25	454970	136%	12
Solution Annealed CRC[3]	E32	M7616	136%	12
Solution Annealed CRC[3]	E34	M0063	136%	12
Solution Annealed CRC[3]	E35	454970	136%	12

NOTES: [1]Percent of 288°C (550°F) 0.2% offset yield strength
[2]Corrosion-resistant cladding
[3]Initial 1.25 cm (0.5 in.) of cladding was solution annealed prior to deposition of remainder.

90014125

Table 4-3
SMALL SPECIMEN TEST MATRIX

Condition	Stress[1]	Cycle Rate	Cycle Shape	Specimens
Reference[2]	136%	0.67/hr	Plateau[3]	4
Reference[2]	136%	0.67/hr	Ramp[4]	4
Reference[2]	136%	3.35/hr	Plateau[3]	4
Reference[2]	110%	0.67/hr	Plateau[3]	4
Reference[2]	90%	0.67/hr	Plateau[3]	4
Reference[2]	90%	3.35/hr	Plateau[3]	4
Reference[2]	90%	3.35/hr	Ramp[4]	4
Ground Before Welding	136%	0.67/hr	Plateau[3]	4[5]
Ground Before Welding	136%	3.35/hr	Plateau[3]	4[5]
Ground Before Welding	90%	0.67/hr	Plateau[3]	4[5]
Ground Before Welding	90%	3.35/hr	Plateau[3]	4[5]
Welded Without Grinding	136%	0.67/hr	Plateau[3]	4[5]
Welded Without Grinding	136%	3.35/hr	Plateau[3]	4[5]
Welded Without Grinding	136%	0.67/hr	Ramp[4]	4[5]
Welded Without Grinding	90%	0.67/hr	Plateau[3]	4[5]
Welded Without Grinding	90%	3.35/hr	Plateau[3]	4[5]

NOTES [1]Percentage of 288°C (550°F) 0.2% offset yield strength
[2]Ground after welding
[3]Identical to pipe test loading
[4]Slowly rising load
[5]Tests not performed

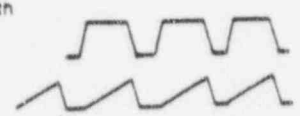

90014126

Table 4-4
STATISTICAL PIPE TEST RESULTS

Pipe Specimen	Pipe Number	Pipe Heat Number	Remarks	Time(s) To Failure (h)
Reference	E18	M7616	Ground after welding	104, 106,[2] 107,[2] 109[2]
Reference	E20-B	M7616	Machined and welded—not ground	620, 838, 1003, 1351, 1362
Reference	E12	454970	Ground after welding	3253, 3342, 3553
Reference	E11	M0063	Ground after welding	1067, 1140, 1144, 2132
Reference	E19-B	M7616	Machined and welded—not ground	101, 140, 145, 150,[2] 163, 430[4]
Solution Anneal	E13	M7616	Solution anneal after welding and grinding	No Failures in 5000 hrs
Solution Anneal	E14	M0063	Solution anneal after welding and grinding	No Failures in 5187 hrs
Solution Anneal	E15	454970	Solution anneal after welding and grinding	No Failures in 5748 hrs
As-Deposited Corrosion Resist Clad	E16	M7616	Ground after welding	714, 856, 1254
As-Deposited Corrosion Resist Clad	E24	M0063	Ground after welding	No Failures in 6806 hrs
As-Deposited Corrosion Resist Clad	E25	454970	Ground after welding	No Failures in 5924 hrs
Solution Annealed Corrosion Resist Clad	E32[3]	M7616	Ground after welding	No Failures in 5204 hrs
Solution Annealed Corrosion Resist Clad	E34[3]	M0063	Ground after welding	No Failures in 6806 hrs
Solution Annealed Corrosion Resist Clad	E35[3]	454970	Ground after welding	No Failures in 5825 hrs

NOTES: [1]Included to provide better estimate of variance on Heat M7616
[2]Assigned time of failure
[3]Initial 1.25 cm (½ in.) of corrosion-resistant clad was solution annealed prior to deposition of remainder.
[4]Failure in a repaired weld

90014127

Table 4-5
COMPARISON OF STRESS CORROSION CRACKING BEHAVIOR OF AS-WELDED 304 SS (Heat M7616) IN SMALL SPECIMEN VARIABLE LOAD TESTS
(HIGH PURITY WATER AT 288°C (550°F) CONTAINING 8 ppm DISSOLVED OXYGEN)

Stress[1]	Cycle Rate	Cycle Shape	Cycles To Failure				Hours To Failure			
			1	2	3	4	1	2	3	4
136%	0.67/h	Plateau[2]	56	82	86	163	84	122	128	244
136%	0.67/h	Ramp[3]	103	415	131	150	153	620	196	224
136%	3.35/h	Plateau[2]	302	355	382	335	90	106	114	100
110%	0.67/h	Plateau[2]	637	405	446	446	950	605	666	666
90%	0.67/h	Plateau[2]	No Failures at 1800 Cycles				No Failures in 2686 Hours.			
90%	3.35/h	Plateau[2]	No Failures at 2100 Cycles				No Failures in 3134 Hours.			
90%	3.35/h	Ramp[3]	No Failures at 6300 Cycles				No Failures in 1880 Hours.			

NOTES: [1]Percentage of 288°C (550°F) 0.2% yield strength
[2]Identical to Pipe Test Laboratory loading
[3]Slowly rising load

90014128

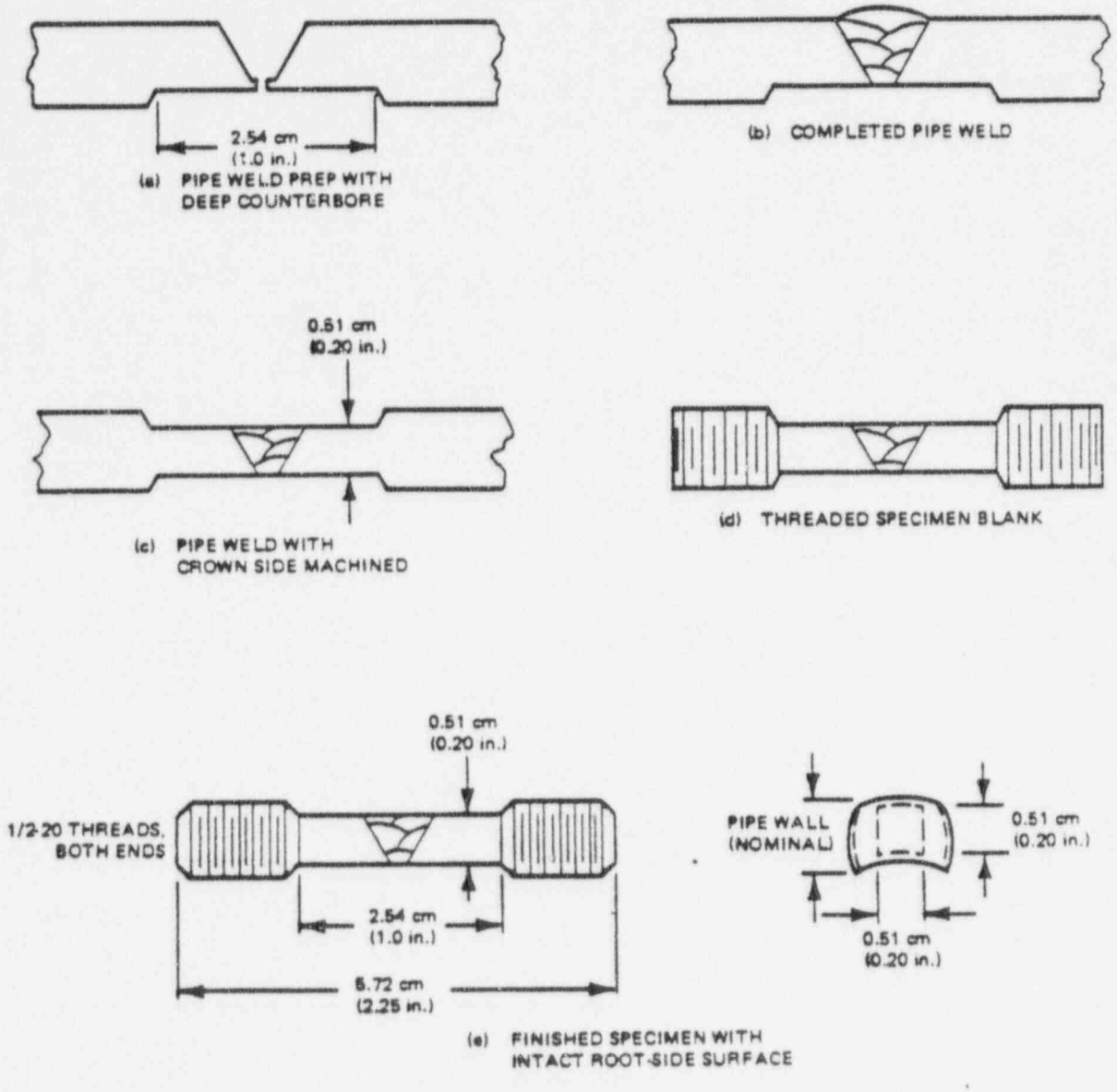

Figure 4-5. Fabrication Sequence for Small Specimens to Produce Centered Gage Section with Undisturbed Root-Side Surface

90014129

considerations, failures of this type were assigned to the next cycle and the time to failure was calculated based on that number of cycles.

4.5.2 Small Specimen Tests

The results of the small specimen tests are shown in Table 4-5. No assignment of failure times was necessary in this portion of the investigation.

4.6 FAILURE ANALYSIS

4.6.1 Reference Type-304 Pipe

As indicated in Table 4-4 all reference Type-304 stainless steel pipes have experienced failures in at least three weld joints. Destructive evaluation has been performed on one or more of the welds from each heat. This evaluation was made to determine, in each case, if the failure was intergranular stress corrosion cracking representative of field failures.

Pipe E18 fabricated from Heat M7616 failed in the pipe test at four welds in a short period of time. All other welds showed large UT indications. Weld K was destructively examined. The crack initiation and growth to the point of ductile fracture is intergranular, Figure 4-6. This failure is typical of Type-304 stainless steel failures in previous pipe tests. Except for the ductile propagation at the end of the crack caused by the load controlled nature of the pipe tests, it is representative of field failures.

Two failures in pipe E11 were examined. Pipe E11 experienced an overload of approximately 33 percent upon reload after the third failure. This had the effect of greatly extending time to the fourth failure. A UT examination after the fourth failure showed deep cracks greater than 100% full screen height in five welds. Because of the increase in failure times, it was decided to destructively examine one failure from before the overload, and one following the overload. Both welds examined showed fully intergranular appearance until the ductile region. Figure 4-7 is an SEM photo of a typical area of the weld F crack while Figure 4-8 shows the crack initiation in weld C in a metallographic section.

It has been previously observed in Type-304 stainless steel that crack growth rates can be temporarily slowed after a short term specimen overload. An overload changes the material at the crack tip by increasing the plastic zone size. Cold work is increased, and residual strains will remain. The net effect is, that even though the crack is driven more rapidly during overload, a net decrease in growth rate is observed if the overload duration was short.

The lowest carbon content heat of Type-304 stainless steel used in this study was the 0.042 carbon heat used for pipe E12. During the tests three weldments developed through wall cracks after greater than 3000 hours. These failures, two of which were destructively examined, were not like typical failures in higher carbon heats or in field piping. Figure 4-9 is a Scanning Electron Microscopy Photograph of the through wall fracture surface of weld B. It is apparent from the enlarged views in Figure 4-10 that the crack initiation and growth to about 60 mils is intergranular. Figure 4-11 is a similar region from weld K with the oxide removed. In weld B, at a depth of about 60 mils a small ductile tear is present which is followed by a fracture surface which is characterized by transgranular cleavage. Some intergranular penetrations and grain facets are also visible in this area. In Figures 4-12 and 4-13, which show this region at about 120 mils and 190 mils depth respectively, features with an appearance similar to striations can be seen. The final crack propagation is ductile to overload caused by the reduced cross section. In Figure 4-9 the region beyond the ductile area (the lower 3.5 cm of the photograph) which goes out of focus is the o.d. surface of the pipe showing the typical surface achieved after grinding.

The appearance of the samples discussed above from Pipe E12, a low carbon heat, (0.042 percent) is not typical of higher carbon material tested in the pipe test or of field piping failures. The intergranular initiation and propagation is typical of field IGSCC cracks, but the region showing cleavage and striation like features appears to be an artifact of the test. Since the pipe test is a cyclic test, it would be easy to conclude that the 'striations' result from fatigue loading. Previous non-cyclic tests at General Electric*, however, have produced fracture surfaces with areas of cleavage very similar to that found in the present pipe test.

* Clarke, W.L., Cowan, R.L. and Walker, W.L., "Comparative Methods for Measuring Degree of Sensitization in Stainless Steel," Intergranular Corrosion of Stainless Steel Alloys, ASTM STP 656, R.F. Steigerwald, Ed., American Society for Testing and Materials, 1978, pp. 99-132.

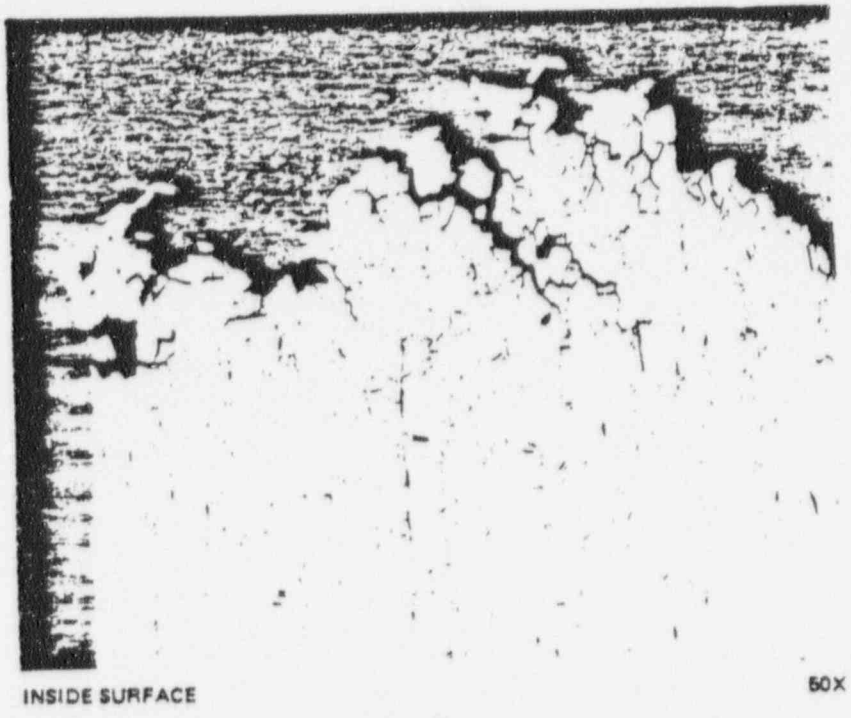

Figure 4-6. Pipe E18, Intergranular Fracture of Weld K

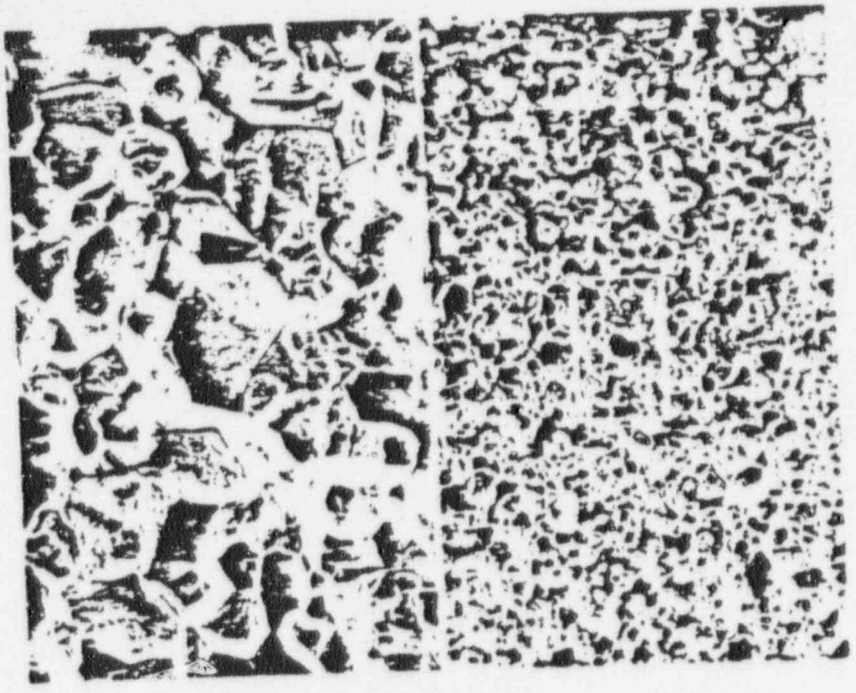

Figure 4-7. Pipe E11, Typical Region of Intergranular Cracking of Weld F (30 and 150X)

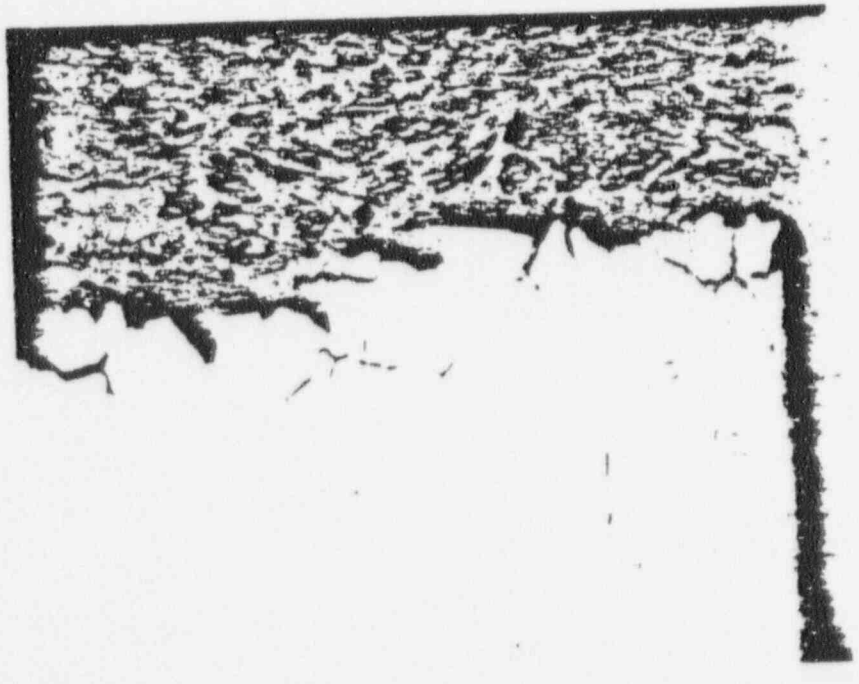

Figure 4-8. Pipe E11, Inside Surface and Intergranular Appearance of the Crack, Weld C

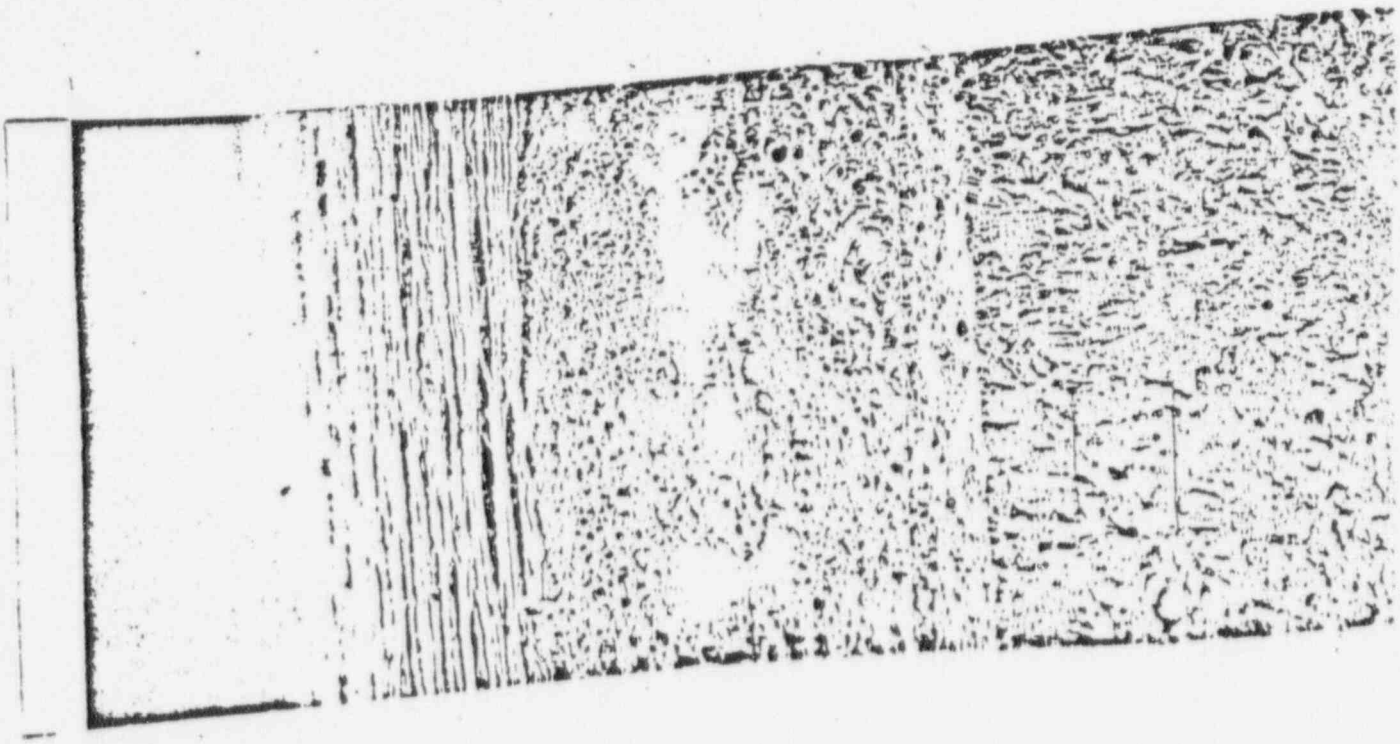

OUTSIDE SURFACE OF PIPE

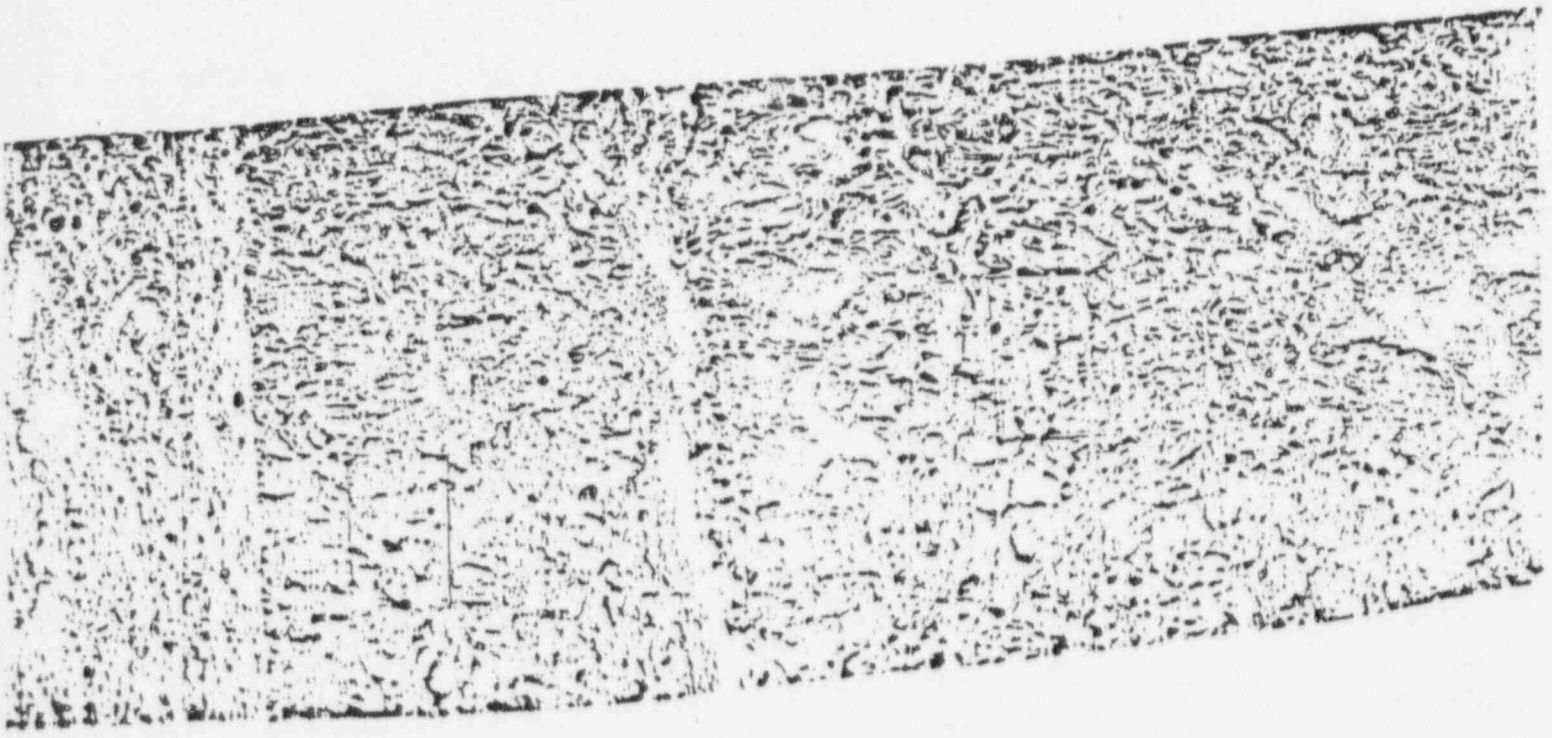

Figure 4-9. Pipe E12, Weld B Intergranular Cr
of Ductile Overload Boxed Areas a

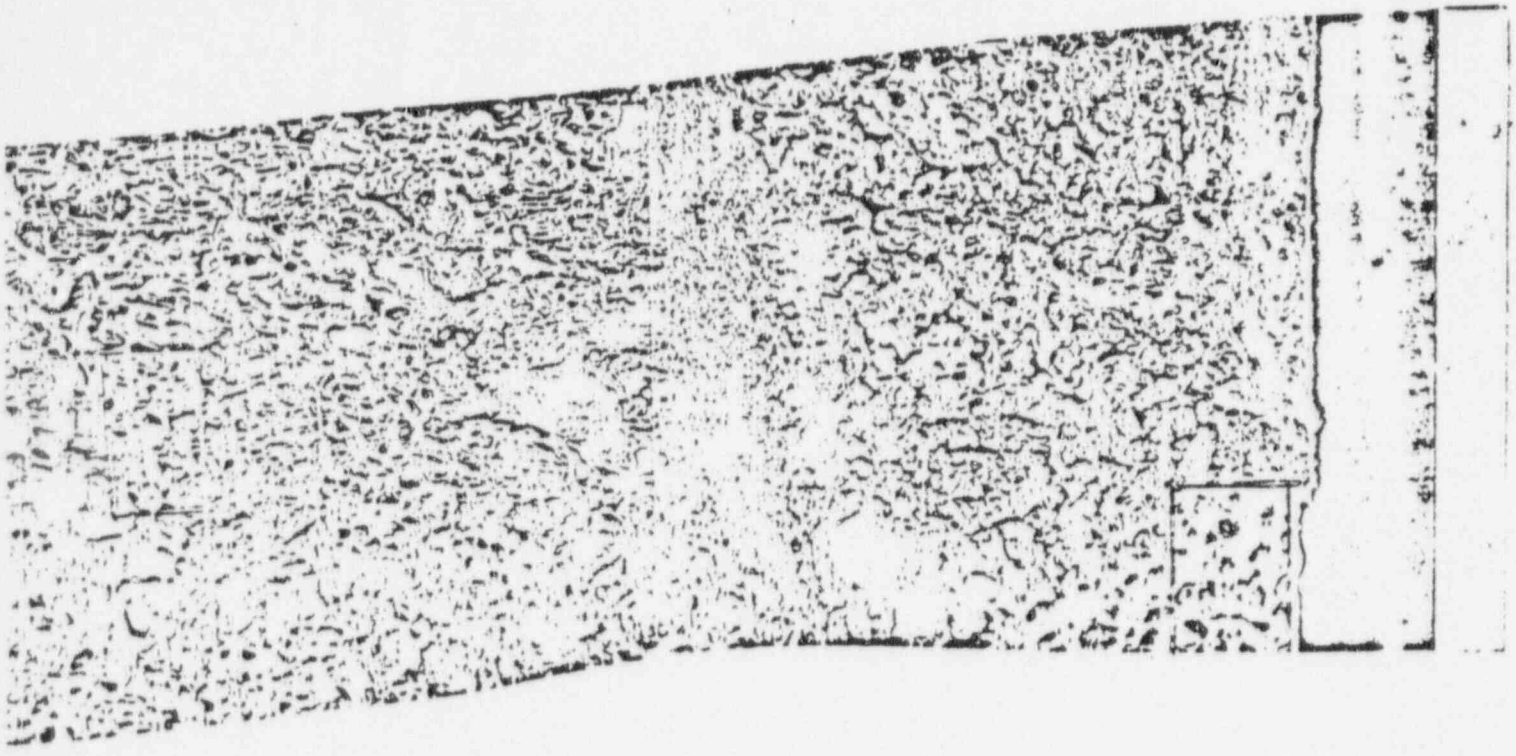

Figure 4-9. Pipe E12, Weld B Intergranular Crack Initiation and Propagation Followed by Cleavage Fracture to Point of Ductile Overload Boxed Areas are Enlarged in Figures 6-5, 6-7 and 6-8

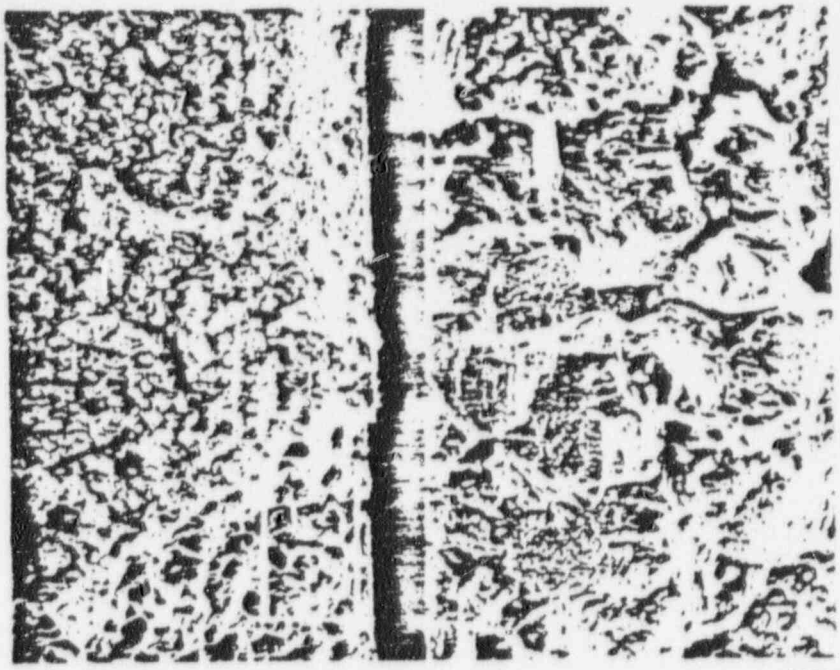

Figure 4-10. Area Near Inside Surface of Weld B (50 and 250X)

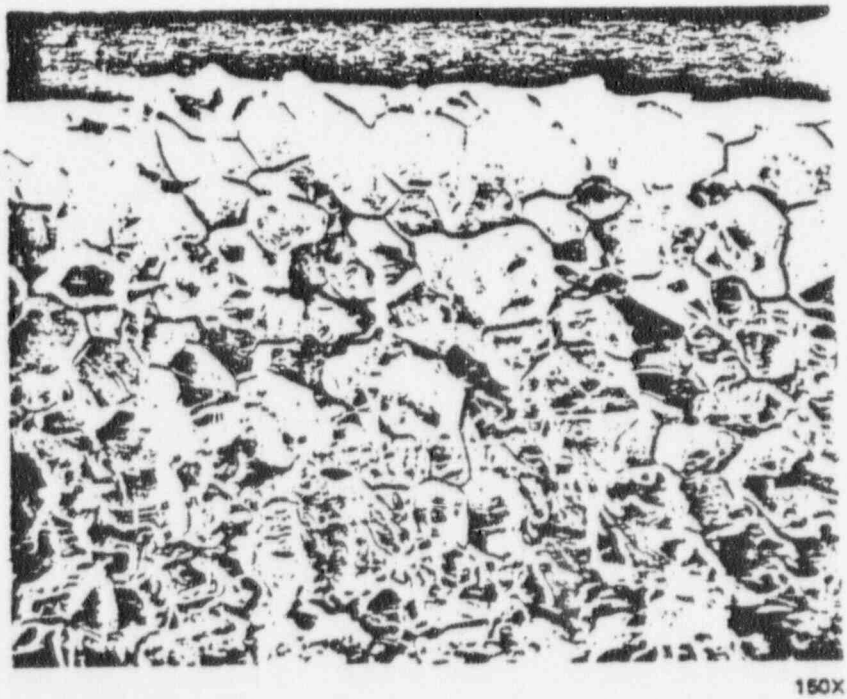

Figure 4-11. Area, Similar to Figure 6-5, from Weld K with Oxide Removed (150X)

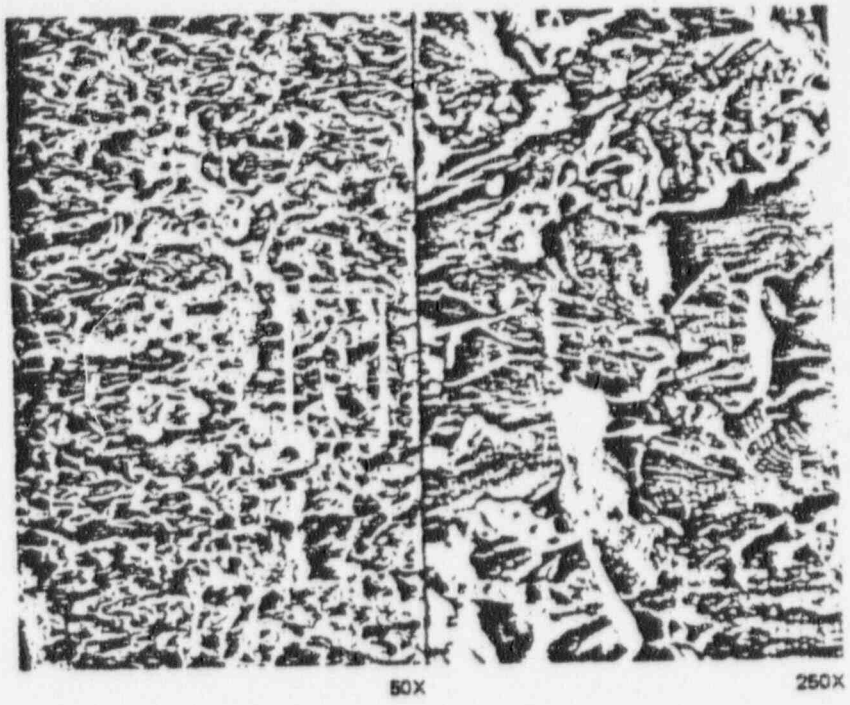

Figure 4-12. Area at Mid-Wall of Weld B (50 and 250X)

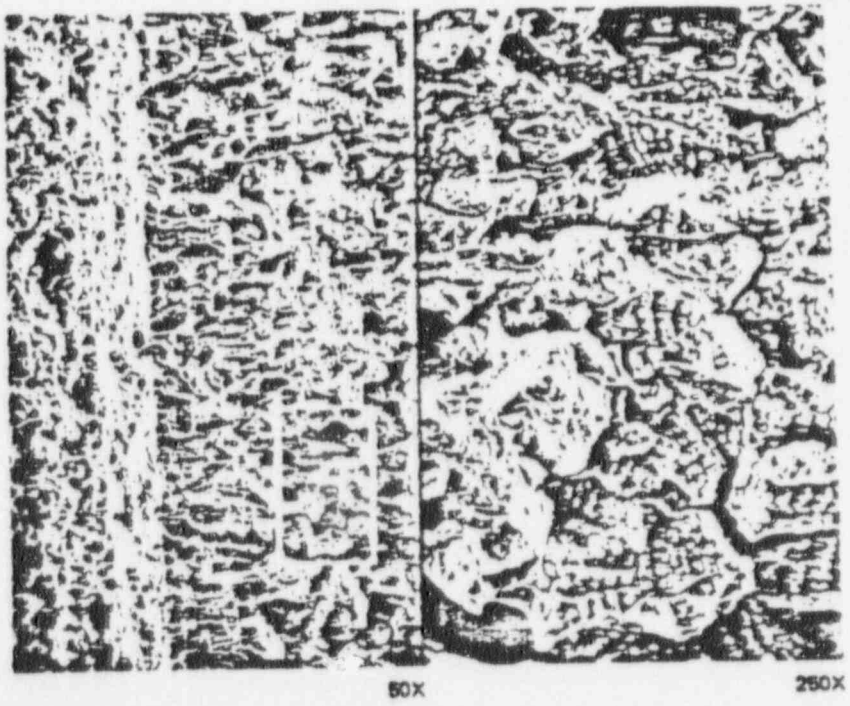

Figure 4-13. Area Near Outside Surface of Weld B (50 and 250X)

It was found that these fracture surfaces occurred in high stress and high strain tests such as the constant extension rate test, and on samples of material which were lightly sensitized. More heavily sensitized materials were generally completely intergranular. This behavior is consistent with the current pipe test results in which this failure and similar ones in Types-316L and 347 have occurred in heats which would be characterized as lightly sensitized. It can be concluded that although this non-intergranular crack propagation may or may not be fatigue, it is an artifact of the test and is not relevant to any BWR service related phenomena.

4.6.2 Solution Heat Treated Welds

No failures have occurred in any of these welds and thus no failure analysis was performed.

4.6.3 Corrosion-Resistant Clad Welds — Shop Version

No failures have occurred in the corrosion-resistant clad remedy in which a portion of the cladding is solution heat treated. Failure analysis was therefore not performed.

4.6.4 Corrosion-Resistant Clad Welds — Field Version

Three pipes were fabricated to test the field version of corrosion-resistant cladding. In the field version (shown in Figure 4-4), a small area of base metal can be sensitized by cladding deposition. Of three heats of Type-304 stainless steel used in this study failures of this remedy have occurred only in Heat M7616 (pipe E16). The first failure in the as-deposited corrosion-resistant cladding weld originated in the base metal of Heat M7616 0.18 cm (0.07 in.) from the edge of the deposited cladding, and propagated in an intergranular manner. The results of dye penetrant examination of the i.d. surface of the failed weld and an adjacent weld with an incipient crack are shown in Figure 4-14 and a metallographic section through the crack is shown in Figure 4-15. The results are consistent with the constant extension rate test results presented in Subsection 3 of this report, in which an as-deposited cladding specimen from weld 26B failed by IGSCC and are predictable since this heat of material was sensitized in the as-received condition.

Because Heat M7616 was sensitized in the as-received condition the repair of the first failure was made with a section of M7616 which was solution heat treated prior to application of cladding. This procedure it was hoped would leave the material in a condition which would not be susceptible to IGSCC. Subsequent to this repair however, another failure occurred similar to the first. This failure was repaired by Heat Sink Welding. A third failure then occurred between the Heat Sink Weld and the edge of the as-deposited cladding. Failure analysis was performed on the third failure. Figure 4-16 shows two different azimuths cut from the failed pipe. Section 1 is at the through wall portion where initiation occurred in the HAZ of the as-deposited cladding. From the ASTM A262 Practice an etch performed, Figure 4-17, it is apparent that the material in this region is heavily sensitized. In Figure 4-18 the Heat Sink Weld is at the right. Here, a shallow intergranular crack has initiated near the weld in a heavily sensitized zone. The base metal appearance of this pipe segment in a region not sensitized by either the cladding or Heat Sink Weld is shown in Figure 4-19. Although this pipe was solution heat treated in the laboratory prior to welding, some of the grain boundaries are ditched reflecting a light degree of sensitization. This degree of sensitization is not enough to cause cracking as evidenced by the successful performance of pipe E13 (Heat M7616). It does represent, however, a material condition in which the sensitization process has already begun and thus is highly susceptible to even slight subsequent thermal treatments like the cladding deposit or the Heat Sink Weld. The fact that the Heat Sink Weld initiated a crack can be explained by one of several possible factors.

1. The close proximity of the corrosion-resistant cladding and butt weld which might interfere with typical residual stress distribution setup after a HSW.

2. Solution Heat Treatment of stainless steel significantly reduces the yield strength due to relief of residual cold work. This would cause greatly increased strains in this region since the pipe was loaded to 136% of the non-SHT yield strength of M7616.

These and other possible causes are being investigated. It should be noted that no failures have occurred in the four Heat Sink Weld pipes which are a part of this study and are fabricated from Heat M7616.

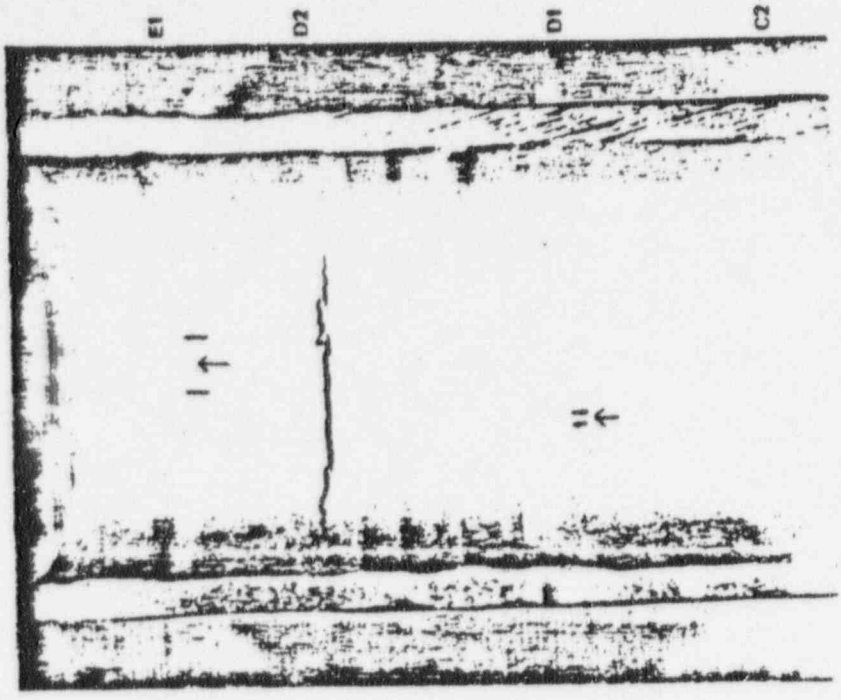

Figure 4-14. Dye Penetrant Examination of Inside Surface of Failure on Pipe E16. A Second Initiated Crack is Visible Near the Adjacent Weld (~0.5X)

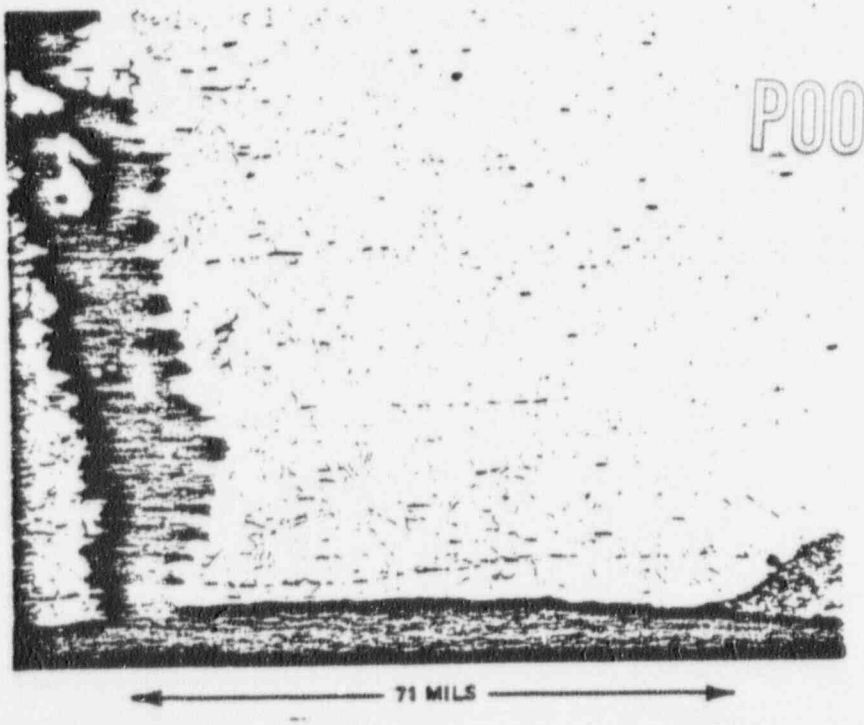

Figure 4-15. Photomicrograph of Failure in Pipe E16. Inside Diameter Surface is at Bottom of Photo, and the Edge of the Cladding is at Bottom Right (45X)

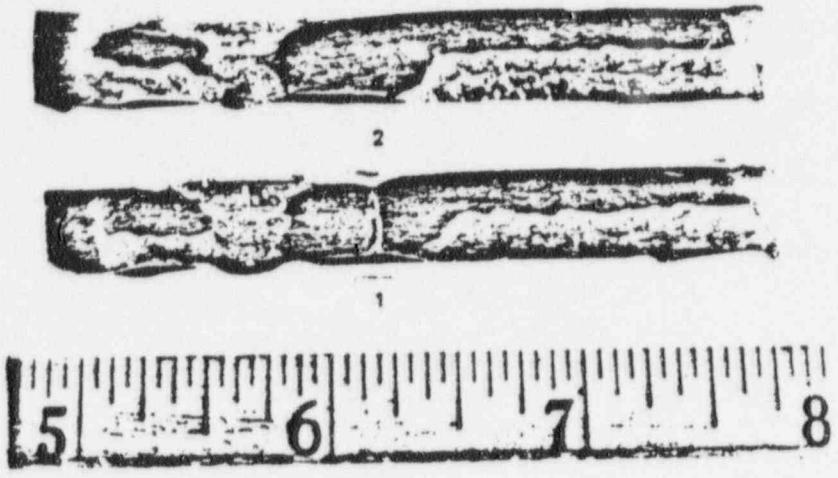

Figure 4-16. Photomicrograph of Through-Wall Crack Near Cladding (1) and Shallow Crack Near Heat Sink Weld (2)

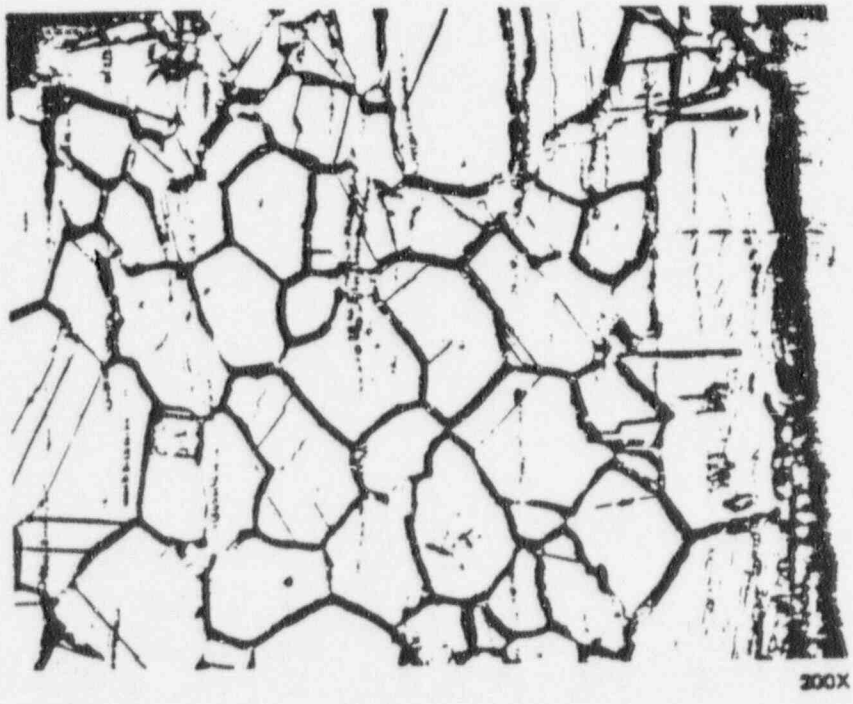

Figure 4-17. Ditching in ASTM A262 Practice A Sensitization Test Near Cladding (200X)

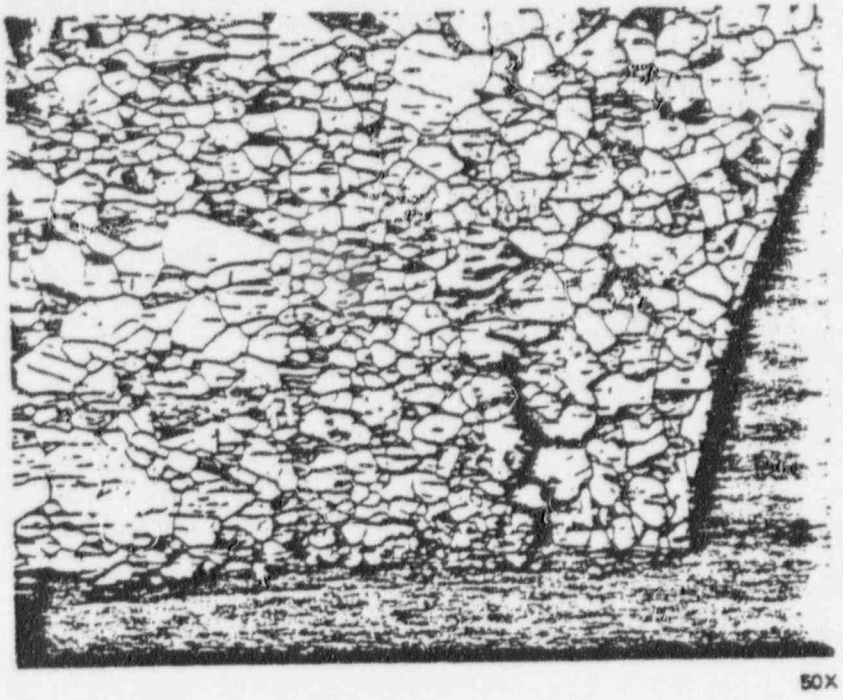

Figure 4-18. Crack Near Heat Sink Weld Repair (50X)

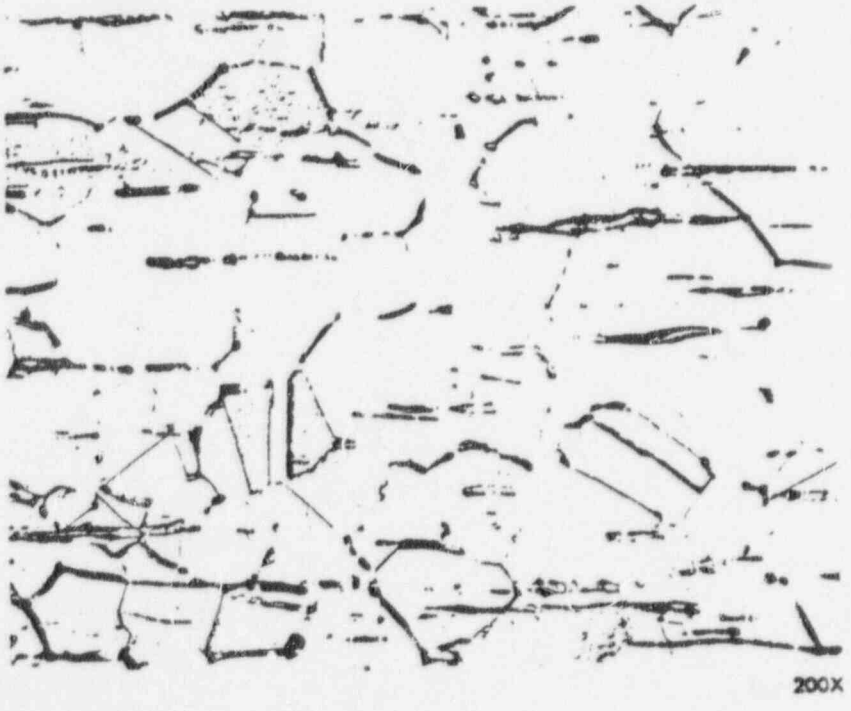

Figure 4-19. ASTM A262 Practice A of Base Metal from Heat M7616 after Solution Heat Treatment (200X)

4.7 CALCULATIONS

4.7.1 Pipe Tests

The model utilized in this investigation assumes that the variances of the distributions of times to failure of materials in the reference condition and in the remedy condition are approximately equal. For calculation purposes, it was also assumed that the distribution of individual times to failure in any condition would be approximately log-normal. This assumption is not critical to the model; the model will accommodate any distribution shape. Since not all reference welds have failed to date, it is not possible to calculate directly the distribution parameters of interest; that is, the mean and the variance of the distribution of individual times to failure of Type-304 stainless steel in the as-welded condition. While these parameters cannot be calculated directly, it is possible with the data generated in this investigation to estimate them using methods developed by Nelson and Schmee*. An additional assumption of normal or a log normal distribution is required for this approach. Plotting the log of failure times on normal hazard paper yields a straight line for each heat; indicating that the log normal approach is valid.

The various remedies can be evaluated on the basis of the behavior of heats individually or on the basis of the three heats combined into one population. Initially, it was believed that calculations based on the entire population (three heats combined) would yield the most useful information. This was found to be incorrect. Two major problems which are interrelated caused difficulties in the calculations and caused the results to be of little value. First, the interheat variance in failures times was very large and tended to overwhelm the intraheat variance. Second, the failure times for reference welds in two heats were so long relative to Heat M7616 that these heats in the reference condition could be considered remedies relative to M7616. In order to show the desired factor of improvement in this situation, one would have to run all remedies more than 230 times as long as the Heat M7616 reference pipe. This was an impractical proposition.

Because the above approach proved to be infeasible, improvement factors were calculated for each heat separately. The formula used for the calculation of the time on test required to demonstrate some given improvement factor is shown below:

$$\text{Log Test Time} = F + G + \sigma \left[-Q + U\,(1/n + r)^{1/2} \right]$$

Where:
- F = mean log time to failure of reference welds
- G = log of desired improvement factor
- σ = standard deviation of log times to failure of reference welds
- Q = factor on σ for expected location of first order statistic ($Q = 1.5864$ for n of 11)'
- U = normal distribution coefficient for 90% one-sided limit ($U = 1.282$)
- ν = number of test welds per remedy ($n = 11$)'
- r = factor on σ^2 for variance of first order statistic ($r = 0.3332$ for $n = 11$)

NOTE:

While there are 12 welds in each test pipe section, one heat-affected zone of each end weld is located in the transition piece rather than in the test pipe material. This results in 10 whole welds and two separate heat-affected zones in the reference material, which were added together for a total of 11.

The Nelson and Schmee approach permits one to estimate the mean and standard deviation of a series of failures, based on time-limited early failures. Using this method, and assuming a log-normal distribution of individual failures, one can arrive at an approximation of the population parameters and from those values; one can estimate the minimum running time required to demonstrate the desired improvement factor of 20 for each heat. For each of the three heats of Type-304 stainless steel pipe, the Nelson and Schmee approach was used to estimate the mean and

* W.B. Nelson and J. Schmee, "Estimates and Approximate Confidence Limits for (log) Normal Life Distributions from Singly Censored Samples by Maximum Likelihood". Report No. 76CRD250, General Electric Co., April 1977.

standard deviation for the reference condition. Substitution of these values and the log of the test time accumulated to date into the above equation yields the anti-log of the current improvement factor. Where failures have occurred in a remedy pipe, the time to first failure is used rather than total accumulated time. One can also substitute the log of 20 for G and calculate the required time to reach a factor of 20 improvements. All of these calculations have been performed and the results tabulated in Table 4-6. A sample calculation is found in Appendix M.

The results of the statistical treatment of test times to show factors of improvements summarized in Table 4-6, reveal that in Heat M7616, two remedies have far surpassed the improvement goal of 20 times. These remedies, solution heat treatment after welding, and solution annealed corrosion-resistant cladding have reached factors of 46.3 and 48.2 respectively. The third remedy in Heat M7616, as deposited corrosion resistant cladding, fell short of the goal with an improvement of 6.6. The causes of this failure are discussed in the failure analysis section 6.0.

The other two Heats M0063 and 454570 have not yet reached the desired goal of 20 times improvement over the reference in any of the remedies. This failure to reach the goal of 20 reflects the time limitation of the current program only and does not represent a failure of any remedy to perfrom satisfactorily. It is apparent from the failure times of these two heats in the reference condition --- Table 4-4 --- that both are relatively resistant to IGSCC in the reference condition. This should not be unexpected since the carbon levels for the two heats are 0.042% and 0.050%. In an analysis performed under EPRI Contract RP 968 it has been shown that most field failures in BWR piping have occurred in greater than 0.050 percent carbon piping. In fact the available data indicate that with a 90% confidence, 90% of the field failures have occurred in greater than 0.050% carbon material. The significance of carbon content is evident in pipe test results when failure times are studied. For all Type-304 stainless steel (more than 10 heats) in the RP 701 and RP 968 programs with greater than 0.050 percent carbon, the average time to first failures for the failures to date is about 100 hours. This is in contrast to the times to first failure of 1067, and 3253 hours for Heats M0063 and 454970 respectively. Thus, attempting to show a factor of 20 improvement when applying a remedy to an already very resistant heat is a very time consuming goal, one that could not be accomplished within the time constraints of this program; and one that is not necessary.

An estimate of the improvement factor obtained utilizing heat sink welding in test pipe E19B on a single heat of Type-304 stainless steel (M7616) can be obtained in the same manner as those for the other remedies. The values of the variables substituted into the equation are different, however, because of the smaller number of specimens involved. Using this approach, yields an improvement factor of 9.3 for the heat sink welds in pipe E18B. No failures have occurred in any of the heat sink welds in pipes E19A, 19B, 20 A or 20B. Pipe E19B shows the largest improvement because the reference welds fail more quickly than in the other three pipes. Efforts to accumulate long test times on these pipes have been hindered by the fact that reference welds were in the same pipe as the remedy resulting in test interruption of the Heat Sink Welds everytime a reference weld had to be repaired. Heat Sink Welding is expected to show a factor of 20 improvement in continued testing.

4.7.2 Small Specimen Tests

The only statistical calculations performed upon the data from this portion of the program were simple tests of the significance of the differences of mean times to failure of reference condition small specimens and reference condition full-size pipes. These tests indicated that the differences were not significant at the 0.10 level, or greater, for small specimens tested under the same conditions as pipes. In addition, the difference in times to failure between small specimens tested at 3.35 cycles/h and 0.67 cycles/h was not significant at the 0.10 level.

Comparisun of the results obtained from plateau loading at rates of 0.67 and 3.35 cycles per hour provides some indication of the rate controlling mechanism in IGSCC. While the number of cycles to failure at the higher rate was approximately five times that at 0.67 cycles per hour, the times to failure were nearly the same. This indicates that, within the range tested, cycling rate has little or no effect on IGSCC initiation and propagation; and that the controlling factor is time under load. This conclusion is also supported by the results obtained from ramp loading at 0.67 cycles per hour. Specimens loaded in this manner exhibited a significantly longer time to failure than those tested at the same stress level and cycle frequency with a plateau loading which would result in greater time at maximum load.

Table 4-6

Heat	Remedy	Factor of Improvement
M7616 (0.060% C)	Solution Heat Treatment	46.3
	Corrosion-Resistant Cladding (solution annealed)	48.2
	Corrosion-Resistant Cladding (as-deposited)	6.6*
	Heat Sink Welding	9.3*
M0063 (0.050% C)	Solution Heat Treatment	4.6
	Corrosion-Resistant Cladding (solution annealed)	6.0
	Corrosion-Resistant Cladding (as-deposited)	6.0
454570 (0.042% C)	Solution Heat Treatment	1.6
	Corrosion-Resistant Cladding (solution annealed)	1.6
	Corrosion-Resistant Cladding (as-deposited)	1.7

*Based on first failure.

90014144

4.8 DISCUSSION

4.8.1 Pipe Tests

All failures observed in this portion of the program have been at least partly intergranular in nature, and have occurred in weld heat-affected zone material. The fracture surface of Pipe E12 (Heat 454970) showed areas of cleavage, a phenomena previously seen in high stress and strain stress corrosion test failures of lightly sensitized specimens. This kind of fracture is considered to be an artifact of the severe test and is not representative of field failures.

While the true mean time to failure of the three heats in the reference condition is not directly available from the data generated at this time, a reasonable estimate can be made; particularly in light of the small relative standard deviations in times to failure of multiple welds from the individual heats of pipe. The principal source of variation in stress corrosion cracking behavior under similar test conditions appears to be due to variations in resistance between different heats of Type-304 stainless steel. The variation due to all other sources combined in relatively small. Heat-to-heat variables would appear to produce differences in susceptibility to stress corrosion cracking by factors as large as 30. As discussed in the calculations section 4.7.1, carbon content is a significant contributor to heat-to-heat variability. A factor related to carbon content and residual cold work, the yield strength of each heat of material, may also be a contributor to variation in failure times. The understanding of the influence of this factor comes with the recognition that while the percentage of yield strength at which the tests were performed was the same for all materials, the absolute stress levels at which they were tested were different.

The test stresses for the three heats were as follows:

M7616 — 269 MPa (39.0 ksi); 454970 — 214 MPa (31.1 ksi);
M0063 — 201 MPa (291 ksi).

If one were to assume that the stress dependency exhibited by both pipe tests and small specimen tests from Heat M7616 applied across all heats of Type-304 stainless steel, then the order in which the three heats have exhibited failures is exactly that which would have been predicted. An analysis of the combined effect of carbon content and test loading could be useful in studying failures in the pipe test.

4.8.2 Small Specimen Tests

All failures were intergranular in nature and occurred in the weld heat affected zone, as shown in Figure 4-20. However, approximately half of the failures originated on the intact weld root-side surface and the other half originated on the crown-side surface which was machined after welding. No failures originated on either of the transverse (circumferentially oriented) sides of any specimen, although these surfaces were also machined after welding. Examination of the three different surfaces revealed that the surface finish on the transverse sides was much finer than that of either the root or crown sides of the specimens, as shown in Figure 4-24. These results would indicate a significant interaction between surface cold work and sensitization in the initiation of IGSCC. The results also indicated that the testing of specimens which had either not been ground, or had been ground prior to welding would not yield results which could be clearly interpreted because the probability of failure initiation on the crown-side surface was equal to that on the root-side surface of the reference condition. Investigation of grinding effects, utilizing small specimens, will require a different fabrication sequence than that used in the preparation of these specimens.

Examination of the data obtained from the small specimen tests shows excellent absolute agreement with data generated in full-size pipe tests, as shown in Table 4-4. The mean times to failure for small specimens tend to be slightly longer than for pipes, but the differences are not significant at the 0.10 level. A bias in this direction is not surprising because the circumferential surface area of a small specimen is only approximately 7% of that of a pipe weld if both the root and crown sides of the small specimen are considered as likely initiation sites. This excellent agreement between the two tests is observed at test loadings of 136% and 110% of the yield strength, although at the lower loading the mean time to failure of the small specimens is slightly less than that of the pipes.

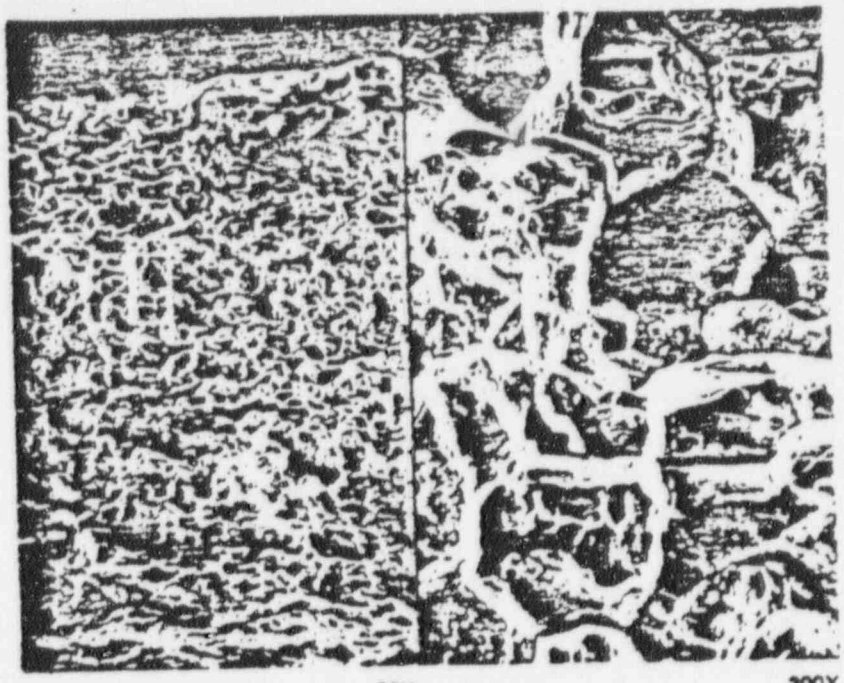

30X 300X

(a) SCANNING ELECTRON PHOTOMICROGRAPH OF FRACTURE FACE OF SPECIMEN

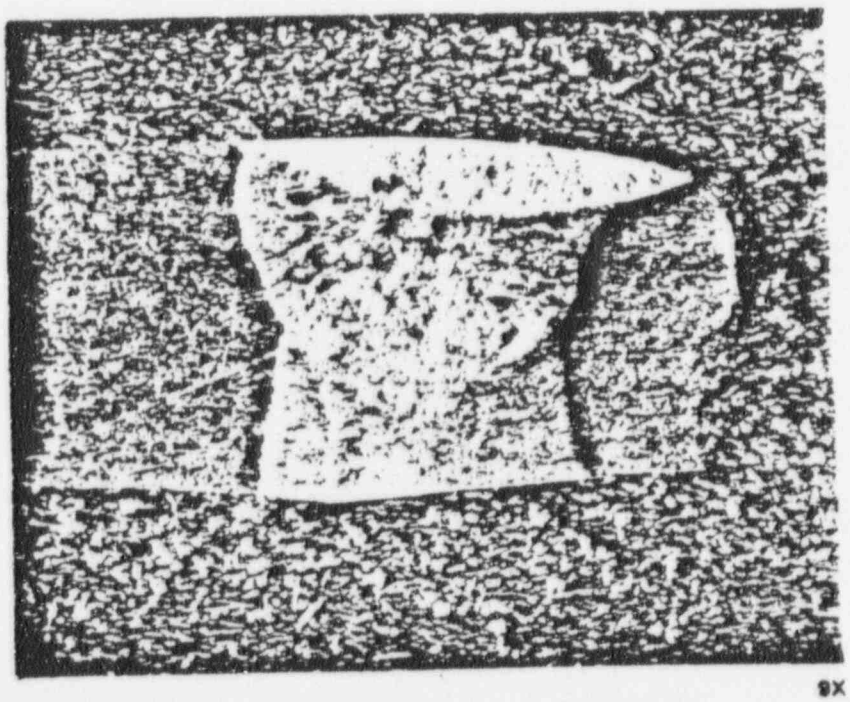

9X

(b) POLISHED AND ETCHED SECTION THROUGH FAILED SPECIMEN

Figure 4-20. Typical Small Specimen Failure

100X

SIDE OF SPECIMEN, GROUND AFTER
LETION OF WELDING

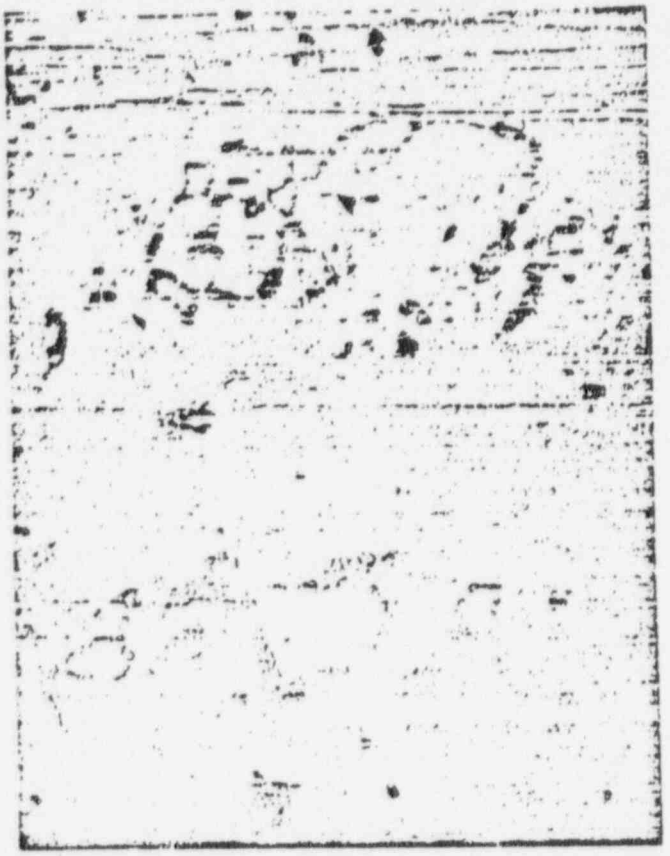

100X

(b) CROWN SIDE OF SPECIMEN, MACHINED AFTER
COMPLETION OF WELDING

(c)

Figure 4-21. Compa

100X

SPECIMEN, MACHINED AFTER
F WELDING

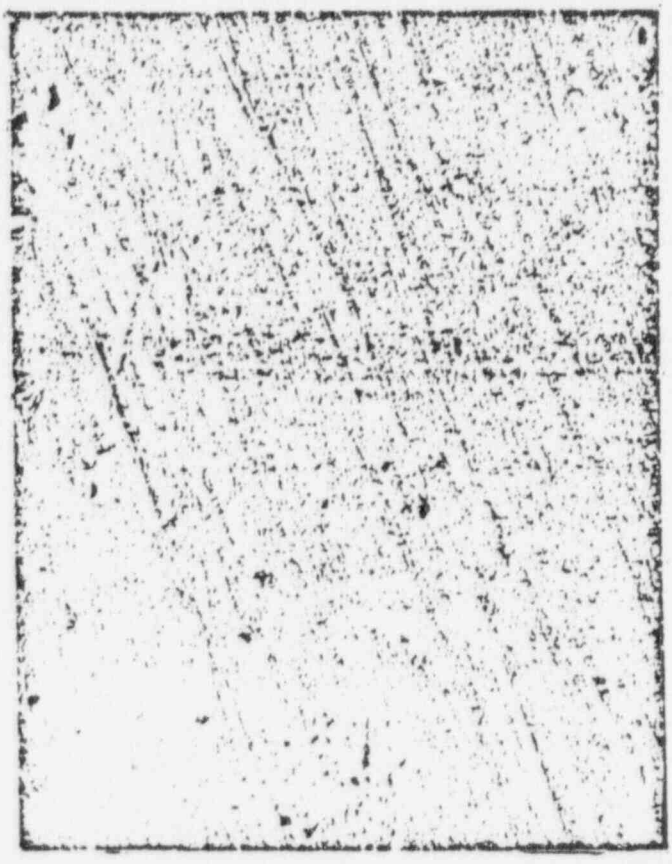

100X

(c) THROUGH-WALL SIDE OF SPECIMEN, MACHINED AFTER COMPLETION OF WELDING

Figure 4-21. Comparison of Small Specimen Reduced Gage Section Surfaces

However, load cycling per se does have a significant effect on IGSCC of welded specimens from Heat M7616. Constant load tests on welded specimens from this heat were performed in 288°C (550°F) high purity water with 8 ppm oxygen at higher stress levels, and the variance of observed times to failure was much greater. Some constant load failures were as short as cyclic load failure times, but the mean time to failure for constant load tests was longer than for cyclic tests.* Stress level has a very pronounced effect on IGSCC, as indicated by the data obtained from plateau loaded specimens at 136% and 110% of the yield strength. If a linear relationship between stress and time to failure is assumed to exist (see Figure 4-22) then the slope of the curve is approximately −0.06. This same approximate slope was obtained from full pipe specimens from Heats M7616 and M0063. If the curve were linear over the major portion of the range, one would predict that failure of the specimens loaded to 90% of the yield strength should occur at approximately 2500 hours or 3700 cycles. As of this writing, the specimens have accumulated only approximately one-half of this exposure. It is recognized that the stress dependency curve is not linear over its entire extent; the upper limit represents a slow strain rate test with both stress corrosion cracking and ductile rupture mechanisms operating in the failure, and the lower limit is that stress level at which IGSCC will not initiate. While the upper limit is relatively well defined, the lower limit is not at this time.

4.9 SPECIAL STUDIES

Three additional special studies were performed in Task 2. A complete presentation of each is found under the following subjects in Appendices J, K, and L.

1. Analysis of Constraint Near Pipe Welds — Comparison Among Different Diameter Pipes
2. Measurement of Constraint Near Pipe Welds — Comparison Among Different Diameter Pipes
3. Effect of Surface Condition on the Surface Integrity of Strained Type-304 Stainless Steel

*W. L. Clarke, Detection of Sensitization in Stainless Steel: 11. EPR Method for Nondestructive Field Tests, GEAP-12697, February, 1978.

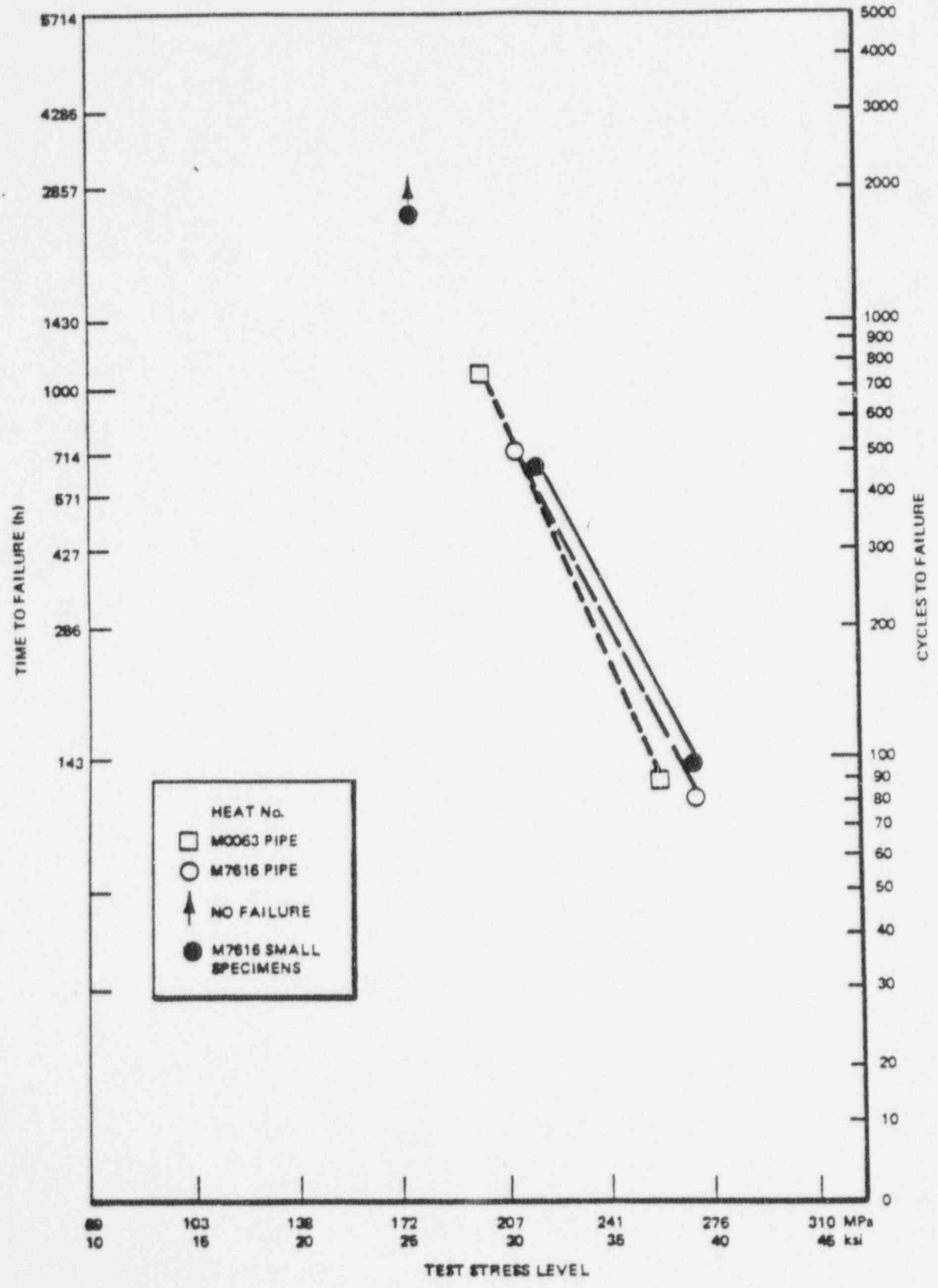

Figure 4-22. Effect of Stress on IGSCC of Welded Type-304 Stainless Steel Pipe and Small Specimens (0.67 cycle/h, air-saturated 288°C water)

5. TASK 3 — ELECTROCHEMICAL MEASUREMENTS

5.1 INTRODUCTION

For stress corrosion to occur in aqueous environments a combination of stress, specific alloy metallurgical condition, and electrochemical potential must exist simultaneously. It is possible to affect the cracking phenomenon by a system change that alters any of these variables. In the studies to be described, specific experiments were performed where the electrochemical potentials of Type-304 stainless steel and related materials were either measured or controlled. In an operating boiling water reactor these potentials were measured during a reactor start-up. The in-reactor potential measurements were then compared to measurements obtained in the laboratory where the chemistry of the environment was carefully controlled. To increase understanding of the alloy environmental interactions that could occur over the wide range of electrochemical potentials of interest to operation of boiling water reactors, potentiokinetic curves were determined on Type-304 stainless steel and alloys that simulated chromium depleted grain boundaries. More specifically, the current-voltage relationships on stainless steel and experimental alloys containing <18% Cr gave insight concerning reactions that could give rise to the rapid chemical attack that can occur during intergranular stress corrosion cracking of weld-sensitized Type-304 stainless steel.

Straining electrode experiments were performed to determine the stress corrosion behavior of as-welded stainless steel. Each experiment was conducted at a controlled potential and the limiting potential (that potential below which initiation and propagation of IGSCC does not occur) was determined and related to the equivalent dissolved oxygen concentration. The straining electrode technique was also used to evaluate specific metallurgical remedies that have been proposed as countermeasures for IGSCC.

Finally, an electrochemical constant load system has been developed that simulates the effect of the reactor start-up transient on the tendency of Type-304 stainless steel toward stress corrosion crack initiation. Initial shakedown tests have given promising results.

5.2 IN-REACTOR STUDIES

The electrochemical potentials of Type-304 stainless steel and platinum have been studied from cold-standby to full power operation in the Vermont Yankee Nuclear Power Station. Similar studies were previously conducted at Dresden-2 Nuclear Power Station[1]. The Dresden-2 measurements were obtained from electrodes inserted in a flange in the "A" 10.2 cm (4-inch) diameter bypass line and were correlated to general and transient plant water chemistry. The measurements in the present study were obtained from electrodes contained in an autoclave that was installed in the reactor water cleanup system. The Vermont Yankee test facility basically consisted of a 1-liter stainless steel autoclave with four ports that contained specimen and reference electrodes. The specimen electrodes used were Type-304 mill-annealed stainless steel and platinum. Two silver/silver chloride electrodes were used for the references. Bottom penetrations in the autoclave were provided for continuous monitoring of temperature and flow. The temperature was measured with a chromel-alumel thermocouple and flow was determined from the output of a differential pressure transmitter. The autoclave with a reference and working electrode is shown in Figure 5-1. Figure 5-2 shows the high temperature reference and working electrodes in complete detail. Similar electrodes were also used in all laboratory electrochemical experiments described in subsequent sections. During operation, reactor water from the "A" recirculation line was pumped to the reactor water cleanup system by the A and B reactor water cleanup pumps. A bypass installed across the cleanup pump delivered water to the autoclave at a rate of about 5 gpm. If required, the bypass containing the autoclave was isolated from the cleanup system by valves. The potentials, temperature, and flow rate were monitored remotely. Corrosion and oxidation potentials were monitored by a multi-station corrosion meter-recorder. Temperature and flow were monitored continuously with a dual-channel recorder.

Figure 5-3 shows the flow diagram and the location of the electrochemical facility in the Vermont Yankee reactor piping system.

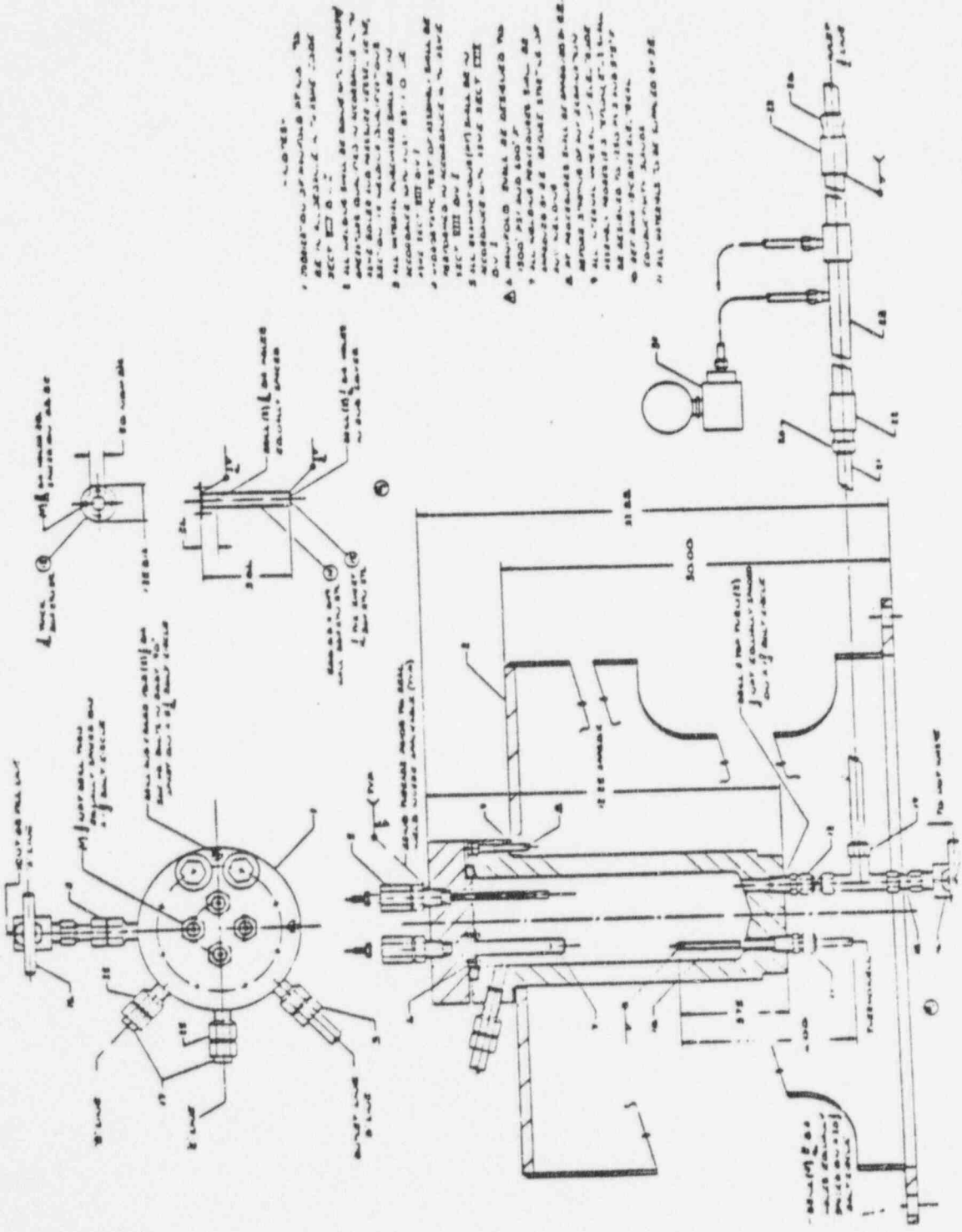

Figure 5-1. Electrochemical Potential Test Probe Assembly in Vermont Yankee

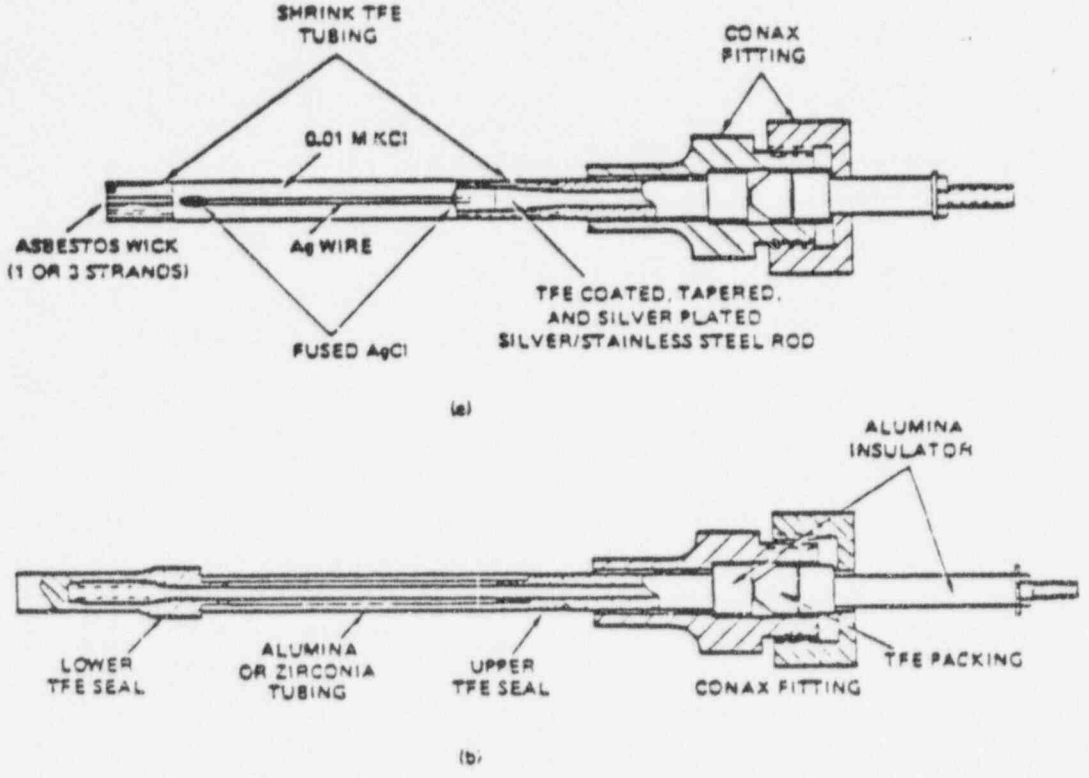

Figure 5-2. Electrochemical Potential Test Probes

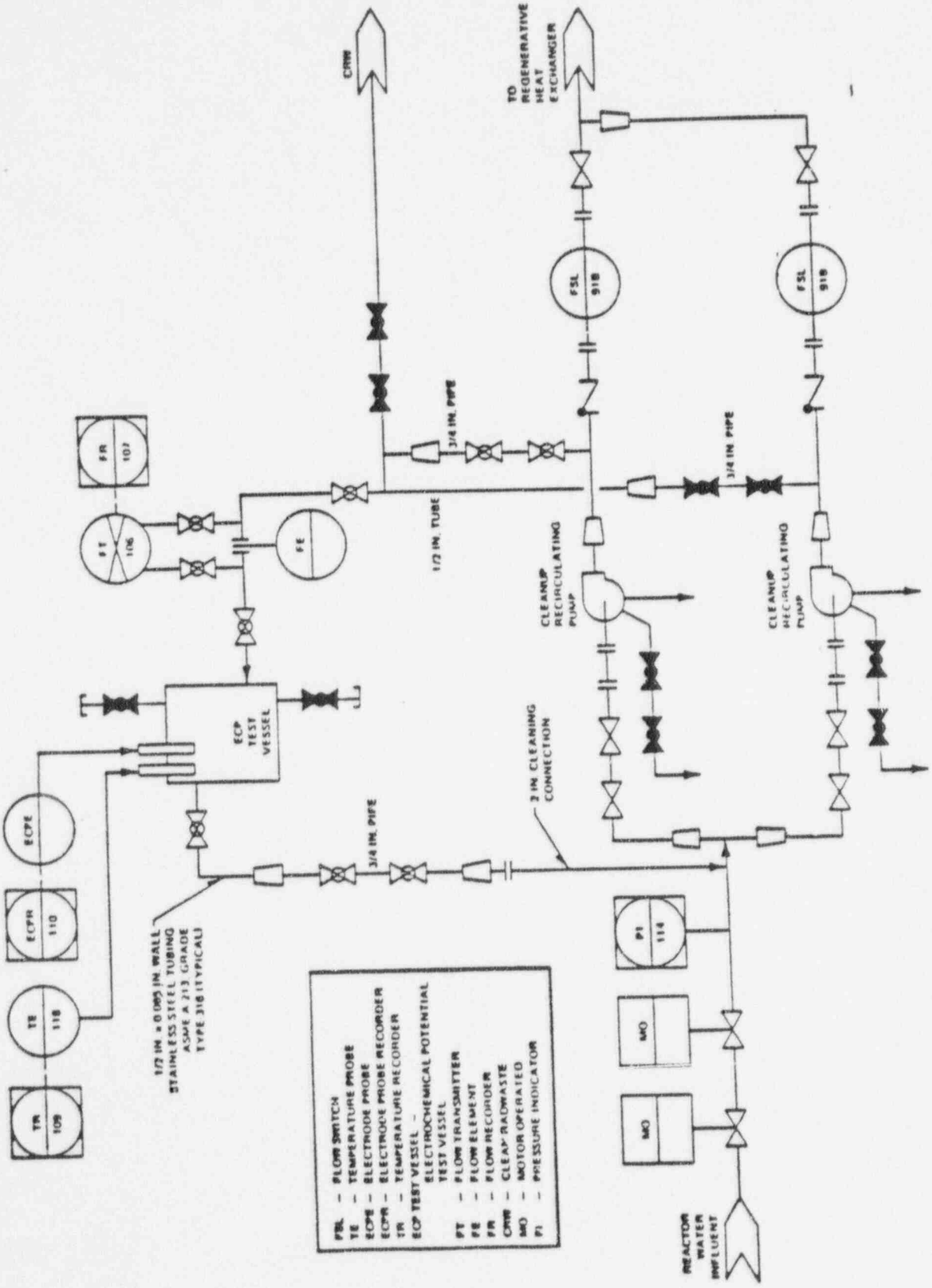

Figure 5-3. Flow Diagram of Electrochemical Potential Test Facility in Vermont Yankee

To increase understanding of the effect of plant water chemistry on the potentials obtained from Type-304 stainless steel (referred to as the corrosion potential) and the potentials obtained from platinum (referred to as the oxidation potentials) detailed chemical analyses were performed on the reactor water coincident with the electrochemical measurements. Of particular interest in the present study were analyses of O_2, H_2, H_2O_2, and conductivity during reactor start-up and high temperature operation. The water chemistry analyses were performed by Nuclear Water and Waste Technology (NWT) and have also been reported[2].

The measurements obtained from Vermont Yankee were especially significant because of a controlled degassing period that was used during the reactor start-up. The degassing was conducted slightly below the boiling point by valving the condensate vacuum pump to the reactor pressure vessel through existing lines, while the head vents were closed. It has been postulated that the start-up transient which includes aqueous environments that contain >200 ppb dissolved oxygen may contribute to crack initiation of weld sensitized Type-304 austenitic stainless steel. Figure 5-4 shows a range of dissolved oxygen in reactor water measured during various BWR start-ups. The presence of dissolved oxygen in water will increase the corrosion potential of stainless steel. Decreasing the concentrations of O_2 and H_2O_2 as during vacuum degassing will lower the corrosion potential of Type-304 stainless steel. It is postulated that at low corrosion potentials the susceptibility toward intergranular crack initiation should be reduced. However, the combinations of O_2 and H_2O_2 or the equivalent corrosion potentials that will result in a susceptible or non-susceptible environment during reactor start-up are not known. Much of these studies and other related studies are aimed at determining proper and reasonable values of the corrosion potential where IGSCC can be avoided. In-reactor studies however, are the first step in identifying the range potentials and chemistry that exist during start-up (de-aerated and non-deaerated) and steady-state operation.

In the Vermont Yankee Nuclear Power Station the controlled vacuum start-up degassing period extended from 0630 to 1350 on August 6, 1976. During this period the potential of the Type-304 stainless steel decreased by about 0.240V. The behavior of platinum was quite different as it exhibited an initial rise in potential and an eventual decrease at the end of the controlled degassing period. The electrode potentials during the degassing period, shown in Figure 4, were dependent on the concentration of oxidizing species in the reactor water. For example, the peak in the stainless steel curve and the drop in platinum curve, shortly after 1100 hours, was the result of a rise in the H_2O_2 concentration from about 100 to 350 ppb.

The level of H_2O_2 and oxygen at the beginning and end of the degassing period are also given in Figure 5-5. Figure 5-6 from NWT shows the oxygen and H_2O_2 concentration during the entire start-up period. Peaks in the H_2O_2 concentrations after the degassing period coincide with increased corrosion potentials. The effectiveness of the vacuum degassing increased with increasing temperature. Thus, it can be noted that the last two hours were more effective in simultaneously lowering the concentration of oxidizing species in the reactor water and the electrochemical potentials of stainless steel and platinum as the temperature was increased from 91.7°C (197°F) to about 96.1°C (205°F).

The corrosion and oxidation potentials and coincident temperatures recorded from cold-standby to high temperature reactor operation, including the vacuum degassing period are shown in Figures 5-7, 5-8, and 5-9. The controlled degassing period is bracketed in Figure 5-7. Before, during and just after the degassing the increases in potential for Type-304 stainless steel, Figures 5-5 and 5-7, are caused mainly by spikes in the H_2O_2 concentration shown in Figure 5-6. Above about 170°C (338°F), H_2O_2 concentration dropped below detection, <10 ppb.

A more complete discussion of the effects of H_2O_2 and O_2 on the corrosion and oxidation potential will be given in the next section. However, the significance of H_2O_2 in affecting the corrosion potential and perhaps the tendency to IGSCC can not be ignored.

The continuous decrease in potential with increasing temperature was observed until a temperature of about 256°C (493°F) was achieved. At this point an increase in potential was measured which persisted several hours (from about 2100 August 6 to 0200 August 7). This rise in potential was coincident with a decrease in the pH of the reactor water. The decrease in pH was caused by decomposition of ion exchange resins which had been dropped into the reactor vessel during shutdown. For this reason and because conductivity also rose, the reactor temperature was lowered to 215°C (420°F) and the reactor water cleanup system was run at maximum duty. During the cleanup period

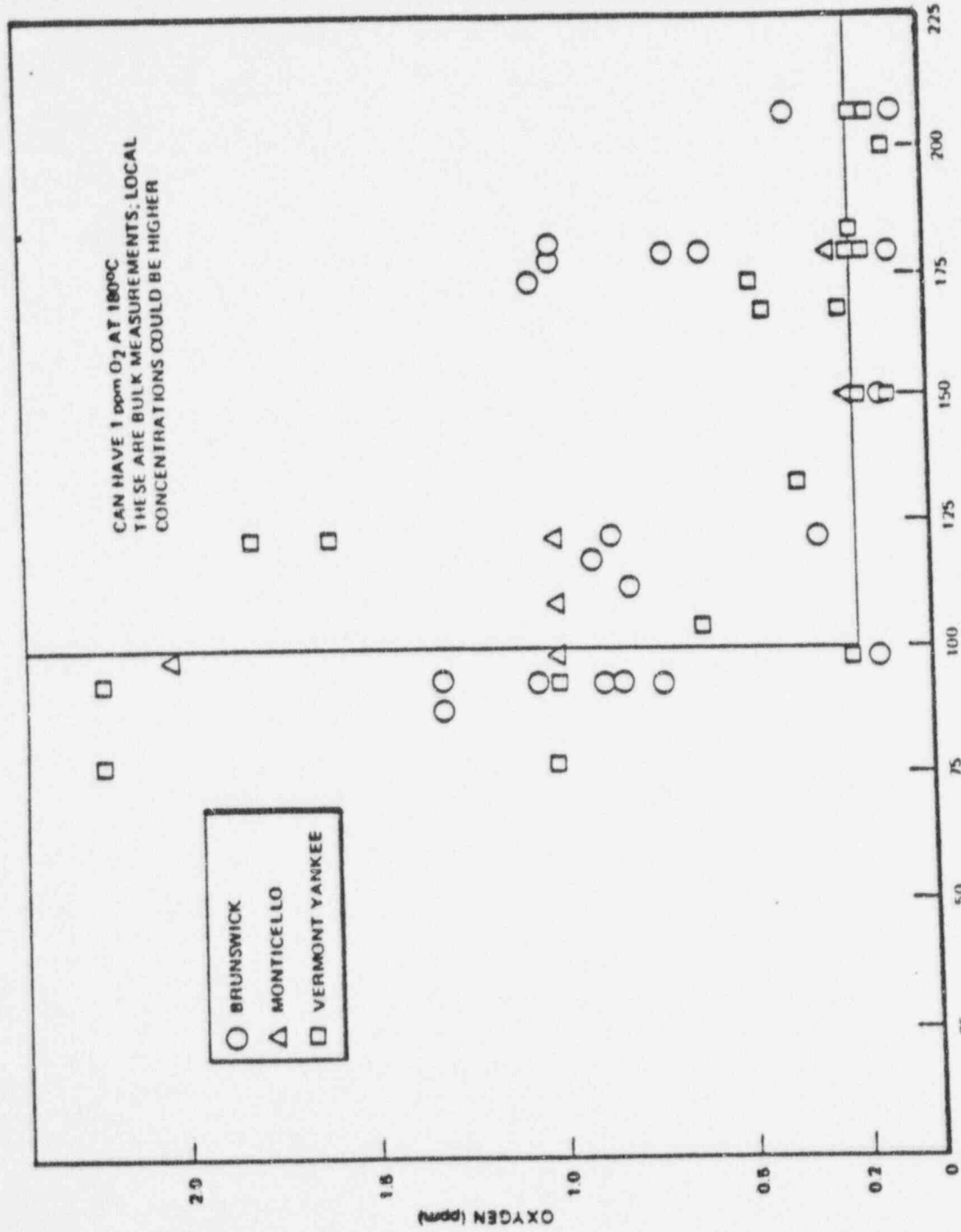

Figure 5-4 Variation of Oxygen with Temperature during Startups

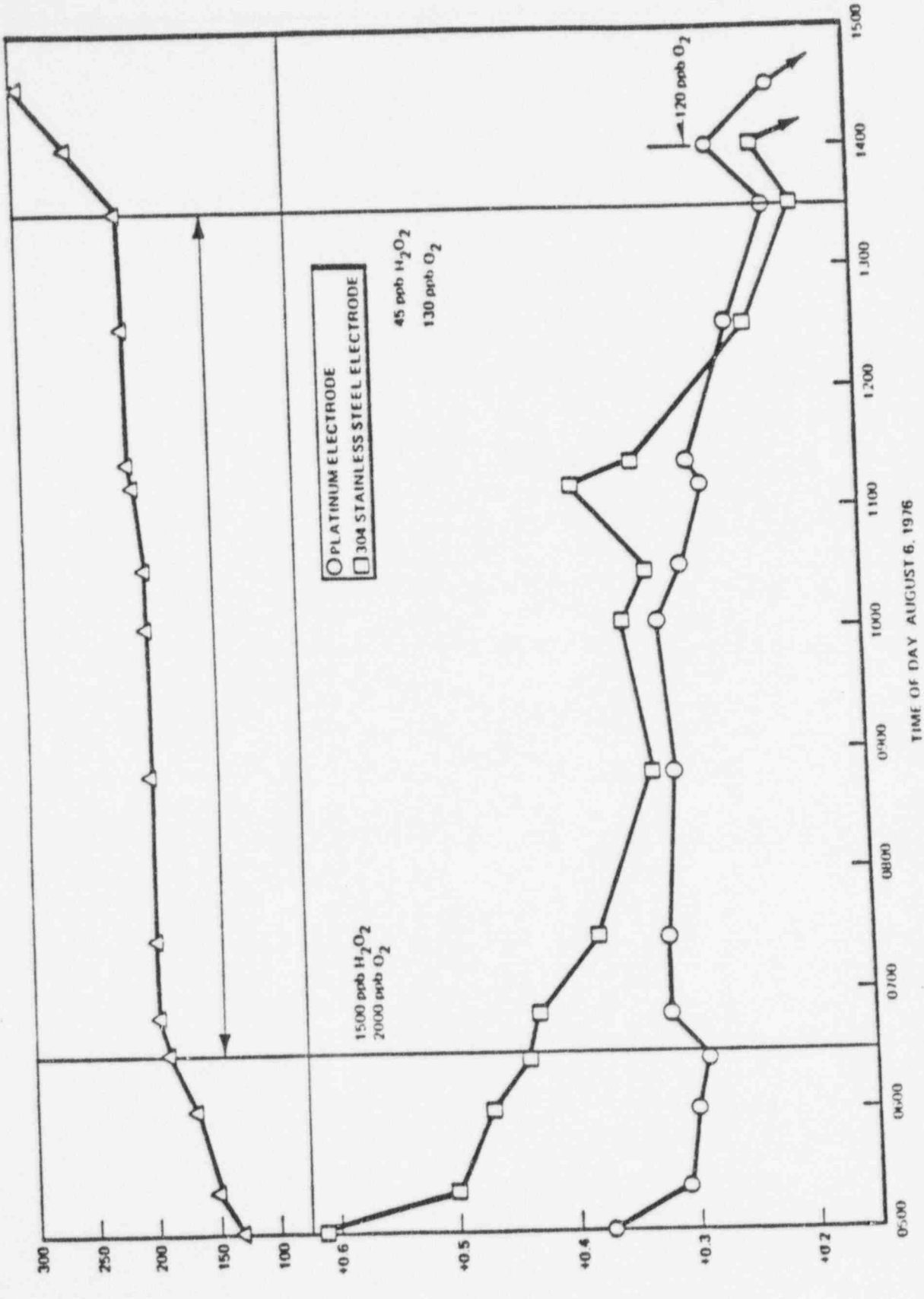

Figure 5.5 Corrosion and Oxidation Potential of Type 304 Stainless Steel and Platinum, Respectively, in Vermont Yankee during Controlled Degassing

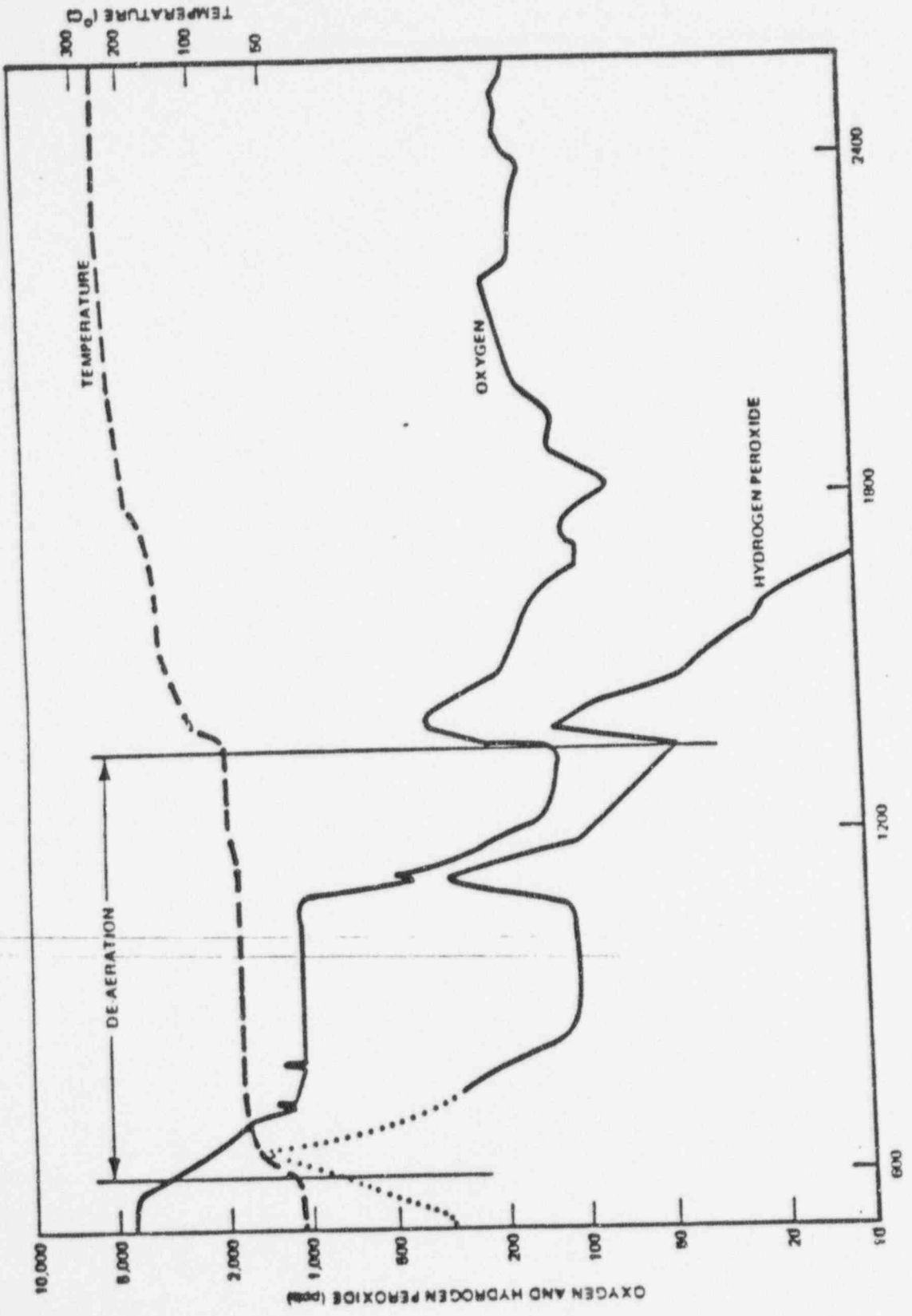

Figure 5-6 Oxygen and Hydrogen Peroxide During Vermont Yankee Startup, August 6, 1976

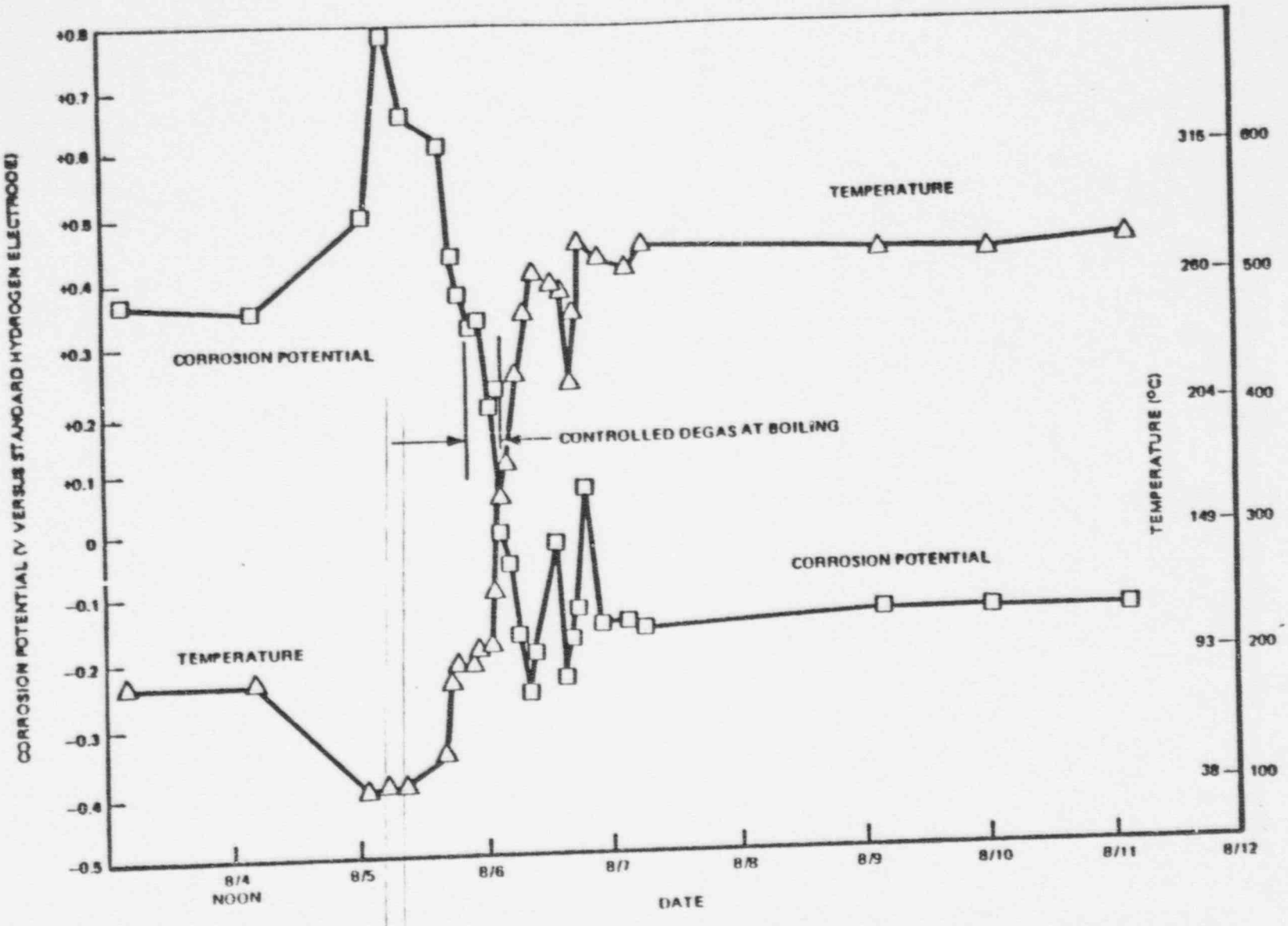

Figure 5-7. Corrosion Potential of Type-304 Stainless Steel During Reactor Startup

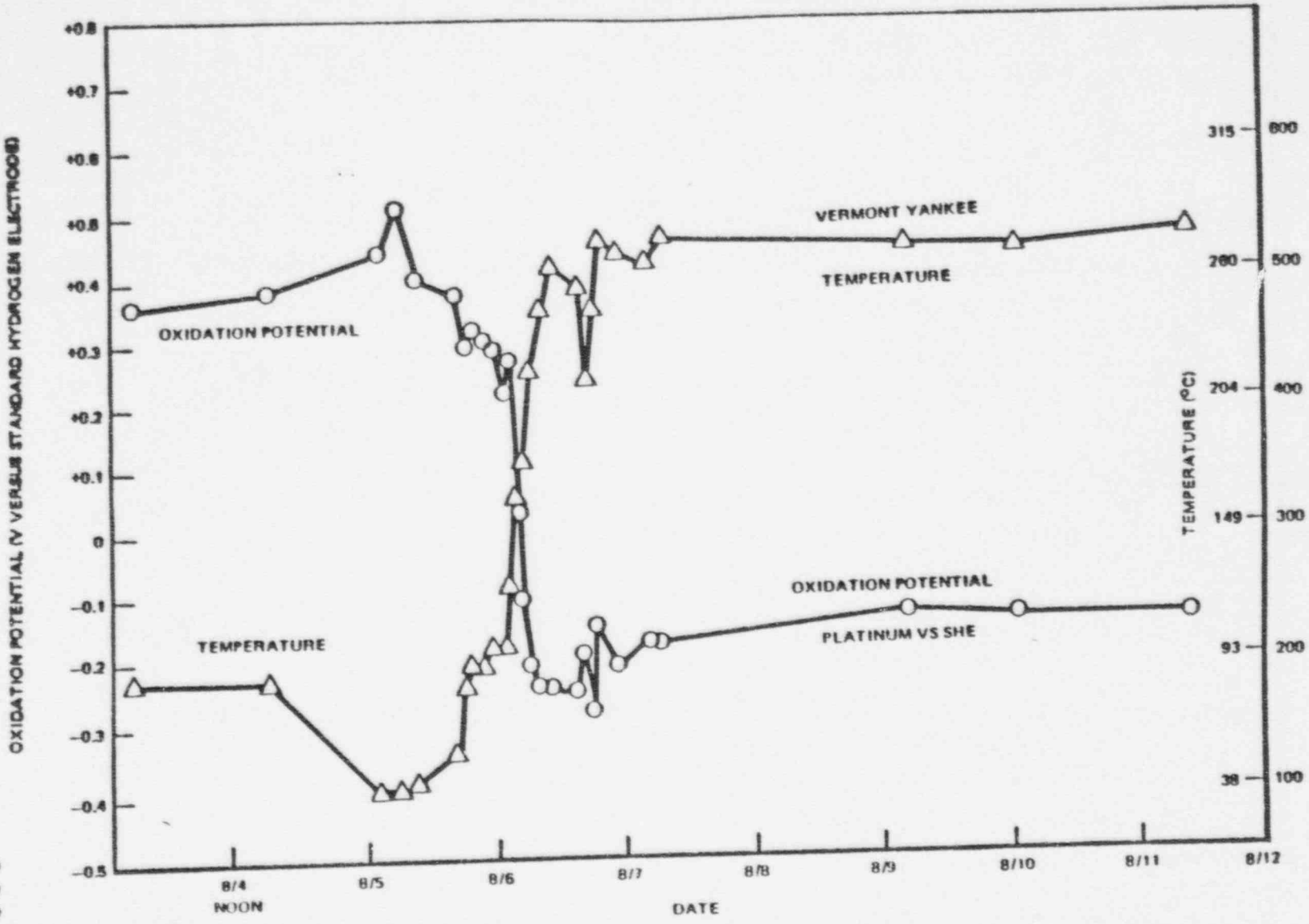

Figure 5-8. Oxidation Potential of Platinum During Reactor Startup

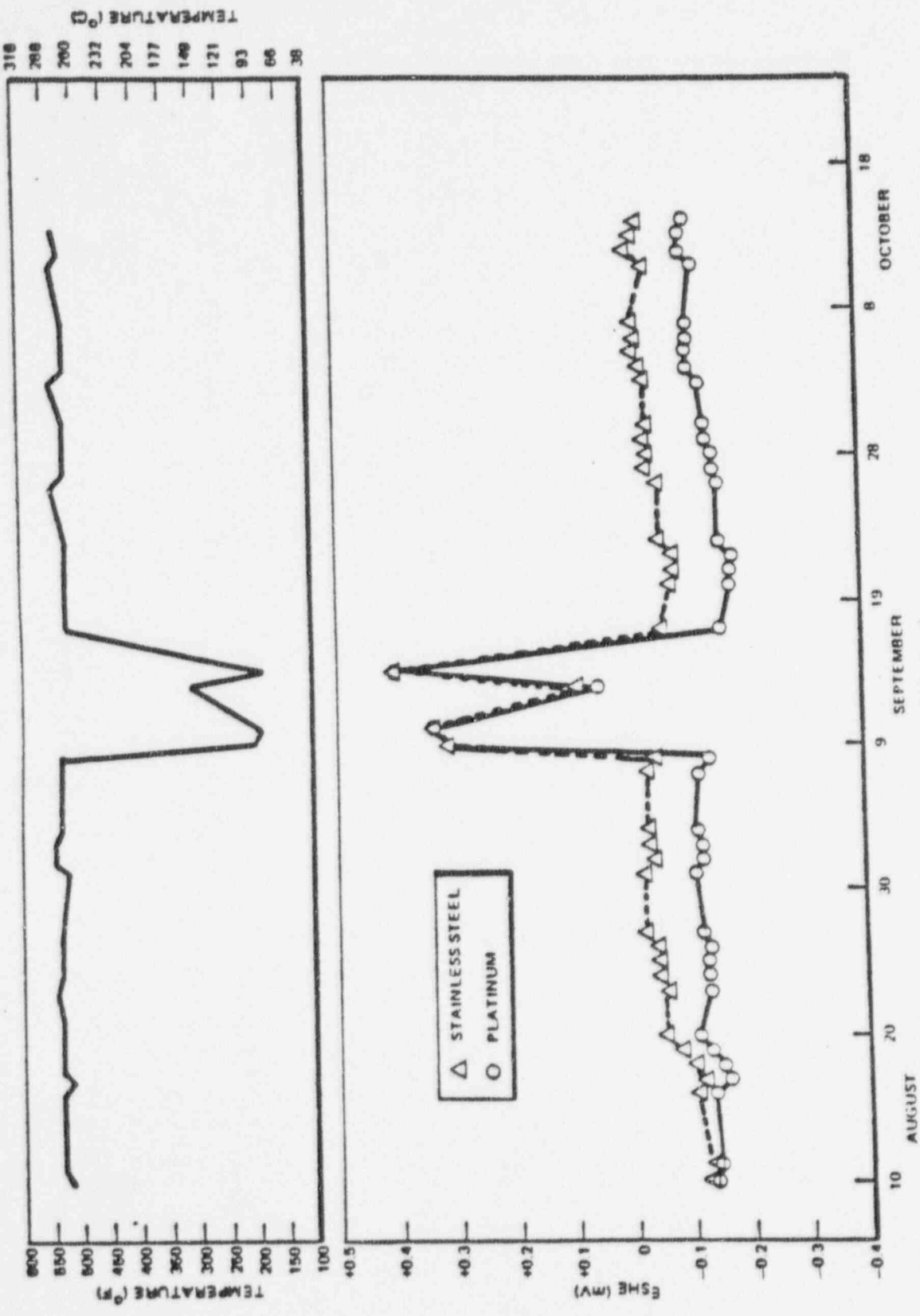

Figure 5-9 Potential versus Time Behavior at Vermont Yankee after Startup

the pH and conductivity returned to acceptable values. In addition, the oxygen concentration dropped due to decrease in radiolysis with temperature. Normally the potential will rise with decreasing temperature; however, the decreasing oxygen conductivity and increasing pH more than compensated for the temperature effect and the potentials dropped. All of these chemical variations were measured by NWT and coincided with the potential behavior. A second large positive spike was recorded after the heat-up period was reinitiated. The potential of the stainless steel electrode rose to almost +0.1 volt versus the standard hydrogen electrode at 276°C (530 F). From previous studies it has been found that potentials above 0 volts can cause cracking of highly stressed sensitized Type-304 stainless steel. Coincident with the first positive spike of stainless steel at 256°C (493°F) and the second spike at 276°C (530°F), similar increases in potential were observed on the platinum electrode. However, the magnitude of the potential changes of the platinum was much less. It is postulated that the platinum electrode is more sensitive to hydrogen than the stainless steel and during the chemistry transient, the hydrogen concentration rose. At constant pH, increases in H_2 concentration in a hydrogen sensitive electrode result in a decrease in potential. Thus, on platinum the increase of potential caused by the decrease in pH was partly compensated by the increase in hydrogen which reduced the magnitude of the positive spike.

After the reactor chemistry returned to normal a steady-state potential of about -0.15 to -0.13 volt standard hydrogen scale was measured on the stainless steel and platinum electrode. With time at temperatures between 270 and 282°C (518 to 540°F) the corrosion potential increased toward 0 volts$_{SHE}$. The corrosion potential on October 15, 1985 was -0.03V_{SHE} at 280°C (536°F). Shortly afterward an electronic malfunction and mechanical leak forced the isolation and shutdown of the test station.

The three month drift of the corrosion potential toward 0 volts at Vermont Yankee was also noted at the experiments performed in the "A" recirculation bypass line at Dresden-2 Nuclear Power Station[1]. The most likely explanation for the apparent increase in potential is the degradation of the silver chloride reference electrode. Hydrogen present in the reactor coolant can diffuse through the Teflon wall of the reference electrode and reduce the silver chloride to silver metal. Thus, as the reference electrode converts to pure silver the potential of the reference would drop (become more negative) which would decrease the potential difference between the reference and test electrodes. Since the correction factor required to bring all voltage to the standard hydrogen scale is based on the Ag AgCl electrode potential, a correction factor larger than necessary would have been applied to the test electrodes. The net result would be an apparent increase in corrosion potential. Post-test examination of the reference electrodes used in the reactor experiment and in more closely regulated laboratory experiments where both O_2 and H_2 were dissolved in the electrolyte, showed complete or significant reduction of the AgCl had occurred. Other designs and container material should offer increased reference electrode life.

The potentials measured in the Vermont Yankee and Dresden-2 experiments are in good agreement when one considers the difficulty of the experiment, that the electrodes were in different locations and that differences in reactor startup procedure and general chemistry may exist. Table 5-1 shows a comparison of these measurements. The major difference appears to be the behavior of the platinum electrode. In the Dresden-2 measurements, the platinum electrode potentials were higher than those measured in Vermont Yankee and with time the differences increased. The reason for this difference is not known.

The potential-time behavior of the stainless steel and platinum electrode after startup is given in Figure 5-9. It should be noted that the potentials have an inverse relationship with temperature (increasing temperature decreases potential) and during the brief low temperature shut-down period the potential difference between platinum and stainless steel became negligible. The sharp increase in potential during the low temperature period is probably the result of H_2O_2 production as oxygen increases by itself could not result in such high potential values of 0.4 V_{SHE} at 85°C (185°F). Thus during the low temperature period H_2O_2 apparently has a significant effect on the corrosion potential. Additional straining electrode experiments will be required to determine whether welded Type-304 stainless steel is susceptible to crack initiation at low temperatures and at a potential of 0.4 V_{SHE}.

5.3 THE EFFECT OF H_2O_2 ON CORROSION AND OXIDATION POTENTIALS, LABORATORY STUDIES

During cold-standby and the initial BWR startup period, measureable concentrations of H_2O_2 are produced by radiochemical reactions. The concentrations during one of these periods are given in Figure 5-6. To establish the

Table 5-1
STARTUP POTENTIALS (SHE)
DRESDEN-2 AND VERMONT YANKEE

Days From Startup		Temperature (°F)		Platinum (V)		Stainless Steel (V)	
D2	VY	D2	VY	D2	VY	D2	VY
0	0	139	131	+0.510	+0.370	+0.370	+0.610
0	0	151	150	+0.450	+0.310	+0.510	+0.500
0	0	206	211	+0.280	+0.220	+0.200	+0.200
0	0	280	296	+0.160	+0.200	+0.140	+0.120
0	0	343	328	+0.090	+0.030	−0.040	0.000
12	10	498	530	−0.080	−0.140	−0.130	−0.110
53	67	535	541	+0.100	−0.120	−0.040	−0.040

relationship between H_2O_2 and the potential of the test electrodes measured against the silver/silver chloride reference electrode several controlled laboratory experiments were conducted. In these experiments, known concentrations of H_2O_2 were added to air saturated water and the potential responses were measured on platinum and stainless steel. The experiments were conducted in a Type-316 stainless steel autoclave at 66°C (150 F) and 94°C (200 F) and the data are shown in Figure 5-10. It was found that the addition of 10 ppm H_2O_2 increased the stainless steel potential about 225 mV and lowered the platinum potential about 94 mV. Similar responses of stainless steel and platinum were detected in the Vermont Yankee startup as discussed in the previous section. The opposite response of the two electrodes to hydrogen peroxide is probably due to platinum acting as an oxygen electrode and stainless steel acting as a peroxide electrode. The potentials of the test electrodes in 8 ppm O_2 is given at time zero on Figure 5-10, and as can be seen, platinum has the higher potential. This is to be expected as platinum behaves as a more reversible oxygen electrode according to the reaction:

$$O_2 + 4H^+ + 4e \rightarrow H_2O;\ E_o = 1.23 \text{ volts}$$

For the above reaction the reduction of oxygen to water does not proceed directly, but occurs by first producing H_2O_2 according to the reaction:

$$O_2 + 2H^+ + 2e \rightarrow H_2O_2;\ E_2 = 0.68 \text{ volts}.$$

The H_2O_2 subsequently disproportionates to water and oxygen. Since the intermediate reaction occurs at a lower potential, increasing the concentration of the kinetic intermediate (H_2O_2) will lower the potential of the platinum/oxygen electrode. On the other hand, the potential of stainless steel does not approach reversibility as an oxygen electrode, and in the presence of H_2O_2 it responds as a peroxide electrode according to the reaction:

$$H_2O_2 + 2H^+ + 2e \rightarrow 2H_2O;\ E_o = 1.77 \text{ volts}.$$

Since this reaction occurs at an extremely high potential, the potential of the stainless steel electrode increased significantly. The effects of hydrogen peroxide were realized at 66°C (150°F) and for a short time (<4 hours) at 94°C (200°F). Holding at 94°C (200°F) eventually decomposed the H_2O_2 and the corrosion potentials of stainless steel and platinum approached their original values.

Hydrogen peroxide can effect the corrosion potential in a BWR significantly below 170°C. Thus, during reactor startups, combinations of H_2O_2 and O_2 can result in ranges of corrosion potentials that can either produce a propensity to IGSCC or mitigate IGSCC. At present, the envelope of these startup environments and oxidizing potentials which can result in IGSCC is not known and should be the subject of future studies.

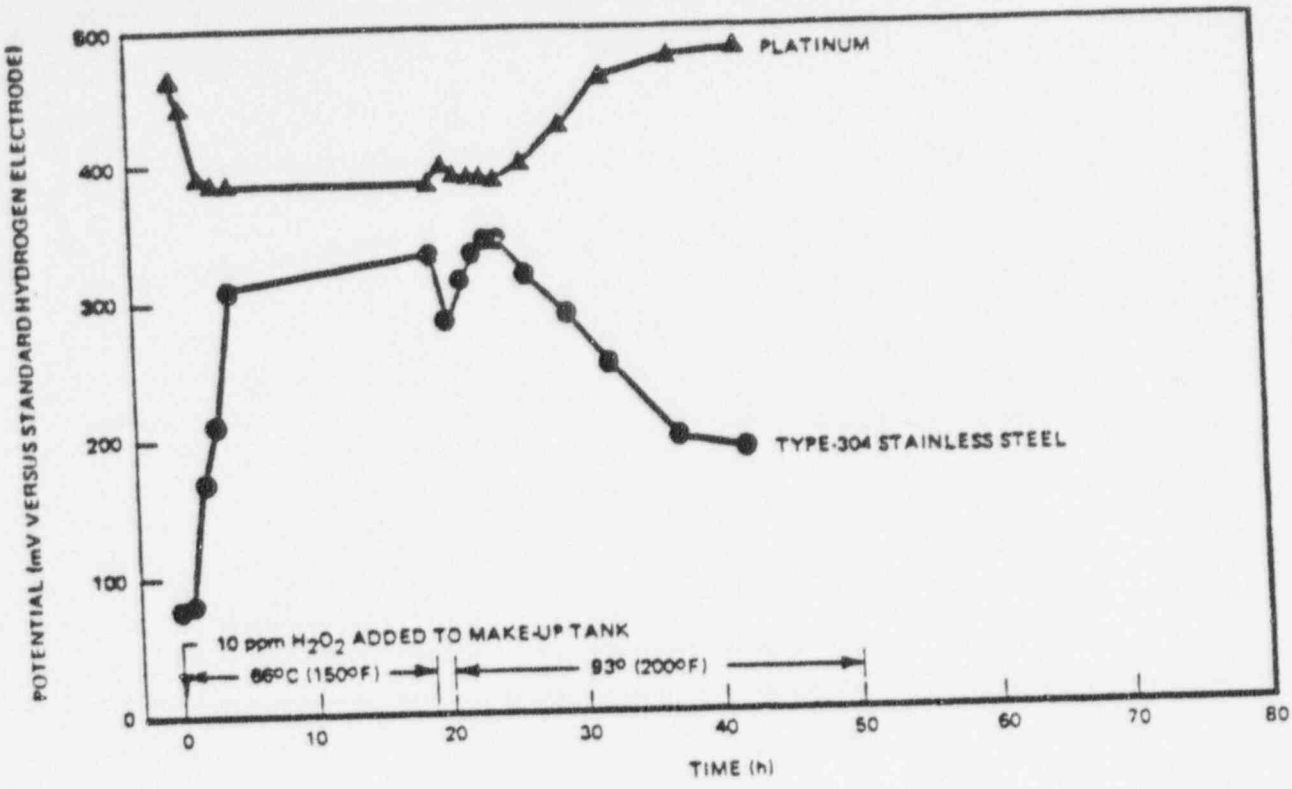

Figure 5-10. Effect of Hydrogen Peroxide on Oxidation and Corrosion Potential of Platinum and Type-304 Stainless Steel in Aerated Water

5.4 THE EFFECT OF OXYGEN ON POTENTIAL

Hydrogen peroxide, hydrogen pH and temperature can all effect the corrosion potential of austenitic stainless steel in boiling water reactors. In general the potential increases with H_2O_2 concentration, decreases with dissolved H_2, and increases with decreasing pH. However, during BWR operation (after startup) the H_2O_2 concentration is too low to have a significant effect on potential. The pH is constant and about neutral and as we will see the hydrogen dissolved in the BWR water exerting only a slight effect on the corrosion potential. Finally, at constant BWR chemistry, increasing the temperature decreases the potential.

The species that has the most profound influence on the corrosion potential appears to be the dissolved oxygen. From electrochemical theory we can predict that the major environmental factor in IGSCC of welded stainless steel is the corrosion potential. Thus, the relation between oxygen and corrosion potential will provide the kinetic driving force of IGSCC in BWRs in a quantified manner. The material response of Type-304 stainless steel under a specific driving force is a function of local metallurgical condition (degree of grain boundary sensitization) and the strain rate (stressed state). It is the interaction of the kinetic driving force and material response that determines whether or not stress corrosion will occur. In addition to providing a value for the driving force for IGSCC, the study of the oxygen/potential relation can aid in characterizing the chemistry within a growing crack or an actively corroding crevice.

As a first approximation, the potential difference between a filmed surface at some temperature exposed to a specific oxygen concentration and an unfilmed surface at zero oxygen concentration gives the potential difference from the solution at an advancing crack tip (bare metal or crevice) to the solution at the mouth of the crack (filmed metal or crevice). The potential/oxygen curves on filmed and unfilmed surfaces to be presented in this section provide

values for the potential differences and by application of the Boltzman equation, $Co = Co\ (\exp Ze/kT \cdot \Delta V)$ the anion concentration at the crack tip can be calculated where:

- C = ion concentration at the crack tip,
- Co = ion concentration in the bulk solution,
- Ze = electronic charge on an ion,
- R = gas constant,
- T = absolute temperature, and
- ΔV = potential difference between the crack tip and the bulk solution.

Assuming a potential difference of 0.6V, a monovalent ion and a temperature of 300°C (572°F) the change in concentration, (C/C_o), = 10^5. The combination of metal oxidation, anion flow into the crack and hydrolysis produces an acid solution at the crack tip. Whether or not a crack will propagate depends on other factors such as the depletion of oxygen in the crack or crevice (differential aeration produces the potential difference), the presence of some anions, and mechanical strain. A decrease in the oxygen concentration of the bulk solution would decrease the potential difference for the formation of crevice chemistry which should reduce the driving force for IGSCC, while a decrease of O_2 in the crevice may re-establish the potential difference. The potential difference for a given bulk oxygen concentration is given in this section.

The studies of the oxygen/potential behavior on stainless steel and platinum electrodes at various temperatures were conducted in a pressure vessel which was part of a refreshed water system. A flow diagram of the system is shown in Figure 5-11. Deionized water was stored in the 100 liter storage tank and was continuously pumped through columns containing deionizing resins, so that the tank water purity as measured by resistivity was ≥5 megohm-cm. The water in the tank was purged with various N_2-O_2 bottled gas mixtures to give the desired concentration of dissolved water. For example, a mixture of 99.5% N_2-0.5% O_2 when bubbled through room temperature water results in a dissolved O_2 concentration of 200 ppb.

A major concern in performing experiments with controlled amounts of dissolved oxygen in high temperature water is minimizing the amount of oxygen gettered in the high temperature portions of the system; the tubing in the regenerative heat exchanger and the inside surfaces of the pressure vessel. Gettering or loss of oxygen before reaching the test electrode gives low potentials and misleading predictions of reactor environments and stress corrosion behavior. The initial studies were conducted in a Type-316 stainless steel autoclave. Although the internal surfaces had a well aged oxide, comparison of the inlet and effluent autoclave water oxygen analyses showed that significant gettering occurred especially at oxygen concentrations ≤200 ppb. The flow diagram, Figure 5-11, shows the oxygen cell which is part of the Beckman 7001 oxygen system analyzer. The cell and analyzer are used for continuous oxygen analyses of the tank or autoclave water. Before installation of the continuous analyses system water samples were analyzed for dissolved oxygen periodically by a colorimetric method.

The potential differences between a cylindrical test specimen and the high temperature silver/silver chloride reference electrode were monitored with a switching circuit and a strip chart recorder. To prevent ground loops all ac powered instruments were removed from virtual ground with an isolation transformer.

The result of the initial tests in the stainless steel autoclave and data obtained at Ohio State University (OSU) are shown in Figure 5-12. Oxygen concentrations were based solely on measurements from the storage tank. The initial data from the stainless steel system which contained an Inconel 600 heat exchanger were in excellent agreement with the OSU data. However, the laboratory potential measurements with 200 ppb dissolved oxygen were significantly lower than those obtained at Vermont Yankee (−0.350 versus −0.150 V_{SHE}). In addition, the data indicated that between 0 and 100 ppb dissolved O_2 the potential remained low, around −0.650 V_{SHE}. Above 100 ppb O_2 the potential increased dramatically. At low potentials, it is theorized that susceptibility to IGSCC is low. This large increase in potential could indicate the onset of IGSCC. Thus, from the initial GE and OSU data it might have been predicted that no IGSCC would occur below 100 ppb dissolved oxygen. System changes that decreased gettering such as removal of the heat exchanger, decreased gettering, moved the curve to left and improved the data. However, the major system improvement was the installation of a titanium autoclave (Ti-6Al-4V) and titanium heat exchanger. After an aging period in air saturated high temperature water for several weeks the oxygen gettering was reduced to a minimum (15 ± 10 ppb) and reliable data were obtained.

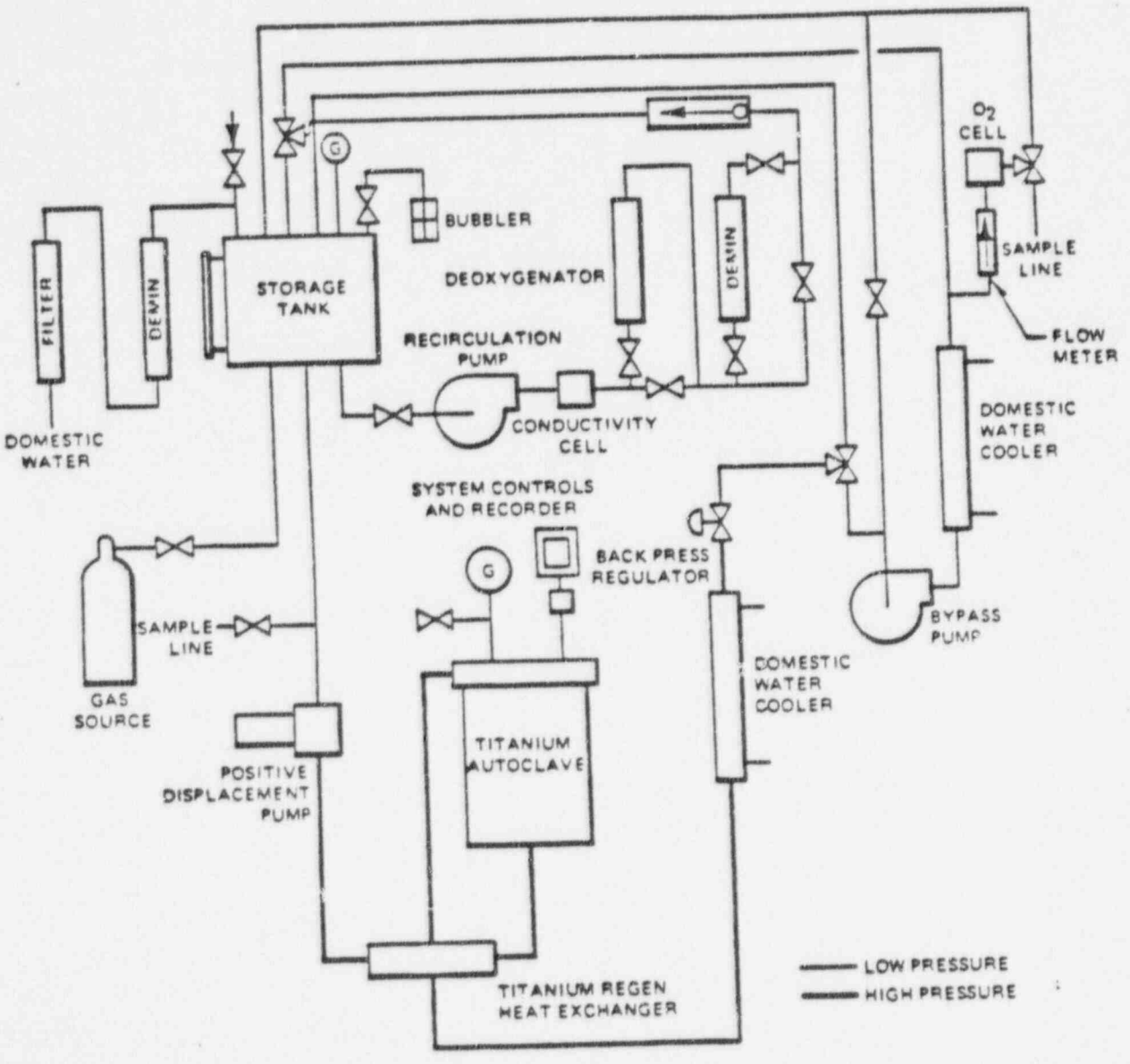

Figure 5-11. Refreshed Water Loop for Electrochemical Studies

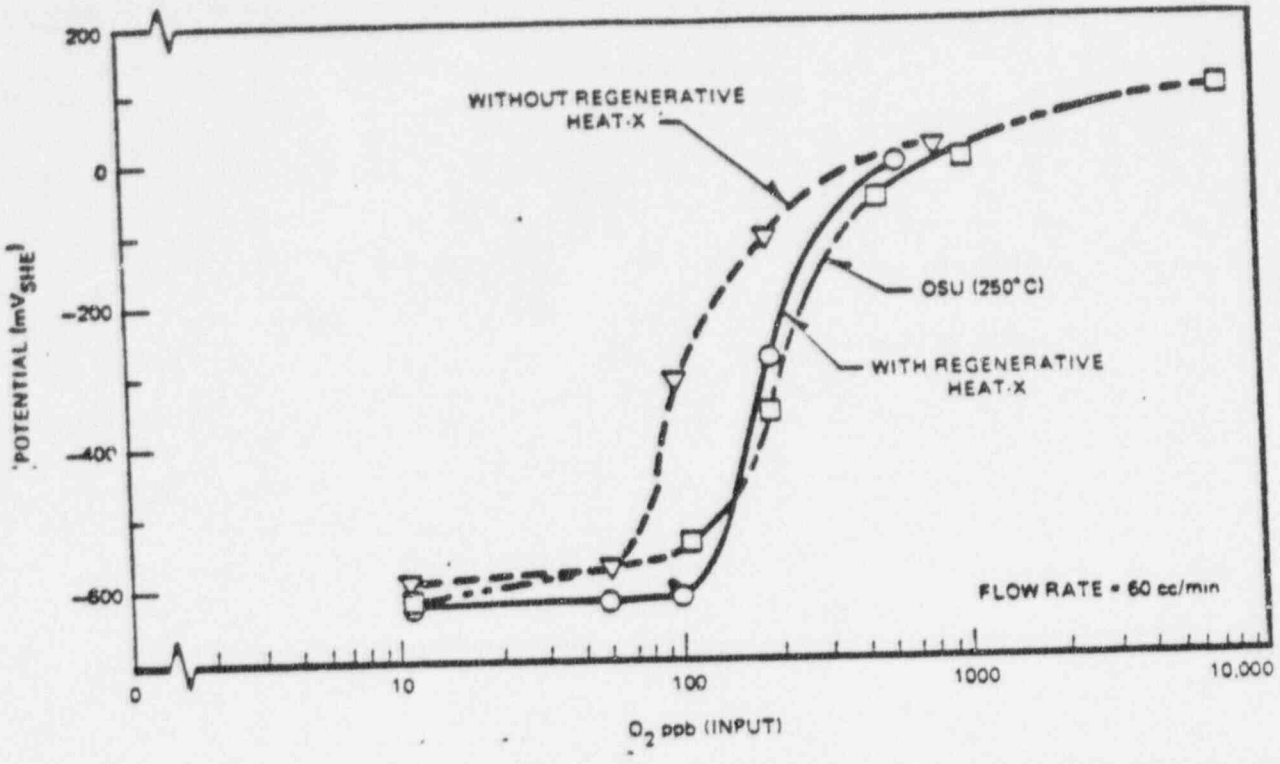

Figure 5-12. The Effect of Dissolved Oxygen on the Oxidation Potential of Platinum in High Purity Water at 274°C (525°F). With and Without Alloy 600 Regenerative Heat Exchanger. (Determined After 24 hours at Each Oxygen Level)

The oxygen/potential curves presented in the following sections were obtained in the titanium system. Figure 5-13 shows the oxygen/potential relationship at 274°C (525°F) for Type-304 stainless steel. The curve is presented as a band to account for experimental scatter in two runs, differences in measured oxygen concentrations in the feedwater (input) and effluent from the autoclave (output) and differences in potential measurements obtained as the dissolved oxygen concentration was increased from 0 to 10,000 ppb or decreased from 10,000 ppb to 0 ppb. At 232°C (450°F) similar behavior was obtained, as shown in Figure 5-14.

At 274°C (525°F), approximate reactor operation temperature, a significant increase in corrosion potential occurs with dissolved oxygen concentration between 10 and 50 ppb. Above 100 ppb the change of potential is about linear with the logarithm of the oxygen concentration with a slope of about 0.100V/decade O_2. Thus, above 100 ppb changes in oxygen concentration do not have a strong influence on electrochemical potential. The results in Figure 5-13 show that to decrease the corrosion potential significantly and thus the propensity for IGSCC by environmental control, the dissolved oxygen concentration must be below 100 ppb. Just how low the corrosion potential must be decreased to avoid IGSCC of weld sensitized Type-304 stainless steel will be given in the results of the "straining electrode" section.

The effect of decreasing the temperature from 274°C (525°F) to 232°C (450°F) was to increase the potential approximately 80 mV at all oxygen concentrations (Figure 5-14). A comparison of the corrosion potentials between a prefilmed and an unfilmed stainless steel specimen is also given in Figure 5-14. The prefilmed specimen had been previously used in the experiments at 274°C (525°F), while the unfilmed specimen had been ground with 600 grit silicon carbide paper prior to use. In general, the filmed specimen exhibited higher corrosion potentials than the unfilmed sample. The potential differences were greatest during the time of the experiment when the oxygen concentration was increased from 0 to 10,000 ppb, and least when the oxygen was reduced from 10,000 to 0 ppb. The maximum potential difference between the stainless steel specimens was about a 0.150V and minimum potential difference was about 0.050V. The potential differences were probably caused by the higher metal oxidation rate of the

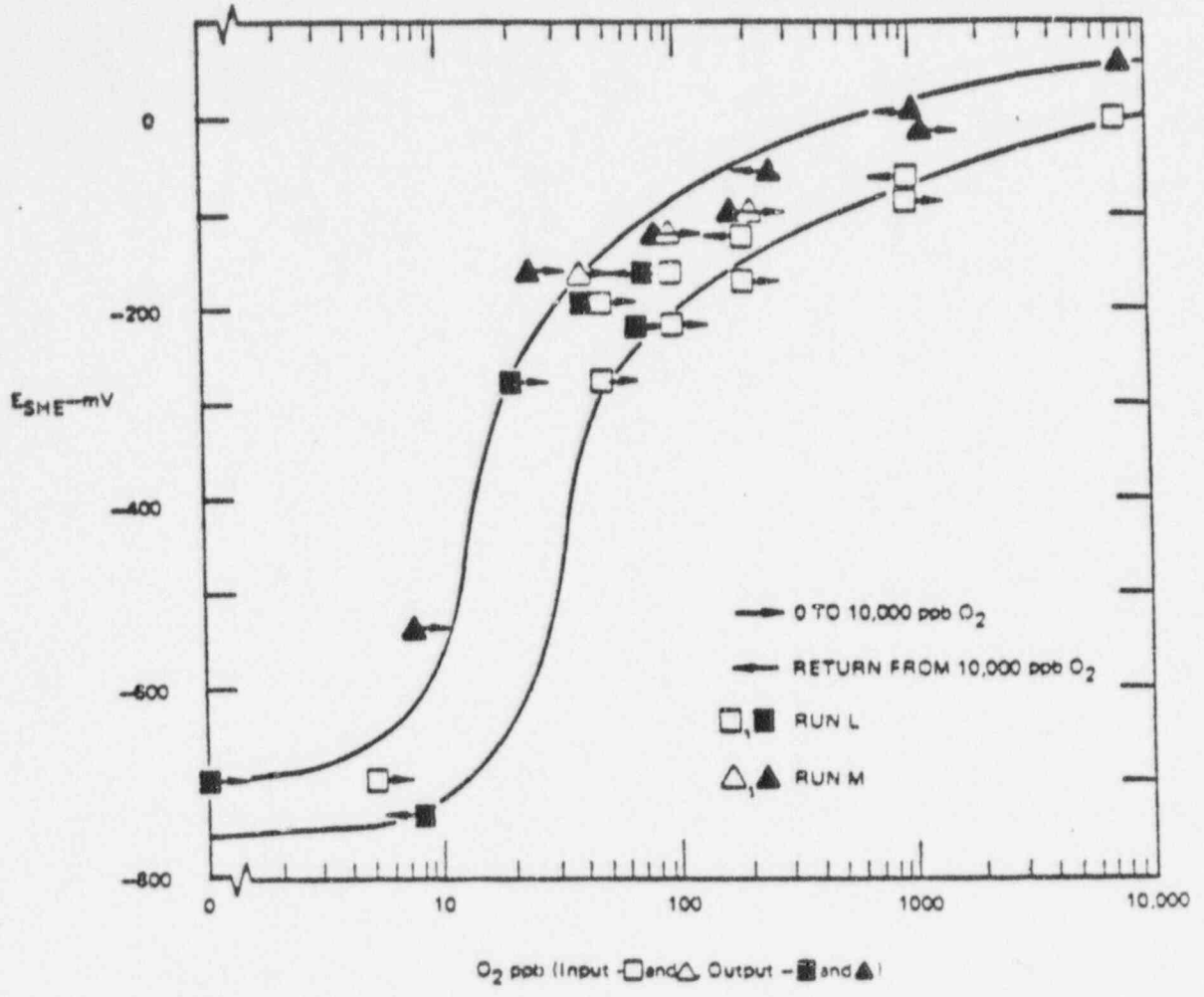

Figure 5-13. The Effect of Dissolved Oxygen on the Corrosion Potential of Type-304 Stainless Steel in High Purity Water at 274°C (525°F)

90014168

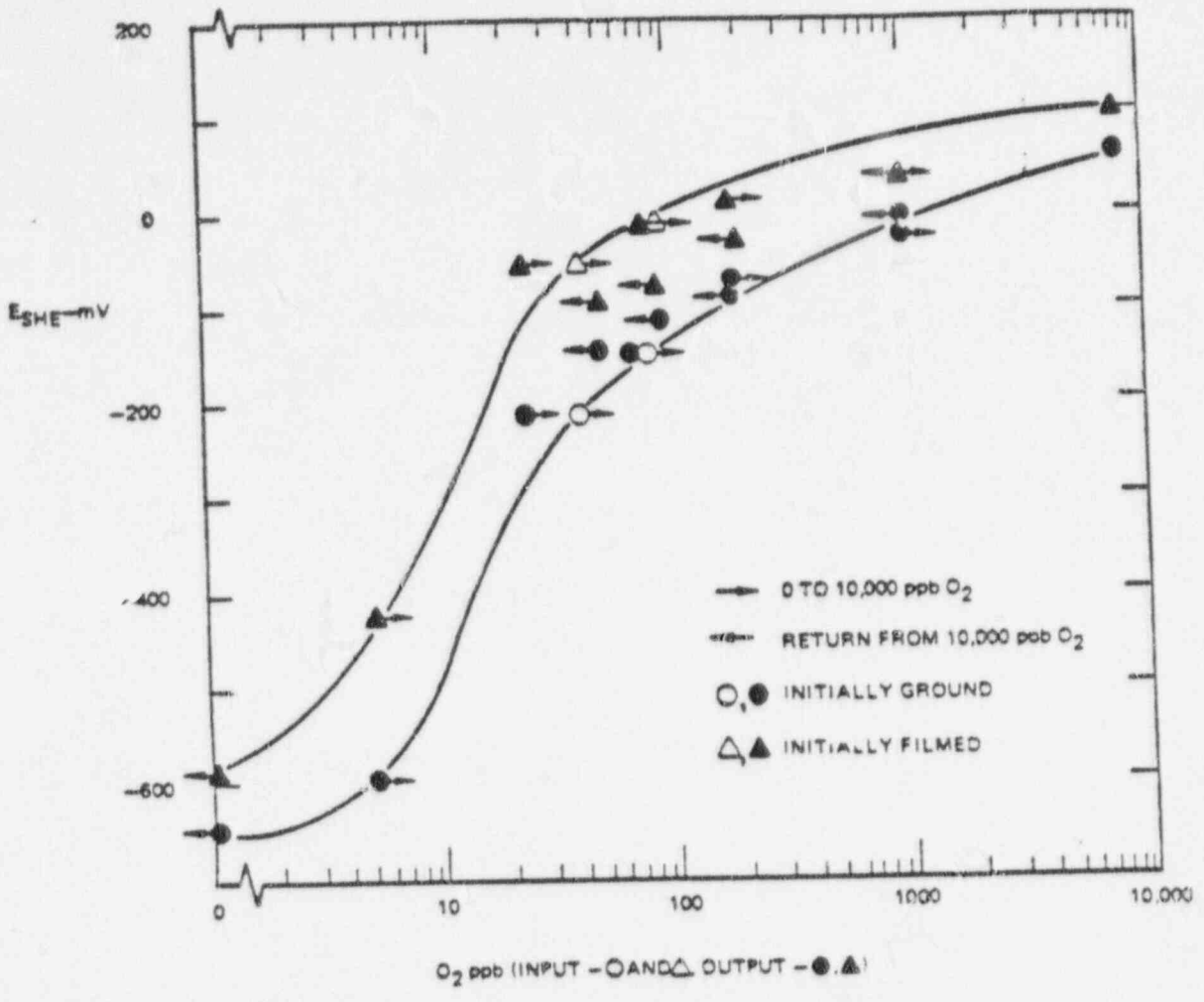

Figure 5-14. The Effect of Dissolved Oxygen on the Corrosion Potential of Type-304 Stainless Steel in High Purity Water at 232°C (450°F)

initially unfilmed specimen. According to electrochemical theory, the increased anodic oxidation current of the unfilmed specimen would cause the intersection of anodic and cathodic currents that comprise the corrosion reaction to occur at a lower potential. As the corrosion film on the unfilmed surface grows, the difference in corrosion rates and the potential differences would decrease.

For simplicity, average curves for the potential oxygen behavior at 274°C (525°F) and 232°C (450°F), are given in Figure 5-15. Included on the curves are BWR stainless steel potentials estimated from reactor startup data. The sigmoidal shape of the oxygen/potential behavior at 274°C (525°F) and 232°C (450°F) is probably due to a change in the potential controlling cathodic portion of the corrosion reaction. At high oxygen concentrations, >100 ppb, the cathodic process is undoubtedly the reduction of oxygen according to the reaction $4e^- + O_2 + 4H^+ \rightarrow 2\,H_2O$. At low oxygen concentrations, less than about 10 ppb, the controlling cathodic process is probably the direct reduction of water according to the equation $2e^- + 2H_2O \rightarrow 2OH^- + H_2$. In the transition region, between 10 and 100 ppb dissolved oxygen, small increases in oxygen concentrations cause a dramatic increase in corrosion potential. It is in this potential/O_2 region that control of the oxygen concentration could have a significant effect on IGSCC. Just how low the corrosion potential must be decreased to avoid IGSCC of welded sensitized Type-304 stainless steel will be given in the section on the "straining electrode" tests.

Others[3] have proposed that the sigmoidal shape of the potential/oxygen curve could be explained by the intersections of portions of the anodic polarization curve with the oxygen reduction curve. However, a similar sigmoidal behavior exists for a noncorroding platinum electrode whose potential is known to respond to the presence or absence of oxidizing or reducing substance (dissolved O_2 or H_2) in the environment. The behavior of platinum at 274°C (525°F) and 232°C (450°F) is shown in Figures 5-16 and 5-17 and justifies the above explanation of the observed potential response for Type-304 stainless steel. The major differences in platinum behavior compared to stainless steel are a much sharper rise in potential above 50 ppb dissolved O_2 and higher potentials above 200 ppb dissolved O_2 than those measured for stainless steel. Higher potentials indicate more reversible behavior as an oxygen electrode.

Figures 5-18 through 5-20 show the potential/oxygen behavior for bright and prefilmed Type-304 stainless steel at 191, 149, and 107°C (375, 300, and 225°F). The prefilmed electrode had been previously used in the 274°C (525°F) and 232°C (450°F) potential/oxygen experiments and thus had a well aged oxide. In this temperature range sigmoidal behavior was not observed on stainless steel, probably because the activation energy for the direct reduction of water is too high. On platinum, sigmoidal behavior was observed at 191°C (376°F) but not at 149°C (300°F) and 107°C (225°F), Figures 5-21 through 5-23. In addition, the changes of potential with oxygen concentrations are greater with platinum than stainless steel. The greater voltage response of platinum reflects the greater reversibility of platinum as an oxygen electrode or sensor compared to stainless steel.

Figures 5-18 through 5-20 also show that the stainless steel electrode that was polished to a bright finish had corrosion potentials that were about 100 to 200 mV lower over the linear oxygen/potential region than did the electrode with the high-temperature oxide.

Reasons for the difference in potential between the filmed and unfilmed electrode have already been discussed. The maximum potential difference between the two surfaces occurred at the 0 ppb oxygen level, while the minimum difference was at 8,000 ppb oxygen. A summary of Figures 5-18 through 5-20 is given in Figure 5-24. It should be noted that for a given oxygen concentration the potential decreases with increasing temperature. At any constant temperature the potential difference between the filmed surface at a specific oxygen concentration and the unfilmed surface at zero oxygen approximates the potential drop from active crack tip to the crack mouth and hence the electrochemical driving force for crack growth.

The combination of a high-temperature silver/silver chloride reference electrode, a stainless steel electrode, and a platinum electrode can be used as analytical tools. Figures 5-13, 5-14, and 5-18 through 5-20 or their summary curves indicate that the stainless steel/silver chloride voltage can be used to determine oxygen concentration in high-temperature water. Presently, this combination is used to monitor oxygen concentrations within autoclaves where high-temperature stress corrosion experiments are conducted. The platinum electrode offers additional analytical capability because of its sensitivity to dissolved hydrogen in water. Hydrogen and oxygen are present in BWRs as a result of radiolysis of the water. The presence of both dissolved gases may affect corrosion processes in a

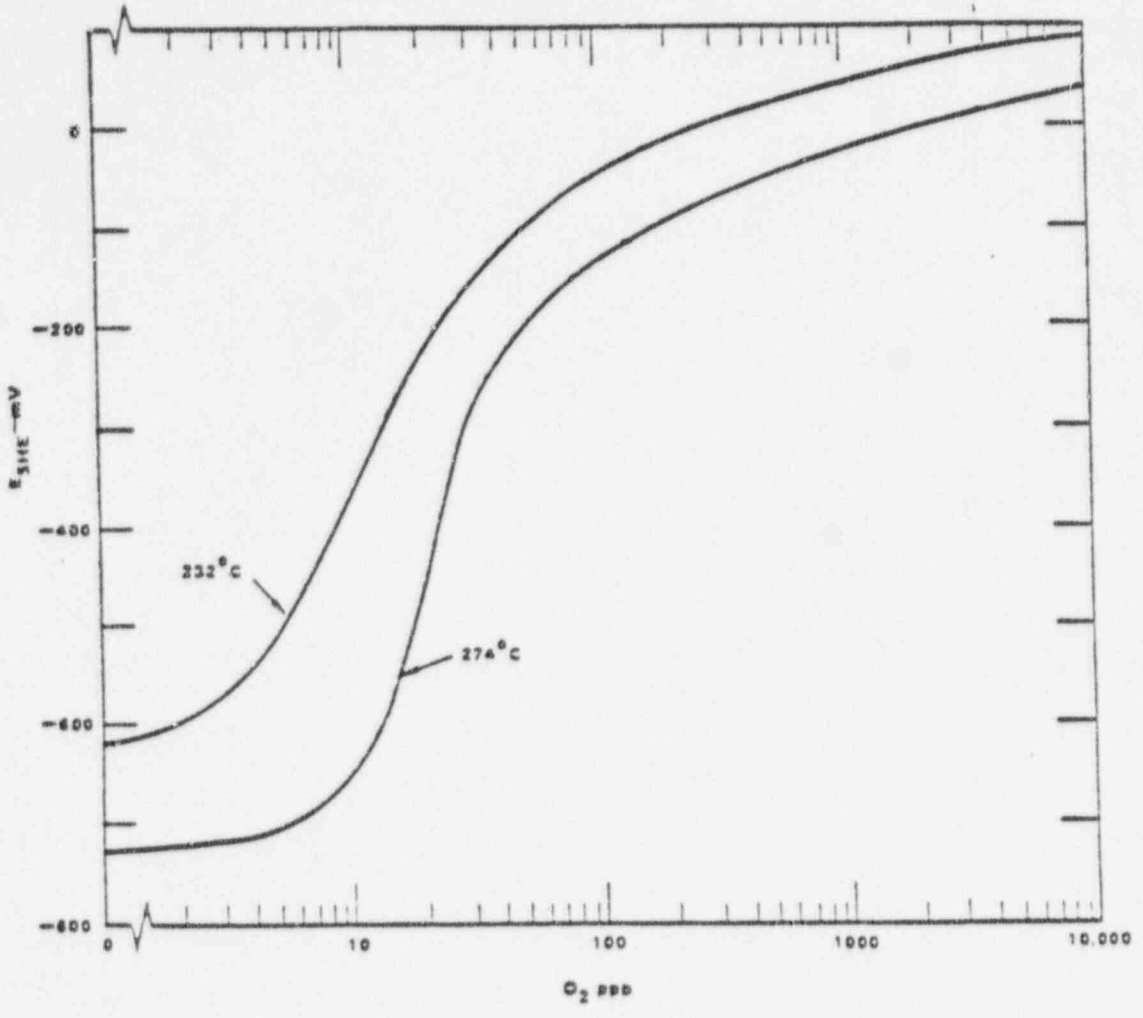

Figure 5-15. The Effect of Dissolved Oxygen on the Corrosion Potential and IGSCC of Type-304 Stainless Steel (Average Curves)

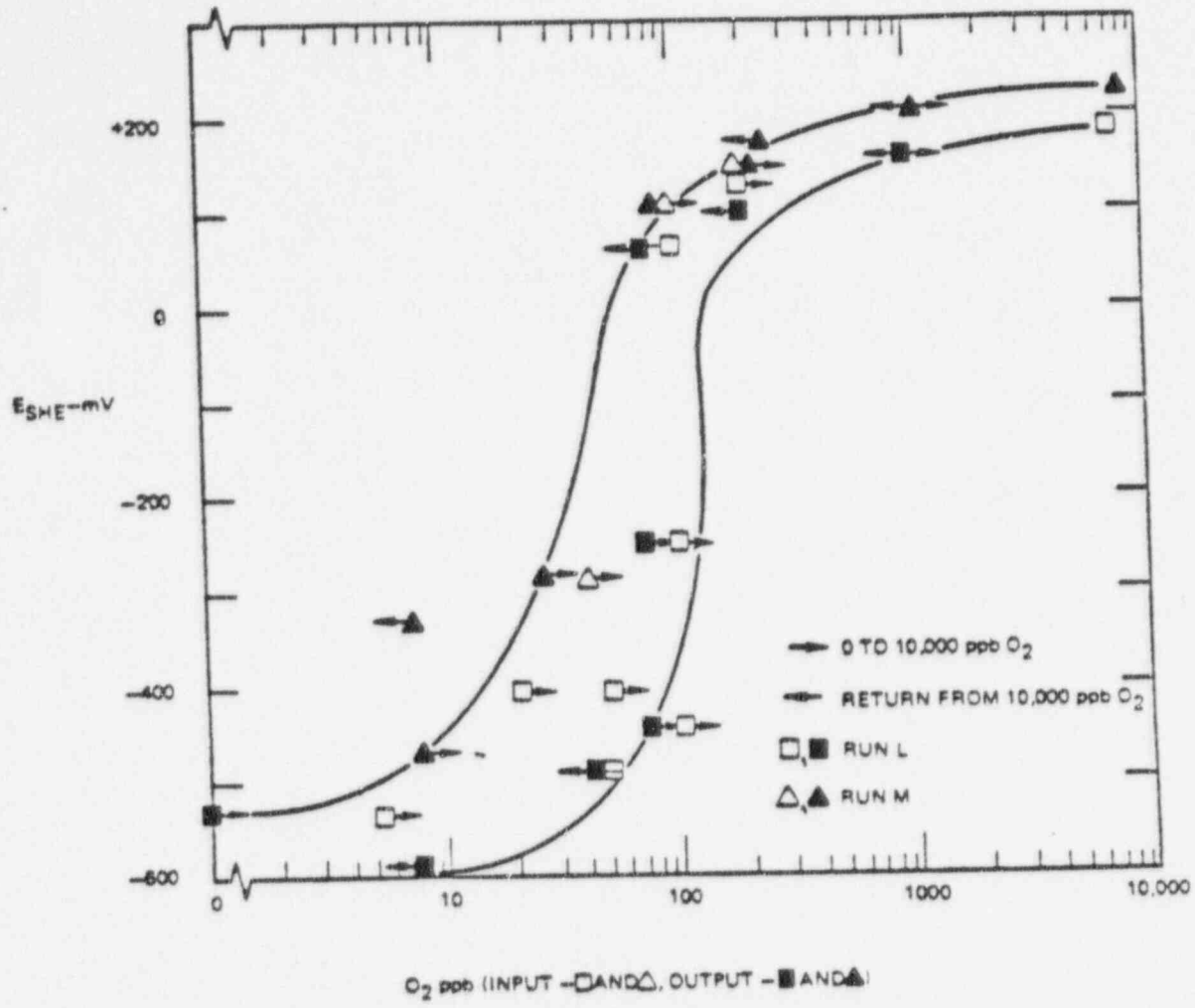

Figure 5-16. The Effect of Dissolved Oxygen on the Oxidation Potential of Platinum in High Purity Water at 274°C (525°F)

90014172

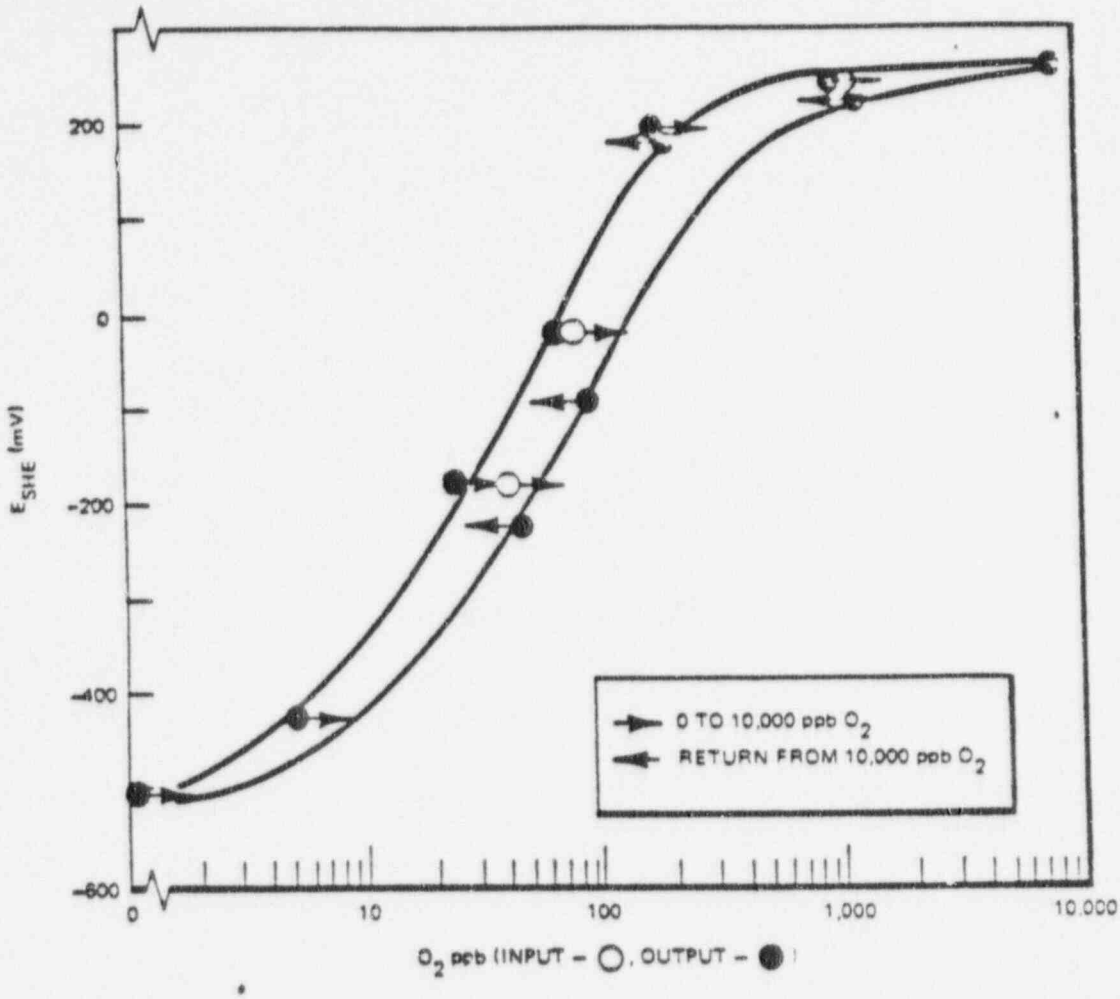

Figure 5-17. The Effect of Dissolved Oxygen on the Oxidation Potential of Platinum in High-Purity Water at 232°C (450°F)

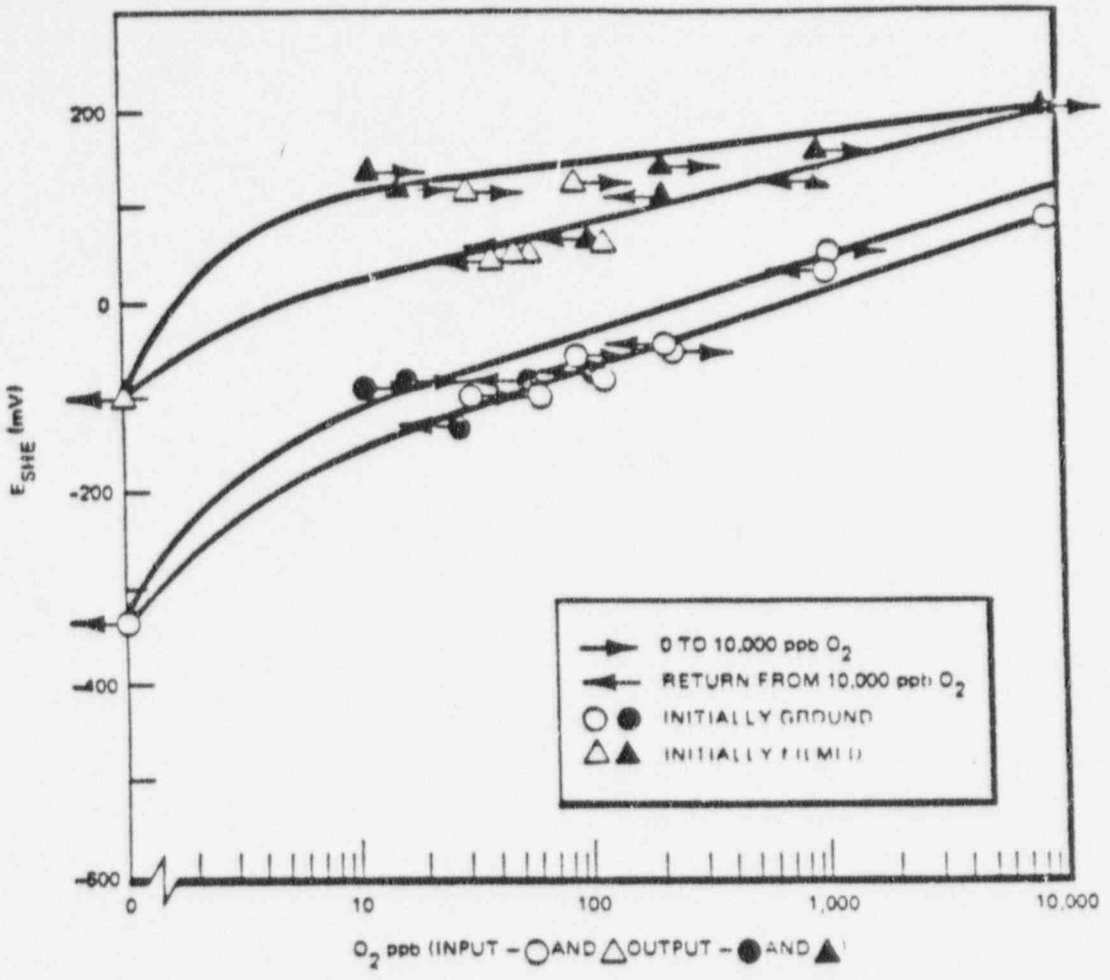

Figure 5-18. The Effect of Dissolved Oxygen on the Corrosion Potential of Type-304 Stainless Steel in High-Purity Water at 191°C (375°F)

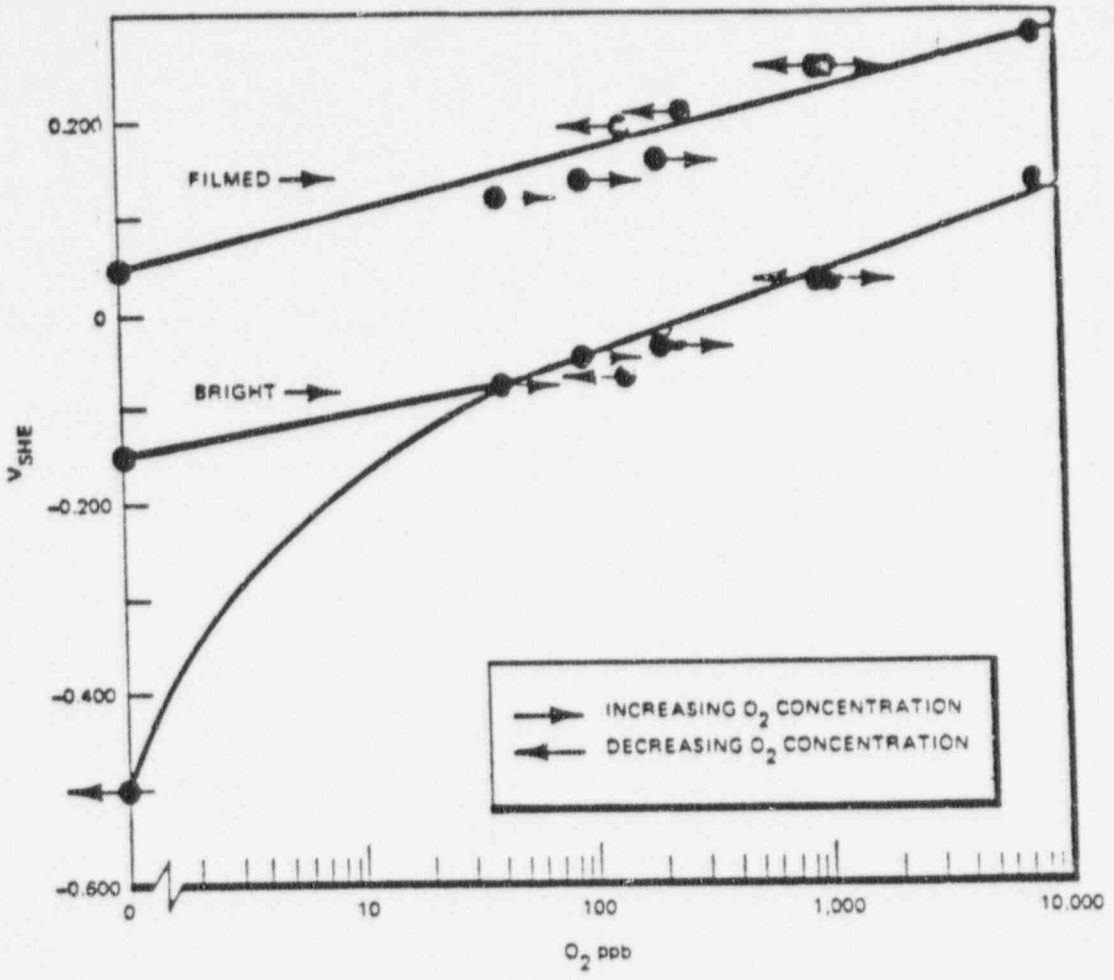

Figure 5-19. The Effect of Dissolved Oxygen on the Corrosion Potential of Bright and Filmed Type-304 Stainless Steel in Water at 149°C (300°F)

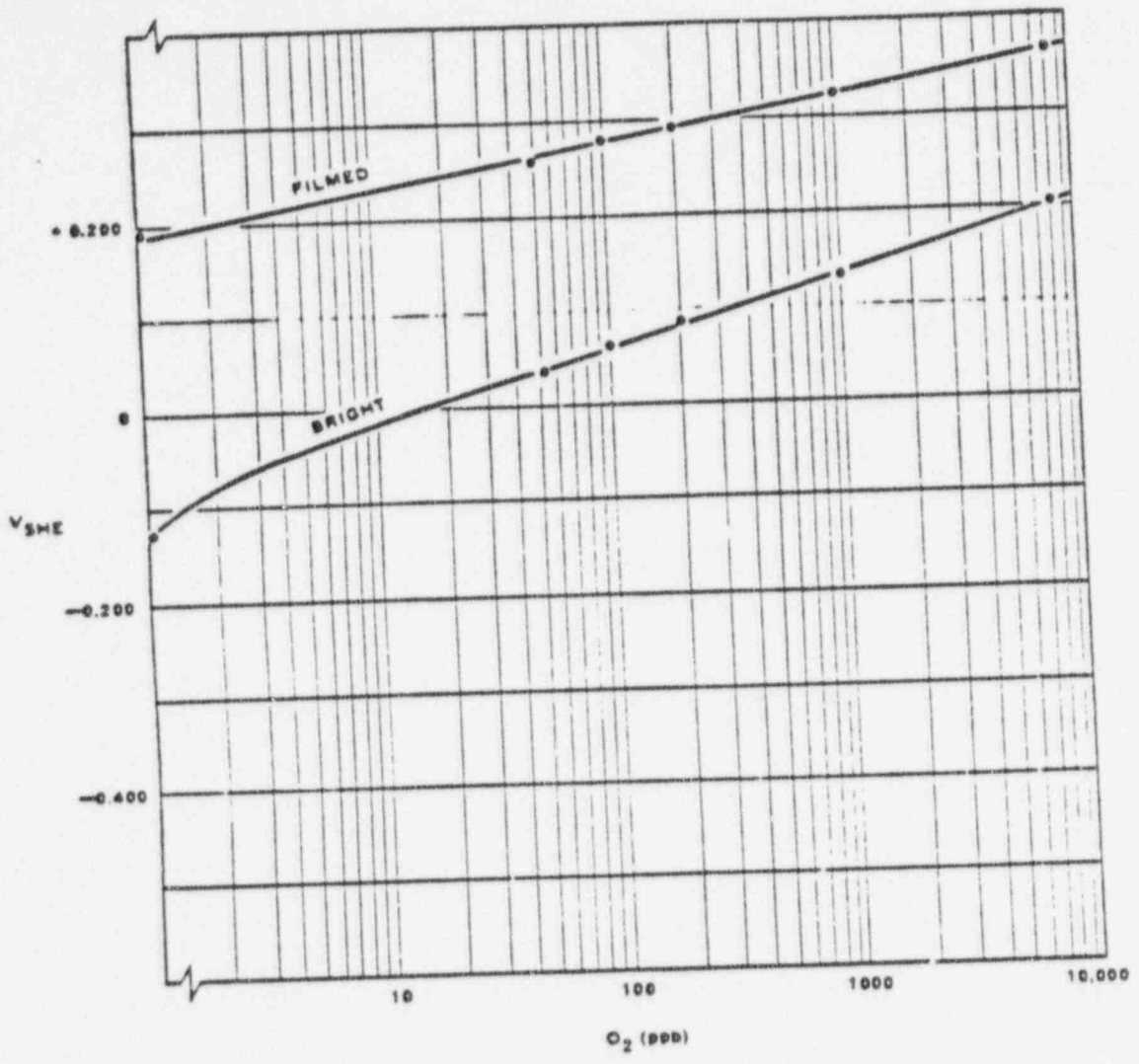

Figure 5-20. The Effect of Dissolved Oxygen on the Corrosion Potential of Bright and Filmed Type-304 Stainless Steel in Water at 107°C (225°F)

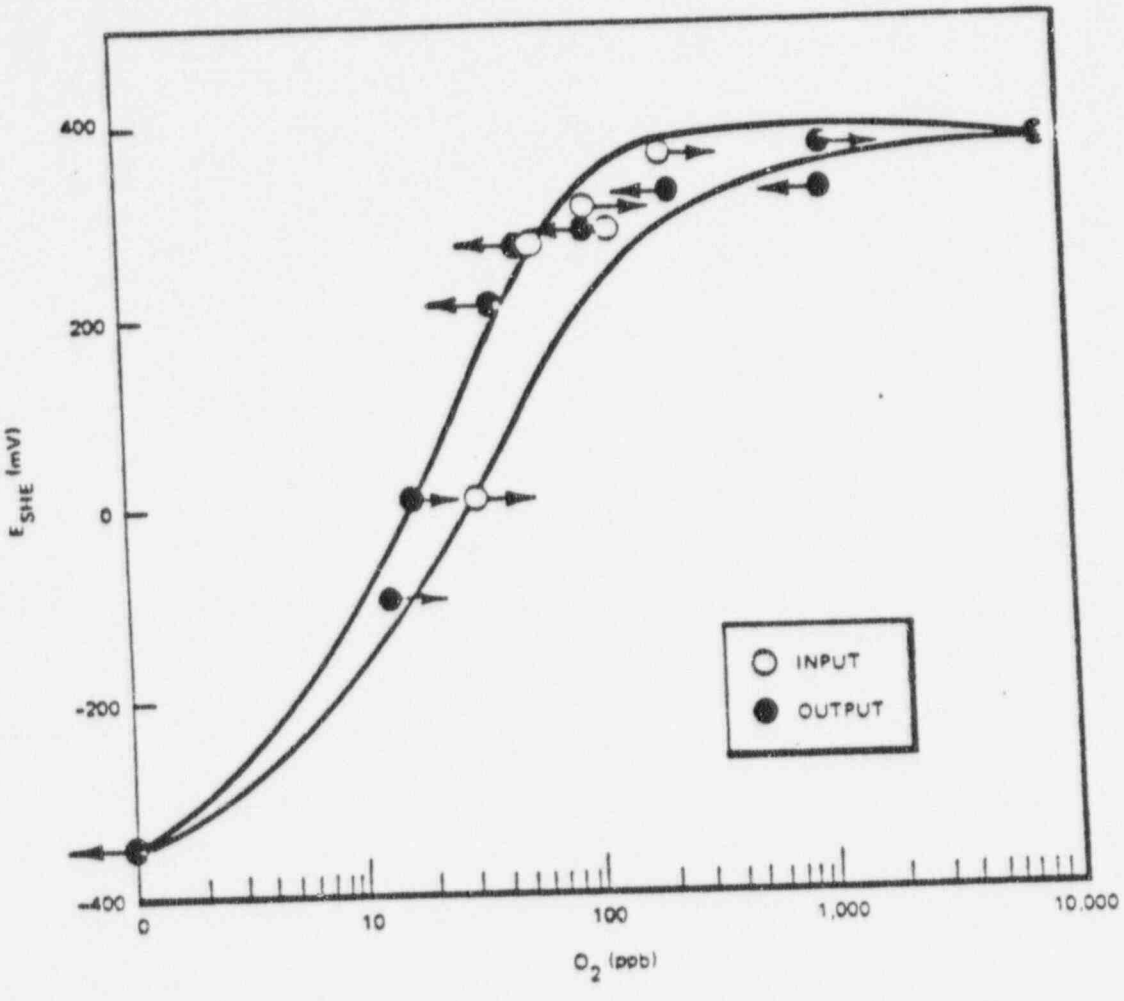

Figure 5-21. The Effect of Dissolved Oxygen on the Corrosion Potential of Platinum in High-Purity Water at 191°C (375°F)

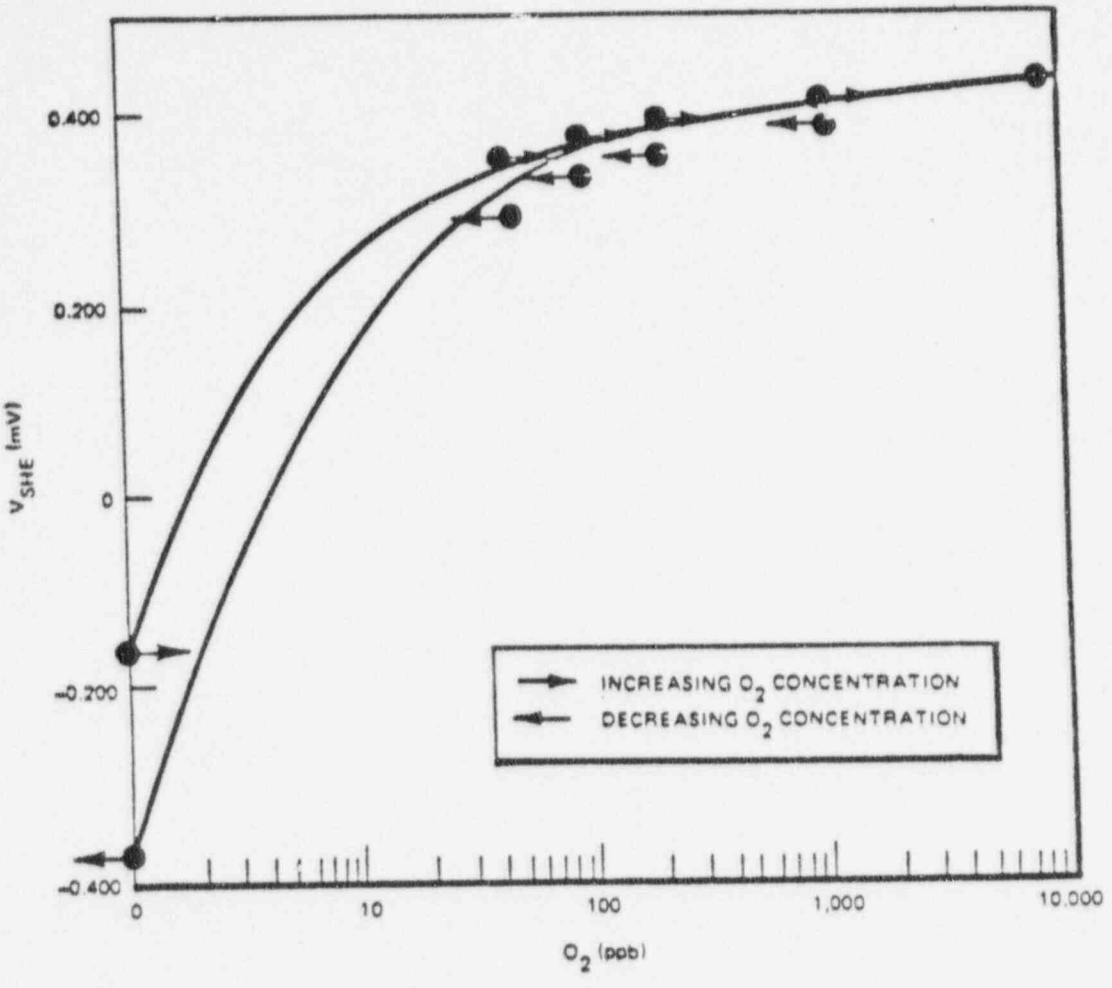

Figure 5-22. The Effect of Dissolved Oxygen on the Oxidation Potential of Platinum in Water at 149°C (300°F)

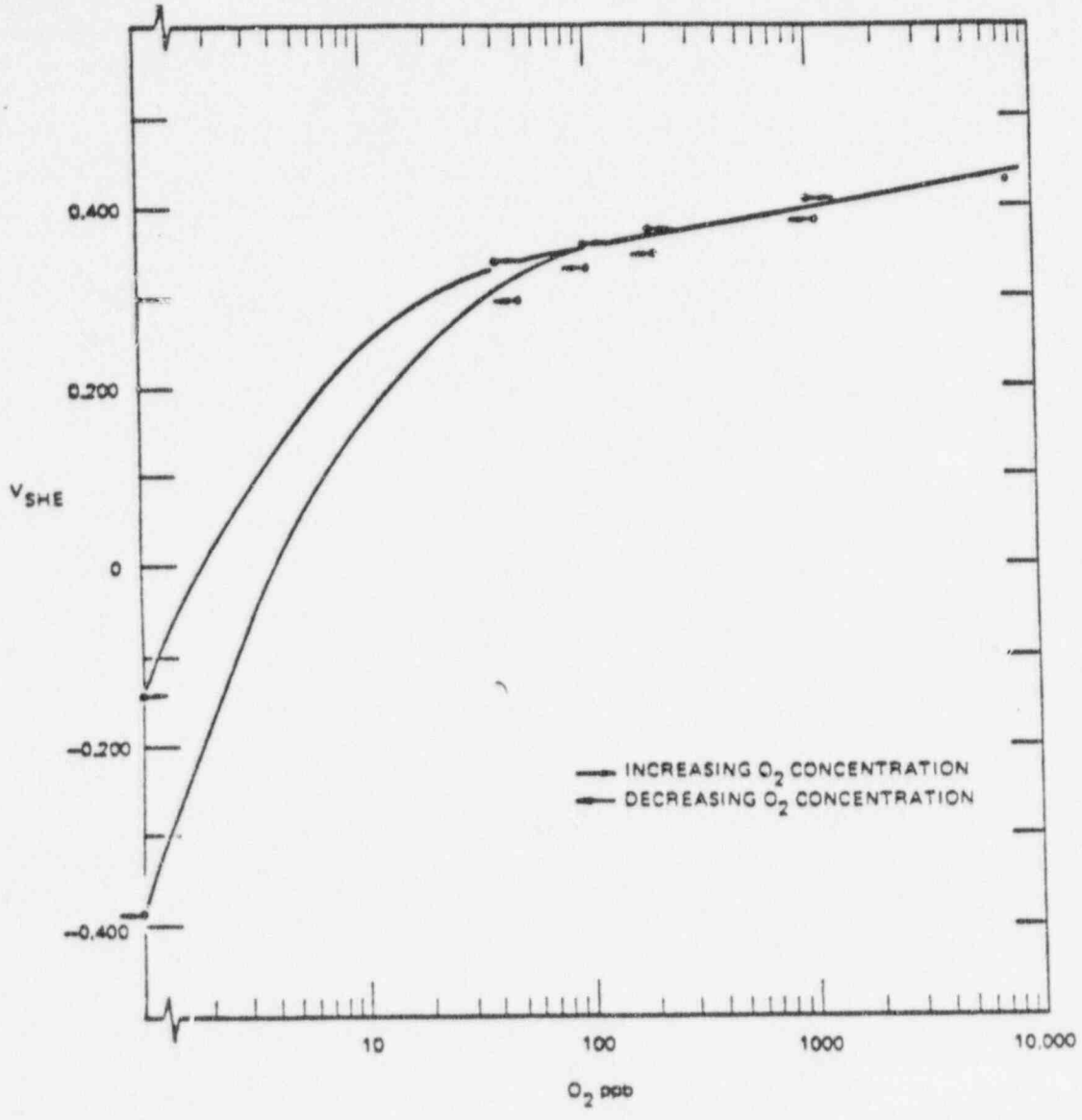

Figure 5-23. The Effect of Dissolved Oxygen on the Potential of Platinum in High Purity Water at 107°C (225°F)

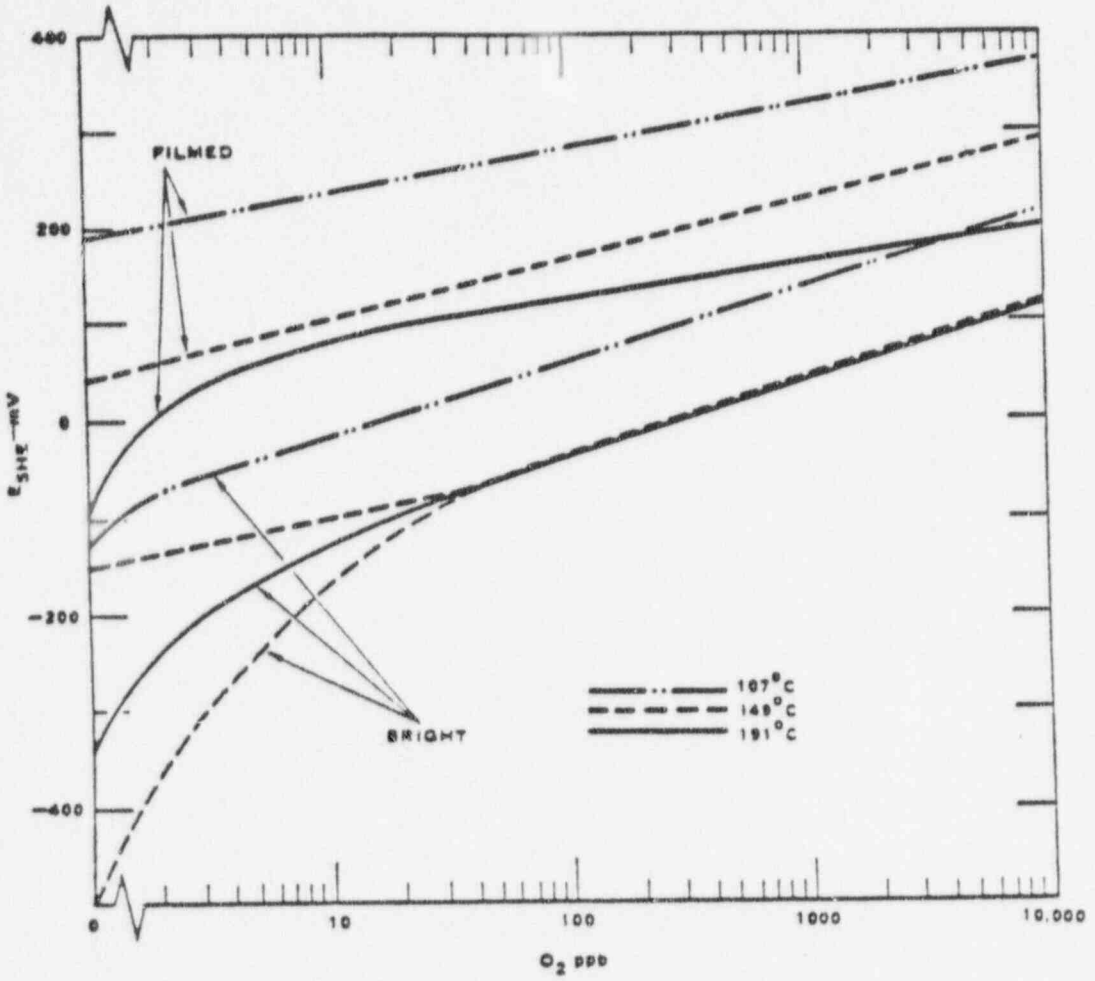

Figure 5-24. The Effect of Dissolved Oxygen on the Corrosion Potential of Bright and Filmed Type-304 Stainless Steel in Water (Average Curves)

different manner than oxygen alone. Table 5-2 summarizes the effect of oxygen and oxygen plus hydrogen on the corrosion potential of stainless steel and platinum at 274°C (525°F) and 232°C (450°F). The corrosion potential of stainless steel did not appear to be significantly affected by the presence or absence of the hydrogen with dissolved oxygen. However, the platinum electrode potential dropped more than 0.700V when 25 ppb hydrogen was present. In the reactor studies at Vermont Yankee it was noted that the platinum electrode responded to changes in hydrogen concentration while the stainless steel electrode was largely unaffected.

Table 5-2
POTENTIALS OF TYPE-304 STAINLESS STEEL AND PLATINUM IN WATER WITH H_2 AND O_2

	Gas Concentrations (ppb)		Potentials (SHE)	
Temperature	O_2	H_2	Type-304 SS	Pt
274°C (525°F)	200	0	~0.170	~0.130
	200	0	~0.097	~0.156
	250	0	~0.048	~0.178
	220	25	~0.085	~0.545
232°C (450°F)	180	0	~0.086	~0.200
	115	25	~0.086	~0.550

At least two concepts appear to emanate from the studies with O_2 and H_2. First, in studies of the specific corrosion behavior of stainless steels (stress corrosion, corrosion fatigue), it is necessary to maintain controlled oxygen concentrations in the water but hydrogen control appears unnecessary. Second, the combination of stainless steel, platinum, and silver chloride electrodes can be used to detect changes in hydrogen concentrations at constant oxygen levels. Such changes in hydrogen concentration have occurred in operating reactors as a result of an upset condition.

5.5 POLARIZATION STUDIES

Experiments where the electrochemical potential is controlled externally cannot be performed in pure water because of the extremely high electrical resistivity. In the polarization studies presented in this section and in the straining electrode experiments given subsequently, an ionic salt was added to decrease the resistivity. The salt, Na_2SO_4, in 0.01 N concentration, was used in these studies because it is not known to cause localized corrosion attack on austentic stainless steel in high-temperature water, nor does the solution have any known inhibiting or accelerating effect on general corrosion. The addition of the proper quantity of Na_2SO_4 to form a 0.01 N solution decreased the resistance between the working and counter electrode three orders of magnitude, from about 3×10^5 to 30 ohms at 274°C (525°F). Because of the properties of pure water the decrease in impedance on addition of Na_2SO_4 is even greater at lower temperatures.

Polarization curves were performed on Type-304 stainless steel and a series of experimental alloys. The experimental alloys were obtained from the General Electric Research and Development Center, Schenectady, N.Y., and had bulk compositions which simulated the local chromium-depleted regions in the vicinity of grain boundary carbides. The compositions of the alloys are given in Table 5-3. In general, the polarization curves were developed at a scan rate of 5 mV/sec (18V/h) starting at $-1200\ mV_{SHE}$, sweeping to $+1200\ mV_{SHE}$ and then reversing the scan back to $-1200\ mV_{SHE}$. The scanning procedure was repeated until six forward and six reverse were completed. A few curves were also developed at slower scan rates. A potentiostat, a programmer, and an X-Y recorder were the main instruments used to produce the curves. The a-c powered instruments were connected to building power through an isolation transformer.

The polarization studies were performed in a 3.8 liter, Type-316 stainless steel autoclave, which was grounded and also used as the counter electrode. The autoclave was part of a refreshed system similar to that shown in Figure 5-11. However, since the electrolyte was 0.01 N Na_2SO_4, purged with nitrogen, those supporting systems used for continuous deionization and oxygen analyses were absent. The reference and working electrode were screwed into

Table 5-3
CHEMICAL COMPOSITION OF MATERIALS USED IN ELECTROCHEMICAL STUDIES

	Heat Number	Composition — Weight Percentage C	Mn	P	S	Si	Cr	Ni
Type-304 SS	M7616	0.060	1.70	0.023	0.012	0.55	18.8	10.34
Experimental Alloy	3696	0.003	1.85	0.005	0.005	0.99	8.1	10.30
Experimental Alloy	3698	0.005	2.06	0.004	0.004	1.00	10.4	10.00
Experimental Alloy	3699	0.003	2.05	0.004	0.004	1.01	12.5	9.40
Experimental Alloy	3697	0.003	1.99	0.004	0.005	0.99	14.3	9.70

tapped holes in the autoclave head. The experimental arrangement was two reference electrodes and three specimen electrodes spaced uniformly around a 12.7-cm (5-in) diameter circle on the autoclave head. Because the potential of the silver chloride reference electrode is known on the standard hydrogen scale at the temperatures used in these tests, all potentials are reported versus the standard hydrogen electrode[1]. The polarization curves also include the voltage loss due to the ohmic resistance of the electrolyte. Voltage losses due to the ohmic component, IR, are non-electrochemical and geometry dependent. Thus, it is preferable to subtract the IR contribution from each potential. Although the polarization curves in general were not IR corrected, the correction factor is known and was small except at high current densities. For example, at 274°C (525°F) significant IR corrections, <50 mV, were necessary at currents above 260 $\mu A/cm^2$.

Figure 5-25 presents the forward and backward polarization scans for mill-annealed Type-304 stainless steel at 274°C (525°F). The IR correction is also given. The scans shown are for the first, second, and fourth through sixth scans. The fourth through sixth scans were identical and thus are shown by a single curve. Although each reverse scan followed each forward scan, for visualization the forward and reverse scans have been separated in Figure 5-25.

During the forward scans (increasing potential), the primary active peak is observed at about −0.500V and a secondary active peak around −0.250V. Following the secondary active peak, the passive region appears to extend from −0.225 to 0.100V. At potentials in excess of the passive region a broad transpassive region which is followed by oxygen evolution occurs in the polarization curves. The transpassive region occurs between about 0.200 to 0.600 V_{SHE} and the onset of oxygen evolution appears to occur at about 0.800V_{SHE}. With successive scans the current associated with the primary and secondary active peak increases, while the transpassive current region decreased in intensity and was absent by the fourth scan. The increase of current in the active region is probably the result of reduced thickness of the corrosion film. Apparently, successive polarization scans thin the surface oxides. The current response in the fourth through sixth scans probably approached the maximum dissolution rate for a film-free surface. With the continual thinning of the corrosion film, less Cr_2O_3 would be present on the surface. Since the transpassive region is the result of the oxidation of Cr_2O_3 to CrO_4^{-2}, the region is absent in the later scans. If the scans are interrupted and the surface oxide allowed to re-form, the transpassive region would reoccur.

Upon reversing the scan direction from oxygen evolution, the current fell sharply. During the first reverse scan the current became cathodic around 0.250V. Cathodic to anodic current changes or anodic to cathodic changes are noted by a discontinuity in the current/voltage behavior. The cathodic current peaked at about 0.200V, then decreased and changed to anodic current at 0.140V.

During successive reverse scans this cathodic region disappeared. This cathodic region, just below the oxygen evolution potential, is thought to be the reverse reaction of the oxidation of Cr_2O_3; or the reduction of Cr^{+6} to Cr^{+3} according to the reaction:

$$6e + 2\,CrO_4^{-2} + 5\,H_2O \rightarrow Cr_2O_3 + 10\,(OH)^-.$$

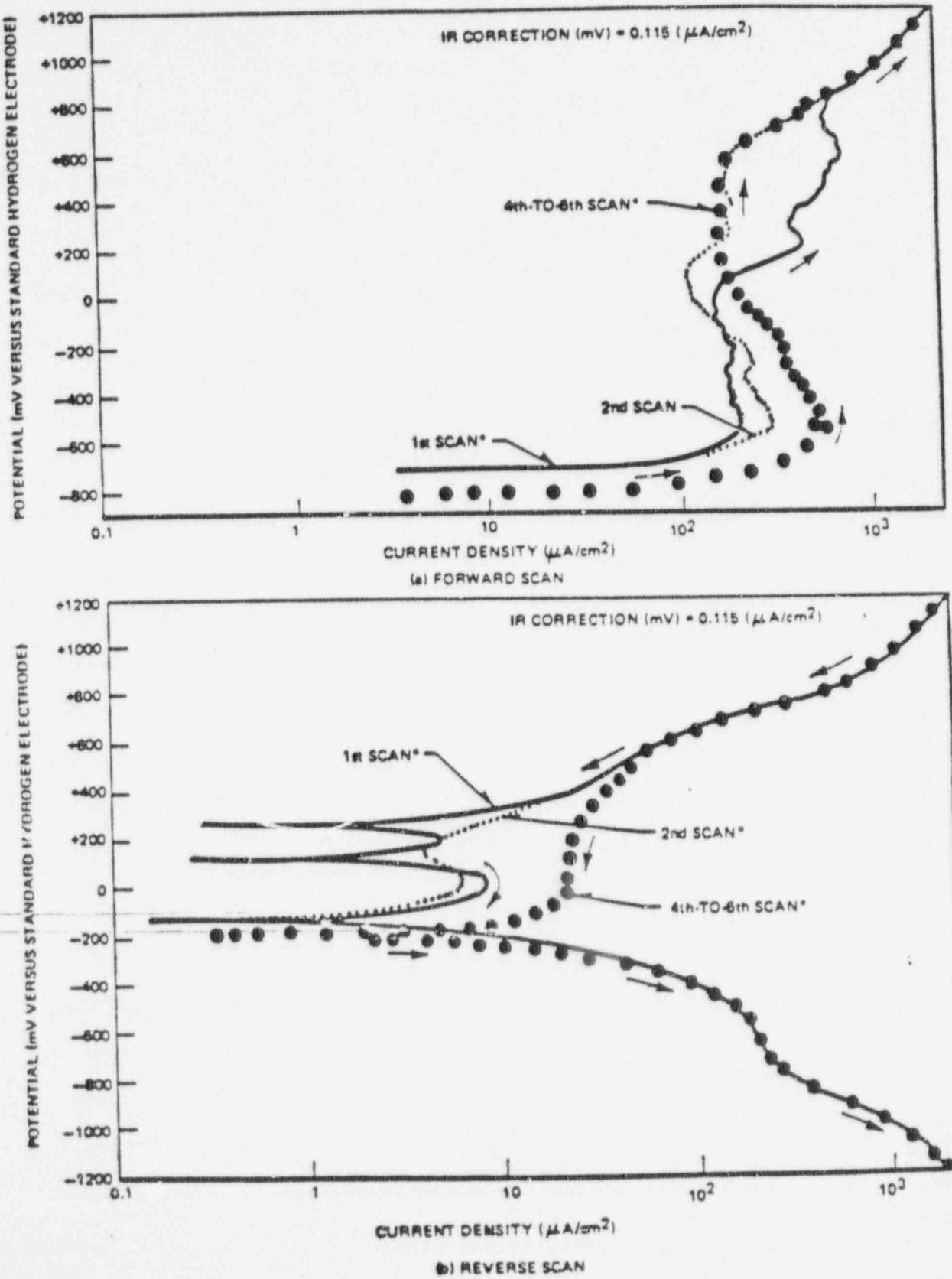

Figure 5-25. Forward (A) and Reverse (B) Scan Polarization Curves of Mill Annealed Type-304 Stainless Steel at 274°C (525°F) in Deaerated Water Containing 0.01 N Na_2SO_4 (Scan Rate 5 mV/sec)

Because the forward scans generated CrO_4^{-2} from Cr_2O_3, the loss of Cr_2O_3 from the surface with successive forward scans resulted in the disappearance of CrO_4^{-2} from the electrolyte and the disappearance of the cathodic region during the reverse scan. However, because the net current measured is the difference between the cathodic and anodic currents, the dip in the anodic current in the second scan just below the oxygen evolution potential region was probably caused by some remaining cathodic current from the reduction of CrO_4^{-2}. By the fourth through sixth reverse scans, no trace of the above reduction reaction remained.

As the potential was lowered below 0.140V the current remained anodic, but below about 0.0V the anodic current began to drop off, signaling the beginning of the final cathodic region. The final cathodic region began around −0.120 to −0.200V and was probably caused by the reduction of a small amount of oxygen in solution according to the reaction:

$$4e^- + O_2 + H_2O \rightarrow 4\,(OH)^-.$$

The oxygen in solution was generated at high potentials at the end of the forward scan, but because of its extremely low partial pressure and the irreversibility of the above reaction, the reduction reaction occurs more than 0.7V below the equivalent oxidation reaction (oxygen evolution reaction). The cathodic current persisted until termination of the reverse scan. However, an inflection occurred at about −0.500V. The inflection or flattening out occurs at the same potential as the peak of active metal dissolution during a forward scan and thus indicates that a metal oxidation (anodic) current is competing with the reduction current (cathodic). Below about −0.700V the reverse scan became the same as the forward scan. This final region of the cathodic current was undoubtedly the result of the reduction of H_2O or the evolution of hydrogen according to the reaction:

$$2e^- + 2\,H_2O \rightarrow H_2 + 2\,(OH)^-.$$

In most of the polarization experiments a fast scan rate, 18V/h, was used. Figure 5-26 compares polarization curves at 177°C (350°F) obtained at the fast scan rate and at a slow rate. The curve developed at the slower scan rate has lower currents at equivalent potentials; the various regions appear more clearly delineated and the current changes indicate a change in the oxidation reaction occurs at a slightly lower potential. The latter difference was probably the result of the lower IR contribution to each potential on the curve. In general, the slower scan rate result in more detail on the polarization curve which may be useful in providing a more complete understanding of the corrosion behavior of alloys of interest over an extremely large potential region. Subsequently, the specific potential regions on the polarization curves will be related to in-reactor measured potentials as a function of temperature.

5.6 EFFECT OF ALLOY COMPOSITION AND TEMPERATURE ON THE POLARIZATION BEHAVIOR

The polarization behavior of alloys that contain <18% Cr can provide understanding of grain boundary environmental reactions that occur during IGSCC. Figure 5-27 shows a comparison of polarization curves obtained at 288°C (550°F) for Type-304 stainless steel and two chromium-depleted alloys. With decreasing chromium content the tendency for alloy passivation becomes less. The 8% Cr alloy exhibited large anodic dissolution currents over a broad potential range. These results indicate that at reactor potentials [$-0.10V_{SHE}$ at 274° (525°F)] the anodic dissolution current for chromium-depleted grain boundary regions would be at least an order of magnitude higher than for the matrix alloy (18% Cr).

The polarization behavior of stainless steel and the experimental alloys that contained <18% Cr were also studied as a function of temperature. Figure 5-28 shows the polarization behavior, first forward scan, of Type-304 stainless steel at 288, 232, 177, and 127°C (550, 450, 350, and 260°F). The major difference between these curves is the shift to higher potentials for each peak and region with decreasing temperature. In general, the lower the temperature the lower the current levels.

Figure 5-29 shows combined forward and reverse polarization scans for Type-304 stainless steel at 127°C (260°F). The curves are quite similar to those at 274°C (525°F) (Figure 5-25 with the exception that the transpassive region persisted in later forward scans.

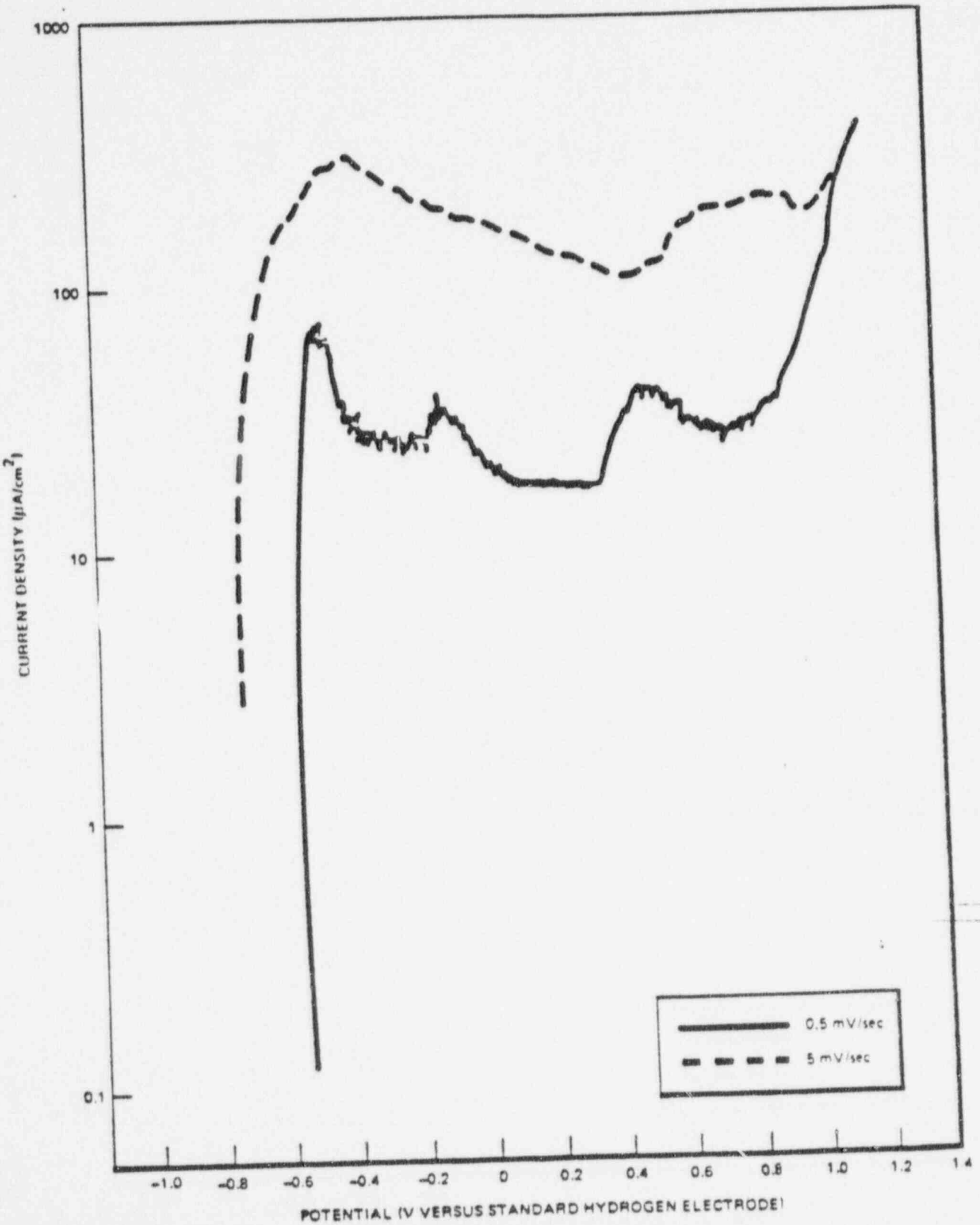

Figure 5-26. Effect of Scan Rate on Mill-Annealed Type-304 Stainless Steel at 177°C (350°F)

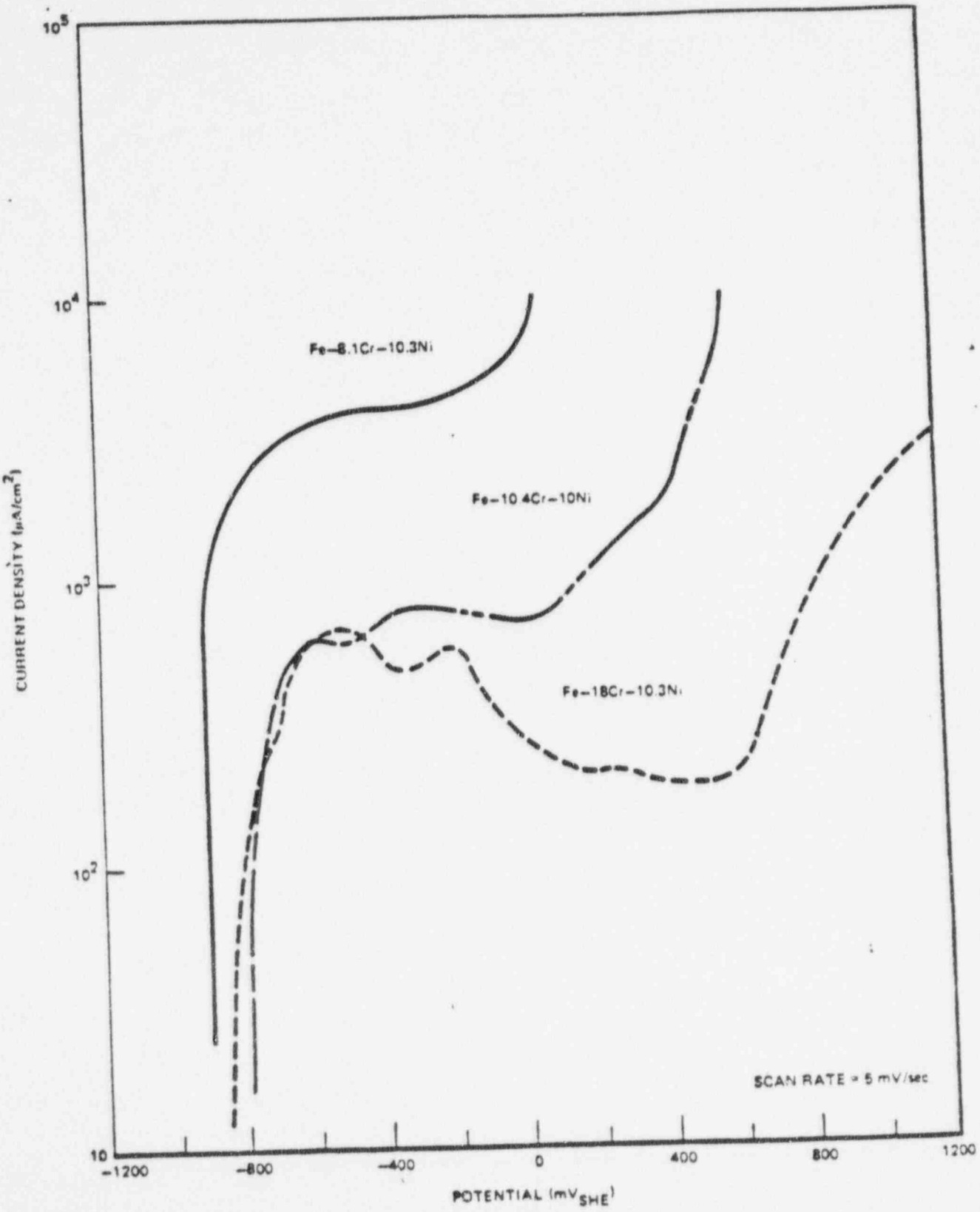

Figure 5-27. Effect of Chromium Content on the Anodic Polarization Behavior of Fe-Cr-Ni-Alloys in Deaerated Water Containing 0.01 N Na_2SO_4 at 288°C (550°F)

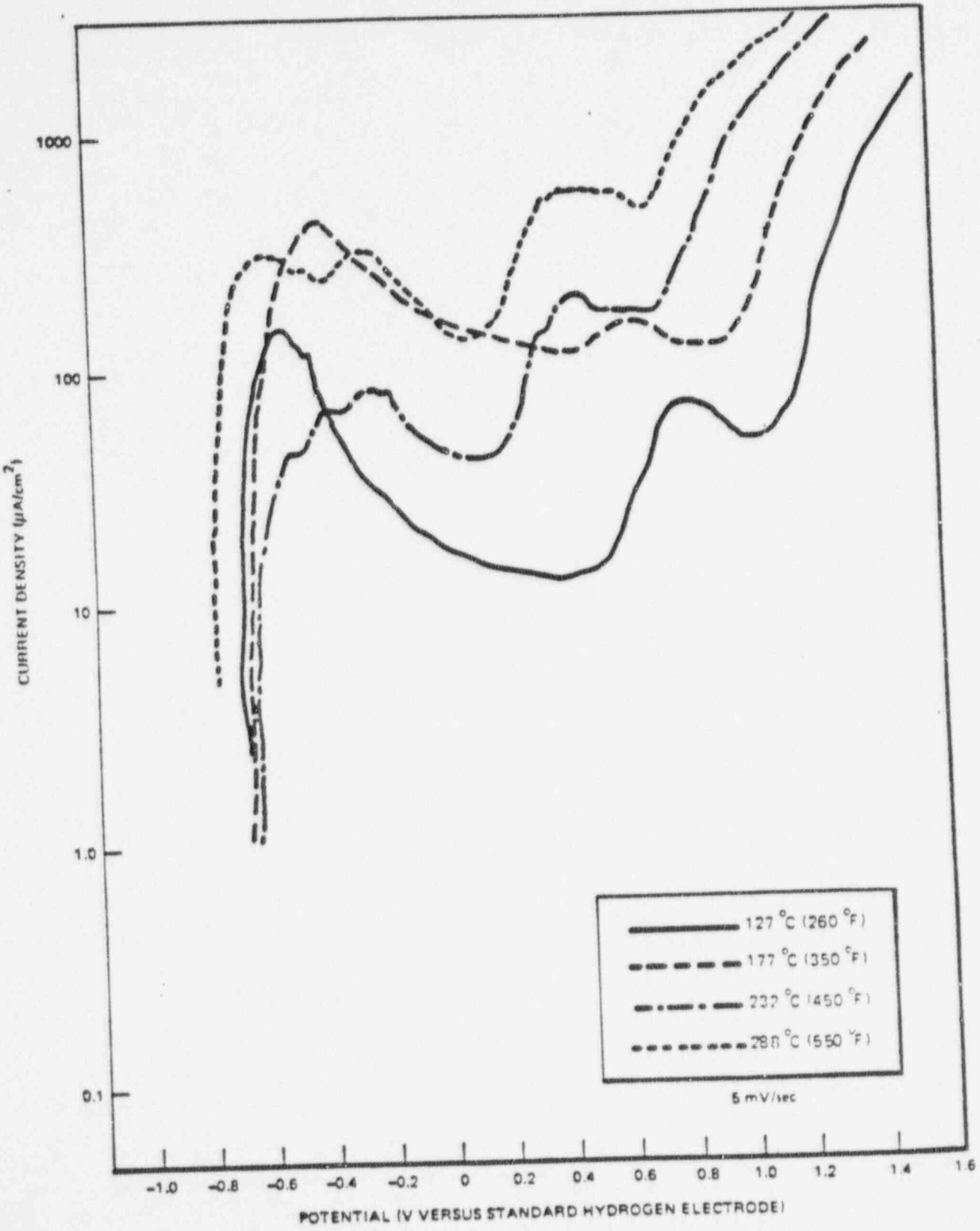

Figure 5-28. Effect of Temperature on Polarization Curves for Type-304 Stainless Steel

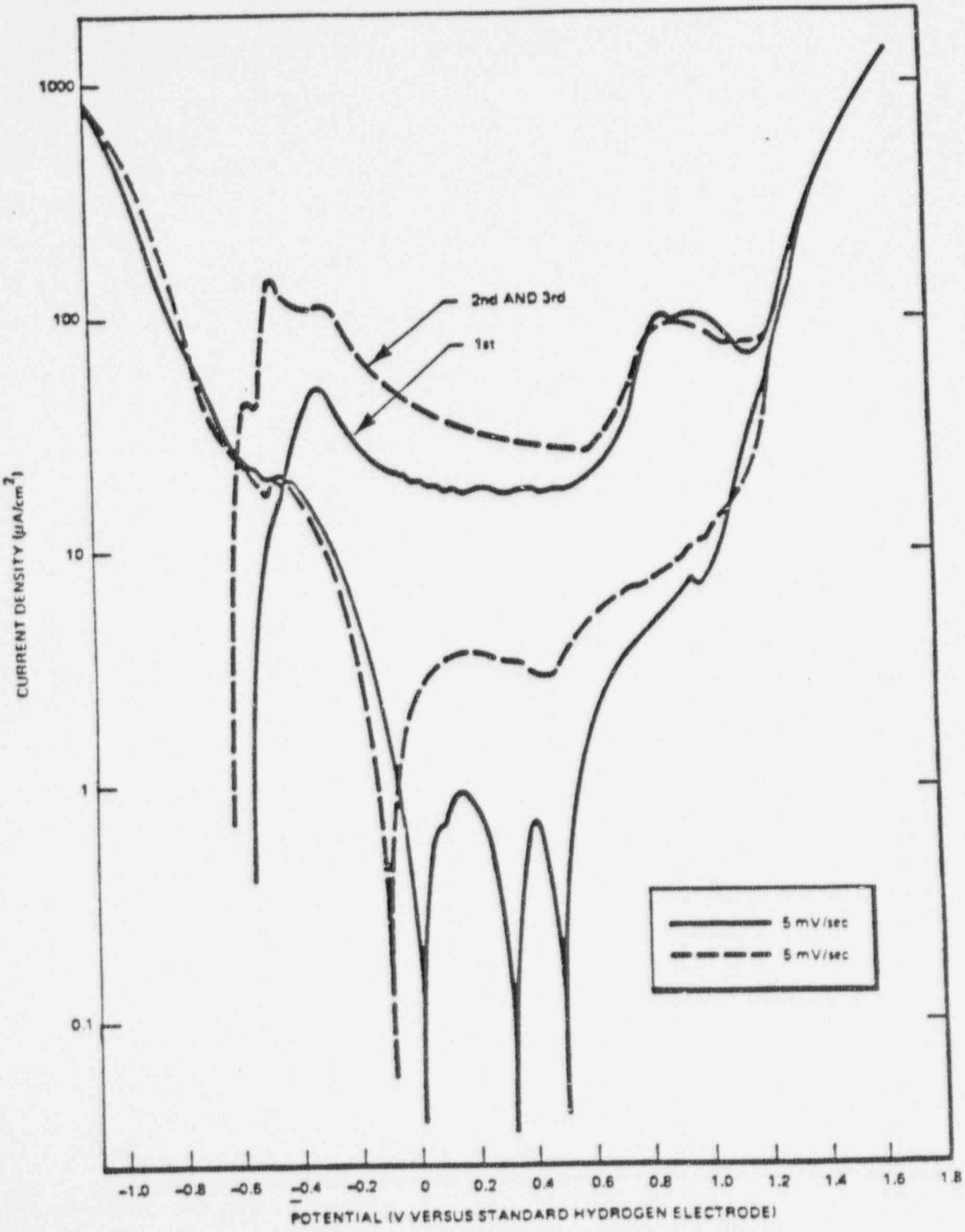

Figure 5-29. Forward and Reverse Polarization Scans of Type-304 Stainless Steel at 127°C (260°F)

Because of the large number and complexity of forward and reverse scans that were performed on Type-304 stainless steel, a schematic representation of the peaks in the polarization curves as a function of temperature was prepared. Figure 5-30 shows the general shape of the polarization curve. The forward scan (increasing potential from hydrogen to oxygen evolution) is the solid curve while the dashed curve (decreasing potential from oxygen to hydrogen evolution) is the reverse scan. The various peaks on the scans are noted by the following symbols.

E_c = open circuit potential
E_{c_1} = primary active peak where active metal dissolution occurs
E_{c_2} = secondary active peak, which may be the result of nickel or hydrogen oxidation
E_{c_3} = transpassive peak; the oxidation of Cr_2O_3 in the corrosion film to soluble $CrO_4^{=}$.
E_{p_2} = initiation of oxygen evolution (the oxidation of water)
$E_{a\text{-}c}$ = the change of current from an anodic to cathodic reaction (oxidation to reduction current) on the reverse scan.

The cathodic reaction that occurs below $E_{a\text{-}c}$ is the reduction of oxygen according to the reaction $4e^- + O_2 + H_2O \rightarrow 4(OH)^-$. $E_{a\text{-}c}$ can occur either close to the transpassive peak E_{c_3} (as shown in Figure 5-30) or several hundred millivolts below. Figure 5-31 presents the potentials of the electrochemical reactions described above for three metallurgical conditions. For comparison the Vermont Yankee startup is also shown. The Vermont Yankee data were, of course, obtained in pure (reactor) water while the polarization curves were in 0.01 N Na_2SO_4. As will be seen subsequently, to correct the pure water data (Vermont Yankee data) to the Na_2SO_4 electrolyte 0.15V should be subtracted from the startup potentials at 275°C and 0.075V should be subtracted from the 232°C (450°F) reactor data point. In any event, the reactor startup data lie just below E_{c_2}. Thus, to understand the electrochemistry of corrosion reactions in BWR piping environments it is not necessary to consider potentials and reactions in excess of E_{c_2}. On the other hand, higher potentials may occur in the core environment.

The polarization curves of the simulated grain boundary alloys (<18% Cr) are shown as a function of temperature in Figures 5-32 and 5-33 for the 8 and 10% Cr alloys. Active-passive behavior was achieved at 177°C (350 F) for the 10% Cr alloy and at 121°C (250°F) for the 8% alloy. Above these temperatures the alloys appear to corrode actively when polarized anodically. From these data it can be predicted that in high-temperature water the sensitized grain boundary region would be attacked with increasing severity with increasing potential, above some minimum potential value. However, where active-passive transitions occur, the grain boundary attack would be limited to some narrow potential region which would be determined by the degree of chromium-depletion and the temperature. Thus, at low temperatures IGSCC could occur only when the combination of oxidizing species in the environment (O_2 and H_2O_2) produced a very specific corrosion potential. Identification and avoidance of these potential and equivalent chemical regions could be significant in preventing crack initiation during BWR startup. In addition, alloys that are only slightly sensitized, for example those that contain ≥10% chromium at the grain boundaries, would be less susceptible to IGSCC with decreasing temperature [<177°C (350°F)]. This latter statement indicates that only a severely sensitized condition (welded + LTS) would be susceptible to low temperature cracking.

5.7 STRAINING ELECTRODE STUDIES

The straining electrode test (SET) is a modification of the constant extension rate test (CERT). In both of these tests a tensile specimen is strained continuously in a controlled environment. In CERT, environmental control is achieved by control of the dissolved oxygen concentration in the influent water. From a previous section in this study, oxygen vs. potential curves, it was seen that a specific dissolved oxygen concentration results in a specific corrosion potential on Type-304 stainless steel. In SET, as in the polarization studies, the corrosion potential was controlled electrochemically with a potentiostat located outside of the controlled environment. Each SET was conducted at a constant potential and a constant temperature and in an electrolyte of 0.01 N Na_2SO_4. These tests were conducted to determine the minimum potential for IGSCC of welded stainless steel (that potential at or below which IGSCC does not occur). Figure 5-34 shows a schematic of the SET facility. Four electrically insulating and sealing glands are screwed into the autoclave cover. The conductors (rod or wire) pass through the glands and are connected internally and separately to the tension sample, the reference electrode, and an unstressed cyclindrical stainless steel electrode. Outside of the autoclave the conductors are connected to the potentiostat and readout systems. The portion of the system that supplies the electrolyte is quite similar to that used in polarization experiments discussed previously.

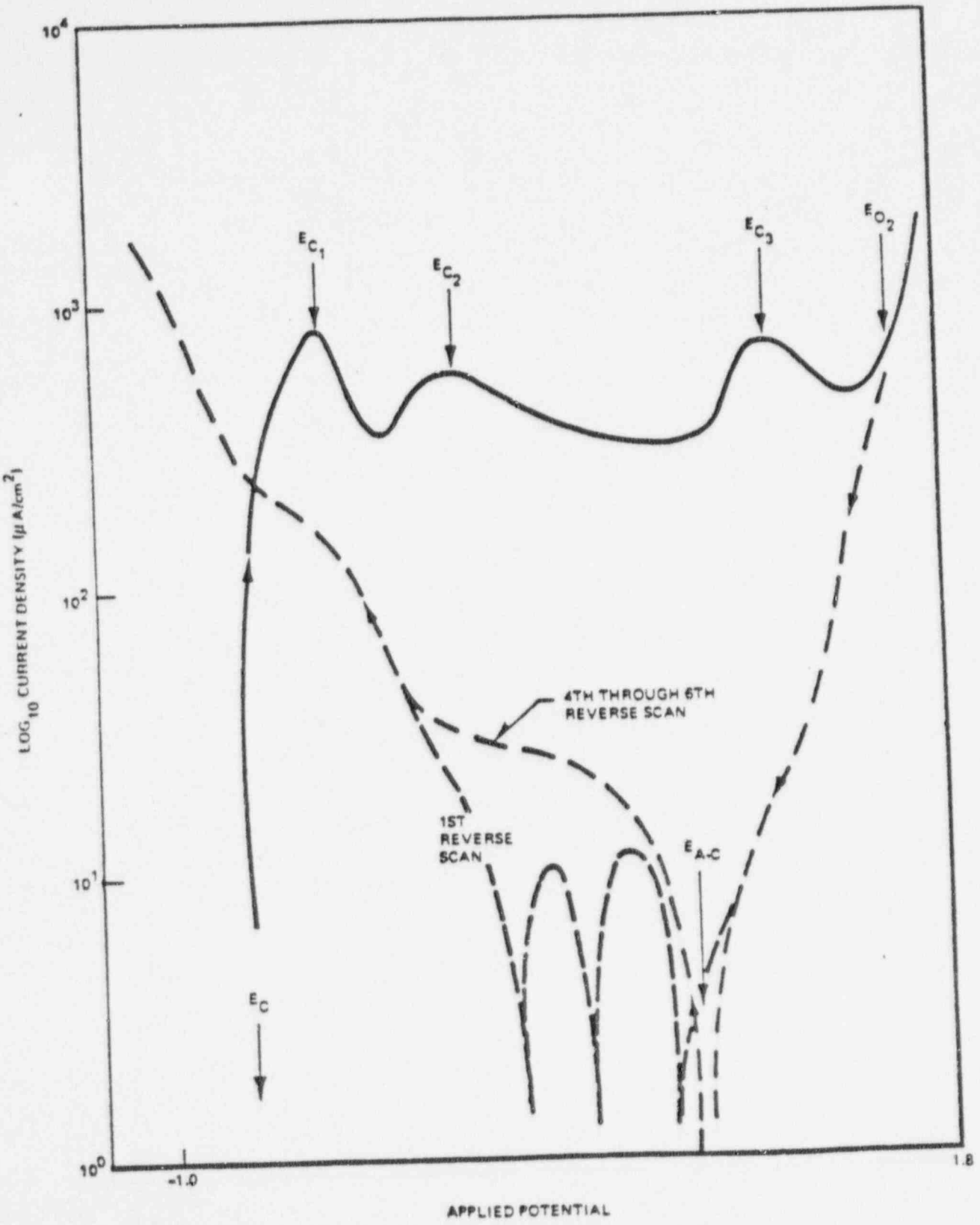

Figure 5-30. Schematic of the Shape of the Polarization Curve for Type-304 Stainless Steel in High Temperature With the Identification of Several Critical Potential Regions

90014190

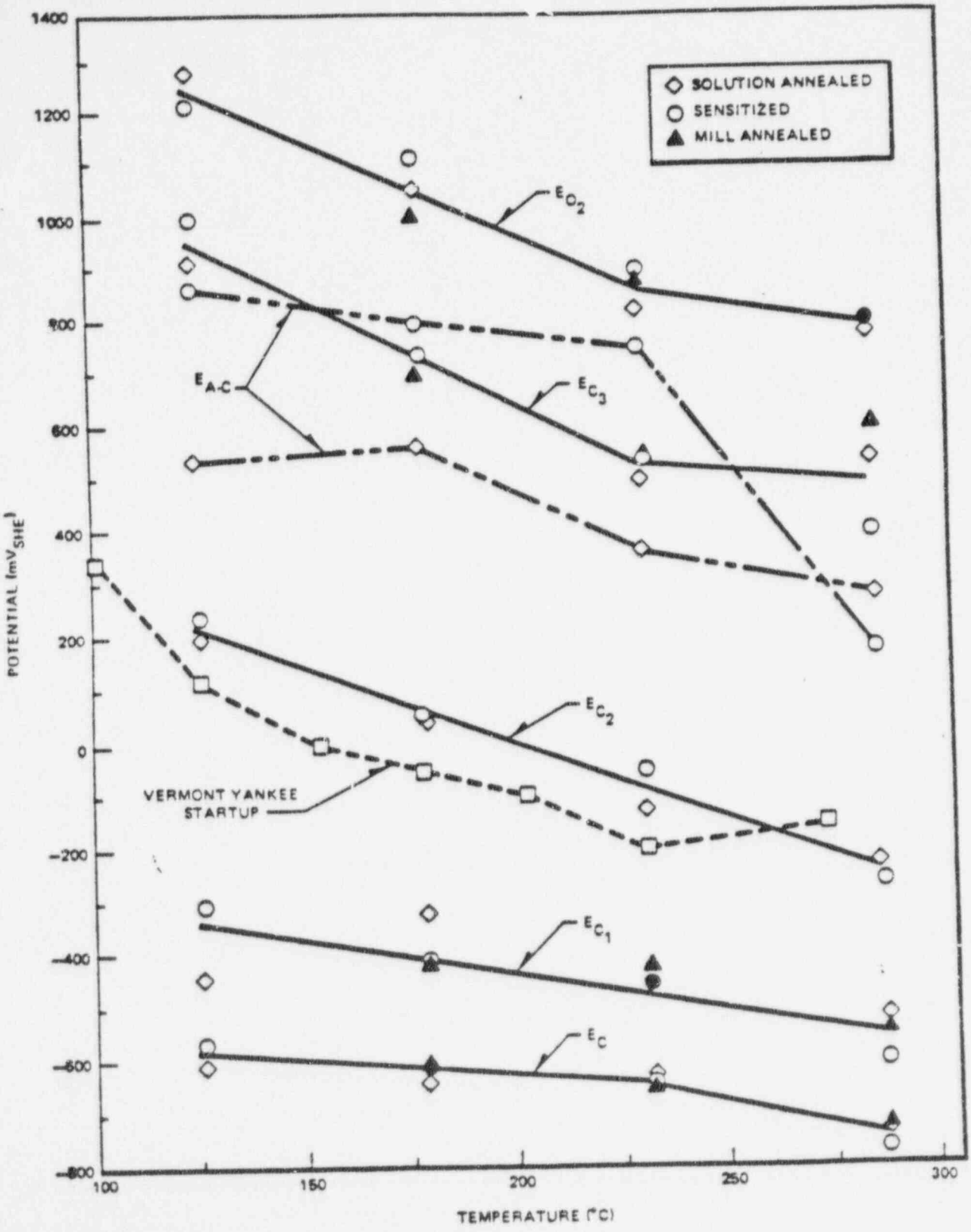

Figure 5-31. Effect of Temperature on Various Potentials of Type-304 Stainless Steel in Water With 0.01 N Na_2SO_4

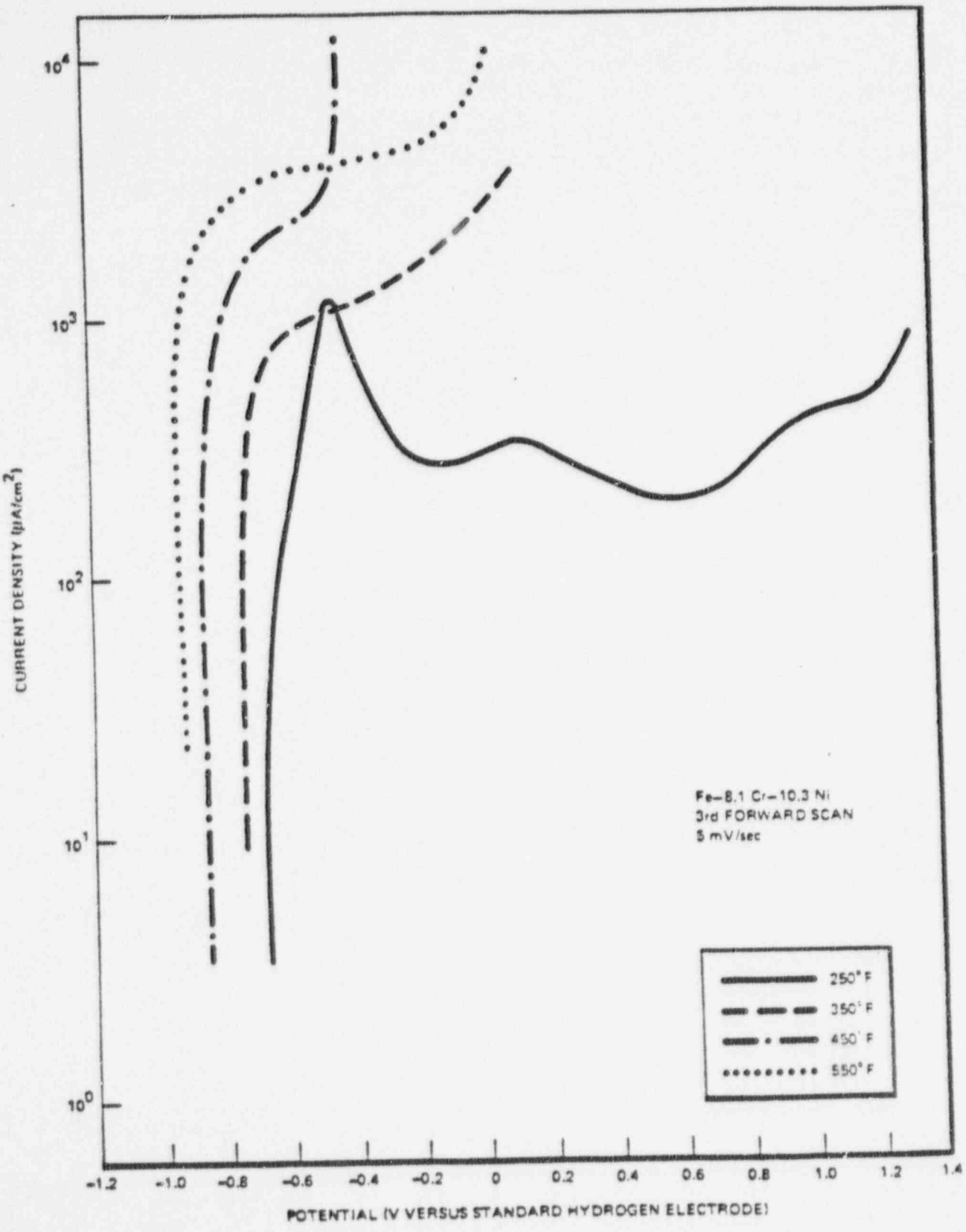

Figure 5-32. Polarization Behavior of 8% Chromium Alloy Versus Temperature

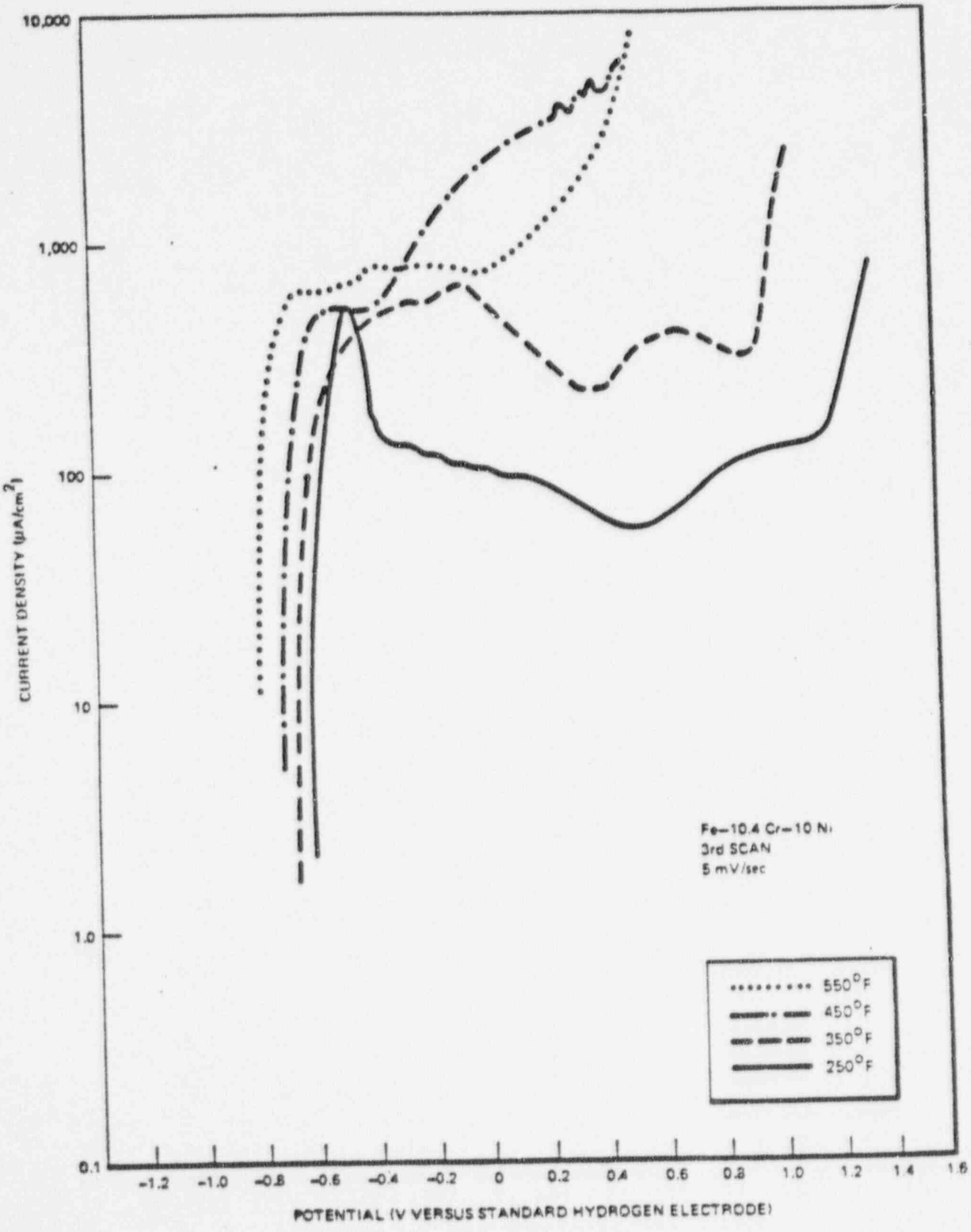

Figure 5-33. Polarization Behavior of 10% Chromium Alloy Versus Temperature

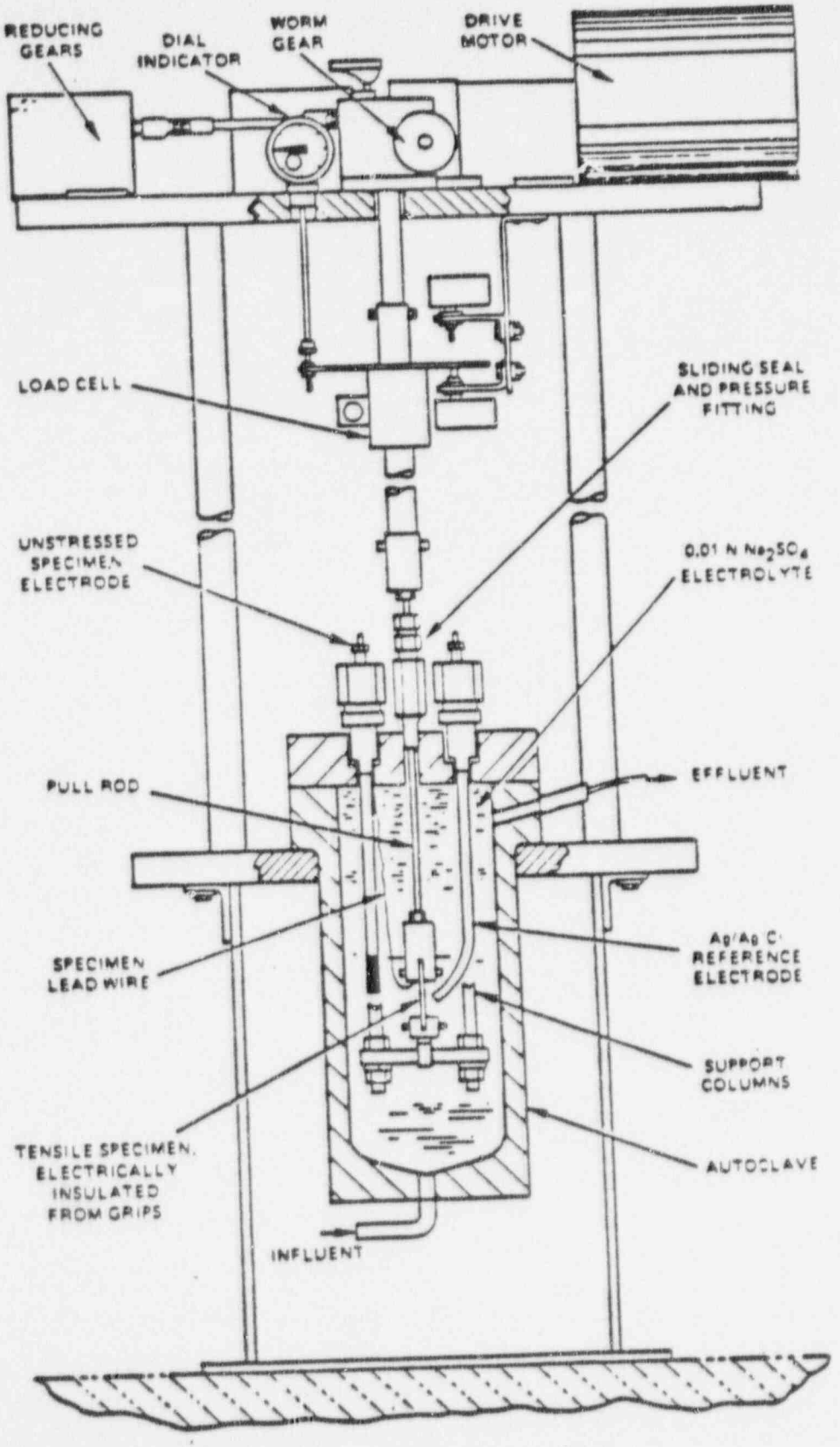

Figure 5-34. Straining Electrode Facility

Above the autoclave is the external drive system that allows the continuous straining of the tension sample. The drive system, anchored on aluminum plate and supporting framework, consists of a variable-speed motor, variable and fixed gear reducers, and a worm gear which transforms rotary motion to vertical movement. While it was possible to change the speed of the vertical movement (sample extension rate) by varying the settings on the motor and gear reducers, all experiments were conducted at a fixed extension rate of 0.001 in/7.1x10^{-7} cm/sec which approximated a strain rate of 2x10^{-8} min^{-1}. The pull rod from the stressing system was linked to the tension specimen pull rod which passed through a Teflon seal in the central sealing gland on the autoclave head. The Teflon seal allowed the rod to pass through the gland with negligible frictional loss. As the pull rod was withdrawn from the autoclave the specimen strained. The load cell, which was connected to the pull rod, and the signal-conditioning system monitored the load required to strain the specimen during a SET.

To control the corrosion potential during straining it was necessary to insulate the tension sample from the grips and pull rod. This was done by using pre-oxidizing insulating Zr-2.5 Nb pins, rather than conducting high strength Fe or Ni base alloy pins and Teflon sheets. The Teflon prevented the faces of the tab sections from touching the slots in the upper and lower grips. A stainless steel wire was spot welded to the tab section of the specimen, and routed through an insulting gland to the potentiostat outside of the autoclave. During SET the potentiostat was used to maintain the required corrosion potential by controlling the potential between the tension sample and the high-temperature reference electrode.

The Type-304 stainless steel tension specimens were fabricated in the form of dog-bones from 10.16-cm (4-in.) schedule 80, high heat input*, welded pipe, Heat M7616. The tensile specimens were taken from the internal surface of the pipes with the weld root in the center of the gage as shown in Figure 5-35. Thus these samples had the inside and welded surfaces preserved. A few samples were also taken from mid-wall of the pipe. Most of the tensile specimens were tested in the as-welded condition. A few welded samples were given a post-weld LTS** heat treatment or were surface ground after welding. The LTS treatment increases the degree of sensitization in the weld heat affected zone and surface grinding results in a cold-worked brittle surface layer and/or martensite transformations, which will initiate cracks upon strain.

In addition to determining the effect of corrosion potential on IGSCC, the SET was also used to determine the behavior of selected pipe remedies at controlled potentials known to cause IGSCC on as-welded Type-304 stainless steel. Tension specimens for the evaluation of pipe cracking remedies were fabricated from welded Type-304 stainless steel pipe, Heat M7616, which was given a specific protective metallurgical treatment, or from a welded pipe of an alternate austenitic alloy thought to be highly resistant to IGSCC. The remedies applied to welded pipe Heat M7616 and studied by the SET technique were heat-sink welding, as-welded plus solution heat treatment, and application of corrosion-resistant cladding with an intermediate solution heat treatment. These remedies are discussed in detail in Task 1 of this report. The alternate austenitic alloys studied by SET were as-welded Type-304L and as-welded CF3A (cast 304L). All straining electrode tests of the pipe cracking remedies were conducted at 274°C (525°F) while SET of as-welded Type-304 stainless steel were conducted at 274°C (525°F) and 232°C (450°F).

The results of the straining electrode experiments conducted at various potentials at 274°C (525°F) on welded Type-304 stainless steel are given in Table 5-4. For a susceptible alloy in a given metallurgical condition, increasing the potential increases IGSCC. The factors used in ranking the resistance of each sample to IGSCC at each potential are the mechanical properties, time to failure, and type of failure (IGSCC or ductile). When a sample failed completely by IGSCC the fracture stress and ultimate tensile strength were about the same, because very little lateral deformation (reduction in area) occurred. Thus, similar but low values of fracture stress and ultimate tensile stress indicate a stress corrosion failure. Other indications of stress corrosion are low reduction of area and low percent elongation. Since all of the samples were tested at the same crosshead speed and had approximately the same dimensions, the longer the time to failure, the greater the resistance to cracking.

It was found that the limiting potential for IGSCC of welded Type-304 stainless steel is not a single value but depends on the metallurgical structure. For example, Table 5-4 indicates that $-0.400V_{SHE}$ appears to prevent IGSCC of

---

* 30,000 J/cm

** LTS-low temperature sensitization, sample heated for 24 hours at 500°C (932°F)

Table 5-4
STRAINING ELECTRODE* RESULTS FOR WELDED T-304 STAINLESS STEEL (HEAT #7616) AT 274°C (525°F) IN 0.01N Na_2SO_4

Process Code[a]	Potential (SHE)	Fracture Stress[c] MPa	Fracture Stress[c] ksi	UTS[d] MPa	UTS[d] ksi	T,[e] (h)	R.A.[f] (%)	Elongation (%)	Failure Morphology
W	-0.100	421	61	372	54	78	11.5	6.9	IGSCC
W	-0.300	614	89	448	65	161	26.7	17.4	70% IGSCC. 30% Ductile
W	-0.400	862	125	483	70	262	44.2	24.6	Ductile
W	-0.400	814	118	531	77	255	38.9	26.1	Ductile
W + grd + LTS	-0.100	317	46	276	40	39	5.0	2.7	IGSCC
W + LTS	-0.400	310	45	303	44	64	2.5	7.5	IGSCC
W + LTS	-0.450	545	79	455	66	234	26.7	13.2	IGSCC, some ductile
W + LTS	-0.750	669	97	489	71	216	26.6	22.8	Ductile, minor transgranular SCC

*Strain Rate of 2×10^{-5} min^{-1}
[a] W = Welded
grd = Ground
LTS = Low Temperature Sensitization (500°C for 24 hours)
[c] Maximum load/failure cross section
[d] Ultimate tensile strength—maximum load/original cross section
[e] Time to failure
[f] Reduction in area
[g] Initiated by short transgranular crack on I.D. machined surface

90014196

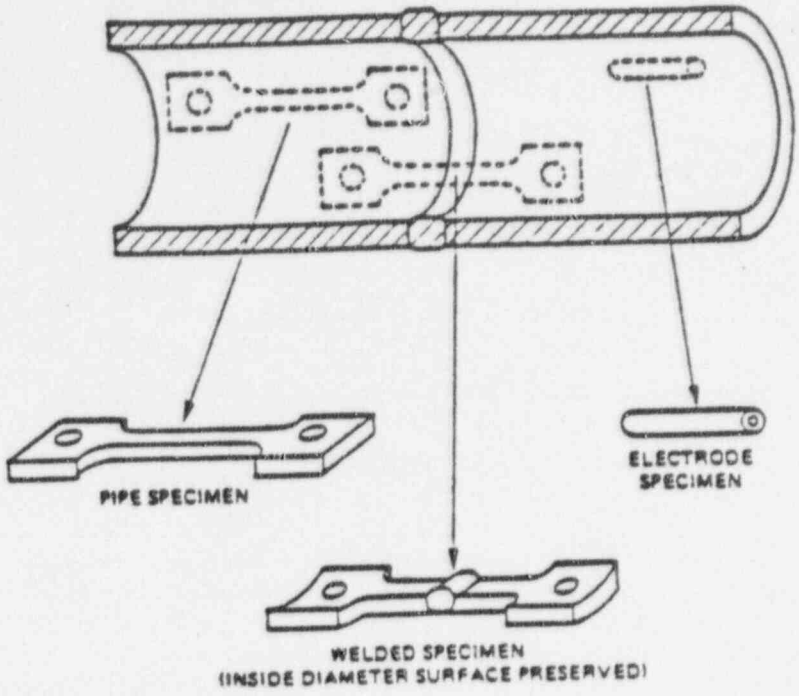

Figure 5-35. Specimens from Pipe Weldment

as-welded (high-heat-input) Type-304 stainless steel. However, if the welded sample ws given an LTS treatment, severe IGSCC occurs at $-0.400V_{SHE}$ in the straining electrode test. Even at $-0.450V_{SHE}$, the welded + LTS condition still exhibits significant susceptibility to IGSCC. Clarke, Cowan, and Danko[4] have shown that significant differences in susceptibility to IGSCC exists among heats of stainless steel. Thus, other heats of welded Type-304 stainless steel or other metallurgical conditions of welded pipe (Heat M7616) could have different values for the minimum potential for IGSCC. At sufficiently low potential, however, IGSCC can be prevented for the welded + LTS condition, as is evident by the final entry in Table 5-4.

Table 5-5 presents a summary of the SET results used to evaluate selected pipe remedies and the alternate austenitic alloys. For comparison, data for as-welded Type-304 stainless steel are included. The initial experiments on pipe remedies were conducted at $-0.100V_{SHE}$. Subsequently, it was determined that $-0.200V_{SHE}$ was an adequate test potential to cause IGSCC of as-welded Type-304 stainless steel and, thus, the evaluation of the alternate austenitic alloys was conducted at this lower test potential. In a later section in this report on the effect of the supporting electrolyte it will be shown that $-0.200V_{SHE}$ in 0.01 N Na_2SO_4 more closely simulates potentials measured in BWRs in pure water than the control potential of $-0.100V_{SHE}$ in the Na_2SO_4 electrolyte, see Figure 5-45

In SET, the welded plus solution heat treated and corrosion-resistant cladding remedies exhibited excellent resistance to IGSCC. However, the heat-sink welding did not offer any apparent improvement over the as-welded sample. The increased resistance to IGSCC for the welded plus solution heat treated and the corrosion-resistant cladding remedies is noted by the high ductilities (elongation and reduction of area), the mostly ductile failure morphology and the increased failure times when compared to the as-welded condition at $-0.100V_{SHE}$. Heat sink welding of pipe results in compressive surface residual stresses which should increase resistance to IGSCC. However, these surface stresses relax when the pipe is cut and a tensile sample is removed. Thus tensile samples from heat sink welded pipe would probably behave similarly to as-welded pipe. On the other hand, stress corrosion testing of a complete pipe section has shown significant improvement over the as-welded condition[3]. The wrought and cast Type-304L both exhibited excellent resistance to IGSCC as the failures were mostly ductile.

Table 5-5
STRAINING ELECTRODE RESULTS FOR WELDED PIPE REMEDIES
AT −0.100 V_{SHE} IN 0.01 N Na_2SO_4 AT 274°C (525°F)

Remedy or Treatment Code	Fracture Stress[a] MPa	ksi	UTS[b] MPa	ksi	T_f[c] (h)	R.A.[d] (%)	Elongation (%)	Failure Morphology
As-Welded	421	61	372	54	78	11.5	6.9	IGSCC
Heat-Sink Welded	406	59	365	53	125	9.8	5.5	IGSCC, some ductile
Welded + Solution Annealed	496	72	379	55	153	23.1	18.7	Mostly ductile, some transgranular SCC, minor IGSCC
Corrosion-Resistant Cladding	655	95	462	67	236	28.9	13.4	Mostly ductile, some transgranular SCC
As-Welded Type-304L	952	138	496	72	246	47.9	20.2	Mostly ductile, some transgranular SCC
As-Welded CF3A	883	128	476	69	196	46.5	24.3	Mostly ductile, some transgranular SCC, ferrite level ~20%

[a] Maximum load/failure cross section
[b] Ultimate tensile strength—maximum load/original cross section
[c] Time to failure
[d] Reduction in area
[e] Tested at −0.200 V_{SHE}

90014198

The results of the straining electrode experiments conducted at 232°C (450°F) are summarized in Table 5-6. From the amount of IGSCC versus ductile failure, it appears that intergranular crack initiation for the as-welded condition is a more difficult process at the lower temperature. For example, post-test microscopy of those samples tested at −0.200 and −0.300V_{SHE} indicated that the fracture initiated at the heat affected zone of the preserved internal pipe surface and propagated mainly by microvoid coalescence in a ductile mode. This method of crack growth suggests that initiation occurred at loads approaching the fracture stress of the material, which is in agreement with the fact that the failure morphology and mechanical properties indicate primarily a ductile failure. Thus, while the minimum potential to completely eliminate IGSCC on as-welded Type-304 stainless steel at 232°C (450°F) appears to be below −0.300V_{SHE} [not very different than the minimum potential at 274°C (525°F)] it appears that crack initiation at or above −0.300V_{SHE} requires significantly high stresses and strains.

Table 5-6
STRAINING ELECTRODE RESULTS FOR WELDED TYPE-304 STAINLESS STEEL (HEAT M7615) AT 232°C (450°F) IN 0.01 N Na_2SO_4

Potential (V_{SHE})	Fracture Stress[a] (ksi)	UTS[b] (ksi)	T_f[c] (h)	R.A.[d] (%)	Elongation (%)	Failure Morphology
−0.100	62	55	82	15	10	0.95 IGSCC, 0.05 Ductile
−0.200[e]	107	75	192	30	22	0.10 IGSCC, 0.90 Ductile
−0.300	115	73	248	37	23	0.10 IGSCC, 0.90 Ductile
−0.350	210	73	246	39	25	Ductile failure

[a] Maximum load/failure cross-section.
[b] Ultimate tensile strength, maximum load/original cross-section.
[c] Time to failure.
[d] Reduction in area.
[e] Electronic malfunction during test. Temperature dropped to room temperature for 30 hours while sample continued to be strained and under potentiostatic control.

5.7.1 Morphology of Failures in the Straining Electrode Tests

As indicated in Table 5-4 stress corrosion failures in the straining electrode tests at 274°C (525°F) were usually intergranular. However, samples having increased resistance to IGSCC failed in a predominantly ductile mode with a small amount of transgranular stress corrosion cracking. Increased resistance to IGSCC occurred when testing at a lower potential or on alloys that are not sensitized. Figure 5-36 shows some shallow transgranular cracks observed on all surfaces of an as-welded sample tested at −0.400V_{SHE}. At a potential of −0.100V_{SHE}, structures that are resistant to IGSCC (selected pipe remedies) show somewhat deeper transgranular stress corrosion cracks. Figure 5-37 shows a portion of the fracture surface on a specimen with corrosion-resistant cladding. The failure was predominantly ductile with a small cleaved region that contained fatigue-like striations. These fracture features are observed occasionally in both straining electrode tests and constant extension rate tests over a large range of potentials and are due to transgranular stress corrosion. Minor transgranular cracks, Figure 5-38, also appeared in wrought material outside of the corrosion-resistant cladding. It is postulated that, for the most part, the transgranular cracks occur at high strains and stresses that approach the ultimate tensile strength of the material. However, in some cases, a cold-worked surface caused by machining, grinding or other surface upsetting processes can produce short transgranular cracks upon small amounts of strain[6].

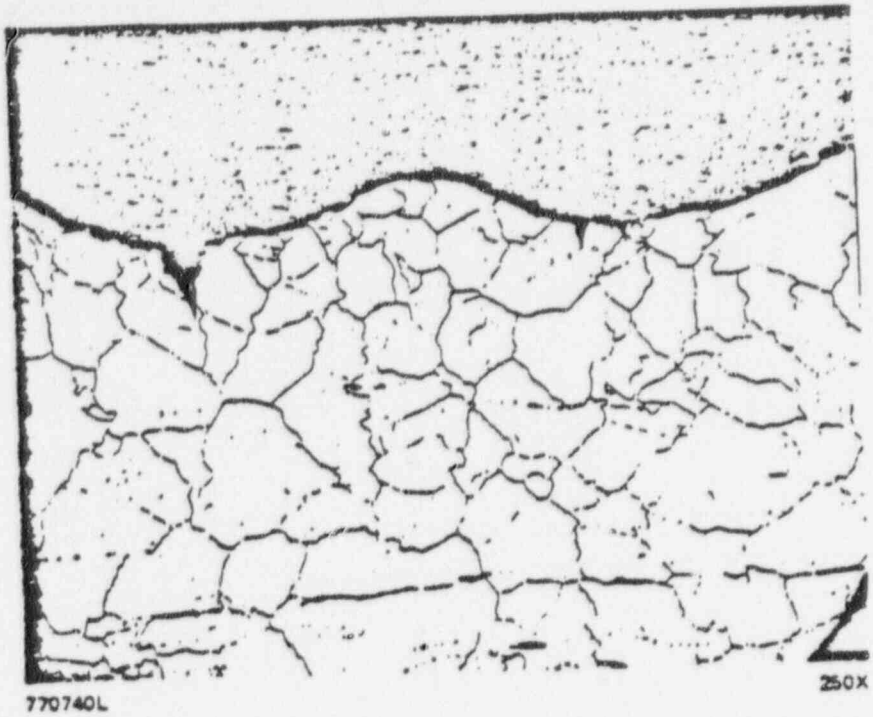

Figure 5-36. Transgranular Cracks on the Surface of an As-Welded Type-304 Stainless Steel Sample (Heat M7616) Tested as a Straining Electrode at $-0.400V_{SHE}$ in 0.01N Na_2SO_4 at 274°C. See Table 5-3

One may suspect that cracks which initiate by a transgranular mode may propagate as an intergranular crack within a susceptible microstructure. This phenomenon is illustrated in Figure 5-39 which shows transgranular cracks in a welded and solution heat treated sample tested at $-0.100V_{SHE}$ in 0.01 N Na_2SO_4 that terminate as intergranular penetrations at the crack tip. Figure 5-40 is a scanning electron micrograph which shows a cleaved portion of the fracture surface of the solution heat treated sample with evidence of grain boundary separations. Material with a microstructure which is extremely susceptible to IGSCC could fail at a potential equivalent to a very low dissolved oxygen concentration if it were possible to initiate a transgranular stress corrosion crack. An example of such a failure is shown in Figures 5-41 through 5-43 for a welded + LTS sample tested at $-0.450V_{SHE}$. Although the sample failed by IGSCC (Figure 5-41), a relatively high stress was required and the sample exhibited a significant amount of ductility, see Table 5-4. Figure 5-42 shows auxiliary cracks along the preserved internal surface of the pipe weld sample. The internal surface was prepared by machining and the cracks originate at the base of the machined grooves. As shown in Figure 5-43, these cracks initiated by a transgranular mode and then propagated into the susceptible microstructure by an intergranular mode. Elimination of the severely upset surface may have eliminated transgranular crack initiation and thus decreased the sample susceptibility to failure by IGSCC. It should be noted however, that the transgranular cracking has only been observed after CERT or SET experiments (high strain tests) of welded or sensitized Type-304 stainless steel. Transgranular cracking has not been observed in constant lead tests or field failures of welded or sensitized Type-304 stainless steel.

5.3 RELATIONSHIP BETWEEN SET POTENTIALS AND OXYGEN CONCENTRATION; EFFECT OF THE SUPPORTING ELECTROLYTE

For the straining electrode experiments to have engineering significance the controlled potentials in each experiment must be related to specific oxygen concentrations. An over-simplified approach would be to determine the equivalent oxygen concentration from the potential/oxygen curves as shown in Figure 5-13 and 5-14. For example, from Figure 5-13, 200 ppb dissolved oxygen at 274°C (525°F) is equivalent to a potential of about $-0.10V_{SHE}$. However, the potential/oxygen curves were determined in pure water and the addition of Na_2SO_4 to form a 0.01 N solution produces a slightly basic solution and a measurable decrease in corrosion potential. The change in solution

Figure 5-37. Cleaved Region of Transgranular Stress Corrosion Cracking Observed on the Fracture Surface of a Type-304 Stainless Steel Sample (Heat M7616) With Corrosion Resistant Clad Tested as a Straining Electrode at −0.100V_{SHE} in 0.01N Na_2SO_4 at 274°C. See Table 5-4

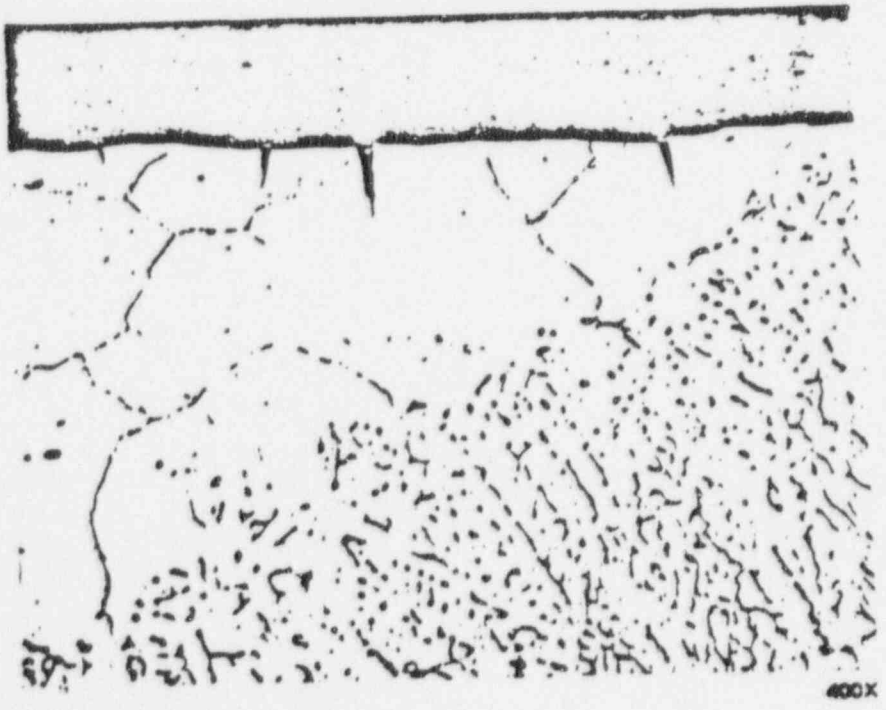

Figure 5-38. Transgranular Cracks Within the Wrought Material of a Type-304 Stainless Steel Sample (Heat M7616) With Corrosion Resistant Clad Tested as a Straining Electrode at −0.100V_{SHE} in 0.01N Na_2SO_4 at 274°C. See Table 5-4

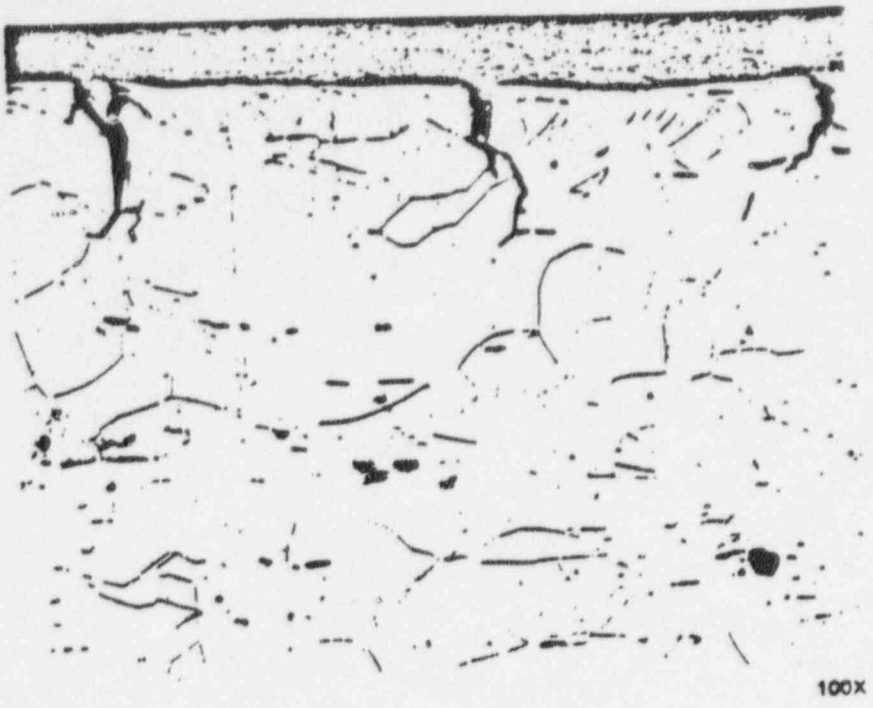

Figure 5-39. Transgranular Penetrations Which Have Changed to Intergranular Penetrations During the Testing of a Welded Plus Solution Heat Treated Sample (Heat M7616) as a Straining Electrode at $-0.100V_{SHE}$ in 0.01N Na_2SO_4 at 274°C. See Table 5-4

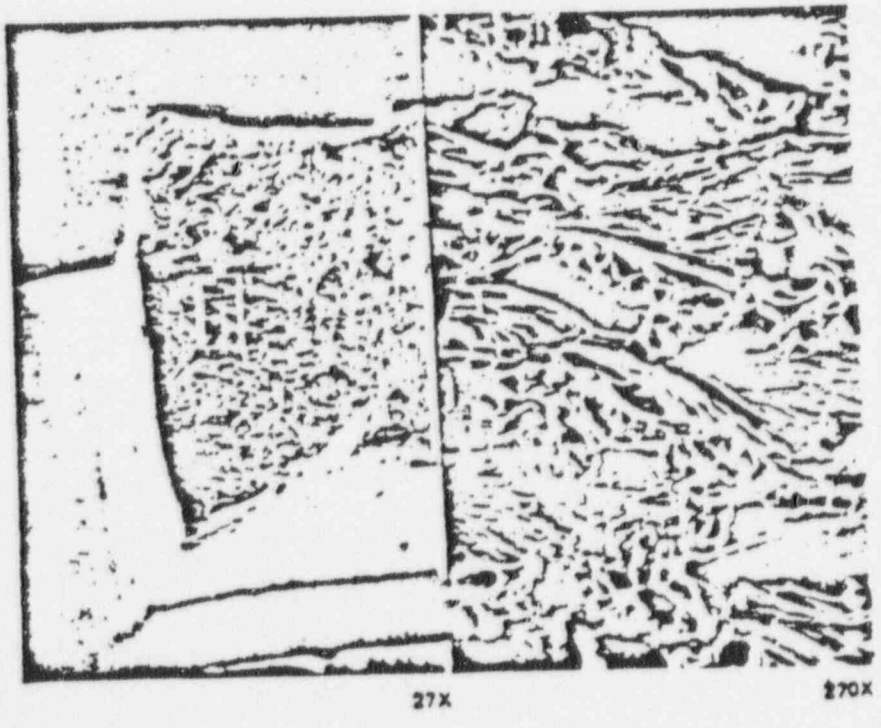

Figure 5-40. Scanning Electron Micrograph of a Cleaved Portion of the Fracture Surface of a Welded Plus Solution Heated Sample (Head M7616) Tested as a Straining Electrode at $-0.100V_{SHE}$ in 0.01N Na_2SO_4 at 274°C. See Table 5-4

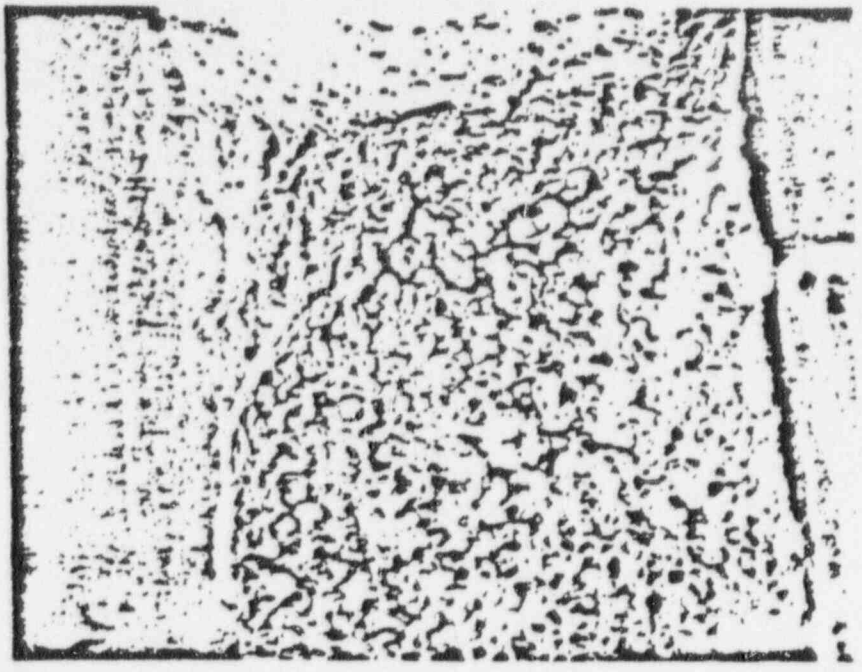

887 (a) 30X

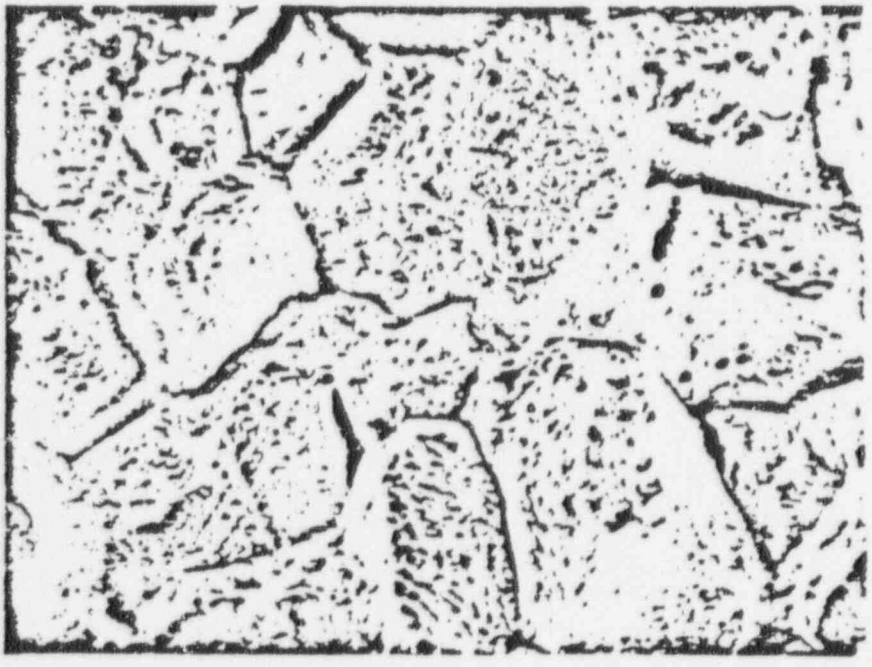

889 (b) 400X

Figure 5-41. Scanning Electron Micrographs of the Fracture Surface of the Heat Affected Zone of a Welded (High Heat Input) Type-304 Stainless Steel (Heat No. M7616) Specimen (Mil-Annealed + Machined + Welded + 24 Hours at 500°C) Strained at $-0.450V_{SHE}$ in 0.01N Na_2SO_4 Water at 274°C. See Table 5-3

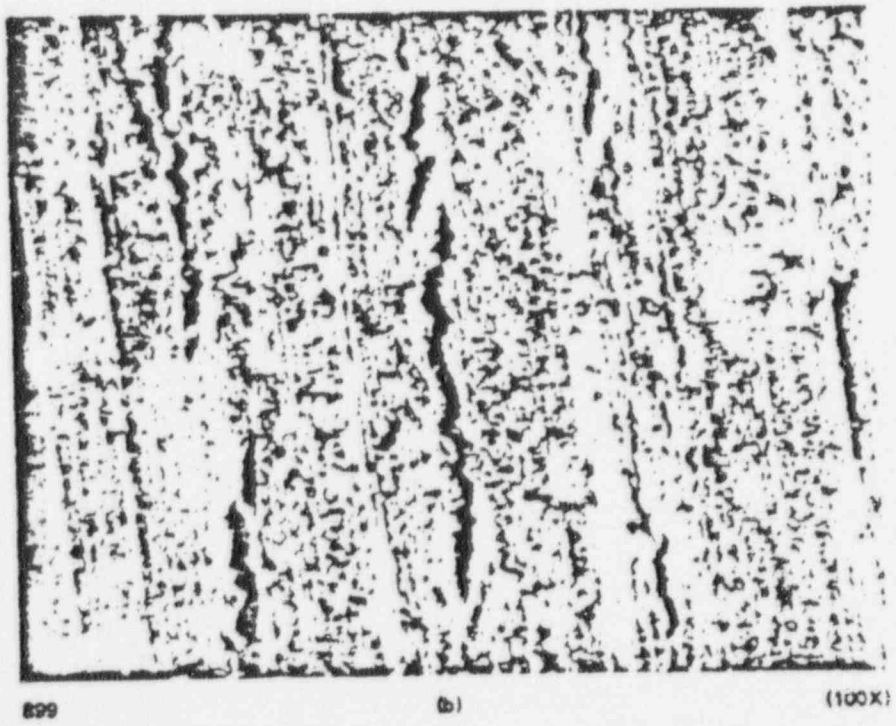

Figure 5-42. Scanning Electron Micrograph of Cracks on the Machined I.D. Pipe Surface of a Welded (High Heat Input) Type-304 Stainless Steel (Heat No. M7616) Specimen (Mill-Annealed + Machined + Welded + 24 Hours at 500°C) Strained at $-0.450V_{SHE}$ in 0.01N Na_2SO_4 Water at 274°C. See Table 5-3

Figure 5-43. Scanning Electron Micrograph of the Fracture Surface of the Heat Affected Zone of the Machined Edge (Right Side) Showing Transgranular Fracture Steps in a Welded (High Heat Input) Type-304 Stainless Steel (Heat No. M7616) Specimen (Mill-Annealed + Machined + Welded + 24 Hours at 500°C) Strained at −0.450V_{SHE} in 0.01N Na_2SO_4 Water at 274°C. See Table 5-3

chemistry, formation of OH^-, occurs in high-temperature water because of the hydrolysis Na_2SO_4 according to the reaction:

$$Na_2SO_4 + H_2O \rightarrow HSO_4^- + OH^- + 2\,Na^+, K_H = \frac{(HSO_4)^- (OH)^-}{(SO_4)^{-2}}$$

The shift in potential must be accounted for by adding a correction factor to each straining electrode potential. The correction factor is constant at a constant temperature and ionic concentration. Using the correction factor, the potentials in 0.01 N Na_2SO_4 can be corrected to potentials in pure water and then the equivalent dissolved oxygen concentration can be determined by reference to the potential/oxygen curve.

From the data presented by Cohen[7], shown in Figure 5-44, the pH at 275°C (527°F) can be expected to increase from 5.75 (pure water) to about 7.1 by the addition of 710 ppm Na_2SO_4 (0.01 N Na_2SO_4). In this case the stainless steel could be considered to behave as a H_2 or O_2 electrode. For an electrode which responds to changing pH at constant O_2 concentration, the Nernst equation at 274°C (525°F) simplifies to $\Delta E = 0.109\Delta pH$. From this equation the increase in pH from 5.75 to 7.1 should decrease the potential by 0.147V. Thus 0.147V must be added to the straining electrode potentials in 0.01 N Na_2SO_4 to convert to potentials in pure water at 274°C (525°F).

The validity of the correction factor was determined in a specific experiment where 0.01 N Na_2SO_4 was added to pure water with about 200 ppb O_2. Potentials on platinum and stainless steel were measured before and after the addition. Table 5-7 presents a summary of the potential changes and dissolved oxygen concentrations with time. After 24 hours the potential decreased on the stainless steel and platinum electrodes by 0.180 and 0.162V, respectively. These experimental measurements indicate that the calculated correction factor is conservative. Use of the correction factor illustrates its importance. From straining electrode results in 0.01 N Na_2SO_4, $-0.400V_{SHE}$ appears to be the limiting potential for intergranular stress corrosion of welded Type-304 stainless steel. Without the correction factor, −0.400V in pure water is equivalent to about 25 ppb dissolved O_2. Using a conservative correction factor of 0.150V, the equivalent concentration is about 50 ppb.

Table 5-7

EFFECT OF Na_2SO_4 ADDITION (0.01 N) TO WATER AT 274°C (°F)

Time (h)	Potential$_{SHE}$ (V) SS	Pt	Dissolved Oxygen (ppb)
0*	−0.193	+0.025	195
1.3	−0.450	−0.100	210
6	−0.485	−0.145	175
24	−0.355	−0.155	170

*Zero Na_2SO_4

Figure 5-45 shows the relationship between the potentials in 0.01N Na_2SO_4 to those in pure water at the equivalent oxygen concentration. Included in Figure 5-45 is the steady-state corrosion potential of Type-304 stainless steel measured in Vermont Yankee and Dresden-2 BWRs during operation and a summary of the IGSCC data for as-welded Type-304 stainless steel Heat M7616 in the straining electrode tests. It should be noted that the stainless steel electrode potentials are raised by 0.150V in relation to the potentials in pure water. For example, $-0.250V_{SHE}$ in 0.01 N Na_2SO_4 is equivalent to $-0.100V_{SHE}$ in pure water. Thus, the SET for the alternate austenitic alloys run at $-0.200V_{SHE}$ were equivalent to $-0.050V_{SHE}$ in pure water which was equivalent to, ~8 ppm O_2, environment.

With decreasing temperature the correction factor decreases due to the decreasing hydrolysis of Na_2SO_4. At 232°C (450°F) the correction factor is about 0.075V. Figure 5-46 summarizes the straining electrode stress corrosion results corrected for the Na_2SO_4 hydrolysis at 274°C (525°F) and 232°C (450°F), with reactor potentials on the average potential/oxygen curves for stainless steel in pure water. The reactor potential at 232°C (450°F) was approximated

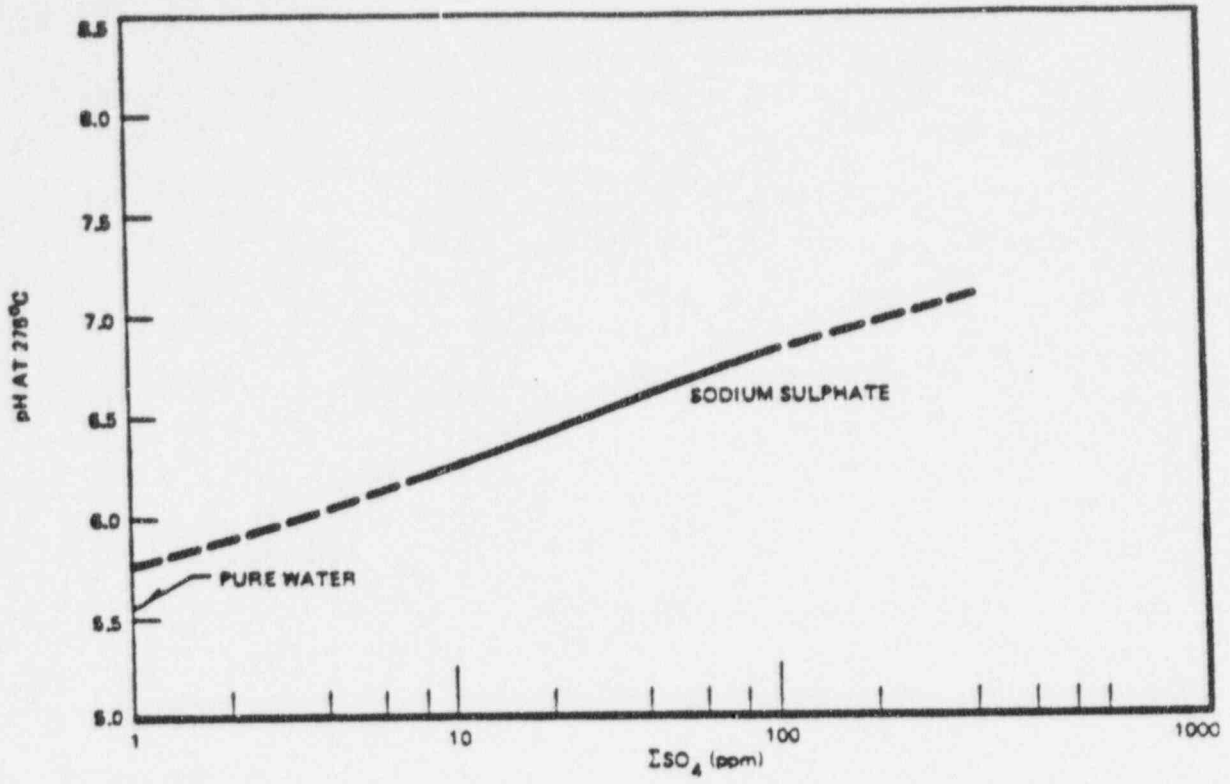

Figure 5-44. pH as a Function of Total PO_4 or SO_4 Concentration — Na_3PO_4, Na_2SO_4, 275°C

from Vermont Yankee startup data. The stress corrosion data on Figure 5-46 were obtained from straining electrode tests. The controlled potentials in 0.01 N Na_2SO_4 were converted to potentials and equivalent oxygen concentrations in pure water. Thus, there may be some question on the superposition of data obtained in one environment to a second environment. For this reason a CERT was recently completed in pure water containing 100 ppb dissolved oxygen at 232°C (450°F). To control the dissolved O_2 concentration at 100 ppb, a preconditioned titanium system was required. The tensile specimen was in the welded + LTS condition. From Figure 5-46 failure by IGSCC would have been predicted and indeed the prediction was correct. Table 5-8 summarizes the CERT data obtained. The major difference in the CERT and the electrochemical SET data in Table 5-6 is in the percent IGSCC. Apparently, electrochemicl control will cause a more highly aggressive crack tip solution and greater IGSCC. From this standpoint SET experiments must be considered to be more aggressive than the equivalent CERT experiments.

Perhaps even more significantly these results indicate that dropping the oxygen concentration to 100 ppb even at 232°C (450°F) does not result in immunity to IGSCC for a highly susceptible microstructure.

5.9 EFFECT OF REACTOR STARTUP ON PIPE CRACKING

The task force organized by the General Electric Company in 1975 to investigate the cause of the Type-304 stainless steel pipe cracking phenomena determined that pipe cracking frequency seemed to be related to the number of reactor startups which followed a cold-standby condition of 24 hours or longer in duration. It can be postulated that crack initiation may be the result of startup transients where welded Type-304 stainless steel is exposed to the combination of a changing chemical environment and some mechanical strain. Electrochemical and chemical studies conducted at Dresden-2 and Vermont Yankee BWRs and described previously indicate that, during startup, the reactor piping can be exposed to a changing environment, which causes a dramatic shift in the corrosion potentials. These electrochemical measurements from the 10.16-cm (4-in.) bypass line in Dresden-2 and from the test vessel installed in the reactor cleanup system in Vermont Yankee indicate that a decrease of 0.7V in the corrosion potential occurred from cold-standby to full-power operation.

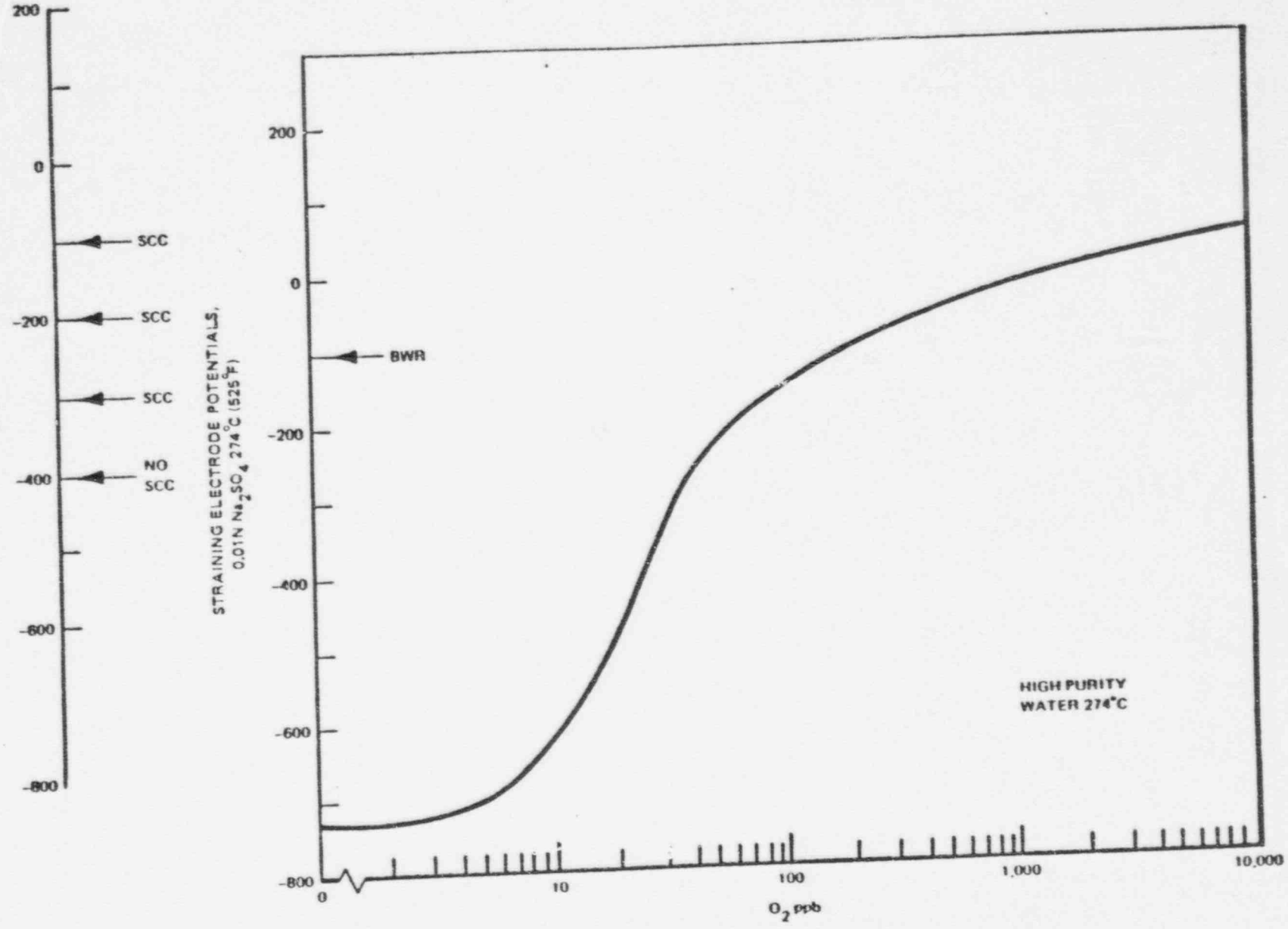

Figure 5-45 *The Effect of Dissolved Oxygen on the Corrosion Potential of Type-304 Stainless Steel in High Purity Water at 274 C (525°F)*

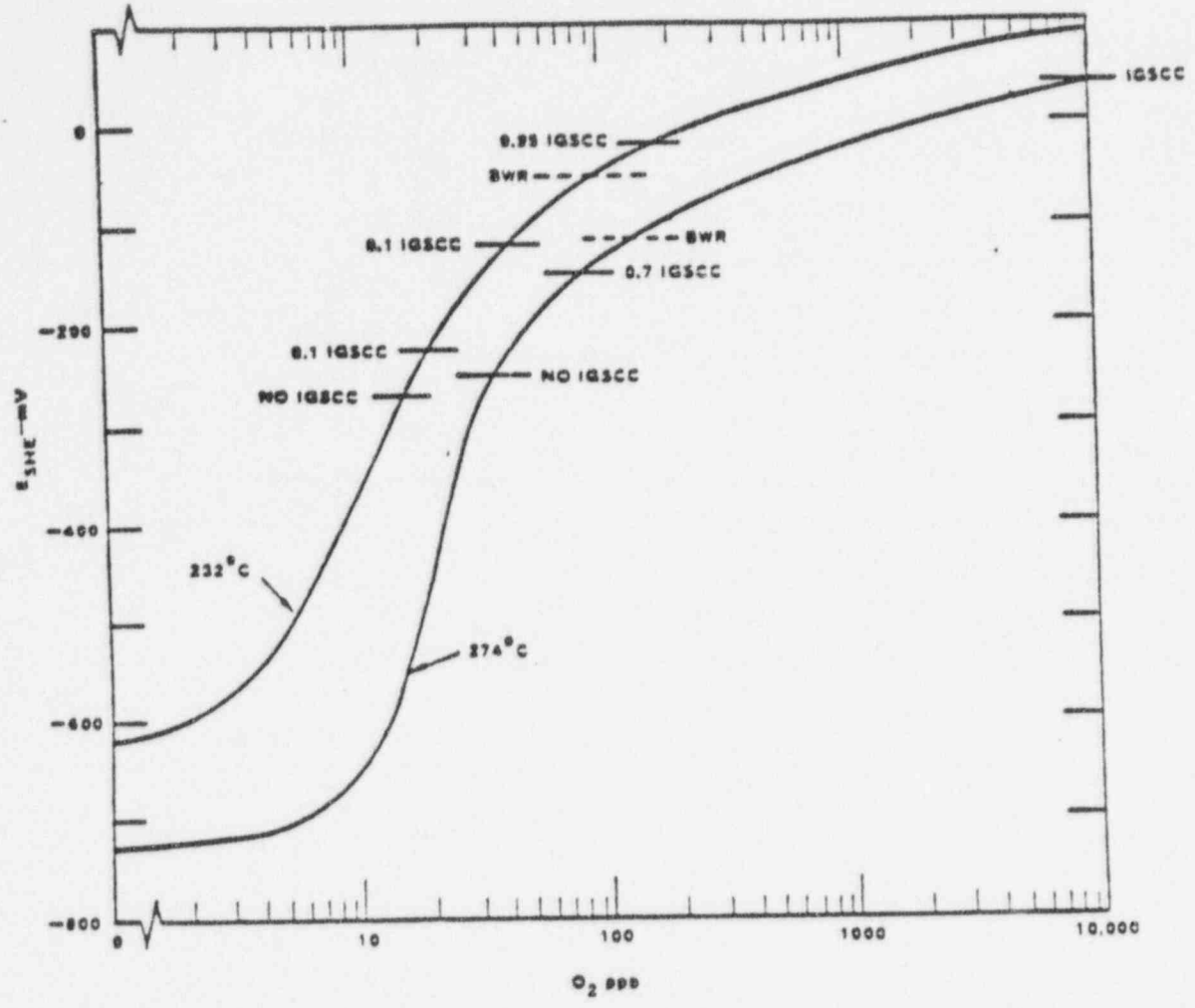

Figure 5-46. The Effect of Dissolved Oxygen on the Corrosion Potential and IGSCC of Type-304 Stainless Steel (Average Curves)

90014209

If cracks could initiate during such startups, then propagation might occur during steady-state operation. In response to the question of the effect of reactor startup relative to pipe cracking, further studies are required to attempt to relate the effect of the changing reactor environment and the resulting change in corrosion and oxidation potentials to crack initiation. Furnace-sensitized and as-welded Type-304 stainless steel tensile specimens need to be subjected to a changing electrochemical potential and a temperature cycle which simulates the reactor startup profile as determined by the electrochemical measurements obtained in reactor startups. Figure 5-47 is a block diagram of a system recently constructed with the capability of performing startup simulation tests. Figure 5-48 shows the electronic system used to control temperature and potential simultaneously.

The system is designed to test four tensile samples. Each tensile sample is connected to an external piston. By pressurizing the pistons to the desired level, a constant stress is applied to each sample while the temperature and corrosion potential are varied. Shakedown runs to determine proper system operating procedures have been completed.

The initial startup simulation run under electrochemical control has been completed with furnace-sensitized tensile samples. The samples were stressed at 30, 40, and 50 ksi (207, 276 and 345 MPa). In a single startup cycle, failure by IGSCC occurred on the sample stressed at 50 ksi at 270°C (519°F) after 390 minutes and on the sample stressed at 40 ksi 274°C (525°F) after 420 minutes. Further experiments are required to determine whether crack initiation occurs in de-aerated cycles the temperature/environmental requirements for crack initiation and crack avoidance during startup, and the effect of metallurgical condition on crack initiation.

Table 5-8
CERT RESULTS FOR AS-WELDED + LTS TENSION SAMPLE AT 232°C (450°F) IN PURE WATER

O_2 Conc. (ppb)	Fracture Stress ksi	Fracture Stress MPa	UTS ksi	UTS MPa	T_f (h)	R.A. (%)	Elongation (%)	Failure Morphology
100	63.9	440	54.5	376	114	11.7	6.8	60% IGSCC, 40% ductile

5.10 REFERENCES

1. M.E. Indig, J.E. Weber, and A.D. Miller, *Corrosion*, 34, 3, 1978.
2. W.L. Pearl, W.R. Kassen, and S.G. Sawochka, *Oxygen Monitoring and Control in BWR Plants*, ANS Meeting, June 1977.
3. Heat Sink Welding Improvement, this report, Task 2.
4. W.L. Clarke, J.C. Danko, and R.L. Cowan, *A Dynamic Straining Stress Corrosion Test for Predicting Boiling Water Reactor Materials Performance*, General Electric Co., May 1977 (NEDO-12670).
5. M.J. Povich, *Corrosion*, accepted for publication.
6. G. Welch, F. Sykes, J.B. Lee, R.D. McCright, J.A. Begley, and R.W. Staehle, *Stress Corrosion Cracking and Electrochemistry in Oxygenated High Temperature Water*, Paper presented at EPRI review meeting, Contract RP-311-1,3 on January 11, 1977.
7. P. Cohen, *The Chemistry of Water at High Temperatures for Application of Corrosion in Power Systems*. Presented at the Seminar on Chemistry and Aqueous Corrosion in Steam Generators, Ermenonville, France, 1972 (WARD-5788).

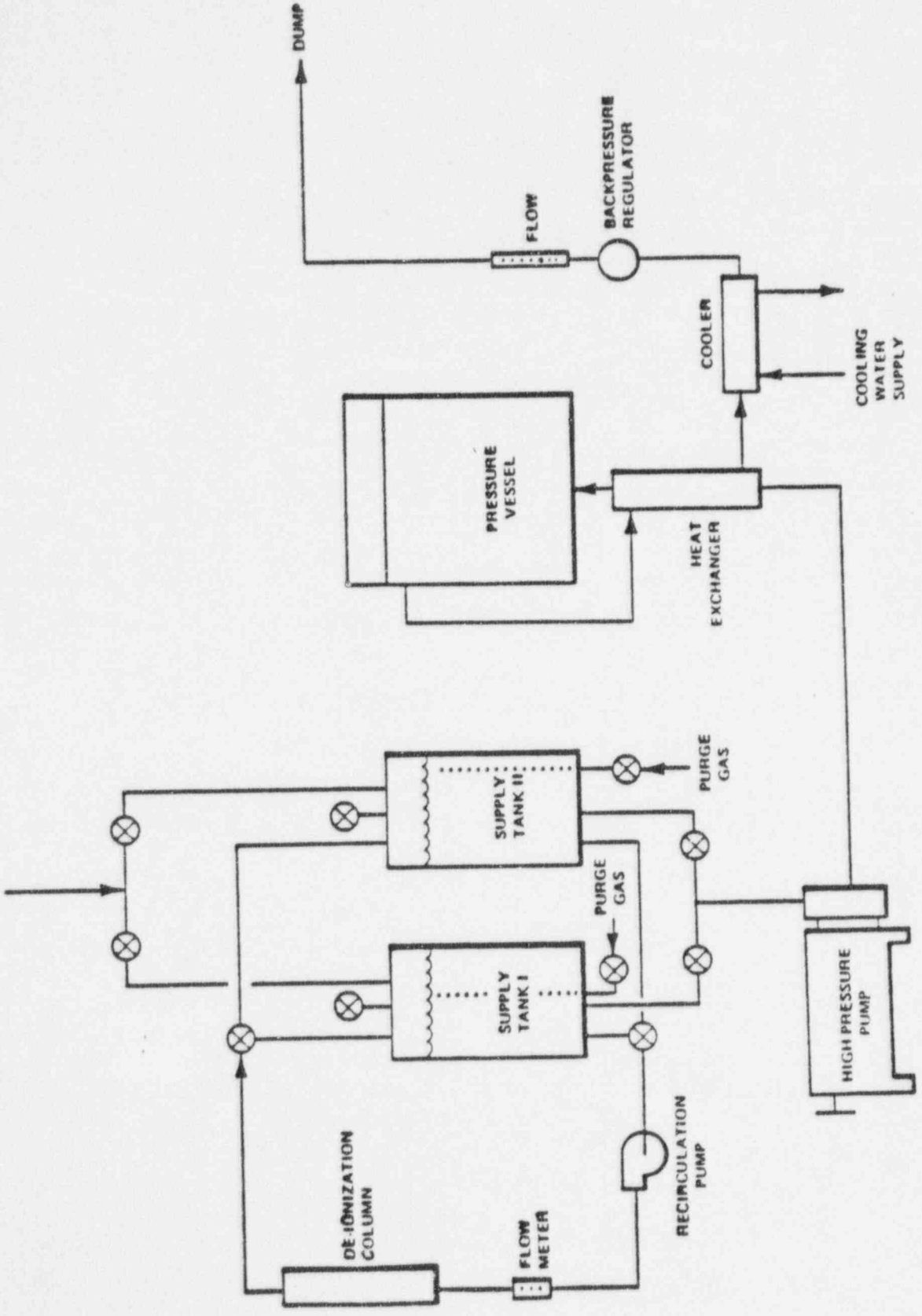

Figure 5-47 Reactor Temperature/Potential Simulator

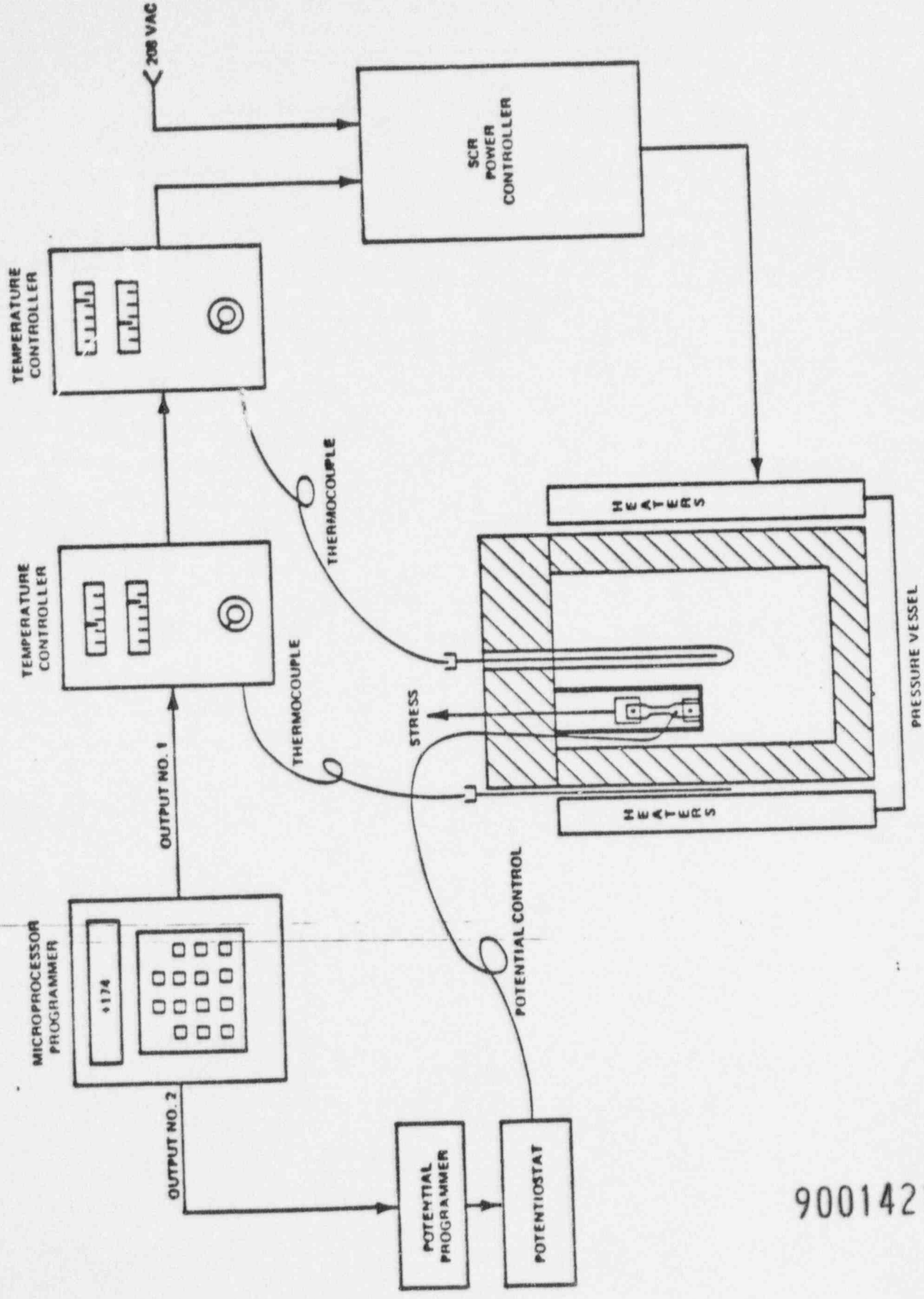

Figure 5-48 Temperature/Potential Electronic Control System

6. TASK 4. FUNDAMENTAL STUDIES OF FERRITE EFFECTS IN DUPLEX STAINLESS STEELS ON RESISTANCE TO INTERGRANULAR STRESS CORROSION CRACKING IN BOILING WATER REACTOR ENVIRONMENT

6.1 INTRODUCTION

Work has been conducted at the General Electric Corporate Research and Development Center to determine the factors which contribute to the resistance of austenitic-based duplex stainless steels to intergranular stress corrosion cracking in the BWR environment. Since this study sought to identify the mechanisms responsible for stress corrosion resistance, it was necessary to study the alloys' responses to a wide variety of thermal treatments. As such, this effort is not intended to be a qualification program for duplex alloys in any specific condition such as the as-welded condition.

In-reactor experience and numerous laboratory studies conducted in simulated boiling water reactor environments have indicated duplex stainless steels to be much more resistant to intergranular stress corrosion cracking than austenitic stainless steels. It was the goal of this task to determine the metallurgical conditions responsible for this resistance to stress corrosion cracking in the various boiling water reactor environments. The minimum amount of ferrite, and the morphology of the ferrite required to inhibit intergranular stress corrosion cracking in simulated boiling water reactor environments was to be determined. The effect of second phase particles such as carbides, σ phase, and α' phase on the stress corrosion cracking of duplex stainless steels was also to be investigated. To expedite testing of the large number of alloys and heat treatments to be examined in this study, a screening test was developed to detect and screen out alloys and/or heat treatments highly susceptible to stress corrosion cracking.

6.2 DEVELOP A TESTING PROCEDURE TO ASSESS THE STRESS CORROSION CRACKING SUSCEPTIBILITY OF DUPLEX STAINLESS STEELS IN THE BOILING WATER REACTOR ENVIRONMENT

6.2.1 Introduction

The primary test employed in this program to assess an alloy's susceptibility to stress corrosion cracking in the Boiling Water Reactor environment is a constant extension rate test of tensile-type specimens immersed in high-purity water with 8 ppm dissolved oxygen at 288°C (550°F). In this test the stress and strain at failure and the amount of intergranular fracture are measured. Because of the limited number of facilities capable of performing this test, an extensive effort was made in this program to develop a screening test capable of assessing an alloy's susceptibility to stress corrosion cracking in the slow extension rate test. Such a test could be used to detect and screen out alloys and/or heat treatments with a high degree of susceptibility to stress corrosion cracking. These alloys and/or heat treatments would not be tested in the constant extension rate test (CERT) facility, freeing the latter for tests on more resistant material. Additionally, the results of such corrosion tests can provide indications of the mechanism of intergranular stress corrosion cracking in the Boiling Water Reactor environment. Finally, looking beyond this program, a corrosion test capable of assessing a duplex stainless steel's resistance to stress corrosion cracking in the Boiling Water Reactor environment could be employed to screen out from large quantities of purchased material those heats which would exhibit inadequate stress corrosion cracking resistance.

The initial screening tests evaluated are ASTM practices A262A, A262C, A262E, and the pitting behavior in low pH, chloride-ion solutions. The ASTM A262A, A262C, and A262E tests were selected because of the long history of their use in assessing the intergranular stress corrosion cracking susceptibility of austenitic stainless steels. The pitting test was selected principally because pitting is a strong function of the chromium content of the alloy. Regions of a material which are low in chromium will pit first and at a lower applied potential than regions higher in chromium. This is very important for two reasons. First a strong correlation exists between intergranular stress corrosion cracking susceptibility in the Boiling Water Reactor environment of austenitic stainless steel and the presence of chromium-depleted zones adjacent to grain boundaries. Because of the dependency of pitting susceptibility on the chromium content, the presence of chromium-depleted grain boundaries in austenitic or any other type of stainless steel would be detected by the pitting tests. Second, many microstructural features in duplex stainless steels are accompanied by chromium-depleted regions. Consequently, the pitting test could be used to detect the presence of

these microstructural features. For example, σ phase, which can form in single phase as well as duplex stainless steels, is a chromium-rich inter-metallic compound of transition elements and is surrounded by a chromium-depleted zone. Similarly, both the intermetallic compounds known as R phase and χ phase, are formed in molybdenum-containing stainless steels, are rich in chromium, and their formation results in the creation of chromium-depleted zones. Finally, α' phase is a chromium-rich phase formed within a miscibility gap existing at low temperatures in the ferrite phase. The α' precipitates contain as much as 90% chromium and result in severe chromium depletion of the ferrite phase as well as embrittlement of the ferrite. Should stress corrosion crack testing show such microstructural features to be deleterious to stress corrosion cracking resistance, then the pitting test will be useful in screening duplex stainless steels containing these harmful phases.

6.2.2 Experimental Procedure

One heat of Type-308 stainless steel whose composition is listed in Table 6-1 was used to evaluate the ability of the various corrosion tests to predict the stress corrosion cracking behavior in CERT. The alloy was obtained in the form of 0.16-cm (1/16-in.) diameter wire from the General Electric Company's Nuclear Energy Division. Specimens were sectioned into 8.9-cm (3.5-in.) lengths, coated with MgO to prevent sintering during high temperature heat treatment, encapsulated in ~1.9-cm (¾-in.) diameter quartz tubes which had been evacuated and then back-filled with ¼ atmosphere of argon, and finally heat treated for 1 hour at temperatures ranging from 1200°C (2192°F) to 1350°C (2462°F). The specimens were cooled by removing the quartz tubes from the furnace and breaking them open in water. The annealed samples were then electropolished for 5 minutes at ~2 amps/cm² in a solution of 60% H_3PO_4 + 40% H_2SO_4 at 40–60°C (104–140°F), wrapped in zirconium foil, encapsulated in evacuated ~1.3 cm (½ in) quartz tubes, and aged for ¼ to 1000 hours at temperatures ranging from 475 to 700°C (889 to 1292°F). After aging, the samples were water quenched by breaking the quartz tubes in water, electropolished as described above, ultrasonically cleaned in detergent solution, and rinsed in distilled water.

Table 6-1
COMPOSITION OF TYPE-308 STAINLESS STEEL, HEAT L-B7

C	Cr	Ni	Mn	Si	S	P
0.040	20.95	9.82	1.76	0.41	0.008	0.016

Accelerated intergranular corrosion tests were performed according to ASTM specifications A262A, A262C, and A262E. Samples for pitting tests were soldered to an electrical test lead which was then masked off from the remainder of the sample with Glyptol® paint. The anodic polarization tests were conducted in a glass polarization cell which contained the specimen and two platinum-mesh counter-electrodes. A Luggin-Haber probe and salt bridge provided a low resistance path between the specimen and a saturated calomel reference electrode located in a separate beaker. The test electrolyte was deoxygenated by bubbling nitrogen through the solution at a rate of 95 cc/min for a minimum of 4 hours. Upon immersion in the test solution, the specimen was cathodically polarized to −1400 mV vs. SCE for 20 sec and then polarized in the anodic direction at a rate of 1 mV/sec., starting at a potential 100 mV lower than the corrosion potential. This particular cathodic pretreatment provided very reproducible results.

Galvanostatic pitting experiments were also performed in 0.1 N HCl to aid in studying pit initiation. In this test a 1 mA/cm² pulse was applied for varying lengths of time while continuously monitoring the potential of the sample. The initiation of pitting was accompanied by an abrupt drop in the potential of the sample. Pit initiation rate was measured by counting the number of pits per unit area following application of a 1 mA/cm² anodic current for five minutes.

Following all corrosion tests the samples were examined for evidence of corrosion by optical microscopy at 250–1200X. Certain samples were further examined by scanning electron microscopy.

The CERT tests were conducted on samples 7.6 cm (3 in.) long which contained a 2.5 cm (1 in.) gage section which was reduced to 0.89 cm (0.035 in.) diameter by electropolishing as described above. Strain rates ranging from 5×10^{-6} min^{-1} to 1×10^{-4} min^{-1} were employed. The specimens were pulled to failure in high resistivity water with 8 ppm

dissolved oxygen at 288°C (550°F). The solution was continuously refreshed at a rate of 1 cc/min in each of the 1-liter stainless steel autoclaves. Some samples were first precorroded in the A262E test solution prior to testing in CERT. Precorrosion times ranged from 1½ hours to 24 hours. Following the immersion in A262E the samples were ultrasonically cleaned in distilled water for 3 hours before testing in CERT. Following failure in CERT, the fracture surface of each specimen was examined in a scanning electron microscope for evidence of stress corrosion cracking.

6.2.3 Results

Figures 6-1 through 6-4 show the microstructures of Heat L-B7 resulting from 1 hour anneals at temperatures ranging from 1350°C (2462°F) to 1200°C (2192°F). The duplex samples are in the electropolished condition. The austenitic material in Figure 6-4 was electropolished and then lightly electroetched in 10% oxalic acid. Figure 6-1 indicates that a 1 h anneal at 1350°C (2462°F) followed by a water quench results in a duplex microstructure consisting of approximately 20 vol % ferrite. Annealing at lower temperatures produces less and less ferrite until at 1200°C (2192°F) the structure is 100% austenitic. Although the 20 vol % ferrite structure was produced by annealing at a temperature 150°C (302°F) higher than that used to produce the all-austenitic structure, the duplex material had a much finer grain size than the all-austenitic structure. Apparently the presence of ferrite inhibits the grain growth of the austenite and vice-versa.

As indicated in Figure 6-1, the ferrite phase was present in two distinct morphologies. In addition to the individual grains of ferrite, there were within the austenite grains regions of ferrite which were twinlike in appearance.

Figures 6-5 through 6-9 summarize the effect of aging treatment on the intergranular corrosion behavior in A262E of Type-308 stainless steel containing varying amounts of ferrite. Solid points indicate complete through-the-thickness intergranular fracture of the specimen during bending after the 72 h immersion period in the boiling acidified copper-copper sulfate solution. Diamond shaped points indicate that bending produced macroscopically visible cracks. Square points indicate that extensive microscopically visible cracking occurred due to bending. However, the intergranular corrosion penetration was not sufficient to result in deep intergranular cracking which would be macroscopically visible. Open points indicate the presence of isolated intergranular cracks one or two grains in length and triangular points indicate no cracking.

The results obtained for the fully austenitic Type-308 stainless steel produced by annealing at 1200°C (2192°F) for 1 hour and presented in Figure 6-5 are similar to those obtained on other austenitic grades of stainless steel such as Type-304. A C-shaped curve can be drawn through the data separating the aging treatments which result in severe intergranular corrosion from those which give rise to only isolated intergranular cracks one or two grains in length. Figure 6-6 depicts the appearance following testing of the sample aged for 20 hours at 600°C (1112°F) and illustrates the intergranular nature of the failure. Although samples were aged for up to 400 hours at 600°C (1112°F), no healing effects were observed. Such samples suffered 100% intergranular penetration.

The A262E results for material initially annealed at 1250°C (2282°F) for 1 hour are presented in Figure 6-7. The material contained only 4 vol % ferrite and the results indicate that this material was at least as susceptible to intergranular corrosion as the all-austenitic material. Corrosion occurred along both the austenite-ferrite and austenite-austenite grain boundaries.

Figures 6-8 and 6-9 illustrate the effect of aging on the intergranular corrosion behavior of the 10 and 20 vol % ferrite alloys, respectively. The results are very similar for both levels of ferrite. In contrast to the all-austenitic material and the 4 vol % ferrite material , both of which exhibited a large zone of susceptibility to severe intergranular corrosion, the 10 and 20 vol % ferrite alloys possessed only a small zone of susceptibility to severe intergranular corrosion. This zone extended at 600°C (1112°F) from aging times of ~1/2 hour to ~7 hours and at 550°C (1022°F) from ~5 hours to ~150 hours. Comparing the influence of aging time on the intergranular corrosion behavior of the 10 and 20 vol % ferrite alloys, the latter material developed a sensitized microstructure earlier and exhibited immunity to intergranular corrosion sooner at each temperature than the 10 vol % ferrite alloy. In further contrast to the all-austenitic material and the 4 vol % ferrite duplex alloy both of which locally corroded along austenite-austenite grain boundaries when sensitized, the 10 and 20 vol % ferrite alloys were locally attacked only along austenite-ferrite boundaries when sensitized at 600°C (1112°F) as shown in Figure 6-10. No intergranular corrosion occurred along

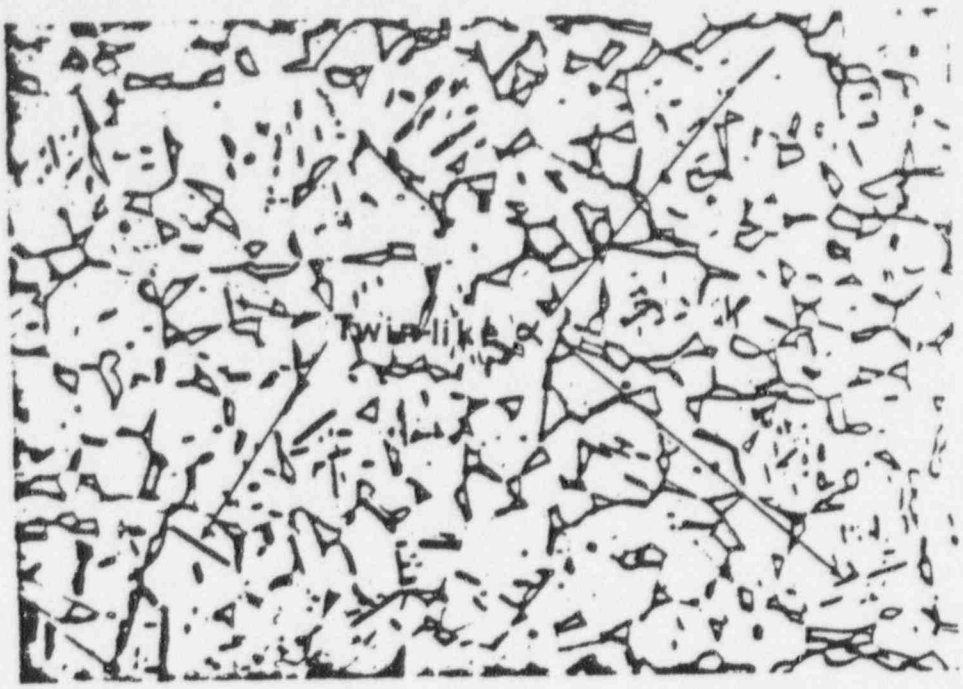

Figure 6-1. Scanning Electron Micrograph of Type-308 Stainless Steel Annealed at 1350°C/1 h, Water Quenched, and Aged at 600°C/50 h, Water Quenched (15% Ferrite)

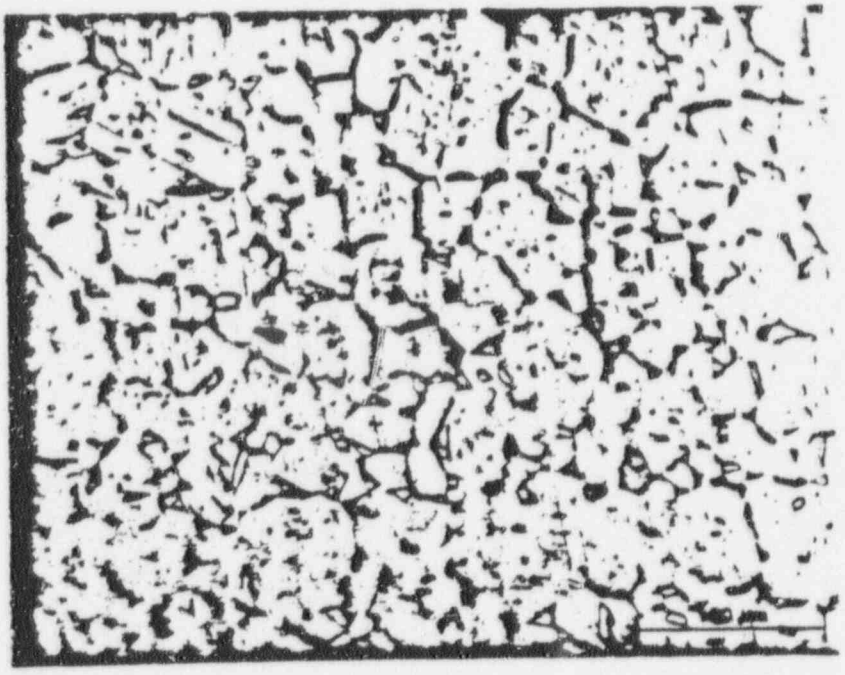

Figure 6-2. As-electropolished Microstructure of Type-308 Stainless Steel Heat Treated at 1300°C (2372°F)/1 h, Water Quenched 250X

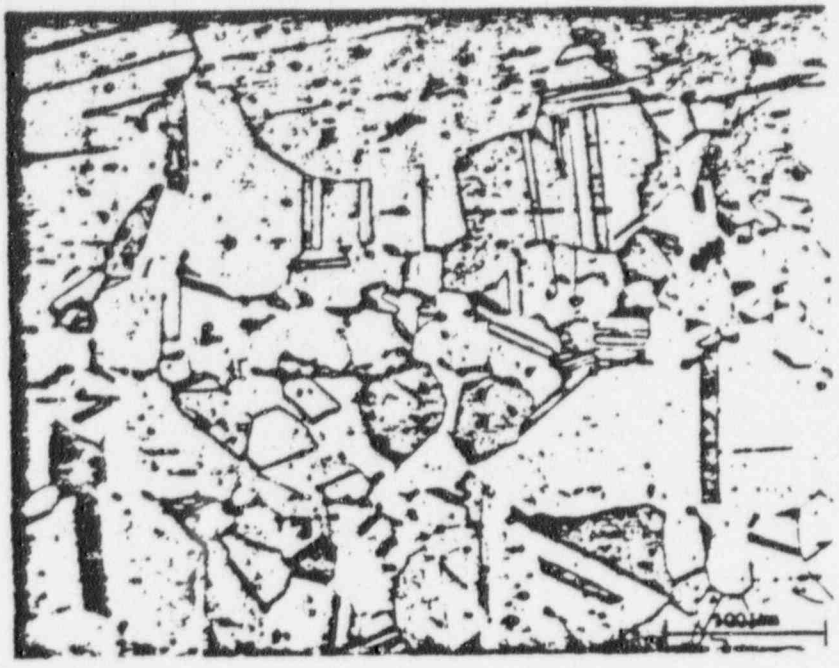

Figure 6-3. As-electropolished Microstructure of Type-308 Stainless Steel Heat Treated at 1250°C (2282°F)/1 h, Water Quenched 250X

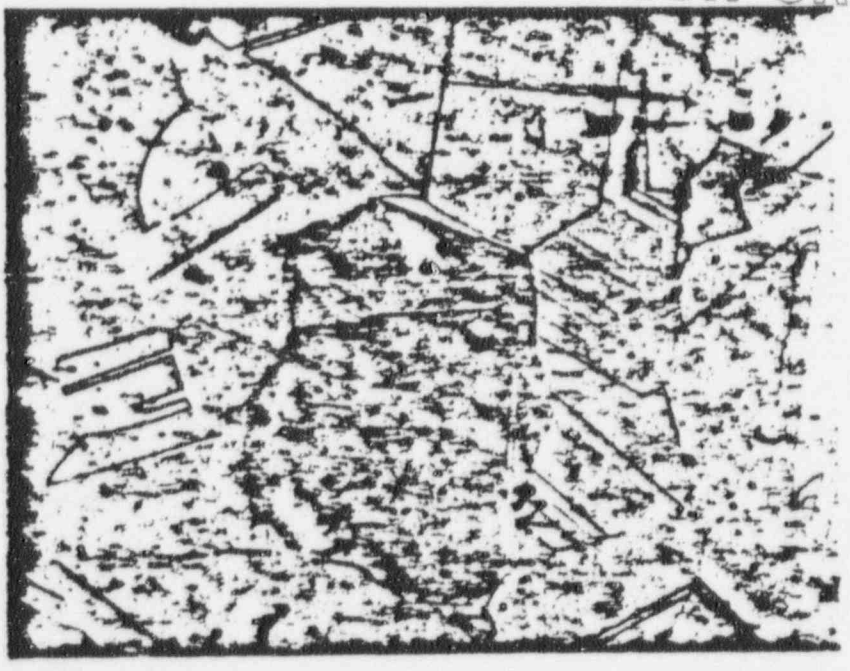

Figure 6-4. As-electropolished Microstructure of Type-308 Stainless Steel Heat Treated at 1200°C (2192°F)/1 h, Water Quenched 250X

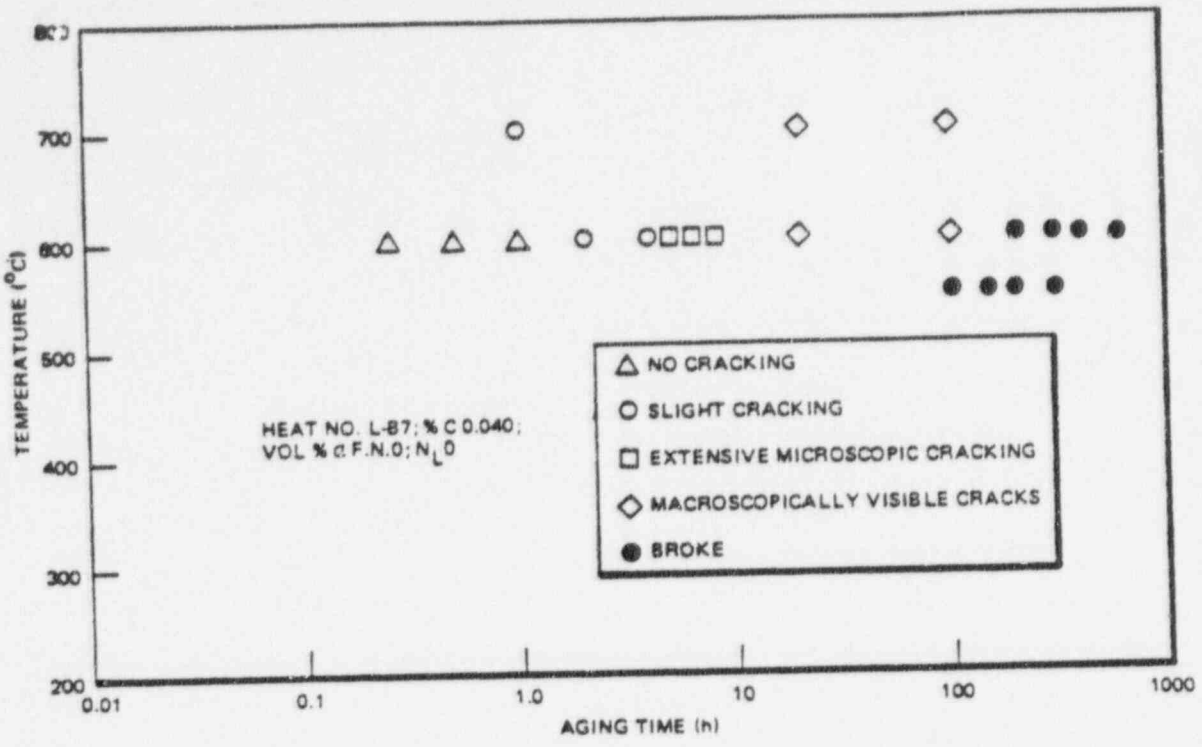

Figure 6-5. Effect of Aging Treatment on the Intergranular Corrosion Behavior of Type-308 Stainless Steel Annealed at 1200°C (2192°F)/1 h, Water Quenched

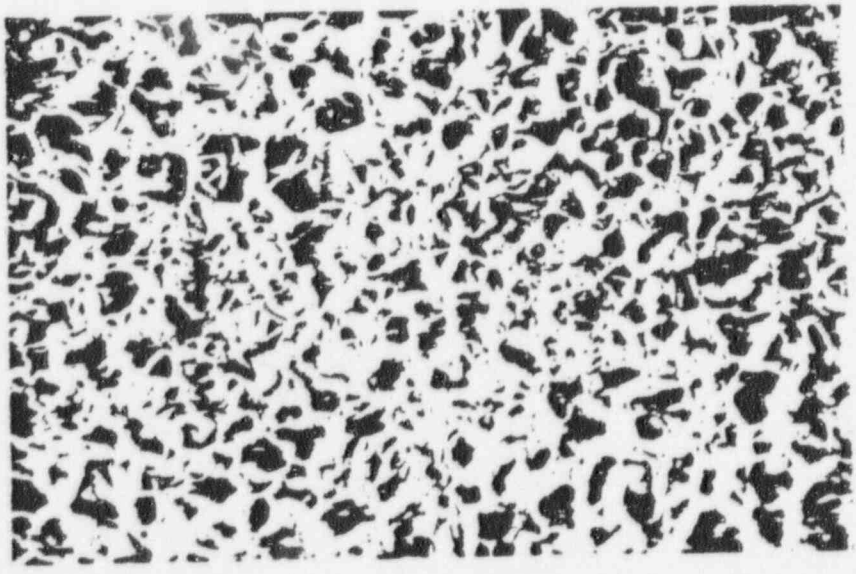

Figure 6-6. Fracture Surface of Type-308 Stainless Steel Heat Treated at 1200°C (2192°F)/1 h, Water Quenched + 600°C (1112°F)/20 h, Water Quenched, and Immersed in A262E for 72 h 250X

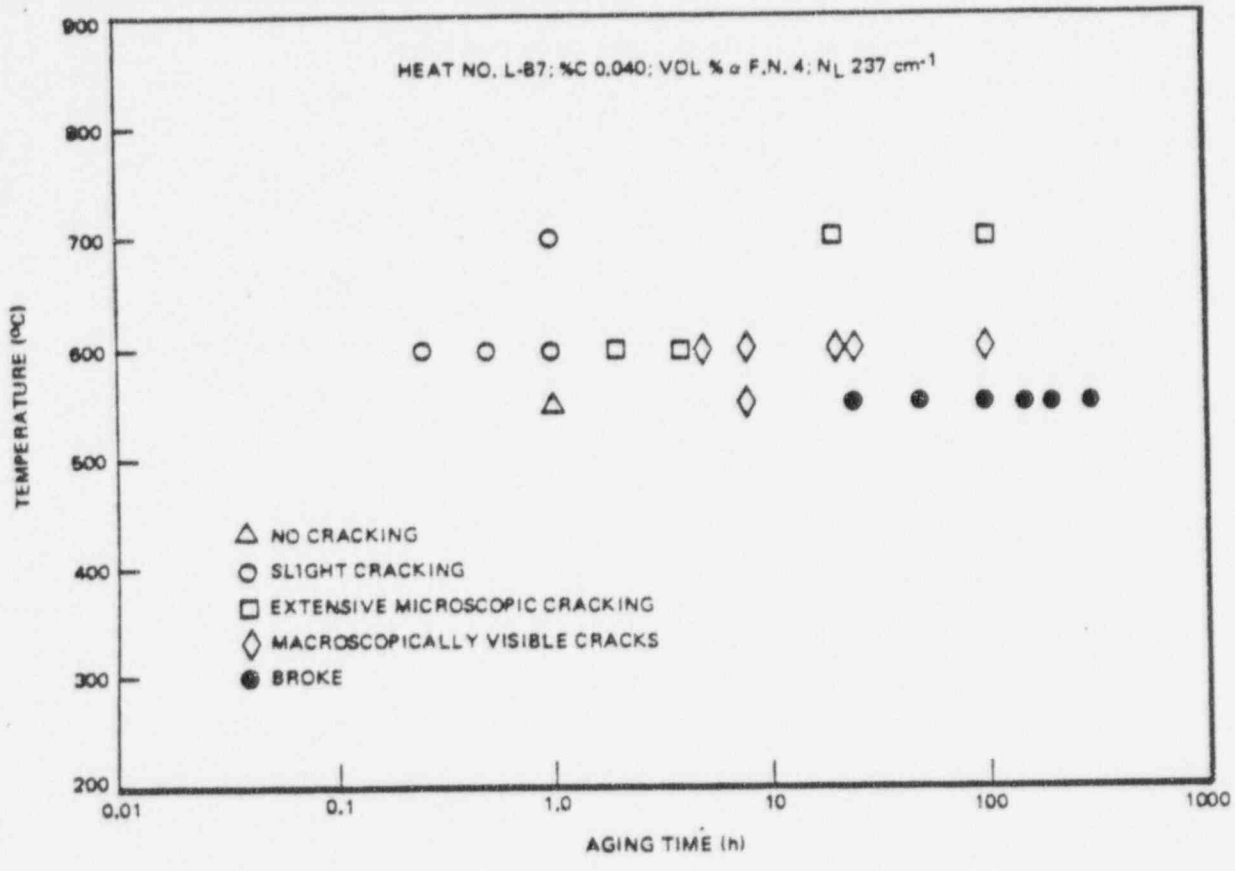

Figure 6-7. Effect of Aging Treatment on the Intergranular Corrosion Behavior of Type-308 Stainless Steel Annealed at 1250°C (2280°F)/1 h, Water Quenched

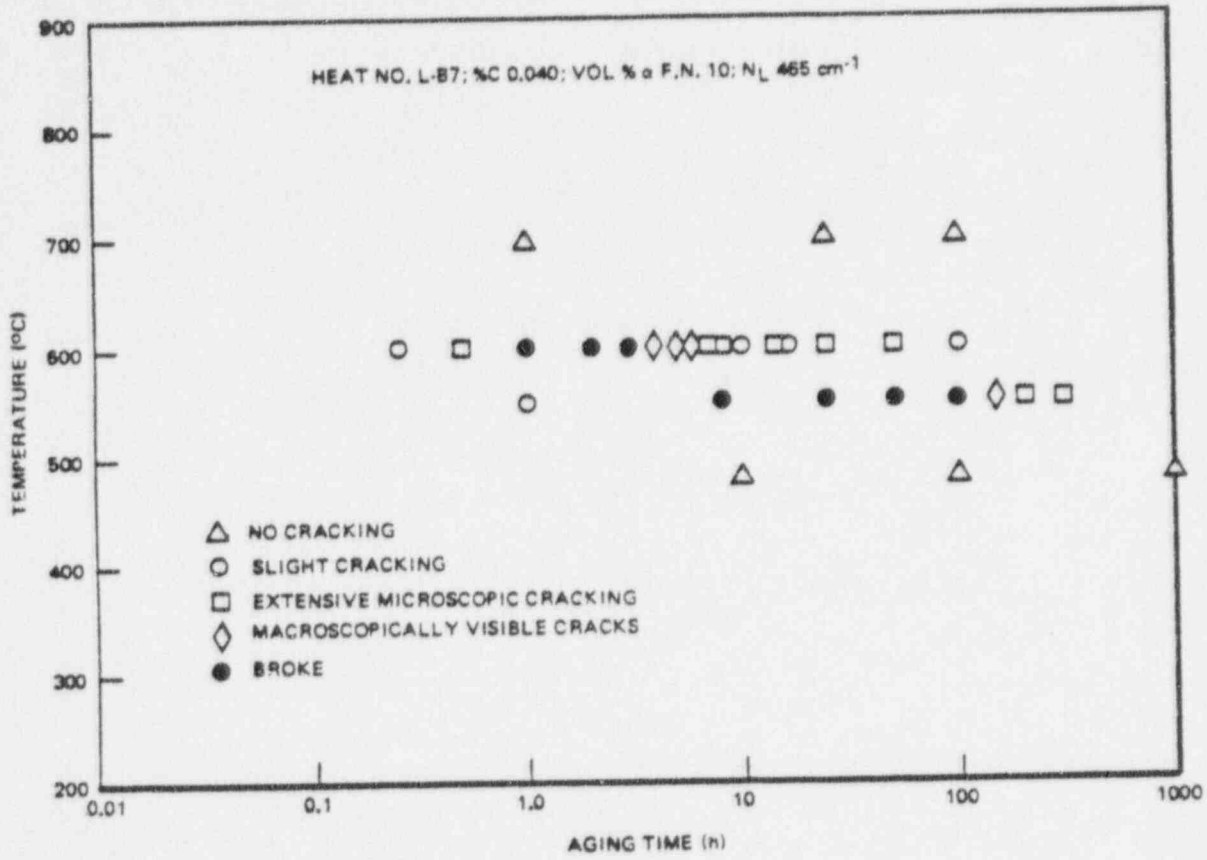

Figure 6-8. Effect of Aging Treatment on the Intergranular Corrosion Behavior of Type-308 Stainless Steel Annealed at 1300°C (2372°F)/1 h, Water Quenched

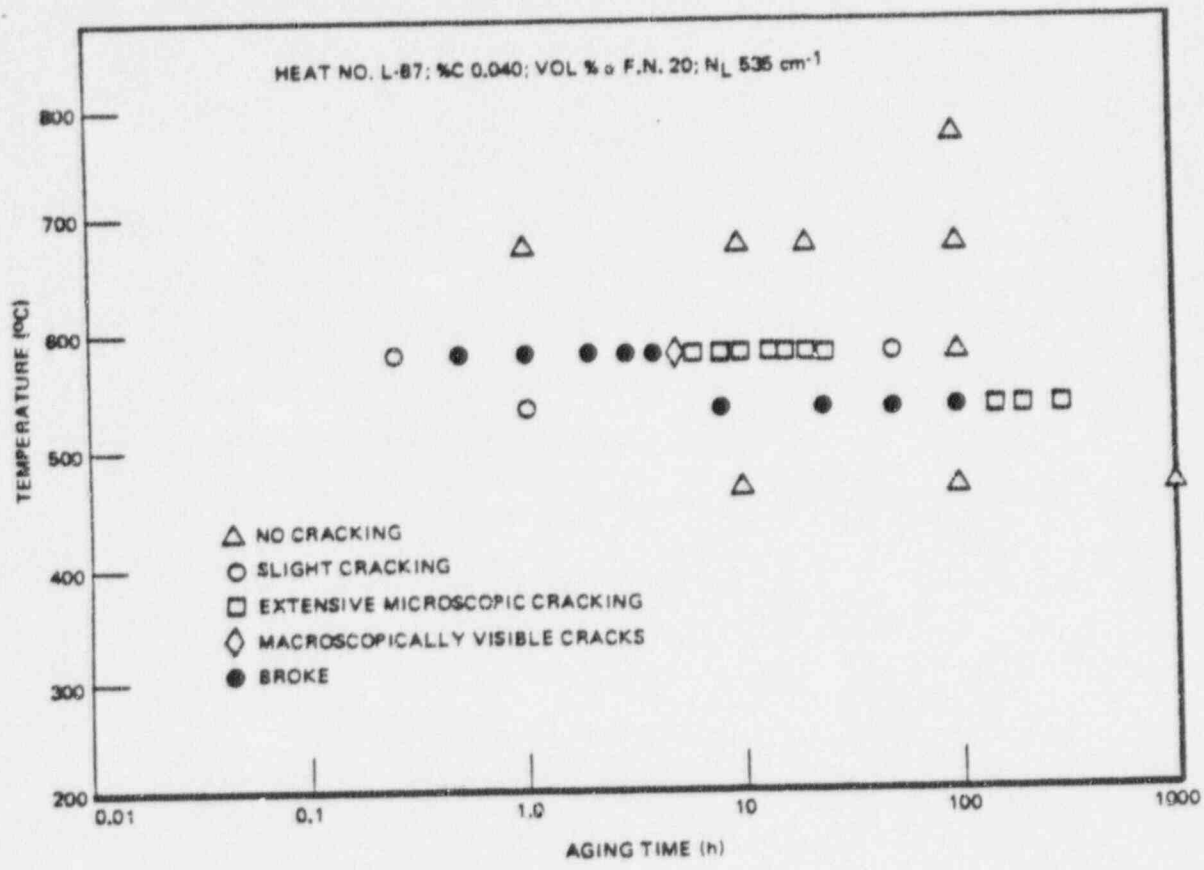

Figure 6-9. Effect of Aging Treatment on the Intergranular Corrosion Behavior on Type-308 Stainless Steel Annealed at 1350°C (2462°F)/1 h, Water Quenched

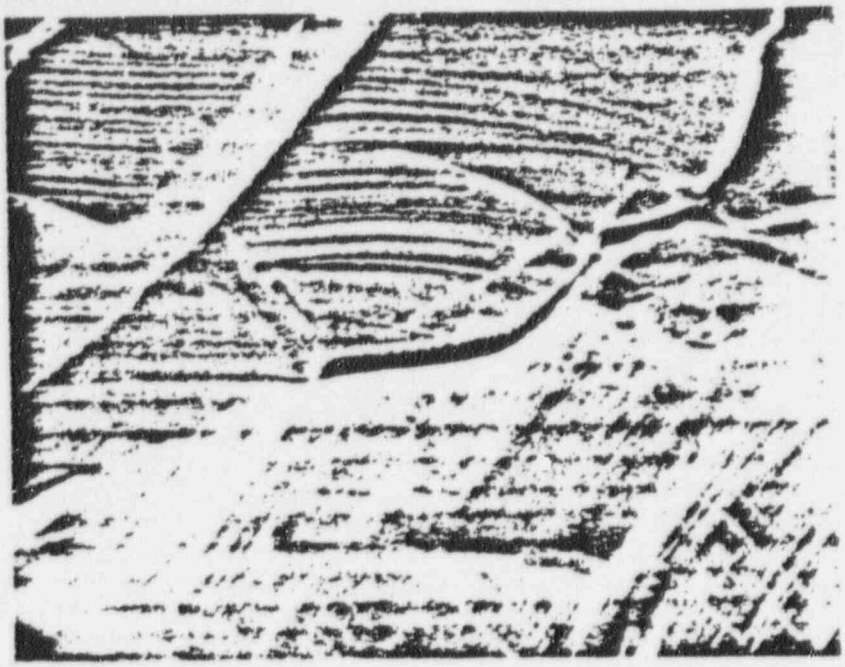

Figure 6-10. Scanning Electron Micrograph of Surface of Type-308 Stainless Steel Specimen Heat Treated at 1300°C (2372°F)/1 h, Water Quenched + 600°C (1112°F)/1 h, Water Quenched, and Immersed in A262E for 72 h 1000X

austenite-austenite grain boundaries in the 10 and 20 vol % ferrite alloys sensitized at 600°C (1112°F). The lack of attack along austenite-austenite boundaries resulted in fracture surfaces with two distinct features for A262E specimens. As shown in Figure 6-11, the fracture surface for the 10 vol % ferrite specimen aged for 1 hour at 600°C (1112°F) has areas of grain boundary fracture caused by localized corrosion of austenite-ferrite phase boundaries. Areas of ductile cracking are also apparent. These result from transgranular fracture of austenite grains during the bending. Interestingly, no localized corrosion attack ever occurred along the austenite-ferrite boundaries separating the austenite grains from the intragranular, twin-like ferrite regions. After aging the 10 and 20 vol % ferrite alloys for 6-8 hours at 600°C (1112°F) or 100-150 hours at 550°C (1022°F) immunity to severe intergranular corrosion attack is restored.

Table 6-2 presents the cumulative weight losses of variously heat treated samples of Type-308 stainless steel following five 48 h immersion periods in boiling 65% nitric acid. In the all-austenitic material the weight loss results from localized corrosion attack down the grain boundaries and subsequent grain dropping. When the 10 and 20 vol % ferrite alloys were aged for 1 hour at 600°C (1112°F), localized corrosion attack occurred along both the austenite-austenite grain boundaries and along the austenite-ferrite boundaries. The attack appeared to be more severe along the latter. Attack also occurred in the A262C test down the austenite-ferrite boundaries separating the austenite grains from the intragranular twinlike ferrite regions. While immunity to intergranular corrosion in A262E occurred with continued aging of the 10 and 20 vol % ferrite alloys at 550-700°C (1022-1292°F), longer aging at 600°C (1112°F) and 700°C (1292°F) resulted in increased intergranular corrosion attack in the A262C test.

Table 6-3 summarizes the results of the A262A tests conducted on Type-308 stainless steel as a function of heat treatment. In the as-annealed conditions the oxalic acid produced a stepped structure regardless of the amount of ferrite present. As shown in Figure 6-12, the stepped structure in the fully austenitic material was the result of differential etching of adjacent grains. Figure 6-13 illustrates the much lower rate of attack in A262A of the ferrite phase relative to the austenite phase in the duplex alloys which leaves the former in relief and results in a stepped microstructure. Aging the duplex material at 550°C (1022°F) for 1 hour results in the ditching of some austenite-ferrite boundaries in the low-ferrite duplex alloys and in the complete ditching of the 20 vol % ferrite duplex alloy. Aging the

duplex alloys at 550°C (1022°F) for 8 or more hours resulted in totally ditched structures from A262A testing. In the duplex alloys aged at 600°C (1112°F) and 550°C (1022°F), ditching occurred along both the austenite-austenite and austenite-ferrite boundaries including the austenite-intragranular ferrite boundaries. As was the case for A262C testing, continued aging of the 10 and 20 vol % ferrite alloys at 600°C (1112°F) and 550°C (1022°F) resulted in higher corrosion rates in the A262A test.

Table 6-2
EFFECT OF HEAT TREATMENT ON
THE CORROSION BEHAVIOR OF STAINLESS STEEL, HEAT L-B7, IN A262C

Heat Treatment	Cumulative Weight Loss After Five 48-Hour Immersion Periods (mg/cm²)
1200°C/1 + 600°C/100	*
1250°C/1 + 600°C/100	138
1350°C/1 + 600°C/100	115
1200°C/1 + 600°C/20	102
1200°C/1 + 700°C/20	96
1250°C/1 + 600°C/20	87
1300°C/1 + 600°C/100	75
1200°C/1 + 700°C/100	70
1250°C/1 + 700°C/1	66
1350°C/1 + 600°C/1	56
1300°C/1 + 700°C/100	54
1250°C/1 + 700°C/20	26
1300°C/1 + 600°C/1	22
1200°C/1 + 700°C/1	19
1250°C/1 + 700°C/100	18
1350°C/1 + 600°C/20	14
1350°C/1 + 700°C/100	13
1350°C/1 + 700°C/1	12
1300°C/1 + 700°C/1	11
1300°C/1 + 700°C/20	10
1350°C/1 + 700°C/20	8
1250°C/1 + 600°C/1	7
1200°C/1 + 600°C/1	5

*Sample disintegrated during fifth immersion period.

Figure 6-14 illustrates the effect of annealing temperature on the pitting potential of Type-308 stainless steel. Recall that the volume percent ferrite in the alloy varies from 0% to 20% as the annealing temperature increases from 1200°C (2192°F) to 1350°C (2462°F). Regardless of the amount of ferrite present in the alloy, considerable scatter is apparent in the measured values of the pitting potential. Several samples did not pit during testing. These were assigned values of 900 mV. All specimens which pitted, regardless of annealing temperature, exhibited only a very few (~10 pits/cm²), but large (~300 μm diameter), pits. As indicated in Figure 6-15, in the duplex material the pits initiated in the ferrite phase at the austenite-ferrite interface.

Regardless of annealing temperature, samples which were aged at 480°C (896°F) for times of 10-1000 hours exhibited the same pitting propensity as the as-annealed material. Very low pit densities were observed in the aged samples following anodic polarization and similar values of pitting potentials were obtained. Figures 6-16 through 6-19 illustrate the effect of aging treatment at 600 and 700°C (1112 and 1292°F) on the pitting potential of Type-308 stainless steel containing different amounts of ferrite. The vertical bar in each figure indicates the range of pitting potentials measured for the as-annealed material. Several points are apparent in these data. First, the scatter in the

data obtained for the aged specimens was much less than that obtained for the as-annealed samples. Second, regardless of annealing temperature the pitting potential obtained on samples aged at 700°C (1292°F) was always greater than that obtained on samples aged at 600°C (1112°F).

Table 6-3
EFFECT OF HEAT TREATMENT ON THE
CORROSION BEHAVIOR OF TYPE 308 STAINLESS STEEL, HEAT L-87, IN A262A

Anneal	1200°C/1h W.Q.	1250°C/1h W.Q.	1300°C/1h W.Q.	1350°C/1h W.Q.
Aging time at 600°C (h)				
0	Step	Step	Step	Step
1/4	Step	Dual	Ditch	Ditch
1/2	Step	Ditch	Ditch	Ditch
1	Dual	Ditch	Ditch	Ditch
2	Dual	Ditch	Ditch	Ditch
4	Ditch	Ditch	Ditch	Ditch
5	Ditch	Ditch	Ditch	Ditch
6	Ditch	Ditch	Ditch	Ditch
8	Ditch	Ditch	Ditch	Ditch
24	Ditch	Ditch	Ditch	Ditch
48	Ditch	Ditch	Ditch	Ditch
96	Ditch	Ditch	Ditch	Ditch
Aging time at 550°C (h)				
1	Ditch	Dual	Dual	Ditch
8	Ditch	Ditch	Ditch	Ditch
24	Ditch	Ditch	Ditch	Ditch
48	Ditch	Ditch	Ditch	Ditch
96	Ditch	Ditch	Ditch	Ditch

As indicated in Figure 6-16 the pitting potentials of the all-austenitic material aged at 700°C (1292°F) were near the lower end of the range obtained for the as-annealed material. The pitting potential of the all-austenitic material decreases as the time of aging at 600°C (1112°F) increases from 1 to 20 hours. In fact, the specimens aged at 600°C (1112°F) for 1 hour behaved exactly like the as-annealed specimens. In both cases, there was a large amount of scatter in the data and the pit density following anodic polarization was very low. For all other aging conditions, the pits were much smaller (~20 μm diameter) and the pit density was much higher (~$10^3/cm^2$) than was obtained for the as-annealed material. This was also the case for the three duplex conditions studied, namely, the pit density following anodic polarization of aged material was much greater than that obtained for the as-annealed material.

Figure 6-17 indicates that the pitting potential of the low volume fraction ferrite duplex alloy formed by annealing at 1250°C (2282°F) for 1 hour and water quenched was a strong function of aging time. The pitting potential obtained by aging at either 700 or 600°C (1292 or 1112°F) decreased as the aging time increased from 1 to 20 hours. The pitting potentials measured for the 4 vol % ferrite duplex condition after 20 and 100 hours at 600 and 700°C (1112 and 1292°F) were much lower than those measured for any aging treatment of the other duplex alloys and for the all-austenitic material as well.

The results of the pitting potential measurements conducted on the 10 and 20 vol % ferrite duplex material are summarized in Figures 6-18 and 6-19, respectively. In contrast to the results obtained for the all-austenitic material and the 4 vol % ferrite duplex material, the pitting potential of specimens aged at 600°C (1112°F) remains relatively unchanged as the aging time increases from 1 to 20 hours. The pitting potential of the 20 vol % ferrite duplex alloy increased abruptly as the aging time at 600°C (1112°F) increased from 20 to 50 hours.

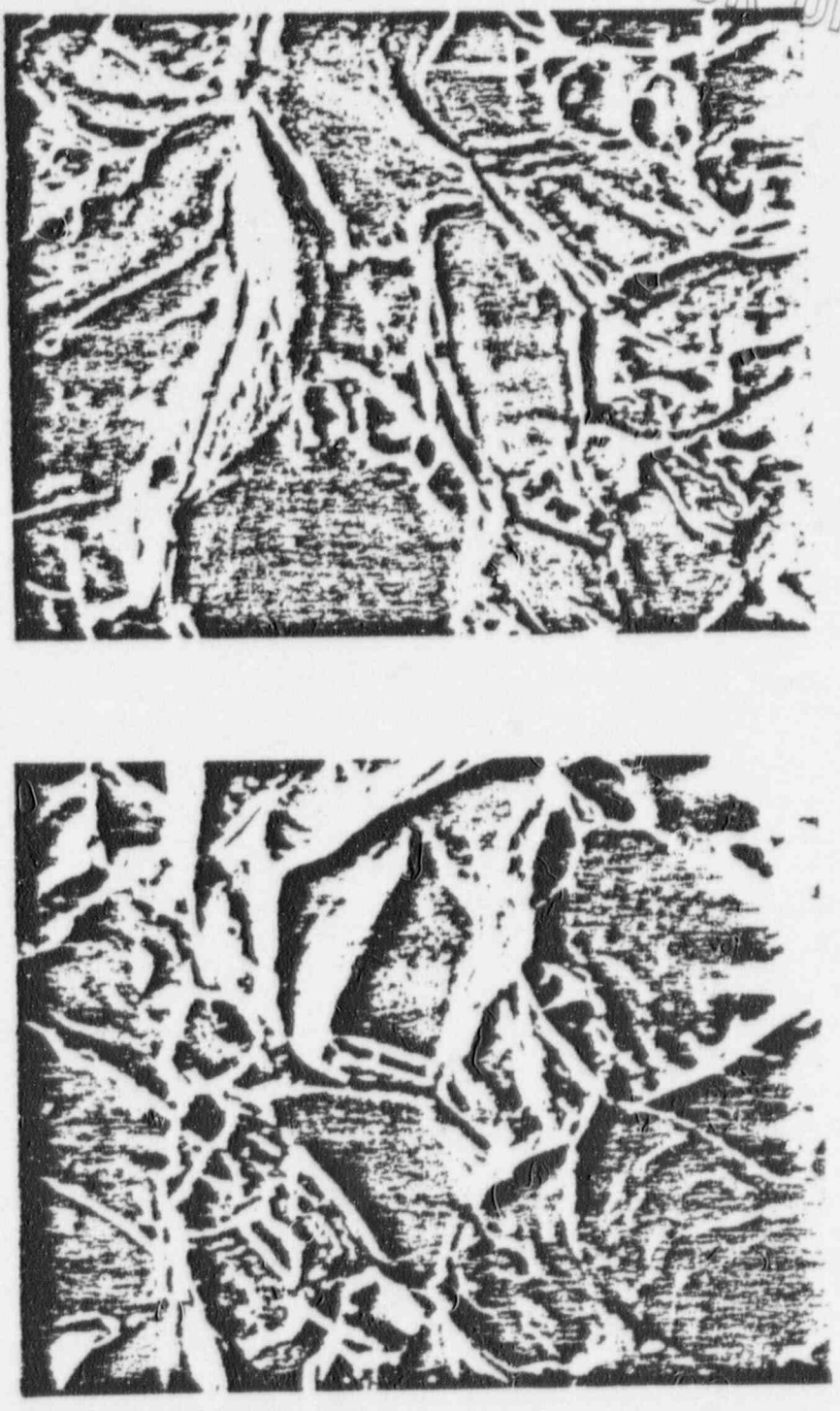

Figure 6-11. Fracture Surface of Type-308 Stainless Steel Heat Treated at 1300°C (2372°F)/1 h, Water Quenched + 600°C (1112°F)/1 h, Water Quenched, and Immersed in A262E for 72 h 3000X

Figure 6-12. Scanning Electron Micrograph of Type-308 Stainless Steel Heat Treated at 1200°C (2192°F)/1 h, Water Quenched and Tested in A262A 1000X

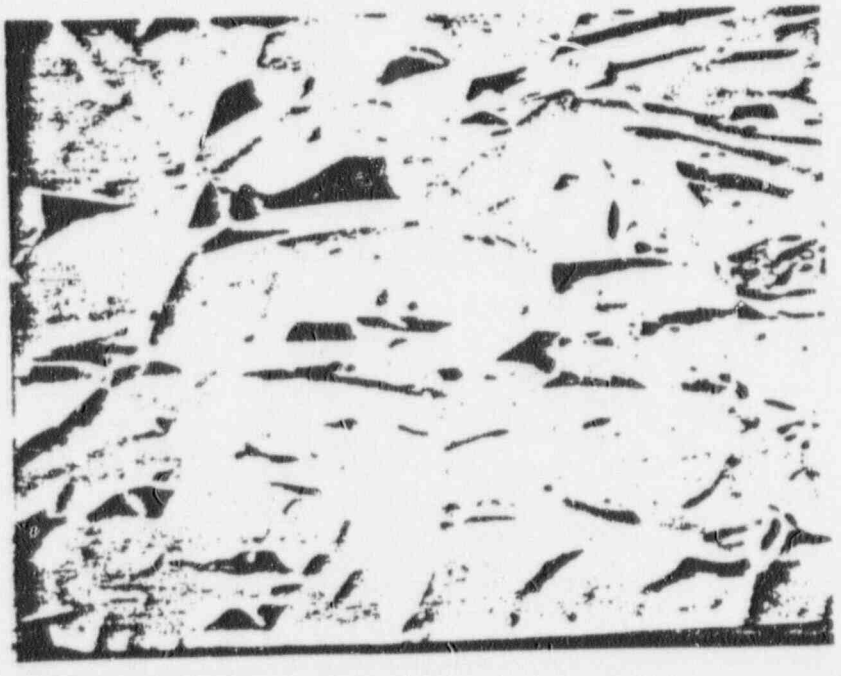

Figure 6-13. Scanning Electron Micrograph of Type-308 Stainless Steel Heat Treated at 1300°C (2372°F)/1 h, Water Quenched and Tested in A262A 750X

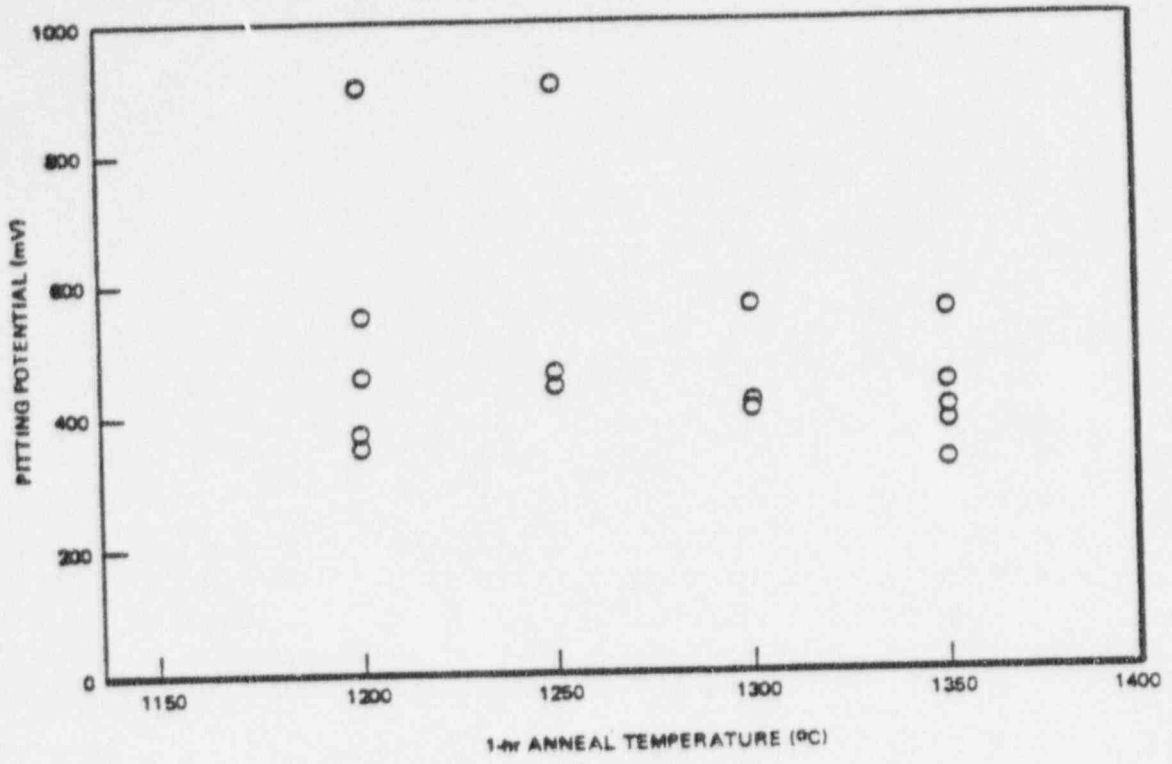

Figure 6-14. Effect of Annealing Temperature on the Pitting Potential of Type-308 Stainless Steel in 0.1 N HCl

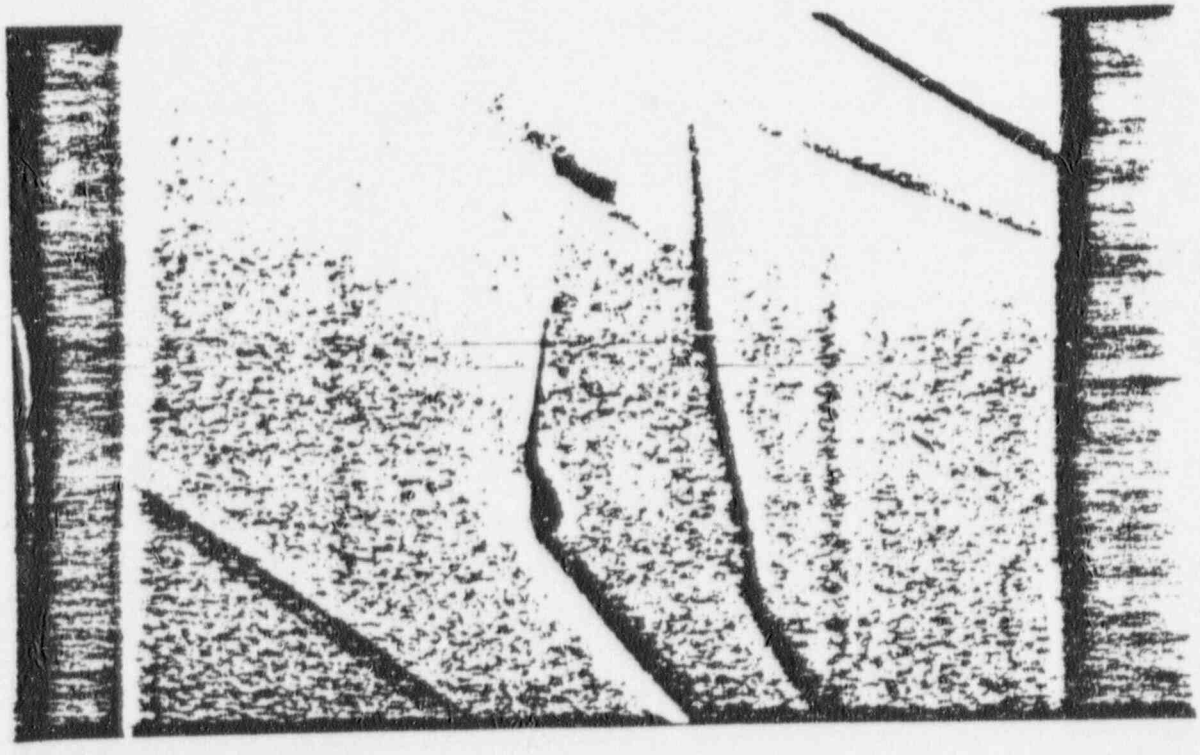

Figure 6-15. Appearance of Type-308 Stainless Steel Heat Treated at 1350°C (2462°F)/1 h, Water Quenched, and Anodically Polarized at 1 mV/sec in 0.1 N HCl

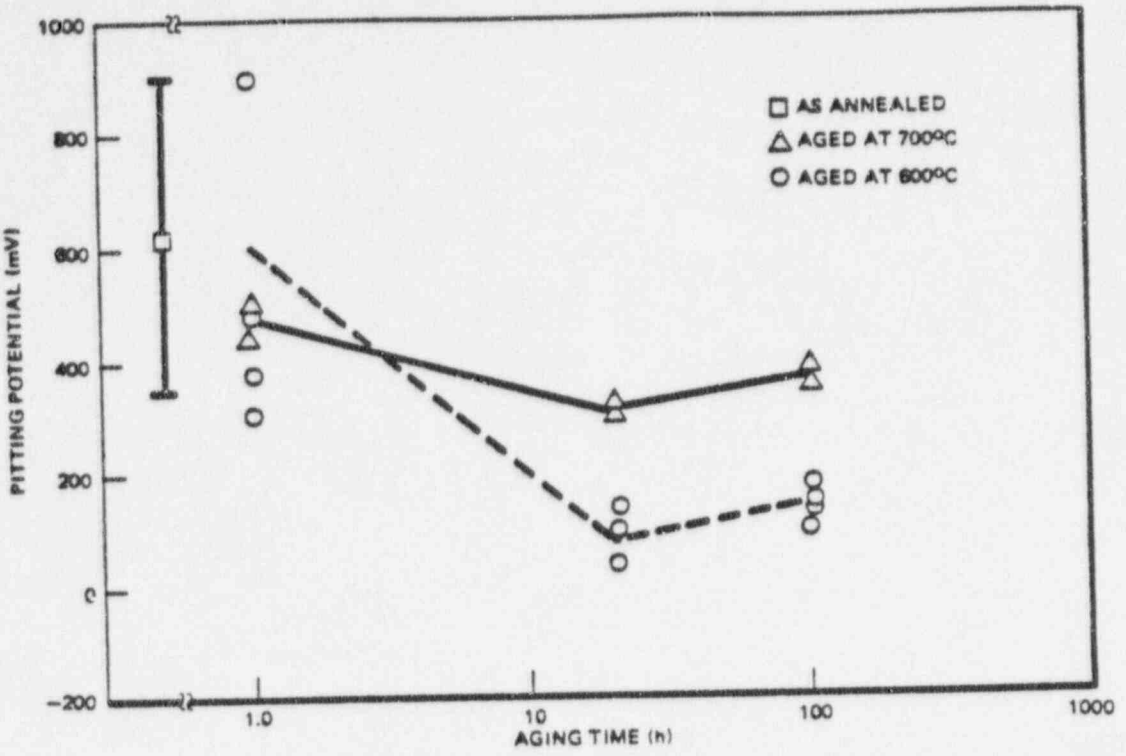

Figure 6-16. Influence of Aging Treatment on the Pitting Potential in 0.1 N HCl of Type-308 Stainless Steel Annealed at 1200°C (2192°F)/1 h, Water Quenched

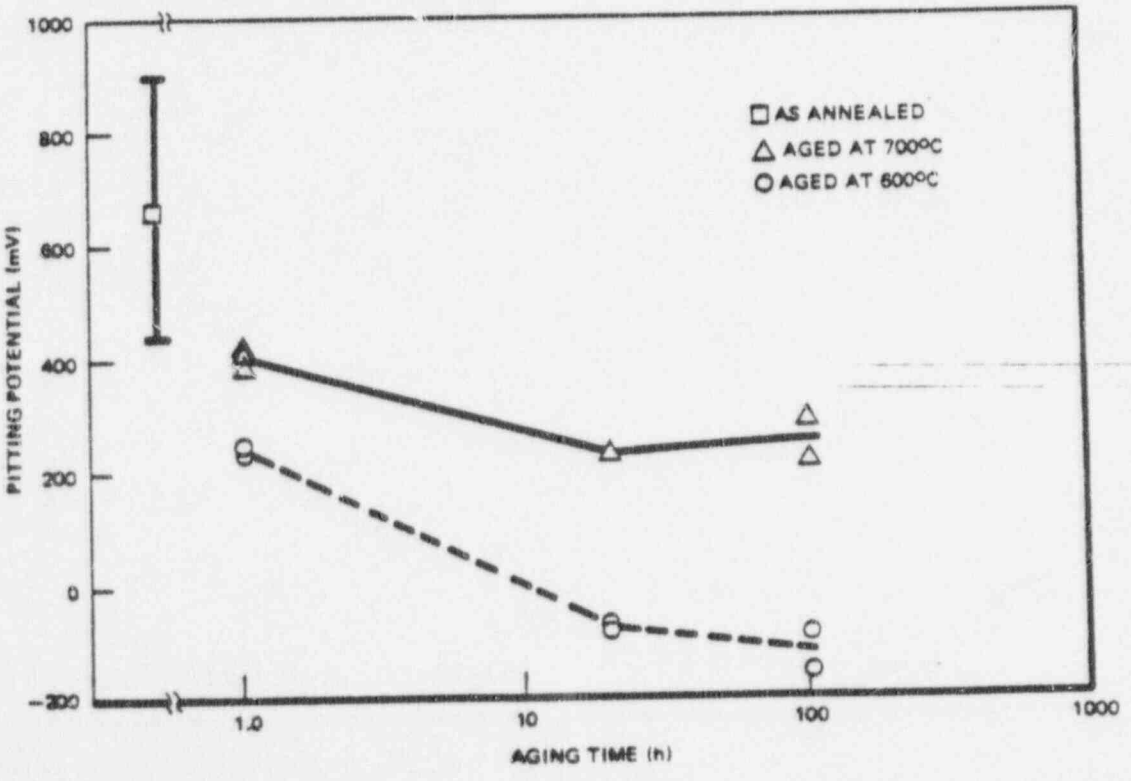

Figure 6-17. Influence of Aging Treatment on the Pitting Potential in 0.1 N HCl of Type-308 Stainless Steel Annealed at 1250°C (2282°F)/1 h, Water Quenched

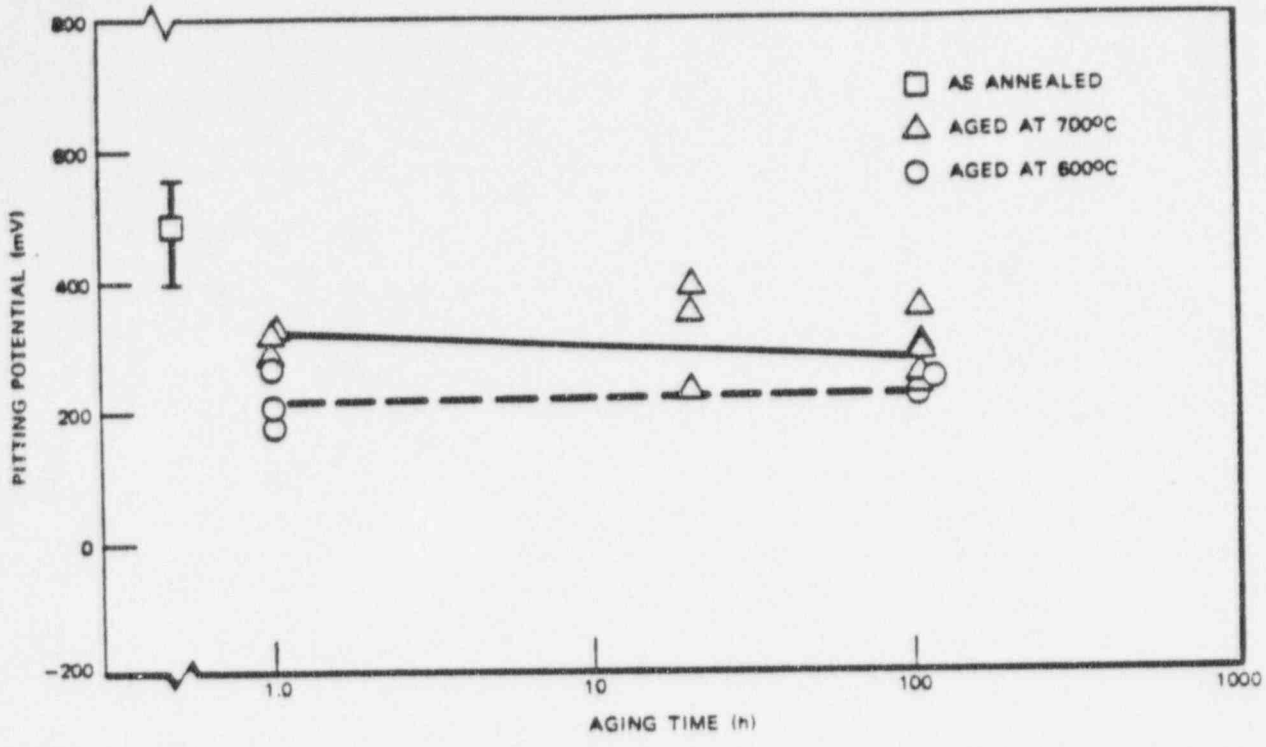

Figure 6-18. Influence of Aging Treatment on the Pitting Potential in 0.1 N HCl of Type-308 Stainless Steel Annealed at 1300°C (2372°F)/1 h, Water Quenched

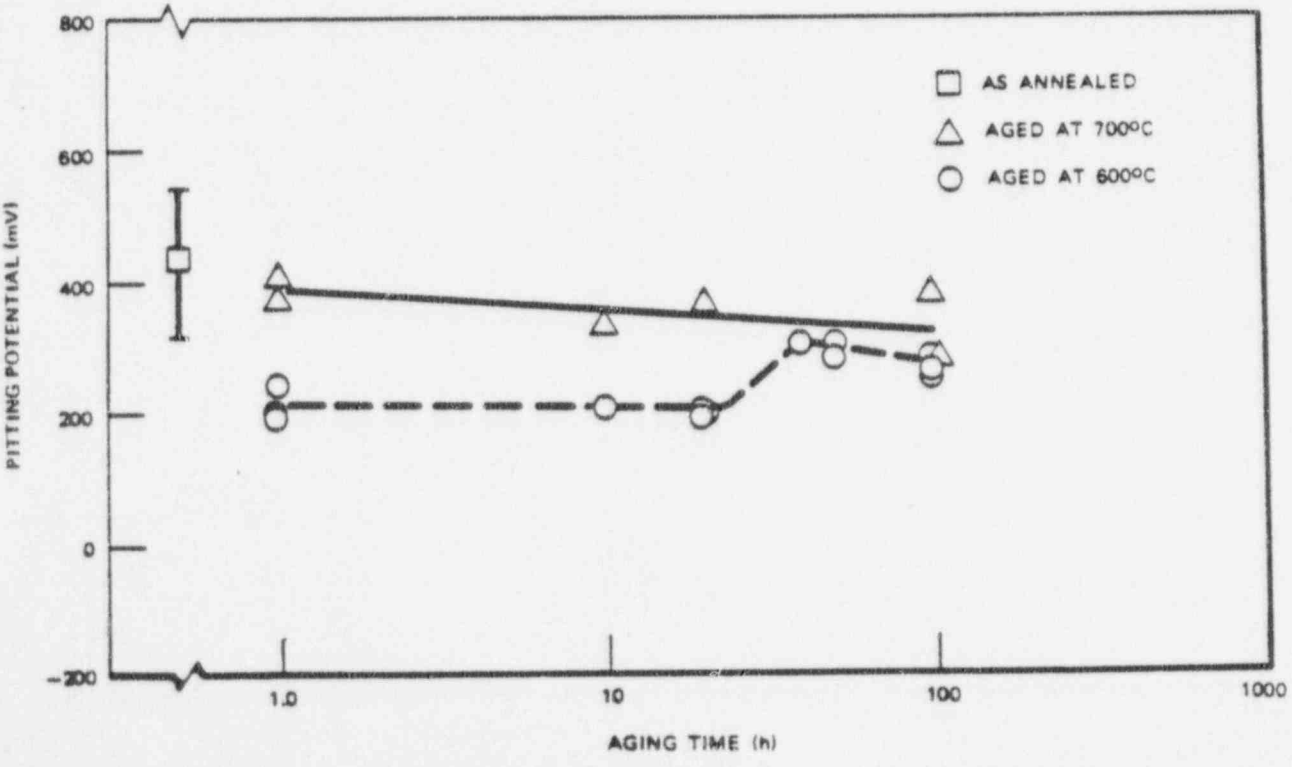

Figure 6-19. Influence of Aging Treatment on the Pitting Potential in 0.1 N HCl of Type-308 Stainless Steel Annealed at 1350°C (2462°F)/1 h, Water Quenched

Although the pitting potential appeared to be sensitive to aging treatment, the most dramatic change in pitting behavior during anodic polarization affected by aging was the change in pit density. To study this effect more closely, galvanostatic pitting experiments were conducted to measure pit initiation rate and to determine the site of pit initiation as a function of aging treatment. Pit initiation rate experiments were conducted by applying a constant 1 mA/cm^2 anodic pulse to the specimen for 5 minutes and then counting the number of pits. The onset of pitting in this test was determined by simultaneously measuring the potential of the specimen. When pitting initiated the potential of the specimen precipitously dropped by ~1 volt. In tests designed to study the site of pit initiation, the galvanostatic current was interrupted as soon as the potential of the specimen dropped. The sample was then immediately removed from the solution and examined in a scanning electron microscope for evidence of pitting.

A 5-minute application of a 1 mA/cm^2 galvanostatic current pulse in 0.1 N HCl to the as-annealed austenitic and duplex conditions of Type-308 stainless steel did not result in pit initiation. Similarly, no pits were initiated in specimens aged at 480°C (896°F) for times up to 1000 hrs. Aging at higher temperatures, however, had a dramatic effect on pitting behavior in the galvanostatic test.

Figure 6-20 illustrates the effect of aging at 600°C (1112°F) on the pit initiation rate of all-austenitic Type-308 stainless steel. Specimens aged for 1 hour at 600°C (1112°F) exhibited the same behavior as the as-annealed material and were free of pits following testing. Aging for 20 or more hours at 600°C (1112°F),however, resulted in a drastic increase in pitting. As depicted in Figure 6-21, the pits initiated at the grain boundaries. This was determined by interrupting the test and examining the sample as soon as the first pits were initiated. The pits propagated rapidly down the grain boundaries, resulting in grain dropping as shown in Figure 6-22. Aging for 100 hours at 600°C (1112°F) resulted in similar behavior. Pits initiated at grain boundaries and propagated down grain boundaries as well as into the grain interiors.

Figure 6-23 summarizes the effect of aging time at 600°C (1112°F) on the 10 and 20 vol % ferrite duplex Type-308 stainless steel. In contrast to the all-austenitic material, the pit initiation rate was very high at very short aging times and decreased somewhat abruptly after aging for 8-10 hours at 600°C (1112°F). Whereas the pit initiation site for the all-austenitic material remained constant with aging time, namely, along the grain boundaries, the pit initiation site of the duplex alloys was a strong function of aging time. Aging for 1/4 to 2 hours at 600°C (1112°F) resulted in pits initiating in the austenite phase at the austenite-ferrite interface, as shown in Figure 6-24. Aging at 600°C (1112°F) for 3 hours or more resulted in the decomposition of the ferrite phase into lamellar $\gamma + M_{23}C_6$, beginning at the austenite-ferrite interface. It was not possible to unambiguously identify the precise site of pit initiation in samples aged for 3-10 hours at 600°C (1112°F). The lamellar $\gamma + M_{23}C_6$ zone was so small in these instances and the pit propagation rate so rapid that pits had grown in the austenite phase at the austenite-ferrite interface as well as in the austenite phase in the two-phase lamellar $\gamma + M_{23}C_6$ region, as shown in Figure 6-25. Consequently, the pits either initiated in the austenite phase at the original austenite-ferrite interface and then propagated into the austenite phase in the two-phase $\gamma + M_{23}C_6$ region, or vice versa. With longer aging times the ferrite continued to decompose and the lamellar $\gamma + M_{23}C_6$ region was easily distinguishable. Here, as shown in Figure 6-26, pits could be clearly seen initiating in the $\gamma + M_{23}C_6$ region. As discussed in depth in another section of this report, the ferrite phase decomposed sequentially into lamellar $\gamma + M_{23}C_6$, single-phase austenite, followed by single-phase sigma, and finally into duplex austenite plus ferrite. The final stages of the decomposition into σ and $\alpha + \gamma$ began after approximately 50 hours at 600°C (1112°F). Pits initiated in specimens aged for this length of time at 600°C (1112°F) in the two-phase $\gamma + M_{23}C_6$ region and propagated into the austenite phase leaving the remaining ferrite phase unattacked as was the case for specimens aged for greater than 10 hours. Approximately 50% of the pits formed in specimens aged for 100 hours at 600°C (1112°F) also initiated in the $\gamma + M_{23}C_6$ region. The remainder initiated in the newly formed duplex $\gamma + \upsilon$ region and propagated through the entire, former all-ferrite region.

The pit initiation rate as a function of aging time at 600°C (1112°F) for the 4 vol % ferrite duplex Type-308 stainless steel is presented in Figure 6-27. Pits initiated preferentially at the austenite-ferrite interface after a 1 h age at 600°C (1112°F) and within the $\gamma + M_{23}C_6$ region after 20 hours at 600°C (1112°F). In the latter aging conditions pits also eventually formed along austenite-austenite grain boundaries as well.

Table 6-4 lists the results of the CERT tests conducted on the 20 vol % ferrite alloy as a function of aging treatment. Specimens were tested in the as-annealed condition, as aged at 475°C (889°F) to precipitate α' within the ferrite, and as aged at 600°C (1112°F) to precipitate $M_{23}C_6$. Regardless of aging treatment, no stress corrosion cracking

was observed, even in samples aged for 1 and 2 hours at 600°C (1112°F) which produced severe austenite-ferrite boundary attack in the A262A, A262C, A262E, and pitting tests. Similar results were found for the 10 vol % ferrite alloy. However, when the duplex alloys aged at 600°C (1112°F) for 1 and 2 hours were first precorroded in A262E and then tested in CERT, they failed in a completely brittle, intergranular fashion as depicted in Figure 6-28. Table 6-5 illustrates the effect of prior intergranular corrosion on the stress corrosion cracking behavior in CERT of the 10 vol % ferrite alloy. Samples aged for 1 hour at 600°C (1112°F) and then tested in CERT without A262E treatment failed ductilely. Specimens aged for 1 hour at 600°C (1112°F) with a subsequent A262B treatment and then tested at nominal strain rates of 1×10^{-5} and 2×10^{-5} min^{-1}, failed intergranularly with low elongations to failure. The specimen tested this way and strained at a nominal rate of 5×10^{-5} min^{-1} failed in a completely ductile fashion. The appearance of the sample following CERT testing is illustrated in Figure 6-29. The influence of precorrosion time in A262E on the failure behavior in CERT is also presented in Table 6-5. Precorroding the sample in A262E for 12 hours and 1-1/2 hours also resulted in complete intergranular failure. When specimens aged for 10, 20, 50, and 100 hours at 600°C (1112°F) were precorroded in A262E for 24 hours and then tested, they failed in a completely ductile fashion.

Table 6-4
EFFECT OF AGING TREATMENT ON THE STRESS CORROSION CRACKING BEHAVIOR OF DUPLEX TYPE-308 STAINLESS STEEL, HEAT L-B7, IN CERT

Heat Treatment	Nominal Strain Rate (min^{-1})	SCC
1350°C/1	1×10^{-3}	No
1350°C/1	2×10^{-4}	No
1350°C/1	2×10^{-5}	No
1350°C/1 + 475°C/10	1.5×10^{-4}	No
1350°C/1 + 475°C/100	1.3×10^{-4}	No
1350°C/1 + 475°C/1000	1.3×10^{-4}	No
1350°C/1 + 600°C/1	1×10^{-5}	No
1350°C/1 + 600°C/2	1.3×10^{-5}	No
1350°C/1 + 600°C/10	1.3×10^{-5}	No
1350°C/1 + 600°C/20	1.3×10^{-5}	No
1350°C/1 + 600°C/20	1.6×10^{-5}	No
1350°C/1 + 600°C/100	1.4×10^{-4}	No
1350°C/1 + 700°C/1	1.3×10^{-4}	No

Table 6-6 illustrates the effect of aging treatment on the stress corrosion cracking behavior in CERT of pre-intergranularly corroded samples of Type-308 stainless steel containing various amounts of ferrite. Aging the all-austenitic and the 4 vol % ferrite alloys at 600°C (1112°F) from 5 to 100 hours resulted in intergranular stress corrosion cracking in CERT. The 20 vol % ferrite material underwent intergranular stress corrosion cracking when aged for 2 and 4 hours at 600°C (1112°F). Aging for 8 or more hours at 600°C (1112°F) resulted in a ductile failure when tested in CERT.

6.2.4 Discussion

All discussion of the mechanisms and causes for the localized corrosion and stress corrosion cracking reported above for Type-308 stainless steel will be presented in subtask 3. The present task is concerned only with the ability of the various tests to assess the stress corrosion cracking susceptibility of duplex stainless steel.

The A262E results presented in Figure 6-5 for the all-austenitic Type-308 stainless steel are similar to results obtained for other austenitic stainless steels such as Types-304 and -316. A C-shaped curve can be drawn through the data separating the region to the left (which represents aging treatments not susceptible to intergranular corrosion) from the region to the right (which represents aging treatments that are susceptible to severe intergranular corrosion). Aging times up to 100 hours at 700°C (1292°F) and 600 hours at 600°C (1112°F) and 550°C (1022°F) were not sufficient to restore immunity to intergranular corrosion.

Table 6-5
EFFECT OF PRIOR INTERGRANULAR CORROSION ON THE STRESS CORROSION CRACKING BEHAVIOR IN CERT OF DUPLEX TYPE-308 STAINLESS STEEL WITH 10 VOL % FERRITE

Aging Treatment	A262E (h)	d (cm)	$\dot{\epsilon}$ (min^{-1})	Failure Mode
600°C/1	0	0.0917	1×10^{-5}	Ductile
600°C/1	24	0.0922	1×10^{-5}	IGSCC
600°C/1	24	0.0940	1.4×10^{-5}	IGSCC
600°C/1	24	0.0920	3.9×10^{-5}	Ductile
600°C/1	12	0.0914	1.2×10^{-5}	IGSCC
600°C/1	1.5	0.0902	1.2×10^{-6}	IGSCC
600°C/(½)	3	0.0841	8.7×10^{-5}	IGSCC
600°C/1	3		1×10^{-5}	IGSCC
600°C/2	3	0.0655	3.6×10^{-5}	IGSCC
600°C/2	3	0.0800	1×10^{-5}	IGSCC
600°C/2	3	0.0699	1.4×10^{-5}	IGSCC
600°C/2	3	0.0716	6.3×10^{-6}	IGSCC
600°C/2	3	0.0737	6.7×10^{-6}	IGSCC
600°C/4	3	0.0813	9.1×10^{-6}	IGSCC
600°C/8	3	0.0762	1×10^{-5}	Ductile
600°C/10	24	0.0940	7.7×10^{-6}	Ductile
600°C/10	24	0.0940	7.4×10^{-6}	Ductile
600°C/20	24	0.0889	7.4×10^{-6}	Ductile
600°C/20	24	0.0864	7.7×10^{-6}	Ductile
600°C/96	3	0.0841	9.5×10^{-6}	Ductile
550°C/24	0	0.0752	6.76×10^{-5}	IGSCC
550°C/24	0	0.0787	2×10^{-5}	IGSCC
550°C/24	0	0.0795	1.95×10^{-5}	IGSCC

Table 6-6
EFFECT OF AGING TREATMENT ON THE STRESS CORROSION CRACKING BEHAVIOR IN CERT OF PRE-INTERGRANULARLY CORRODED TYPE-308 STAINLESS STEEL

Heat Treatment	A262E (h)	d (cm)	$\dot{\epsilon}$ (min^{-1})	Failure Mode
1200°C/1 + 600°C/5	3	0.0711	9.1×10^{-6}	IGSCC
1200°C/1 + 600°C/96	3	0.0716	1×10^{-5}	IGSCC
1200°C/1 + 600°C/100	3	0.0663	3.6×10^{-5}	IGSCC
1250°C/1 + 600°C/1	3	0.0699	1.1×10^{-5}	Ductile
1250°C/1 + 600°C/5	3	0.0671	9.1×10^{-6}	IGSCC
1250°C/1 + 600°C/20	3	0.0737	5×10^{-5}	IGSCC
1250°C/1 + 600°C/100	3	0.0729	6.7×10^{-5}	IGSCC
1350°C/1 + 600°C/2	3	0.0528	1×10^{-5}	IGSCC
1350°C/1 + 600°C/4	3	0.0630	1.2×10^{-5}	IGSCC
1350°C/1 + 600°C/8	3	0.0798	1.33×10^{-5}	Ductile
1350°C/1 + 600°C/20	3	0.0787	1.1×10^{-5}	Ductile
1350°C/1 + 600°C/100	3	0.0841	9.1×10^{-6}	Ductile

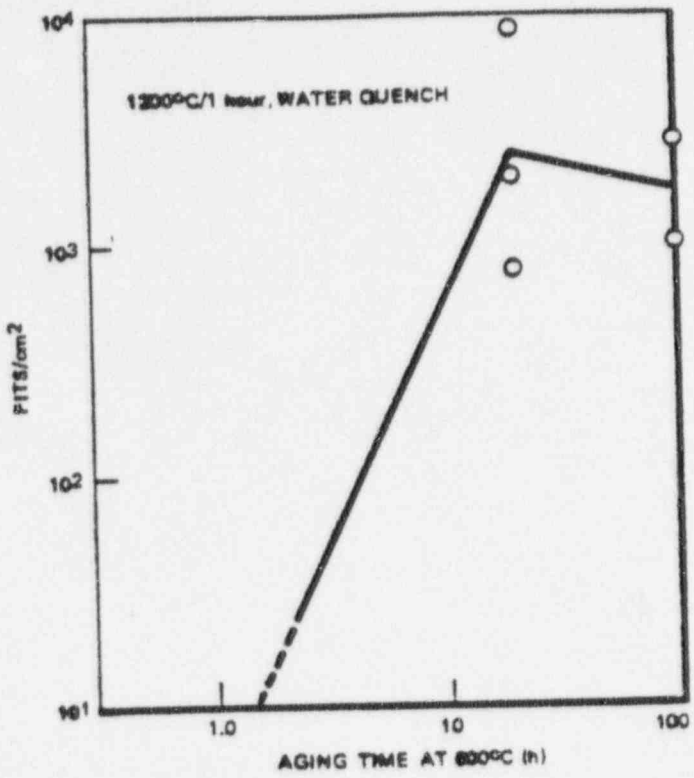

Figure 6-20. Influence of Aging Treatment on the Pit Initiation Rate in 0.1 N HCl of Type-308 Stainless Steel Annealed at 1200°C (2192°F)/1 h, Water Quenched

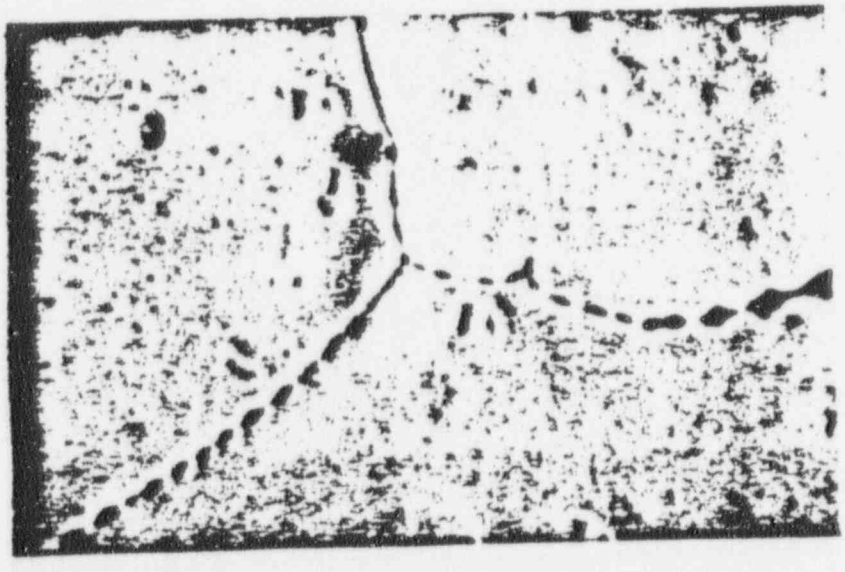

Figure 6-21. Pit Initiation at Grain Boundaries in Sample of Type-308 Stainless Steel Heat Treated at 1200°C (2192°F)/1 h, Water Quenched + 600°C (1112°F)/20 h, Water Quenched, and galvanostatically corroded at 1 mA/cm² for 3 seconds 3000X

Figure 6-22. Appearance of Sample of Type-308 Stainless Steel Heat Treated at 1200°C (2192°F)/1 h, Water Quenched + 600°C (1112°F)/20 h, Water Quenched, and galvanostatically corroded at 1 mA/cm² for 5 minutes 750X

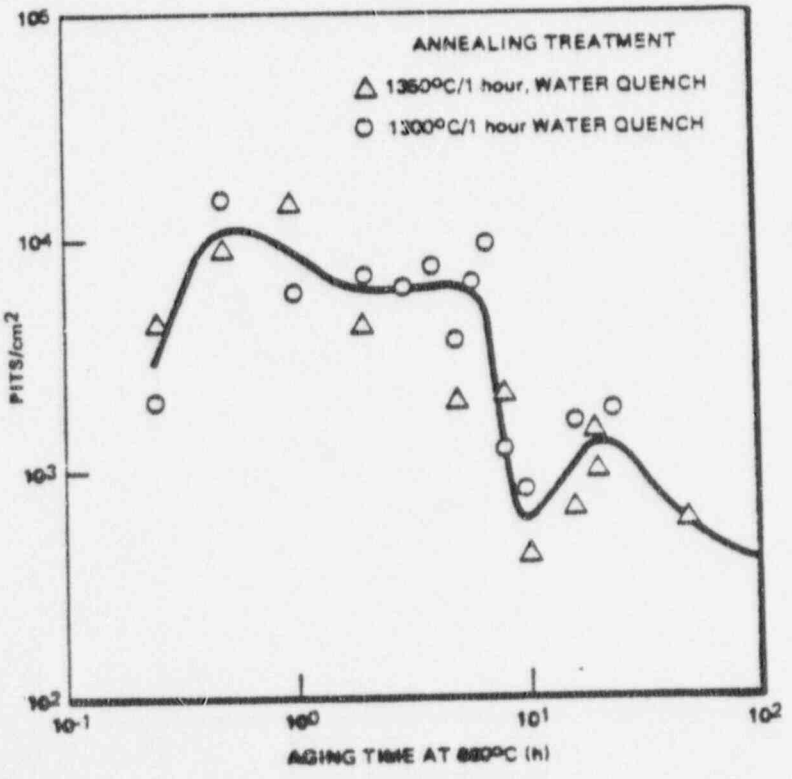

Figure 6-23. Influence of Aging Time at 600°C (1112°F) on the Pit Initiation Rate in 0.1 N HCl of Type-308 Stainless Steel Annealed at 1300°C (2372°F)/1 h, Water Quenched and 1350°C (2462°F)/1 h, Water Quenched

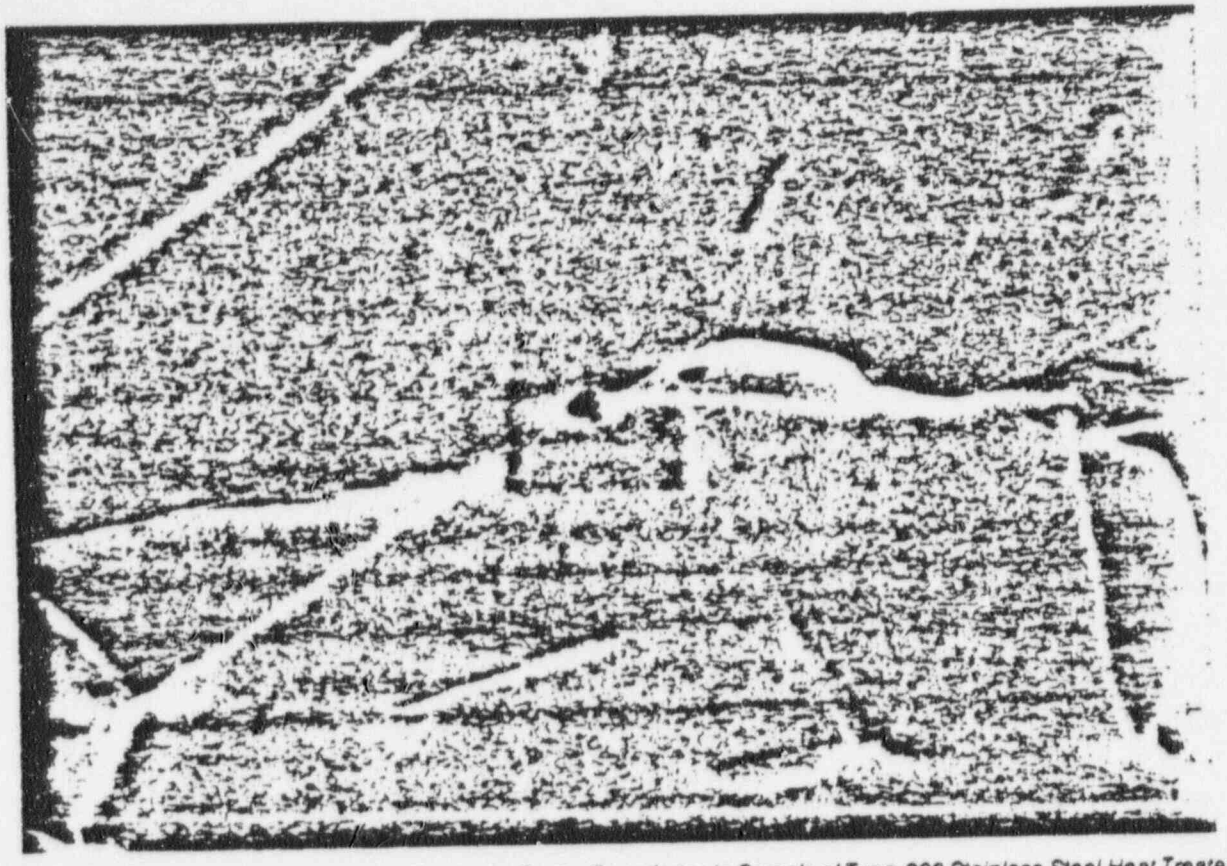

Figure 6-24. Pit Initiation in Austenite at Austenite-Ferrite Boundaries in Sample of Type-308 Stainless Steel Heat Treated at 1350°C (2462°F)/1 h, Water Quenched + 600°C (1112°F)/1 h, 3860X

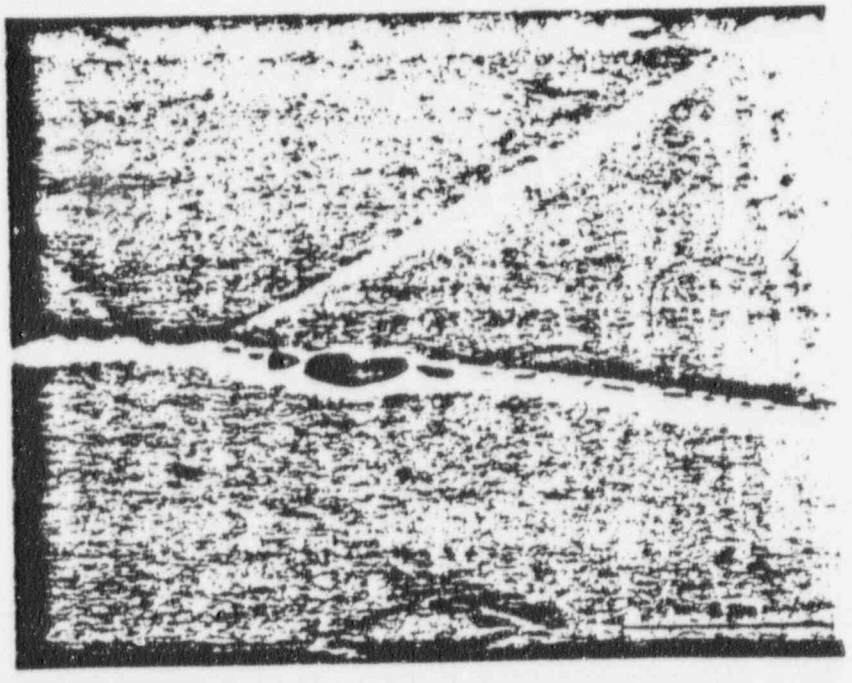

Figure 6-25. Pit Initiation at Austenite-Ferrite Boundaries in Sample of Type-308 Stainless Steel Heat Treated at 1350°C (2462°F)/1 h, Water Quenched + 600°C (1112°F)/5 h, Water Quenched 5000X

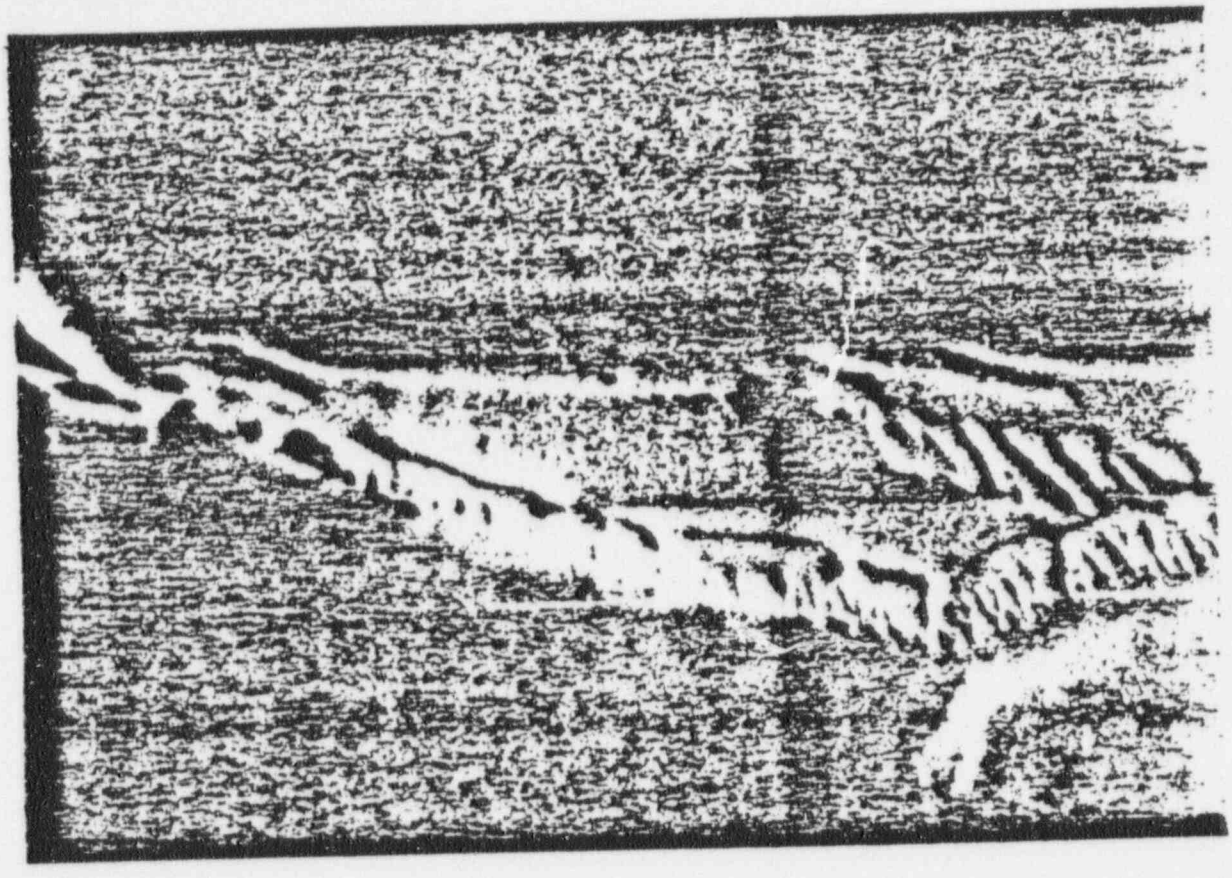

Figure 6-26. Pit Initiation at Austenite in Cellular γ + $M_{23}C_6$ Zone in Sample of Type-308 Stainless Steel Heat Treated at 1350°C (2462°F)/1 h, Water Quenched + 700°C (1292°F)/1 h, Water Quenched + 700°C (1292°F)/1 h, Water Quenched 6430X

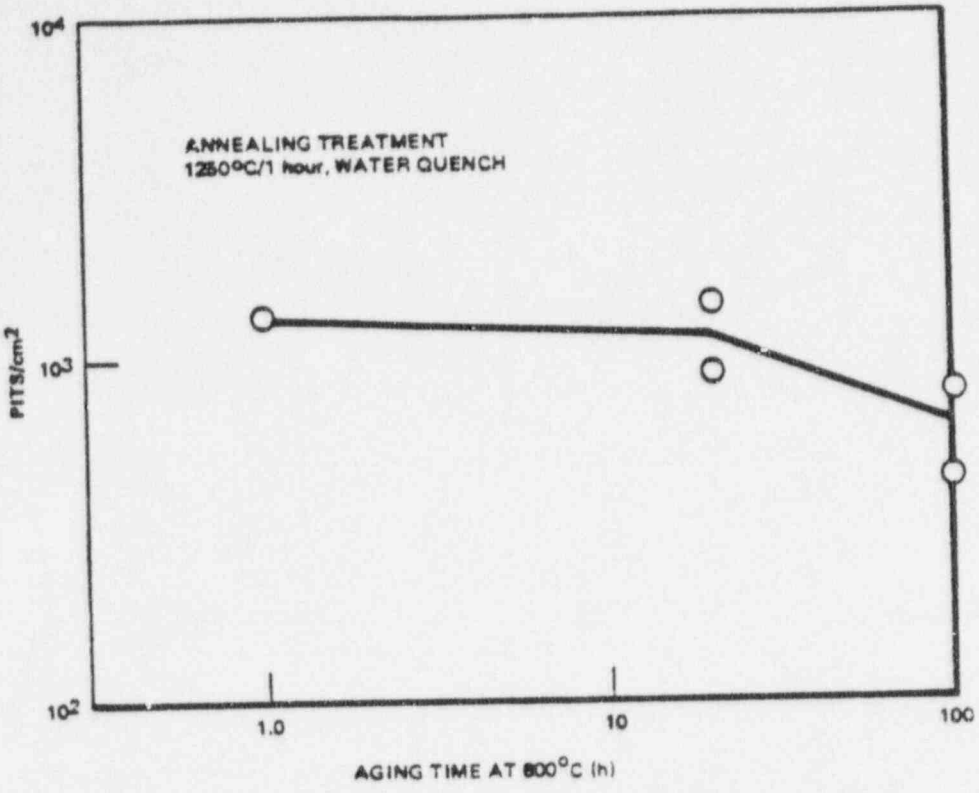

Figure 6-27. Influence of Aging Time at 600°C (1112°F) on the Pit Initiation Rate in 0.1 N HCl of Type-308 Stainless Steel Annealed at 1250°C (2282°F)/1 h, Water Quenched

Figure 6-28. Fracture Surface of Type-308 Stainless Steel Heat Treated at 1300°C (2372°F)/1 h, Water Quenched + 600°C (1112°F)/1 h, Water Quenched, Immersed in A262E for 24 h, and Tested in CERT at 1 x 10^{-4} min^{-1} 100X

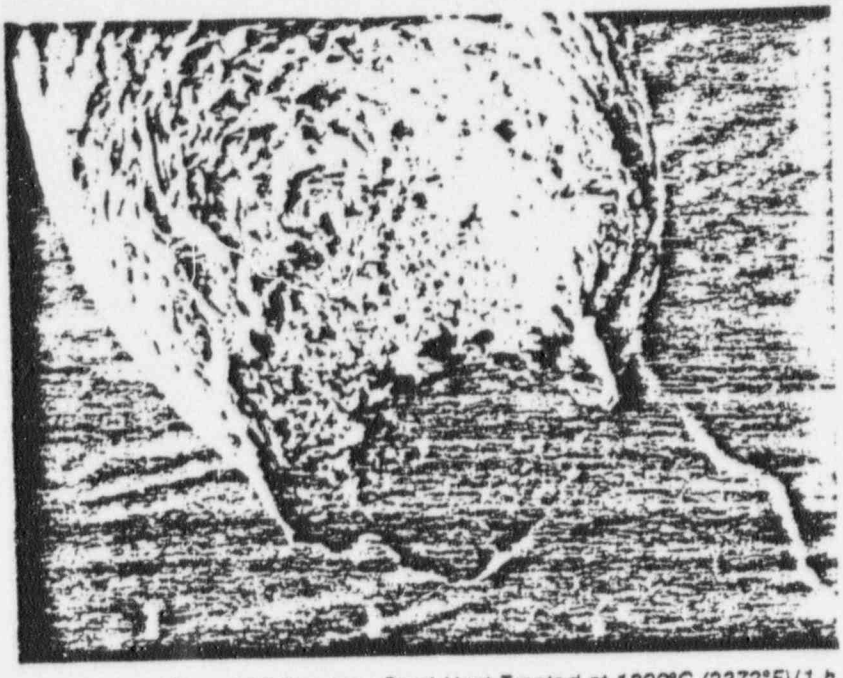

Figure 6-29. Fracture Surface of Type-308 Stainless Steel Heat Treated at 1300°C (2372°F)/1 h, Water Quenched + 600°C (1112°F)/1 h, Water Quenched, Immersed in A262E for 24 h, and Tested in CERT at 5 x 10^{-6} min^{-1} 100X

The intergranular corrosion behavior in A262E of the duplex material containing 4 vol % ferrite was similar to that of the fully austenitic material. Aging up to 100 hours at 600°C (1112°F) and 300 hours at 550°C (1022°F) did not restore immunity to intergranular corrosion.

The 10 and 20 vol % ferrite alloys exhibited similar intergranular corrosion behavior in A262E as a function of aging treatment. Contrary to the results found for the all-austenitic and 4 vol % duplex alloys, immunity to intergranular corrosion could be restored in the 10 and 20 vol % ferrite alloys by aging for longer than ~10 hours at 600°C (1112°F) and ~150 hours at 550°C (1022°F).

The A262C and A262A results were very similar and, for the all-austenitic and 4 vol % ferrite alloys, closely correlated with the A262E results. This was not the case for the 10 and 20 vol % ferrite alloys. Unlike the A262E results, the A262C and A262A corrosion rates of the 10 and 20 vol % ferrite alloys increased with aging time at 550°C (1022°F) and 600°C (1112°F). This is consistent with the observations of several other investigators who reported the A262E test to be sensitive to the presence of chromium-depleted grain boundaries while the more oxidizing solutions A262C and A262A were sensitive to the presence of chromium-rich carbides.[1,2,3,4]

Of the two pitting tests, the galvanostatic pit initiation test was by far the more sensitive to aging treatments. Both the site of pitting and the pit initiation rate varied strongly with the aging treatment. While a significant difference existed between the pitting potentials of the annealed and aged materials and between the pitting potentials of samples aged at different temperatures, there was little effect of aging time on the pitting potential even though the site of pitting and the rate of pitting were changing markedly with aging time. Furthermore, the large scatter in the measured values of the pitting potential of the as-annealed material requires that many measurements of the pitting potential be made in order to confirm the presence of a sensitized microstructure in aged material.

The pit initiation rate of the all-austenitic material as a function of aging treatment agreed quite closely with the results of the three intergranular corrosion tests. The scanning electron microscopy showed the pitting attack to be confined to the grain boundaries. The pit initiation tests of the 10 and 20 vol % duplex alloys also agreed quite well with the A262E results. The healing phenomenon in these high ferrite alloys were demonstrated by a decrease in the number of pits and a change in the site of pit initiation from the austenite phase at the austenite-ferrite interface to the austenite phase in the $\gamma + M_{23}C_6$ cellular zone.

The CERT results obtained for the 10 and 20 vol % ferrite alloys exhibited a distinct healing phenomenon identical to that observed for the A262E and pit initiation tests. The A262C and A262A tests are too conservative to function as indicators of the intergranular stress corrosion cracking behavior in CERT. Both the A262E and pit initiation tests of the 10 and 20 vol % ferrite alloys exhibit a healing phenomenon for aging times longer than 8 hours at 600°C (1112°F) which coincides with the restoration of immunity to intergranular stress corrosion cracking in CERT. The A262C and A262A tests do not reveal this healing effect and consequently could deem material which is immune to intergranular stress corrosion cracking as being susceptible to intergranular stress corrosion cracking. It is important to realize that the A262E test cannot unambiguously predict the outcome of CERT tests on the 10 and 20 vol % ferrite alloys.

While the A262E results on the high ferrite alloys indicate that a healing phenomenon occurs with increasing aging time, there is a broad span of aging time extending from 6 to 15 hours at 600°C (1112°F) in which the A262E test results in extensive microscopic cracking, and it is within this span of aging time that the material goes from susceptible to immune to intergranular stress corrosion cracking in CERT. Consequently, if, following A262E testing, the duplex alloy is extensively microscopically cracked, the material may or may not be susceptible to intergranular stress corrosion cracking in CERT. It is true, however, that if the duplex alloy exhibits macroscopic cracking in A262E, it will be susceptible to intergranular stress corrosion cracking in CERT, and if it exhibits only isolated, nonconnected, one-grain-length, intergranular cracks in A262E, it will be immune to intergranular stress corrosion cracking in CERT.

The results of the CERT tests conducted on the all-austenitic and 4 vol % ferrite alloys are consistent with the results of the three intergranular corrosion tests and the pit initiation tests. The aging treatments investigated which resulted in intergranular corrosion attack also resulted in intergranular stress corrosion cracking in CERT. However, one may speculate that if samples were aged for the very long aging times (greater than 600 hours for the all-austenitic alloy) required to heal the chromium depleted boundaries, then the all-austenitic and 4 vol % ferrite alloys would fail in a ductile fashion in CERT, but still suffer intense intergranular corrosion in A262C and A262A.

6.3 SUBTASK 2 DETERMINE THE INFLUENCE OF SECOND PHASE PARTICLES ON THE STRESS CORROSION CRACKING SUSCEPTIBILITY OF DUPLEX STAINLESS STEEL

6.3.1 Introduction

The thermal and mechanical history experienced by a weld and its heat-affected-zone (HAZ) during welding encompasses a wide range of temperatures and heating and cooling rates. During welding the stress operating in conjunction with the temperature can introduce a number of microstructural changes. In the case of austenitic stainless steel the most detrimental microstructural change introduced by the welding process is the intergranular precipitation of chromium-rich $M_{23}C_6$. This reaction depletes the material adjacent to the grain boundary of chromium and results in susceptibility to localized grain boundary corrosion and stress corrosion cracking. Similar carbide precipitation can occur in duplex stainless steels. Additionally, because of the presence of the ferrite phase, the latter alloys are susceptible to precipitation of other second phases such as σ and α', the latter being a chromium-rich phase which can decrease the corrosion resistance of the alloy as well as embrittle the alloy. In this task we attempt to determine the microstructural changes which can result in sensitization of Type-308 stainless steel as a result of isothermal aging treatments and to determine what effect, if any, such microstructural changes can have on the corrosion and stress corrosion cracking resistance of the alloy.

6.3.2 Procedure

Heat L-B7 whose composition is given in Table 6-1 was employed to evaluate the effects of isothermal aging treatments on the corrosion and stress corrosion cracking resistances of Type-308 stainless steel. The thermo-mechanical processing, specimen preparation, and testing procedures of this material have been described in Section 6.2.2.

6.3.3 Results

6.3.3.1 Physical Metallurgy

As noted in Section 6.2.3, annealing Heat L-B7 at temperatures higher than 1200°C (2192°F) introduces ferrite into the austenite matrix. The higher above 1200°C (2192°F), the more ferrite that is produced. Annealing at 1200°C (2192°F) or lower produces a single-phase austenitic matrix.

The fully austenitic structure, obtained by heat treatment at 1200°C (2192°F) for 1 hour, and water quenched, is supersaturated with interstitial carbon. When aged for 1 hour at 600°C (1112°F), it remained free of any precipitation. When specimens were heat treated for 20 hours at 600°C (1112°F) or 1 hour at 700°C (1292°F), extensive intergranular precipitation occurred as illustrated in the transmission electron micrograph in Figure 6-30. The precipitates were too small to unambiguously identify them by selected area electron diffraction. However, the diffraction patterns obtained were consistent with the grain boundary precipitate being chromium-rich $M_{23}C_6$. Longer aging times at 600°C (1112°F) and 700°C (1292°F) increased the amount of intergranular precipitate.

Aging the duplex material at 480°C (896°F) for times up to 1000 hours produced no microstructural changes within the austenite grains. Similarly, no changes could be seen in the ferrite regions of Type-308 stainless steel following 10 hours at 480°C (896°F). However, after 100 hours at 480°C (896°F) significant quantities of an extremely fine precipitate could be observed within the ferrite as shown in Figure 6-31. Selected area electron diffraction of the α grains following heat treatment for 100 hours and 1000 hours at 480°C (896°F) indicated the presence of only bcc diffraction spots and only one set of bcc diffraction spots. These observations are consistent with the precipitate being α', a chromium-rich bcc phase whose lattice parameter is nearly identical to that of α.

Precipitation occurred in the duplex Type-308 stainless steel following extremely brief aging times at 600°C (1112°F). As short a time as 30 minutes was sufficient to produce extensive precipitation. In the 10 and 20 vol % ferrite material formed by heat treating for 1 hour at 1300°C (2372°F) and 1350°C (2462°F), respectively, the precipitation occurred exclusively along austenite-ferrite phase boundaries. In the low-volume-fraction ferrite material formed by heat treating for 1 hour at 1250°C (2282°F) precipitation eventually occurred along austenite-austenite grain boundaries as well. Figure 6-32 depicts the boundary precipitation resulting from a 1 h age at 600°C (1112°F) of the duplex material formed at 1350°C (2462°F). The diffraction patterns were consistent with this precipitate being $M_{23}C_6$. The figure illustrates the confinement of the precipitation to the austenite-ferrite phase boundries. Grain A was identified by selected area electron diffraction as ferrite, grains B and C were identified as austenitic. Microchemical analysis using a 200 keV JEOL scanning transmission microscope indicated the precipitate (carbide) to contain ≈65wt% chromium, ≈30wt% iron, and ≈2wt% nickel. Similar carbide precipitation occurred as a result of aging for less than 1 hour at 700°C (1292°F). With further aging at 600°C (1112°F) and 700°C (1292°F), carbide precipitation continued, accompanied by decomposition of the ferrite phase.

Decomposition of the ferrite phase occurred in samples aged for only 2 hours at 600°C (1112°F). As illustrated in the bright and dark field transmission electron micrographs in Figure 6-33, decomposition of the ferrite phase began as austenite extending into the ferrite region. As indicated in Figure 6-34, a region of columnar $M_{23}C_6$ + austenite was gradually formed. The cellular $\gamma + M_{23}C_6$ zone grew deeper into the ferrite phase with continued aging. Eventually, the cellular zone ended and the ferrite decomposed into single phase austenite then into sigma phase and finally into a duplex austenite-plus-ferrite region as shown in Figure 6-35.

6.3.3.2 Intergranular Corrosion

The influence of aging treatment on the intergranular corrosion behavior in A262E of Heat L-B7 has previously been illustrated in Figures 6-5 through 6-9. As noted in Section 3.3, the results obtained for the fully austenitic material produced by annealing at 1200°C (2192°F) for 1 hour and presented in Figure 6-5 are similar to those obtained on other austenitic grades of stainless steel such as Type-304. The 10 and 20 vol % duplex alloys, however, exhibited a much smaller zone of susceptibility to intergranular corrosion. The 10 and 20 vol % ferrite alloys developed a sensitized microstructure within ~1/2 hour at 600°C (1112°F) and within ~5 hours at 550°C (1022°F). Significant susceptibility to intergranular corrosion in the austenitic alloy required at least 5 hours at 600°C (1112°F). Immunity to intergranular

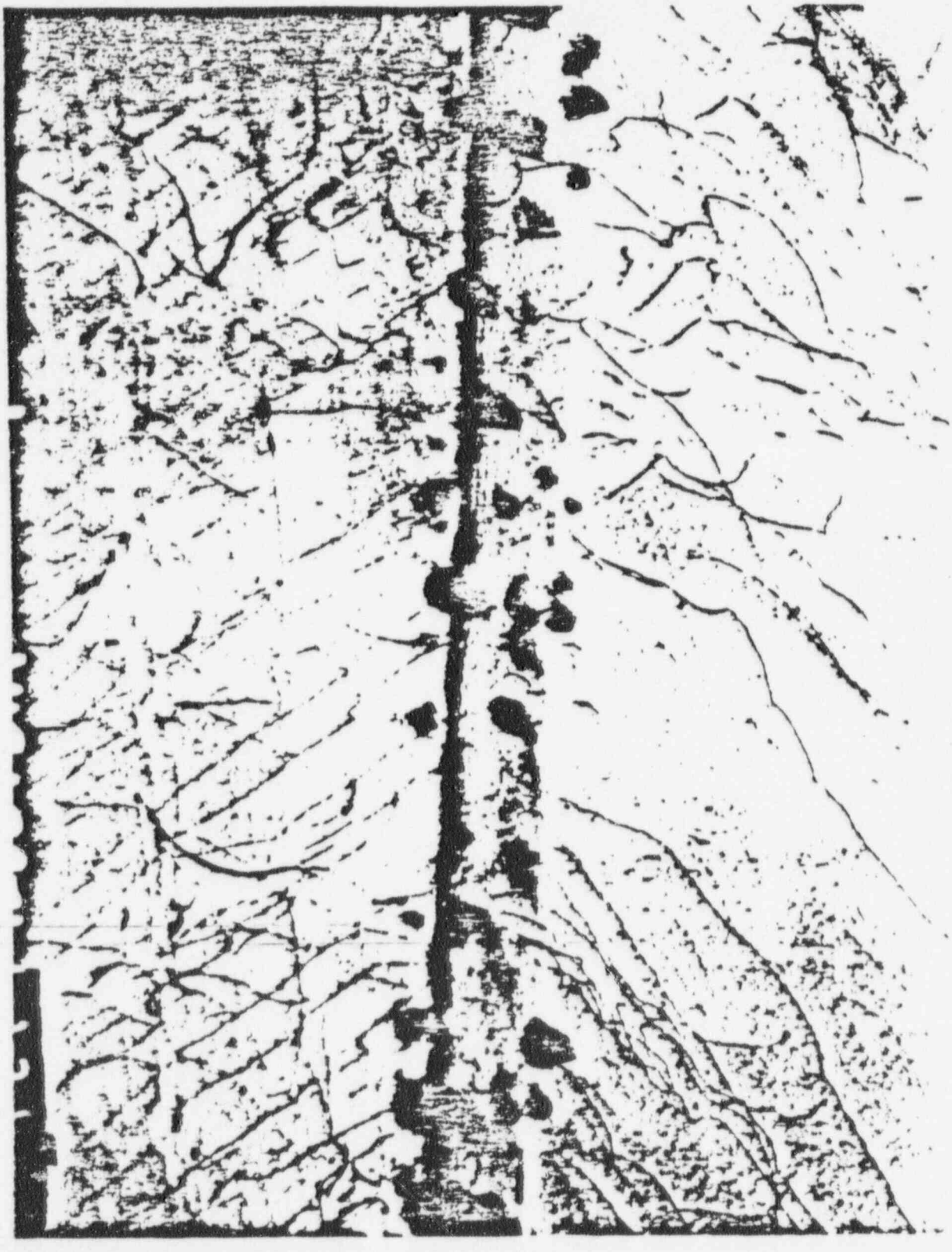

Figure 6-30. Transmission Electron Micrograph of Type-308 Stainless Steel Heat Treated at 1200°C (2192°F)/1 h, Water Quenched + 600°C (1112°F)/20 h, Water Quenched 75,000X

Figure 6-31. Transmission Electron Micrograph of Type-308 Stainless Steel Heat Treated at 1350°C (2462°F)/1 h, Water Quenched + 480°C (896°F)/100 h, Water Quenched 90,000X

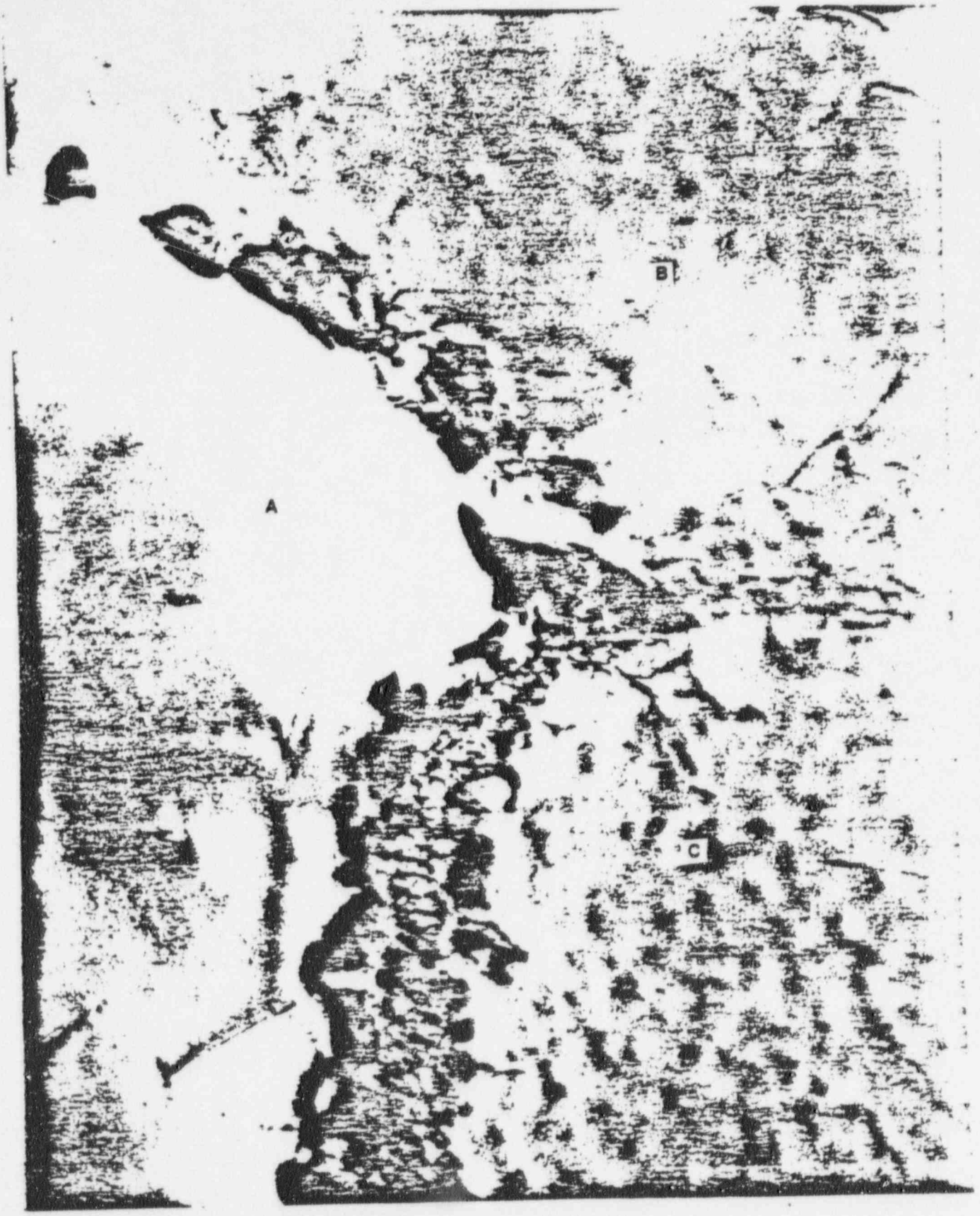

Figure 6-32. Transmission Electron Micrograph of Type-308 Stainless Steel Heat Treated at 1350°C (2462°F)/1 h, Water Quenched + 600°C (1112°F)/1 h, Water Quenched 110,000X

Figure 6-33a. Light Field Transmission Electron Image of Type-308 Stainless Steel Heat Treated at 1350°C (2462°F)/1 h, Water Quenched + 600°C (1112°F)/4 h, Water Quenched 60,000X

Figure 6-33b. Dark Field Transmission Electron Image of Type-308 Stainless Steel Heat Treated at 1350°C (2462°F)/1 h, Water Quenched + 600°C (1112°F)/4 h, Water Quenched 60,000X

Figure 6-34a. Transmission Electron Micrograph of Type-308 Stainless Steel Heat Treated at 1350°C (2462°F)/1 h, Water Quenched + 700°C (1292°F)/1 h, Water Quenched 25,000X

Figure 6-34b. Transmission Electron Micrograph of Type-308 Stainless Steel Heat Treated at 1350°C (2462°F)/1 h, Water Quenched + 700°C (1292°F)/1 h, Water Quenched 25,000X

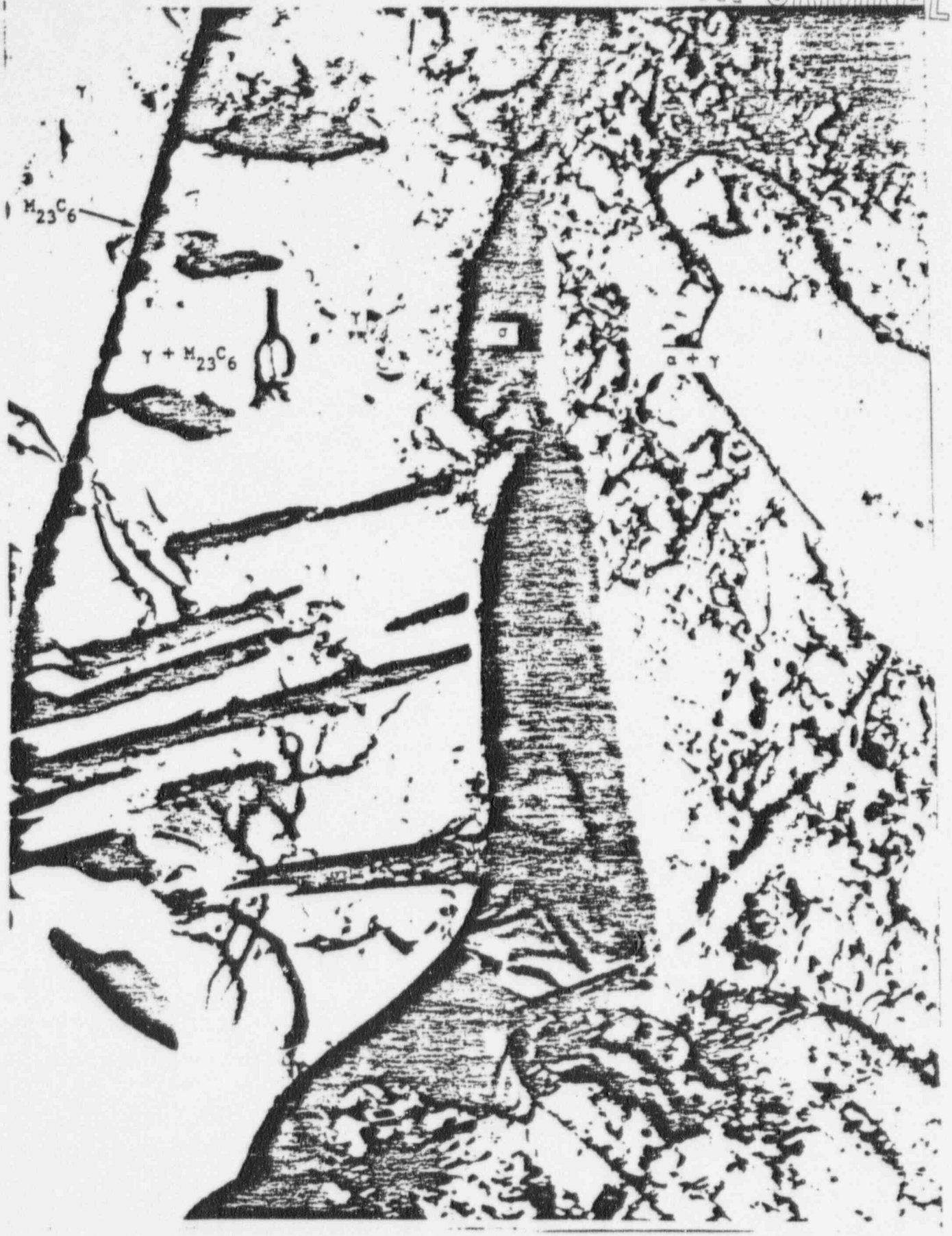

Figure 6-35. Transmission Electron Micrograph of Type-308 Stainless Steel Heat Treated at 1350°C (2462°F)/1 h, Water Quenched + 700°C (1292°F)/100 h, Water Quenched

corrosion was restored in the 10 and 20 vol % ferrite alloys after ~8 hours at 600°C (1112°F) and ~150 hours at 550°C (1022°F). Aging the austenitic material up to 600 hours at 600°C (1112°F) still produced a fully sensitized microstructure. Since no intergranular corrosion occurred along the austenite-austenite grain boundaries in the 10 and 20 vol % ferrite alloys sensitized at 600°C (1112°F), the fracture surfaces resulting from bending of corroded samples have two distinct features. As previously noted in Figure 6-11, the fracture surface for the 10 vol % ferrite specimen aged for 1 hour at 600°C (1112°F) has areas of grain boundary fracture caused by localized corrosion of austenite-ferrite boundaries. Areas of ductile cracking result from transgranular fracture of austenite grains during the bending.

Figure 6-36 illustrates the fracture surface of the specimen annealed at 1300°C (2372°F) for 1 hour and aged at 600°C (1112°F) for 5 hours. Again, areas of grain boundary fracture and transgranular cracking can be seen. An additional feature is also apparent on this fracture surface — the rumpled appearance of the ferrite grains caused by the localized corrosion attack of the $\gamma + M_{23}C_6$ cellular zone. Corrosion attack in the A262E test propagated along the original austenite-ferrite boundary as indicated by the smooth, faceted appearance of the austenite grains on the fracture surface in Figure 6-36. This localized attack separated the austenite grains from the $\gamma + M_{23}C_6$ cellular zone. Simultaneously the austenite within the $\gamma + M_{23}C_6$ cellular region was preferentially attacked, causing the irregular surface appearance of the ferrite grains on the fracture surface. Aging at 600°C (1112°F) for times longer than 6 hours results in immunity to intergranular corrosion. Nevertheless, localized corrosion attack continues in selected areas of the microstructure. This is illustrated in Figure 6-37 which is a scanning electron micrograph of a specimen aged at 600°C (1112°F) for 50 hours and then tested in A262E. The columnar $\gamma + M_{23}C_6$ zone at the original austenite-ferrite interface as well as the austenite formed within the ferrite phase have been preferentially corroded. The penetration of corrosion down the columnar $\gamma + M_{23}C_6$ zone is less than 1 grain diameter.

One rather interesting microstructural characteristic of the aged duplex samples was that carbide precipitation occurred along only 50% of the austenite-ferrite boundaries. In addition to the ferrite regions which appeared along austenite grain boundaries, there were also ferrite regions within austenite grains. These ferrite regions were twinlike in appearance as shown in Figure 6-1. There were no instances of carbide precipitation along these austenite-ferrite boundaries.

As indicated in Figures 6-8 and 6-9, the 10 and 20 vol % ferrite alloys were susceptible to intergranular corrosion at 550°C (1022°F) as well as 600°C (1112°F). In fact, the grain boundary penetration rate in the duplex alloys sensitized at 550°C (1022°F) was much greater than at 600°C (1112°F). Similarly, the duplex alloys sensitized at 550°C (1022°F) were much more susceptible to intergranular stress corrosion cracking in high-purity water with 8 ppm dissolved oxygen at 288°C (550°F) than when sensitized at 600°C (1112°F). As shown in Table 6-5, the 10 and 20 vol % ferrite alloys sensitized at 600°C (1112°F) would not fail CERT unless first precorroded in A262E. Duplicate smooth-bar samples (Table 6-5) of 10 vol % ferrite material aged at 550°C (1022°F) for 24 hours and tested at 288°C (550°F) in high-purity water with 8 ppm dissolved oxygen at nominal strain rates of 1, 2, and 3×10^{-6} min^{-1} failed by intergranular stress corrosion cracking without any pre-A262E treatment.

Aging the duplex material for up to 1000 hours at 480°C (896°F) did not result in any intergranular corrosion attack in A262E. Nevertheless, aging for as little as 100 hours at 480°C (896°F) did result in intense uniform attack of the ferrite grains themselves. Entire grains of ferrite in specimens aged at 480°C (896°F) for 100 hours were completely dissolved during A262E testing. Nevertheless, as indicated in Table 6-4, samples of the 20 vol % ferrite alloy aged for up to 1000 hours at 480°C (896°F) still exhibited ductile, transgranular cracking in CERT. Similarly, samples of the 10 and 20 vol % ferrite alloys aged for 100 hours at 600°C (1112°F) to introduce σ phase into the microstructure exhibited ductile, transgranular cracking in CERT.

6.3.4 Discussion

6.3.4.1 Physical Metallurgy

From the high-temperature annealing experiments it is clear that the equilibrium structure of the matrix phase of Type-308 stainless steel is austenitic below 1200°C (2192°F). At higher temperatures, increasing amounts of ferrite are stable. From available phase diagrams, the equilibrium structure of Type-308 stainless steel at 600-700°C (1112-1292°F) is $\gamma + M_{23}C_6$. Consequently, if the duplex structures were aged for sufficiently long periods at these

Figure 6-36a. Fracture Surface of Type-308 Stainless Steel Heat Treated at 1300°C (2372°F)/1 h, Water Quenched + 600°C (1112°F)/5 h, Water Quenched, and Immersed in A262E for 72 h 2000X

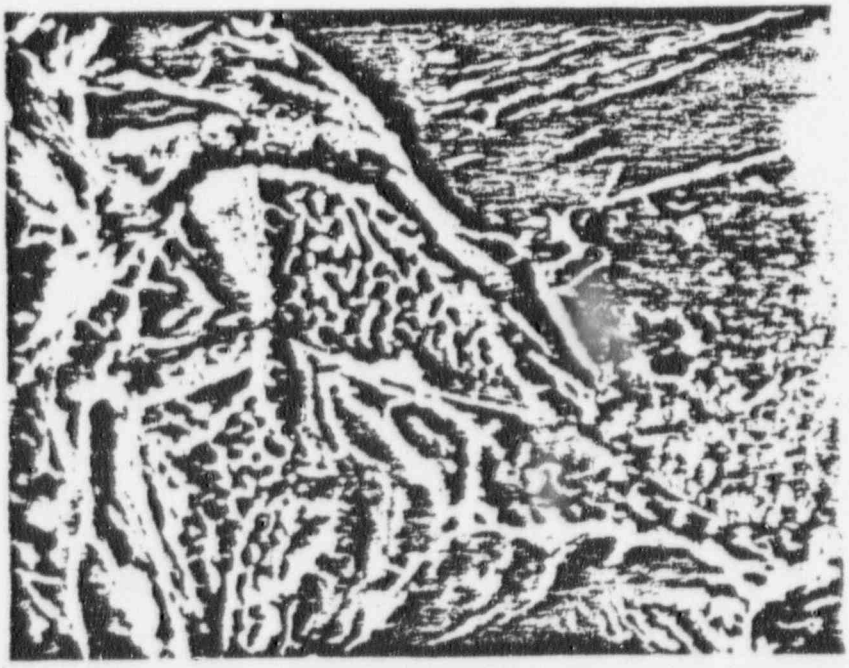

Figure 6-36b. Fracture Surface of Type-308 Stainless Steel Heat Treated at 1300°C (2372°F)/1 h, Water Quenched + 600°C (1112°F)/5 h, Water Quenched, and Immersed in A262E for 72 h 3000X

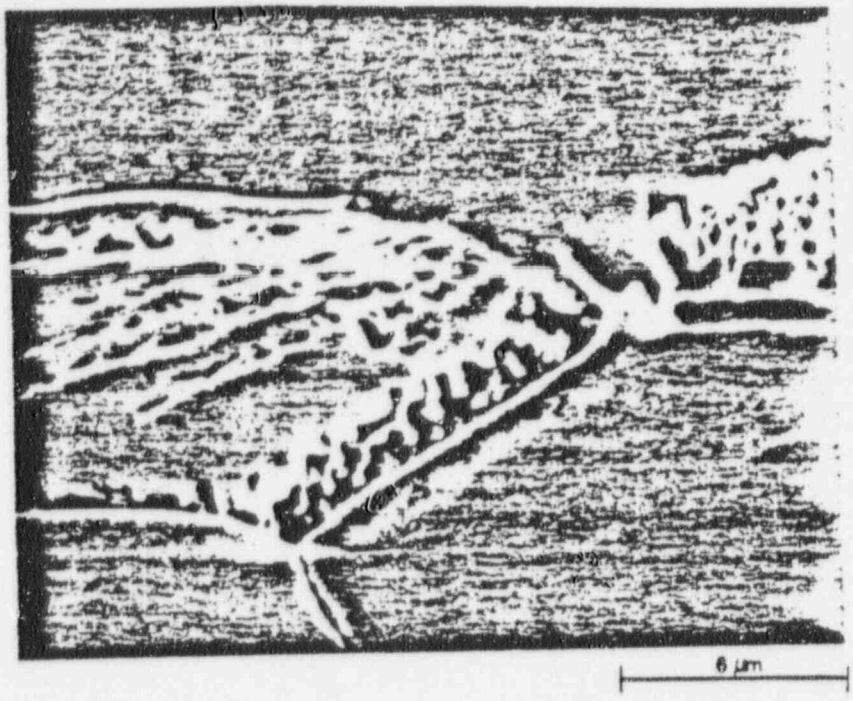

Figure 6-37. Scanning Electron Micrograph of Surface of Type-308 Stainless Steel Heat Treated at 1350°C (2462°F)/1 h, Water Quenched + 600°C (1112°F)/50 h, Water Quenched, and then Tested in A262E

temperatures, they would eventually transform into the equilibrium $\gamma + M_{23}C_6$ structure. The composition of the ferrite phase obtained from microprobe measurements is such that its equilibrium structure at 600°C (1112°F) consists of α, γ, $M_{23}C_6$, and σ as shown in the phase diagram in Figure 6-38. Although the bulk alloy composition dictates an equilibrium structure of $\gamma + M_{23}C_6$, the ferrite phase first decomposes to a metastable structure of α, γ, $M_{23}C_6$, and σ.

The decomposition of the ferrite phase is accelerated by its chromium depletion caused by the early precipitation of $M_{23}C_6$ along the austenite-ferrite boundaries. In the 10 and 20 vol % ferrite duplex stainless steel, $M_{23}C_6$ precipitation occurs exclusively along the austenite-ferrite boundaries. The austenite-austenite grain boundaries were free of $M_{23}C_6$ precipitation. This results because chromium diffusion is the rate-controlling step in the precipitation reaction. Since the diffusivity of chromium in the ferrite phase is approximately 1000 times greater than in the austenite at 600°C (1112°F), $M_{23}C_6$ forms first along austenite-ferrite boundaries (there are no ferrite-ferrite boundaries as each ferrite region is a single grain) probably by both chromium and carbon diffusing from the ferrite. The available carbon content of the ferrite is quickly exhausted and subsequent carbon comes almost exclusively from the austenite. This depletes the austenite of carbon. The feasibility of carbon depletion of the austenite is demonstrated by the fact that carbon in austenite at 600°C (1112°F) has a characteristic 1.2 h diffusion distance of 35μm, which is the average grain size. Thus, the austenite-austenite grain boundaries are free of $M_{23}C_6$ precipitation. The chromium and iron in the $M_{23}C_6$ precipitate are supplied principally by the ferrite phase. The decomposition of the ferrite phase initiates at the $\gamma - M_{23}C_6 - \alpha$ interface since this ferrite is the most unstable because of its low chromium content as it lies in the chromium-depleted zone produced by the $M_{23}C_6$ precipitate. The α decomposes to cellular $M_{23}C_6 + \gamma$. This is because chromium diffusion (probably in the austenite phase) is the rate-determining step in the transformation. Consequently, the overall reaction rate is speeded up by shortening the chromium diffusion distance and enhancing boundary diffusion. This is achieved by cellular precipitation of the $M_{23}C_6$ and austenite. From the phase diagram in Figure 6-38, we can estimate the maximum chromium content of the austenite phase in the cellular $\gamma + M_{23}C_6$ product to be approximately 14 wt% chromium. This is the chromium content of the austenite phase in the three phase $\gamma + \alpha + \sigma$ region of the Fe-Ni-Cr ternary diagram at 600°C (1112°F) depicted in Figure 6-38. It should also be the maximum amount of chromium which can be dissolved in the austenite phase in the three phase $\alpha + \gamma + M_{23}C_6$ region of the Fe-Cr-Ni-C quarternary since the solubility of carbon in γ is so low at 600°C (1112°F). Consequently, the austenite phase in the $\gamma + M_{23}C_6$ cellular product has a rather low chromium content.

The initial decomposition of the ferrite phase into cellular $\gamma + M_{23}C_6$ is halted when the available carbon content of the ferrite phase is exhausted. Subsequent decomposition of the ferrite phase occurs by direct transformation into austenite. The latter transformation occurs with a significant amount of chromium rejection into the remaining untransformed ferrite so that an abrupt dropoff in chromium concentration occurs at the ferrite-austenite interface. The chromium-enriched ferrite phase at the austenite-ferrite interface then transforms to σ, containing approximately 40 wt% chromium and 4 wt% nickel. The remaining ferrite phase transforms to duplex $\alpha + \gamma$. From the Fe-Ni-Cr ternary diagram in Figure 6-38, this γ phase contains, at most, 14 wt% chromium.

The lack of carbide precipitation along many of the austenite-ferrite boundaries in the duplex material is quite interesting. The fact that carbide precipitation was never observed along the austenite-ferrite interface formed between the austenite matrix and the intergranular, twinlike ferrite regions leads one to speculate that all austenite-ferrite boundaries which are free of carbide precipitation are low-energy boundaries. If indeed carbide precipitation is confined to high-energy austenite-ferrite boundaries, then one explanation for the phenomenon would be that nucleation occurs along high-energy boundaries so as to minimize strain-energy in the lattice and/or precipitate.

At 480°C (896°F) chromium has insufficient mobility for $M_{23}C_6$ to form. Instead, aging at 480°C (896°F) results in the ferrite phase transforming to a metastable structure of $\alpha + \alpha'$. The latter, a chromium-rich body centered cubic phase which is responsible for the embrittlement of ferritic stainless steels aged at this temperature, may form by either a nucleation and growth process or by spinodal decomposition. From the transmission electron microscopy, the α' precipitates appear to be approximately 30 Å in diameter and spaced approximately 50 Å apart. No effort was made in this program to determine the composition of α'. Other investigators have estimated the composition of α' to be around 70% chromium.[5]

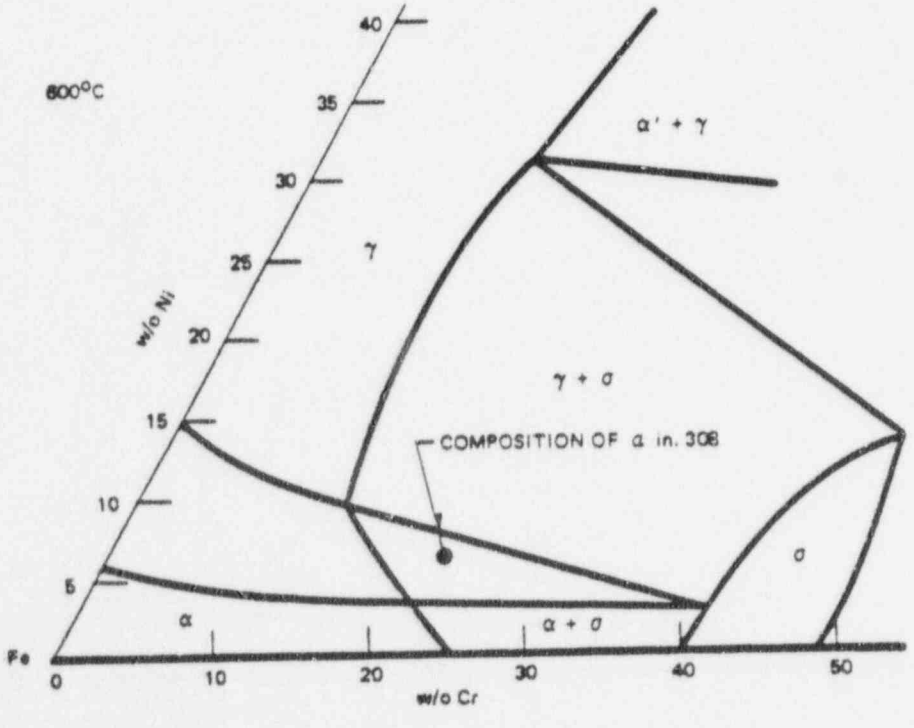

Figure 6-38. Fe-Ni-Cr Ternary at 600°C Showing Composition of α Phase

90014252

6.3.4.2 Intergranular Corrosion

The A262E results obtained on the all-austenitic Type-308 stainless steel are quite consistent with those results reported for other grades of austenitic stainless steel such as Type-304. The cause of intergranular corrosion is no doubt the same as that in Type-304, namely, the presence of chromium-depleted zones lying along grain boundaries caused by the intergranular precipitation of $M_{23}C_6$. This is consistent with the transmission electron microscopy results which indicated a one-to-one correspondence between the presence of intergranular precipitation and intergranular corrosion susceptibility.

Observing the effect of heat treatment on the intergranular corrosion resistance in A262E of the 10 and 20 vol % ferrite containing duplex material produced by heat treating at 1300°C (2372°F) for 1 hour and 1350°C (2462°F) for 1 hour and water quenching, respectively, there are three principal questions to be answered. First, why does sensitization occur so readily during short-time anneals at low temperatures, e.g., 600°C (1112°F) 1/2 hour. Second, why does intergranular corrosion occur exclusively along austenite-ferrite boundaries. And third, what mechanism is responsible for the immunity of duplex stainless steel to intergranular corrosion following longer time aging at 600°C (1112°F), i.e., more than 6 hours?

As discussed in the Physical Metallurgy Section, $M_{23}C_6$ precipitation occurs exclusively along the $\alpha-\gamma$ boundaries in the 10 and 20 vol % ferrite duplex stainless steels. Since the austenite-austenite grain boundaries are free of $M_{23}C_6$ precipitates and their accompanying chromium-depleted zones, the austenite-austenite grain boundaries are immune to intergranular corrosion. Although the chromium in the $M_{23}C_6$ precipitates is supplied principally by the ferrite phase, a small but significant amount of chromium is contributed by the austenite phase. In fact, the small amount of chromium contibuted by the austenite phase creates a small (in width) chromium-depleted zone in the austenite at the original austenite-ferrite interface. Although the chromium-depleted zone in the austenite phase is very narrow, the amount of chromium in the austenite at the austenite-$M_{23}C_6$ interface is less than that in the ferrite at the ferrite-$M_{23}C_6$ interface and it is the narrow chromium-depleted zone in the austenite phase that causes intergranular corrosion along the austenite-ferrite boundaries in A262E. This is indicated by the pitting corrosion experiments in which pits always initiated in the austenite at the austenite-ferrite interface in material which was susceptible to intergranular corrosion. That the pits initiated on the austenite side of the interface indicates that this region possessed the lowest chromium content.

The aging times at 600 and 700°C (1112 and 1292°F) which result in the decomposition of the ferrite phase into cellular $\gamma + M_{23}C_6$ nearly coincide with the aging treatments which confer immunity to intergranular corrosion on the alloy. However, the separation of the $M_{23}C_6$ carbides from the $\alpha-\gamma$ interface which occurs during the decomposition of the ferrite phase is not responsible for the immunity of the alloy to intergranular corrosion. Indeed, the decomposition of the ferrite into cellular $\gamma + M_{23}C_6$ occurs after aging at 600°C (1112°F) for times greater than 4 hours while intergranular corrosion attack continues with aging times up to 6 hours. The smooth, featureless appearance of the austenite grains on the fracture surface of the specimen aged at 600°C (1112°F) for 6 hours indicate that the corrosion attack, even in the samples in which the ferrite has begun to decompose, occurs within the austenite phase along the original austenite-ferite interface. Were the corrosion attack occurring along the cellular $\gamma + M_{23}C_6/\alpha$ interface, for example, the austenite grain boundary surface would not be smooth but would show some indication of the presence of the cellular $\gamma + M_{23}C_6$. The ferrite grain boundary surface is highly rumpled because of the localized corrosion attack of the austenite phase in the cellular $\gamma + M_{23}C_6$ zone. The latter occurs because of the low chromium content of the austenite phase ($\lesssim$14% Cr from above calculation) in the cellular $\gamma + M_{23}C_6$. Immunity to the intergranular corrosion occurs when the small chromium-depleted zone in the austenite phase at the original austenite-ferrite interface is replenished with a critical amount of chromium required to restore the corrosion resistance of the area. This healing of the chromium depleted zone in such a short time ($\approx$7 hours) is made possible by virtue of the unusually small width of the zone. The zone is narrow because the carbon content of the austenite phase was exhausted before sufficient time was permitted for chromium diffusion in the austenite phase to result in any significant loss of chromium. The bulk of the carbon was tied up as $M_{23}C_6$ by chromium supplied from the ferrite phase. Only a small amount of chromium from the austenite reacted with carbon to form $M_{23}C_6$. Consequently, it was relatively easy for subsequent chromium diffusion in the austenite to replenish the small austenite chromium-depleted zone. It is worth emphasizing that the small austenitic chromium-depleted zone was healed by chromium coming from the interior of the austenite grain and not by chromium coming from the decomposing chromium-rich ferrite phase. The latter is true

since pit initiation studies on material heat-treated for times longer than 6 hours at 600°C (1112°F) revealed that pits initiated preferentially in the austenite phase in the cellular $\gamma + M_{23}C_6$ zone. If healing was accomplished by chromium coming from the ferrite phase, such chromium would first heal the low-chromium austenite in the cellular $\gamma + M_{23}C_6$ zone.

The same mechanism can explain the intergranular corrosion behavior of duplex Type-308 stainless steel at 550°C (1022°F) at 600°C (1112°F). Because the kinetics are slower at 550°C (1022°F) as at 600°C (1112°F) and because the chromium depletion is more severe at 550°C (1022°F) than at 600°C (1112°F), the time to start sensitization and the time to produce healing are longer at 550°C (1022°F) than at 600°C (1112°F). The chromium depletion is more severe at 550°C (1022°F) than at 600°C (1112°F) because of the temperature dependencies of the chromium and carbon activities as well as of the equilibrium coefficient for $M_{23}C_6$. The more severe chromium depletion at 550°C (1022°F) is the cause of the more rapid grain boundary penetration in A262E of alloys sensitized at 550°C (1022°F) relative to those sensitized at 600°C (1112°F). The chromium depletion in alloys sensitized at 600°C (1112°F) is not sufficient to cause initiation of intergranular stress corrosion cracking in CERT. However, it is sufficient to propagate intergranular cracks initiated by prior exposure in A262E. The chromium depletion in alloys sensitized at 550°C (1022°F) is sufficient to both initiate and propagate intergranular stress corrosion cracking in CERT.

The 4 vol % ferrite duplex Type-308 stainless steel exhibited essentially the same intergranular corrosion behavior as the all-austenitic material. There was insufficient austenite-ferrite boundary area to tie up all of the available carbon as $M_{23}C_6$ along austenite-ferrite boundaries. Intergranular carbide precipitation occurred along austenite-austenite grain boundaries which resulted in chromium depletion and susceptibility of these boundaries to localized attack in A262E. This result emphasizes the need for a critical amount and distribution of ferrite throughout the austenite matrix in order that the carbon in the austenite be within easy access of an $\alpha-\gamma$ boundary so that the carbon supply of the austenite can be quickly exhausted by reacting with chromium and iron in the ferrite to form $M_{23}C_6$ along $\alpha-\gamma$ boundaries.

The accelerated, uniform dissolution of the ferrite phase, which occurs in duplex samples heat treated for 100 or more hours at 480°C (896°F) and immersed in A262E, is the result of α' precipitation. The formation of this chromium-rich precipitate results in chromium depletion of the matrix. Sufficient chromium depletion has occurred to prevent passivation in the A262E test solution. It is interesting to note that the formation of α' did not result in enhanced susceptibility to pitting corrosion as samples heat treated at 480°C (896°F) were as resistant to pitting attack as the fully annealed specimens. Apparently, chromium depletion has a greater effect on passivation tendencies (as is measured in A262E) than on passivation breakdown (as is measured by pitting tests).

6.3.4.3 Pitting Corrosion

Previous investigators have demonstrated the enhanced pitting corrosion resistance accompanying increased chromium additions to ferrous base alloys. Consequently, lowering the chromium content in an area by, for example, a phase transformation should increase the pitting susceptibility of that region. In fact, Rarey and Aronson[6] have already demonstrated the enhanced pitting susceptibility of a ferritic stainless steel following the formation of chromium depleted zones adjacent to carbide precipitates. Given the phase transformations which occur in austenitic and duplex Type-308 stainless steel during aging at 480–700°C (896–1292°F), marked changes in pitting resistance should result from such heat treatments. And, in fact, this is what the pitting potential and pit initiation results reported in this study have shown.

The galvanostatic pit initiation tests were by far the most sensitive to aging treatments. Both the site of pitting and the pit initiation rate varied strongly with the aging temperature and time. While a significant difference existed between the pitting potentials of the annealed and aged materials and between the pitting potentials of samples aged at different temperatures, there was little effect of aging time on the pitting potential. Furthermore, the large scatter in the measured values of the pitting potential of the as-annealed material requires that many measurements of the pitting potential be made to confirm the presence of a sensitized microstructure.

The poor reproducibility in the pitting potentials measured for the as-annealed conditions probably results from the lack of reproducibility in the pit initiation site. Pitting probably initiates in the as-annealed material at highly soluble inclusions such as manganese sulfides as was shown by Eklund for Type-316 stainless steel.[7] The inclusions dissolve out and the aggressive solution produced, which now fills the void once occupied by the inclusion, results in propagation of the corrosion attack into the metal matrix. Samples in which pitting did not occur during anodic polarization was probably free of such inclusions. The lack of reproducibility in the size and shape of such inclusions probably contributes to the scatter in the pitting potentials.

In the as-annealed duplex material, pits appear to initiate preferentially in the ferrite at the austenite-ferrite interface. This may be the result of a high concentration of sulfur at the interface or a high density of sulfides along the interface. This results from the sulfur preferentially partitioning into the ferrite phase during the high-temperature anneal due to the lower activity coefficient of sulfur in ferrite than in austenite [activity coefficient of sulfur in austenite is four times that in ferrite at 1365°C (2489°F)].[8] During quenching, sulfur in the ferrite phase segregates to the austenite-ferrite interface or sulfides precipitate out of the supersaturated ferrite phase along the austenite-ferrite boundary.

Aging austenitic and duplex specimens of Type-308 stainless steel at 600 and 700°C (1112 and 1292°F) resulted in a marked decrease in the scatter of the measured values of the pitting potential as well as a decrease in its numerical value. In addition, the pit density was orders of magnitude greater in aged samples than in as-annealed samples. In fact, by far the most dramatic influence of aging treatment on the pitting behavior was the drastic increase in pit density as a result of aging. The influence of aging treatment on pit density was more closely examined by means of the galvanostatic pit test.

Streicher[9] has shown that the number of pits is not a function of the potential of the sample but rather is a function of the corrosion current density. The relative pit initiation rates of different materials, therefore, can be determined by galvanostatically corroding samples at a relatively high anodic current density for a specified length of time. As in the anodic polarization test, a dramatic increase in pit density was observed in the galvanostatic pit test as a result of aging. The galvanostatic pitting test was evidently a less aggressive test than the anodic polarization test. In the former, pitting never occurred in as-annealed samples whereas pits usually formed during the latter test, albeit only a very low pit density was exhibited.

Aging the all-austenitic Type-308 stainless steel at 600°C (1112°F) for 1 hour did not result in any increase in pitting susceptibility. No pitting occurred during the galvanostatic corrosion test. This behavior was exactly the same as that of the as-annealed material. This is similar to the pitting potential measurements in which the behavior of the as-annealed material and that aged for 1 hour at 600°C (1112°F) was the same, relatively high values of pitting potential, relatively large scatter in the measured values of the pitting potential, and very low pit density following anodic polarization. These results are consistent with the transmission electron microscopy which revealed no intergranular precipitation and with the A262E findings which indicated heat treating for 1 hour at 600°C (1112°F) did not cause intergranular corrosion.

Increasing the aging time at 600°C (1112°F) to 20 hours dramatically increased the pit initiation rate to ~10^4 pits/cm^2 as measured by the galvanostatic pit corrosion test. By interrupting the applied current immediately after pitting began the first pits were seen to initiate in the grain boundaries. Undoubtedly these pits were forming in the chromium-depleted zones adjacent to the intergranular precipitates of $M_{23}C_6$. Similar behavior was observed for the samples aged for 100 hours at 600°C (1112°F) and for samples aged even for as little as 1 hour at 700°C (1292°F). The pits propagated rapidly down the chromium-depleted grain boundaries resulting in grain dropping as shown in Figure 6-22. These results are again consistent with the A262E results which indicated aging at 600°C (1112°F) for 20 hours or longer and at 700°C (1292°F) for more than 1 hour resulted in severe intergranular corrosion attack. Several points are of interest in the pitting potentials measured on samples aged for any time at 700°C (1292°F) and for 20 or more hours at 600°C (1112°F). First, the amount of scatter in the pitting potentials measured for these aged conditions is much less than that obtained for the as-annealed condition. Second, the value of the pitting potential is lower for these aged conditions than for the as-annealed condition. And, finally, the pitting potential of material aged at 700°C (1292°F) is greater than that of material aged at 600°C (1112°F). Since the pitting potential is a measure of the resistance of the passive film to initiation of breakdown, the lower pitting potential resulting from aging is due to the

chromium-depleted zones formed adjacent to the intergranular carbides which are more susceptible to pitting than is the matrix. The latter, in fact, is presumably strongly resistant to pitting with pits actually forming at inclusions and then growing (by a crevice corrosion type mechanism) into the matrix. The pitting potentials of the aged conditions are more reproducible than those for the as-annealed conditions because the pit initiation site of the aged material, namely, the chromium-depleted zone, is a more reproducible defect than the pit initiation site of the as-annealed material. That the pitting potentials measured on samples aged at 700°C (1292°F) are greater than those measured for samples aged for 20 or more hours at 600°C (1112°F) is as predicted from thermodynamic considerations.[16] Due to the temperature dependencies of the carbon and chromium activities as well as for the equilibrium constant for the formation of $M_{23}C_6$, the chromium content in the matrix at the precipitate matrix interface is lower during precipitation at 600°C (1112°F) than at 700°C (1292°F). The lower chromium content results in greater pitting susceptibility and a lower pitting potential.

As the aging time at 600°C (1112°F) increased from 30 minutes to 10 hours the narrow chromium-depleted zone in the austenite at the austenite-ferrite interface in the 10 and 20 vol % ferrite alloys was replenished with chromium and the site of pit initiation shifted to the austenite region within the two phase columnar $\gamma + M_{23}C_6$ zone. This austenite region is susceptible to pitting since its chromium level is less than 14 wt % as discussed in the previous section (Figure 6-22). With longer aging times the remaining ferrite phase began to transform to both σ phase and duplex austenite plus ferrite. Corresponding to this microstructural change, the pit initiation site shifted from the columnar $\gamma + M_{23}C_6$ zone to within the austenite phase in the duplex austenite plus ferrite region formed in the transformed ferrite.

The pitting potential of the 20 vol % ferrite duplex material increased by ≈90 mV as the aging time at 600°C (1112°F) increased from 20 to 50 hours. Other than this no changes in pitting potential of the duplex material were observed to accompany the major microstructural changes which were occurring. Consequently, the pitting potential is an inadequate parameter to study the microstructural changes which occur during aging at 600 and 700°C (1112 and 1292°F).

In addition to the pitting which occurred at the austenite-ferrite interface and within the transformed ferrite phase of aged samples, pits also initiated at austenite-austenite grain boundaries in the Type-308 stainless steel containing only 4 vol % ferrite. These pits apparently initiated in the chromium-depleted zones adjacent to $M_{23}C_6$ carbides which formed along austenite-austenite grain boundaries as well as along austenite-ferrite boundaries in the 4 vol % ferrite duplex material.

Annealing Type-308 stainless steel at temperatures greater than 1200°C (2192°F) results in the introduction of ferrite into the austenitic matrix. The amount of ferrite formed increases with the temperature. At 1350°C (2462°F) 15 vol % ferrite is formed. Below 1200°C (2192°F) the matrix structure is 100% austenitic. Annealing at 1200°C (2192°F) and water quenching produces a 100% austenitic structure supersaturated with carbon. Aging this material at an intermediate temperature of 600°C (1112°F) results in the intergranular precipitation of chromium-rich $M_{23}C_6$. A chromium-depleted zone is formed adjacent to the intergranular precipitate which results in susceptibility to intergranular corrosion attack in boiling acidified copper-copper sulfate solution (A262E) and grain boundary pitting in 0.1 N HCl.

Whereas $M_{23}C_6$ precipitation occurs intergranularly during aging of austenitic Type-308 stainless steel, $M_{23}C_6$ precipitation is exclusively confined to austenite-ferrite boundaries in duplex Type-308 stainless steel containing a critical amount and distribution of ferrite. In such structures, because most of the chromium in the carbide comes from the ferrite phase and only a very small amount comes from the austenite phase, a chromium-depleted zone is formed within the austenite phase at the austenite-carbide interface which is susceptible to localized corrosion attack but which is very narrow compared to that which exists in sensitized austenitic stainless steel. Continued aging for only 7 hours at 600°C (1112°F) replenishes the narrow chromium-depleted zone so that it is no longer susceptible to corrosion attack in the A262E test. Similar healing of the much wider chromium-depleted zone formed in fully austenitic Type-308 stainless steel does not occur even after 100 hours at 600°C (1112°F).

In addition to the precipitation of $M_{23}C_6$ along austenite-ferrite boundaries, aging at 600°C (1112°F) results in decomposition of the ferrite phase into cellular $\gamma + M_{23}C_6$, single-phase austenite, σ phase, and duplex austenite +

ferrite. The corrosion behavior of these new phases is consistent with their chemical compositions as estimated from phase diagrams.

When duplex Type-308 stainless steel is aged at 480°C (896°F) an extremely fine chromium-rich precipitate, α', forms throughout the ferrite. The chromium depletion of the ferrite phase resulting from the α' precipitation causes corrosion of the ferrite regions in A262E test.

Two major points are made by this research. First, the corrosion behavior of Type-308 duplex stainless steel is a very strong function of the microstructure. Second, the presence of a critical amount and distribution of ferrite will restrict the intergranular corrosion susceptibility of austenitic stainless steel.

6.4 SUBTASK 3 — EFFECT OF VOLUME PERCENT AND MORPHOLOGY OF FERRITE ON THE INTERGRANULAR STRESS CORROSION CRACKING BEHAVIOR OF TYPE-308 DUPLEX STAINLESS STEEL

6.4.1 Introduction

The mechanism of intergranular corrosion of duplex stainless steels proposed in the previous section states that the critical amount of ferrite required to impart a significant reduction in susceptibility to intergranular corrosion be expressed not in terms of the amount of ferrite present but rather in terms of the amount and distribution of austenite-ferrite boundary area. In this task the intergranular corrosion behavior of duplex Type-308 stainless steel with different ferrite morphologies is investigated in an attempt to determine the appropriate manner in which to express the critical amount and distribution of ferrite required to impart resistance to intergranular corrosion.

6.4.2 Procedure

In addition to the data already supplied by Heat L-B7 in Sections 6.2 and 6.3 of this report, three laboratory heats of Type-308 stainless steel whose compositions are listed in Table 6-7 were used to evaluate the effects of carbon content and aging treatment on the intergranular corrosion behavior of wrought Type-308 stainless steel. The three heats were cast as 30-lb tapered ingots, 7.6 × 5.7 × 27.9 cm (3 × 2-1/4 × 11 inches), hot forged at 1200°C (2192°F) to 3.8 × 6.35 cm (1-1/2 × 2-1/2 inches) rectangular cross section, hot rolled to 0.229 cm (0.090 inch) thickness at 1175°C (2149°F), and cold rolled to 0.127 cm (0.050 inch) thick sheet. The sheet was then annealed at 1100°C (2012°F), water quenched, and sheared into test coupons [17.8 × 1.27 cm (7 × 1/2 inch)]. Samples were electropolished in a solution of 60% H_3PO_4 + 40% H_2SO_4 at 40-60°C (104-140°F) using ~2 amps/cm² for 5 minutes. Following electropolishing, samples were ultrasonically cleaned in a detergent solution and then distilled water, dried, and encapsulated in quartz tubes which were first evacuated and then back-filled with 1/4 atmosphere of argon. Following heat treatment, specimens were water quenched by plunging the tubes into water and breaking them. The samples were then electropolished and cleaned as described above, wrapped in zirconium foil, encapsulated in evacuated quartz tubes, and aged at temperatures ranging from 480 to 700°C (896 to 1292°F) for times of 1/4 hour to 1000 hours. Following aging the samples were again electropolished and cleaned and tested for susceptibility to intergranular corrosion by immersing the samples wrapped in copper wire in acidified copper-copper sulfate solution for 72 hours. The latter was conducted according to ASTM specification A262E. Upon removal from the solution, the samples were bent open and examined with an optical microscope for evidence of intergranular corrosion.

Identical intergranular corrosion tests were conducted on Type-308 weld metal deposited onto fully annealed 1.27-cm-thick × 10.2-cm wide × 15.24-cm-long (1/2-in. × 4-in. × 6-in.) plate of Type-304L stainless steel containing 0.027% carbon. The compositions of the five stick electrodes and the uncoated wire are listed in Table 6-8. The TIG weld was deposited at a nominal rate of 12.7 cm/min (5 in./min) using 105 amps and 16 volts. The stick electrodes were manually deposited at a nominal rate of 15.8 cm/min (6 in./min) using 95 amps and 23 volts. Ferrite numbers were measured for each weld deposit using a Magne Gauge and the Draw File procedure recommended by the Welding Research Council.[11] The weld deposits were tested for intergranular corrosion resistance in both the as-welded and as-aged conditions. Prior to corrosion testing the welds were electropolished and cleaned as described above.

Table 6-7
COMPOSITION OF WROUGHT TYPE-308 STAINLESS STEEL HEATS

Heat	Cr	Ni	Mn	Si	S	P	C
292	20.5	10.0	1.7	0.5	0.02	0.02	0.025
293	20.5	10.0	1.7	0.5	0.02	0.02	0.038
294	20.5	10.0	1.7	0.5	0.02	0.02	0.055

Table 6-8
COMPOSITION OF TYPE-308 STAINLESS STEEL WELD DEPOSITS

Heat	Cr	Ni	Mn	Si	S	P	C
				Manual Metal Arc			
1N10B	18.92	10.30	1.71	0.32	0.018	0.020	0.056
5410	20.97	9.52	1.65	0.33	0.015	0.027	0.050
G6976	20.65	9.83	1.70	0.20	0.017	0.019	0.053
2E7L	20.23	9.32	1.69	0.31	0.019	0.015	0.044
2E11L	20.03	8.88	1.84	1.05	0.019	0.019	0.036
				Tungsten Inert Gas			
4S983	20.95	9.82	1.76	0.41	0.008	0.016	0.040

The amount of $\alpha-\gamma$ boundary area in each sample was measured metallographically by superposing a test grid on 250X-750X optical micrographs, measuring the number of intercepts of the test grid with $\alpha-\gamma$ boundaries and using the relationship

$$S_v^{\alpha-\gamma} = 2N_L^{\alpha-\gamma} \quad (6\text{-}1)$$

where $N_L^{\alpha-\gamma}$ = number of intercepts of a random test line with austenite-ferrite boundaries per unit length of test line,

and $S_v^{\alpha-\gamma}$ = amount of austenite-ferrite boundary area per unit volume of alloy.

6.4.3 Results

Table 6-9 summarizes the influence of annealing temperature and carbon content on the volume percent ferrite and the amount of austenite-ferrite boundary area in the three laboratory heats investigated. For each carbon content the amount of ferrite and the amount of austenite-ferrite boundary area increased with increasing annealing temperature. For each annealing temperature the amount of ferrite increased with decreasing carbon content.

Figures 6-39 through 6-42 summarize the effect of aging treatment on the intergranular corrosion behavior in A262E of the 0.055% C Type-308 stainless steel as a function of the amount of ferrite. The 2 vol % ferrite material produced by annealing for 1 hour at 1200°C (2192°F) behaved like a fully austenitic alloy. Sensitized microstructures developed after 1 hour at 600°C (1112°F) and ~10 hours at 550°C (1022°F). Healing effects were not observed within 100 hours at 600°C (1112°F) and 200 hours at 550°C (1022°F). Increasing the ferrite content to 4 vol % produced a sensitized microstructure sooner at each aging temperature. While healing was not observed within 200 hours at 550°C (1022°F), healing effects were exhibited within 100 hours at 600°C (1112°F). The 9 and 20 vol % ferrite alloys exhibited nearly the same aging behavior. In both alloys, sensitization began before 1/2 hour at 600°C (1112°F) and 1

hour at 550°C (1022°F). However, significant healing of sensitization occurred for both alloys within 8 hours at 600°C (1112°F) and 200 hours at 550°C (1022°F).

Figures 6-43 through 6-46 present the influence of aging treatment on the intergranular corrosion behavior in A262E of the 0.038% C Type-308 stainless steel as a function of the amount of ferrite. Even the 6 vol % ferrite material produced by annealing at 1200°C (2192°F) possessed sufficient ferrite to exhibit significant healing within 48 hours at 600°C (1112°F). Minor healing occurred within 200 hours at 550°C (1022°F) but the alloy remained quite susceptible to intergranular corrosion. Significant healing resulted in the 9 vol % ferrite alloy within 24 hours at 600°C (1112°F) and 200 hours at 550°C (1022°F). The 17 and 25 vol % ferrite alloys exhibited nearly identical behavior. Each alloy was sensitized before 1/2 hour at 600°C (1112°F) and before 1 hour at 550°C (1022°F). Each alloy exhibited significant healing within 24 hours at 600°C (1112°F) and 150 hours at 550°C (1022°F).

Finally, Figures 6-47 through 6-50 illustrate the influence of aging treatment on the intergranular corrosion behavior in A262E of the 0.025% C Type-308 stainless steel as a function of ferrite content. Regardless of annealing temperature, aging at 600°C (1112°F) did not result in significant sensitization. As the amount of ferrite increased, the time to develop a sensitized microstructure and to heal the same at 550°C (1022°F) decreased. Further, as the amount of ferrite increased, the intergranular corrosion attack became more severe.

Table 6-10 lists the ferrite number and amount of austenite-ferrite boundary area for each of the weld deposits. The effect of aging treatment on the intergranular corrosion behavior in A262E of each of these weld deposits is summarized in Figure 6-51. Two heats, IN10B and G6976, possessed insufficient ferrite to be able to undergo a healing phenomenon at 600°C (1112°F). Heat 2E7L exhibited a healing phenomenon in less than 96 hours at 600°C (1112°F). Heat 5410 exhibited a significant healing effect in less than 24 hours at 600°C (1112°F) and Heat 45983 was immune to intergranular corrosion after aging at 600°C (1112°F) and only slightly susceptible to intergranular attack following 24 and 96 hour ages at 550°C (1022°F).

Table 6-9
INFLUENCE OF ANNEALING TEMPERATURE AND CARBON CONTENT ON FERRITE CONTENT AND AUSTENITE-FERRITE BOUNDARY AREA

Heat	Heat Treatment	Ferrite (vol %)	N_L = One-Half Austenite-Ferrite Boundary Area Per Unit Volume (cm^{-1})
L-B7	1200°C/1	0	0
	1250°C/1	4	237
	1300°C/1	10	465
	1350°C/1	20	535
292	1200°C/1	14	350
	1250°C/1	17	355
	1300°C/1	21	428
	1350°C/1	31	433
293	1200°C/1	6	155
	1250°C/1	9	285
	1300°C/1	17	310
	1350°C/1	25	388
294	1200°C/1	2	123
	1250°C/1	4	153
	1300°C/1	9	255
	1350°C/1	20	410

90014259

Table 6-10
FERRITE NUMBER AND AUSTENITE-FERRITE BOUNDARY AREA OF WELD DEPOSITS

Heat	Heat Treatment	Ferrite No.	N_L = One-Half Austenite-Ferrite Boundary Area Per Unit Volume (cm^{-1})
1N10B	As Deposited	2.25	145
5410	As Deposited	4.50	476
G6976	As Deposited	2.95	279
2E7L	As Deposited	4.15	308
2E11L	As Deposited	5.14	1061
45983	As Deposited	8.28	1241

6.4.4 Discussion

The conclusion reached in Section 6.3 of this report states that the susceptibility of a duplex stainless steel to sensitization is a function of the amount and distribution of austenite-ferrite boundary area. The importance of the distribution of austenite-ferrite boundary area can be illustrated by considering the results obtained for the two wrought alloys, Heat L-B7/1250°C (2282°F)-1 hour which contained 0.040 carbon (Figure 7) and Heat 294/1250°C (2282°F)-1 hour (Figure 6-48), and the weld deposit Heat 5410 (Figure 6-51). All three had approximately 4 vol % ferrite. Since both Heat L-B7/1250°C (2282°F)-1 hour which contained 0.040% carbon and Heat 294/1250°C (2282°F)-1 hour which contained 0.055% carbon behaved like fully austenite stainless steel and did not show a healing phenomenon at 600°C (1112°F) or 550°C (1022°F), the weld deposit Heat 5410 which contained 0.050% carbon might also be expected to not show a healing phenomemon. However, the results indicate that this weld deposit does, in fact, exhibit a healing effect at 600°C (1112°F). As shown below, all of these results are completely consistent with a model which requires a critical amount and distribution of austenite-ferrite boundary area for resistance to intergranular corrosion.

There are two analytical approaches that can be taken to develop expressions for the required amount and distribution of austenite-ferrite boundary area. In the first, it is simply required that there be sufficient austenite-ferrite boundary area to accommodate the available carbon supply as a 1000-Å-thick carbide layer covering the austenite-ferrite boundaries. Earlier work indicated this to be the average carbide thickness along the austenite-ferrite boundaries following a 2-hour age at 600°C (1112°F).[12] The available carbon supply is defined as the carbon content of the austenite minus 0.015%. The latter is the maximum amount of carbon which a fully austenitic 19% chromium-10% nickel alloy can contain and not be susceptible to intergranular corrosion following isothermal aging treatments at 600°C (1112°F). Thus, the requirement is that there be sufficient $\alpha-\gamma$ boundary area to exhaust the carbon supply of the austenite to 0.015% within 2 hours at 600°C (1112°F). A 2-hour aging time was selected since intergranular precipitation of $M_{23}C_6$ will begin within 2 hours at 600°C (1112°F) in Type-304L austenitic stainless steel containing 0.017% carbon.[13] This leads to the following expression for the amount of austenite-ferrite boundary area as a function of carbon content of the alloy.

$$S_v^{\alpha-\gamma} = 2N_L^{\alpha-\gamma} = 7.13 \times 10^3 (\%\ C - 0.015) \qquad (6\text{-}2)$$

The second approach to developing an expression for the critical amount of austenite-ferrite boundary area is to require that the ferrite phase be distributed throughout the austenite phase in such a manner that each carbon atom within the austenite phase has easy access to an austenite-ferrite boundary. This is analogous to requiring that the mean free path of the austenite-phase is sufficient to deplete the carbon content of the austenite matrix to some low value $\bar{c}$ within a specified time t. We therefore equate the austenite mean free path length to a diffusion distance over which the average carbon content of the austenite phase is reduced to $\bar{c}$ in time t.

$$\lambda_\gamma = \frac{\pi^2\ Dt}{\ell n\ \frac{8}{\pi^2}\ \frac{Co}{\bar{c}}}^{1/2} \qquad (6\text{-}3)$$

90014260

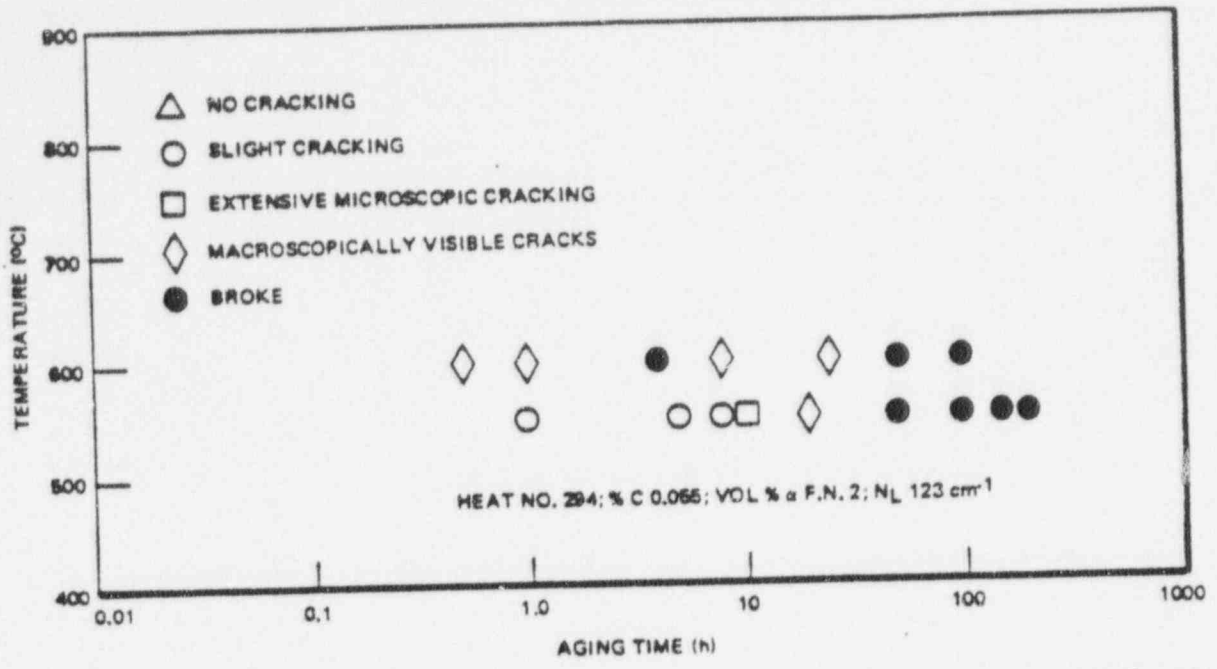

Figure 6-39. Influence of Aging Treatment on the Intergranular Corrosion Behavior of Type-308 Stainless Steel Containing 0.055% Carbon and 2 vol % Ferrite

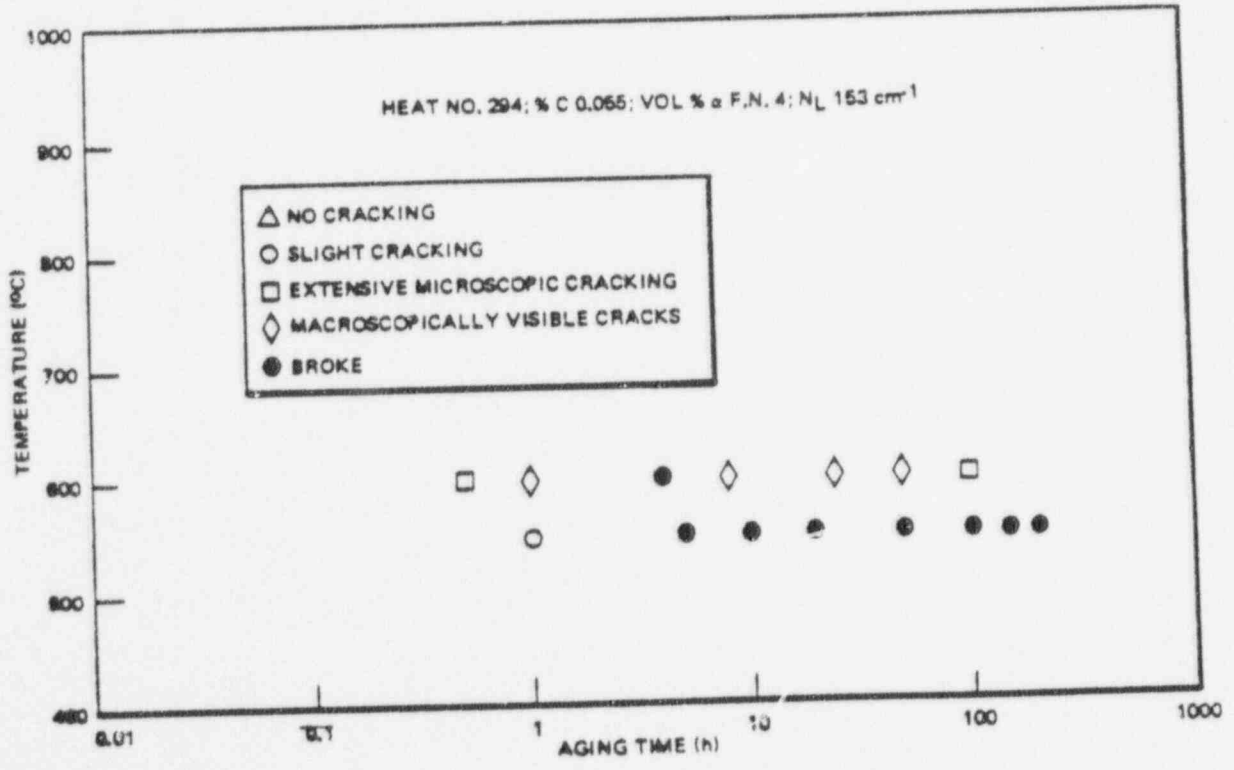

Figure 6-40. Influence of Aging Treatment on the Intergranular Corrosion Behavior of Type-308 Stainless Steel Containing 0.055% Carbon and 4 vol % Ferrite

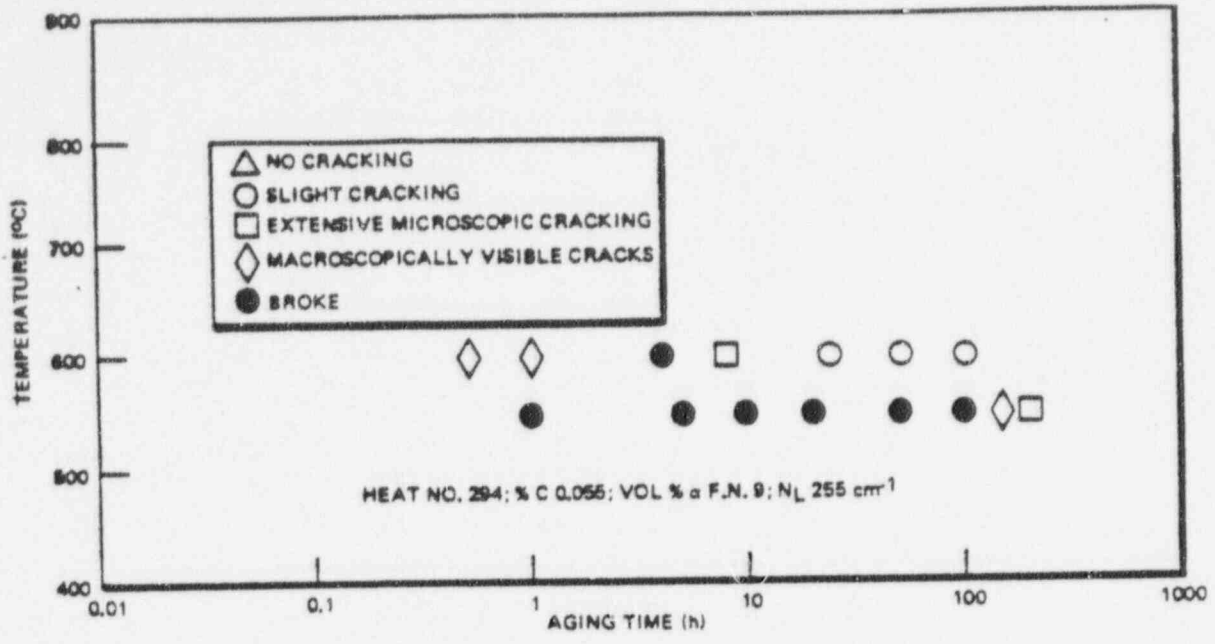

Figure 6-41. Influence of Aging Treatment on the Intergranular Corrosion Behavior of Type-308 Stainless Steel Containing 0.055% Carbon and 9 vol % Ferrite

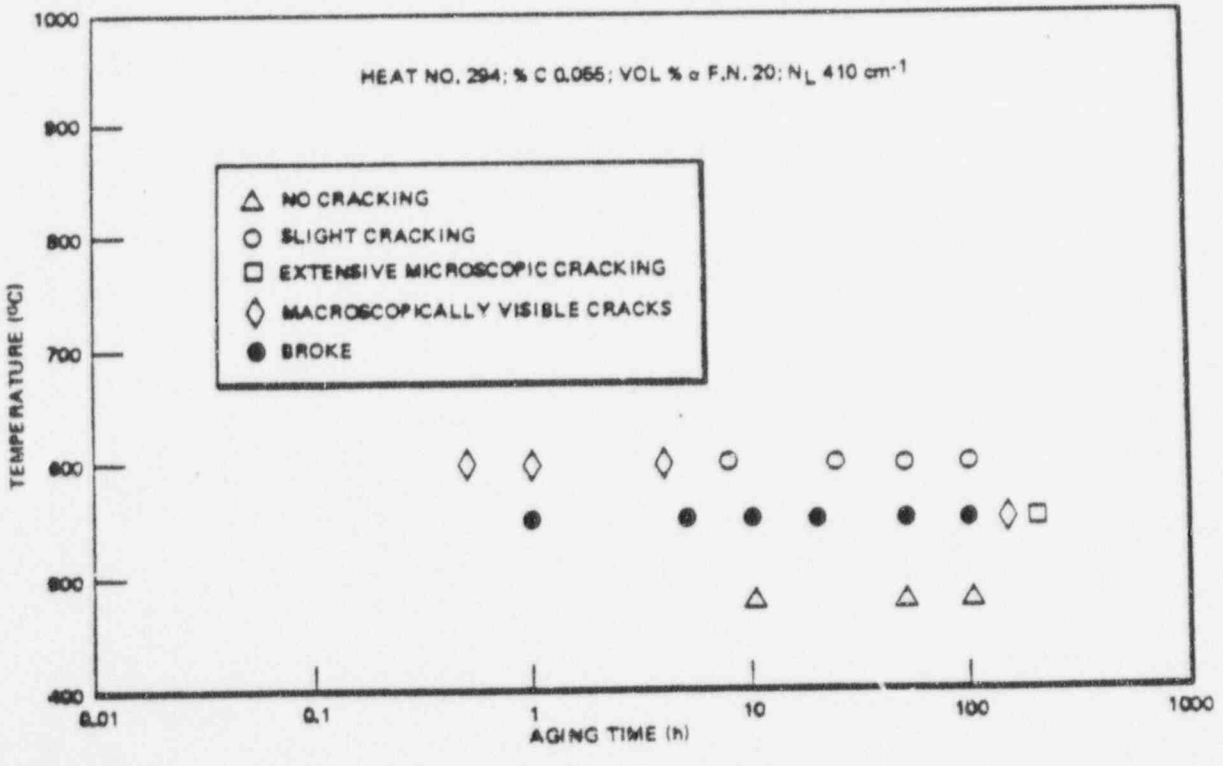

Figure 6-42. Influence of Aging Treatment on the Intergranular Corrosion Behavior of Type-308 Stainless Steel Containing 0.055% Carbon and 20 vol % Ferrite

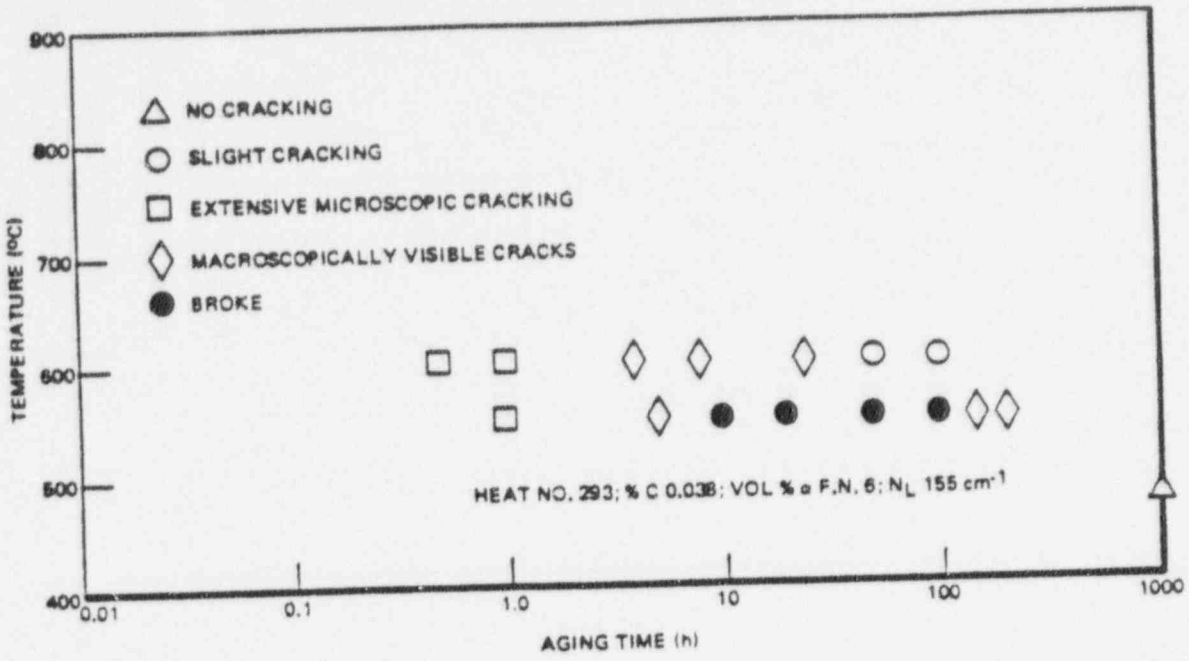

Figure 6-43. Influence of Aging Treatment on the Intergranular Corrosion Behavior of Type-308 Stainless Steel Containing 0.038% Carbon and 6 vol % Ferrite

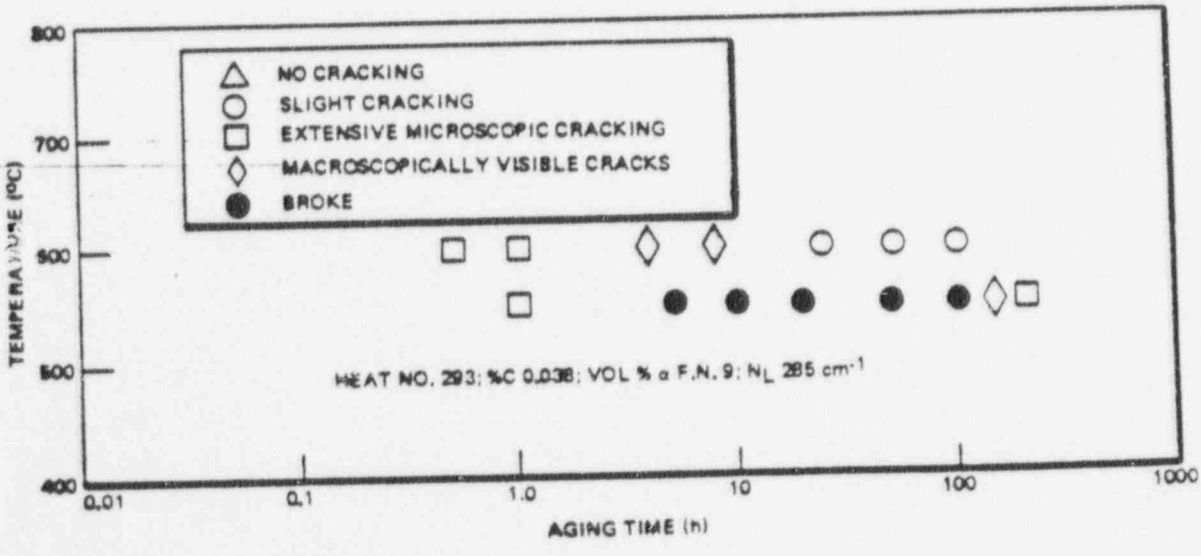

Figure 6-44. Influence of Aging Treatment on the Intergranular Corrosion Behavior of Type-308 Stainless Steel Containing 0.038% Carbon and 9 vol % Ferrite

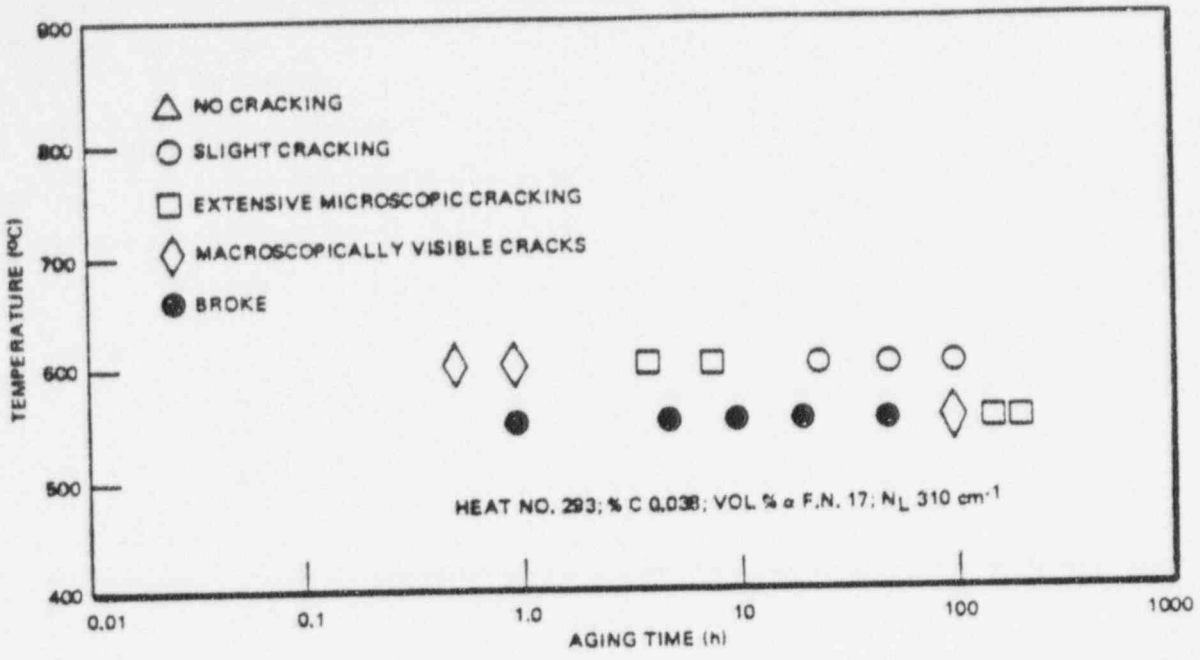

Figure 6-45. Influence of Aging Treatment on the Intergranular Corrosion Behavior of Type-308 Stainless Steel Containing 0.038% Carbon and 17 vol % Ferrite

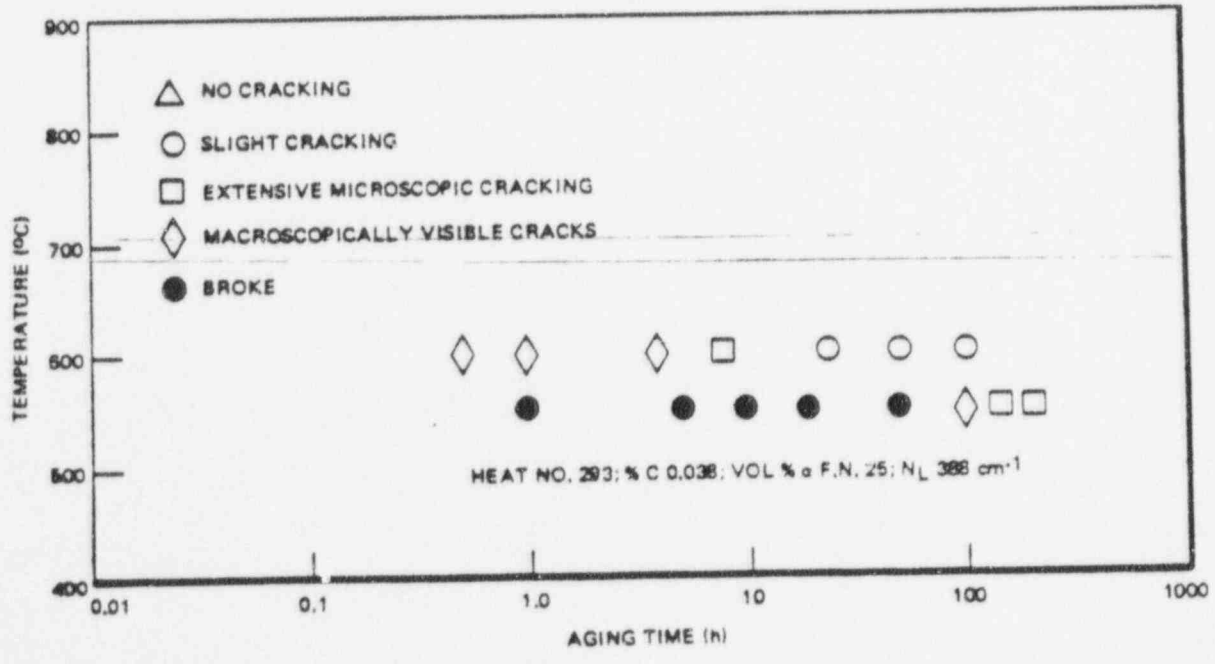

Figure 6-46. Influence of Aging Treatment on the Intergranular Corrosion Behavior of Type-308 Stainless Steel Containing 0.038% Carbon and 25 vol % Ferrite

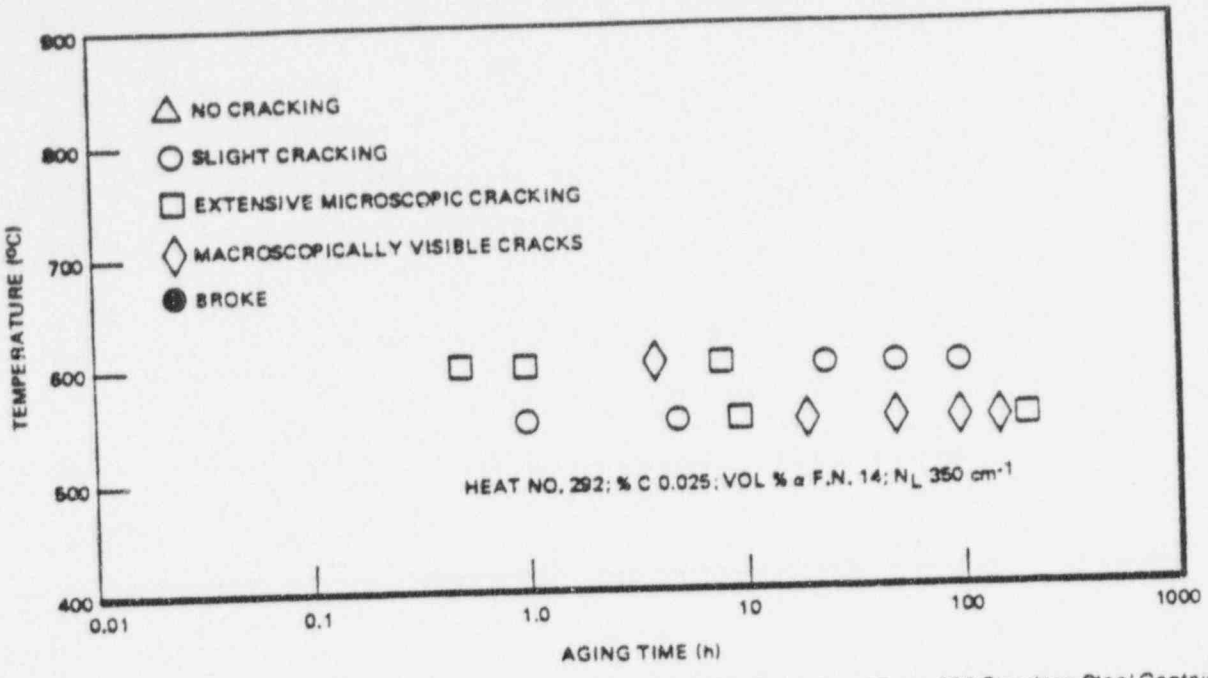

Figure 6-47. Influence of Aging Treatment on the Intergranular Corrosion Behavior of Type-308 Stainless Steel Containing 0.025% Carbon and 14 vol % Ferrite

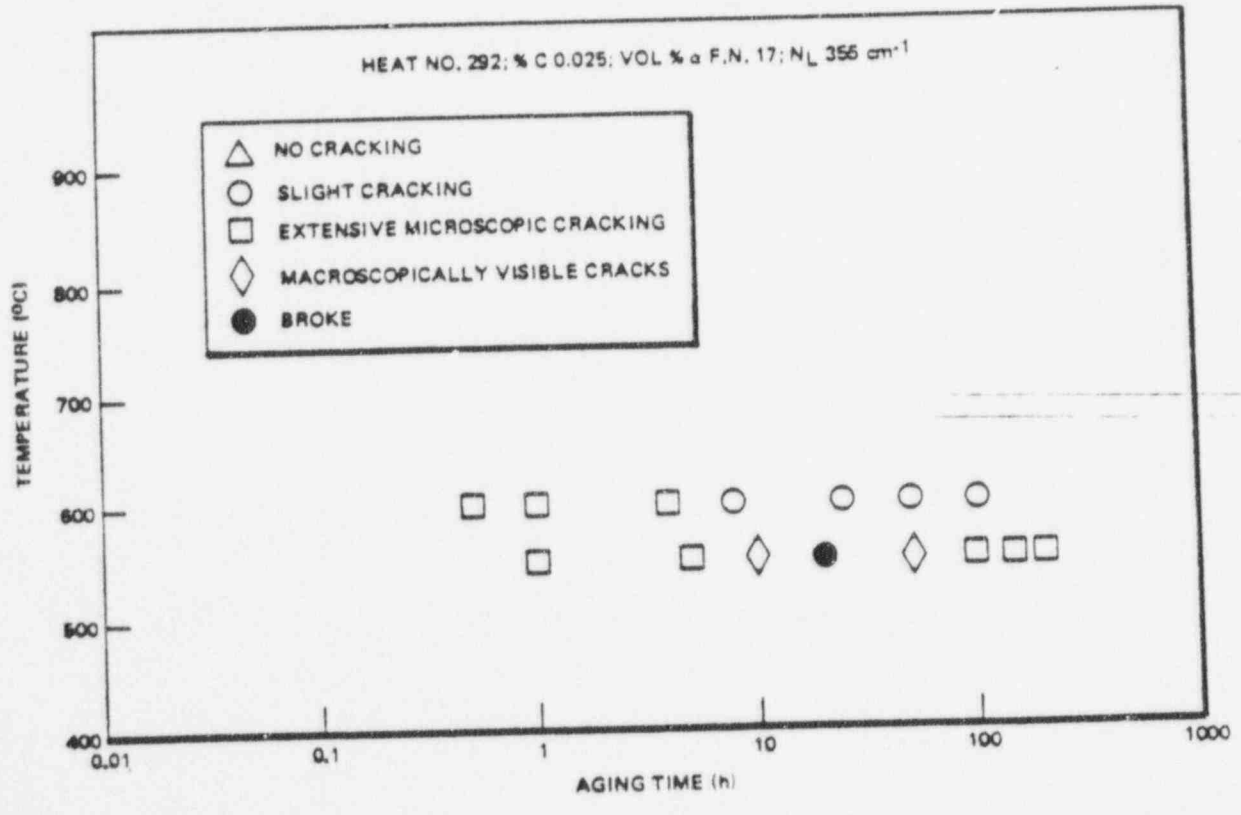

Figure 6-48. Influence of Aging Treatment on the Intergranular Corrosion Behavior of Type-308 Stainless Steel Containing 0.025% Carbon and 17 vol % Ferrite

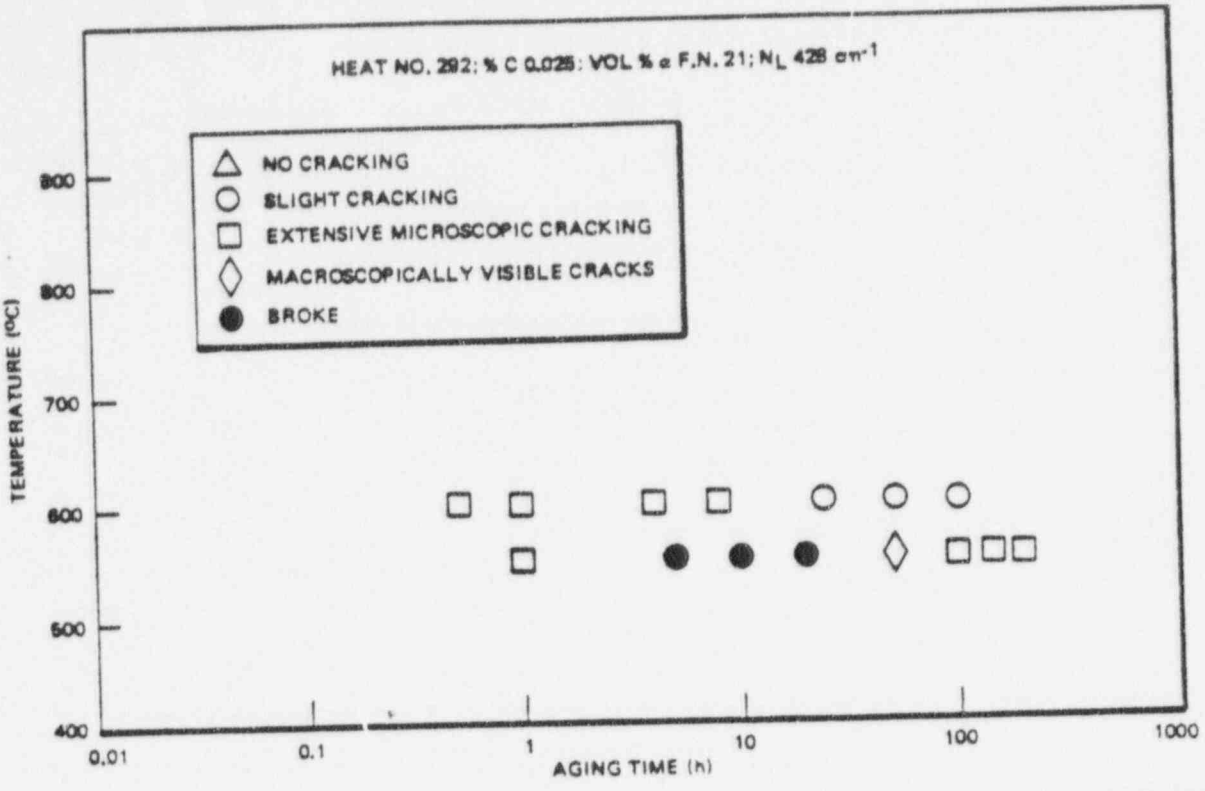

Figure 6-49. Influence of Aging Treatment on the Intergranular Corrosion Behavior of Type-308 Stainless Steel Containing 0.025% Carbon and 21 vol % Ferrite

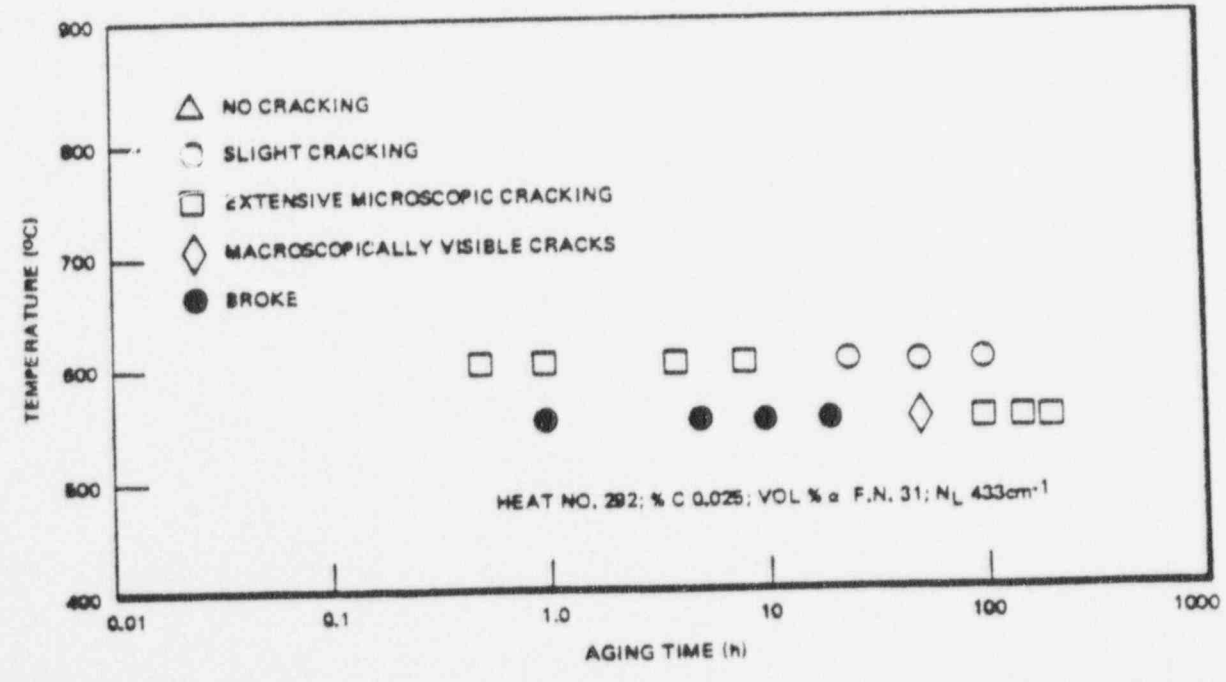

Figure 6-50. Influence of Aging Treatment on the Intergranular Corrosion Behavior of Type-308 Stainless Steel Containing 0.025% Carbon and 31 vol % Ferrite

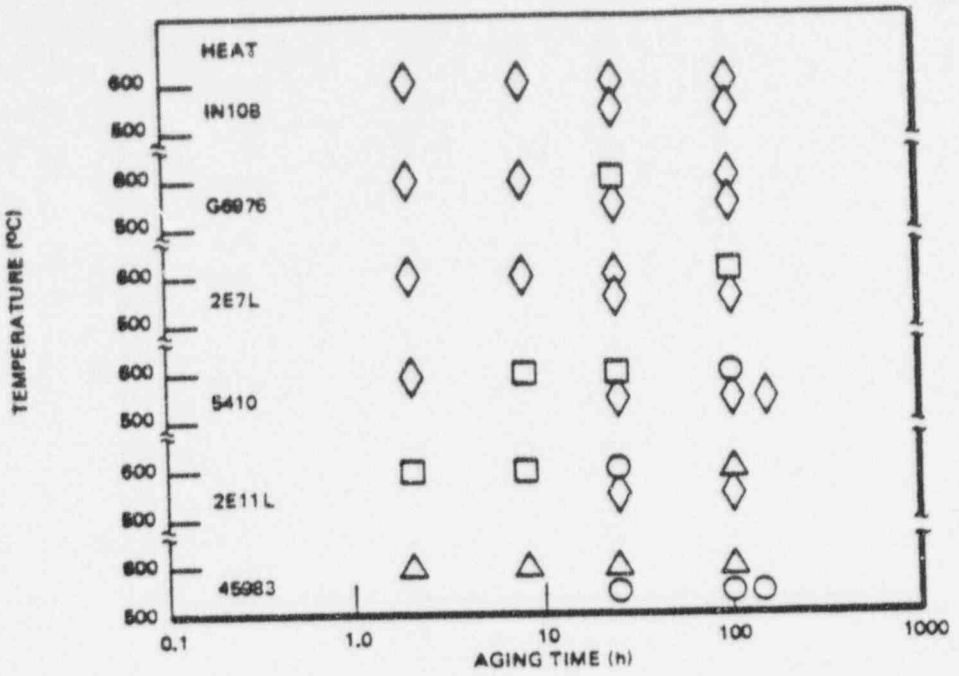

Figure 6-51. Influence of Aging Treatment on the Intergranular Corrosion Behavior of Type-308 Weld Deposits

where
- D = diffusivity of carbon in austenite
- t = aging time
- Co = initial carbon content of austenite
- $\bar{c}$ = mean carbon content of austenite after aging for time t

using the additional metallographic relationship

$$\lambda_\gamma = \frac{1 - L_v^{\alpha}}{1/2\, N_L^{\alpha-\gamma}} \tag{6-4}$$

we can rewrite Equation 6-3 as

$$N_L^{\alpha-\gamma} = 2V_v^{\gamma} \left(\frac{\pi^2 \, Dt}{\ell n \, \frac{8}{\pi^2} \, \frac{Co}{\bar{c}}} \right)^{-1/2} \tag{6-5}$$

Thus we can express each criterion in terms of N_L and carbon content of the alloy.

Figure 6-52 is a plot of Equation 6-2 and describes the amount of austenite-ferrite boundary area required to accommodate all of the available carbon as a 1000-Å-thick $M_{23}C_6$ precipitate. The second curve in this figure plots twice this amount of austenite-ferrite boundary area. The latter may be a more realistic criterion since it has been shown in a separate investigation that only one-half of the austenite-ferrite boundaries contain $M_{23}C_6$ precipitates.[14]

Figure 6-53 is a plot of Equation 6-5 for three different values of $\bar{c}$. In each case it is required that λ_γ be such that the carbon content of the austenite is reduced to $\bar{c}$ within 2 hours at 600°C (1112°F).

It is worth emphasizing that the criteria expressed in Figures 6-52 and 6-53 are not based on immunity to intergranular corrosion. Rather, each is concerned with the amount and distribution of $\alpha-\gamma$ boundary area required to inhibit sensitization of $\gamma-\gamma$ grain boundaries. However, the rapid healing which occurs along these boundaries if a critical amount and distribution of them exists, can limit the aging treatments which will result in sensitization of the alloy.

Figure 6-54 plots the data obtained for the 16 wrought alloys (L-B7 and three laboratory heats, each given four different ferrite levels) and six weld deposits considered in this investigation. The solid points indicate the material was immune to intergranular corrosion when aged at 600°C (1112°F) for longer than 24 hours. The open points indicate that in spite of the amount of ferrite present, the alloy behaved like a fully austenitic stainless steel in that it did not exhibit a healing phenomenon with continued aging at 600°C (1112°F). As shown, the data are reasonably well separated by the two curves drawn. The straight line requires twice the amount of austenite-ferrite boundary area than that required to tie up all the available carbon as $M_{23}C_6$. The curved line expresses the distribution of austenite-ferrite boundaries required in a 10 vol % ferrite alloy to have an austenite-ferrite boundary within easy carbon diffusion distance throughout the austenite so as to be able to reduce the mean bulk austenite carbon content to 0.015% after 2 hours at 600°C (1112°F). That the data are described well by the criterion requiring twice the amount of austenite-ferrite boundary area than that required to tie up all of the carbon as $M_{23}C_6$ along austenite-ferrite boundaries is consistent with the mechanism of intergranular corrosion in duplex stainless steels described in Section 6.3 and the observation made in Section 6.3.3 that only 50% of all the austenite-ferrite boundaries are covered with carbides. This criterion assumes that the ferrite is randomly distributed. For this reason the austenite mean free path criterion is superior as it describes the distribution as well as the amount of austenite-ferrite boundary area. That the data are characterized well by the criterion requiring that the austenite mean free path be such that the carbon content of the austenite be reduced to 0.015% after 2 hours at 600°C (1112°F) is consistent with the work of Bleton, *et al.*,[15] who reported that fully austenitic Type-304L stainless steels with 0.020% carbon or less are extremely resistant to intergranular corrosion and with the calculations of Tedmon and Vermilyea[10] which state that fully austenitic Type-304L stainless steels with 0.015% carbon or less are immune to intergranular corrosion in A262E.

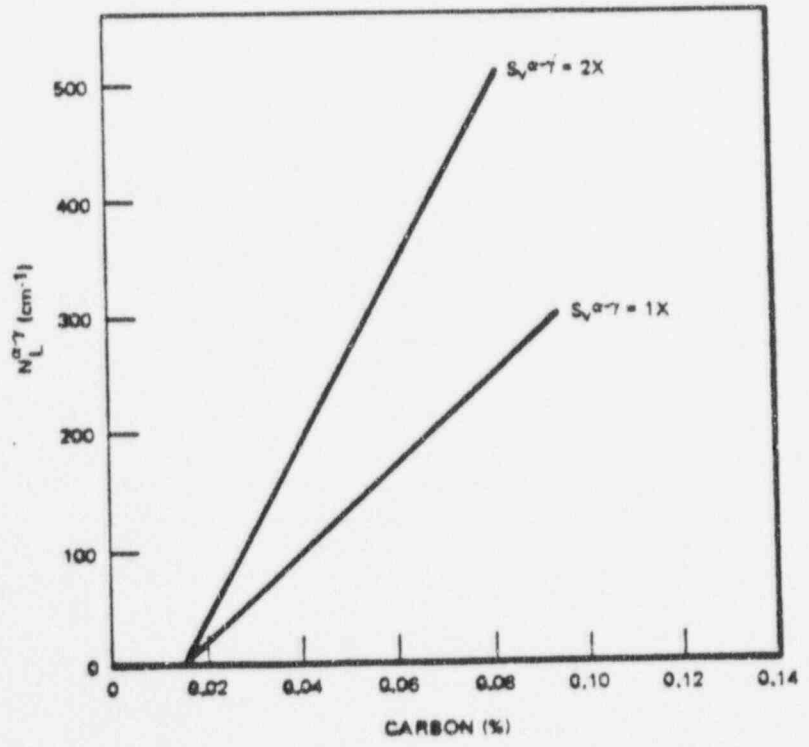

Figure 6-52. The Value of $N_L^{\alpha-\gamma}$ Required to Provide Sufficient Austenite-Ferrite Boundary Area to Inhibit Sensitization of Type-308 Stainless Steel

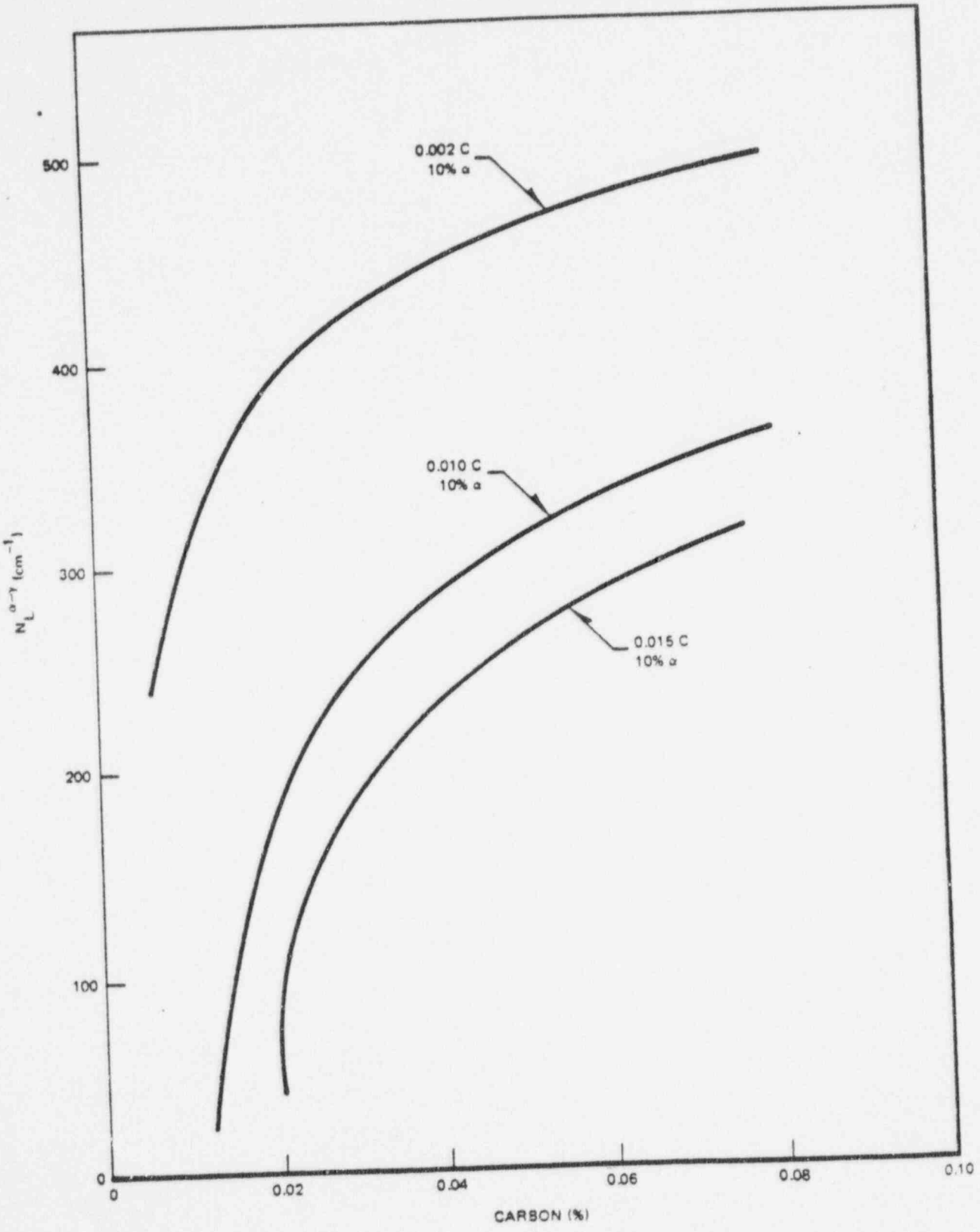

Figure 6-53. The Value of $N_L^{\alpha\gamma}$ Required to Reduce the Austenite Mean-Free-Path to a Level Sufficient to Inhibit Sensitization of Type-308 Stainless Steel

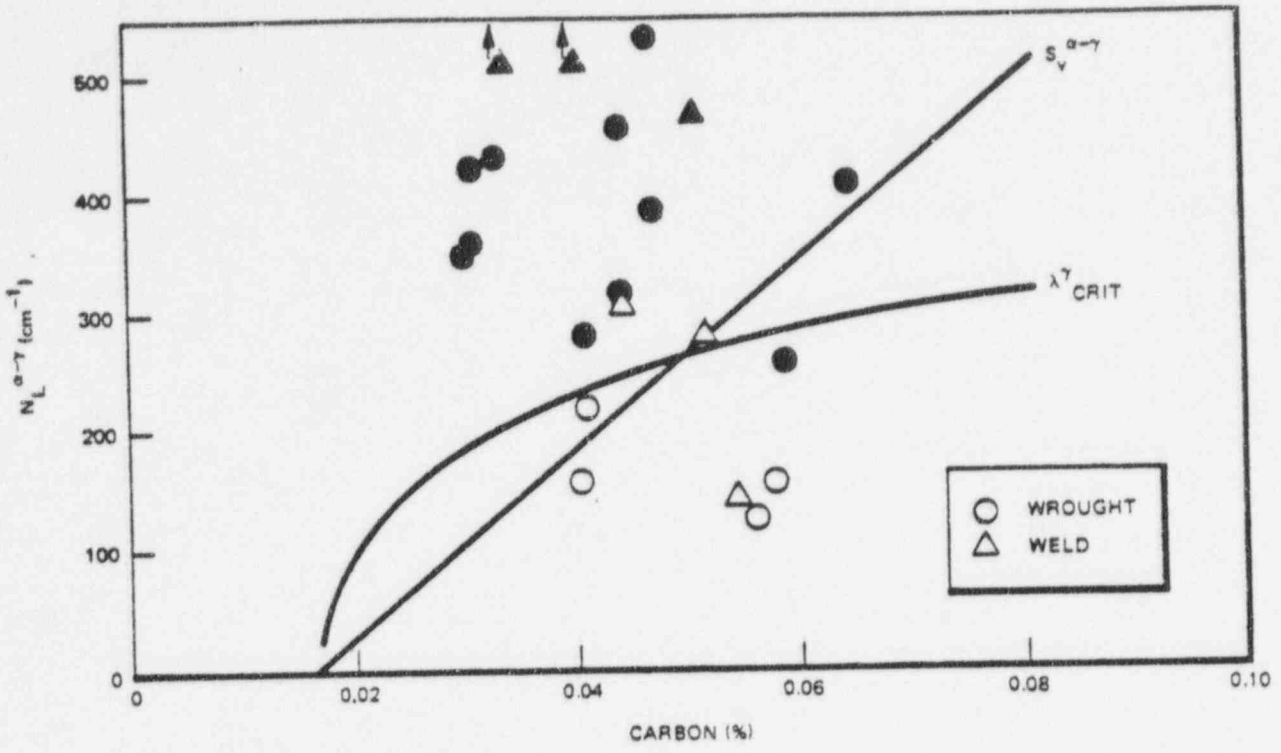

Figure 6-54. The Influence of $N_L^{\alpha\gamma}$ on the Intergranular Corrosion Behavior of Aged Samples of Wrought and Weld-Deposited Type-308 Stainless Steel

The ability to accurately describe the intergranular corrosion behavior of duplex stainless steels with the austenite mean-free-path criterion is illustrated in the A262E tests conducted on the wrought alloys 294/1300°C (2372°F)-1 hour, 293/1350°C (2462°F)-1 hour, 294/1250°C (2282°F)-1 hour, 294/1350°C (2462°F)-1 hour, and on the weld deposits IN10B, 5410, and 2E7L. For convenience in comparison, these results are summarized in Figures 6-55 and 6-56. Figure 6-55 illustrates the similar intergranular corrosion behavior exhibited by the weld deposit of Heat 5410 (which contained 4.5 vol % ferrite and 0.050% carbon) and the wrought alloy 294/1350°C (2462°F)-1 hour (which contained 20 vol % ferrite and 0.055% carbon). These alloys exhibit similar intergranular corrosion behavior because they have similar carbon contents and similar values of $N_L^{\alpha-\gamma}$. Likewise, Figure 6-56 depicts the similar intergranular corrosion behavior of the weld deposit of Heat 2E7L (which contained 4.15 vol % ferrite and 0.044% carbon) and the wrought alloys 293/1300°C (2462°F)-1 hour and 293/1350°C (2462°F)-1 hour (both of which contained 0.038% carbon but 17 and 25 vol % ferrite, respectively). Again, these alloys exhibit similar intergranular corrosion behavior in spite of their widely different ferrite contents because they have similar carbon contents and similar values of $N_L^{\alpha-\gamma}$.

The above model can be extended to predict what amount and distribution of austenite-ferrite boundary area (*i.e.*, λ_γ) is required for a given carbon content to produce an alloy which is immune to intergranular corrosion. That is, an alloy in which no aging treatment can produce a sensitized microstructure. The approach is to first calculate the time, t_s, required to produce a sensitized microstructure and then to calculate the λ_γ required to reduce the carbon content of the austenite phase to less than 0.015% in time t_s. The time to develop a sensitized microstructure is assumed to be the time required to develop a zone of some critical width, w, along the grain boundaries in which the chromium content is less than 13%. This width w is given approximately by[16]

$$w = 2\sqrt{D_{cr}^{\gamma} t_s}\left[\frac{13 - X_{cr}^{\gamma}{}_{i}}{19 - X_{cr}^{\gamma}{}_{i}}\right] \qquad (6\text{-}6)$$

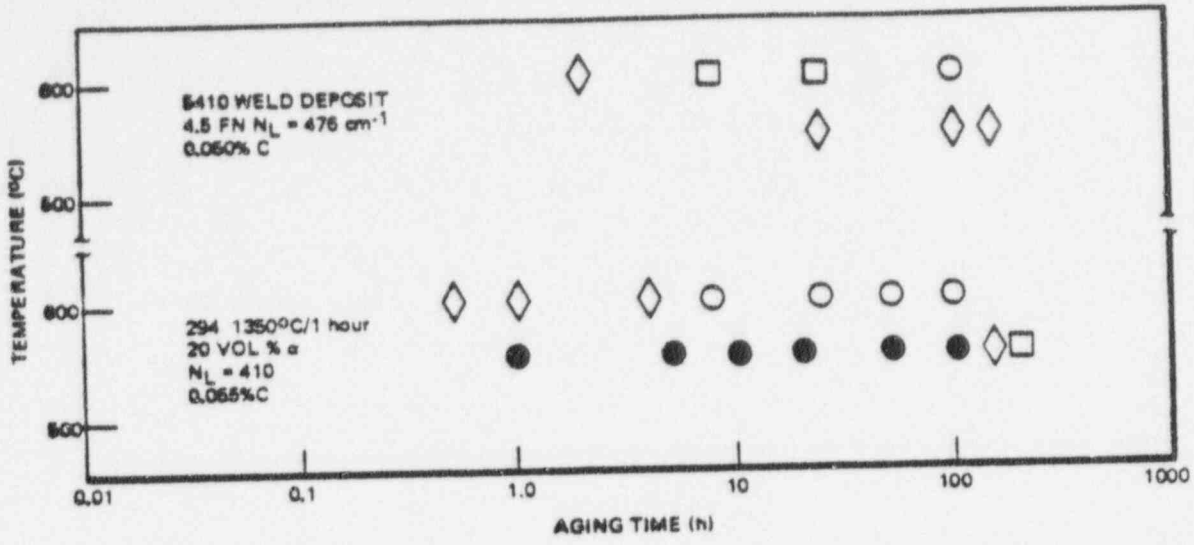

Figure 6-55. Similarity in the Sensitization Behavior of a Wrought Heat and a Weld-Deposited Heat of Type-308 Stainless Steel which Possess Nearly the Same N_L[a7] and Carbon Content

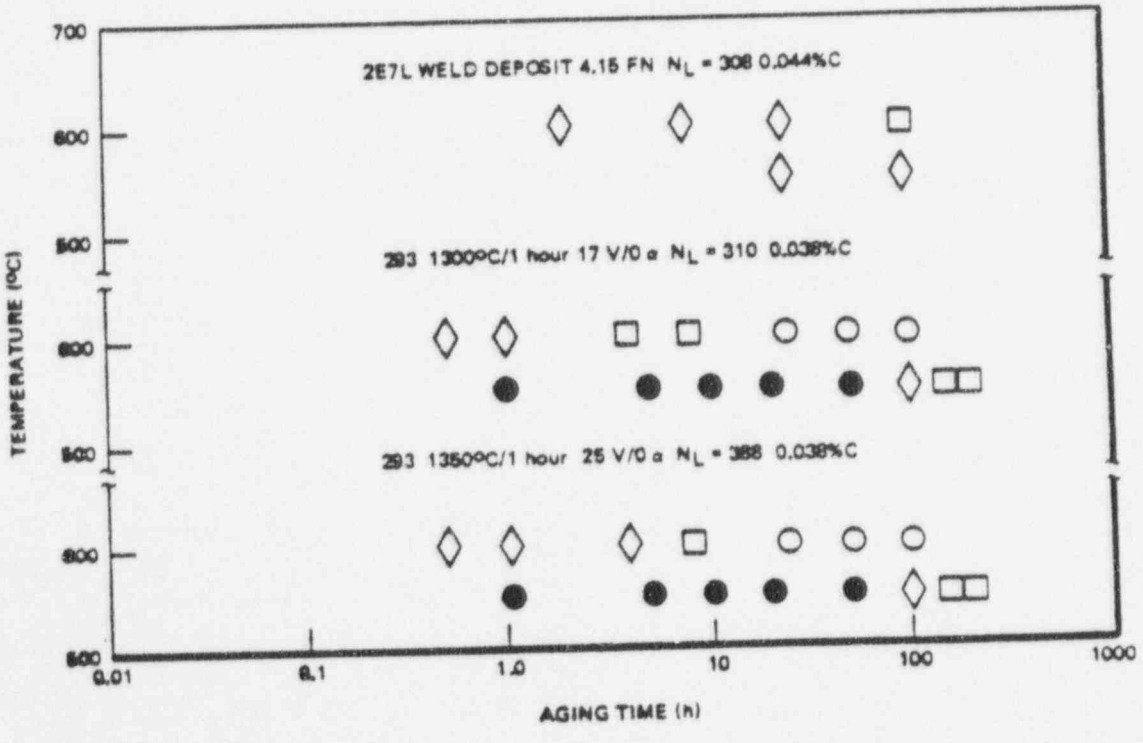

Figure 6-56. Similarity in the Sensitization Behavior of Three Different Heats of Type-308 Stainless Steel which Possess Nearly the Same N_L[a7] and Carbon Content

where the bulk chromium content is 19%, and $X_{cr}^{\gamma}{}_{i}$ is the chromium content in the matrix at the matrix-carbide interface. $X_{cr}^{\gamma}{}_{i}$ is a function of the carbon content. For a given value of w and carbon content t_s can be calculated. With the aid of Equation 6-7 the λ_γ required to reduce the austenite carbon content to 0.015% in time t_s can be calculated. Thus, for an immune duplex alloy

$$\lambda_\gamma \leq \frac{\pi w}{2}\left[\frac{D_c^{\gamma} D_{cr}^{\gamma}}{\ell n \frac{8}{\pi^2}\frac{Co}{c}}\right]^{1/2}\left[\frac{19 - X_{cr}^{\gamma}{}_{i}}{13 - X_{cr}^{\gamma}{}_{i}}\right] \qquad (6\text{-}7)$$

This equation is plotted in Figure 6-57 as a function of carbon content assuming w = 25 Å and for two different ferrite levels. Also shown in this figure is the λ_γ required to prevent sensitization of austenite-austenite grain boundaries and thereby ensure rapid healing kinetics for the alloy. The two points represented as stars in Figure 6-57 are alloys which were immune to sensitization. The one at $N_t^{\alpha-\gamma}$ = 1261 corresponds to the weld deposit 45983 and the one at $N_t^{\alpha-\gamma}$ = 840 corresponds to data obtained in a separate investigation on a heat of Uranus 50, a duplex alloy which contained 0.032% carbon and 33 vol % ferrite. The data are reasonably well described by the theory.

6.4.5 Summary and Conclusions

Based on the mechanism of intergranular corrosion of duplex stainless steels described in Section 6.3, a model is developed which accurately describes the intergranular corrosion behavior of sixteen wrought alloys and six weld deposits of Type-308 stainless steel. The model requires for each carbon content a critical amount and distribution of austenite-ferrite boundary area in order for the alloy to exhibit a healing phenomenon within short aging times. This is of importance to duplex parts given nitriding treatments or high-temperature stress relief anneals. A model is also developed which describes for each carbon content the amount and distribution of austenite-ferrite boundary area required to produce an alloy immune to sensitization.

6.5 ACKNOWLEDGMENTS

It is a pleasure to acknowledge the outstanding contributions of the following people. Miss B.J. Drummond conducted the electrochemical and corrosion tests, and assisted in the heat treatment and specimen preparation of all samples. Ms. A.M. Ritter performed the transmission electron microscopy. Messrs. R.F. Berning, J.H. Steadwell, W.R. Catlin, P.T. Hill, M. Heiberger, and C.P. Palmer designed, constructed, and operated the high-temperature stress corrosion cracking facility. Deformation processing of sheet and wire specimens was performed by T.E. Douglas, F. Clark, J.R. Greening, L.C. Perocchi, and R.J. Petterson. Heat treatments were conducted by D.P. Horney and E.S. Nagy. Welding was performed by Messrs. G. Pagnotta and L.A. Wojcik. Helpful discussions were conducted with Drs. M.G. Benz, R.E. Hanneman, M.F. Henry, M.R. Jackson, H.D. Solomon and D.F. Taylor.

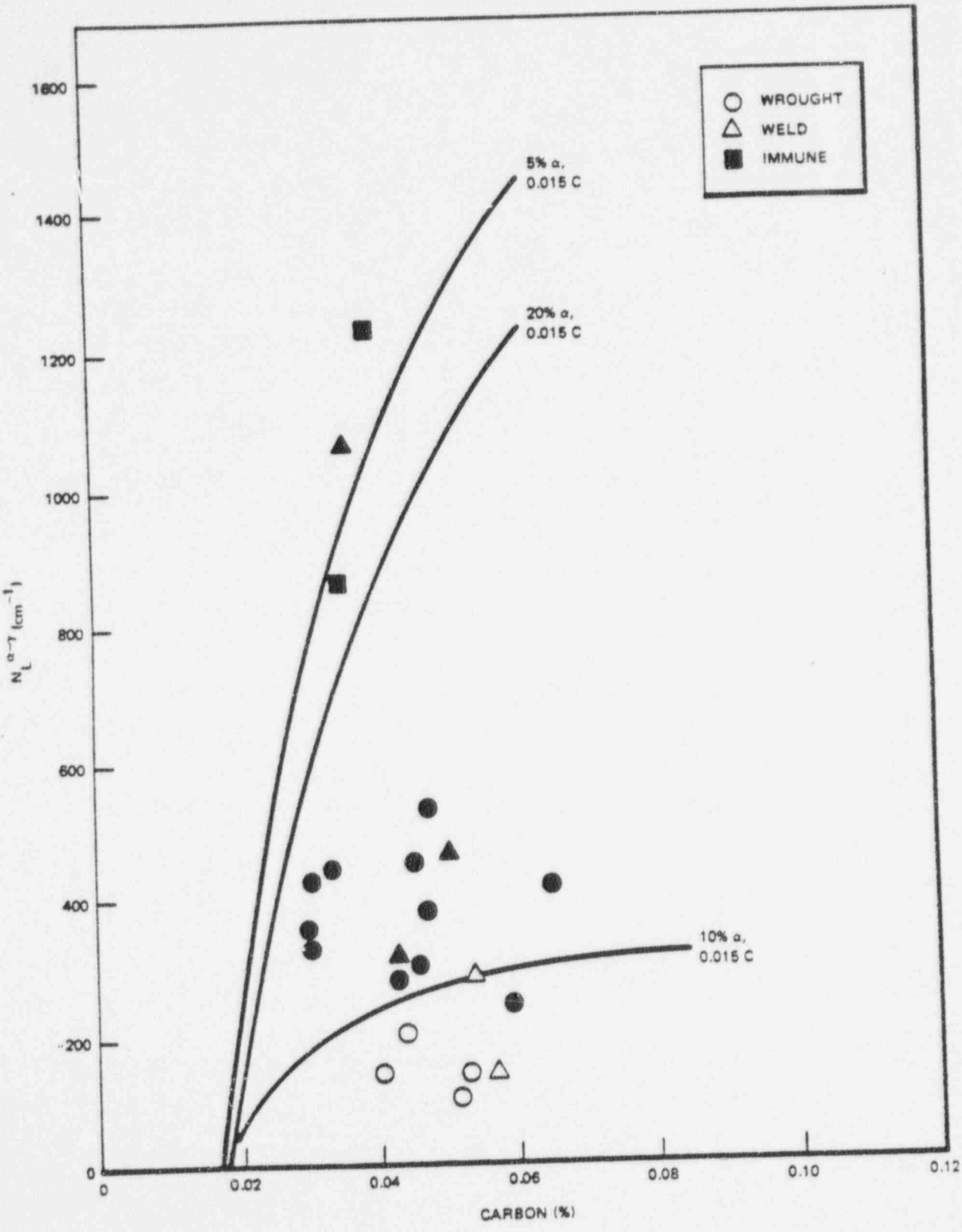

Figure 6-57. The Values of $N_L^{\alpha-\gamma}$ Required to Reduce the Austenite Mean-Free-Path to Levels Sufficient to (a) Restrict and (b) Prevent Sensitization of Type-308 Stainless Steel

90014273

7. REFERENCES

1. M. A. Streicher, The *J. Electrochemical Society*, **106**, 161, (1959).
2. K. Osozawa, K. Bohnekamp and H. J. Engell, *Corrosion Science*, **6**, 421, (1966).
3. H. Coriou, J. Hure, and G. Plante, *Electrochemica Acta*, **5**, 105, (1961).
4. J. H. Payer and R. W. Staehle, *Corrosion*, **31**, 30, (1975).
5. R. M. Fisher, E. J. Dulis, and K. G. Carroll, *Transactions AIME*, 690, (1953).
6. C. R. Rarey and A. H. Aronson, *Corrosion*, **28**, 255, (1972).
7. G. Eklund, *J. Electrochemical Society*, **121**, 467, (1974).
8. M. Hansen, "Constitution of Binary Alloys," McGraw-Hill, New York, 1958, p. 705.
9. M. A. Streicher, *J. Electrochemical Society*, **103**, 375, (1956).
10. C. S. Tedmon, D. A. Vermilyea, and J. H. Rosolowski, *J. Electrochemical Society*, **118**, 192, (1971).
11. "WRC Development Program for Standard Weld Metal Sample Preparation Procedures," Advisory Subcommittee for Welding Stainless Steels, High Alloys Committee, Welding Research Council, December 1972.
12. T. M. Devine, "Task 6 in Evaluation of Near-Term BWR Piping Remedies, Third Semi-annual Progress Report," (NEDC-21463-3).
13. Private Communication, Sumitomo Metal Industries, Ltd., June 1977.
14. T. M. Devine, *J. Electrochemical Society*, **126**, 374, (1979).
15. L. Columbier and J. Hochmann, "Stainless and Heat-Resisting Steels," St. Martin's Press, New York, 1968, p. 153.
16. C. Stawstrom and M. Hillert, *J. Iron and Steel Institute*, 77, (1969).

APPENDIX A. FOUR POINT BEND TESTING PROCEDURE

The four-point bend pipe test pair was loaded in bending (as shown in Figure A-1) at 288°C (550°F) in high purity water with 8 ppm dissolved oxygen and a maximum outer fiber tensile stress of 136% of the Type-304 stainless steel 288°C (550°F) yield strength applied to the weld. In this loading configuration, approximately 14% of the circumference of the pipe is loaded to at least 90% of the maximum load; and approximately 25% of the circumference of the pipe was loaded above the yield strength of Type-304 stainless steel at temperature. The pipes were load cycled periodically (typically daily) to simulate reactor startup and shutdown conditions.

The four-point bend test fixture, shown in Figure A-2, tests two companion pipes by loading the pipes against each other using hydraulic jacks and fixed position ends. The pipes are loaded in bending and the region between the hydraulic jacks is at the same load throughout the length of pipe. In this manner, a large number of test welds can be exposed to the same loading conditions.

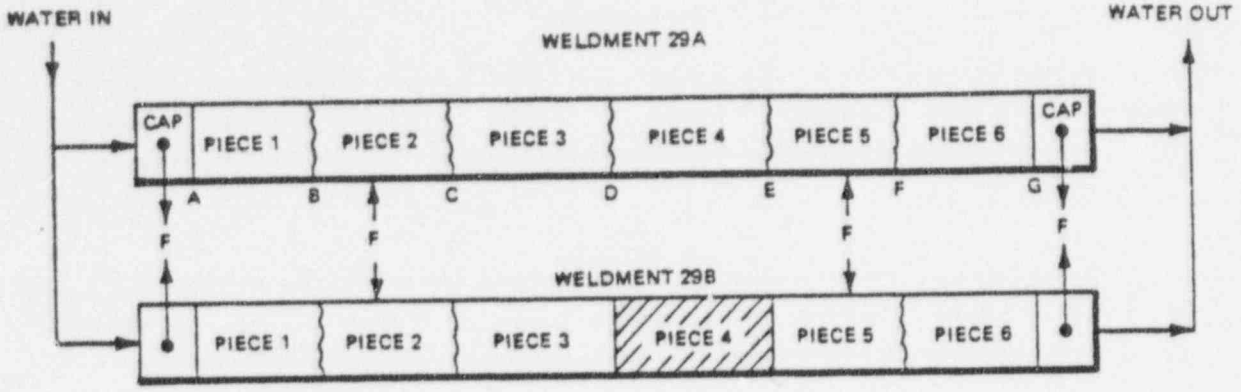

Figure A-1. Typical Weldment

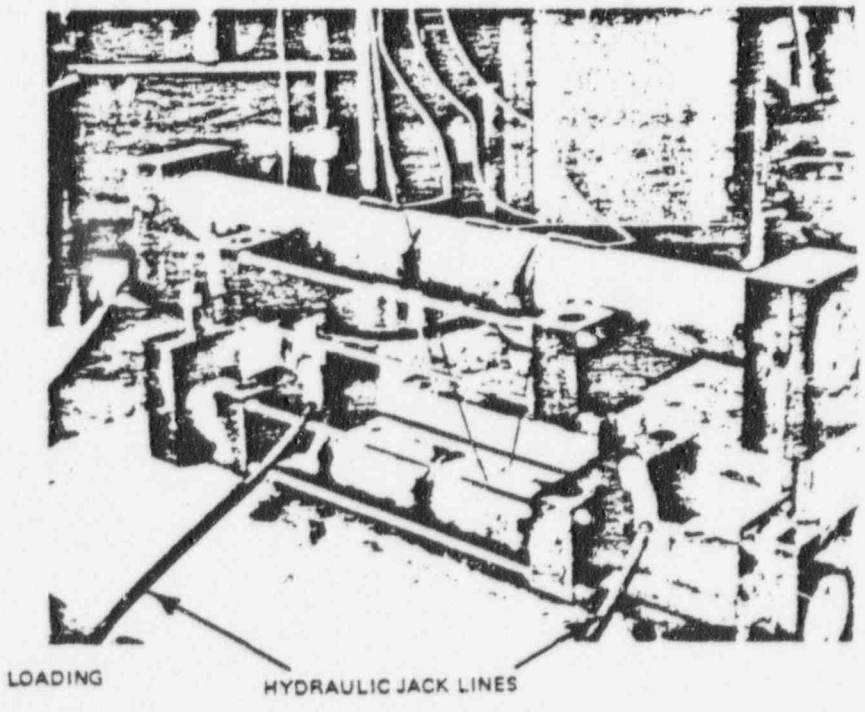

Figure A-2. Test Fixture

APPENDIX B. AXIAL TENSION TESTING PROCEDURE

B.1 MAXIMUM STRESS

The maximum stress for each of the Large Environmental Fatigue Test Facility tests was selected to be equal to the maximum bending stress used in the CL-4 bending tests. The stress level was 38,800 psi (268 MPa) which is 136% of the 280°C (550°F) yield strength of the test material. The calculated stress level did not include pressure or residual stresses.

During later phases of the second and fourth Large Environmental Fatigue Test Facility tests the maximum stress level was increased to 175% of the 280°C (550°F) yield strength to further accelerate cracking.

B.2 CYCLIC WAVE SHAPE

The cyclic wave shape or control wave form used during all phases of each Large Environmental Fatigue Test Facility test was trapezoidal with a period of 1.5 hours (see Figure B-1). During each cycle, the specimen was subjected to 5 minutes at minimum load 5000 lb (2268 kg), 5 minutes during rising load, 75 minutes at full load, and 5 minutes during decreasing load. The test frequency was therefore 0.67 cycle per hour.

B.3 TEST ENVIRONMENT

During all phases of the testing a high oxygen (8–12 ppm) demineralized water environment at 285°C (545°F) and 1120 psig (7.7 MPa) was circulated through the inside of the specimen. The flow rate was approximately 2–3 gpm (7.5-11.4 l/min). The electrical conductivity of the water was maintained below 1 mho/cm (2.54 mho/in.) Load was not applied until these conditions were established.

B.4 TEST OBJECTIVE

The cyclic tensile tests in the Large Environmental Fatigue Test Facility were designed to use axial cyclic loading on full-size 10.16-cm (4-inch) schedule 80 welded pipe specimens of reference Type-304 stainless steel and potential remedy methods to evaluate the relative intergranular stress corrosion cracking performance of the respective welds in full-size pipes. Accelerated test conditions were employed to reduce the required testing time. The accelerants used included high stress, cyclic loading, high oxygen water environment, heavy grinding on the inside surface of the weld heat affected zones, and welds made with high heat input. The accelerants vary from test to test and from condition to condition.

B.5 SPECIMEN DESCRIPTION AND FABRICATION

Each of the test weldments was fabricated by butt welding eight 10.16-cm (4-in.) long segments of 10.16-cm (4-in.) schedule 80 pipe together to form a 81.26-cm (32-in.) long test section. Machined end caps were butt welded to each end of the test section to provide the closure necessary for pressurization. Both end caps were provided with threaded parts to allow the pressurized water environment to flow through the test sections. Loading adapters were welded to both end caps to provide a means to connect the specimens to the test machine.

The general test specimen configuration is presented in Figure B-2. The test section includes eight butt welds (Welds A through I). Each butt weld has two separate heat affected zones for a total of 18 possible crack initiation sites. However, Welds A1, A2, I1, I2 were fabricated from 10.16-cm (4-in.) schedule 160 pipe for the second Large Environmental Fatigue Test Facility test to avoid unwanted cracking in the end cap welds. Thus, 14 weld heat affected zones were tested at the high stress level in the second Large Environmental Fatigue Facility test. An additional transition piece was prepared for the third and fourth Large Environmental Fatigue Test Facility tests so that 18 heat affected zones were tested at the high stress level in these Large Environmental Fatigue Test Facility Tests. An assembled pipe specimen is shown in Figure B-3.

B.6 LOADING

The cyclic axial load was applied to the ends of the specimen using the Large Environmental Fatigue Test Facility 226,800 kg (500,000 pound) universal test machine. The deflection feedback control mode was selected for the universal test machine based on safety considerations. As cracking occurs in this mode, the specimen stiffness decreases and therefore the resulting load decreases.

During the first few cycles of testing, the applied deflection range was adjusted to maintain the desired stress range. These adjustments were made until a stable load-deflection relationship was established. This shakedown process to stable behavior is shown in Figure B-4.

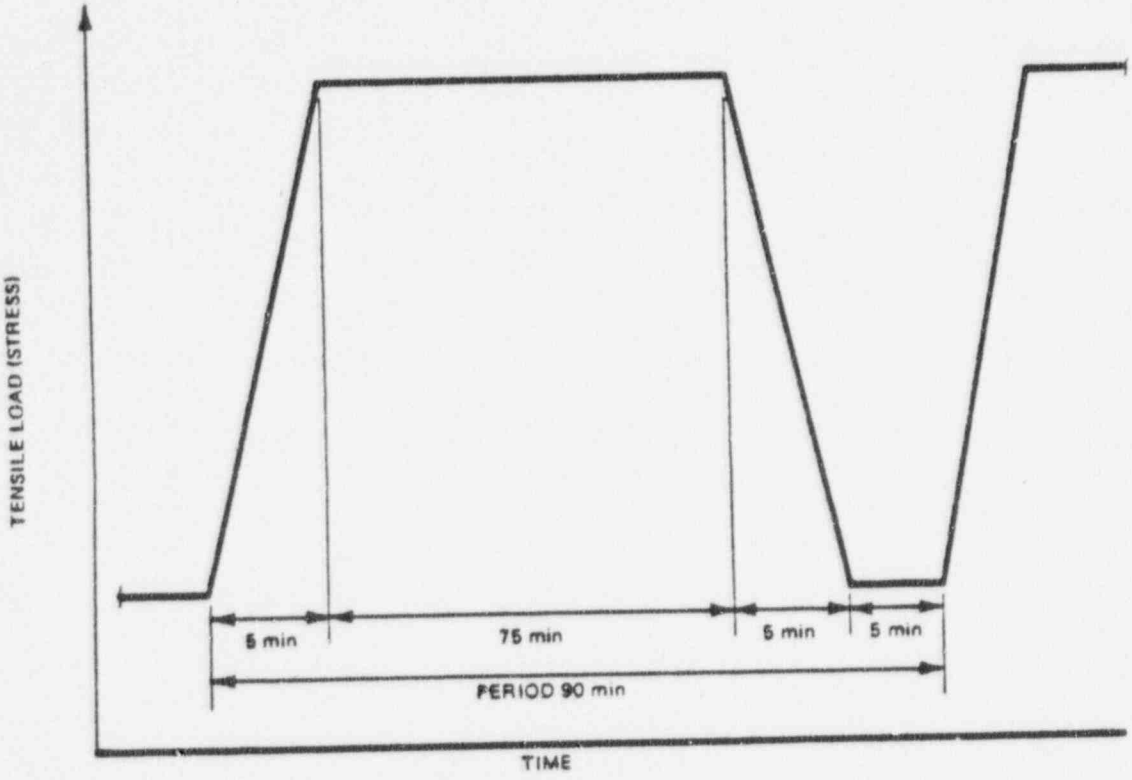

Figure B-1. Cyclic Test Waveform

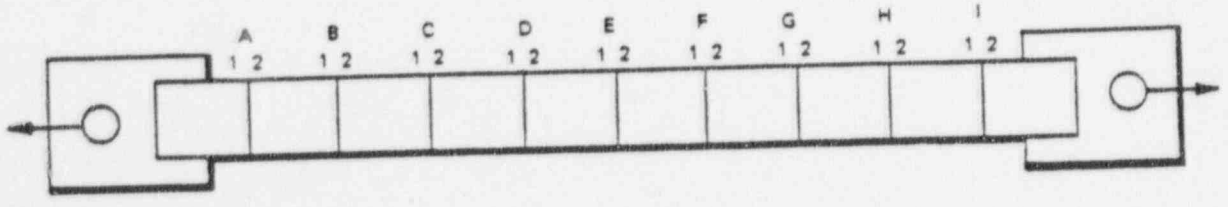

Figure B-2. Typical Weldment Makeup for Large Environmental Fatigue Pipe Tests

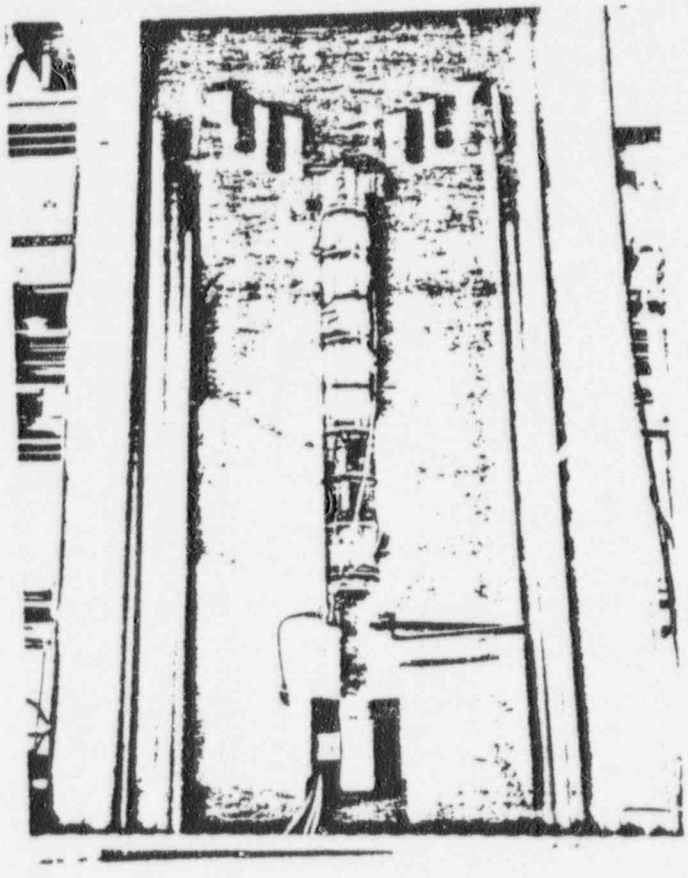

Figure B-3. Pipe Weldment for Second Cyclic Tension Test in Large Environmental Fatigue Test Facility

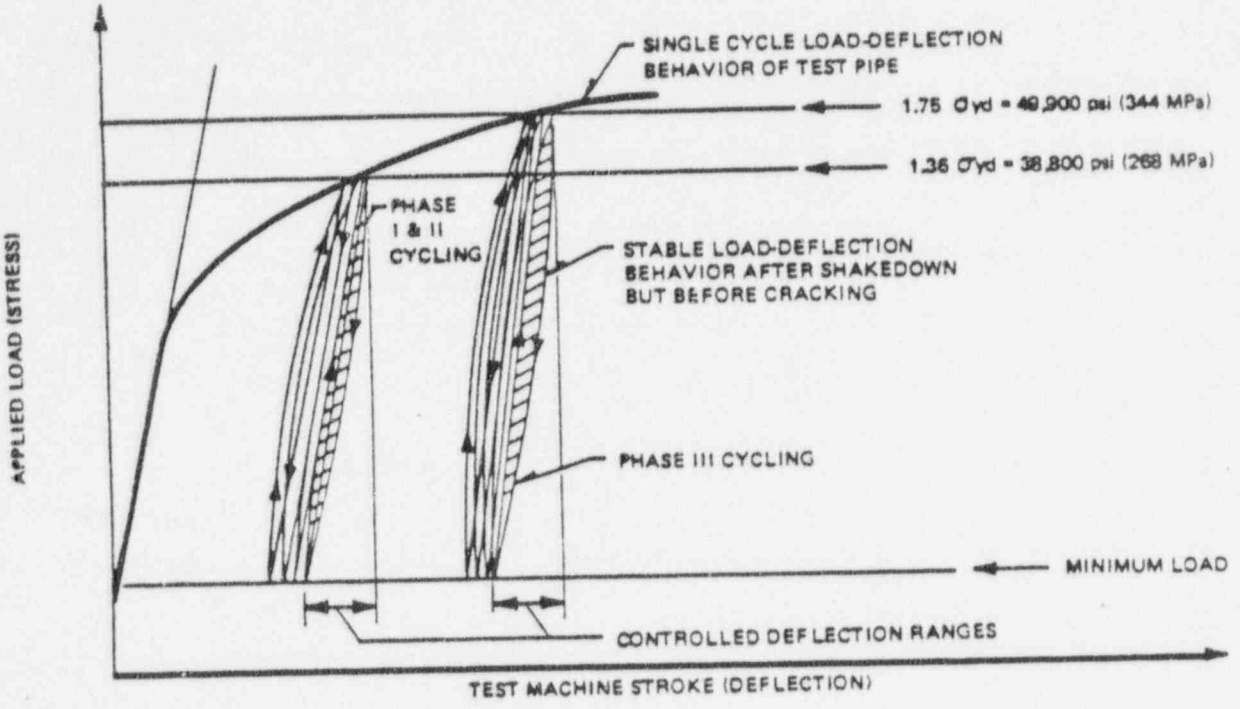

Figure B-4. Demonstration of Shakedown Behavior

APPENDIX C. PIPE TEST LABORATORY

The Pipe Test Laboratory consists of two recirculation loops. One loop is constructed from Type-316 stainless steel for testing pipe specimens under normal BWR environments. The second loop, fabricated from Inconel-600, is used for testing under normal or transient water chemistries. Each loop has 36 pipe test stands for testing 10.16-cm (4-in.) diameter welded pipes 44 inches long in axial loading. In addition, one large axial loaded test stand for testing 40.64-cm (16-in.) or 25.4-cm (10-in.) diameter pipes is available. A special horizontal test stand for testing 25.4-cm (10-in.) diameter pipe in 4 point bending is under construction.

A 10.16-cm (4-in.) pipe test stand specimen is loaded in tension by a hydraulic cylinder at the bottom of the stand through a clevis and pin connection at the bottom end of the test specimen. A hydraulic controller can be programmed to control the loading and unloading ramp rates and holding times at minimum and maximum loads for cyclic loading. On leakage or rupture of the pipe test specimen related to IGSCC, the steam is completely contained within the housing and is vented through an exhaust line to a safe remote location. The steam shield and seals were designed to handle safely the full test loop operating temperatures and pressures. The steam shield was designed to meet ASME code pressure vessel requirements. A pressure switch in the vent line senses the leak in the test specimen and unloads the specimen. A drop in specimen pressure activates check valves that close the supply and return lines and isolates the specimen from the loop. This allows the continuation of testing on the remaining pipe test specimens.

The 10.16-cm (4-in.) pipe test stands have a maximum load capacity of 118,000 kg (260,000 lb) and the large 40.64-cm (16-in.) test stand 1,360,000 kg (3,000,000 lb). Hydraulic cylinder pressure is used to indicate and record the applied load. The pipe test stands are load calibrated with a tension load cell at 6-month intervals.

For the 10.16-cm (4-in.) diameter test specimen, up to 12 butt welds may be included. Each end of the test section is welded to the transition piece fabricated from a 10.16-cm (4-in.) Schedule-160, Type-316 stainless steel pipe. In turn, the transition pieces are welded to the end loading adapters.

The upper end adapter provides the means for sealing and fixing the pipe test specimen at the top of the test stand. The inlet and outlet lines that connect to the system loop water are located in the upper end adapter. The lower adapter provides the connection for the pipe test specimen to the loading cylinder and also the sealing surface for the lower sliding seal. The frictional forces of the seal members have been measured and found to be negligible.

The influent and effluent water for each loop are continuously monitored and the conductivity, pH, and dissolved oxygen concentration are recorded. A Millipore filter is installed in each loop for undissolved solid analysis. Water temperature is monitored at the inlet and outlet of each test station.

The PTL also includes an acoustic emission system for monitoring cracking for up to 80 pipe test specimens. There are 120 parametric data channels available for collecting load and deflection data. A minicomputer is used for data acquisition and post-data processing.

APPENDIX D. PIPE MATERIALS FOR SCREENING TESTS

D.1 Significant Heats of Pipe

Identification	Carbon (%)	Yield Strength (psi)
304 SS, Heat M7616	0.060	45,800
304 SS, Heat 454970	0.042	37,000
304 SS, Heat M7772	0.058	40,500
304 SS, Heat M0063	0.051	38,900
316L, Heat 00630	0.018	47,525
316 SS, Heat M6985	0.065	36,500
316 SS, Heat 2P5801	0.052	52,000
316 SS, Heat M9965	0.057	51,000

D.2 Certifications

The test reports received from the manufacture are attached.

Tubular Products Division

ALLIANCE, OHIO-1 BEAVER FALLS, PA.-2 MILWAUKEE, WISCONSIN-3

TEST REPORT

CUSTOMER'S ORDER NO. 3 20- 5-92 52 DATE 11 4 75 CUSTOMER'S ORDER NO. 2100390

60-2838 316 55

CUSTOMERS TRUCK

SMLS B&W CROLOY 316 EF CD AW PIPE TO ASTM A 312-73 AND ASME SA 312

STEEL WAS MELTED IN THE USA

NO OIL PICKLED

ITEM	O.D.	WALL	LENGTH	SPECIAL MARKS	PCS	FOOTAGE	BURST TEST LBS PER SQ INCH	TESTS MADE
00935 0-361722 00035 091 10000								
01	4.500	.337	SL 17-24		32	723.25	2247 5 sec. hold	ETCH BEND FLATTENING ok FLANGE EXPANSION FLARE CORROSION RACING ULTRASONIC DYE PENETRANT

MIDCO PIPE & TUBE, INC.

THESE TEST REPORTS APPLY TO YOUR

PURCHASE ORDER 0249V1AA11

PIECES SHIPPED 2

FOOTAGE 11'-11" cut

ITEM	HEAT NO.	GAGE	DIAMETER	ECCENTRICITY	PROOF	ELONGATION IN 2"	GRADIENT	C	Mn	P	S	Si	Cr	Ni	Mo	Cu	Co	Cb	V	W	Ti	Al	B	Ca	Fe
	C8468	.057	1.54	.011	.025	.53	17.13	13.15	2.40																
	M9965	.057	1.42	.016	.020	.57	16.63	13.14	2.25																

ITEM	HEAT NO.	ULTIMATE STRENGTH	YIELD POINT	% ELONG IN 2"	REDUCT. IN AREA	HARDNESS
	C8468	85700	49900	55		
	M9965	89700	51700	55		

STAMP X STD BD FULL SECTION

SWORN TO AND SUBSCRIBED BEFORE ME 11-4-75

Alice J. [illegible] Notary Public
W. Mayfield Borough, Bea. County, Pa.
MY COMMISSION EXPIRES
OCT. 3, 1978

THIS IS TO CERTIFY THE ABOVE TUBES AND PIPE HAVE BEEN INSPECTED AND TESTED IN ACCORDANCE WITH AND HAVE MET ALL THE REQUIREMENTS OF THE SPECIFICATIONS.

[illegible]

COMMISSION EXPIRES

4. C8468 M9965

90014283

MIDCO Pipe & Tube Inc.

Houston, Texas Sales & Warehouse
12335 Almeda Road · 77045
Phone: 713-10 3-0331

P.O. Box 326 • 11500 W. Irving Park Road • Bensenville, Illinois 6
Phone 766-6000 • Chicago 921-1070 (312) • Telex 8-54077 TWX 910-756-

316 S.S.

CERTIFICATE OF TESTS

DATE May 6, 1976

CUSTOMER General Electric Company — ORDER OR CONTRACT NO. 529V0A11

CITY San Jose, CA. 95125 — OUR FILE C 60174 — DATE SHIPPED 4-13-76

ATTENTION: Mr. Velez

MATERIAL: WELDED ☐ SEAMLESS ☒ — HOT FINISHED ☐ COLD DRAWN ☒ — SPECIFICATION ASTM A-312 T-316 — MANUFACTURER

SHIPMENT: CONSIGNEE
DESTINATION

1) 4" Sch 80 (.337" wall) Stainless Steel Pipe 23'-10"
2)
3)
4)
5)
6)
7)
8)
9)

CHEMICAL ANALYSIS

	HEAT NUMBER	C	MN	P	S	SI	CR	MO	NI	TI	CB	CU		
1)	2P5801	.052	1.75	.027	.013	.54	16.84	2.23	13.37					
2)														
3)														
4)														
5)														
6)														
7)														
8)														
9)														

PHYSICAL TESTS

	HEAT NUMBER	TENSILE STRENGTH LBS PER SQ. IN.	YIELD STRENGTH LBS PER SQ. IN.	% ELONGATION IN 2 IN.	OTHER TESTS OR REMARKS
1)	2P5801	85,400	52,000	60.0	Hydrostatic & Flattening Tests OK
2)					
3)					
4)					
5)					
6)					
7)					
8)					
9)					

I HEREBY CERTIFY THAT THE HEAT NUMBERS, ANALYSES AND TESTS DETAILED HEREON, ARE CORRECT AS CONTAINED IN THE RECORDS OF THIS CORPORATION.

SIGNED Carol Fuller
MIDCO PIPE & TUBE, INC.

Form 91

Babcock & Wilcox

Tubular Products Division

ALLIANCE, OHIO-1 BEAVER FALLS PA-2 MILWAUKEE, WISCONSIN-3

TEST REPORT

F-807

NUC NUCLEAP
-09

MIDCO PIPE AND TUBE INC
11500 WEST IRVING PARK ROAD
BENSENVILLE, ILLINOIS 60106

STEEL WAS MELTED IN THE USA

SMLS CRO 316 EF CD AW PIPE TO ASTM 312-74 AND ASME SA-312
ASME SECTION III, 1974 ISSUE PLUS SUMMER ADDENDA 1974
CLASS 3 ARTICLE ND 2000.

NO OIL PICKLED

ITEM	O.D.	WALL	LENGTH	SPECIAL MARKS	PCS	FOOTAGE	HYDRO TEST LBS PER SQ. INCH	TESTS MADE
- 020179-2017220003509111000								ETCH
01	4.500	.337	PL 17/24				2250 5 sec. hold	BEND
								FLATTENING OK
								FLANGE
								EXPANSION
								FLARE
								CORROSION
								MICRO
								ULTRASONIC
								DYE PENETRANT

CORRECTED COPY - CHANGES DEPT. OF ... MFG. & FINISH CODE ... TO YOUR NOTED -- JBC 5/14/75.

PL...
PIECES SHIPPED ...
FOOTAGE ...

ITEM	HEAT NO	CARB	MANG	SUL	PHOS	SIL	CHROM	NI	MO	CU	C B	TI
	15985	.065	1.72	.014	.021	.52	17.07	13.58	2.44			
	check	.065	1.70	.014	.021	.50	17.18	13.30	2.36			

ITEM	HEAT NO	ULTIMATE STRENGTH	YIELD POINT	% ELONG IN 2	REDUCT IN AREA	HARDNESS
		81900	36500	63		

STRIP [X] STD RD [ ] FULL SECTION [ ]

SWORN TO AND SUBSCRIBED BEFORE ME 7/29/75

RITA J. PYLE, Notary Public
W. Mayfield Borough, Bvr. County, Pa.
MY COMMISSION EXPIRES
OCT. 3, 1978

COMMISSION EXPIRES

THIS IS TO CERTIFY THE ABOVE TUBES AND PIPE HAVE BEEN INSPECTED AND TESTED IN ACCORDANCE WITH AND HAVE MET ALL THE REQUIREMENTS OF THE SPECIFICATIONS.

VJ

THE BABCOCK & WILCOX COMPANY BY

SANDVIK

MATERIAL CERTIFICATE

SANDVIK, INC. SCRANTON, PA.
P.O. BOX 1220 SCRANTON, PA. 18501 PH. 717-587-5191
PLANT LOCATION INTERSTATE 81, WAVERLY EXIT 53

304 S7

25640	529-VOA35	5-18-76	7-29-76	671344	5/20/76	7/15/76	28220	6/17/
				SCRANTON PPC				
12	SC	91 SMITH	61300					2

SOLD TO:
KILSBY TUBE COMPANY
2077 PIKE AVENUE
SAN LEANDRO, CALIFORNIA 94577

SHIP TO:
KILSBY TUBE COMPANY
2077 PIKE AVENUE
SAN LEANDRO, CALIFORNIA

SPECIFICATION AND MATERIAL: ASME SA-376 40' 0"

SANDVIK SEAMLESS STAINLESS STEEL ANNEALED PIPE TYPE 304 4" SCH 80 40'1"

Analysis, %

Heat	C	Si	Mn	P	S	Cr	Ni	Mo
454970	.042	.33	1.09	.018	.012	18.1	10.1	

Mechanical Tests

Heat	Yield Str. psi	Tensile Str. psi	Elong. 2",%	Hydr. Pres. Test psi
454970	36,300 38,400	80,900 81,100	60 62	2390

FLATTENING TEST: OK

ON H: BAY

For Bengt H. Berg, Quality Assurance Manager

B. H. Berg (P-SA-2) ch

TEST REPORT — A. M. CASTLE & CO.

SOLD TO:	SHIPPED TO:
(: RAL ELEC CO APED 7?5 CURTNER AVENUE SAN JOSE CALIF 95125	SAME

CUST. ORDER NO.	Castle-Pacific Order No. 89709	SPECIFICATION NO.
205 J3R 03		ASTM A 312

ITEM NO. — MATERIAL

1 — 1 LOT — S/S T 316L WELDED PIPE 4" SCH 80 x 20' RDM

PHYSICALS

ITEM	HEAT NO.	YIELD POINT P.S.I.	TENSILE STRENGTH P.S.I.	% ELONG 2"	% RED AREA	BRINELL	ROCK-WELL	BEND TEST	MACRO	ENDURIT-MENT	IZOD IMPACT	OT
1	00630	47,525	83,250	47.0								
	HYDRO TEST: OK	FLATTENING TEST: OK										

CHEMICALS

ITEM	HEAT NO.	% C	% MN	% P	% S	% SI	% NI	% CR	% CU	% AL	% TI	% MG	% MO	% CO
1	00630	.018	1.68	.025	.003	.38	11.62	16.22					2.15	

(SIGNED AND SWORN TO BEFORE ME THIS
___ DAY OF _____ 19___
___ NOTARY PUBLIC
MY COMMISSION EXPIRES _____
IN AND FOR THE COUNTY OF _____,
STATE OF _____

I CERTIFY THAT THESE ARE CORRECT COPIES OF REPORTS NOW ON FILE AT

A. M. CASTLE & CO.

BY _____
SAN FRANCISCO ☒ LOS ANGELES ☐ SALT LAKE CITY ☐

11-25 CKM — 4" XH (80) A376 TP304

ALLIANCE OHIO — Tubular Products Division — LEAVETTSBURG PA. — MILWAUKEE, WISCONSIN

MAIN IMPORT — 11 26 75 11212382 — 304

cc: WAW

205 J5 P88-1
HR 245178

Material was given a heat treatment consisting of heating to a minimum of 1900°F for a minimum of 10 minutes and water quenched.

Both raw materials and finished products on this order have been produced in the USA.

SEAMLESS CROLOY 304 WITH .04 MIN C., E.F., CD, AU, PIPE TO ASTM A-376-74 AND ASME SA-376 PRODUCT ANALYSIS PER PARA 8

SSI
NO OIL PICKLED

WAS MELTED IN THE USA

ITEM	O.D.	WALL	LENGTH	SPECIAL MARKS	PCS	FOOTAGE	TESTS MADE
-	05 7925-201		2000350911	0000			
01	4.500	.337	42 2				2247 5 Sec. Hold
02	4.500	.337	RL 17-24				ETCH, BEND, FLATTENING OK, FLANGE, EXPANSION, FLARE, CONDUCTIVITY, MICRO, BLTN ANALYSIS, PMI

KIWI-Y J- 47541

APPROX 100' REC'D IN 17-24' LENGTHS

M0063	.051	1.71	.009	.025	.62	18.57	10.48
Tube Ck.	.049	1.73	.010	.025	.62	18.65	10.48
Tube Ck.	.051	1.71	.010	.025	.63	18.64	10.43

HEAT NO.	YIELD STRENGTH	TENSILE STRENGTH	ELONG. IN 2"	REDUCTION OF AREA	HARDNESS
	82300	98900	68		

Longitudinal Tensile Specimen

SPECIAL [X] STD NO [ ] FULL SECTION [ ]

SWORN TO AND SUBSCRIBED BEFORE ME 11/28/75

THIS IS TO CERTIFY THE ABOVE TUBES AND PIPE HAVE BEEN INSPECTED AND TESTED IN ACCORDANCE WITH AND HAVE MET ALL THE REQUIREMENTS OF THE SPECIFICATIONS

ph

[illegible], Notary Public
[illegible] Borough, Bvr. County, Pa.
MY COMMISSION EXPIRES
Oct. 2, 1978

COMMISSION EXPIRES

ALLIANCE, OHIO-1 — BEAVER FALLS, PA.-2 — MILWAUKEE, WISCONSIN-3

TEST REPORT

4A05080 — 17 — 12/17/12-11/72

GUYON ALLOYS INC
950 S FOURTH ST
HARRISON NJ 07029

Material was given a heat treatment consisting of heating to a min of 1900°F for a min of 10 minutes & water quenched

STEEL WAS MELTED IN THE USA

SMLS CROLOY 304 EF CD AU PIPE TO ASTM A 312-73 & ASME SA 312 W/CK ANAL
2 PIPES EA LOT & HT PER PARA 8 OF ASTM A 312-73 AND 7 OF ASME SA 312

RECEIVED INSPECTION DEPT
3-2-75

AND OIL PICKLED & PASSIVATED

ITEM	ORDER NO. O.D.	WALL	LENGTH	SPECIAL MARKS	PCS.	FOOTAGE	HYDRO TEST LBS. AT PSI	TESTED MADE
	S040257-3617220003509110000							
01	4500	337	RL 17-24		32	656	2247	

APPROVED
AS
QC DEPT.
DATE 3/04/75
SIGNED

C.A. APPROVED
BY: [signature]
DATE 3/4/75
GUYON ALLOYS INC

HEAT NO.	C	MN	SI	P	S	CR	NI	MO
17616	.050	1.70	.012	.023	.55	18.60	10.34	
TUBE CK	.060	1.71	.012	.025	.53	18.65	10.41	
	.064	1.72	.012	.025	.54	18.61	10.42	
[illegible]								
TUBE CK	.057	1.67	.011	.023	.53	18.60	10.38	
	.058	1.69	.014	.028	.52	18.63	10.42	

HEAT NO.	ULTIMATE STRENGTH	YIELD POINT	% ELONG IN 2"	% AREA	HARDNESS
17616	83700	45000	58		CC-775
[illegible]	86100	40500	57		-76

STRIP [X] STD. RD [ ] FULL SECT. [ ]

SWORN TO AND SUBSCRIBED BEFORE ME 12/19/72

Job #18645

THIS IS TO CERTIFY THE ABOVE TUBES AND PIPE HAVE BEEN INSPECTED AND TESTED IN ACCORDANCE WITH AND HAVE MET ALL THE REQUIREMENTS OF THE SPECIFICATIONS.

THE BABCOCK & WILCOX COMPANY BY [signature]

RITA [illegible]
NOTARY PUBLIC
[illegible] COUNTY, FL
MY COMMISSION EXPIRES
COMMISSION EXPIRES OCT 1 1973

TUBULAR PRODUCTS DIVISION
BEAVER FALLS, PA.-2

ALLIANCE, OHIO-1

MILWAUKEE, WISCONSIN-1

TEST REPORT

4405060

GUYON ALLOYS INC
950 S FOURTH ST
HARRISON NJ 07029

NUCLEAR

Material was given a heat treatment consisting of heating to a min of 1900°F for a min of 10 minutes & water quenched

STEEL WAS MELTED IN THE USA

SMLS CROLOY 304 EF CD AU PIPE TO ASTM A 312-73 & ASME SA 312 W/CK ANAL
2 PIPES EA LOT & HT PER PARA 8 OF ASTM A 312-73 AND 7 OF ASME SA 312

RECONVEN INSPECTION CO.
3-21-75

NO OIL FICKLED & PASSIVATED

ITEM	O.D.	WALL	LENGTH	SPECIAL MARKS	PCS.	FOOTAGE	WEIGHT PER LIN. FT. AS ORDERED	WEIGHT MADE
E040257-3617200035C9110000								
01	4.500	.337	RL 17-24		32	656.61	2247	

APPROVED
ARDE
Q.C. DEPT.
DATE 2/25/75
SIGNED

Arde Pac Eng. Co.
4145-2 (2)

Q.A. APPROVED
BY: DATE 2/21/75
GUYON ALLOYS INC

ITEM	HEAT NO.	C	MN	P	S	SI	CR	NI	CU	CB	TI
	HT026	.050	1.70	.012	.003	.55	18.22	10.21			
	Tube CK	.050	1.71	.025	.025	.53	18.21	10.21			
		.050	1.76	.012	.026	.54	18.21	10.14			
17112		.058	1.87	.014	.028	.50	18.63	10.36			
	Tube CK	.057	1.83	.014	.030	.43	18.60	10.20			
		.058	1.83	.014	.028	.42	18.63	10.42			

ITEM	HEAT NO.	TENSILE STRENGTH	YIELD POINT	% IN 2"	% AREA	HARDNESS
15616	03500	85500	45000	58	77	B-775
17112	86100	84000	40500	57	82	B-776

STRIP [X] STD. OD [ ] FULL SECTION [ ]

SWORN TO AND SUBSCRIBED BEFORE ME 12/18/74

Tag #18645

RITA A. [illegible]
NOTARY PUBLIC
W. [illegible] COUNTY, FL
MY COMMISSION EXPIRES
COMMISSION EXPIRES OCT 1 1975

THIS IS TO CERTIFY THE ABOVE TUBES AND PIPE HAVE BEEN INSPECTED AND TESTED IN ACCORDANCE WITH AND HAVE MET ALL THE REQUIREMENTS OF THE SPECIFICATIONS.

dcs

THE BABCOCK & WILCOX COMPANY BY

APPENDIX E. TEST HISTORY OF THE FINAL SCREENING PIPE TESTS (IN PTL FACILITY)

E.1 WELDMENT E21A

Weld HAZ*	Description of Joint Fabrication Type	Test Results
A1	CRC overlay — SHT	No failure in test life**
A2	CRC overlay — SHT	No failure in test life
B1	CRC inlay — SHT	No failure in test life
B2	CRC inlay — SHT	No failure in test life
C1	Weld backlay	No failure in test life
C2	Weld backlay	No failure in test life
D1	Extended weld bevel	Failed in 177 cycles
D2	Extended weld bevel	Failed in 177 cycles
E1	CRC from licensee — SHT	No failure
E2	CRC from licensee — SHT	No failure
F1	CRC from licensee — SHT	No failure
F2	CRC from licensee — SHT	No failure
G1	Extended bevel	Failed in 267 cycles
G2	Extended bevel	Failed in 267 cycles
H1	Weld backlay	No failure in test life
H2	Weld backlay	No failure in test life
I1	CRC inlay — No SHT	No failure in test life
I2	CRC inlay — No SHT	No failure in test life
J1	CRC inlay — SHT	No failure in test life
J2	CRC inlay — SHT	No failure in test life
K1	CRC inlay — No SHT	Failed in 337 cycles (one HAZ only)
K2	CRC inlay — No SHT	No failure in test life
L1	CRC inlay — SHT	No failure in test life
L2	CRC inlay — SHT	

* Heat affected zone
** 435 test cycles to date

90014291

E.2 WELDMENT E21B

Weld HAZ*	Description of Joint Fabrication Type	Test Results
A1	316 SS pipe	No failure in test life**
A2	CF3 cast pipe	No failure in test life
B1	CF3 cast pipe	No failure in test life
B2	316 SS pipe (HT M6985)	No failure in test life
C1	316 SS pipe (HT M6985)	Failed in 1166 cycles
C2	316 SS pipe (HT 2D5801)	No failure in 1166 cycles
D1	316 SS pipe (HT 2D5801)	No failure in test life
D2	Extended bevel-304 SS (HT 70063)	No failure in test life
E1	Unprotected 304 SS (HT M0063)	Failed in 1794 cycles
E2	Unprotected 304 SS (HT 454970)	No failure in 1794 cycles
F1	Unprotected 304 SS (HT 454970)	No failure in 607 cycles
F2	Unprotected 304 SS (HT M0063)	Failed in 607 cycles
G1	Heat sink weld 304 SS (HT M0063)	No failure in test life
G2	Heat sink weld 304 SS (HT M7616)	No failure in test life
H1	Unprotected 304 SS (HT M7616) — prior SHT	Failed in 92 test cycles
H2	Replaced at 92 cycles with extended bevel repair	Failed in 169 test cycles
I1	Extended bevel (HT M7616) prior SHT	Replaced at 1328 test cycles***
I2	Type-316L SS (HT 00630)	No failure at 1328 test cycles
J1	Type-316L SS (HT 00630)	No failure in test life
J2	Type-347 SS (HT 88622)	No failure in test life
K1	Type-347 SS (HT 88622)	No failure in test life
K2	Type-304L SS (HT 00575)	No failure in test life
L1	Type-304L SS (HT 00575)	No failure in test life
L2	Type-316 SS (HT 482337)	No failure in test life

* Heat affected zone

** 2013 cycles to date at Max/min in. test stress of 1.36 × 288°C (550°F) yield strength of 304SS. HT M7616

*** Replaced prior to through wall failure (due to liquid penetrant indications and U.T. indications) for evaluation.

NOTE: Weld Heat Affected Zones C2, F1, and I2 were removed from the weldment without failing. This was necessitated by the failure of the opposite weld heat affected zone.

90014292

E.3 WELDMENT E19A*

Weld HAZ*	Description of Joint Fabrication Type	Test Results****
1A	Type-316 SS (end transition)	No failure at 585 cycles
1B	Unprotected Type-304 SS (HT M7616)*	Failed at 585 cycles
2A	Heat Sink weld**, Type-304 SS (HT M7616)	No failure in test life***
2B	Heat Sink weld, Type-304 SS (HT M7616)	No failure in test life
3A	Heat Sink weld, Type-304 SS (HT M7616)	No failure in test life
3B	Heat Sink weld, Type-304 SS (HT M7616)	No failure in test life
4A	Heat Sink weld, Type-304 SS (HT M7616)	No failure in test life
4B	Heat Sink weld, Type-304 SS (HT M7616)	No failure in test life
5A	Heat Sink weld, Type-304 SS (HT M7616)	No failure in test life
5B	Heat Sink weld, Type-304 SS (HT M7616)	No failure in test life
6A	Heat Sink weld, Type-304 SS (HT M7616)	No failure in test life
6B	Heat Sink weld, Type-304 SS (HT M7616)	No failure in test life
7A	Heat Sink weld, Type-304 SS (HT M7616)	No failure in test life
7B	Heat Sink weld, Type-304 SS (HT M7616)	No failure in test life
8A	Unprotected Type-304 SS (HT M7616)*	No failure in test life
8B	Unprotected Type-304 SS (HT M7616)	No failure in test life
9A	Unprotected Type-304 SS (HT M7616)	No failure in test life
9B	Unprotected Type-304 SS (HT M7616)	No failure in test life
10A	Unprotected Type-304 SS (HT M7616)	No failure in test life
10B	Unprotected Type-304 SS (HT M7616)	No failure in test life
11A	Unprotected Type-304 SS (HT M7616)	Failed at 556 cycles
11B	Unprotected Type-304 SS (HT M7616)	Replaced at 556 cycles
12A	Unprotected Type-304 SS (HT M7616)	Failed at 585 cycles
12B	Type-316 SS (end transition)	Replaced at 585 cycles

* All inner surface weld heat affected zones were ground and polished after the root pass.
** Automatic GTA weld in 2G position with following water inner surface cool after root pass.
*** 1397 test cycles in December 1978.
**** Tested at 1.36 × 550°F yield strength of HT M7616.

NOTE: Welds 1 and 12 replaced by manual heat sink welds, and Weld 11 was replaced with a "backlay" joint.

90014293

E.4 WELDMENT E20A*

Weld HAZ	Description of Joint Fabrication Type	Test Results****
1A	Type-316 SS End transition	Replaced at 1034 cycles
1B	Unprotected Type-304 SS (HT M7616)*	Failed at 1034 cycles
2A	Heat Sink weld**, Type-304 SS (HT M7616)	No failure in test life***
2B	Heat Sink weld, Type-304 SS (HT M7616)	No failure in test life
3A	Heat Sink weld, Type-304 SS (HT M7616)	No failure in test life
3B	Heat Sink weld, Type-304 SS (HT M7616)	No failure in test life
4A	Heat Sink weld, Type-304 SS (HT M7616)	No failure in test life
4B	Heat Sink weld, Type-304 SS (HT M7616)	No failure in test life
5A	Heat Sink weld, Type-304 SS (HT M7616)	No failure in test life
5B	Heat Sink weld, Type-304 SS (HT M7616)	No failure in test life
6A	Heat Sink weld, Type-304 SS (HT M7616)	No failure in test life
6B	Heat Sink weld, Type-304 SS (HT M7616)	No failure in test life
7A	Heat Sink weld, Type-304 SS (HT M7616)	No failure in test life
7B	Heat Sink weld, Type-304 SS (HT M7616)	No failure in test life
8A	Unprotected Type-304 SS (HT M7616)*	No failure in test life
8B	Unprotected Type-304 SS (HT M7616)	No failure in test life
9A	Unprotected Type-304 SS (HT M7616)	Replaced at 862 cycles
9B	Unprotected Type-304 SS (HT M7616)	Failed at 862 cycles
10A	Unprotected Type-304 SS (HT M7616)	No failures in test life
10B	Unprotected Type-304 SS (HT M7616)	No failure in test life
11A	Unprotected Type-304 SS (HT M7616)	Failed at 391 cycles
11B	Unprotected Type-304 SS (HT M7616)	Replaced at 391 cycles
12A	Unprotected Type-304 SS (HT M7616)	No failure in test life
12B	Type-316 SS end transition	No failure in test life

* Inner surfaces ground and polished after root pass.
** Automatic GTA weld in 2G position with flowing water inner surface cool after root pass.
*** 1100 Test Cycles
**** Tested at 1.10 x 288°C (550°F) yield strength of HT M7616.

NOTE: Welds 1 and 9 were replaced by re-beveling and manual heat sink welding after cutting out the failed weld weld 11 was cut out and replaced by a splice section (HT M0063) which involved two manual heat sink welds.

90014294

E.5 WELDMENT E19B*

Weld HAZ*	Description of Joint Fabrication Type	Test Results****
1A	Type-316 SS end transition	Did not fail (replaced)
1B	Unprotected Type-304 SS (HT M7616)*	Failed at 106 cycles
2A	Heat Sink Weld**, Type-304 SS (HT M7616)	No failure in test life***
2B	Heat Sink Weld, Type-304 SS (HT M7616)	No failure in test life
3A	Heat Sink Weld, Type-304 SS (HT M7616)	No failure in test life
3B	Heat Sink Weld, Type-304 SS (HT M7616)	No failure in test life
4A	Heat Sink Weld, Type-304 SS (HT M7616)	No failure in test life
4B	Heat Sink Weld, Type-304 SS (HT M7616)	No failure in test life
5A	Heat Sink Weld, Type-304 SS (HT M7616)	No failure in test life
5B	Heat Sink Weld, Type-304 SS (HT M7616)	No failure in test life
6A	Heat Sink Weld, Type-304 SS (HT M7616)	No failure in test life
6B	Heat Sink Weld, Type-304 SS (HT M7616)	No failure in test life
7A	Heat Sink Weld, Type-304 SS (HT M7616)	No failure in test life
7B	Heat Sink Weld, Type-304 SS (HT M7616)	No failure in test life
8A	Unprotected Type-304 SS (HT M7616)*	Failed at 97 cycles
8B	Unprotected Type-304 SS (HT M7616)	Failed at 97 cycles
9A	Unprotected Type-304 SS (HT M7616)	Failed at 98 cycles
9B	Unprotected Type-304 SS (HT M7616)	Failed at 98 cycles
10A	Unprotected Type-304 SS (HT M7616)	Failed at 94 cycles
10B	Unprotected Type-304 SS (HT M7616)	Failed at 94 cycles
11A	Unprotected Type-304 SS (HT M7616)	Failed at 68 cycles
11B	Unprotected Type-304 SS (HT M7616)	Failed at 68 cycles
12A	Unprotected Type-304 SS (HT M7616)	Failed at 106 cycles
12B	Type-316 SS end transition	Replaced at 106 cycles

* Inner surfaces at the HAZ were not ground and polished (as machined counterbore).
** Automatic GTA weld in 2G position with flowing water inner surface cool after root pass.
*** Test cycles to date — 863 (Dec. 1978)
**** Tested at 1.36 × 288°C (550°F) yield strength of Heat M7616.

NOTE: Weld 8 replaced by a standard girth weld which was "skin" fused by GTAW after girth weld at the inner joint surface to "recondition" the critical HAZ. Welds 9–12 were removed and a CF3 splice pipe inserted by manual HSW practice.

90014295

E.6 WELDMENT E20B*

Weld HAZ	Description of Joint Fabrication Type	Test Results****
1A	Type-316 SS End Transition	Did not fail — replaced
1B	Unprotected Type-304 SS (HT M7616)*	Failed at 896 cycles
2A	Heat sink weld, Type-304 SS (HT M7616)	No failure in test life***
2B	Heat sink weld, Type-304 SS (HT M7616)	No failure in test life
3A	Heat sink weld, Type-304 SS (HT M7616)	No failure in test life
3B	Heat sink weld, Type-304 SS (HT M7616)	No failure in test life
4A	Heat sink weld, Type-304 SS (HT M7616)	No failure in test life
4B	Heat sink weld, Type-304 SS (HT M7616)	No failure in test life
5A	Heat sink weld, Type-304 SS (HT M7616)	No failure in test life
5B	Heat sink weld, Type-304 SS (HT M7616)	No failure in test life
6A	Heat sink weld, Type-304 SS (HT M7616)	No failure in test life
6B	Heat sink weld, Type-304 SS (HT M7616)	No failure in test life
7A	Heat sink weld, Type-304 SS (HT M7616)	No failure in test life
7B	Heat sink weld, Type-304 SS (HT M7616)	No failure in test life
8A	Unprotected Type-304 SS (HT M7616)	Failed in 643 cycles
8B	Unprotected Type-304 SS (HT M7616)	Failed in 643 cycles
9A	Unprotected Type-304 SS (HT M7616)	Failed in 538 cycles
9B	Unprotected Type-304 SS (HT M7616)	Failed in 538 cycles
10A	Unprotected Type-304 SS (HT M7616)	Failed in 887 cycles
10B	Unprotected Type-304 SS (HT M7616)	Failed in 887 cycles
11A	Unprotected Type-304 SS (HT M7616)	Failed at 435 cycles
11B	Unprotected Type-304 SS (HT M7616)	Failed at 435 cycles
12A	Unprotected Type-304 SS (HT M7616)	No failure in test life
12B	Type-316 SS End Transition	No failure in test life

* Inner surfaces at the weld HAZ were not ground and polished (as machined counterbore).
** Automatic GTA weld-2G position with flowing water inner surface cool after the root pass.
*** 954 test cycles.
**** Tested at 1.10 × 288°C (550°F) yield strength of HT M7616.

NOTE: Weld 9 was replaced by an automatic HSW and the other failed joints by manual HSW.

90014296

APPENDIX F. INITIAL HEAT SINK WELD PIPE TEST

F.1 INTRODUCTION

The third full-size cyclic intergranular stress corrosion cracking pipe test was designed to test exclusively the heat sink welding pipe remedy. The welded pipe was fabricated by joining eight 10.16-cm (4-in.) long 10.16-cm (4-in.) diameter schedule 80 pipe segments of Type-304 stainless steel as shown in Figure F-1.

This full-size-pipe test was performed to explore potential benefits to be derived from heat sink welding of Type-304 stainless steel pipe. Prior laboratory work at General Electric on inside surface water cooled Type-304 stainless steel pipe welds indicated that inside surface water cooling reduced the time that weld heat affected zones spent in the sensitizing temperature range. This third Large Environmental Fatigue Test Facility test was designed to explore the benefits indicated in the laboratory tests.

F.2 MATERIALS

The test welds were fabricated from Heat M7616 Type 304 stainless steel piping, which had failed readily in the second Large Environmental Fatigue Test Facility cyclic tension test (as welded pipe) in both the ground and unground conditions and at both high and low heat input welds

F.3 FABRICATION

Pre- and post-weld grinding was applied to quadrants of each weld. The weld fabrication description and summary of fabrication treatments are presented in Figure F-2.

F.4 DESCRIPTION AND HEAT SINK COOLING PROCEDURE

The inside surface cooling procedure for the heat sink welds originates from prior General Electric laboratory tests. A description of this technique as applied to this weldment follows:

F.4.1 Heat Sink Weld Description

The heat sink welding practice used to prepare this welded pipe did not include any cooling of the root layer, other than the normal gas back purging. Subsequent weld passes were water spray cooled on the inside surface using the following procedure:

- A 2.54-cm (1-in.) outer diameter spray nozzle was fabricated from galvanized pipe.
- At the pipe end 16 holes, each 0.16-cm (1/16-in.) in diameter were drilled in an equally spaced pattern.
- A water flow rate of 2 gpm (0.15 l/sec) was employed for spray cooling. This was obtained by use of a regulator providing 9 psi (0.0063 kg/mm^2) water pressure.
- The spray nozzle was inserted in the pipe a correct distance to completely cover the weld area with water spray.
- The pipe was rotated during welding while the welder added filler metal at the 12 o'clock position (1 g).

It was possible to visually observe the pipe inside surface during this operation and a momentary bright red color was visible in the area under the weld arc. However, the outside surface temperature of the weld immediately after welding was approximately 21°C (70°F). Standard-heat-input welds were limited to 40,000 J/in. (15,750 J/cm). The welding procedures for the reference Type-304 stainless steel welds were similar except no i.d. cooling was involved.

F.4.2 Description of Third Cyclic Tension Test in the Large Environmental Fatigue Test Facility

The third cyclic intergranular stress corrosion cracking pipe test was performed in the Large Environmental Fatigue Test Facility using the same cyclic loading conditions, water chemistry, and test temperature as described in the generalized test procedure for the Large Environmental Fatigue Test Facility tests. The maximum load applied to this pipe was 136% of the Type-304 stainless steel yield strength at test temperature. The test consisted of one phase which lasted 122 test cycles (183 hours) when a through-wall leak developed in the heat affected zone of one of the reference welds. Subsequent ultrasonic testing and liquid penetrant examination revealed cracks in 14 of the 16 Type-304 stainless steel weld heat affected zones (8 of 8 reference and 6 of 8 inside-surface-cooled-weld heat affected zones). No cracking was observed in the two Type-316 stainless steel weld heat affected zones. A post-test examination including macro and micro photography was instituted to identify the extent of cracking and the fracture morphology of the last welds.

F.4.3 Post-Test Nondestructive Testing and Metallurgical Examination

The nondestructive examination of the test weldment used in the third test included acoustic emission monitoring of cracking noise during this test and ultrasonic examination of the test welds before and after the test. The acoustic emission monitoring program was performed in hope that one could discern a recognizable pattern which would provide useful information regarding the onset of crack initiation and crack propagation rates as well as predicting specimen failure.

The ultrasonic post test inspection identified crack indications in 15 of the 16 welds. The indications ranged from multiple cracks extending 360 degrees around the pipe (as shown in unprotected weld heat affected zones A2, D1, and I1), to small indications of 1.27-cm (1/2-inch) in length (as presented in heat sink weld heat affected zone F2). A schematic display of the ultrasonic test results is presented in Figure F-3 along with the welding and grinding specimen details.

Following the ultrasonic examination, the pipe was cut axially into two halves and liquid red dye penetrant measurements were performed on the inside surface of the pipe to confirm the findings of the posttest ultrasonic examination of the pipe. The penetrant indications on the pipe confirmed the ultrasonic test indications and revealed cracks in 14 of the 16 heat affected zones in the welded pipe. These heat affected zones included all eight of the reference heat affected zones and six of eight of the heat-sink-welded heat affected zones. No cracking was found in the two Type-316 stainless steel heat affected zones. A schematic summary of the liquid penetrant indications is also presented in Figure F-3. The results are nearly identical to those presented in the ultrasonic test summary, as shown in Figure F-3. The only discrepancies occurred in the heat sink welds E2 and F2 where small-amplitude ultrasonic test indications were observed which were not confirmed by liquid penetrant.

It is noteworthy that the cracking in the six heat affected zones of the heat sink welds is almost exclusively associated with post-weld grinding. Only in weld heat affected zone E1 does the cracking appear to extend appreciably beyond the post-weld ground region and the weld-E is a high-heat-input weld. Another observation is that the cracking is much more extensive in the reference Type-304 stainless steel welds with eight out of eight heat affected zones cracked and the cracking generally extends into the unground and ground welding regions as well as being on the post-weld ground pipe surface. Table F-1 summarizes the dramatic difference in degree of cracking between the reference and heat sink welds when measured on a quadrant-by-quadrant basis. It appears clear that almost all (if not all) of the cracking in the heat sink weldments was associated with post-weld grinding. Post-weld grinding typically introduces high tensile residual stresses on Type-304 stainless steel piping surfaces. This post-weld grinding procedure probably overwhelmed the more favorable stress state which existed following heat sink welding, thus providing a condition of initiation of intergranular stress corrosion cracking. These results show the dominant effect of state of surface stress on the intergranular stress corrosion cracking susceptibility of Type-304 stainless steel in this environment. The differences in the extent of intergranular stress corrosion cracking between the heat sink welds and the reference welds are shown in Figures F-3 and F-4. Heat sink welds G and H are shown at 3X magnification on the pipe inside surface. The linear crack indications in the ground regions in the heat affected zone of each weld can be observed (wtih the aid of liquid penetrant). The cracks are exclusively associated with the grinding and are very

tight. One was unable to see the cracks visually without the aid of liquid penetrant. A section through one of the cracks in the heat affected zone of weld H identified the crack as an intergranular stress corrosion crack with a depth of approximately 1 millimeter (40 mils).

Table F-1
HEAT AFFECTED ZONE CRACKING COMPARISON BETWEEN REFERENCE AND HEAT SINK WELDS OF TYPE-304 STAINLESS STEEL (LIQUID PENETRANT RESULTS)

Surface Condition	HAZ* Quadrants Cracked/Total HAZ* Quadrants Reference Welds	Heat Sink Welds
Ground Before Butt Welding	4/8	0/8
Ground After Butt Welding	8/8	6/8
Unground	13/16	1/16

*HAZ—Heat Affected Zone

Figure F-5 shows the extent of cracking in welds B, C, and D which are reference unprotected Type-304 stainless steel welds. Cracking is seen to occur in both ground and unground sections in the weld heat affected zone. As evidenced by the amount of red dye observed in Figure F-5, the cracks are rather open and deep. No metallography was performed for any of the reference pipe cracks as one crack penetrated the outside surface and leaked. Further, the results of the second Large Environmental Fatigue Test Facility test clearly identified this cracking mode as intergranular stress corrosion cracking.

F.5 CONCLUSIONS

The results of the third Large Environmental Fatigue Test Facility cyclic tension test resulted in the following conclusions:

1. Acoustic emission is not yet well enough understood to be used as an on-line nondestructive test discriminator of intergranular stress corrosion cracking in stainless steel piping systems.

2. Heat sink welding appears to improve the resistance of Type-304 stainless steel to intergranular stress corrosion cracking in pipe tests in the absence of post-weld grinding.

3. Post-weld grinding of Type-304 stainless steel weld heat affected zones is a strong accelerant to intergranular stress corrosion cracking. Pre-weld grinding has less effect.

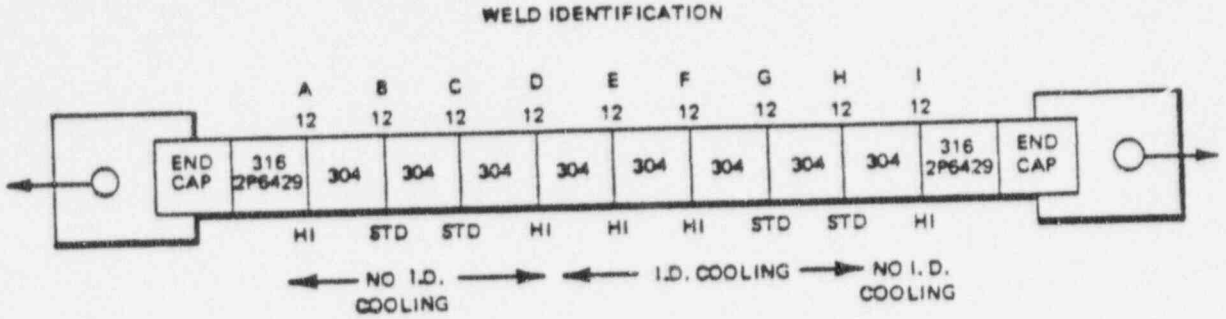

NOTES:

1. WELD HEAT INPUT
   - HI ≃ 70,000 J/in. (27,560J/cm)
   - STD ≃ 40,000J/in. (15,750J/cm)
2. GRINDING DETAILS ALL TEST WELDS A THROUGH I
   - 0 - 90° GRIND PRIOR TO WELDING
   - 90 - 180° NO GRINDING
   - 180 - 270° GRIND AFTER WELDING
   - 270 - 360° NO GRINDING
3. ALL TYPE-304 STAINLESS STEEL FROM HEAT M7616 (THE MOST SUSCEPTIBLE HEAT)

Figure F-1. Test Configuration, Third Cyclic Tension Test in Large Environmental Fatigue Test Facility

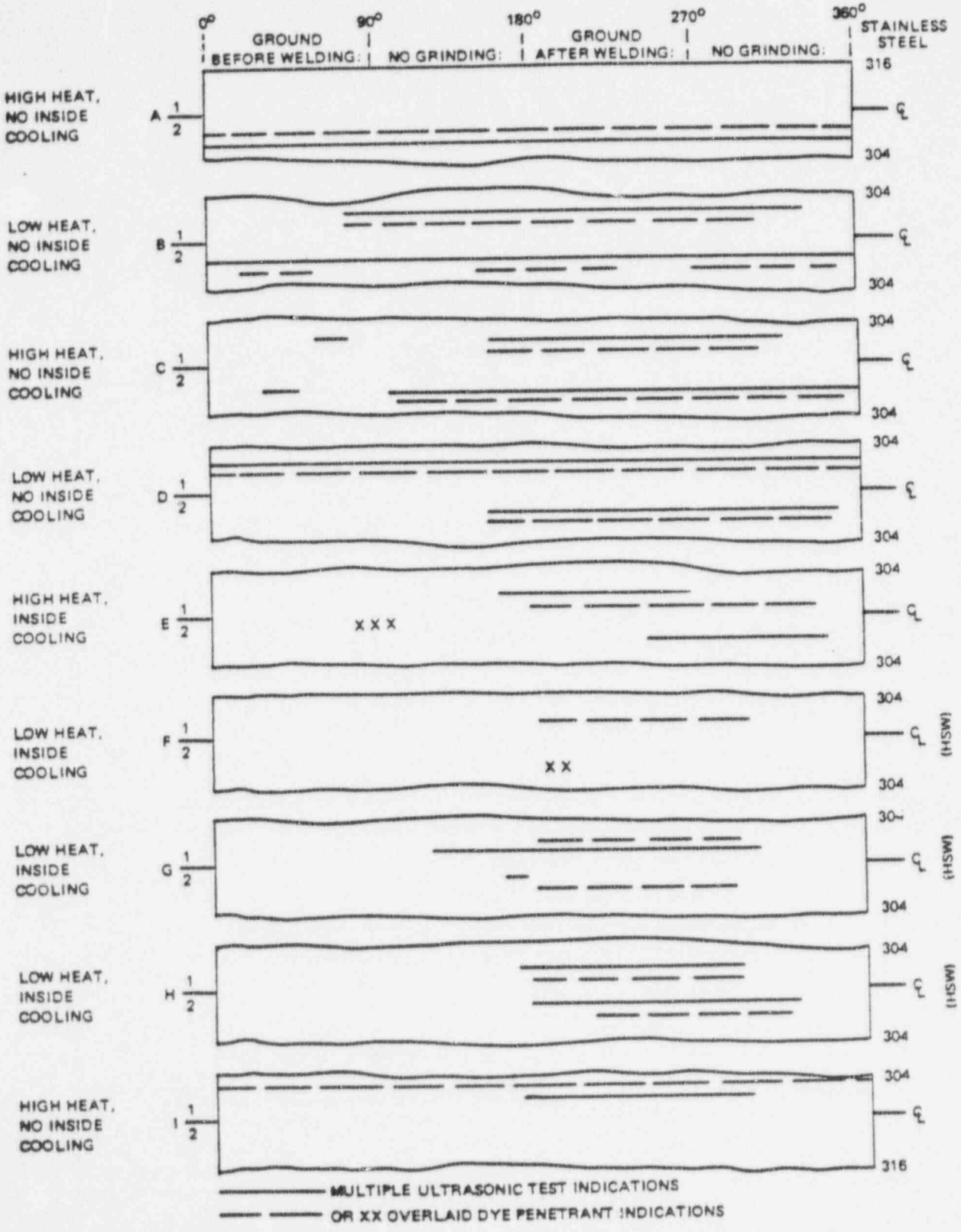

Figure F-2. Ultrasonic Inspection and Liquid Penetrant Results for Third Cyclic Tension Test in Large Environmental Fatigue Test Facility

17

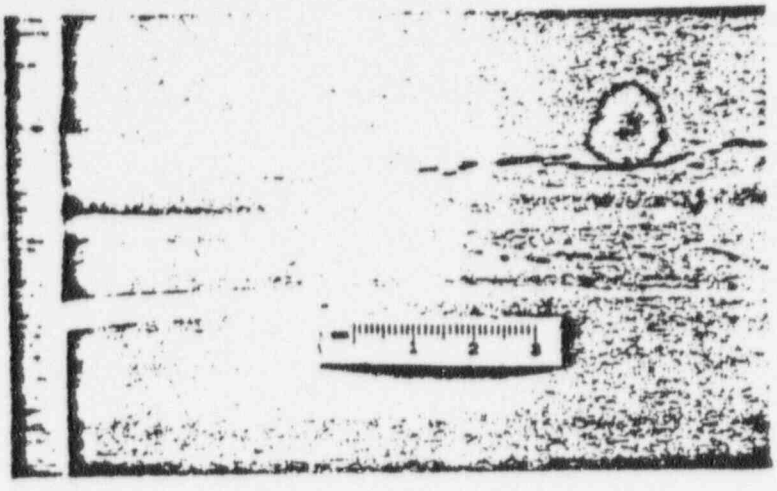

WELD G

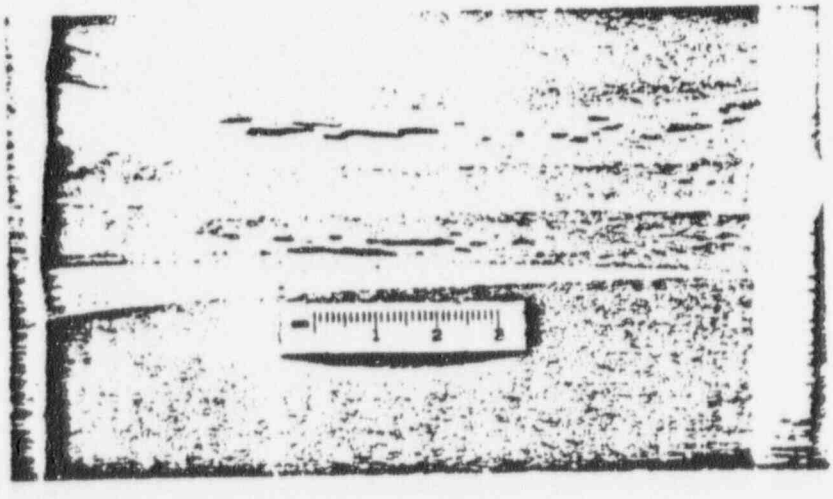

WELD H

Figure F-3. Heat Sink Welds Showing Cracking on Inside Surface

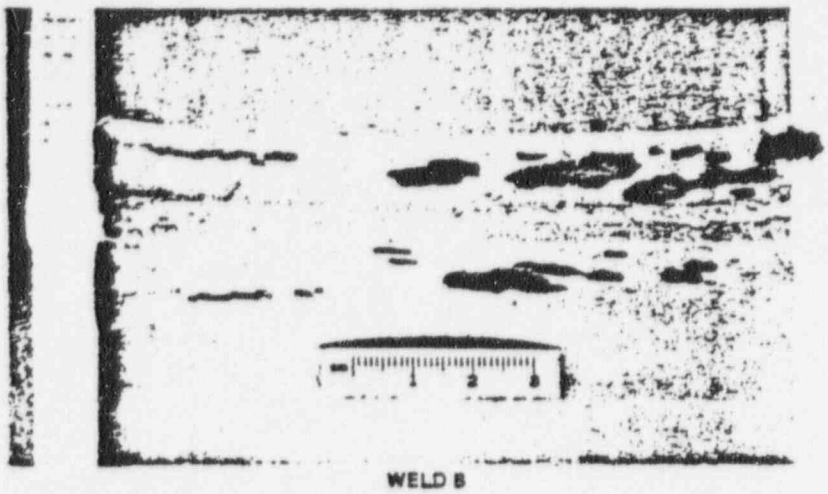

WELD B

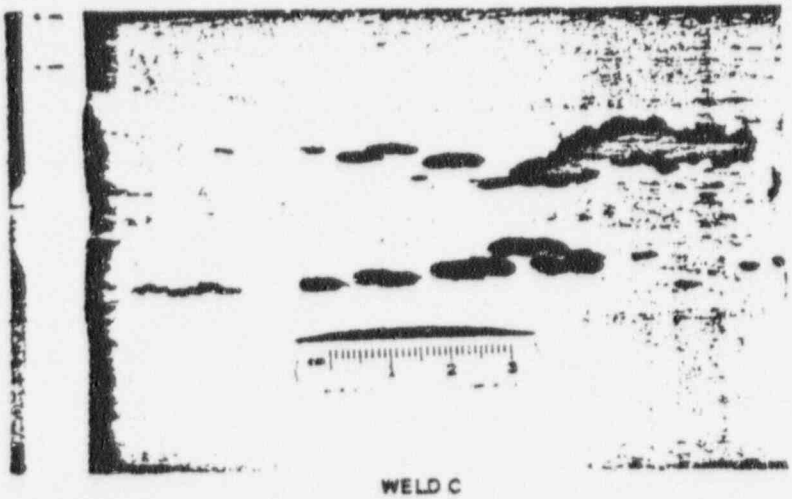

WELD C

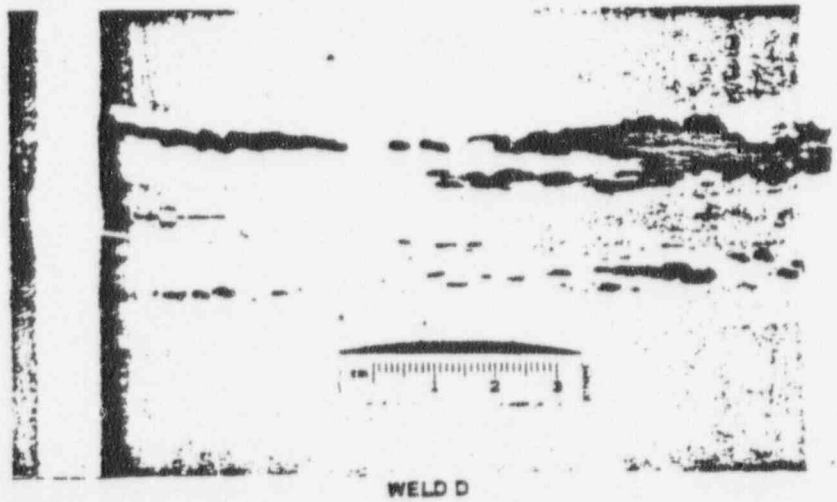

WELD D

Figure F-4. Reference Unprotected Welds Showing Evidence of Cracking

APPENDIX G. HEAT SINK WELD SCREENING TESTS (EXCERPTS FROM CONTRACT QUARTERLY REPORTS)

G.1 INTRODUCTION

A total of four pipe weldments, each containing 12 test welds, were fabricated for this test program by Bechtel Corporation using a machine welding technique. The fabrication details for these pipe weldments and recommended welding procedures for field welding were presented in the Second Semiannual Progress Report (NEDC-21463-2). The test weldment fabrication information is presented in the attached Table G-1 and Figure G-1. Two of the four pipes (E19A and E19B), each containing six reference and six heat sink welds, were initially placed on test in the axial CL4 Test Loop. The remaining two pipes (E20A and E20B) along with E19A and E19B were later placed on test in the "PTL" when it became operational. The designation "A" for each pipe specimen means that the weld HAZs were ground and polished after the root pass. Designation "B" means that the weld HAZs were tested in the as-machined condition.

Table G-1
HEAT SINK WELDMENTS—10.16 cm DIAMETER SCHEDULE 80 PIPE[4]

Bechtel Identification Number	EPRI Identification Number	Pipe Test Maximum Load Level	Test Joint Types[1,2,3] Reference Welds Joints 1 and 8 through 12	Heat Sink Welds Joints 2 through 7
A-1 to A-12	E19-A	1.36σ	6	6
A-1 to B-12	E20-A	1.10σ	6	6
C-1 to C-12	E19-B	1.36σ	6	6
D-1 to D-12	E20-B	1.10σ	6	6

NOTES
1. All welds made in the 2G position.
2. Each weld was made with a fully automatic pipe welder.
3. All weld deposits were made by the GTAW process.
4. Type-304 SS pipe, Heat No. M7616.
5. Specific data for passes not located—Joules/inch × 1000.
6. Heat-sink welding began after deposition of the root pass.

Reference
Bechtel Bi-Monthly
Report No. 6, Job No. 11789

Ground and Polished Inside Diameter After Root Pass	Weld Heat Input[5] Root Pass Reference	Root Pass HSW[6]	Others Reference	Others HSW[6]
Yes	—	19.5 K	—	32.3 K
Yes	—	19.5 K	—	32.3 K
No	—	19.5 K	—	32.3 K
No	—	19.5 K	—	32.3 K

G.2 APPLICATION OF INSIDE SURFACE HEAT SINK WELDING CONTROL DURING WELDING

Field and laboratory intergranular stress corrosion cracking data reveal that high tensile residual welding stresses coupled with the applied stresses plus weld sensitization provide conditions for intergranular stress corrosion cracking of Type-304 stainless steel in the Boiling Water Reactor environment. If a pipe can be welded without producing a significant sensitized structure and high residual tensile stresses in the weld heat affected zone, the resultant component should be resistant to intergranular stress corrosion cracking in the Boiling Water Reactor environment. The inside surface heat sink welding program is directed to the development and qualification of procedures that change the state of surface residual welding stresses from tension to compression, and reduce the

sensitization produced on the inside surface of welded pipe. This approach is proposed for shop or field applications where either post weld solution heat treatment or the use of a corrosion resistant cladding are not practical.

Laboratory Type-304 stainless steel butt welds have been produced by General Electric licensees evaluating the inside surface heat sink welding techniques. It has been found that inside surface residual stress in the critical HAZ area is changed from tension to compression as a result of this approach.

The inside surface heat sink welding can be performed using flowing or turbulent water, or water spray cooling of the inside surface by means of various arrangements. In all cases the water cooling is not applied during the initial root weld layer deposit. The weld is fabricated with normal field welding practice but with the addition of the inside surface water cooling following the initial root pass or passes.

G.3 DESCRIPTION OF HEAT SINK WELDING PIPE TESTS

The environmental and mechanical testing conditions used for the heat sink welded pipe (Weldments E19A and E19B) are basically the same as the test conditions described for other pipe remedy screening tests. The two pipe weldments were load cycled in the CL4 Test Facility at a frequency of 0.67 cycles/hr to a maximum tensile stress of 136% of the Type-304 stainless steel 288°C (550°F) yield strength in 8 ppm oxygen high purity water for pipes E19A and E19B. Weldments E20A and E20B were loaded to a maximum tensile stress of 110% of the Type-304 stainless steel 288°C (550°F) yield strength in the PTL at a frequency of 0.7 cycles/hr.

Following 68 cycles and 102 hours on test, a throughwall failure occurred in pipe E19B in reference weld 11 (see Figure G-1 for weld location). Visual observation of the pipe at that date confirmed probable cracking in reference welds 8, 9 and 10. Ultrasonic examination of the remaining welds confirmed possible crack indications in reference welds 1, 8, 9 and 10. Post-test examination confirmed the failure in weld 11 to be intergranular stress corrosion cracking. No ultrasonic indications were observed in any of the heat sink welds.

Following the removal of pipe E19B, the companion pipe (E19A) continued on test for an additional 94 cycles (162 cycles total) until a loop shutdown provided the opportunity to remove the pipe for ultrasonic examination. This examination, performed following 162 cycles and 243 hr on test detected significant crack indications in three of the reference welds of pipe E19A, welds 1, 8 and 11. No ultrasonic indications were detected in any of the heat sink weld HAZs.

Weld joint 11 in heat sink welded pipe E19B was removed and replaced by a splice involving two manual heat sink welds. This pipe and the companion pipe (E19A) were returned to test.

Following an additional 26 cycles on test (188 total), pipe E19B suffered a throughwall failure in reference weld 10. The pipe weldment was removed from test and an ultrasonic examination was performed on all weld HAZs of pipe E19B. Significant ultrasonic indications were observed in the remaining reference weld HAZs: (Welds 1, 8, 9 and 12). No indications were observed at any of the original heat sink welds nor for the manual heat sink welded pipe repair splice (with 26 test cycles).

Meanwhile, the companion pipe weldment E19A accumulated a total of 188 cycles and 282 hours on test. It was removed from test and both pipes, pipe weldment E19A as well as pipes E20A and E20B, were given a final checkout prior to transfer to the PTL for continued testing.

At this point, the modified CL4 Test Loop was decommissioned and all future axial pipe testing was transferred to the new pipe test facility, capable of handling 36 weldments simultaneously in each of two loops.* Several reference weld failures have occurred in the four Bechtel-prepared pipe weldments since the pipes were placed on test in the PTL. A summary of the reference weld failures is presented in Table G-2. All repairs with the exception of the repaired Weld E19B-8 were performed using manual heat sink welding techniques. The repair to weld E19B-8 will be discussed elsewhere since it was not a heat sink weld repair.

*One loop of Type-316 stainless steel and one loop of Inconel-600.

It is noteworthy that no failures or ultrasonic indications have been detected in the original heat sink welds in these four pipe specimens. This observation does not include those welds repaired by manual welding. In view of the extended test cycles the weldments have received and in view of the number of failures or ultrasonic crack indications for the reference welds, the heat sink weld technique has demonstrated a significant improvement in resistance to IGSCC.

One manual heat sink weld repair (E19B-11A) failed in testing and the failed location is undergoing examination to determine the cause of failure. This manual HSW replaced reference weld E19B-11 after the reference weld failed at 68 test cycles.

Table G-2
REFERENCE WELD PIPE TEST RESULTS

Pipe-Weld	Stress (% of 288°C Yield)	Failure Summary Time (hours)	Failure Summary Cycles	Failure Description
1. E19B-11	136	92	68	IGSCC in weld HAZ
2. E19B-10	136	141	94	IGSCC in weld HAZ
3. E19B-8	136	150	97	IGSCC in weld HAZ
4. E19B-9	136	150	97	IGSCC in weld HAZ
E19A	136	377*	254*	Specimen overload (No Failure)
5. E19A-11	136	807	556	IGSCC in weld HAZ
6. E20A-11	110	529	371	IGSCC in weld HAZ
7. E20B-11	110	620	435	IGSCC in weld HAZ
8. E20B-9	110	838	538	IGSCC in weld HAZ

*Solenoid valve lead resulted in unintentional specimen overload. Ultrasonic examination following specimen removal showed no crack indications in heat sink welds. Decision was made to return pipe to test.

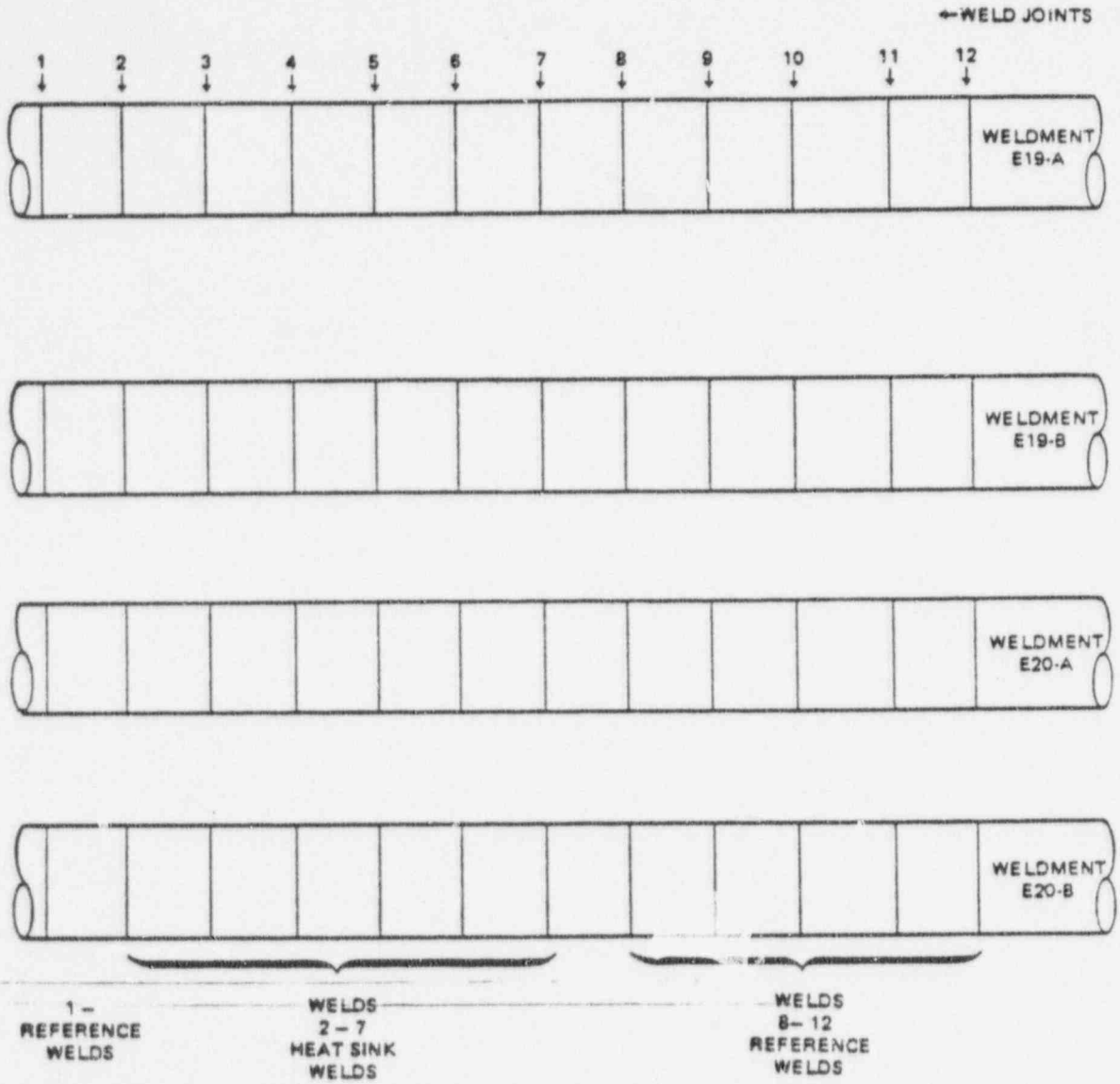

NOTES:
- WELDMENTS E19-A AND E20-A WERE GROUND AND POLISHED ON THE INSIDE SURFACE AFTER ROOT PASS WELDING AND PRIOR TO THE HEAT SINK WELD PASS DEPOSITION
- WELDMENTS E19-B AND E20-B WERE NOT GROUND AND POLISHED ON THE INSIDE SURFACE AFTER ROOT PASS WELDING
- E19 WELDMENTS: MAXIMUM TEST LOAD STRESS – 1.36 x 288°C YIELD
- E20 WELDMENTS: MAXIMUM TEST LOAD STRESS – 1.10 x 288°C YIELD

Figure G-1. Bechtel Fabricated Heat Sink Weldments (Fully Automatic-2G Position — Type-304 Stainless Steel Pipe)

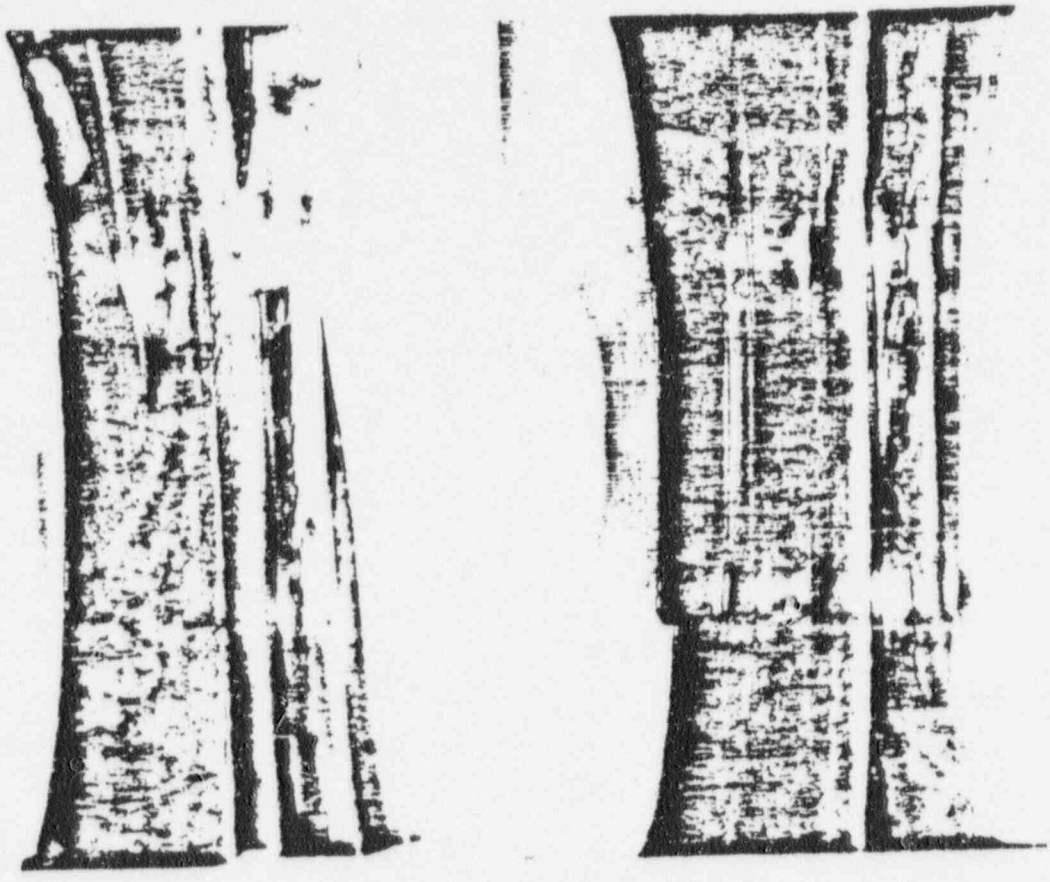

Figure G-2. Heat Sink Weld Pipe Specimen E19B (Weld II), Showing Extent of Cracking in Machined Surfaces of Reference Weld or Weld Heat Affected Zones

APPENDIX H. BACKLAY PRACTICES

Two backlays* sent from the General Electric Corporate Research and Development Center were included in screening tests. A fabrication summary of these welds follows:

Fabrication Summary:

Pipe Butt Joint—Made similar to NEED* developed procedures.
—G.T.A.W. of Grinnel insert (9FN Ferrite, Magnagage)
—G.T.A.W. of 1st fill pass (9FN Ferrite, Magnagage)
—S.M.A.W. of 2nd and 3rd fill passes

Backlay—Made in three layers, using short longitudinal beads. A ¼" thick x 3" wide weld backlay was deposited. This deposit was water-spray quenched on the I.D. during welding.

All three layers were deposited by shielded metal arc welding (11.4 Ferrite, Magnagage).

H.1 MATERIALS:

H.1.1 Test Pipe

10.16 cm (4 m.) diameter schedule 80 Type-304 stainless steel Heat M7616.

H.1.2 Filler Metals

1 Grinnel Insert, E.R. -308L, Heat Arcos-73797, 1/16" x 3/16" cross-section, Ferrite content 9FN as deposited.

2 GTAW wire, E.R. -308L, Heat C3203R, 3/32"ϕ, 9FN as deposited (Arcos).

3 SMAW rods, E308L-16 A.C., D.C., McKay, Heat 336153, Lot 2567907, A.W.S., A5.4-69; ASME SFA5.4, Ferrite content NEED 11.4 FN (Magnagage).

NOTE: Samples 59 and 60 were both machined per NEED drawing (std weld prep.). It was later decided that one set of pipes should be given a heat treatment of 530°C (1950°F) for ½ hour in an argon atmosphere, then water-quenched (10 seconds max./min. time from furnace to H_2O). Sample 59 was heat-treated in this manner. To clean off the surface oxide, the parts were pickled in 30% nitric acid, 5% Hydrofluoric acid and 65% H_2O. Surface appearance was not 100% bright after pickling but fair.

H.2 FABRICATION OF GIRTH WELDS

Welding Details:
Process, Gas Tungsten Arc used for Tack Welding—Grinnel Insert Root Fusion—Second Layer Welding.

H.2.1 Root Insert Fusion (Grinnel):

—Process—G.T.A.W.
—Amps—100 D.C.S.P.
—Volts—14 (on machine voltmeter) (21,000 Joules/inch)
—Travel Speed—2.2 I.P.M.
—Torch Gas—Argon 15 C.F.H.
—Back-up Gas—Argon 15 C.F.H. (inside pipe)
—Continuous Pass—start at 0° past 90°→
—Position—IG (semi automatic)

90014309

*GE Nuclear Energy Engineering Division

H.2.2 Second Layer:

—Process—G.T.A.W. using 3/32" ϕ wire
—Amps—100 D.C.S.P.
—Volts—14 (on machine voltmeter) (21,000 Joules/inch)
—Travel Speed—2.2 I.P.M.
—Torch Gas—Argon 15 C.F.H.
—Back-up Gas—Argon 15 C.F.H. (inside pipe)
—Continuous pass—started at 90° past 180°, ending just past 90°
—Position—IG (semi automatic)

H.2.3 Third Layer:

—Process—S.M.A.W.
—Amps—100
—Volts—22–23 (33,000 Joules/inch)
—Travel Speed—4 I.P.M.
—Argon gas backup inside pipe
—Position IG
—59—started weld at 0° towards 90°
—60—started weld at 90° towards 0°

H.2.4 Fourth Layer 59, 60 pipe welds:

—Same parameters as third layer
—59—started weld at 45° towards 90°
—60—started weld at 45° towards 0°

Note: Both 3rd and 4th layers of the SMAW fill passes were made at an interpass temperature not exceeding 199°C (300°F).

H.3 BACKLAY WELDING

This was made with the SMAW process in three layers to end up approximately 7.62 cm (3 in.) wide 3.81 cm (1½ in.) either side of pipe weld) and 0.635 cm (¼ in.) minimum total height. The inside of each pipe was cooled with the "Internal Water Spray Quench Unit."

H.3.1 First Layer of Backlay 59:

—Process—SMAW
—Amps—95–100
—Volts—22–23 (22,000 Joules/inch)
—Travel Speed—6 I.P.M. (approximately)
—Started at 0° in the 90° direction. Welding direction was toward cooling water outlet end.

H.3.2 Second Layer of Backlay 59:

—Used same parameters as first layer.
—Started weld at 240°, progressed toward the 180° direction.
—Weld bead direction toward fill end (or opposite of first layer weld).

H.3.3 Third Layer of Backlay 59:

—Again, same parameters as first and second layers.
—Started weld at 240° and progressed toward 180°. Weld bead direction toward fill end.

H.3.4 First Layer of Backlay 60:

—Process—S.M.A.W.
—Amps—95–100

—Volts—22-23
—Travel Speed—6 I.P.M. (approximately)
—Started weld at 0° and progressed toward 270°. Welding direction of beads toward drain end of water-cooling flow.

H.3.5 Second Layer of Backlay 60:
—Same parameters as first layer.
—Weld started at 210°—towards 220°. Weld direction of beads was toward fill end of pipe.

H.3.6 Third Layer of Backlay 60:
—Same parameters as first and second layer.
—Weld started at 90° and progressed toward 0°, welding direction of beads toward drain end of cooling water.

---

*Sample 59, 60 (designation at GE CR&D)

Please note

—Volts—22–23
—Travel Speed—6 I.P.M. (approximately)
—Started weld at 0° and progressed toward 270°. Welding direction c
flow.

H.3.5 Second Layer of Backlay 60:

—Same parameters as first layer.
—Weld started at 210°—towards 220°. Weld direction of beads wa

H.3.6 Third Layer of Backlay 60:

—Same parameters as first and second layer.
—Weld started at 90° and progressed toward 0°, welding direction of

2nd Fatigue I can't find where it is referring to.

*Sample 59, 60 (designation at GE CR&D)

90014312

APPENDIX I. THE EFFECT OF POST-GROUND INSIDE SURFACE TREATMENT ON THE INTERGRANULAR STRESS CORROSION CRACKING OF WELDED TYPE-304 STAINLESS STEEL PIPE

I.1 INTRODUCTION

Prior full-size pipe test results revealed the strong influence of grinding at inside surface weld heat affected zones on the acceleration of intergranular stress corrosion cracking initiation. Since grinding has been an accepted technique in shop and field fabrication practices, numerous ground joints are in existence in various stages of BWR plant construction and operation.

This investigation was conducted to explore remedial measures for ground weld joints already fabricated and in various fabrication stages. Two pipe weldments were placed on test in the axial loaded CL-4 Test Loop as part of this study. The first pipe tested, test weldment 56-C, was loaded to 136% of the 288°C (550°F) Type-304 stainless steel yield strength in high purity water with 8 ppm dissolved oxygen. This pipe developed a through wall failure following 92 cycles and 138 hours on test. The fabrication details for this pipe test weldment were described in the Second Semiannual Progress Report (NEDC-21463-2). The post test metallurgical examination of this pipe weldment is described in this report.

The second pipe test weldment, Weldment E-36, was loaded to 120% of the 288°C (550°F) Type-304 stainless steel yield strength in high purity water with 8 ppm dissolved oxygen. The fabrication and test details for this weldment are described in the report.

I.2 POST TEST EXAMINATION OF INSIDE DIAMETER SURFACE CONDITIONED PIPE (WELDMENT 56-C)

The fabrication details for the inside diameter surface conditioned pipe weldment, Weldment 56-C, were presented in the Second Semiannual Progress Report (NEDC-21463-2). Figure 3-14 from that report is repeated here as Figure I-1 for the benefit of the reader. In this test, weld heat affected zones on the inside pipe surface were initially post weld ground and subsequently modified to provide the following final test surfaces:

a. As ground
b. Ground plus flapper wheel sanded
c. Grit Blasted
d. Polished with a diamond impregnated wheel
e. Combinations of b, c and d

In addition, one "as machined" test weld was included for comparison purposes as shown in Figure I-1.

The pipe weldment was placed on test in the axial CL-4 Pipe Test Loop loaded to 136% of the Type-304 stainless steel yield strength at 288°C (550°F) in high purity water with 8ppm dissolved oxygen. Following 92 cycles and 138 hours on test, a through wall failure occurred in Weld A and the pipe weldment was removed from test for post test non destructive and destructive examination.

I.2.1 Non Destructive Examination

Ultrasonic baseline inspections were performed on each completed weld prior to test and following the 92 cycles on test. The post test ultrasonic examination revealed possible crack indications in every weld heat affected zone examined with the exception of heat affected zones K1 and K2 (both as machined), G1 (Ground plus Flapper sanded + polished + grit blasted) and L2, a heat of Type-304 stainless steel which does not sensitize readily and which was used as the transition piece (Heat 482375). In addition, the other heat affected zone from this transition piece showed very slight ultrasonic indications. A decision was made to section the pipe longitudinally and perform a dye penetrant and metallographic examination on the pipe inner surface.

I.2.2 Destructive Examination

Red dye liquid penetrant measurements were performed on the two longitudinal sections of the inside surface conditioned pipe weldment, 56-C. The results, presented in a layout sketch in Figure I-2, confirmed the post test ultrasonic measurements on the pipe. Following the liquid penetrant examinations, one of the longitudinal sections, the 225° to 45° section shown in Figure I-3, was submitted to the metallography laboratory for examination. The examination locations were selected from the dye penetrant results and are shown by arrows in Figure I-2, the layout sketch of the dye penetrant results.

The microscopic examination which was performed had the following objectives:

1. Characterization of crack indications (failure mode, crack depth and distance from weld fusion line).

2. Surface finish comparison (roughness, cold work, surface recrystallization and grain size).

A summary of the post test ultrasonic, liquid penetrant and metallographic results (the metallographic results are for the one section only) are presented in Table I-1. As shown in Table I-1, the mode of cracking was predominantly intergranular, although shallow blunt transgranular separations were also observed, similar to those observed in the Fourth Large Environmental Fatigue Test Facility cyclic tension test (see NEDC-21463-2 for test results). These blunt transgranular indications are probably the result of the grinding operation which alone can introduce separations in Type-304 stainless steel (see Section 4-3 for a discussion of surface condition studies). The stress corrosion cracking was typical of the intergranular stress corrosion cracking previously experienced in pipe tests and in field failures. It occurred exclusively in weld heat affected zones and varied in depth from a few grains to the through wall crack in heat affected zone A2.

In comparing the effects of the various surface preparation techniques, it appears that the "cratex" diamond polish produced a smoother post ground surface than did any of the other surface conditioning techniques. However, even these smooth surface treatments did not appear to provide significant improved resistance to intergranular stress corrosion cracking when compared to post weld grinding. The fact that some rough "as-ground" and "as-matching" pipe heat affected zones showed no evidence of cracking casts some doubt that significant improvement can be achieved by post ground surface conditioning. It may be noteworthy that the only heat affected zone pair of specimens to survive these tests without evidence of intergranular stress corrosion cracking were "as-machined" heat affected zones.

In summary, none of the post ground inside surface conditioning treatments provided a significant improvement over as ground welded Type-304 stainless steel pipe in this very severe pipe test. Although some slight improvement in resistance to intergranular stress corrosion cracking may have occurred using some of the surface conditioning treatments, the high stress (136% of the 288°C (550°F) yield strength) totally overwhelmed whatever subtle improvement may have been attributable to the conditioning treatments. Therefore, a second inside surface conditioned pipe test was initiated at a lower stress level to investigate the possible performance improvement of the most promising inside surface conditioning treatments.

Table I-1

SUMMARY OF EXAMINATION RESULTS—PIPE WELDMENT-56C—INSIDE SURFACE CONDITIONED

Type 304SS Pipe

WELD/ HAZ	HAZ SURFACE	I.D. CONDITION	HEAT NUMBER	UT Results (Indications)	DPT Results (Indications)	"MICRO" Exam. (At Specific Azim.)
A1	Rough	Ground ABW	482375	90°–180°	0–90° and 270 to 360°	272°–12 defects mostly blunt & shallow
A2	Rough	Ground ABW	M0063	Through crack	45° to 180°	272°–8 defects blunt & shallow
B1	Rough	Ground after 1st pass	M0063	45°–135°	0 to 90°	32°–1 IGSCC 17 mils deep
B2	Rough	Ground after 1st pass	M7616	All around	Intermit. all around	32°–5 shallow cracks
C1	Rough	Ground ABW	M7616	All around	Intermit. all around	353°–9 IGSCC (105 mils deep)
C2	Rough	Ground ABW	M7616	All around	Intermit. all around	353°–6 IGSCC (98 mils deep)
D1	Slightly Rough	Ground and Flapper	M7616	90° to 135°	0° to 170°	352°–1 IGSCC (20 mils)
D2	Slightly Rough	Ground and Flapper	M7616	135° to 360°	135 to 360 & 10 to 40°	352°–2 IGSCC (shallow)
E1	Slightly Rough	Ground and Flapper	M7616	0° to 180°	Intermitt. All around	22°–1 IGSCC (34 mils)
E2	Slightly Rough	Ground and Flapper	M7616	0° to 45° & 135° to 360°	0 to 45° & 135° to 360°	22°–1 IGSCC (48 mils deep)
F1	Slightly Rough	Ground and Flapper and Cratex	M7616	All around	All around	278°–2 IGSCC (28 mils deep)
F2	Slightly Rough	Ground and Flapper and Cratex	M7616	All around	80° to 100° & 270° to 360°	278°–2 IGSCC (30 mils)

Table I-1 (Continued)

SUMMARY OF EXAMINATION RESULTS—PIPE WELDMENT-58C—INSIDE SURFACE CONDITIONED

Type 304SS Pipe

WELD/ HAZ	HAZ SURFACE	I.D. CONDITION	HEAT NUMBER	UT Results (Indications)	DPT Results (Indications)	"MICRO" Exam. (At Specific Azim.)
G1	Very Smooth	G+F+C+GB	M7616	None	None	306°-no cracks
G2	Very Smooth	G+F+C+GB	M7616	210° to 360°	270° to 315°	306°-1 IGSCC (shallow)
H1	Rough	Ground and Grit Blast	M7616	180 to 360°	180° line 350° spot	246°-2 IGSCC (25 mils)
H2	Rough	Ground and Grit Blast	M7616	All around	Intermitt. all around	246°-1 IGSCC (32 mils)
I1	Rough	Ground and Grit Blast	M7616	All around	170° spot-200° spot	304°-2 Shallow
I2	Rough	Ground and Grit Blast	M7616	All around	0° to 90° - 210° to 360°	304°-2 IGSCC (55 mils)
J1	Smooth	G+F+C	M7616	Near 0°	30° to 100° & 310° line	315°-2 IGSCC (31 mils)
J2	—	G+F+C	M7616	One at 270°	210° to 240°	315°-no cracks
K1	—	Machined	M7616	None	None	—
K2	—	Machined	M0063	None	None	—
L1	Rough	Ground ABW	M0063	One at 135°	None	—
L2	Rough	Ground ABW	482375	None	270° to 360°	315°-slight separation
L2	Rough	Ground ABW	482375	None	270° to 360°	315°-2 shallow surface sep.

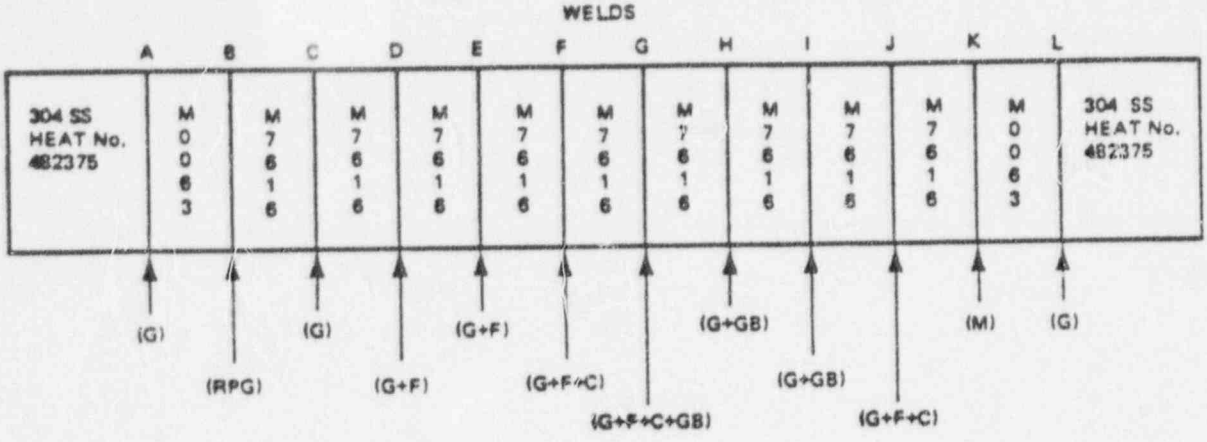

KEY TO ABBREVIATIONS:	
RPG	– ROOT PASS GROUND ON i.d. PRIOR TO DEPOSITION OF OTHER WELD LAYERS
G	– GROUND ON i.d. AFTER WELDING IS COMPLETED
M	– MACHINED COUNTERBORE
F	– FLAPPER WHEEL SANDED ON WELD i.d.
C	– CRATEX WHEEL (DIAMOND IMPREGNATED) POLISH
GB	– GRIT BLASTED ON i.d. SURFACE (Al_2O_3)

*NOTE: ALL PIPE WELDS WERE FABRICATED USING HIGH WELD HEAT INPUT TECHNIQUE [APPROXIMATELY 20,000 J/cm (50,000 J/inch)].

Figure I-1. Fabrication Information on Inside Diameter Surface Conditioned Pipe Weldment

90014317

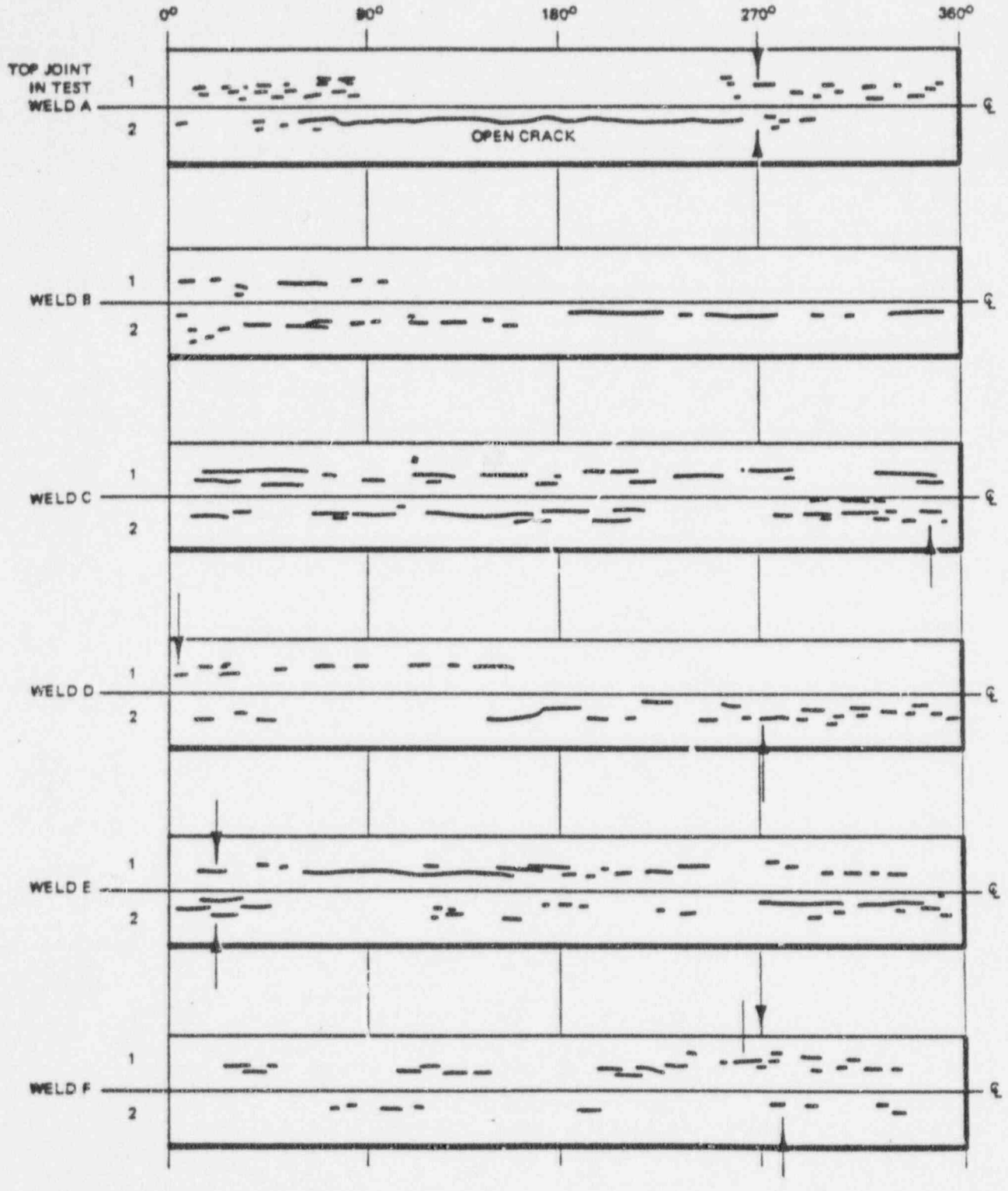

Figure I-2. Dye Penetrant Test Results (Lay-Out of Weld Joint I.D. Surfaces)

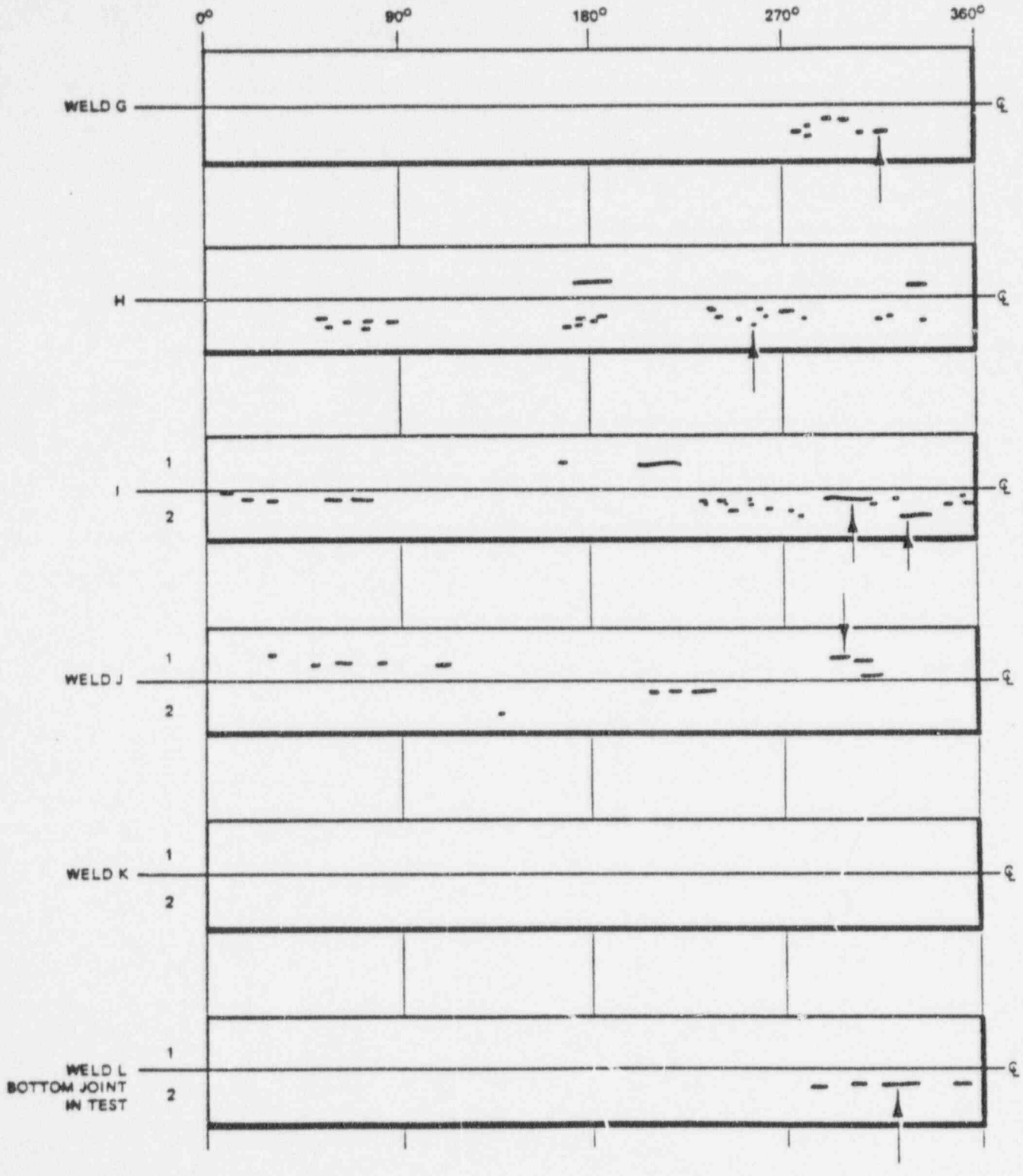

Figure I-2. Dye Penetrant Test Results (Lay-Out of Weld Joint I.D. Surfaces) (Continued)

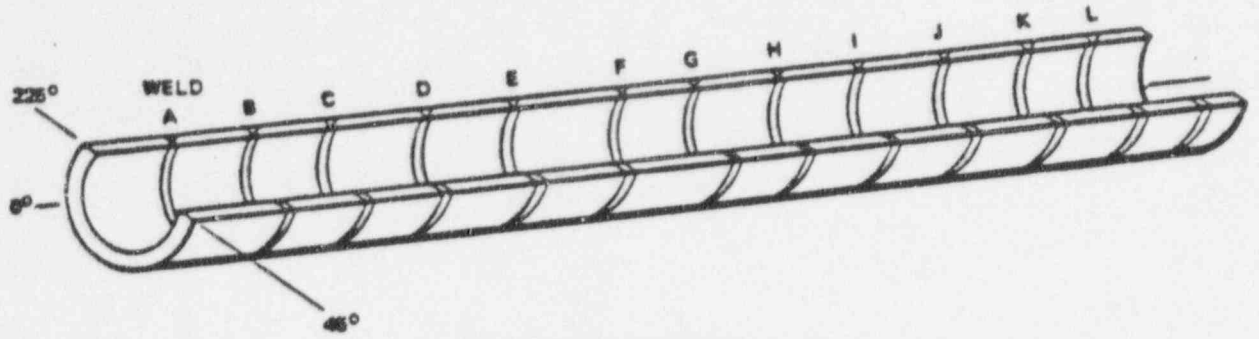

LOCATION OF LONGITUDINAL CUT

(NOTE: THIS HALF SUBMITTED TO METALLOGRAPHIC LAB FOR FURTHER SECTIONING)

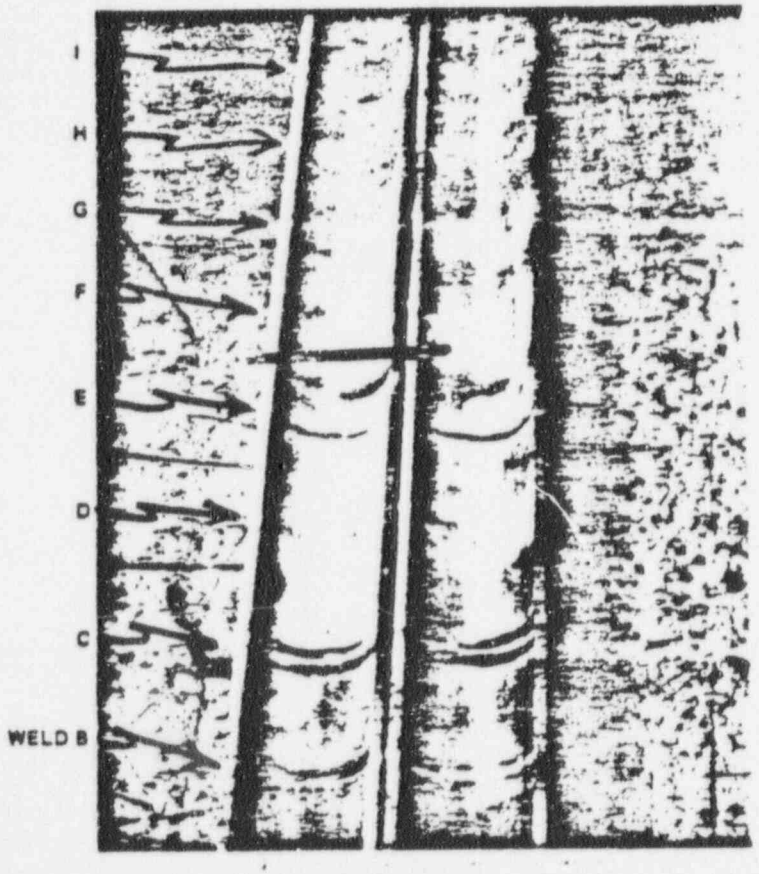

BOTTOM END DURING IGSCC TEST

TOP END DURING IGSCC TEST

APPEARANCE OF I. D. SURFACE AFTER DYE-CHECK

Figure I-3. Weldment 56-C Cut Longitudinally and Dye Penetrant Tested on the I.D. Surfaces

APPENDIX J. ANALYSIS OF CONSTRAINT NEAR PIPE WELDS— COMPARISON AMONG DIFFERENT DIAMETER PIPES

J.1 INTRODUCTION

Cracking in certain Type-304 stainless steel piping systems has been shown to be due to a critical combination of factors.[1] These factors include sensitized material in the weld heat affected zone, water environment and sustained or periodic local plastic deformation. To better evaluate remedies and to predict behavior of piping systems which to date have not experienced cracking, a number of investigations have been undertaken to quantify these factors.[2,3]

This task describes an analytical investigation of plastic deformation of material in the weld HAZ as a function of applied load. The effect of local geometry distortion, residual stress and pipe size are explored. This work is meant to compliment detailed residual stress measurements, local yield strength measurements, and testing of full-pipe sections currently underway.

In the following sections, details and results of elastic-plastic finite element analyses of schedule 80 butt welded Type-304 stainless steel pipes loaded in axial tension are presented. Analysis results for a 10.16-cm (4-in.) diameter pipe at room temperature (with and without weld distortion and residual stress) are compared with test results obtained earlier. Predictions for 10.16-cm (4-in.) and 66-cm (26-in.) diameters at 288°C (550°F) are also carried out. Implication of the results and additional work in progress are mentioned.

J.2 ANALYSIS OF 10.16-cm (4-in.) AND 66-cm (26-in.) IDEALIZED PIPE GEOMETRY

J.2.1 Finite Element Model Description

The ANSYS finite element computer program was used for local pipe deformation analysis. This program is a large scale general purpose computer program suitable for solution of several classes of engineering problems. The matrix displacement method of analysis based upon finite element idealization is employed throughout the program. The ANSYS constant strain element, Stif2 (axisymmetric), was used.

Finite element models for the 10.16-cm (4-in.) and 66-cm (26-in.) diameter pipes are shown on Figures J-1 and J-2, respectively. The models are based on idealized weld prep geometries taken from weld prep drawings before welding. Small size elements were used on the inside pipe surface near the weld where deformation is of most interest. Because of symmetry, the pipes were modeled from the weld centerline to a length of slightly over 10.16 cm (4 in.) for the 10.16-cm (4-in.) diameter pipe, and approximately 38 cm (15 in.) for the 66-cm (26-in.) diameter pipe. Numbers 1 and 2 shown on the two models refer to the two materials used: No. 1—Type-304 stainless steel, No. 2—Type-308 weld metal. The models for the 10.16-cm (4-in.) and 6-cm (26-in.) diameter pipes are identical near the weld and inside surface. Dimensions are shown in inches.

Displacements were constrained in the axial direction at the weld centerline due to symmetry. In addition, nodes at the top of the models were coupled such that axial displacement for these nodes were identical. (One case with the 10.16-cm (4-in.) diameter model was run without the top nodes coupled. This showed that because of the length of the model, coupling of nodes made little difference.) There was no restraint of nodes in the radial direction.

The axial load was applied as a tensile stress at the top of the finite element models using an incremental technique. The first load step was applied at the estimated elastic limit of the models. Subsequent load steps resulted in plastic behavior.

Idealized stress-strain curves used in the analysis for Type-304 stainless steel pipe material and Type-308 weld metal at room temperature and at 288°C (550°F) are shown on Figures J-3 and J-4, respectively. Other properties for both materials are shown below:

Stainless Steel 304 and Stainless Steel 308 Elastic Material Properties	Room Temperature	288°C (550°F)
Young's Modulus	29.2 x 10^6 psi (201 x 10^3 MPa)	26.5 x 10^6 psi (183 x 10^3 MPa)
Poisson Ratio	0.30	0.30

J.2.2 10.16-cm (4-in.) Diameter Pipe Predictions at Room Temperature

Figure J-5 shows the calculated total axial strain plotted as a function of the distance from the weld centerline on the pipe i.d., or weld prep for two different applied axial loads (stress). All strains are calculated at the centroid of the elements. The asterisk denotes the strains for the element located 1.58 inches from the weld centerline on the outside surface (see Figure J-1). The top curve represents the total axial strains at the maximum applied nominal stress of 51,000 psi. The lower curve shows strains at an applied stress of 35,000 psi. Note that the strains on the inside near the weld and outside surfaces away from the weld are nearly equal at a given load. The strains peak at the weld prep notch, 1.3 cm (0.51 in.) from the weld centerline and, also, where the two different materials join 0.28 cm (0.11 in.) from the weld centerline (see Figure J-1). Lower strains are observed in the higher strength weld metal (0 to 0.25 cm (0.0 to 0.10 in.) from the weld centerline.

Figure J-6 shows the location (shaded area) where material first yields under loading on the 10.16-cm (4-in.) diameter model. By an iterative technique, the applied nominal stress was increased from 17,000 psi (117 MPa) (elastic solution) to 18,000 psi (plastic solution) shown on Figure J-6. Yielding occurred within this 1,000 psi interval.

J.2.3 Comparison of Predictions with Room Temperature Pipe Test

In a separate program[1] a 10.16-cm (4-in.) diameter pipe was strain gaged and loaded in axial tension to determine local strains near the weld. Strain gages were attached to a butt welded Type-304 stainless steel pipe and the pipe was loaded in axial tension. Gages were located at four positions around the circumference in the weld prep region near the weld and on the outside surface away from the weld (see Figures J-1 and J-7). The load on the pipe was increased in steps and strains were recorded at each step.

For the applied stress of 35,000 psi (241 MPa), measured strains are compared to the predicted strains in Figure J-5. The inside surface measured strains are shown at a distance from weld centerline of 0.79 cm (0.31 in.), the location of the strain gage. The outside surface measured strains are compared to the outside surface prediction indicated with an asterisk. Note that the measured strains differ from the predicted strains. On the outside surface measured strains are higher than predicted, while on the inside surface they are lower. The analysis does not show constraint (retarded plastic flow) near the weld while the test does.

Before proceeding with the analyses of the larger pipe, a number of modeling changes were made. These included lengthening the model, using a higher order finite element (Stif42) and applied displacement, rather than load at the free end of the pipe. A model of a simple tensile specimen was made to evaluate the adequacy of the Stif42 element, to check ANSYS solution technique for large plastic solutions, to assess the effect of relative element size.

Incorporation of all these modeling changes had little effect on the finite element local strain predictions. Predicted strains near the weld on the inside of a pipe continued to be much higher than measured in the room temperature pipe test.

J.2.4 66-cm (26-in.) Diameter Predictions

In spite of the poor agreement between analysis and test for the 10.16-cm (4-in.) diameter pipe, analysis of a 66-cm (26-in.) diameter pipe was carried out for relative comparison purposes.

Figure J-8 shows the calculated total axial strain plotted as a function of the distance from the weld centerline along the inside diameter for both the 10.16-cm (4-in.) diameter and 66-cm (26-in.) diameter pipes at 288°C (550°F). Again, the asterisk denotes the strains on the outside surface away from the weld. The top two curves represent the total axial strains at the maximum applied nominal stress, 42,800 psi (295 MPa), for both pipes. The lower curves are the strains at a lower nominal load, 23,800 psi (164 MPa). According to this finite element analysis, the axial strains in the weld prep region are greater in the 66-cm (26-in.) diameter pipe than in the 10.16-cm (4-in.) diameter pipe.

Figure J-9 shows the location (shaded area) where material first yields under loading on the 66-cm (26-in.) diameter pipe. Considerable yielding has occurred within a 1,000 psi load step interval (6.9 MPa). A smaller load increment would have shown more detail, possibly yielding starting next to the weld since the strains are higher at that point, as shown on Figure J-8.

Higher strains than expected in the HAZ are due in large part to local bending near the weld and there appears to be more bending in the large pipe. If the plane sections through the thickness remained a plane constant under loading, that is, if no local bending occurred, then the strains would remain constant through the thickness.

The fact that local bending is causing higher strains near the weld was demonstrated in a preliminary analysis of the pipe where the inside diameter was erroneously set equal to zero. The inability of the pipe to move inward and, therefore, the lack of local bending caused the strains to be higher on the pipe material away from the weld than in the weld prep region. However, when the proper inside diameter was used, the pipe could move inward. Local bending occurred and strains were higher near the weld.

To improve finite element predictions, the models were altered to include weld distortion and residual stress.

J.3 EFFECT OF WELD DISTORTION (CAUSED BY WELDING)

Figure J-10 shows a photo of the cross section of a pipe butt weld. Weld shrinkage has caused a distortion on the inside surface of the pipe. In order to more realistically approach the geometry of a butt welded pipe, a modified finite element model was developed.

Distorted 10.16-cm (4-in.) Diameter Pipe Model

Figure J-11 shows the modified geometry for the 10.16-cm (4-in.) diameter pipe. A row of elements was added along the weld prep on the inside surface. At the weld two rows of elements were added. The additional elements increased the thickness of material Type-304 stainless steel by 0.05 cm (0.02 in.) in the weld prep, which is the actual dimension of the test pipe being compared.

Figure J-12 shows the total axial strains on the 10.16-cm (4-in.) diameter pipe with weld distortion. The strains on the outside diameter remain as before, but the strains on the inside diameter near the weld are lower. Comparison with the strains shown on Figure J-5 at the applied nominal load of 35,000 psi (241 MPa) indicates that the strains on the inside diameter, 0.79 cm (0.31 in.) from the weld centerline where the test strain gages were located, are closer to the test measurements when the weld distorted model is used.

Figure J-13 shows the location (shaded area) where material first yields for the 10.16-cm (4-in.) diameter pipe with weld distortion. Comparison with Figure J-6, which shows first yielding on the model without weld distortion, indicates the following:

a. Yielding occurs at a higher nominal load on the model with weld distortion: 19,000 psi versus 18,000 psi near the weld, 20,000 psi versus 18,000 psi in the weld prep notch.

b. Location of first yielding has shifted away from the weld on the model with weld distortion.

J.4 EFFECT OF RESIDUAL STRESS

During welding of pipes, cooling of the weld metal and surrounding material results in shrinkage in both the axial and radial directions. The shrinkage in turn produces residual stress throughout the welded region.

The transient, asymmetric, and elastic-plastic aspects of this process prevent calculation of the resulting residual stress distribution. On the other hand, residual stress measurements on the inside pipe surface have been made. Figure J-14 shows an example of measurements made on a 10.16-cm (4-in.) diameter pipe. For this example, axial residual stresses are tensile in the weld metal, quickly becoming compressive as one moves away from the weld. The magnitude of residual stress varies from 10 ksi (69 MPa) tensile at the weld centerline to −40 ksi (−276 MPa) compressive between 1.02 cm (0.4 in.) and 1.53 cm (0.6 in.) away from the weld centerline. At other azimuthal locations different distributions might be noted, but in all cases residual stresses become compressive 0.3 to 0.6 inch from the weld centerline.[4]

To better understand the influence of residual stresses on local deformation due to an applied load, residual stresses were introduced into the finite element models. This was accomplished by introducing fictitious temperature differences among the finite elements as an initial condition, keeping material properties independent of temperature. The result is to produce an internal initial stress distribution for no externally applied load. This is equivalent to residual stresses which may have been produced by nonuniform plastic deformation.[4]

10.16-cm (4-in.) Diameter Pipe Model with Residual Stress

Figure J-15 shows the elements which were subjected to a higher temperature than the neighboring material as an initial condition. As stated before, expansion of these (shaded) elements is inhibited by the cooler neighboring material. This results in compressive stresses acting on the elements subjected to a higher temperature and tensile residual stress on the neighboring elements.

Figure J-16 shows the axial stress distribution on the inside surface versus distance from the weld centerline on the 10.16-cm (4-in.) diameter pipe model at no load. Comparison of predicted stress distribution, with measurements shown on Figure J-14, indicates a fair approximation in the distribution of residual stresses within the range 0.5 to 1.0 cm (0.2 to 0.4 in.) away from the weld centerline; i.e., residual stresses fall in the −30 and −40 ksi range (−207 to −276 MPa). The actual residual stress in the weld centerline is tensile, whereas the stresses on the model are compressive. The residual stresses 1.27 to 1.52 cm (0.50 to 0.60 in.) away from the weld centerline in the model are close to zero.

Figure J-17 shows the total axial strain versus distance from weld centerline for the 10.16-cm (4-in.) diameter pipe model with weld distortion and residual stresses. Comparison with the strain distribution shown on Figure J-12, for the same model without residual stresses, indicates the following:

a. At the lower nominal load, the predicted strain on the outside surface (asterisk) remains almost the same as before; however, the predicted strains on the inside surface in the weld prep are now lower than the measured strains. These strains have been reduced from approximately 0.2% to close to zero by adding residual stresses to the model.

b. The effect of residual stresses on local strain seems to wash away at the higher nominal loads. That is, the predicted strains on the inside diameter are about as they were without residual stress at high load (see Figure J-12). The predicted strain on the outside diameter (asterisk) has increased slightly.

Figure J-18 shows the location (shaded area) where tensile yielding first occurs on the 10.16-cm (4-in.) diameter pipe model with weld distortion and residual stresses. Residual stress addition has shifted the location of tensile plastic strains from the inside surface (see Figure J-13) toward the outside surface. Yielding also occurs at a lower nominal load, 17,000 psi (117 MPa) versus 19,000 psi (131 MPa), shown on Figures J-18 and J-13, respectively.

J.5 ANALYSIS OF 10.16-CM (4-IN.) AND 66-CM (26-IN.) DIAMETER PIPES AT 288°C (550°F)

Figure J-19 shows a modification of the original case shown in Figure J-15. The residual stress modeling was changed because the stress distribution shown on Figure J-16 did not agree with measured stress distribution shown on Figure J-16 at two points. The measured stresses are tensile at the weld fusion line, whereas the predicted stresses for the first case are compressive there; the measured stresses are still compressive 1.52 cm (0.6 in.) away from the weld centerline, whereas the predicted stresses are tensile.

In the second case (see Figure J-19) the fictitious residual stresses have been shifted away from the weld centerline to more realistically approximate the stress distribution of a real pipe. This residual stress case was used for both the 10.16-cm (4-in.) and the 66-cm (26-in.) diameter pipes with weld distortion. Figure J-20 shows the resultant stress distribution versus distance from the weld centerline for both the 10.16-cm (4-in.) diameter pipe (lower curve) and the 66-cm (26-in.) diameter pipe (top curve). The two curves are nearly identical. These stress distributions are in better agreement with the stress distribution in a real pipe, although it is still slightly compressive at the weld centerline.

Figure J-21 shows a comparison of total axial strain between 10.16-cm (4-in.) diameter and 66-cm (26-in.) diameter pipes with weld distortion and residual stress. As before (see Figure J-9) the strains in the weld prep are larger in the 66-cm (26-in.) diameter pipe than in the 10.16-cm (4-in.) diameter pipe. This suggests that both local weld distortion and residual stress influence deformation near welds although pipe size itself appears to have little influence on deformation.

It needs to be pointed out that local weld distortion and residual stress have not been scaled up in going from a 10.16-cm (4-in.) to a 66-cm (26-in.) diameter pipe model. That is, the same absolute magnitude of distortion and residual stress was used on each model. It is clear that if more distortion and/or more residual stress were present in either model, further suppression of plastic flow in the weld HAZ would have occurred.

J.6 DISCUSSION AND CONCLUSIONS

The analysis of deformation of material near pipe welds was undertaken because plastic flow has been identified in the present working model as a necessary ingredient for stress-corrosion cracking. Further, better understanding of parameters that control plastic deformation is essential if one is to develop remedies that involve restrictions of plastic behavior in the HAZ, or if one is to be able to more accurately predict behavior of existing piping systems. These analyses are part of a larger effort to understand local deformation. Other work which relates to the same phenomena includes measurement of residual stresses, measurement of yield strength in the weld, HAZ and neighboring pipe, and tests of pipes and test sections of pipes.

Earlier consideration of the local pipe deformation question led to speculation that deformation in the HAZ would be limited by neighboring high strength weld metal. This effect was called geometric weld constraint or weld shadowing and would be true if during loading plane sections remained plane. Further, it was reasoned that this effect would cover a larger absolute area of HAZ in a large pipe than in a small pipe. That is, constraint or shadowing might have a size effect which explains why large pipes are less prone to cracking than small.

Finite element analyses of 10.16-cm (4-in.) and 66-cm (26-in.) diameter pipes having idealized geometries and without residual stress show that neighboring higher strength weld metal by itself does not retard plastic flow of the HAZ material near the inside diameter surface. The reason this does not occur is that plane sections do not remain plane during loading. There is local bending near the weld and for the large pipe more bending is occurring than in the small. This bending tends to increase plastic flow in the HAZ near the inside diameter where constraint would retard it. Consequently, geometry itself does not produce a size effect which might explain why large diameter pipes do not crack in service.

To pursue the question further and because predictions showed poor agreement with results of a 10.16-cm (4-in.) pipe tested earlier, additional parameters were introduced into the finite element model. These were local weld distortion and residual stress.

Both these parameters influence local deformation. Distortion due to welding reduces plastic flow because it reduces local bending. This effect is present at both small and large loads. Compressive residual stress near the inside diameter reduces plastic flow because material initially in compression can carry more load before going plastic. This effect is present at small loads but is washed out at large loads.

The analyses of 10.16-cm (4-in.) and 66-cm (26-in.) diameter pipes which included weld distortion and residual stress do not demonstrate that these parameters result in a size effect. In this model the same absolute distortion and residual stress were used for both pipe diameters. This treatment may have been an oversimplification. Work in progress[5] indicates that the weld distortion is greater for large diameter pipes and that residual stresses are more compressive. Both these trends would suggest reduced plastic flow in large diameter pipes.

What this analysis does clearly demonstrate is that there is much less plastic flow in the higher strength weld metal than in the lower strength neighboring base material. Note that strains in the weld are half of those in the HAZ. The reason for this is clear. The weld metal can carry more stress without going plastic. If the HAZ material should have higher yield strength, strains in the HAZ would be lower.

Recently, Hanneman[6] has shown that the yield strength of material in the HAZ is higher than the base pipe material. Further, he has shown that the region of this higher strength material is larger in large diameter pipes.

Both these observations are significant to the question of deformation near welds. First, plastic flow in the HAZ would be reduced from that predicted by these analyses. This factor alone can explain the discrepancy between the 10.16-cm (4-in.) diameter pipe model and the 10.16-cm (4-in.) diameter pipe tests. Second, a larger high strength HAZ in large pipe means a larger region of retarded plastic flow in large pipe. This factor alone accounts for a size effect in deformation. Figure J-22 shows the expected local strain behavior when the yield strength of the HAZ material is higher than the parent pipe.

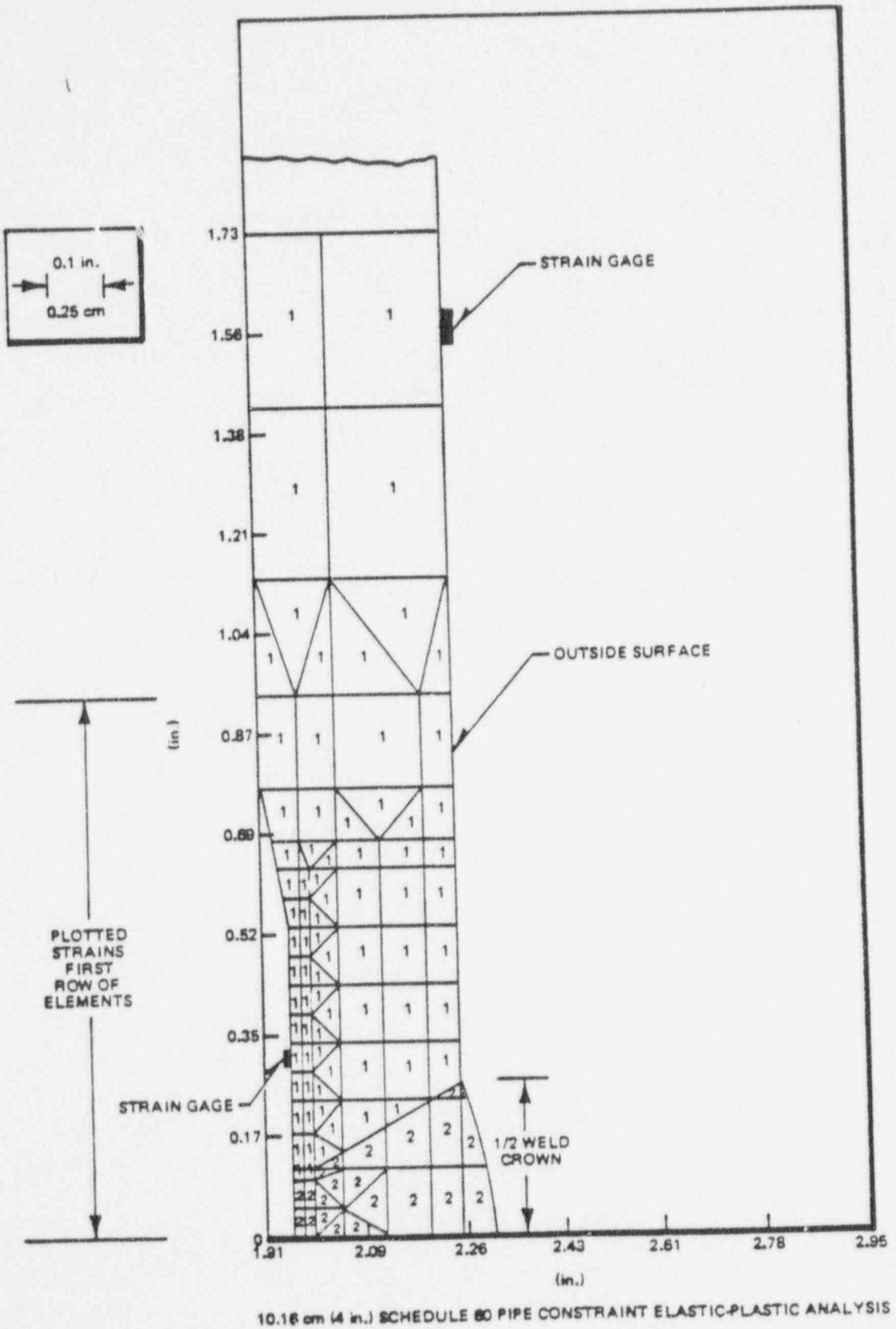

Figure J-1. Finite Element Model for 10.16-cm (4-in.) Diameter Pipe

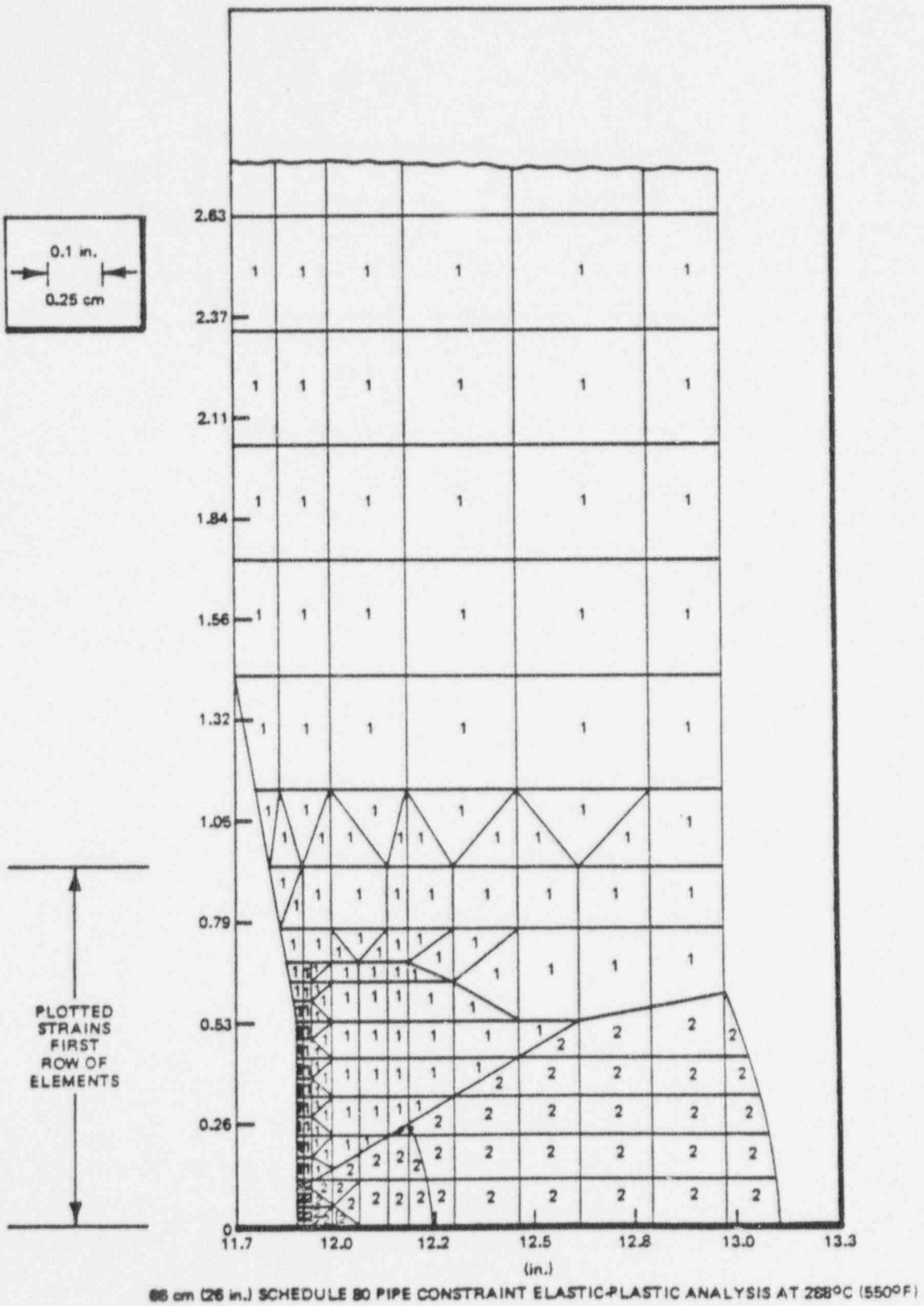

Figure J-2. Finite Element Model for 66-cm (26 in.) Diameter Pipe

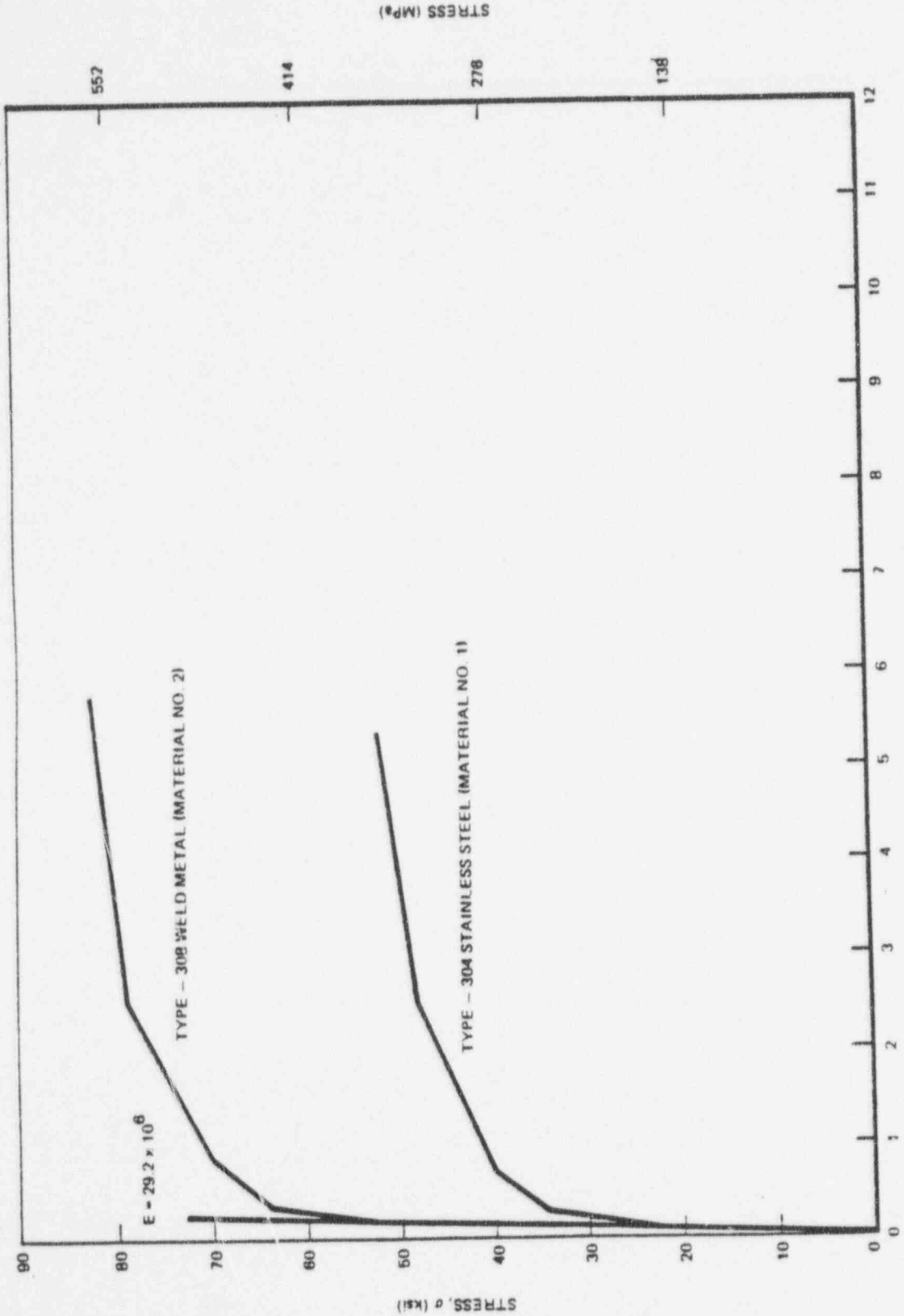

Figure J-3. Room Temperature Material Stress / Strains Properties Used in Analysis

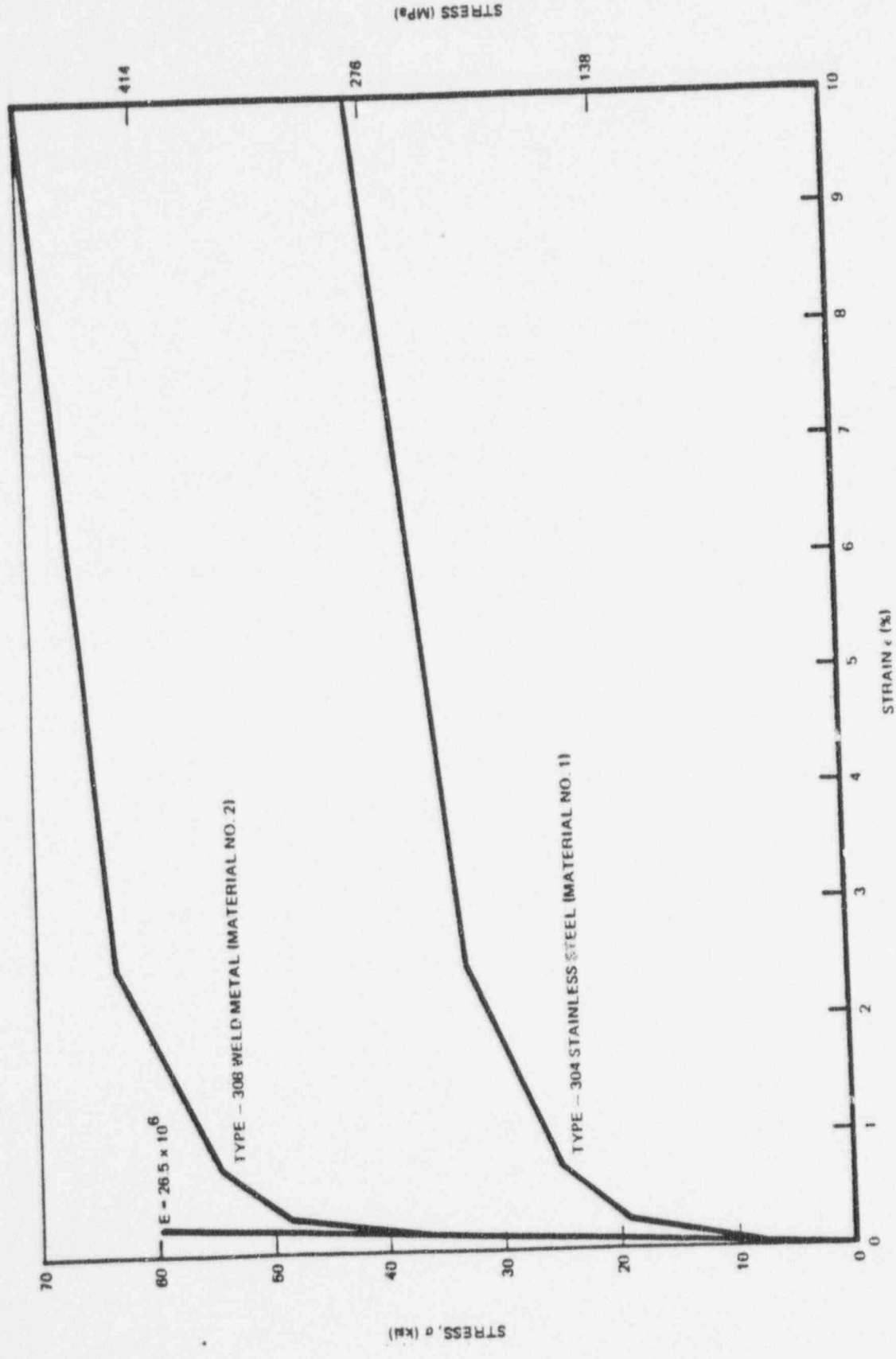

Figure J-4. 228°C (550°F) Material Stress/Strain Properties Used in Analysis

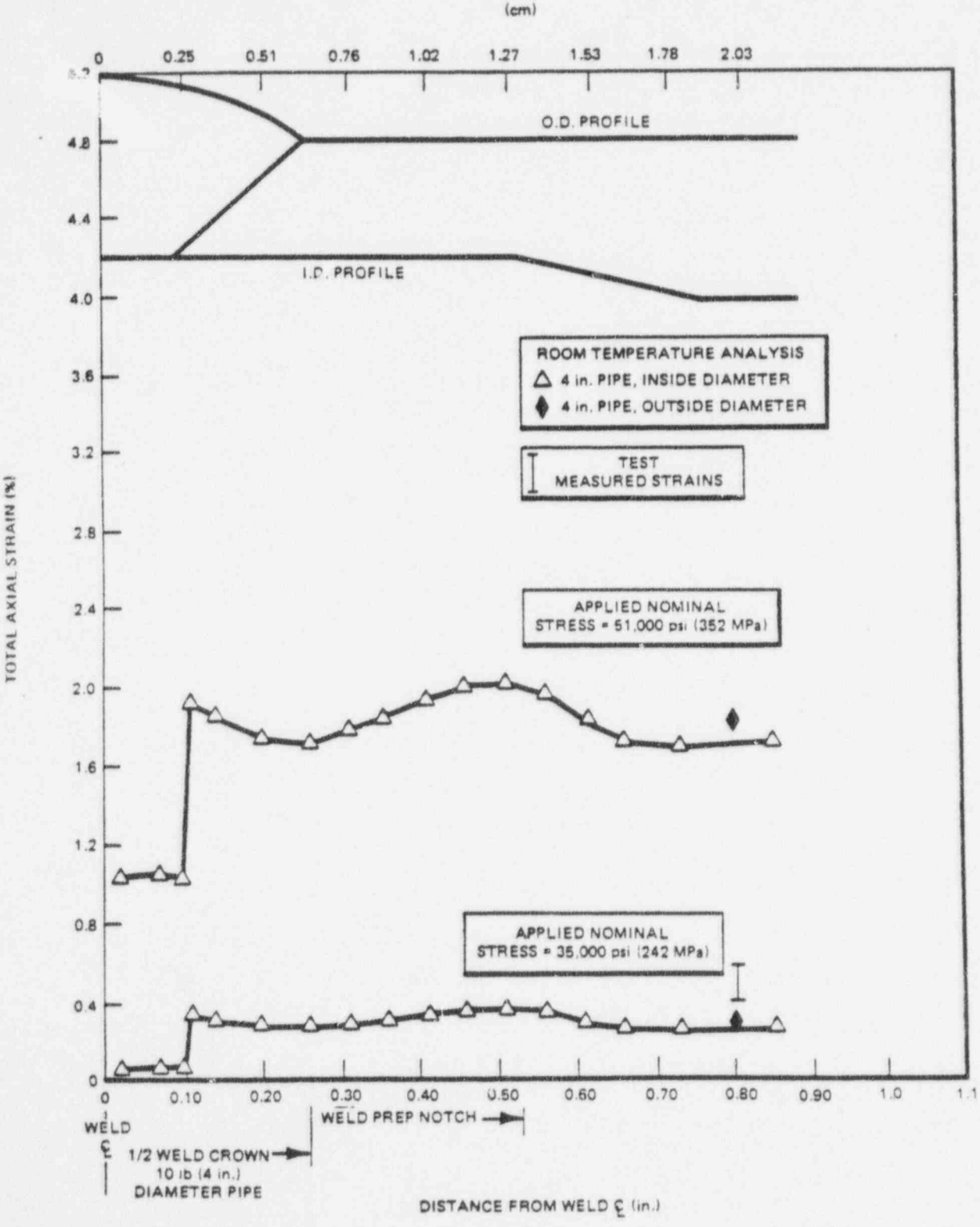

Figure J-5. 10.16-cm (4-in.) Diameter Pipe Total Strain at Room Temperature

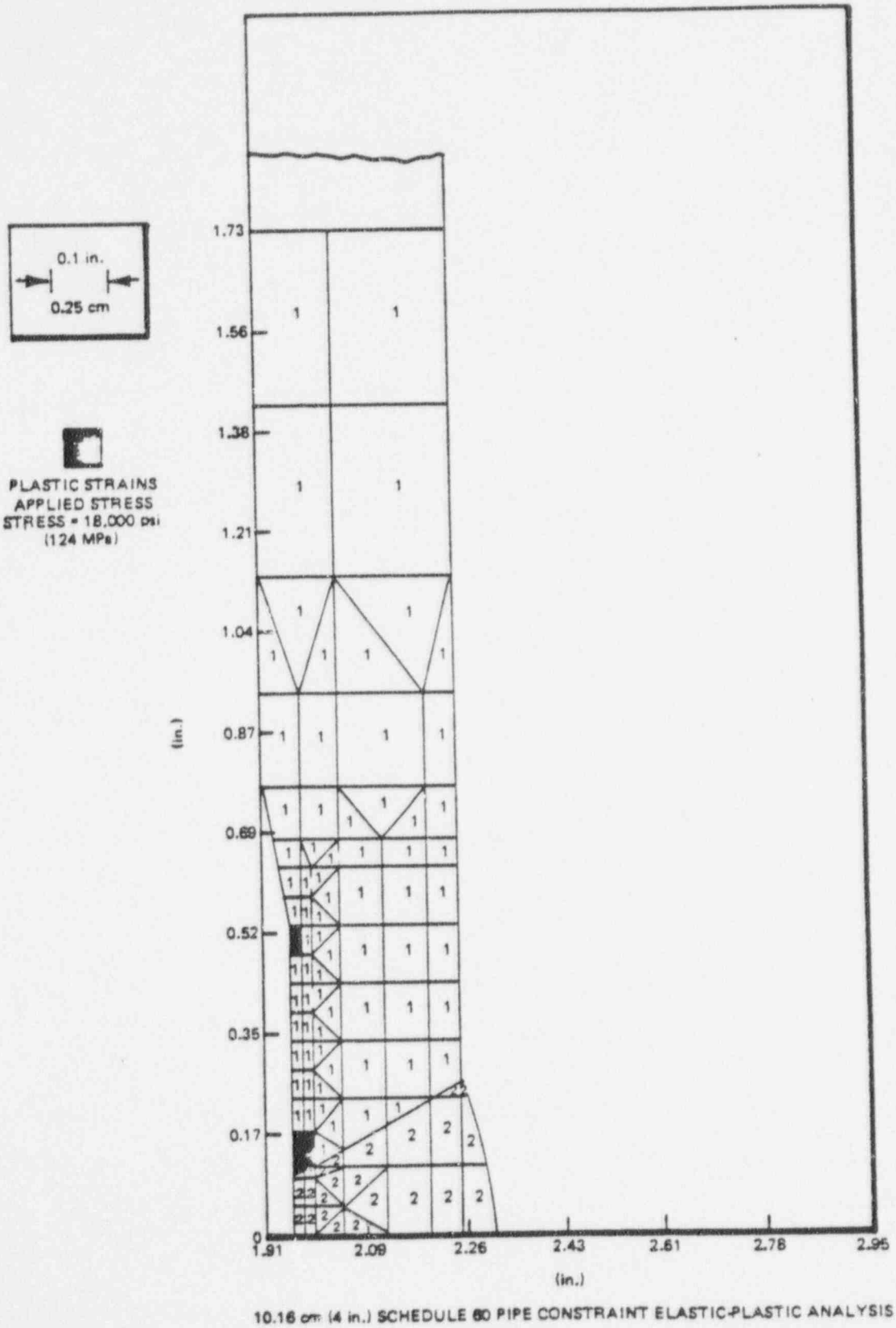

Figure J-6. Mapping of Plastic Strains as They First Appear on 10.16-cm (4-in.) Diameter Pipe at Room Temperature

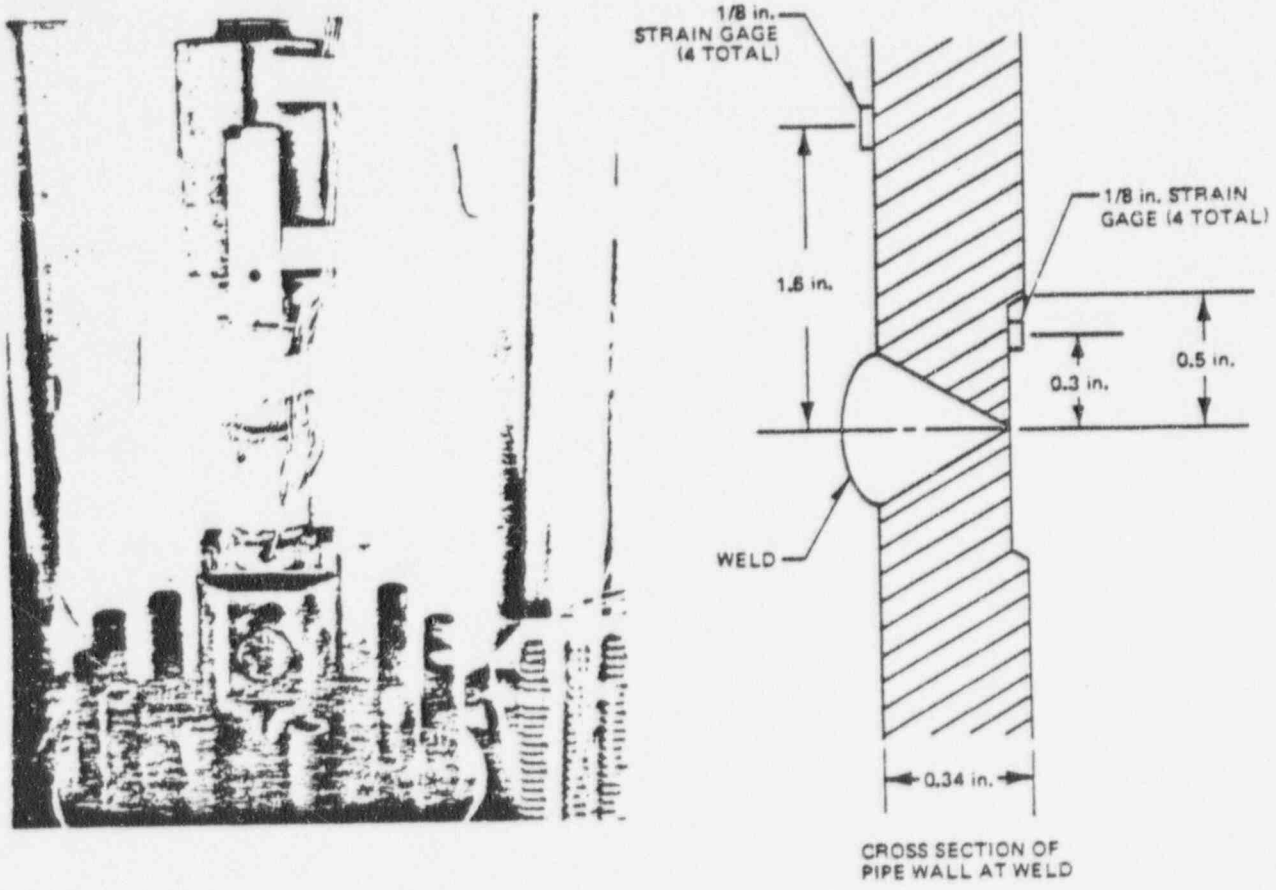

Figure J-7. Instrumented Type-304 Schedule Butt Welded Pipe

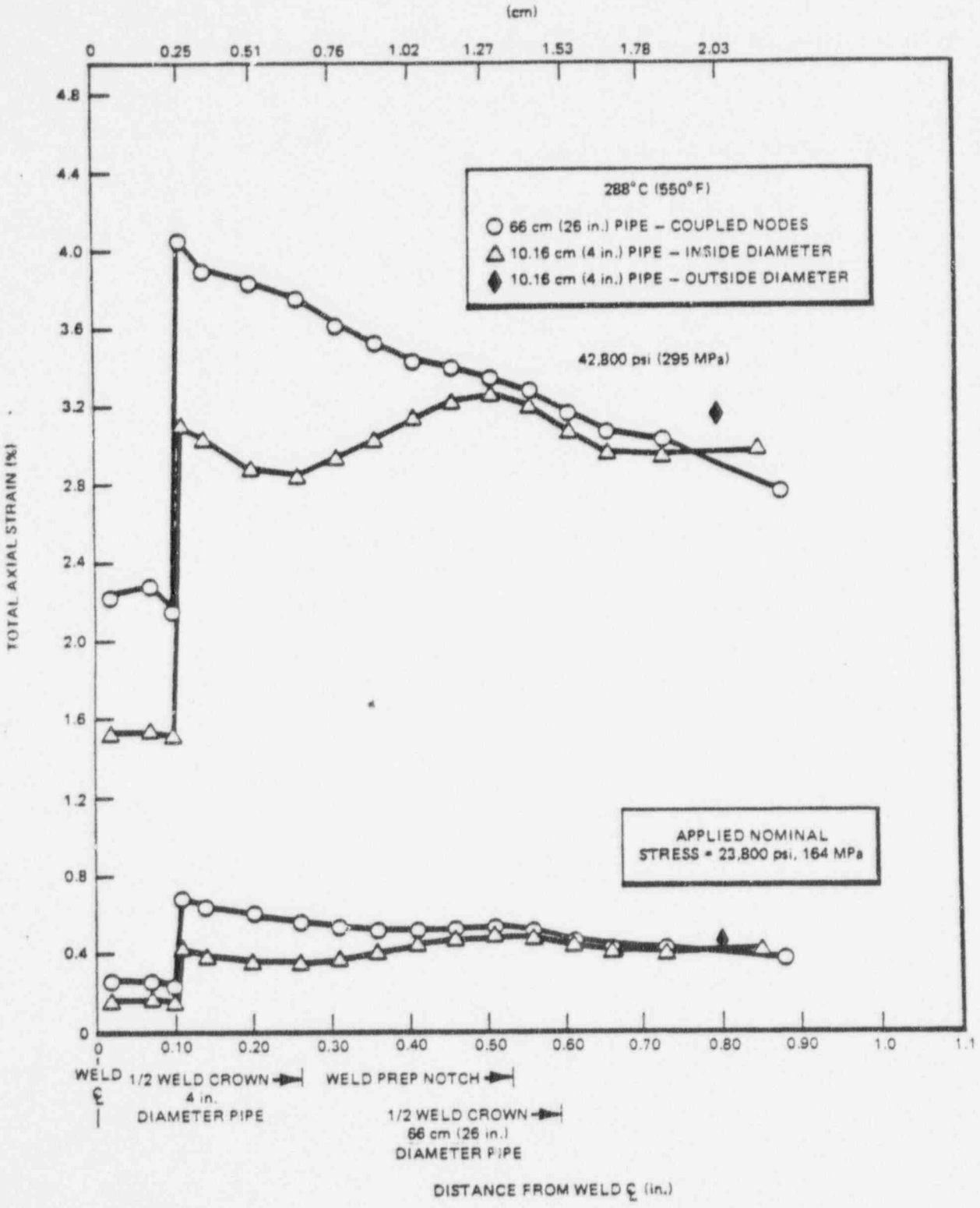

Figure J-8. Comparison of 10.16-cm (4-in.) Diameter and 66-cm (26-in.) Diameter Pipe Strains

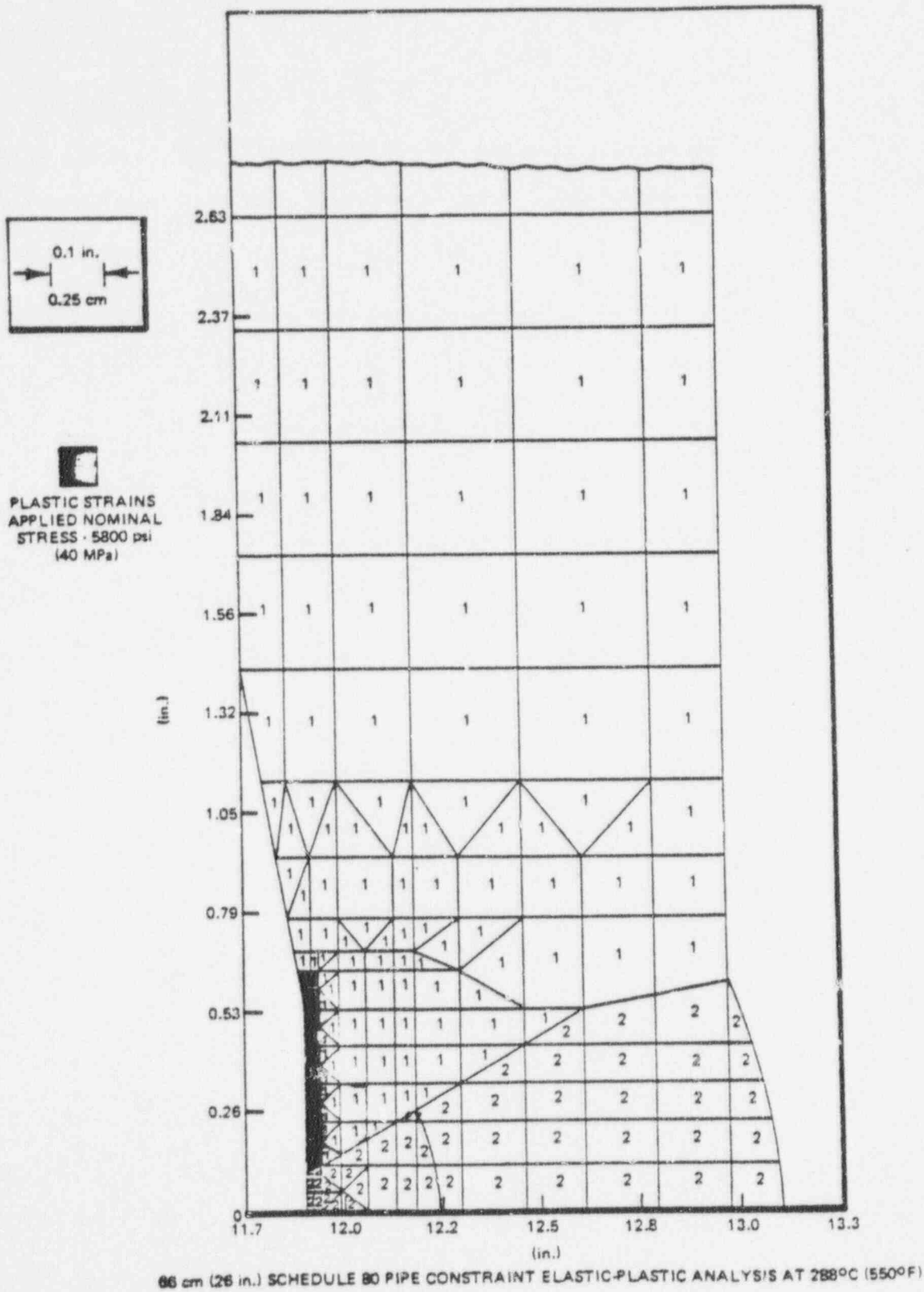

Figure J-9. Mapping of Plastic Strains as They First Appear on 66-cm (26-in.) Diameter Pipe at 288°C (550°F)

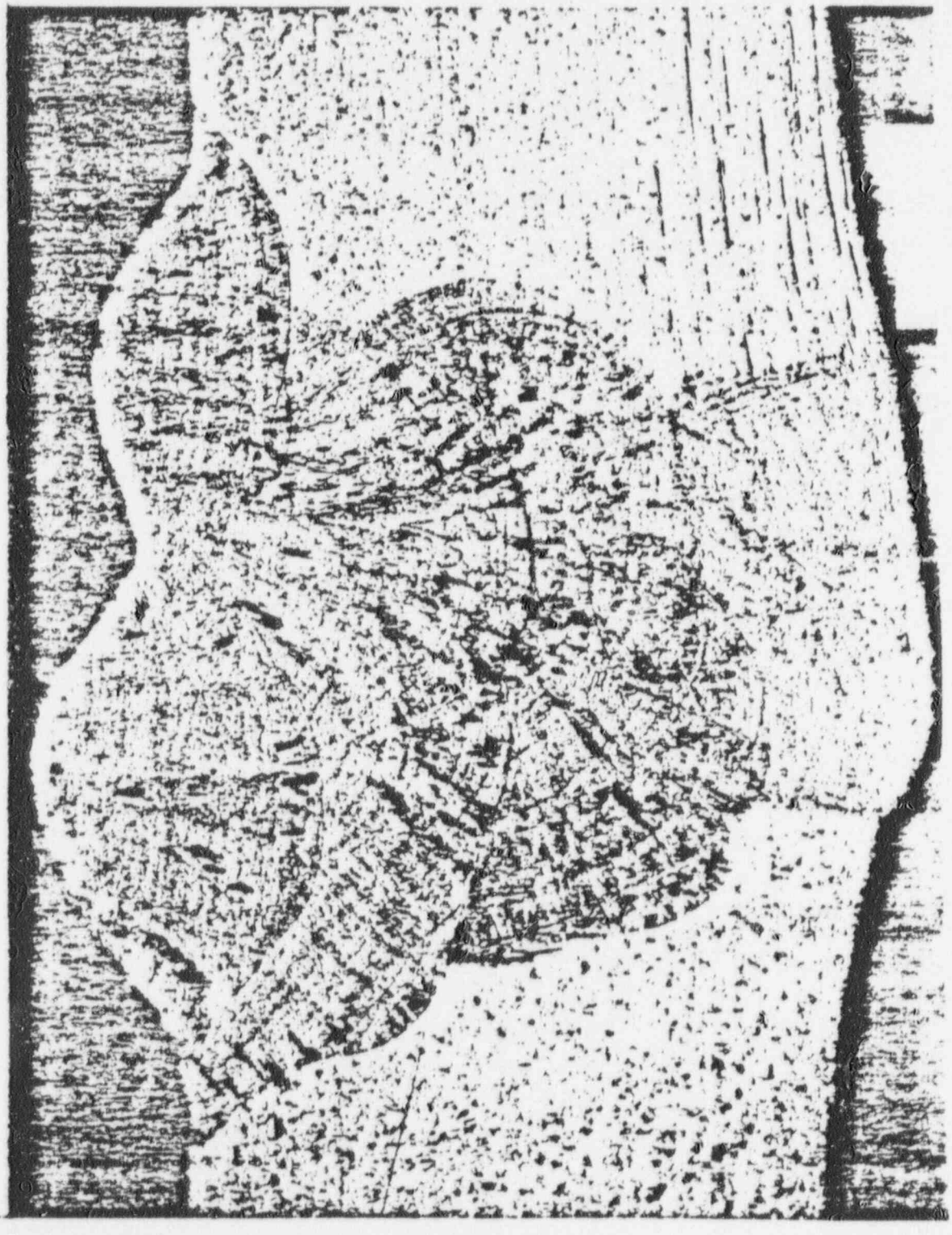

Figure J-10. 10.16-cm (4-in) Diameter Stainless Steel Butt Welded Pipe

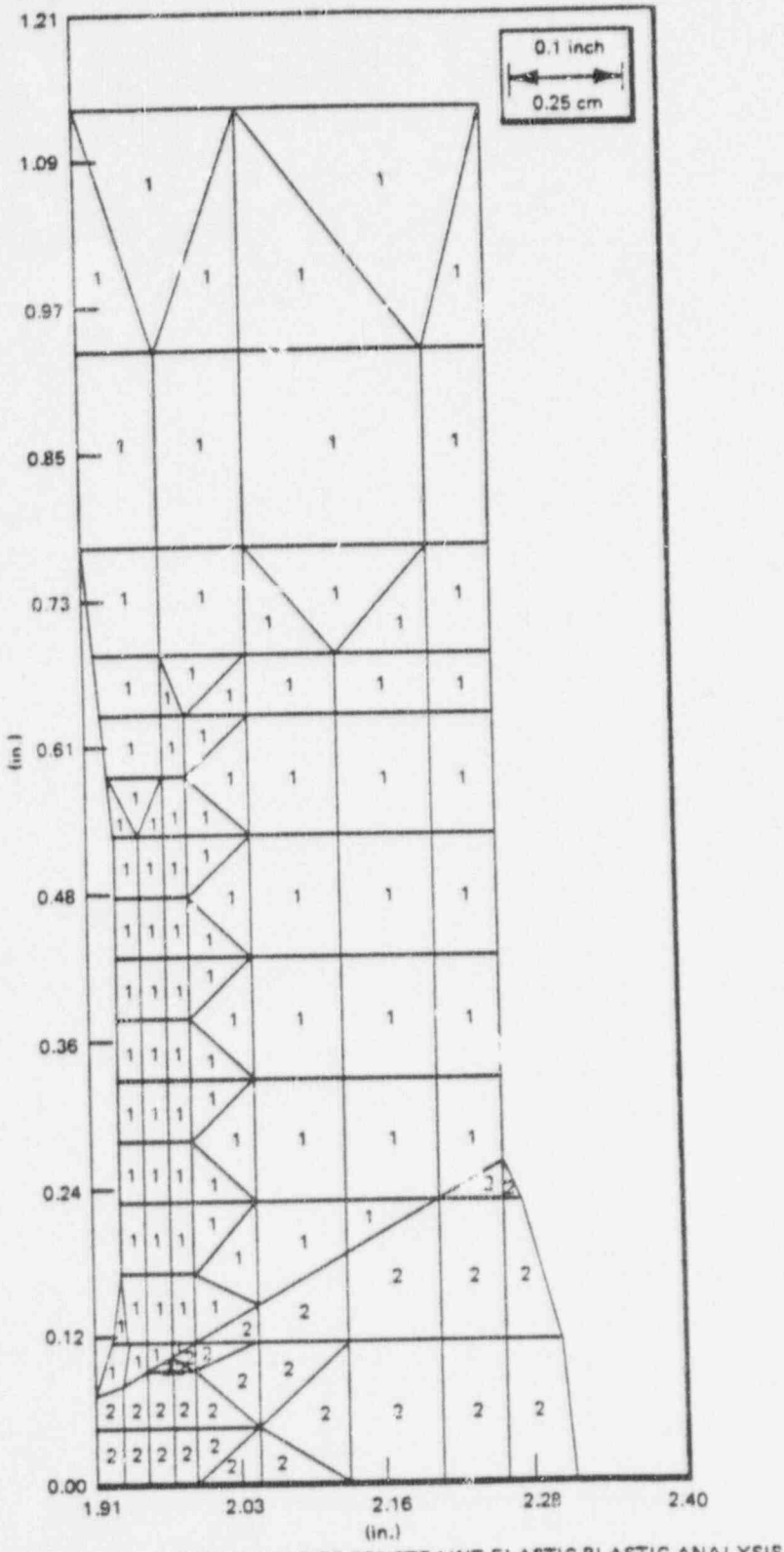

Figure J-11. Finite Element Model of Pipe with Weld Distortion

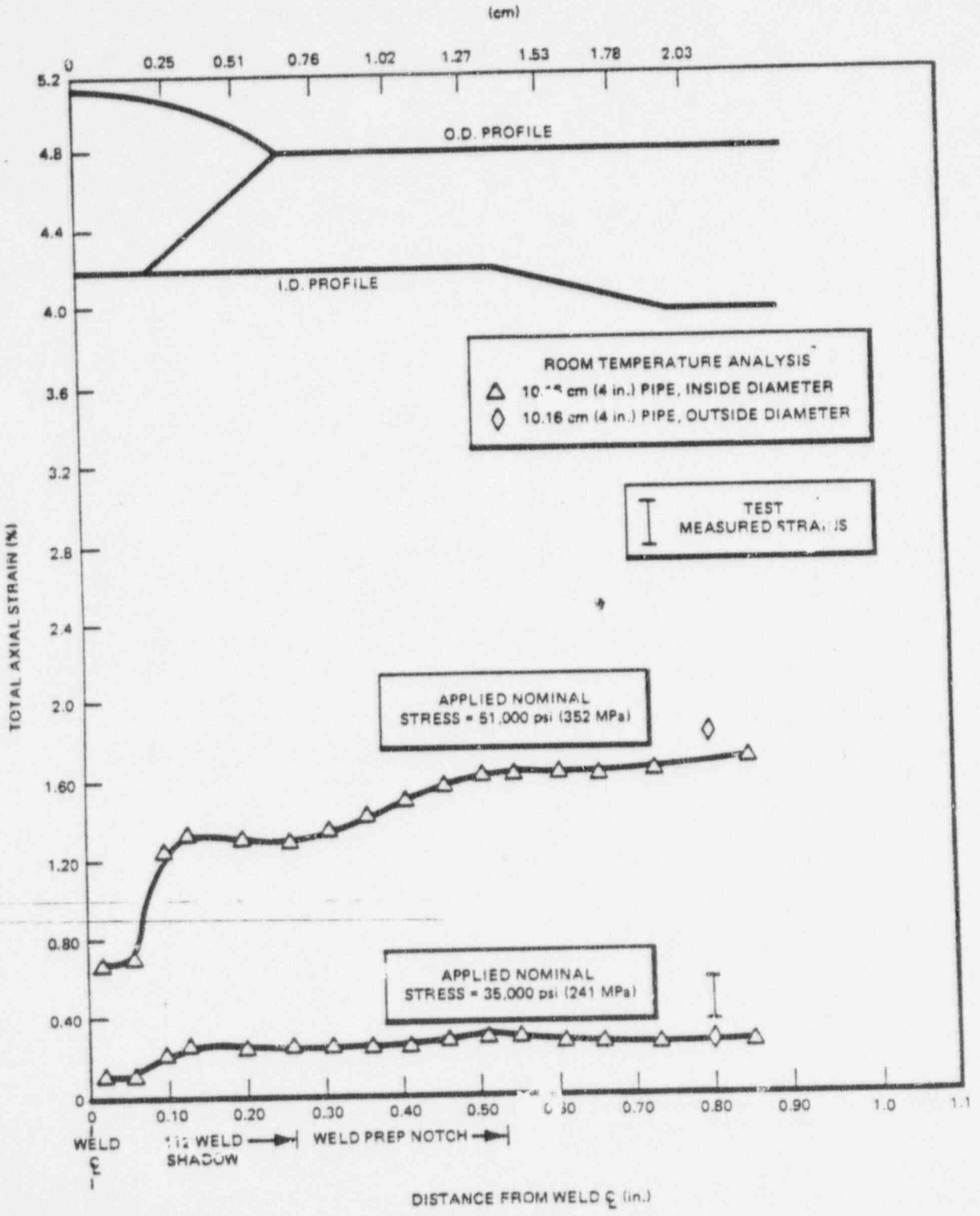

Figure J-12. 10.16-cm (4-in.) Diameter Pipe with Weld Distortion at Room Temperature — Total Strain versus Distance from Weld Centerline

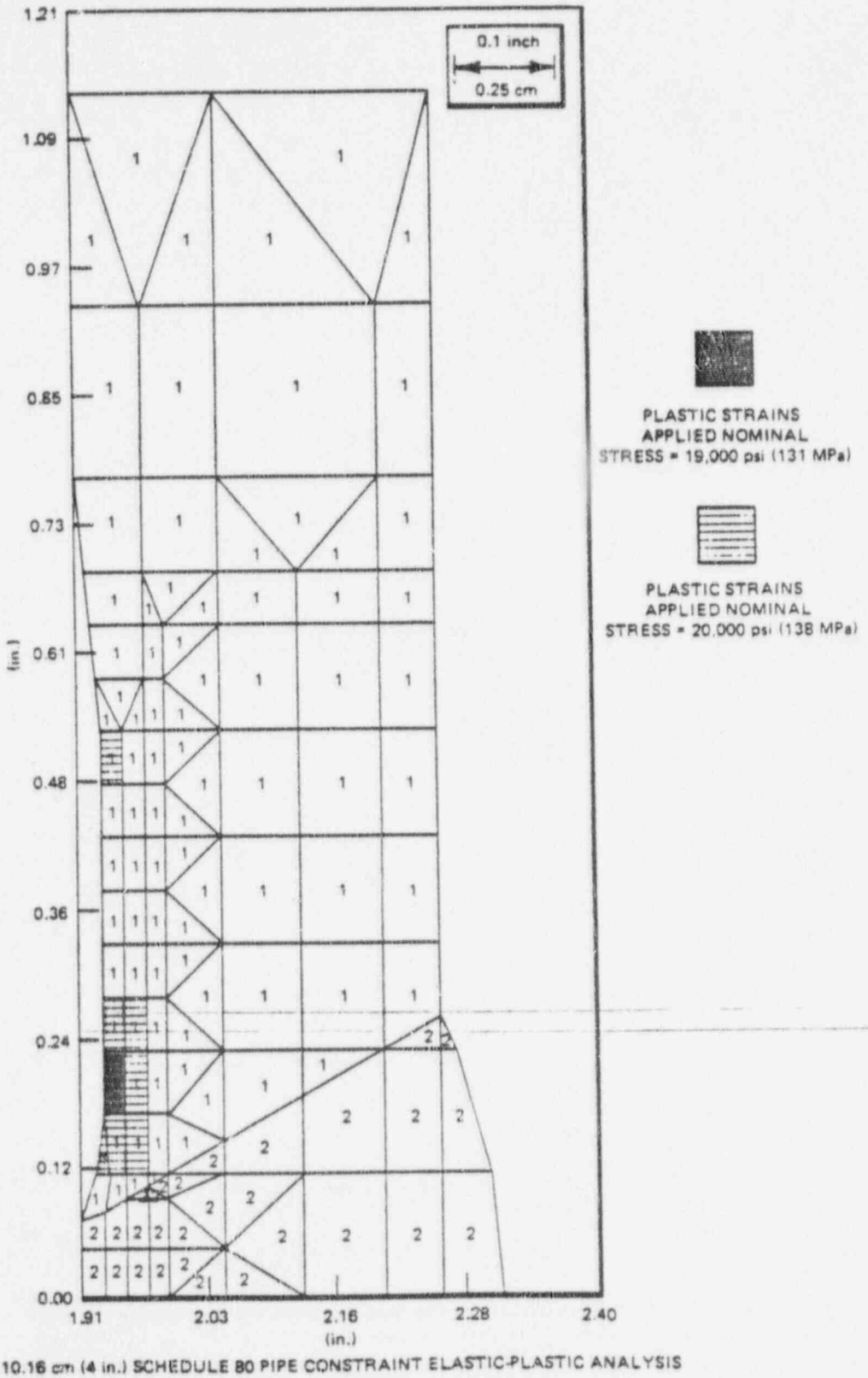

Figure J-13. Mapping of Plastic Strains as They First Appear on 10.16-cm (4-in.) Diameter Pipe with Weld Distortion, at Room Temperature

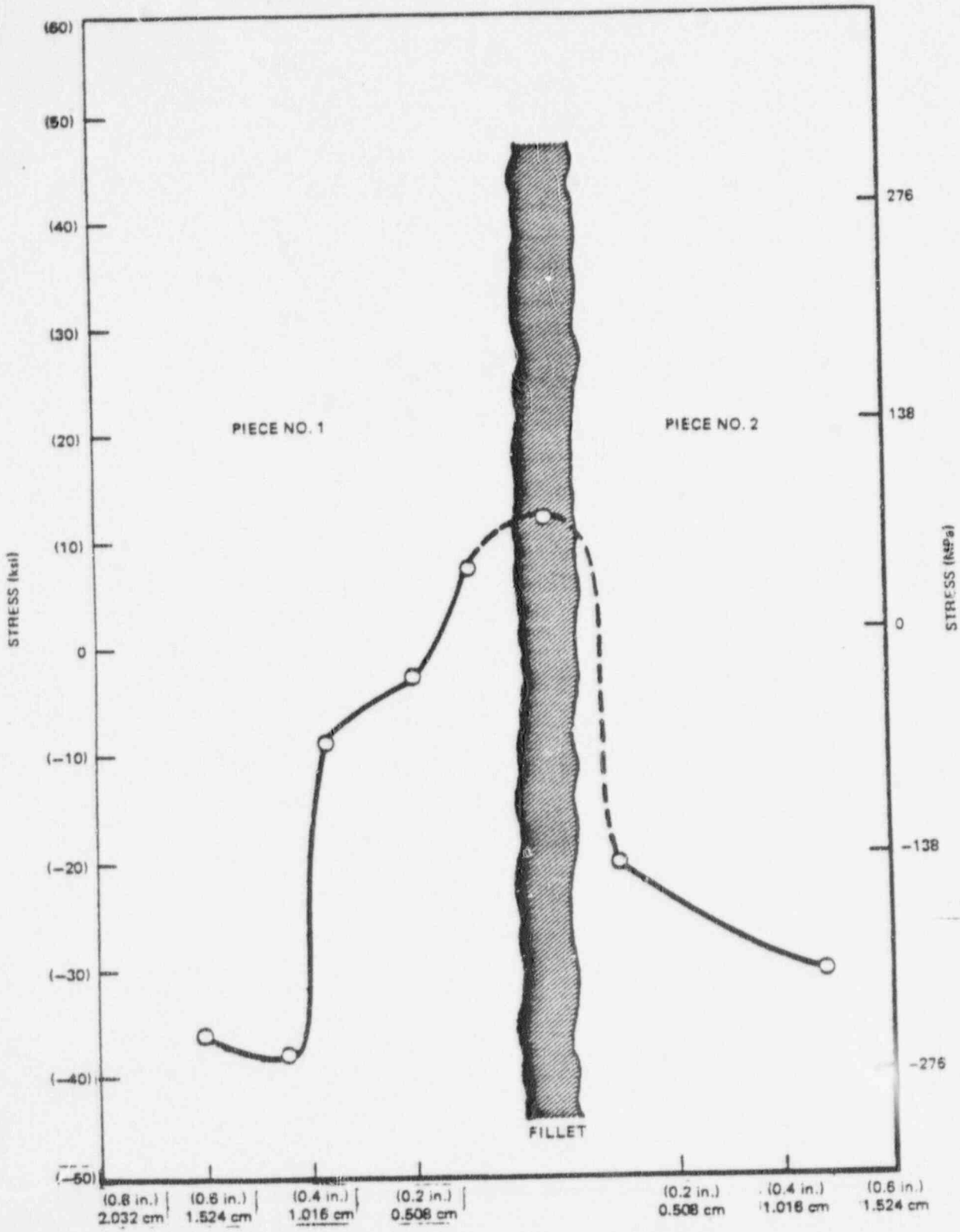

Figure J-14. Maximum Principal Residual Stress for the 10.16-cm (4-in.) Pipe i.d. Strips versus Distance from the Weld Fusion Line at the 225° Azimuth

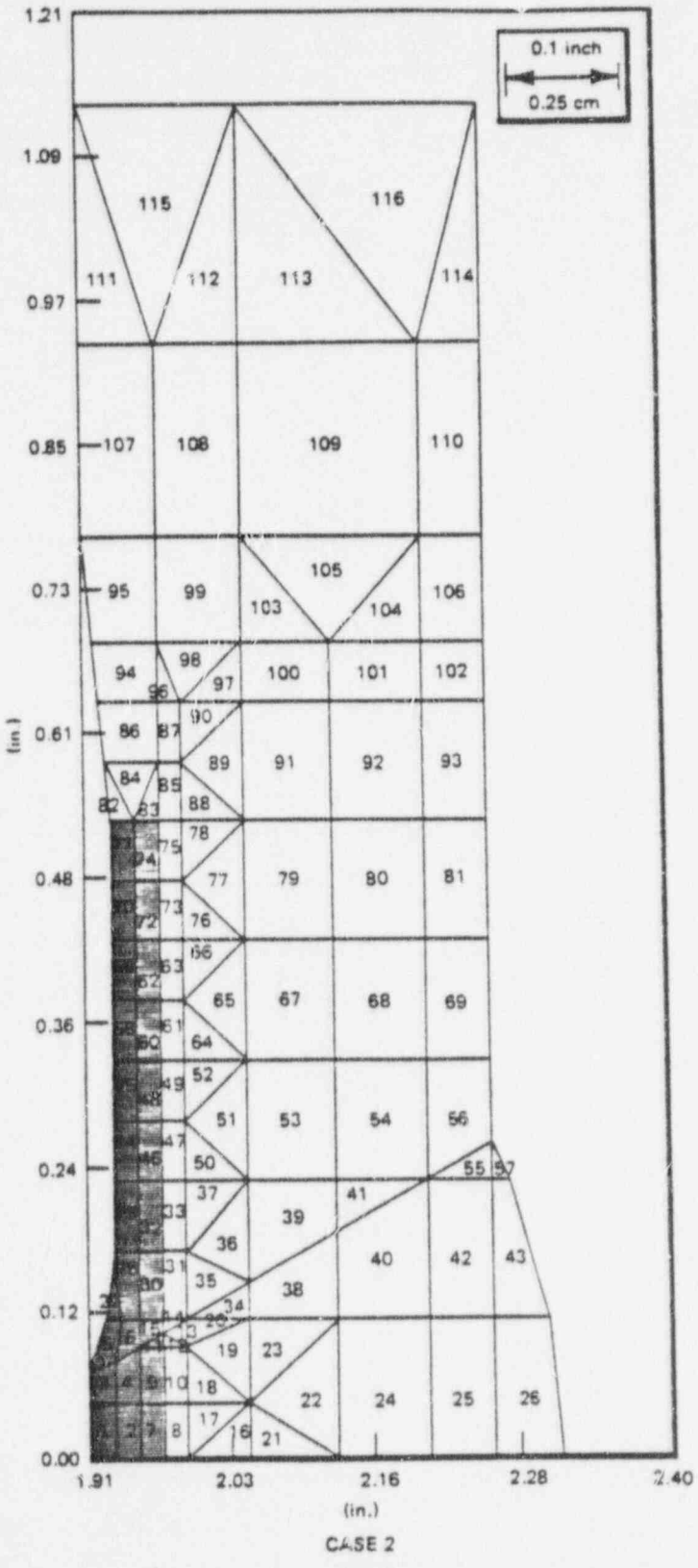

Figure J-15. Location of Residual Stresses on Pipe Finite Element Model

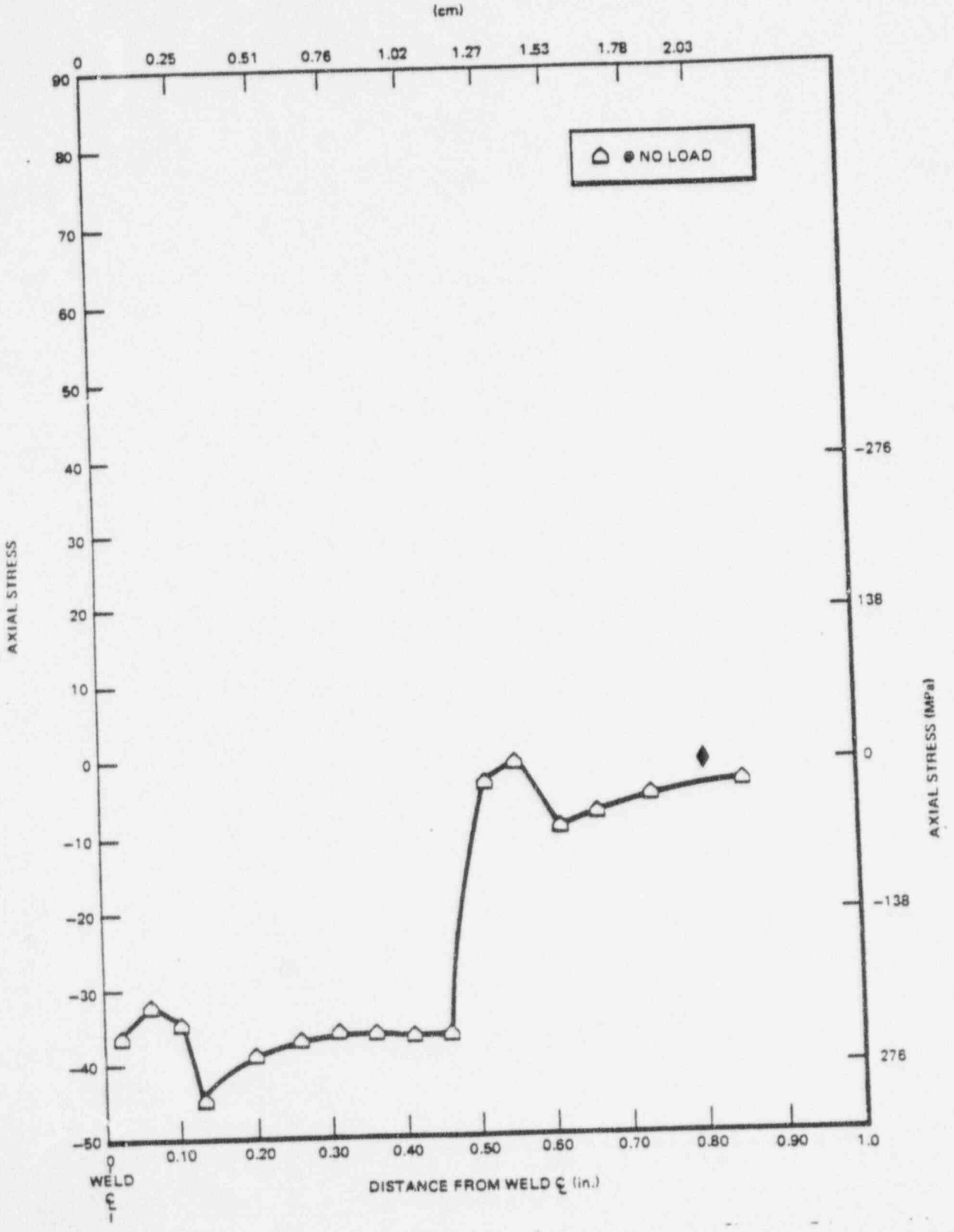

Figure J-16. Role of Residual Stress on 10.16-cm (4-in.) Diameter Pipe with Weld Distortion at Room Temperature — Axial Residual Stress Distribution

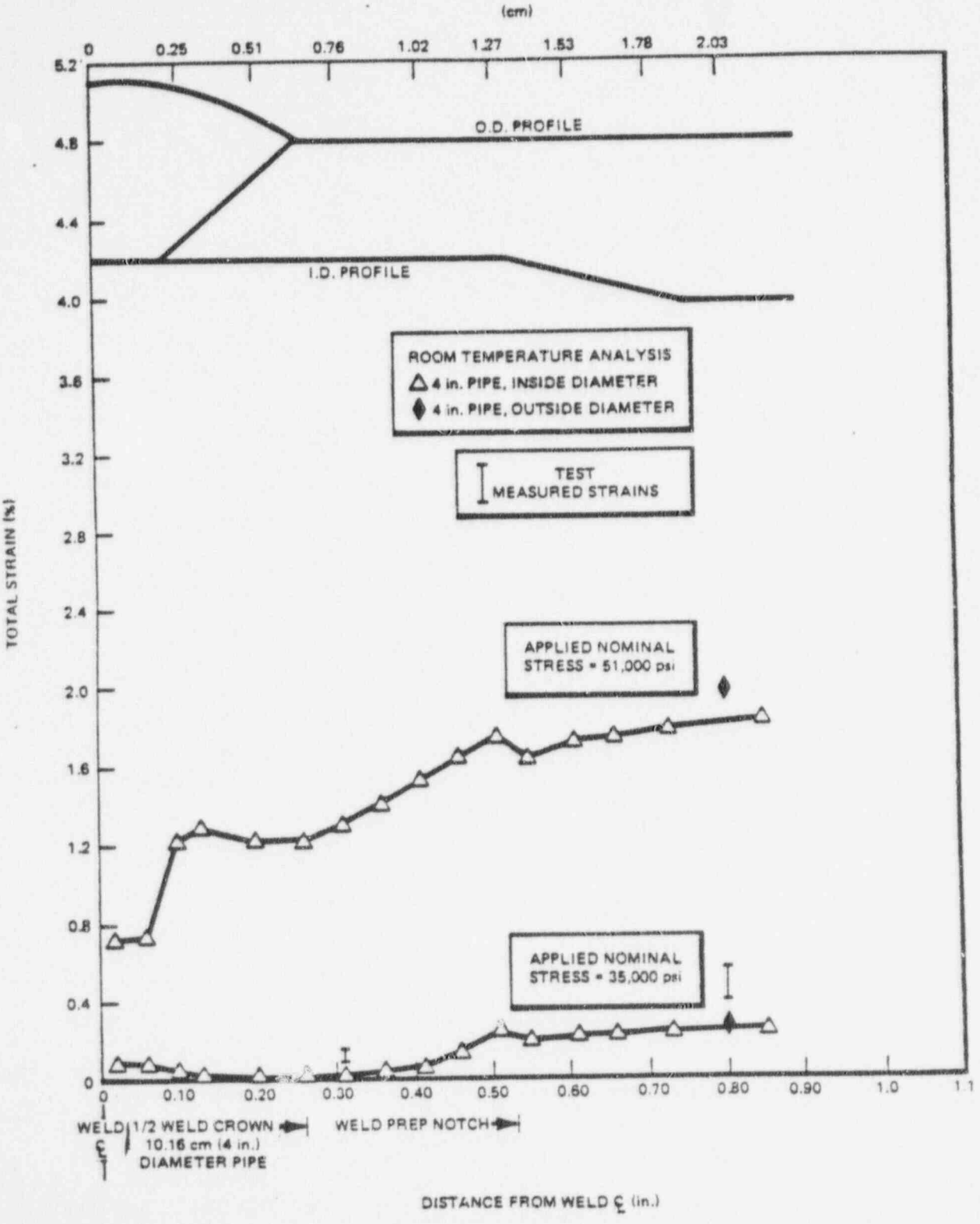

Figure J-17. Role of Residual Stress on 10.16-cm (4-in.) Pipe with Weld Distortion, at Room Temperature — Total Strain versus Distance from Weld Centerline

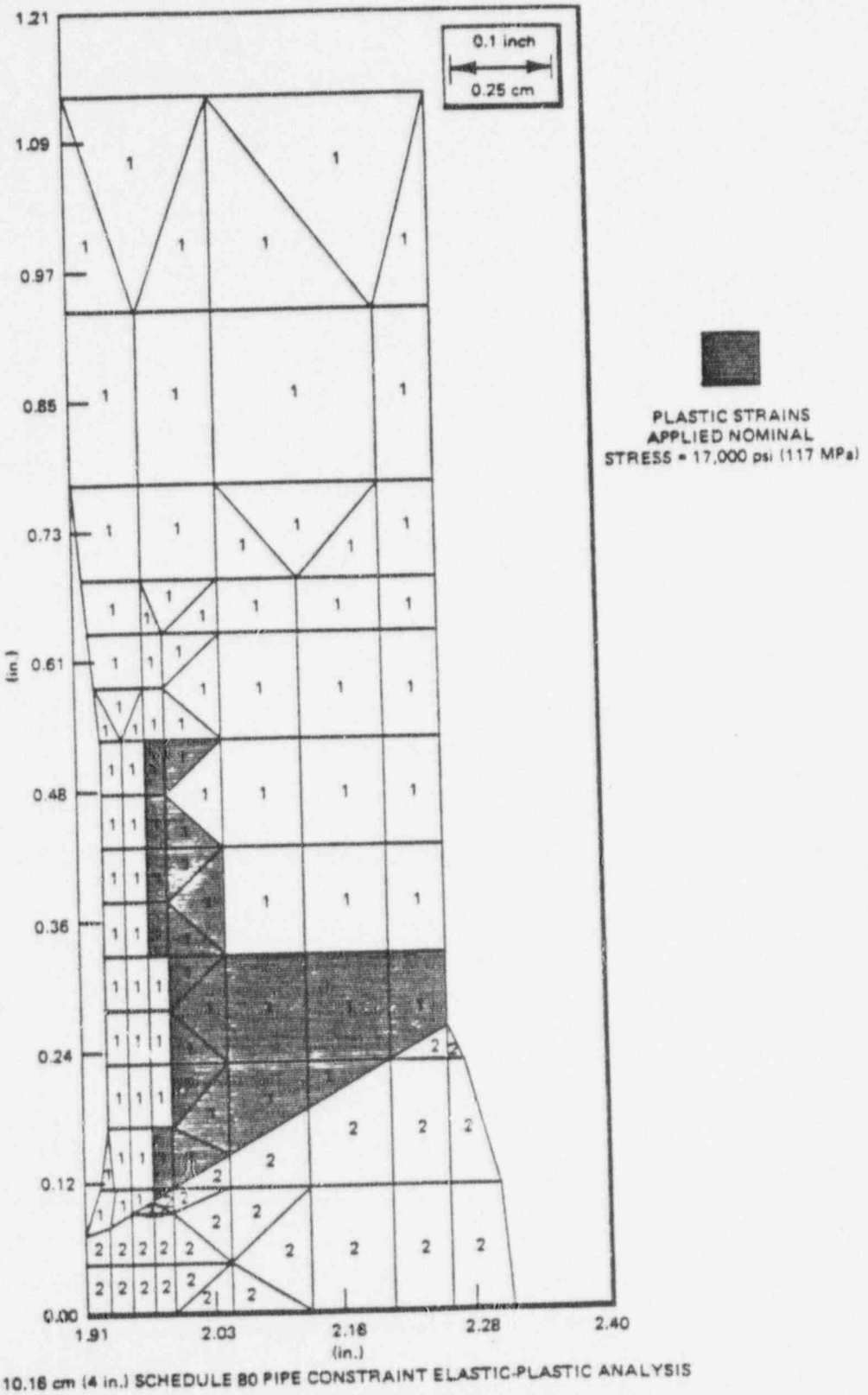

Figure J-18. Mapping of Plastic Strains as They First Appear on 10.16-cm (4-in.) Diameter Pipe with Weld Distortion and Residual Stresses, at Room Temperature — Case 2

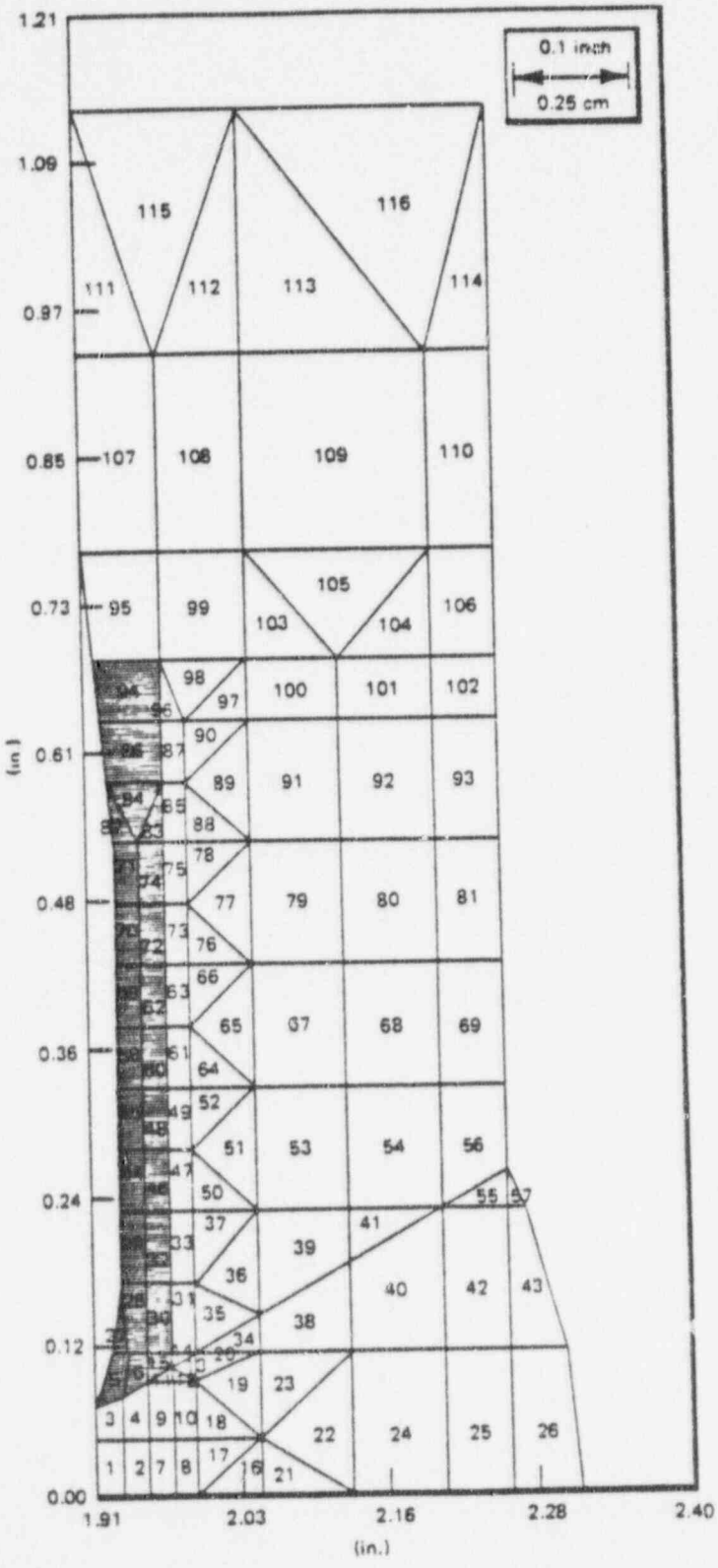

Figure J-19. Location of Residual Stresses on Pipe Finite Element Model

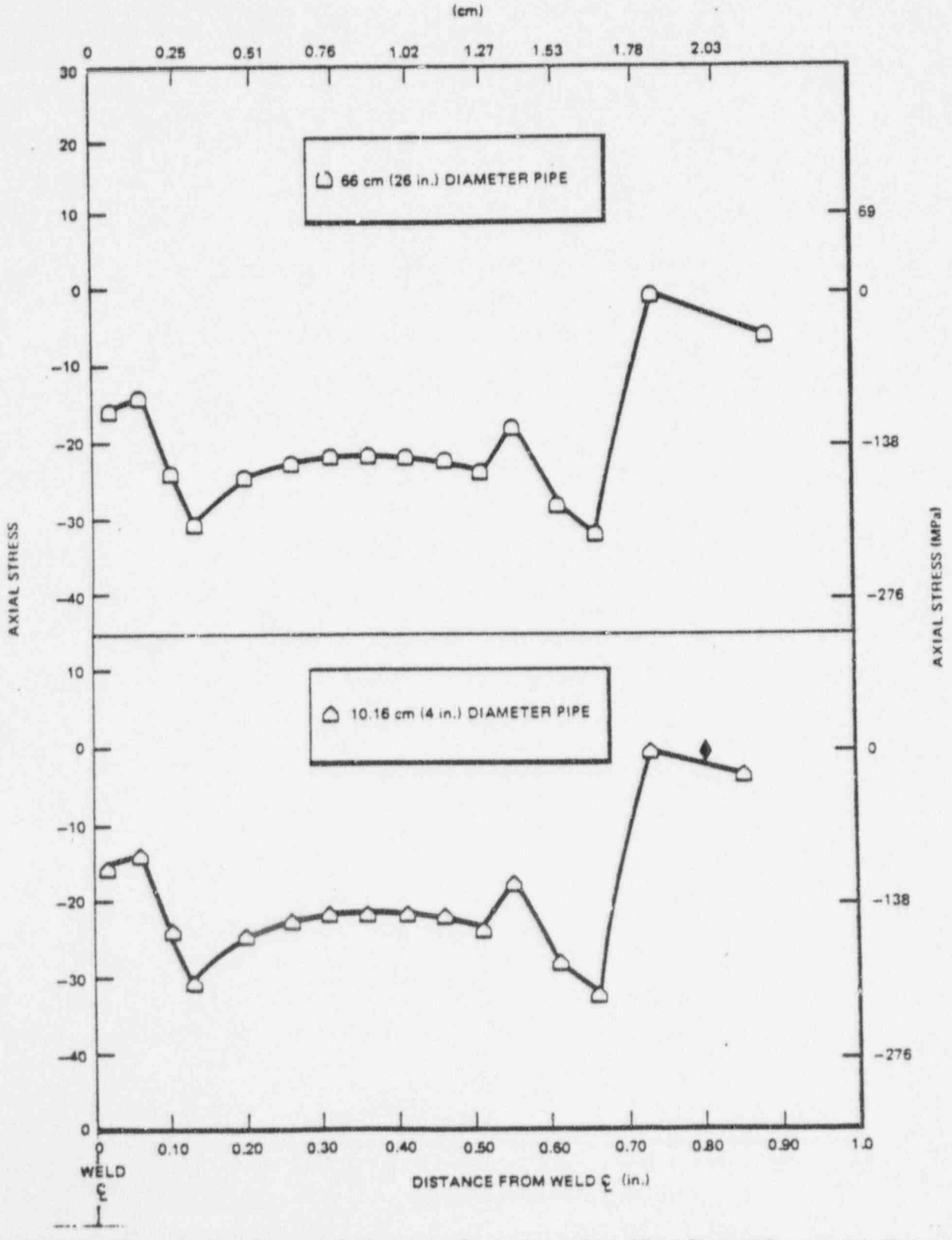

Figure J-20. Role of Residual Stress on 10.16-cm (4-in.) Diameter and 66-cm (26-in.) Diameter Pipe with Weld Distortion, at 288°C (550°F), and at No Load

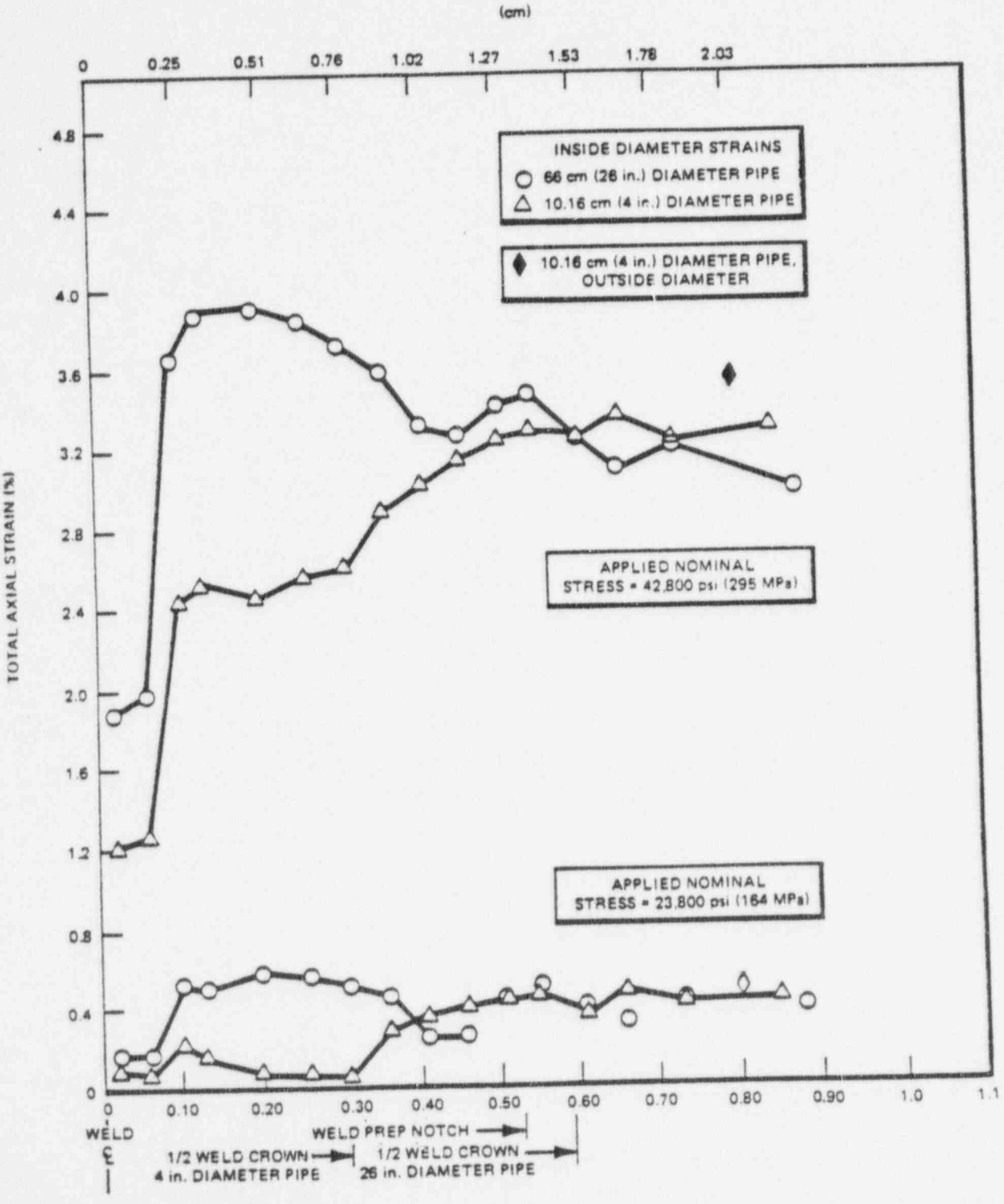

Figure J-21. Comparison of Total Axial Strain Between 10.16-cm (4-in.) and 66-cm (26-in.) Diameter Pipes with Weld Distortion and Residual Stress

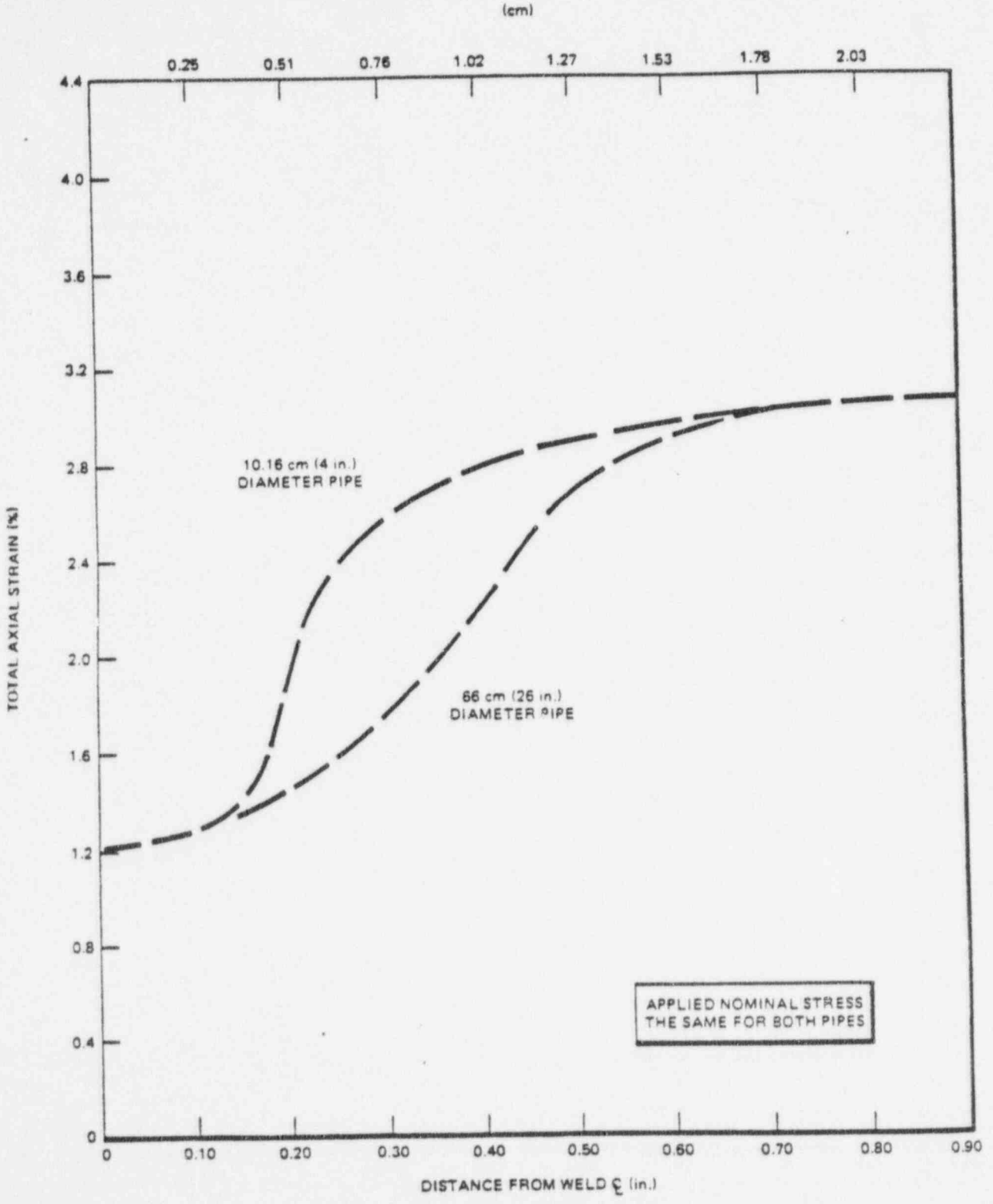

Figure J-22. Assumed Behavior of 10.16-cm (4-in.) and 66-cm (26-in.) Diameter Pipe with Weld Distortion, Residual Stress and High Strength HAZ

APPENDIX K. MEASUREMENT OF CONSTRAINT NEAR PIPE WELDS— COMPARISON AMONG DIFFERENT DIAMETER PIPES

K.1 INTRODUCTION

The cracking observed in certain Type-304 stainless steel piping systems has been shown to be due to a critical combination of factors.[1] These factors include sensitized material in the weld heat affected zone, the water environment and sustained or periodic local plastic deformation. The specific purpose of this study has been to determine the relative strain distributions near the weld in the heat affected zone of a 10.16 cm (4 in.) and a 66 cm (26 in.) diameter schedule 80 Type-304 stainless steel pipe and to evaluate the differences in local plastic strain (if they exist) between large and small diameter piping.

The results of the elastic plastic finite element modeling of the pipe deformation of small and large diameter pipes was presented in the prior section. In the analysis, idealized weld metal and base metal mechanical properties were used. The program predicted no geometric constraint for either pipe diameter. In addition, the modeling predicted that the strain distributions were similar in the heat affected zones for the 10.16 cm (4 inch) and 66 cm (26 inch) diameter pipes. Although residual stress had some influence at low nominal pipe strain, it was rapidly washed out at higher strain.

This task then extends the effort to a series of experimental pipe section tensile tests on 10.16 cm (4 inch) and 66 cm (26 inch) Type-304 stainless steel welded pipe at 500°F to help clarify the understanding of the strain distribution in the heat affected zone of large and small diameter pipes.

K.2 TEST DESCRIPTION

A total of three specimens were tested in this program. These pipe specimens were 20° segments cut out of 10.2 cm (4 inch) and 66 cm (26 inch) pipe cross sections. The specimens were cut out in 20° segments to maintain geometric similarity between the small and large diameter pipe segments so a relative comparison of their strain distributions could be made. Two of the three segments were from the 10.16 cm (4 inch) pipe, one of which was heat treated and partially annealed for ½ hour at 585°C (1250°F) to relieve residual stresses. The third specimen was from an as-welded 66 cm (26 inch) pipe. For all specimens, the base metal was Type-304 stainless steel and the weld metal was Type-308 stainless steel. These specimens and their end pieces are shown in Figures K-1, K-2 and K-3.

The temperature of the piping lines where cracking has been observed was 550°F. This temperature would have been used in the tests but it was believed that the strain gauge epoxy might not survive. Because of this concern, a slightly lower temperature of 500°F was used in the tests.

The specimens were loaded in steps to 4.5% strain. This limit was picked because past tests on full cross sections of piping have shown that at 3% strain, cracking occurred on the inner surface of the pipe near the weld. The loading of the specimens was in the axial direction since the cracks found in the field were oriented such that they indicated axial strain and not hoop strain as the major strain normal to the cracks.

Strain distribution data were obtained from high temperature strain gages, punch marks and a weldable strain gage on each specimen. These are described in the Test Setup Section, following.

K.3 TEST SETUP

A 500,000 pound and a 100,000 pound Universal test machine were used to load the specimens. Furnaces were mounted on both testing machines to provide for the 500°F air environment as shown in Figures K-4 and K-5. The temperature of the furnaces was monitored by chromel-alumel thermocouples adjacent to the weld area. Four additional thermocouples were located on the specimen to assure a uniform temperature throughout the specimens before loading. The thermocouples read out onto a multipoint temperature recorder. The locations of these thermocouples are shown in Figure K-6.

The specimens were then pulled in tension by the 100,000 pound Universal machine, 10.16 cm (4 inch) specimens, and the 500,000 pound Universal machine, 66 cm (26 inch) specimen. The loading of specimens was deflection controlled and loaded in 0.126 cm (.050 inch) increments until an approximate strain of 4.5% was reached for each specimen. The 10.16 cm (4 inch) specimens were loaded to a maximum of 0.80 cm (.320 inch) and the 66 cm (26 inch) specimen was loaded to a maximum of 1.4 cm (.550 inch). The loading was controlled by reading the specimen's deflection on a X-Y recorder.

The deflection versus load for the specimens was recorded on two instruments. One was an X-Y recorder, the other was a two-pen recorder located on the console of each testing machine.

The strain data were measured in three different ways:

1. High temperature strain gages were attached in the vicinity of the weld for all three specimens. These gages were fully encapsulated K-alloy strain gages with integral high-endurance lead ribbon with a backing and encapsulation matrix consisting of high temperature epoxy phenolic resin system enforced with fiberglass. The strain gage accuracy limits were to ±3%. These gages lasted the duration of the test; however, at large strains, the epoxy came loose and the gages became detached so that in some cases, the total data was not usable.

   The output of the high temperature strain gages was recorded on a multichannel strain gage data logger. Ten gages were attached to the 10.16 cm (4 inch) pipe specimens as shown in Figure K-7. Twenty gages were applied to the 66 cm (26 inch) pipe specimen. The ten gages located closest to the weld were the same gages used for the 10.16 cm (4 inch) specimen. Further away from the weld larger gages were used. A sketch and photograph shown in Figure K-8 displays the use of strain gages on the 66 cm (26 inch) pipe specimen.

2. A weldable strain gage was attached to each specimen away from the weld on the inside diameter surface to measure nominal strains in the pipe. This gage provided another data point in the overall strain distribution of the pipe. It's data was read using a BLH single channel strain indicator. These weldable gages were located on each specimen as shown in Figures K-9, K-10 and K-11.

3. Punch marks were made on the specimen as shown in Figures K-12, K-13, K-14 and K-15. The instruments used to measure distance between the punch marks was an X-Y-Z Sheffield Cordex measuring machine. This measurement was repeated four times and averaged, both before and after the test.

K.3 RESULTS

The results of the pipe deformation tests are summarized into several graphs. The coordinate system utilized in presenting the results is shown in Figure K-17.

K.3.1 Stress Versus Local Strain

Three graphs (one for each specimen) were made of stress versus local strain. The various curves on each of these plots represented the stress (load/initial local cross section area) versus the local strain for different locations as measured from the center of the weld.

These graphs are shown in Figures K-17, K-18 and K-19 for the respective test specimens.

K.3.2 Strain Versus Distance from Centerline of Weld

These graphs show only the area near the weld since the object of the tests was to look at the strain distributions in the heat affected zone. This set of graphs was generated by plotting the normalized strain against the distance from the weld centerline for 0.1% (Figure K-20), 1% (Figure K-21), 2% (Figure K-22) and 4.5% (Figure K-23) nominal pipe strain. The normalized strain was obtained by dividing the local inside surface strain at different locations by the

nominal pipe strain measured by the weldable strain gage mounted away from the weld. Each graph contained three curves: one for the 10.16 cm (4 in.) pipe specimen (as-welded), 10.16 cm (4 in.) pipe specimen stress relieved and 66 cm (26 in.) pipe specimen.

K.3.3 Summary of Available Strain Data

Figures K-24, K-25 and K-26 show all strain data obtained from the tests in graphs of strain (in/in) versus distance from weld centerline (in). These strain data were obtained from the high temperature gages, weldable strain gage and punch marks.

K.4 DISCUSSION OF RESULTS

This section contains the discussion of trends shown by the data obtained from these tests. These trends led to conclusions about the relative strain distributions near a weld for the different test specimens.

K.4.1 Stress Versus Local Strain Curves (Figures K-17, K-18 and K-19)

The stress versus local strain curves for the 10.16 cm (4 in.) pipe specimen (as-welded) and the 10.16 cm (4 in.) stress relieved pipe specimen differed slightly. The 10.16 cm (4 in.) annealed specimen's curves were always below the 10.16 cm (4 in.) specimen's (as-welded) curves at corresponding locations away from the weld. This appears to be due to the lower yield strength associated with the 677°C (1250°F) heat treatment. The two 10.16 cm (4 in.) pipe specimen's stress versus local strain curves in the elastic region were essentially the same.

The 66 cm (26 in.) pipe specimen's stress versus strain curve in the elastic region has a lower slope than the 10.16 cm (4 in.) specimen's curves. Comparing the 66 cm (26 in.) curve to the 10.16 cm (4 in.) pipe specimen's curves for plastic strain in the heat affected zone, the curves are almost the same.

K.4.2 Normalized Axial Strain Versus Distance from Centerline of Weld (Figures K-20, K-21, K-22, K-23, K-24)

The normalized axial strain versus the distance from the weld centerline plots for the 10.16 cm (4 in.) heat treated pipe specimen and the 10.16 cm (4 in.) pipe specimen (as-welded) are essentially the same in the heat affected zone. This would imply that the heat treatment on the 10.16 cm (4 in.) pipe specimen did not change the strain distribution in the area around the weld in the heat affected zone.

The 66 cm (26 in.) pipe specimen's strain curve was slightly higher than the 10.16 cm (4 in.) specimen's curve at 1% nominal pipe strain. At 2% nominal pipe strain, the strain curves for all three specimens for locations in the heat affected zone were found to be the same. At 1% and 2% nominal strain, the pipe in the HAZ was still in elastic strain so this result would be expected. The plastic nominal strain of 4.5% curve showed the 66 cm (26 in.) pipe specimen's strain in the HAZ near the weld to be below the 10.16 cm (4 in.) pipe specimen's strain. The curves, however, were quite close to each other. The expected result of the 66 cm (26 in.) pipe axial strain data being considerably less than the 10.16 cm (4 in.) pipe axial strain data was not obtained.

K.4.3 Measurement Accuracy

The high temperature gage data was influenced by several factors which could have caused error. The gage itself has a possibility of ±1% error in gage factor. The signal conditioning equipment used was only capable of calibration within ±50 microstrain or ±2%, whichever was greater. The high temperature strain gages then could have a total error of ±3% in their readings.

The weldable strain gage data will have a ±3% error associated with the gage and the same ±2% error due to calibration of the read-out equipment. Thus, a maximum 5% error could be in the strain readings obtained by the weldable strain gage.

The repeatability of the reading of the punch marks was within 0.5 mils out of 100 mils or ±5% strain. For nominal strains of 4.5% strain, there is an error of 11%.

Another type of error could have been introduced in the elastic curves. This specimen bending comparison of predicted strains and measured strains suggests that there may have been an error due to the clamping of the specimen into the test machine before pulling. This would not have that much effect on the plastic region because when it has reached that point, the strain would be mostly axial. The relative shape of the strain distributions and their relative relationships to each other still would hold true.

K.5 CONCLUSIONS FROM TEST RESULTS

The primary focus of this testing work was to investigate the relative strain behavior of 10.16 cm (4 in.) and 66 cm (26 in.) pipe near butt welds. Based on comparisons of the test data, the following conclusions can be drawn:

- When pipes are loaded beyond their elastic limit, constraint is observed near the weld. The amount of constraint decreases as the distance from the weld increases.
- When equal nominal strain levels were applied to pipe sections in this test, there was no significant difference in the strain distributions near the weld for 10.16 cm (4 in.) and 66 cm (26 in.) pipe.
- Partial stress relief of one of the 10.16 cm (4 in.) weld specimens for ½ hour at 677°C (1250°F) had no apparent effect on the applied strain distribution or constraint near the weld.
- The measured stress strain data imply a strength gradient in the heat affected zone of the weld. This strength gradient is probably the result of strain hardening due to weld shrinkage and may be the primary contributing factor in constraint observed in Type-304 stainless steel pipes.
- Additional tests, including tests with complete circumferential pipe sections, are needed to clarify the deformation behavior in large and small diameter pipes.

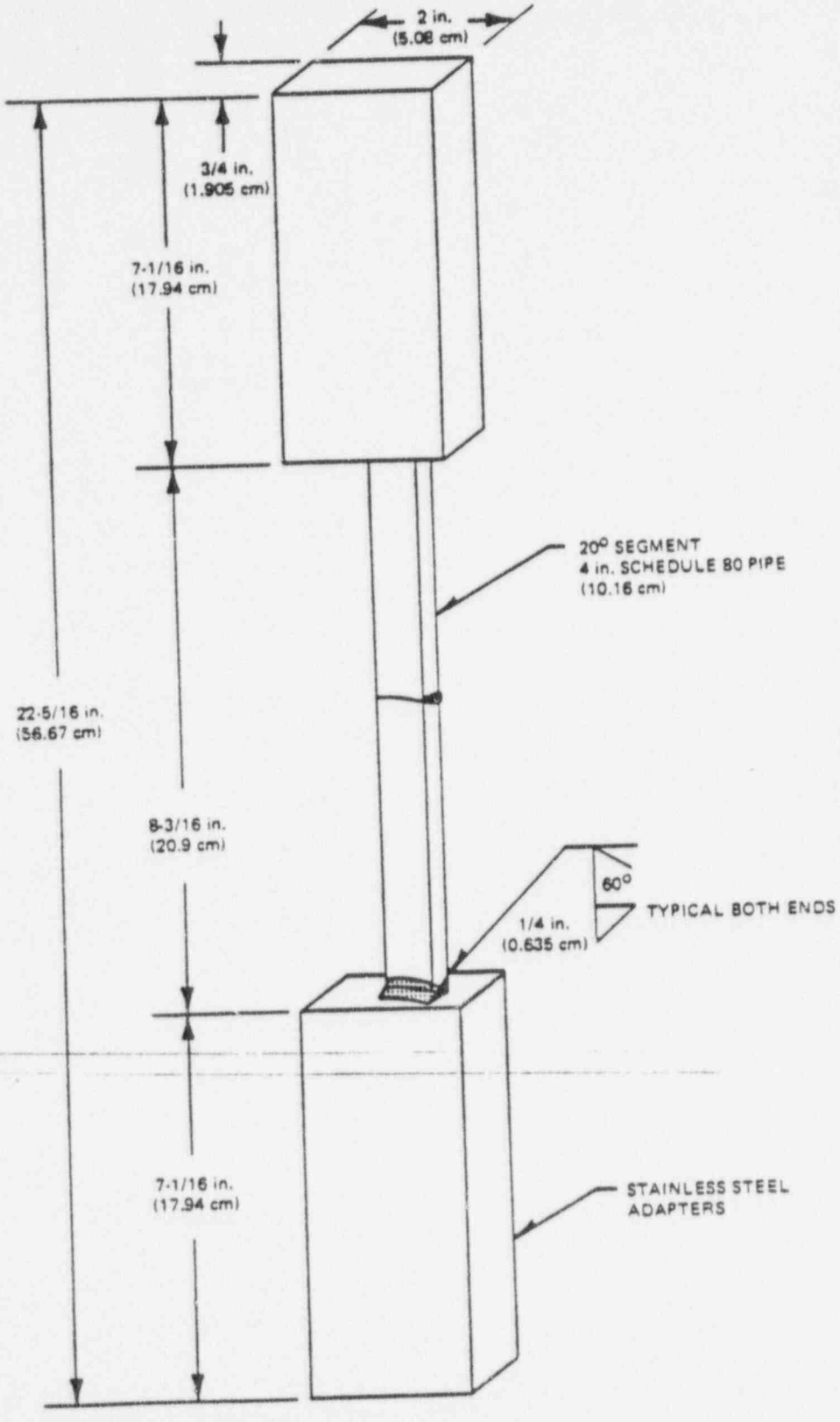

Figure K-1. 10.16-cm (4-in.) Schedule 80 Pipe Test Specimen with End Pieces

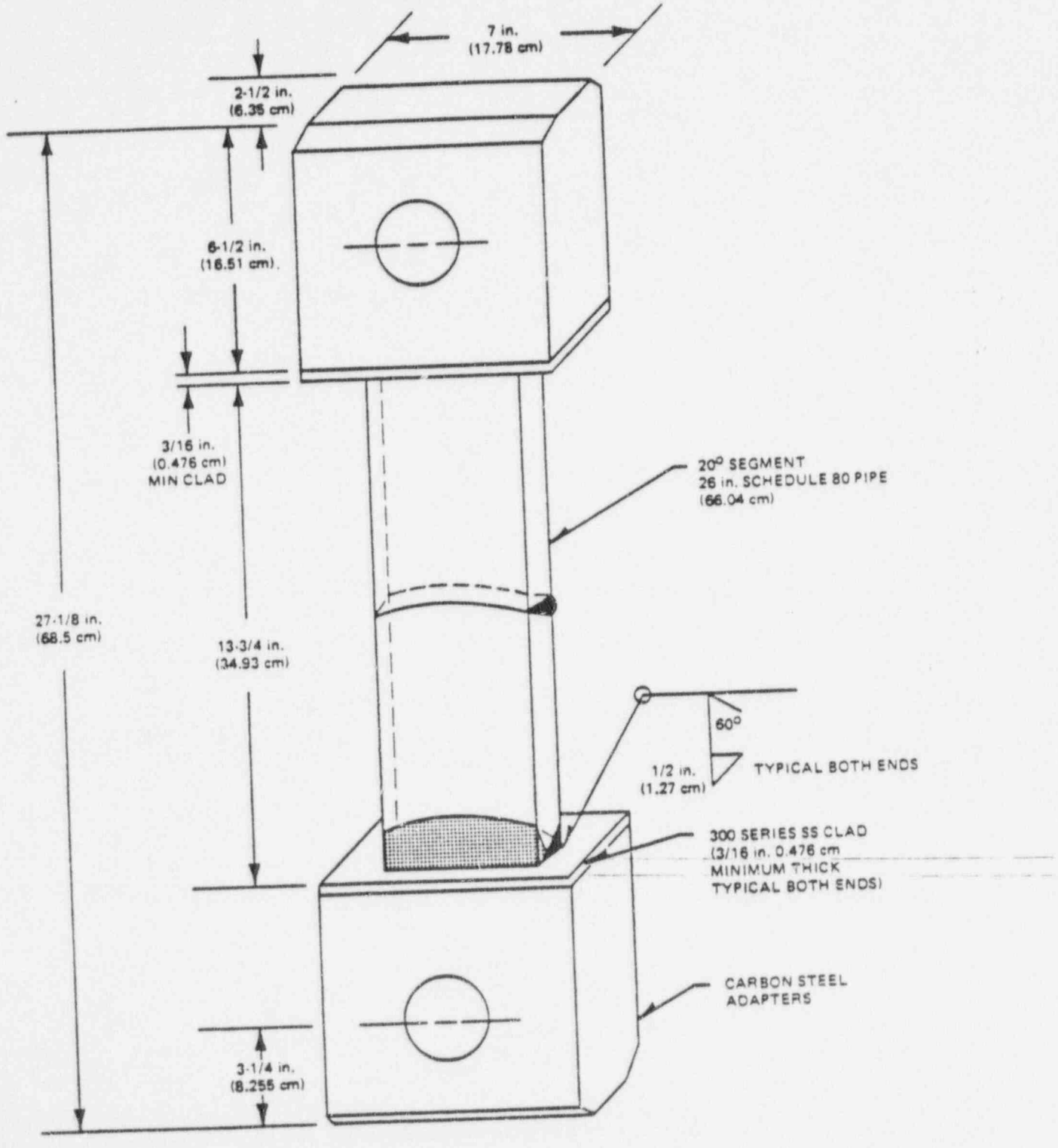

Figure K-2. 66-cm (26-in.) Schedule 80 Pipe Test Specimen with End Pieces

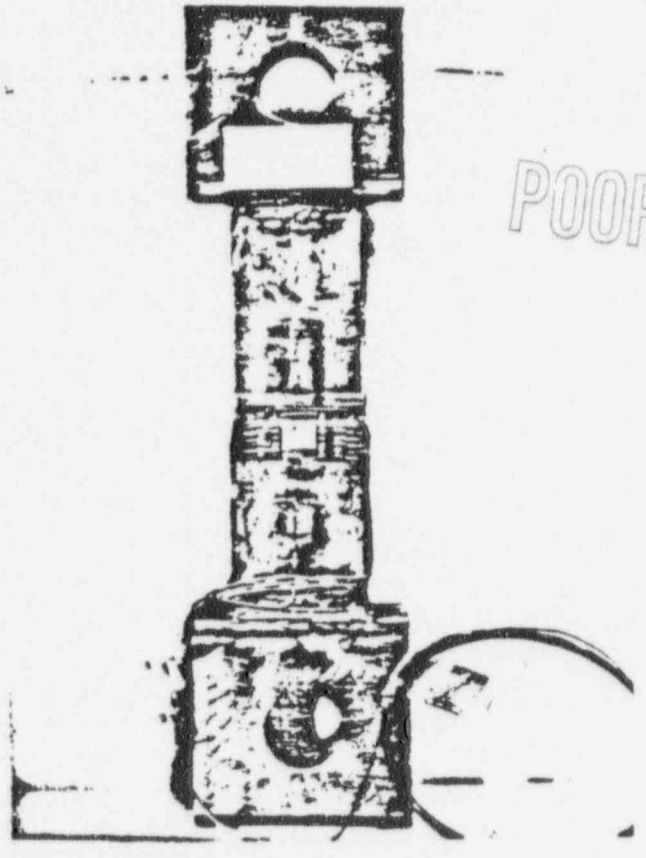

Figure K-3. Photograph of 66-cm (26-in.) Pipe Test Specimen

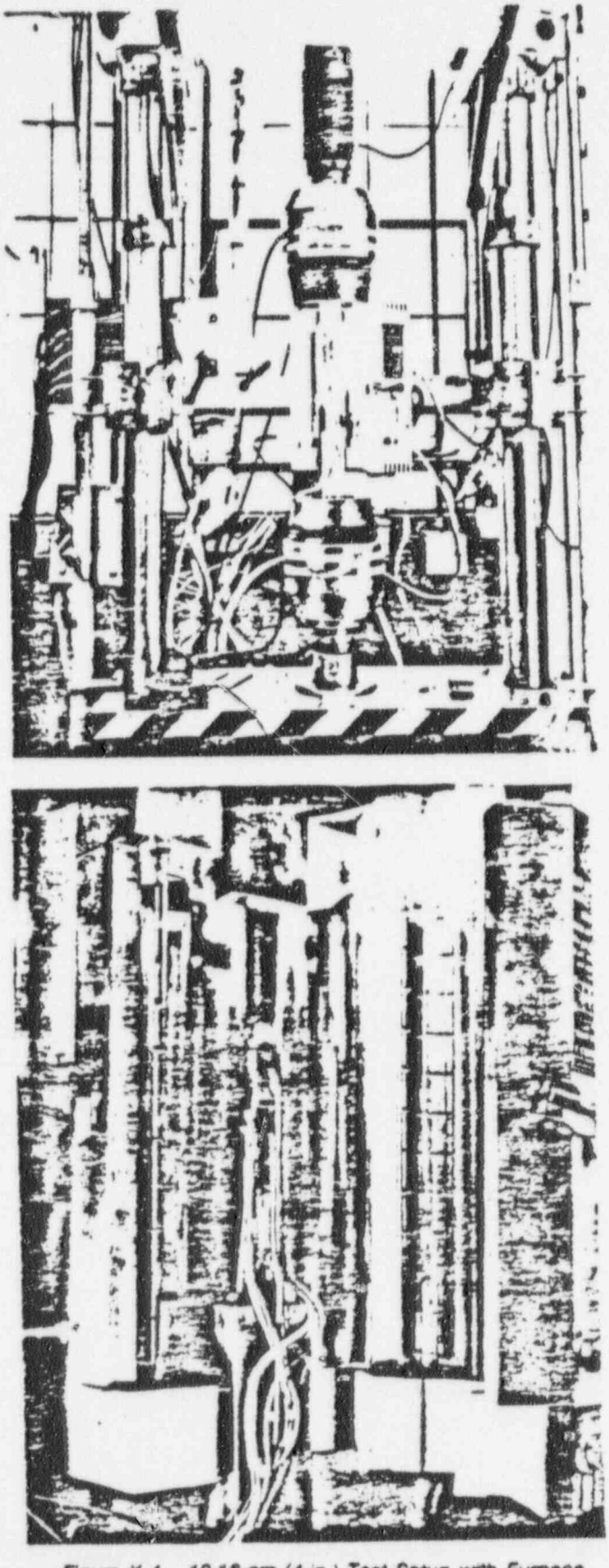

Figure K-4. 10.16-cm (4-in.) Test Setup with Furnace

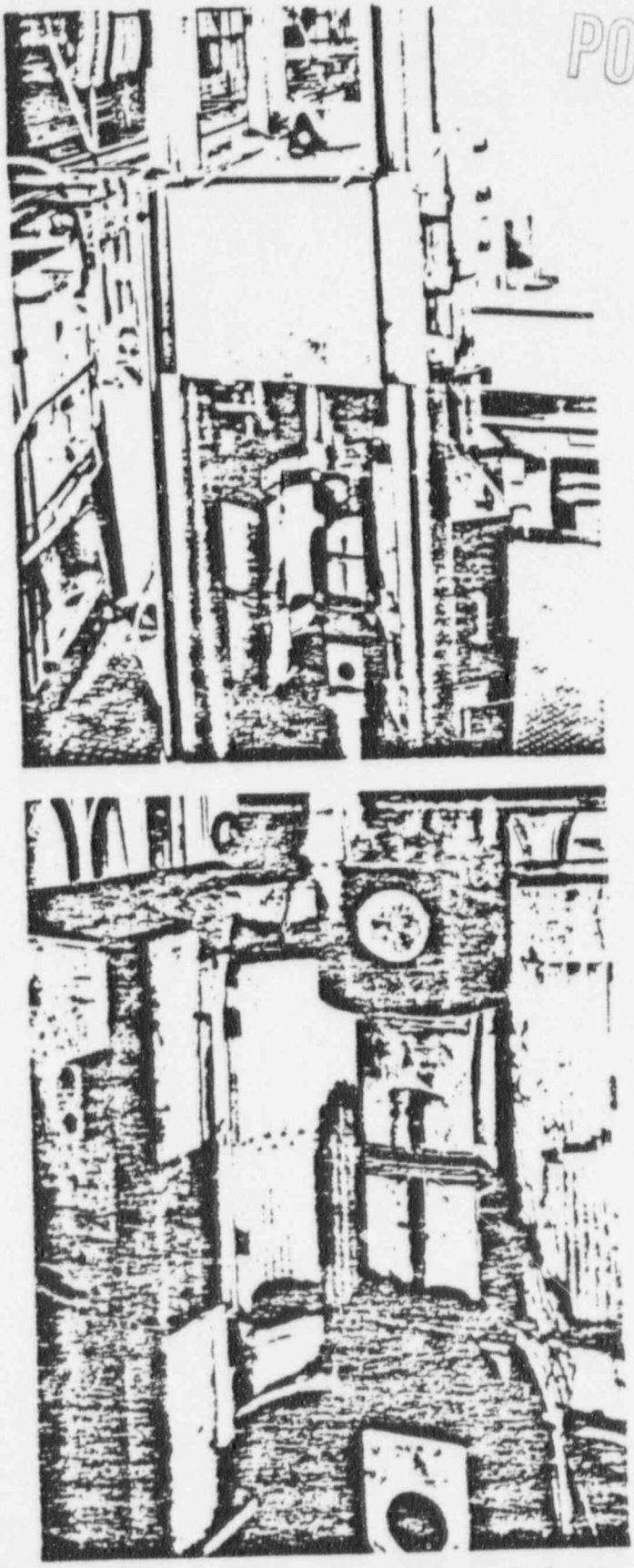

Figure K-5. 66-cm (26-in.) Pipe Test Setup with Furnace

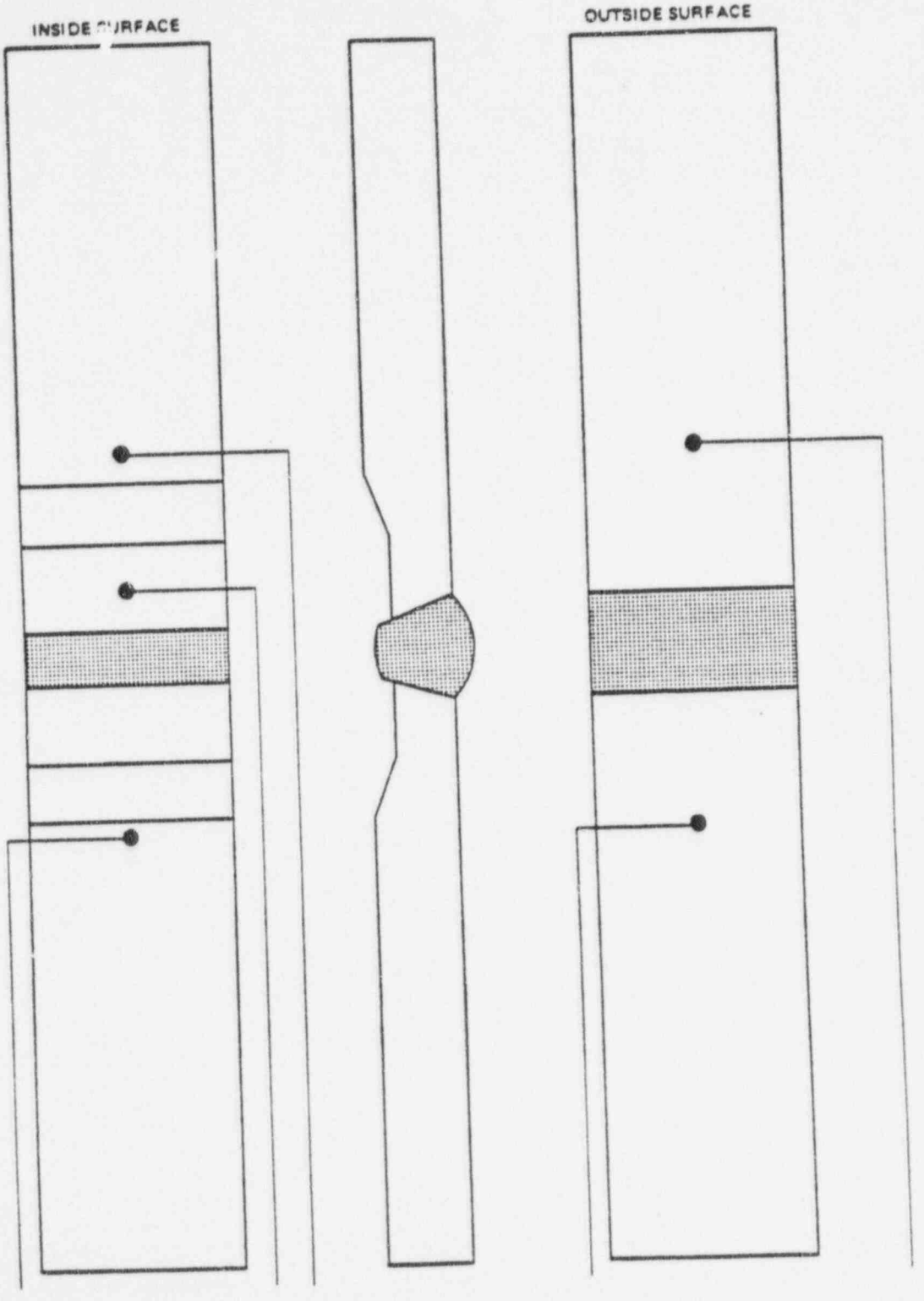

Figure K-6. Relative Location of Thermocouples for the Pipe Test Specimens

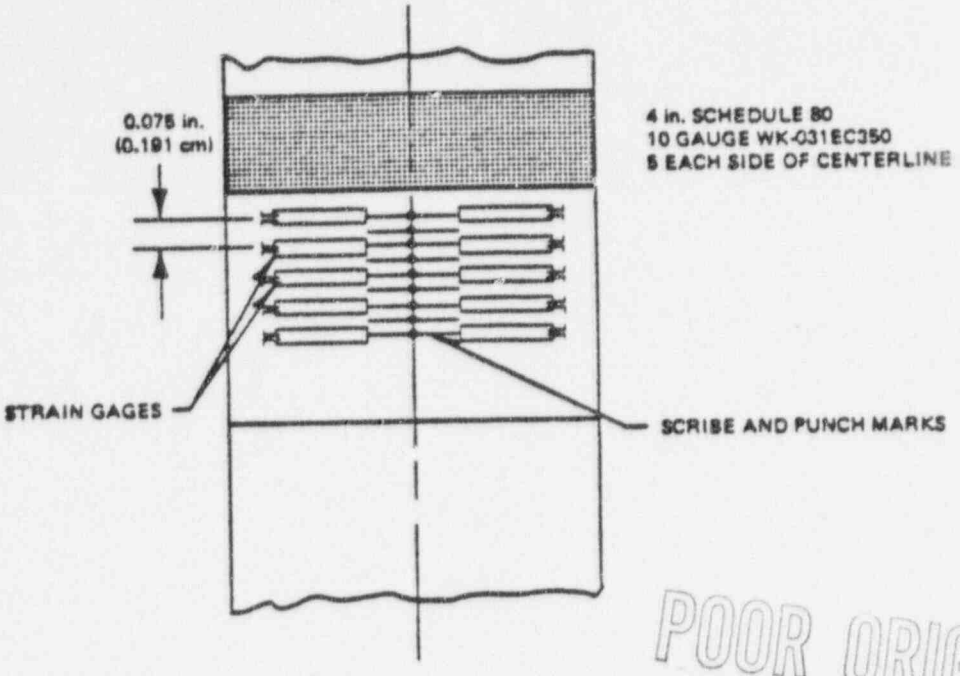

Figure K-7. Location of High Temperature Strain Gages for 10.16-cm (4-in.) Pipe Specimens

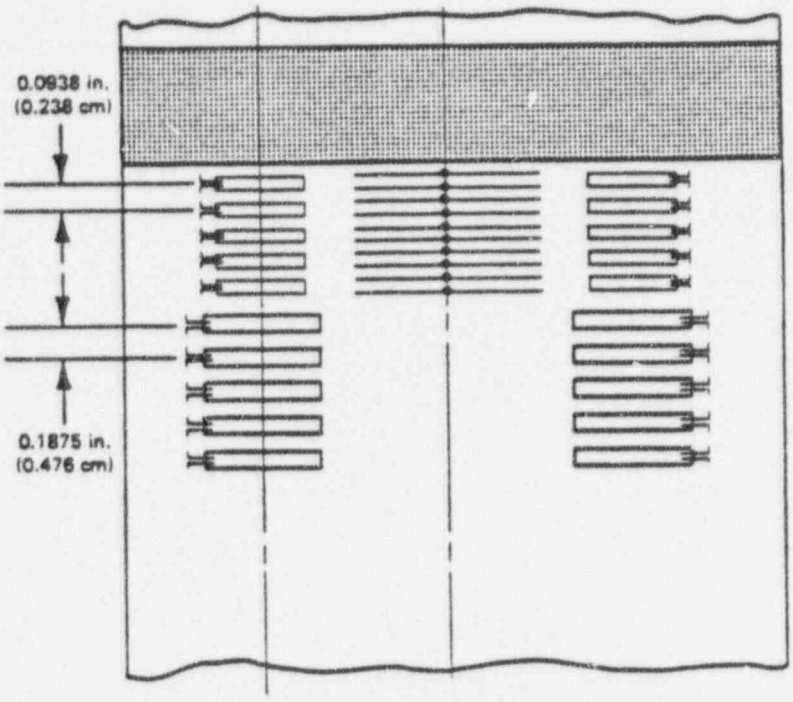

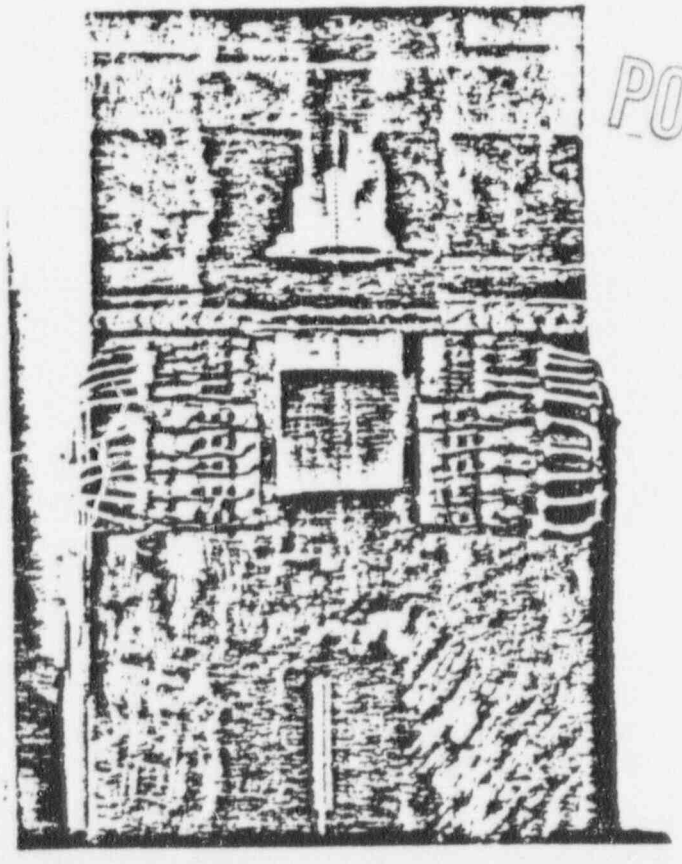

Figure K-8. Location of High Temperature Strain Gages for 66-cm (26-in.) Pipe Specimen

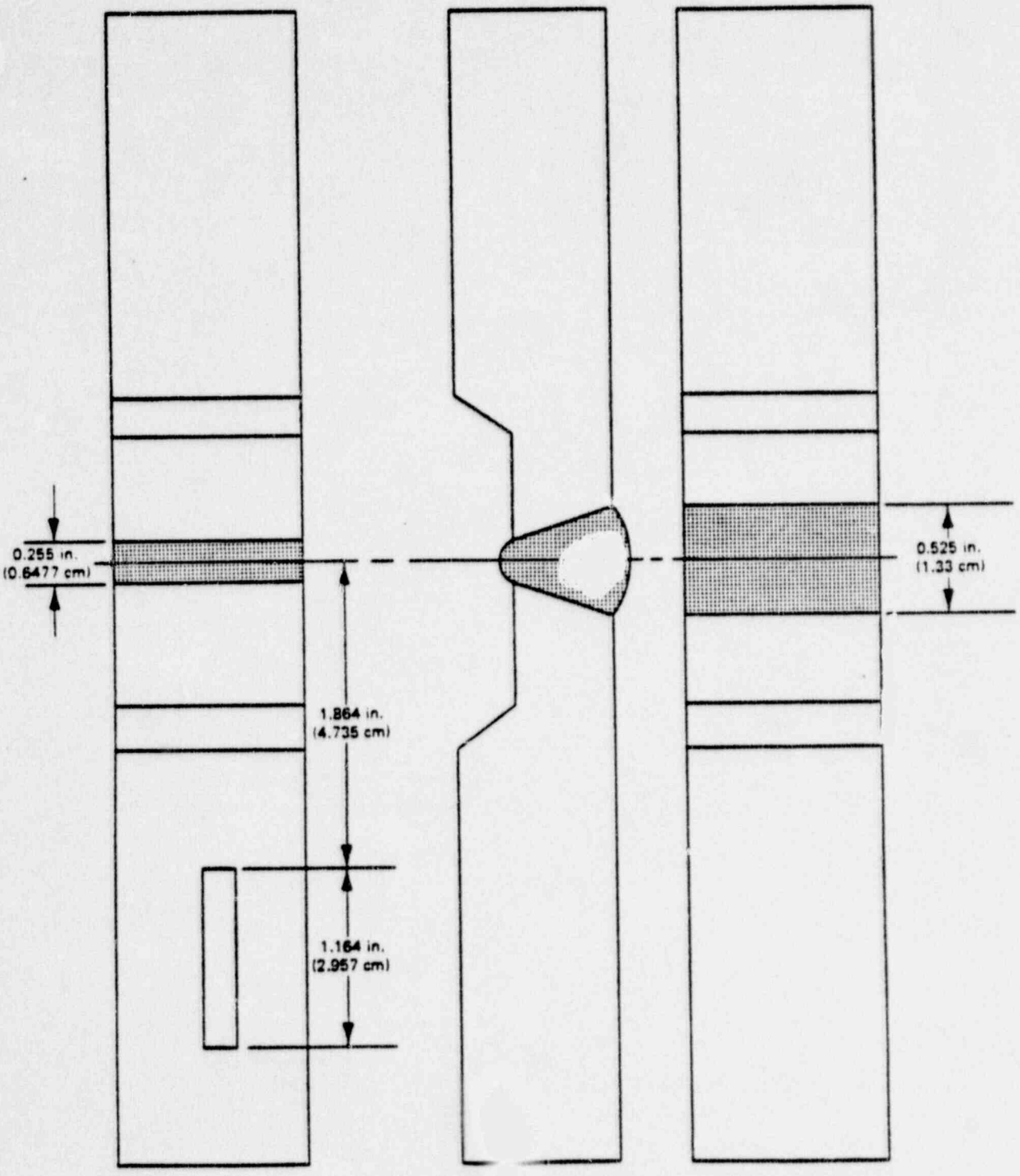

Figure K-9. Location of Weldable Strain Gage on 10.16-cm (4-in.) Pipe Specimen (As-Welded)

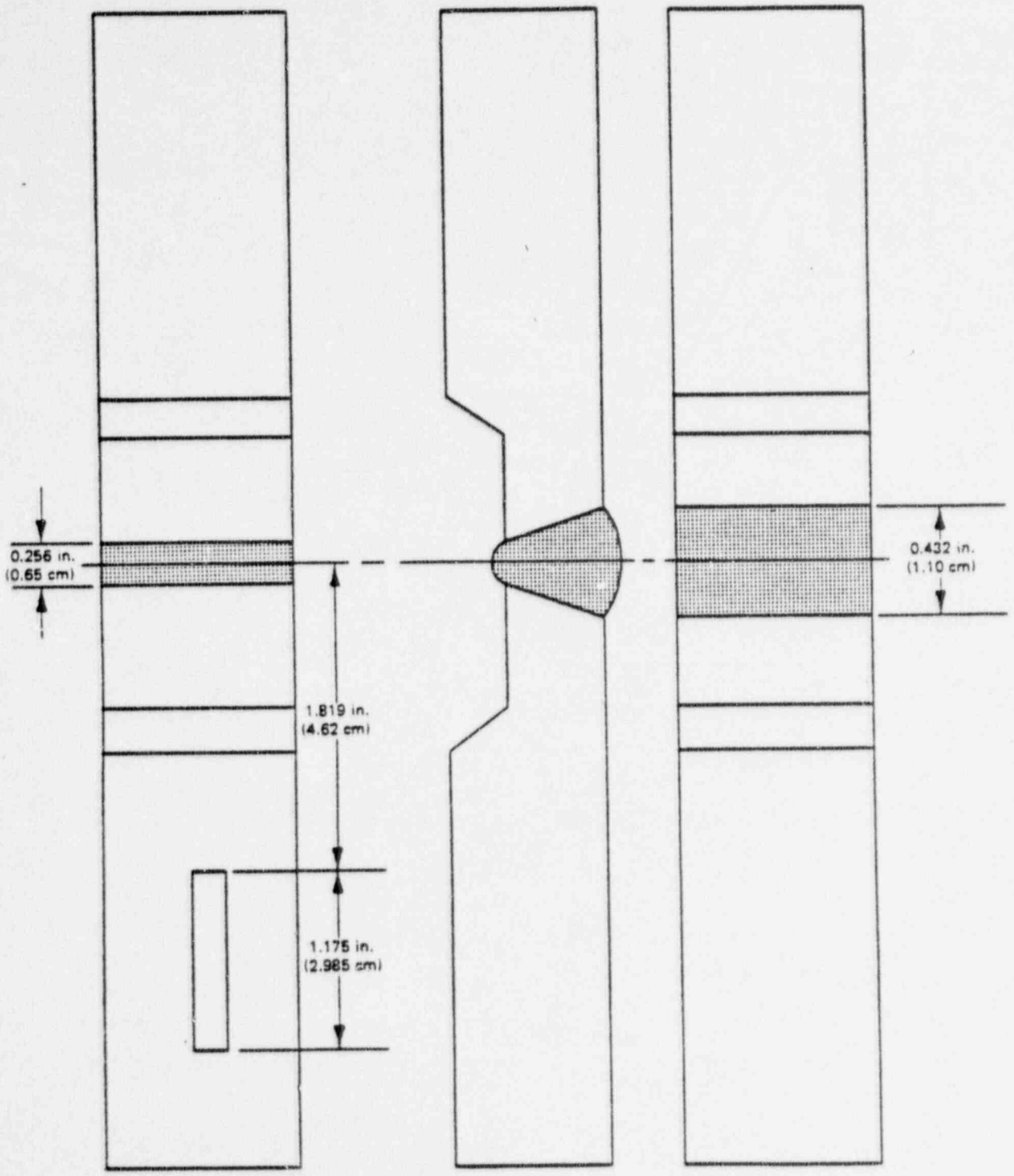

Figure K-10. Location of Weldable Strain Gage on 10.16-cm (4-in.) (Stress Relieved) Pipe Specimen

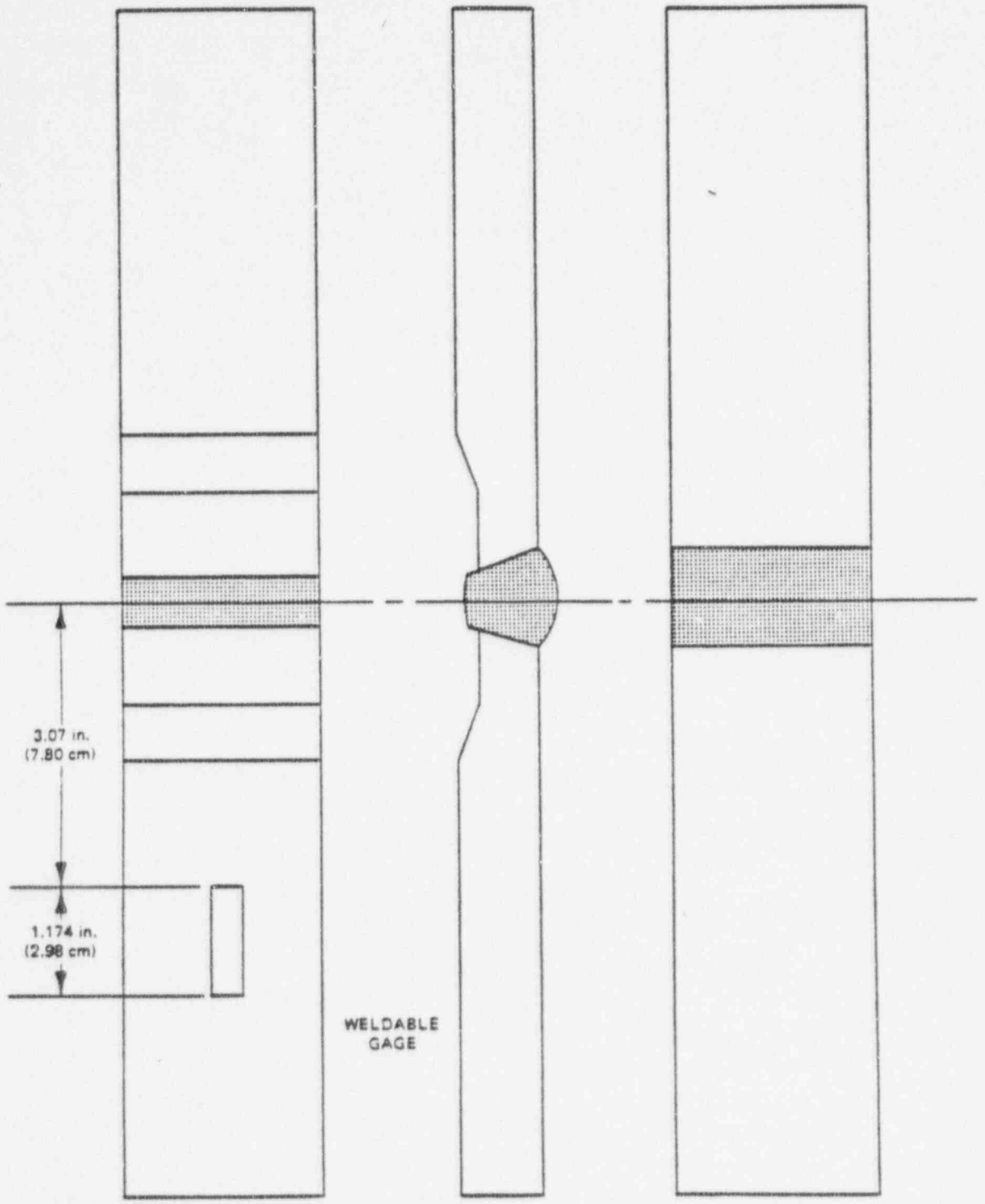

Figure K-11. Location of Weldable Strain Gage on 66-cm (26-in.) Pipe Specimens

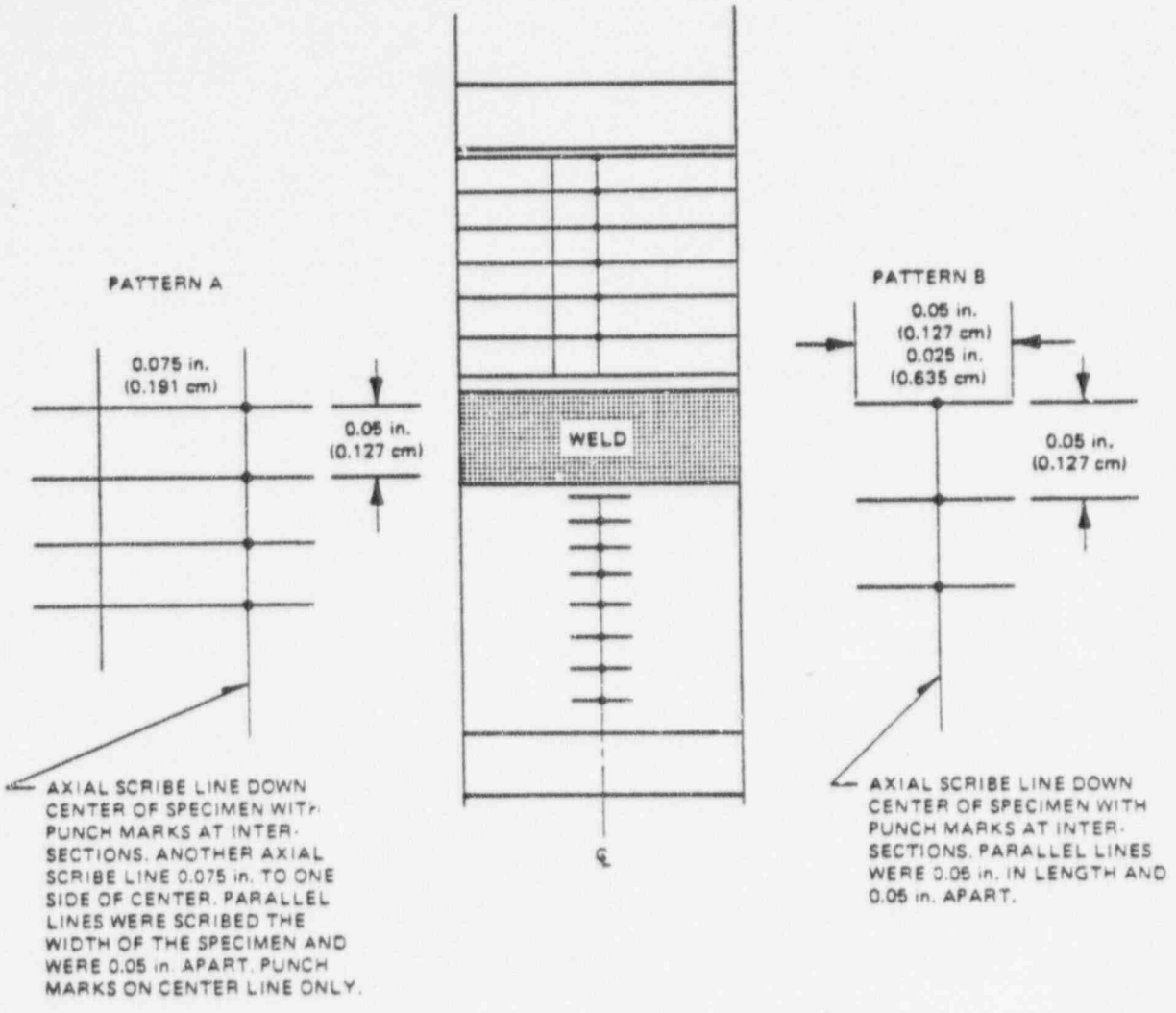

GENERAL DESCRIPTION – TWO DIFFERENT SCRIBE AND PUNCH PATTERNS WENT ON EACH SIDE OF THE WELD, AS SHOWN ABOVE. AS MANY PARALLEL LINES AS WOULD FIT 0.05 in. APART WERE SCRIBED FROM THE EDGE OF THE WELD TO THE INCLINED SECTION.

Figure K-12. Description of Punch Mark Patterns on 10.16-cm (4-in.) Pipe Specimen

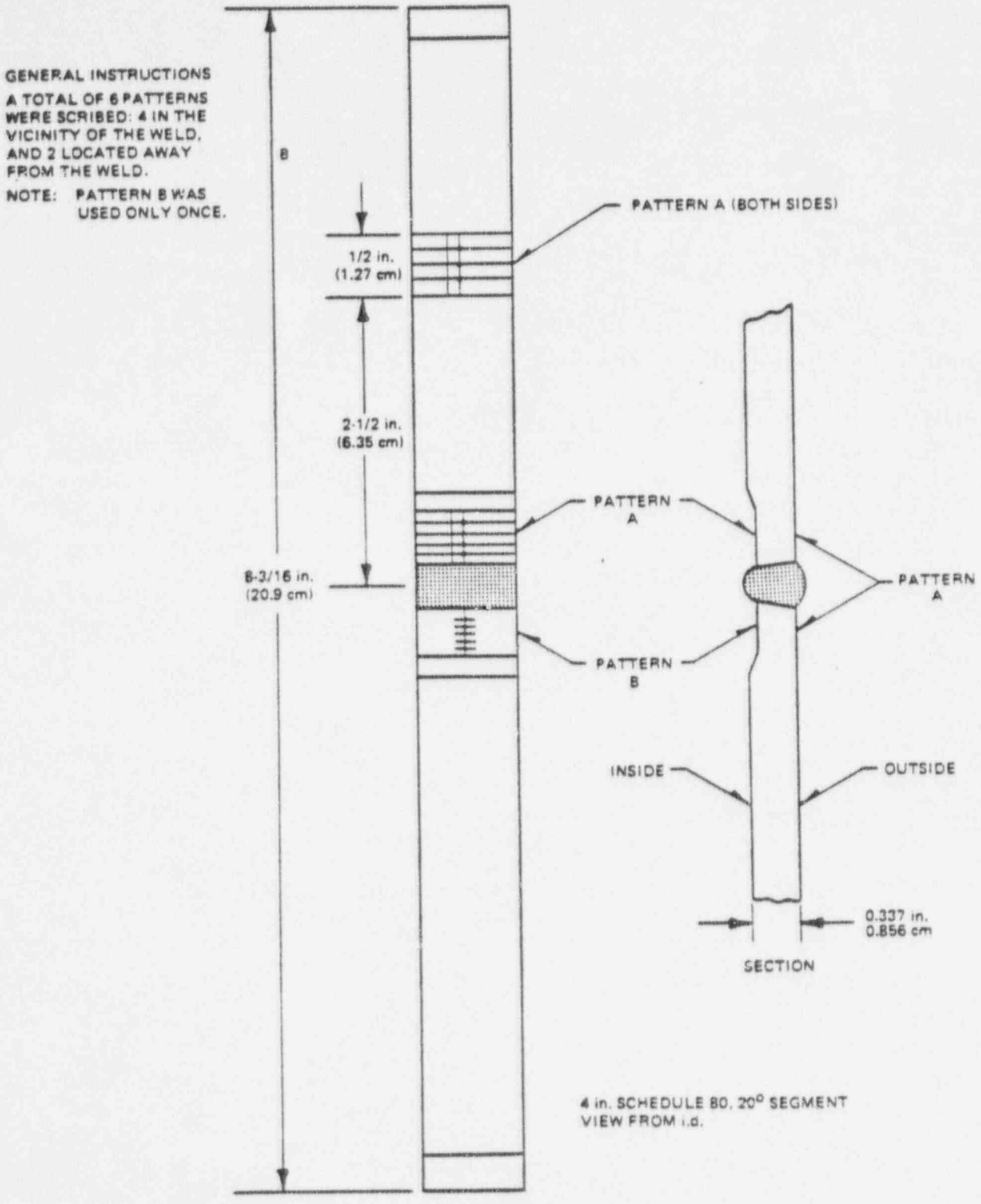

Figure K-13. Location of Punch Mark Patterns on 10.16-cm (4-in.) Pipe Specimen

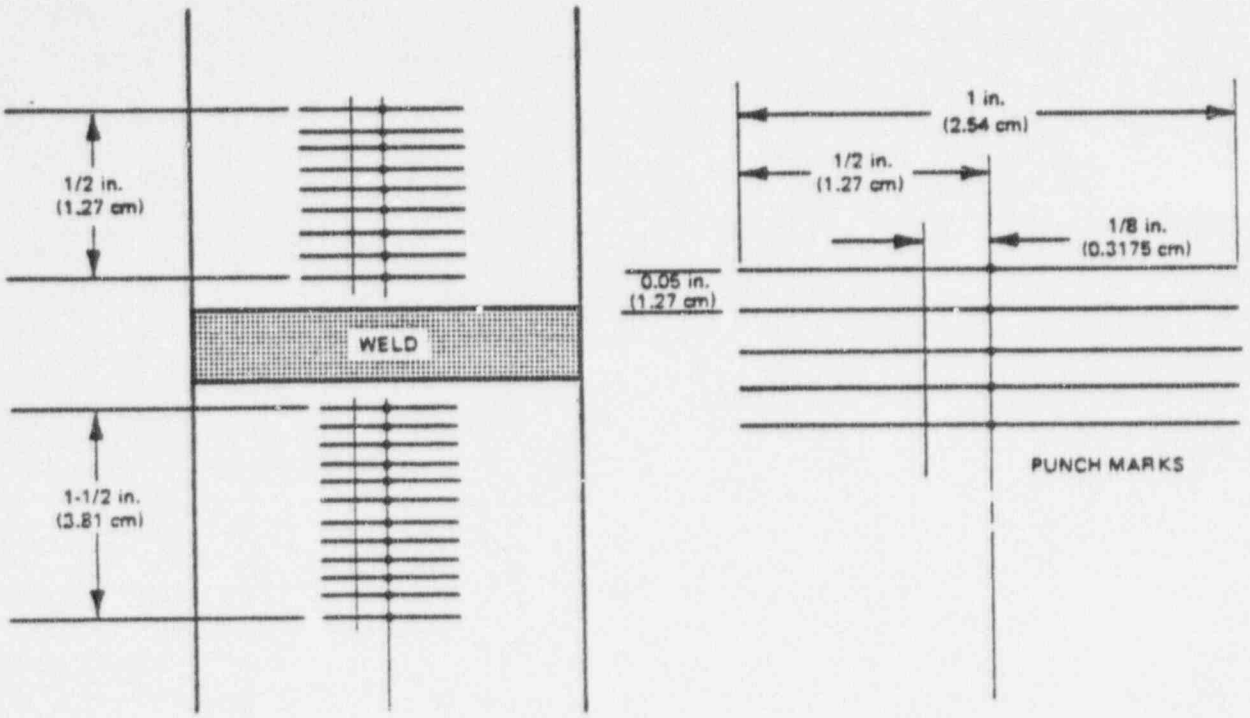

GENERAL DESCRIPTION – PUNCH MARKS WERE MADE AT INTERSECTIONS ALONG CENTERLINE SCRIBE LINE.

Figure K-14. Description of Punch Mark Patterns on 66-cm (26-in.) Pipe Specimen

90015006

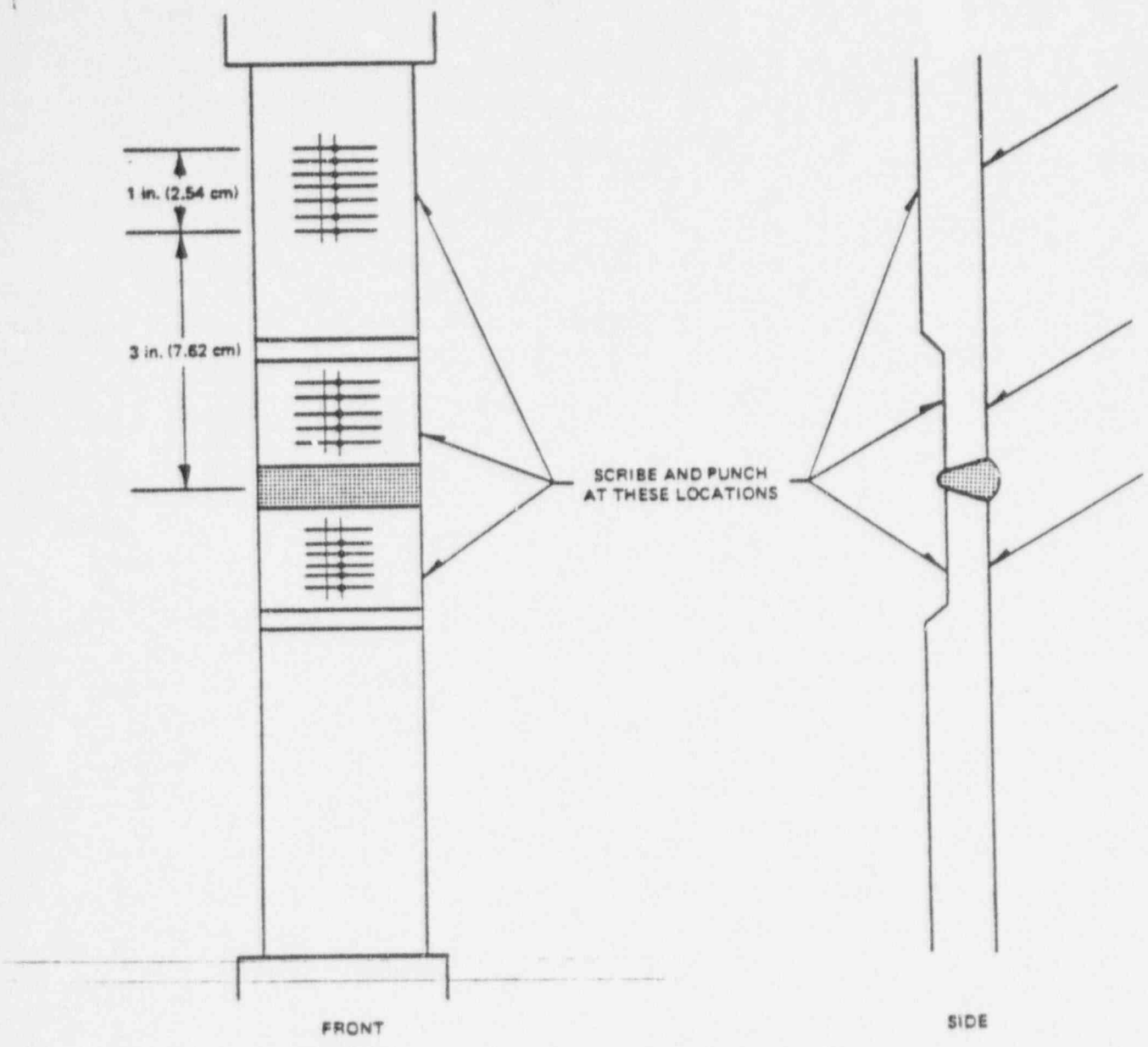

GENERAL DESCRIPTION – THE 26 in. SPECIMEN WAS SCRIBED AND PUNCHED AT A TOTAL OF 6 LOCATIONS, 4 IN THE VICINITY OF THE WELD AND 2 AWAY FROM THE WELD.

Figure K-15. Location of Punch Mark Patterns on the 10.16-cm (4-in.) Pipe Specimen

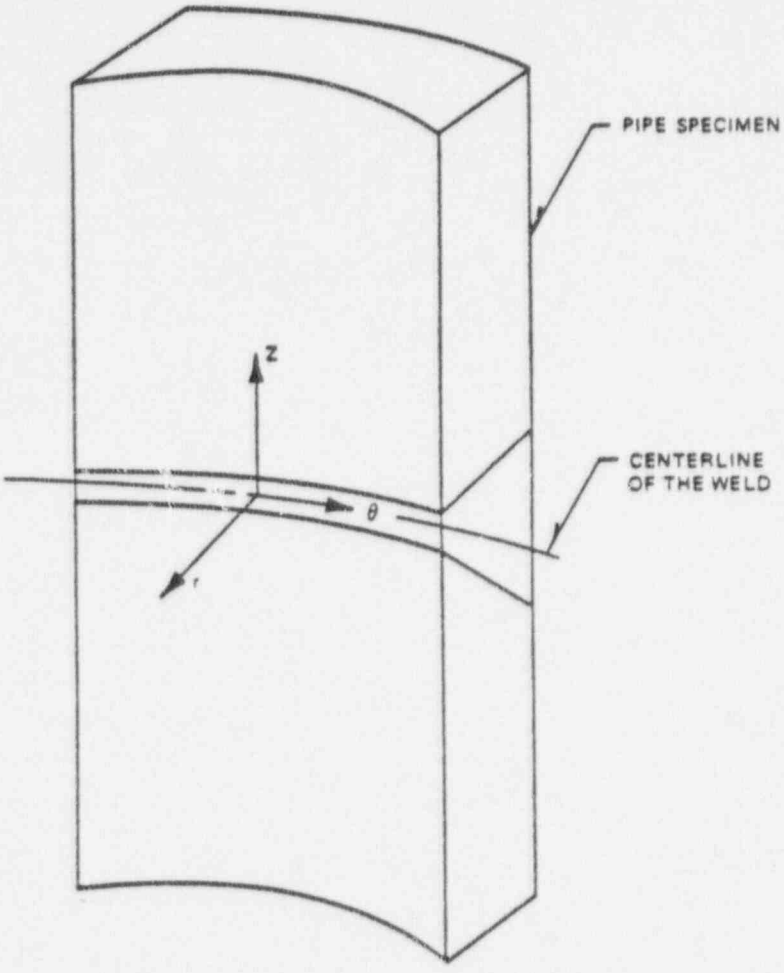

Figure K-16. Coordinate System on the Pipe Weld Used in Plotting Up the Results of the Test

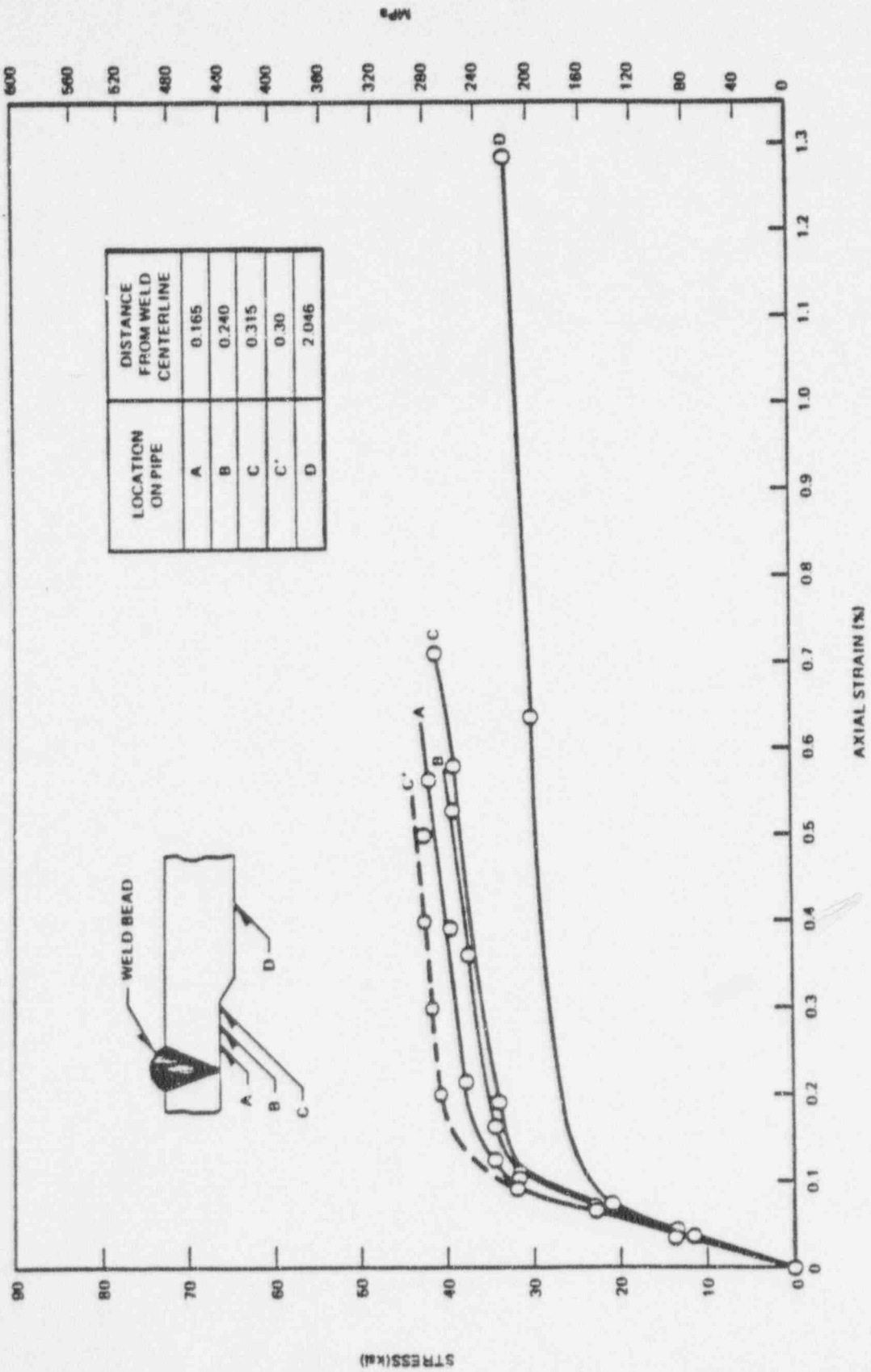

Figure K-17. 10.16-cm (4-in.) Pipe Specimen (As-Welded) Stress Versus Strain % (σ_{zz} vs ε_{zz}, %) for Several Locations in the Axial Direction Away from the Weld Centerline

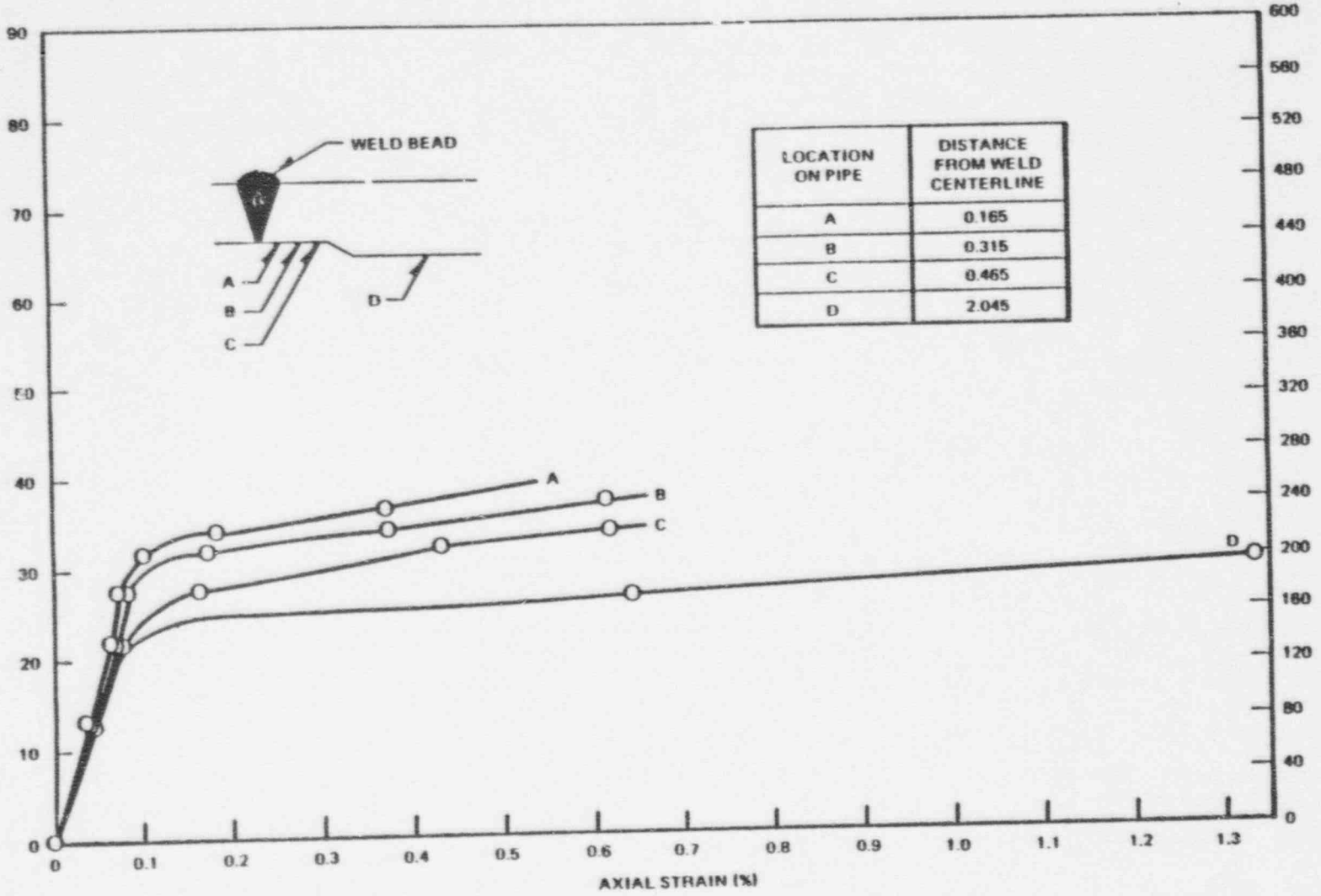

Figure K-18. 10.16-cm (4-in.) Pipe Specimen (Stress Relieved) — Stress Versus Strain % — (σ_{zz} vs Σ_{zz} %) — for Several Locations in the Axial Direction Away from the Weld Centerline

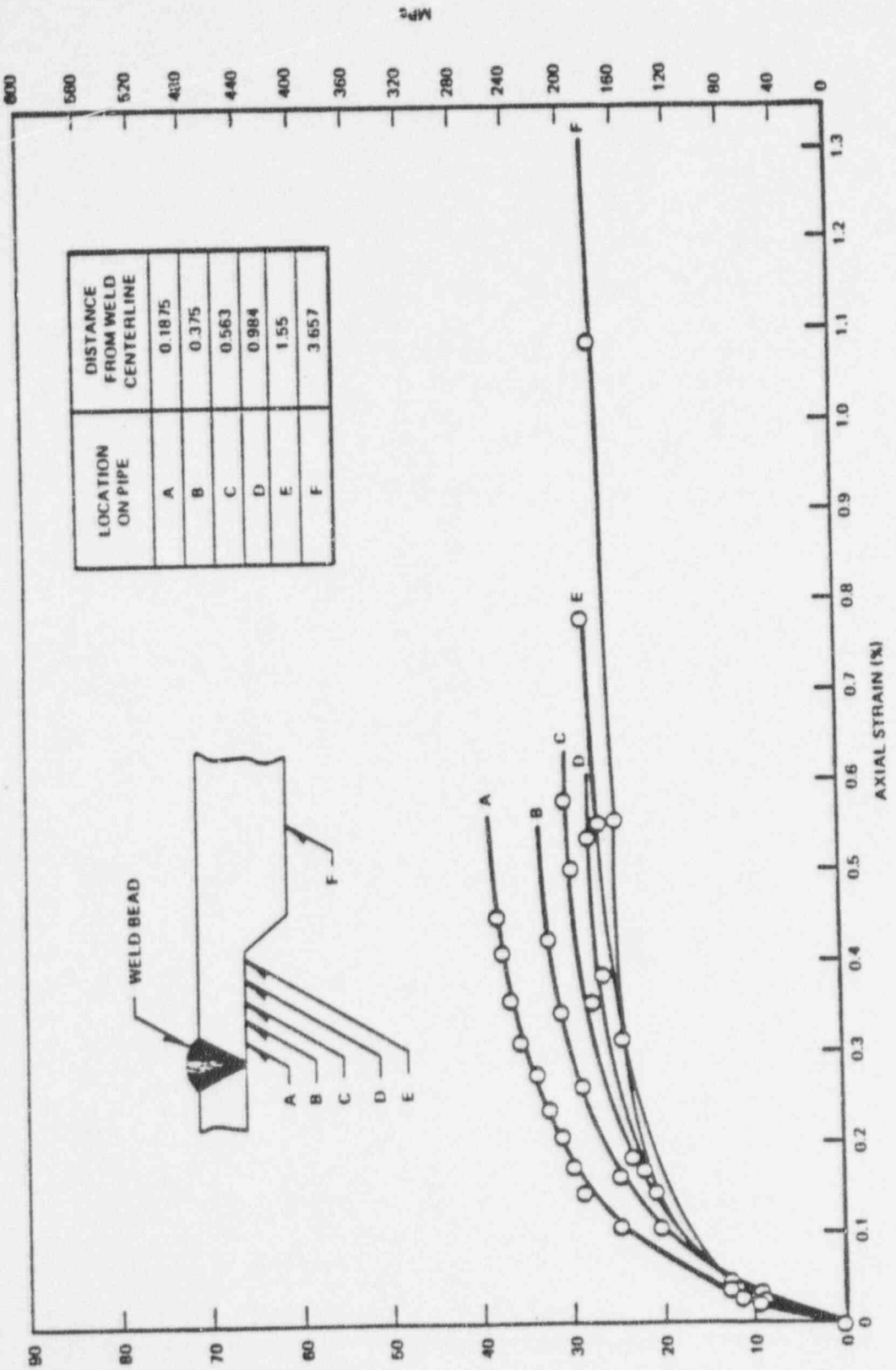

Figure K-19. 66-cm (26-in.) Pipe Specimen (As-Welded) — Stress Versus Strain % — (σ_{zz} vs Σ_{zz}, %) — for Several Locations in the Axial Direction Away from the Weld Centerline

90015011

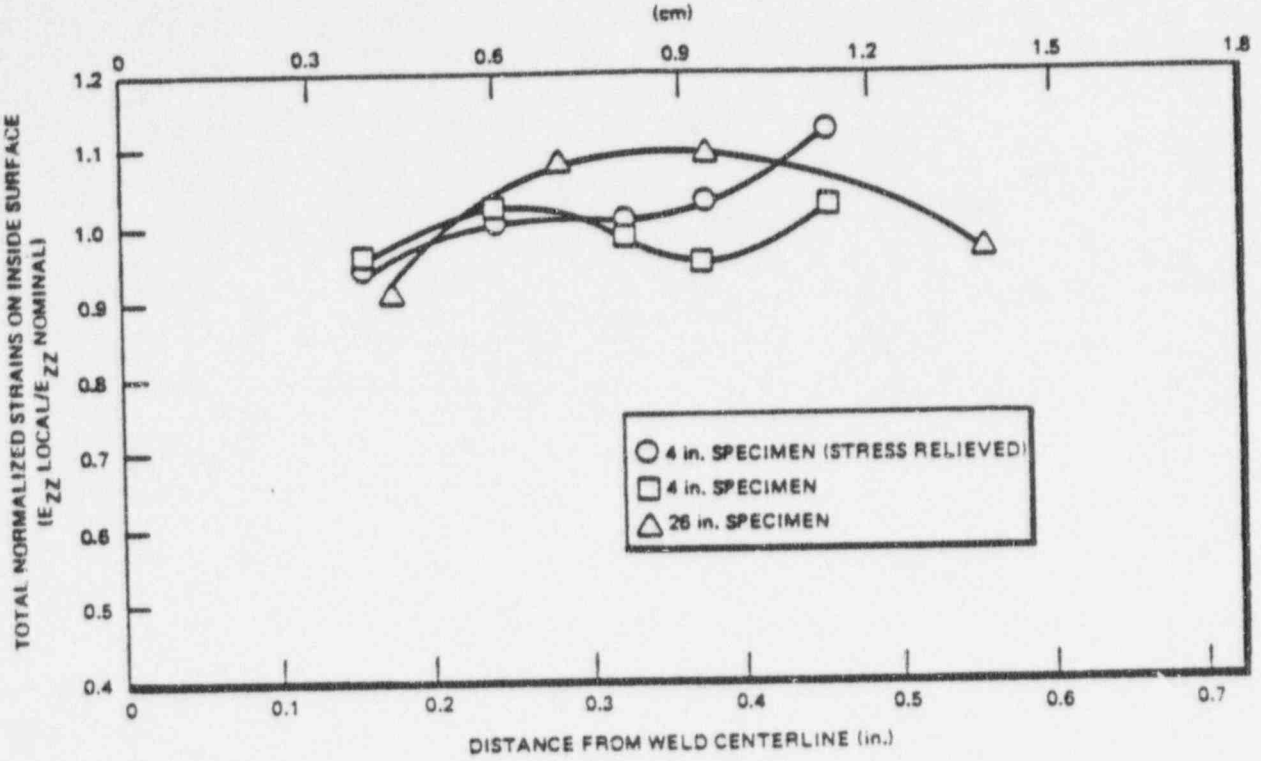

Figure K-20. Normalized Strain Versus Distance from Weld Centerline for 0.04% Nominal Pipe Strain

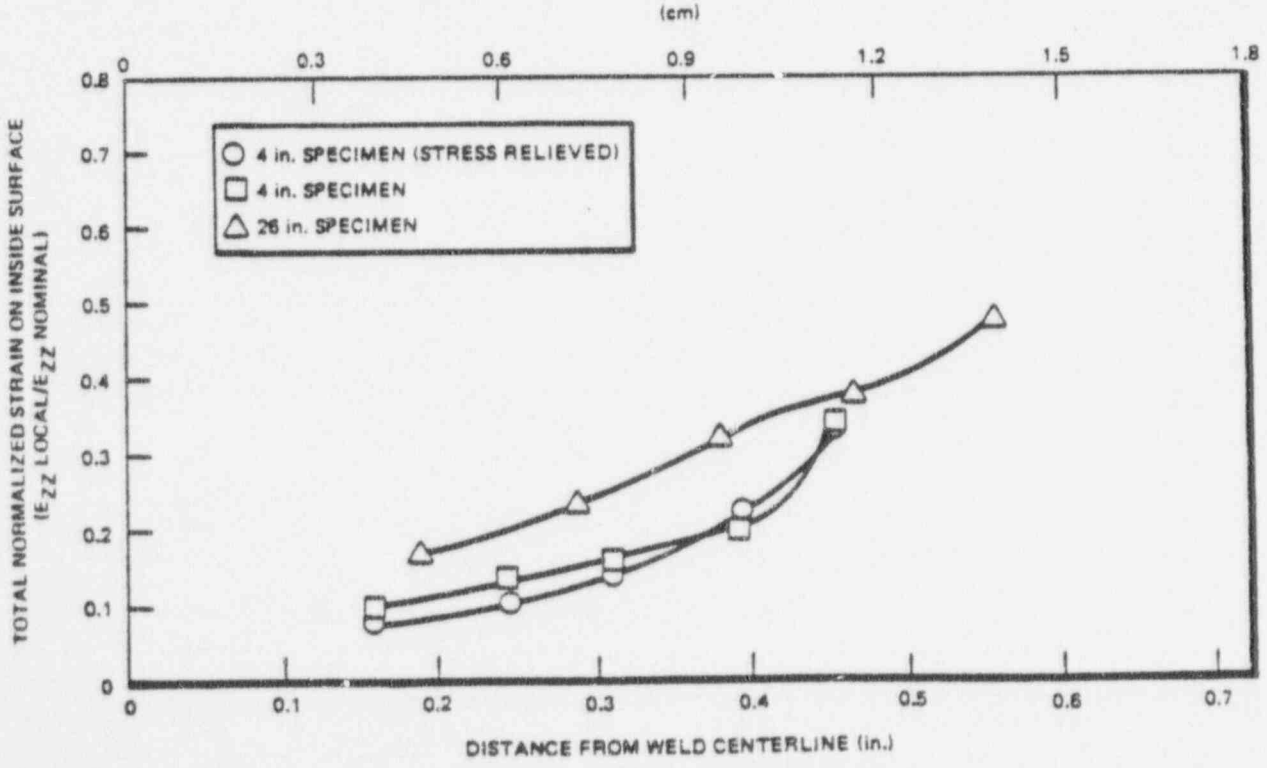

Figure K-21. Normalized Strain Versus Distance from Weld Centerline for 1% Nominal Pipe Strain

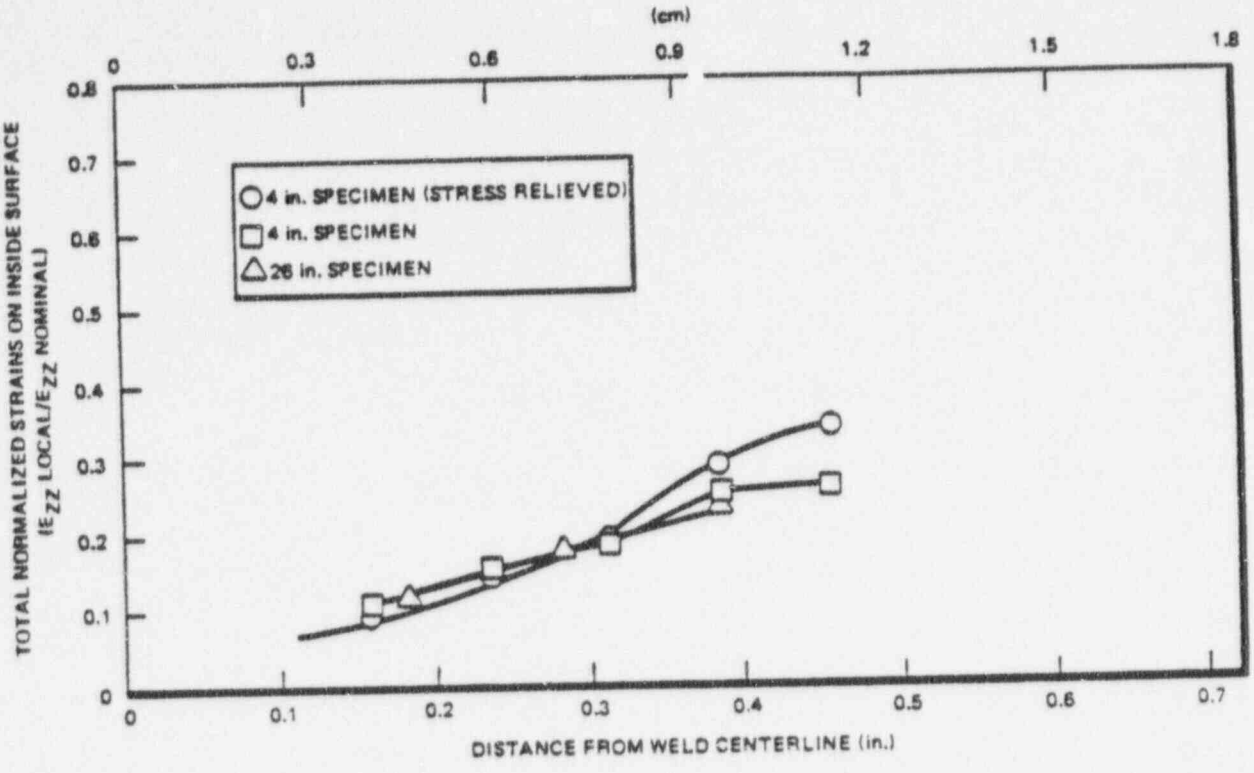

Figure K-22. Normalized Strain Versus Distance from Weld Centerline for 2% Nominal Pipe Strain

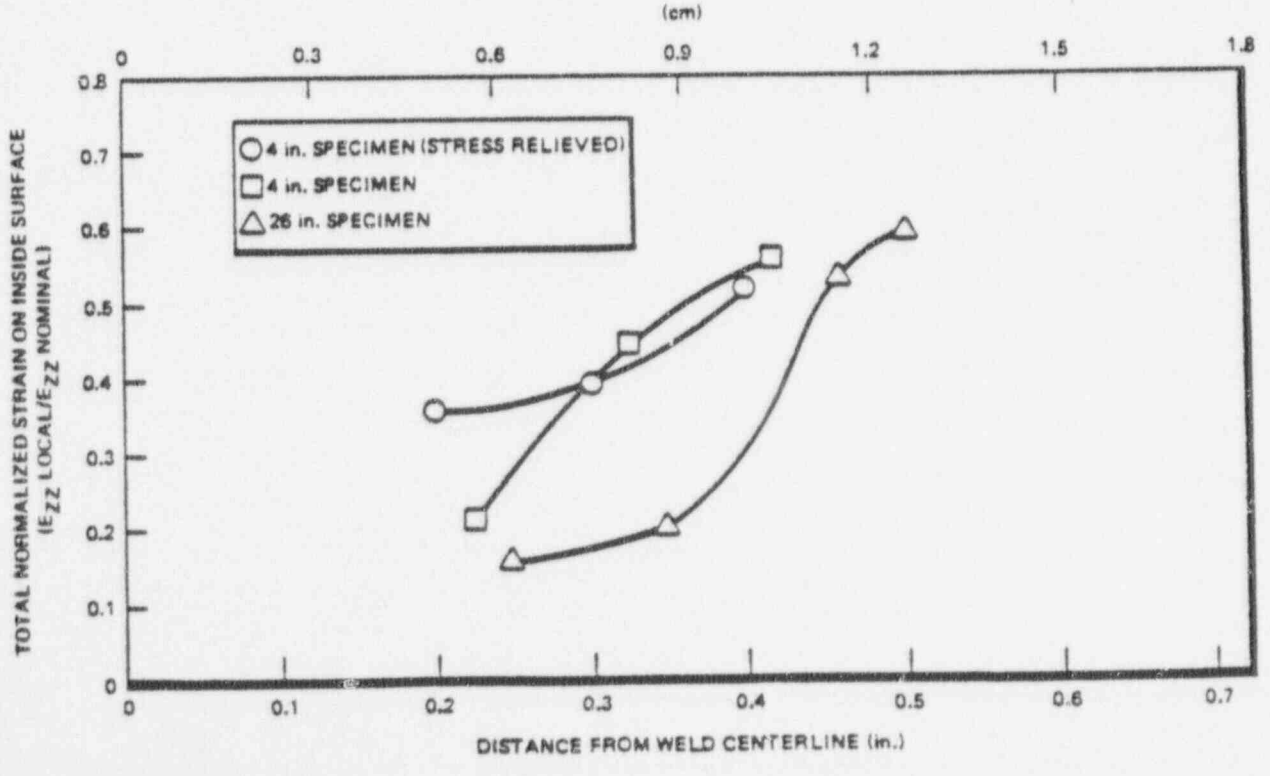

Figure K-23. Normalized Strain Versus Distance from Weld Centerline for 4.5% Nominal Pipe Strain

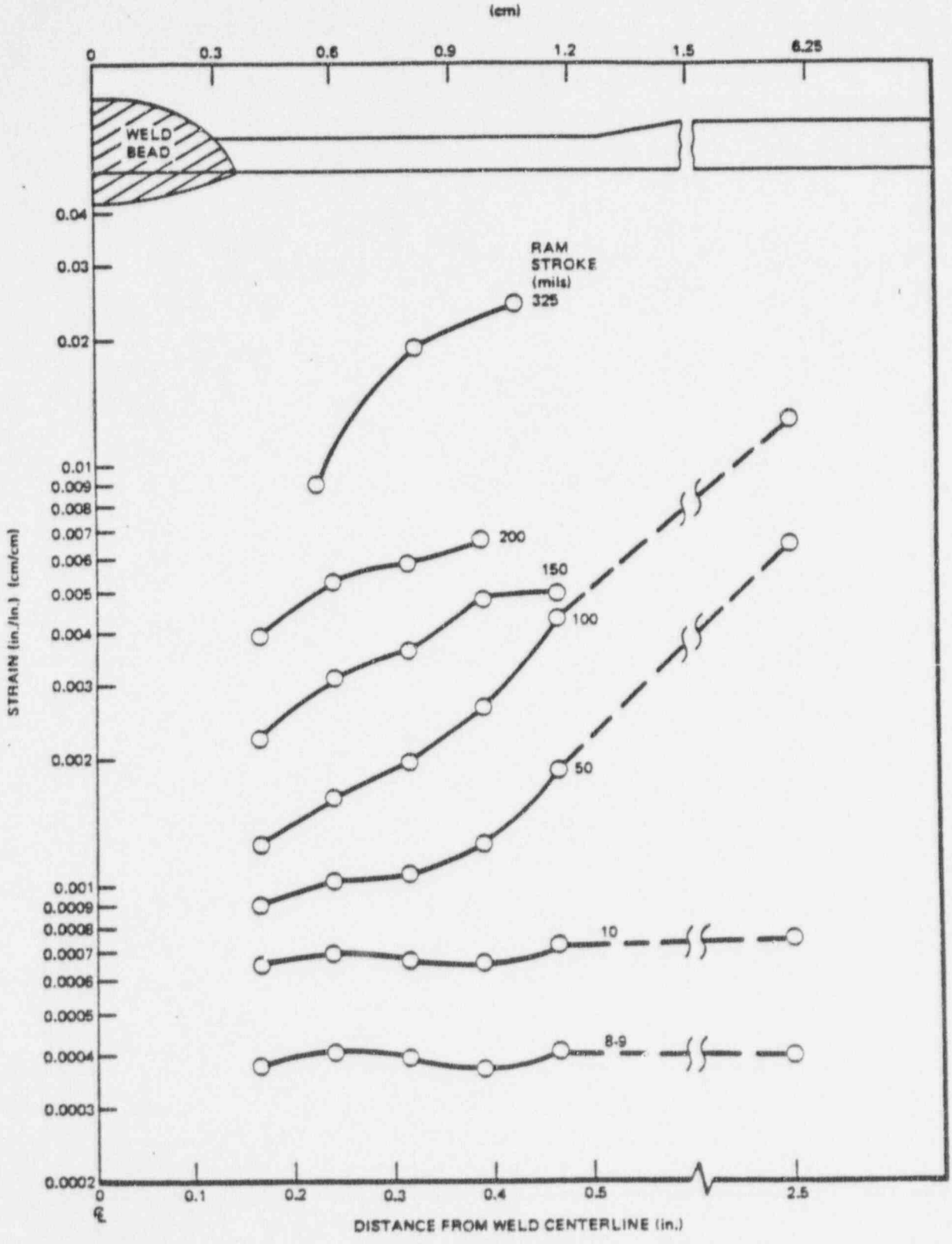

Figure K-24. Strain Versus Distance from Centerline of Weld Showing All the Strain Data from the Test for the 10.16-cm (4-in.) Pipe Specimen (As-Welded)

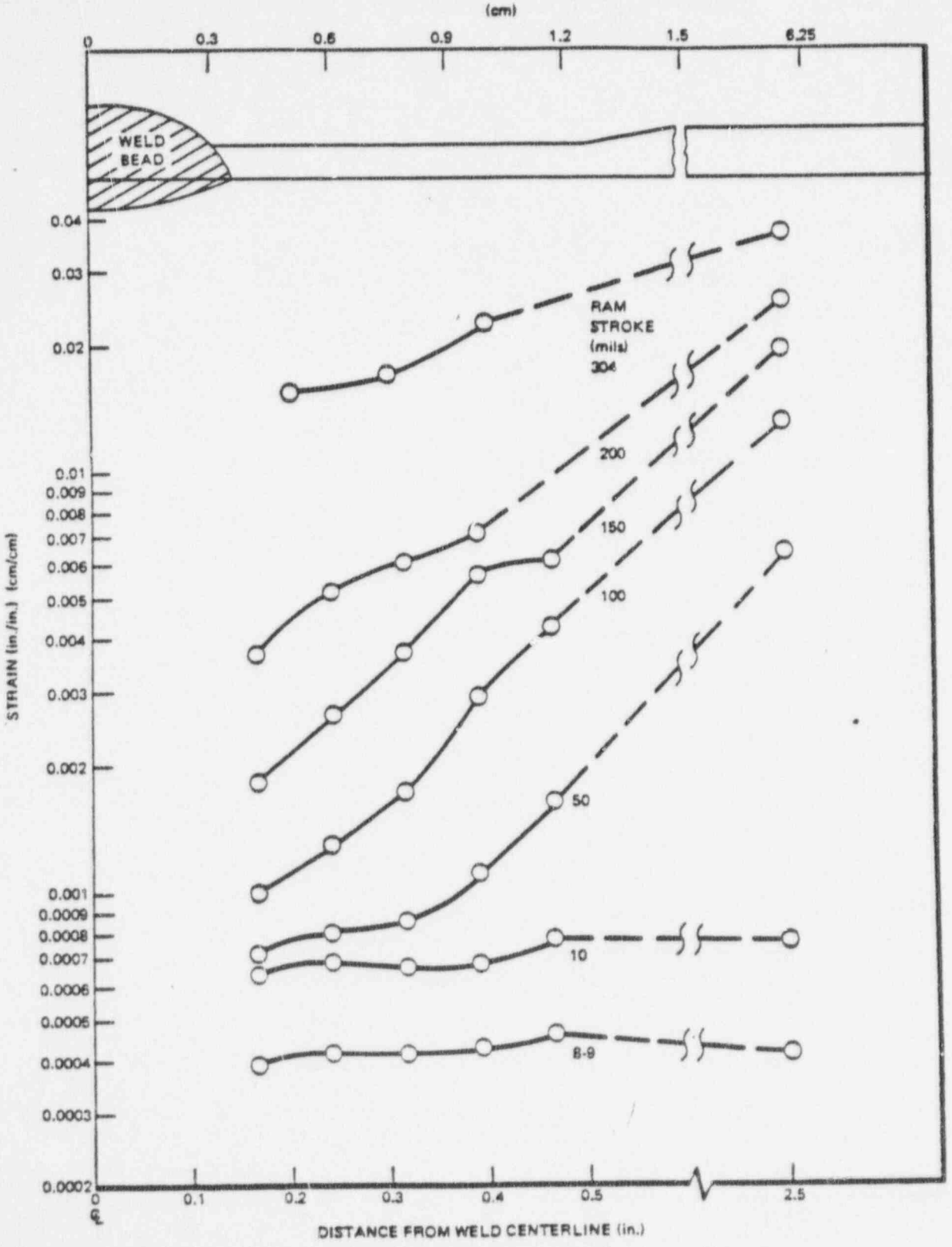

Figure K-25. Strain Versus Distance from Centerline of Weld Showing All the Strain Data from the 10.16-cm (4-in.) Pipe Specimen (Stress Relieved)

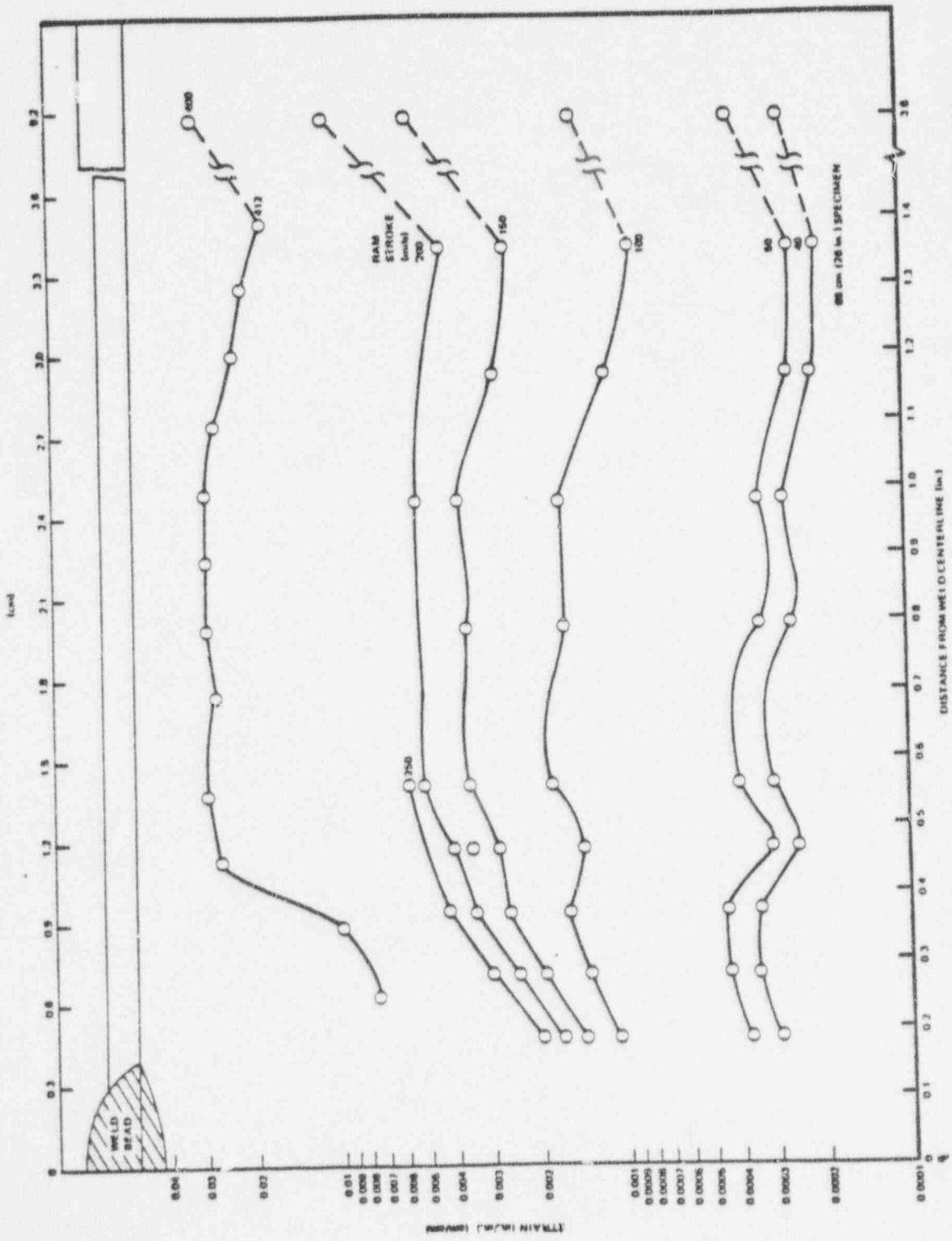

Figure K-26. Strain Versus Distance from Centerline of Weld Showing All the Strain Data from the Test for the 66-cm (26-in.) Pipe Specimen

APPENDIX L. EFFECT OF SURFACE CONDITION ON THE SURFACE INTEGRITY OF STRAINED TYPE-304 STAINLESS STEEL

L.1 INTRODUCTION

Welded pipes are often finished with a ground surface finish on the inside diameter in the pipe weld region. This ground surface has been found to have a cold worked subsurface extending 75 to 125μ (0.003 to 0.005 in.) deep with numerous grinding laps that penetrated into the surface 25 to 75μ (0.001 to 0.003 in.). It has also been found that the susceptibility of Type-304 stainless steel to intergranular stress corrosion is enhanced by surface grinding or machining[1,2] and surface separations have been suggested to play an important role in the initiation of the stress corrosion cracking.

The objective of this investigation was to determine the effects of three different surface abrasion conditions on the surface integrity of sensitized Type-304 stainless steel before and after being strained.

L.2 TEST PROCEDURE

Tensile specimens were machined from 10.16 cm (4 in.) diameter schedule 80 Type-304 stainless steel pipe representing two heats of material. Two test phases were performed in this program. The objective of the first phase was to determine the interaction of grinding and subsequent strain on the surface integrity while the objective of the second phase was to evaluate the effects of various surface finishes on the surface integrity after undergoing cyclic strains. The as-received pipes were initially sectioned for heat treating. One piece of each heat was solution annealed at 1049°C (1920°F) for 30 minutes and another was sensitized at 621°C (1150°F) for 30 minutes and another was sensitized at 621°C (1150°F) for 40 hours and furnace cooled. Twelve flat rectangular coupons were cut from the heat treated sections. Four of the coupons received a machined surface finish on both sides. The remaining coupons received a ground surface finish with a 24 grit grinding wheel on both sides. The specifications for these surface finishes are given in Table L-1.

The grinding was performed by hand using the same type of hand grinder and wheel used in site fabrication to grind pipe welds. Since pipe welds are generally ground circumferentially, the grinding on the specimens was normal to the tensile axis. The coupons were then machined into flat dog bone tensile specimens. The specimen dimensions are given in Figure L-1. Table L-1 shows the test matrix and gives details of the machining and grinding operation.

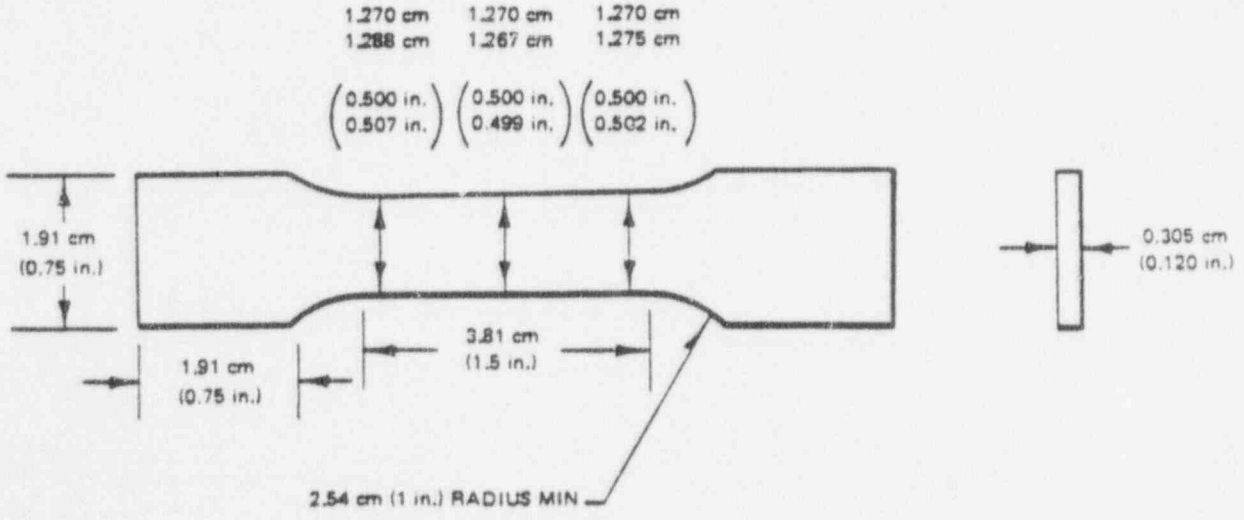

Figure L-1. Specimen Dimensions

90015017

After grinding, one specimen of each heat was subjected to magnetic response—ferrite scope—to measure the martensite (α), and microhardness measurements to determine the depth of coldwork.

The tensile specimens were tested at 550°F in air at a constant extension rate of 0.1270 cm/min (0.05 in./min) to the levels of total strain shown in Table L-1. Specimens SG3 and SG22 were also cycled ten times from 100% to 10% of the load at 5% strain. Solvent dye penetrant was used to check for surface defect indications. To increase the sensitivity of this test, solvent dye penetrant was applied to the surface while the specimens were still warm and under a small amount of load. The penetrant was allowed to set for ten minutes before it was wiped off. The load was then released and the specimen was checked for crack indications.

The second test phase evaluated the effects of three different surface abrasion conditions on the surface integrity after undergoing cyclic strains using material from Heat M7616 of Type-304 stainless steel. Table L-2 shows the surface preparation of the tensile specimens and blanks. The tensile tests were performed in air at 288°C (550°F). The specimens were strained to 5% and cycled ten times from ~0 to 5% strain. The strain rate was the same as previously described. The specimens and blanks were then examined for surface defects with the scanning electron microscope. The chemical compositions of the two heats of material are given in Table L-3.

L.3 RESULTS AND DISCUSSION

The microhardness profile of Specimen SG1 (sensitized, ground, 0% strain) is shown in Figure L-2. These measurements indicate that the depth of cold work was between 0.15 and 0.23 mm (0.006 and 0.009 in.). One side of Specimen SG1 was 80 Knoop hardness greater at 0.07 mm (0.003 in.) from the ground surface than the other side. This may indicate excessive heating of the specimen when it was ground. Ferrite scope readings gave zero magnetic response after grinding indicating the lack of deformation induced martensite on the surface. Table L-1 shows the result of the dye penetrant examination. No dye penetrant indications were found on any specimen.

The behavior of the two heats of material to the different strain levels with and without cycling appeared to be quite similar. The surface separations or fissures appeared to be quite similar.

Evidence of these surface separations was found at strains as low as 1.7%. Figure L-1 shows a typical surface separation in the specimen pulled to 1.7% strain. When the strain was increased to 5%, the number of surface separations increased. A further multiplication of defects occurred with cycling. Figure L-4 shows the surface separations found in a specimen pulled to 5% strain and cycled ten times. The surface separations appeared larger as the strain and number of cycles was increased.

The specimen which was annealed before grinding had the smallest and least number of surface separations compared with those which were as received and sensitized before grinding.

A lack of similar surface separations was found in specimens which had been machined and strained.

The second test phase evaluated the effects of various surface finishes on the surface integrity after undergoing cyclic strains. The hand grinding of these test specimens produced a surface with variable roughness. From optical metallography, it was observed that the degree of surface roughness varied across the surface. The cross section from Specimen A1 (Condition 1 in Table L-2) is shown in Figures L-5A and B. The micrograph shown in Figure L-5A indicated the cold worked layer was vaguely discernable while in an adjacent location the cold worked layer appeared to be approximately 0.025 mm (0.001 in.) thick (Figure L-5B). The depth of cold work appeared to be greater in Specimen B1 (Condition 2 in Table L-2) as shown in Figure L-6. In contrast, the cold work layer of Specimen C1 (Condition 3 in Table L-2) with the cratex polish appeared to be less severely cold worked and approximately 0.006 mm (0.00025 in.) thick as shown in Figure L-7.

The majority of the cold worked subsurface appeared to be created by the 24 grit grinding wheel. With the subsequent grinding operation with the flapper and cratex wheel, the cold worked subsurface was reduced but in a non-uniform manner. The flapper wheel and cratex polish appeared to create a very small cold worked subsurface.

Surface separations or fissures were observed in the unstrained as ground specimens. Surface separations were observed in the as-ground Specimen 1B. Specimen 1B was machined and subsequently ground with a 24 grit grinding wheel. Figure L-8 shows an example of the type of separations observed. The separations appeared to open parallel to the grinding laps and seams. The surface separations in the unstrained specimen with a Condition 2 surface finish is shown in Figure L-9. In Condition 2, the flapper wheel grinding direction was perpendicular to the grinding wheel direction. The surface separations were parallel to the flapper wheel grinding direction. It was concluded that the surface separations were induced by the flapper wheel abrasion. It is, however, important to note that the cold work layer created by the 24 grit grinding wheel may have contributed to the surface separation produced during the flapper wheel operation. The surface separation appeared to occur in regions of rougher surface texture. The surface separations found in the finish from the cratex polish Condition 3 are shown in Figure L-10. The surface separations again were located parallel to the grinding laps and seams and in regions of rougher surface texture. In both the flapper and cratex finishes, the surface separations appeared less frequently than in the 24 grit ground surface.

The surface separations found in the cyclically strained specimens appeared to be larger and more frequent as compared to the as-ground unstrained specimens. The surface separations were found, in Specimens A1 and A2, C1 and C2, to lie perpendicular to the tensile axis, Figure L-11. In both cases, the final grinding was perpendicular to the tensile axis and the 24 grit grinding wheel direction was in the direction perpendicular to the tensile axis. In Condition 2, the flapper wheel abrasion was performed parallel to the tensile axis (or perpendicular to the grinding direction). As shown in Figure L-12, the surface separations appeared perpendicular to the flapper wheel grinding laps and seams. It appeared that these surface separations could have been induced by the cyclic straining or were created by the 24 grit grinding which was not removed by the flapper wheel grinding. As seen in the micrograph of Specimen B1 in Figure L-6, the cold work layer of the 24 grit grinding was not significantly reduced by the flapper wheel grinding, thus, leaving a majority of the surface defects on the surface to be opened up during the test.

L.4 CONCLUSIONS

This study demonstrated that abrasive grinding operations are sufficient to create surface separations in unstrained specimens or Type-304 stainless steel. The depth of cold work resulting from the 24 grit grinding wheel was found to range from 0.15 to 0.23 mm (0.006 to 0.009 in.). The surface separations lay parallel to the grinding laps and seams. The number of surface separations found in the 24 grit ground surface increased with both applied strain and cycles. The solution annealing heat treatment before grinding appeared to reduce the surface damage. The as-machined specimen did not show any indications of surface separations.

Hand polishing with a flapper wheel and cratex polish after grinding produced a large variability in the depth of the cold worked subsurface. However, the two operations did not eliminate the surface separations. The surface separations found in the flapper and cratex finishes appeared in the rougher regions of the unstrained specimens and were again parallel to the grinding laps and seams.

The flapper and cratex grinding operations did not in general remove the cold worked subsurface created by the previous abrasive grinding.

With the application of a tensile load, these surface separations which were created by the abrasive grinding increased in size in the direction perpendicular to the tensile axis. It appears then that the effect of the tensile load is not necessarily only to create microcracks but also to increase the size of the cracks created during the previous grinding operation.

Table L-1
SPECIFICATIONS FOR SURFACE FINISHES

Specimen Number	Heat Number	Heat Treatment	Surface Condition	% Strain	Dye Penetrant Indications
SM25	M7772	as received, sensitized 1150°F, 40 hr, F.C.	machined[a]	0	none
SM26	M7772	as received, sensitized 1150°F, 40 hr, F.C.	machined[a]	1.2	none
SM28	M7772	as received, sensitized 1150°F, 40 hr F.C.	machined[a]	5.7	none
SM5	M7616	as received, sensitized 1150°F, 40 hr F.C.	machined[a]	5.2	none
SG21	M7772	as received, sensitized 1150°F, 40 hr F.C.	ground[b]	0	none
SG23	M7772	as received, sensitized 1150°F, 40 hr F.C.	ground[b]	4.5	none
SG22	M7772	as received, sensitized 1150°F, 40 hr F.C.	ground[b]	4.9[c]	none
SG1	M7616	as received, sensitized 1150°F, 40 hr F.C.	ground[b]	0	none
SG2	M7616	as received, sensitized 1150°F, 40 hr F.C.	ground[b]	1.7	none
SG4	M7616	as received, sensitized 1150°F, 40 hr F.C.	ground[b]	5.0	none
SG3	M7616	as received, sensitized 1150°F, 40 hr F.C.	ground[b]	5.1[c]	none
AG12	M7616	solution annealed 1920°F, 30 min.	ground[b]	5.3	none

[a] Machining conditions are

Speed 1115 rpm
Feed 4 in/min
Cutting fluid soluble oil
Finish 24 μin

Cutter detail

Type Agr In-Dex
Tool number EM-125-R6
Tp-2
2 carbide cutters 370 grade
TPG-323-0 360 rad
0.006 inches of material removed

[b] Hand ground with a 3 in. diameter 1/8 in. thick wheel. The wheel designation is A24TBNA. The rpm used was 18,000 and the surface finish is approximately 125μin according to GE surface roughness scale number 342X60 and number 342X61

[c] Pulled to 5% strain and cycled 10 times from 100% to 10% of the load at 5% strain

Table L-2
SPECIMEN SURFACE CONDITIONS

Tensile Specimens	Blanks		Surface Conditions
A1, A2	2A	Condition 1:	a) 24 grit grinding wheel ground perpendicular to longitudinal axis (125 finish)
			b) 80 grit flapper wheel ground perpendicular to longitudinal axis (32 finish)
B1, B2	2B	Condition 2:	24 grit grinding wheel ground perpendicular to longitudinal axis (125 finish)
			b) 80 grit flapper wheel ground parallel to longitudinal axis (32 finish)
C1, C2	1A	Condition 3:	a) Condition 2 plus cratex polish ground perpendicular to longitudinal axis (16 finish)
D1, D2	1B	Condition 4:	a) 24 grit grinding wheel ground perpendicular to longitudinal axis (125 finish)

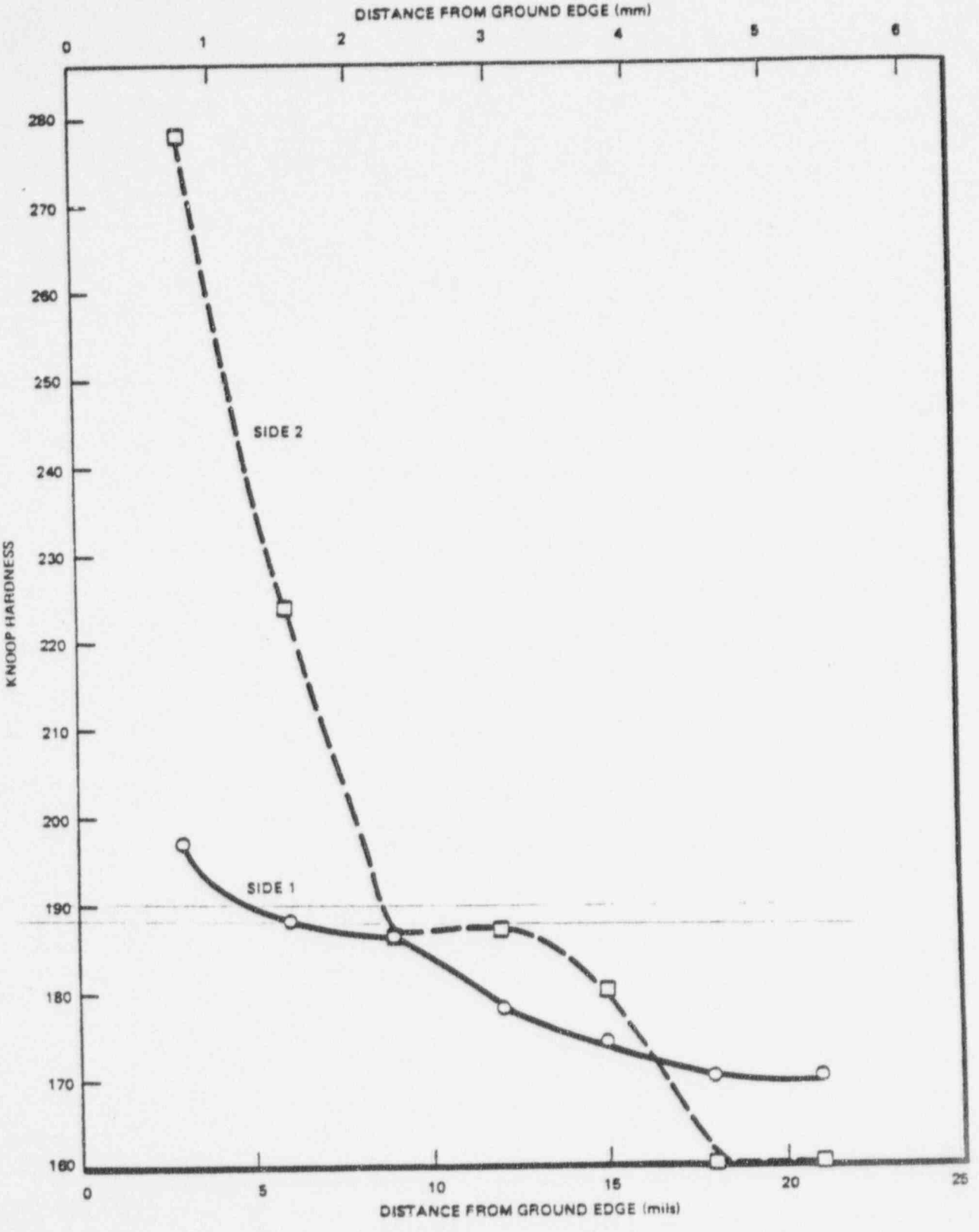

Figure L-2. Microhardness Profile for Specimen SG1, Heat Number M7616, 0% Strain

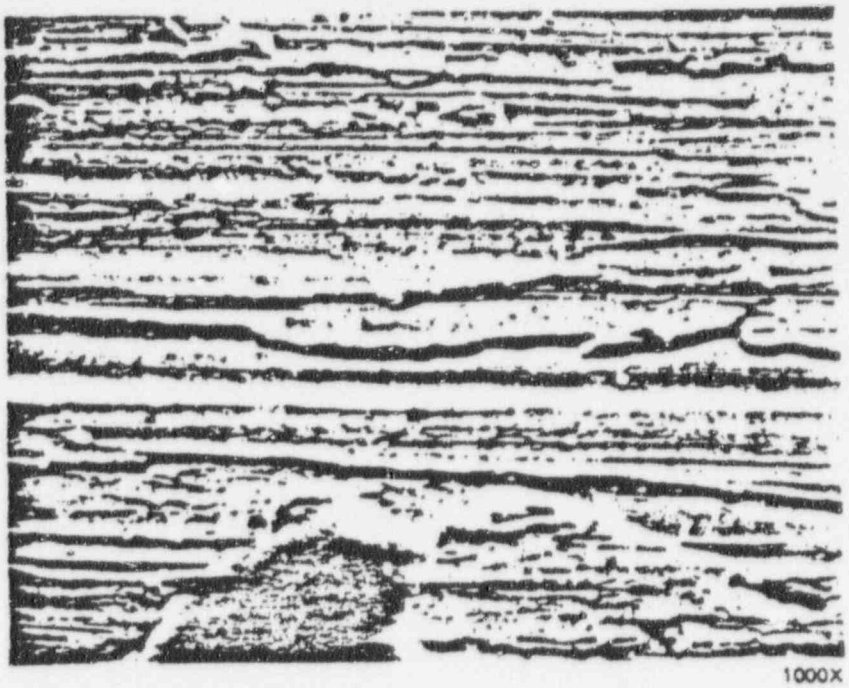

Figure L-3. SEM Micrograph of Specimen SG2 Sensitized, Ground, 1.7% Strain — Heat Number M7616

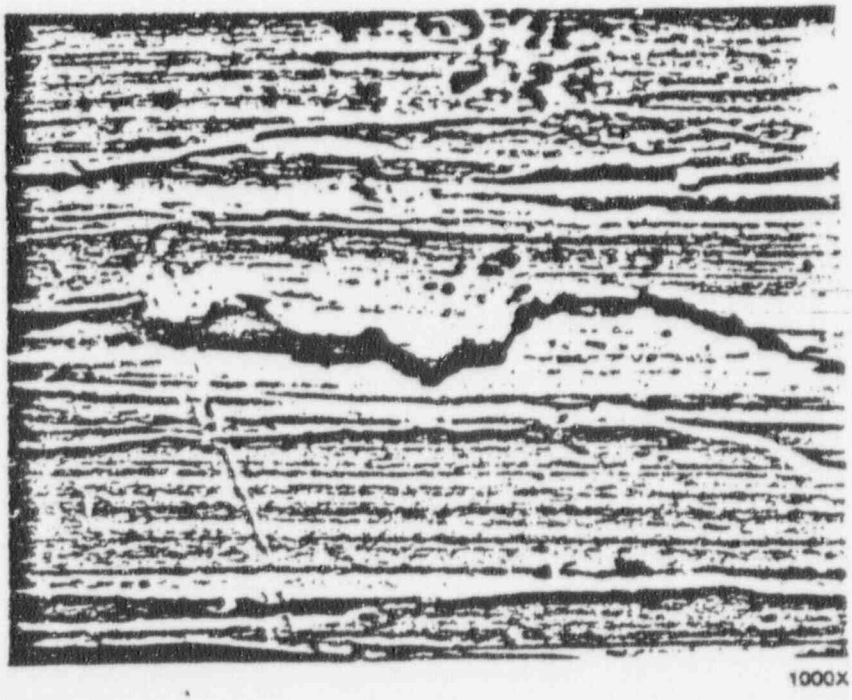

Figure L-4. SEM Micrograph of Specimen SG3 Sensitized, Ground, 5.1% Strain + 10 Cycles — Heat Number M7616

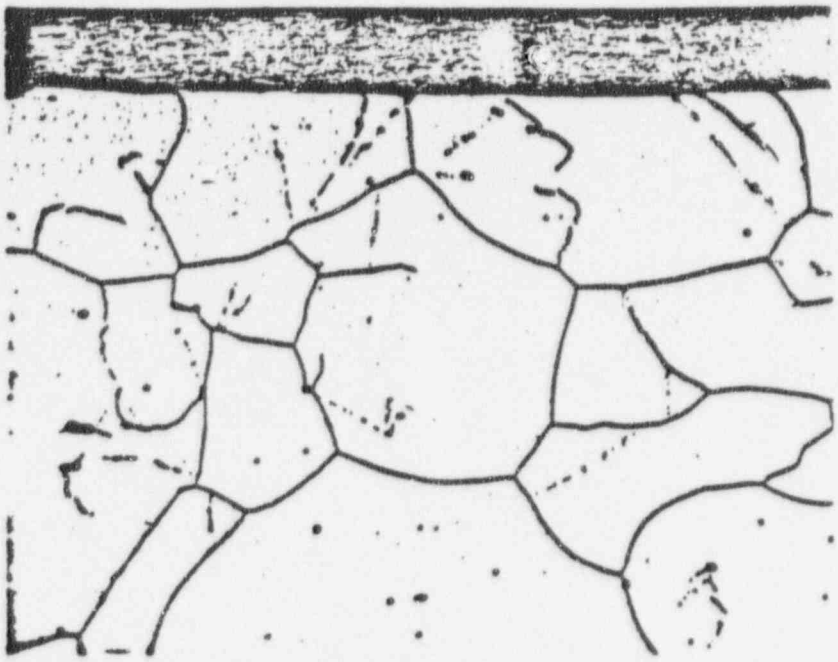

(a) TYPICAL GROUND SURFACE APPEARANCE 400X

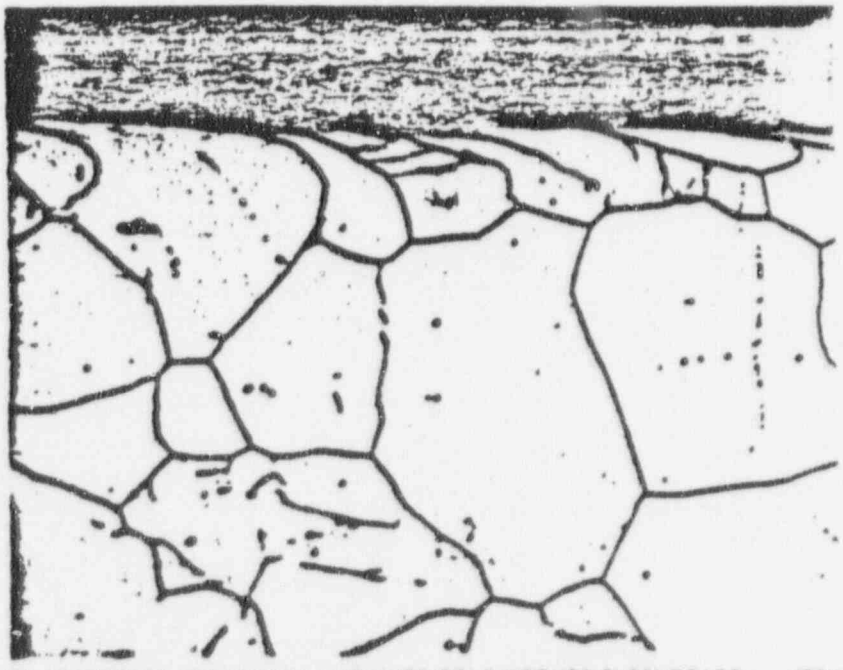

(b) SCATTERED AREAS WITH A HEAVIER COLD-WORKED SUBSURFACE 400X

CONDITION 1: (a) GRINDING DIRECTION
(b) FLAPPER WHEEL DIRECTION
(c) TENSILE AXIS PERPENDICULAR TO MICROGRAPH

Figure L-5. Optical Micrograph of Specimen A1

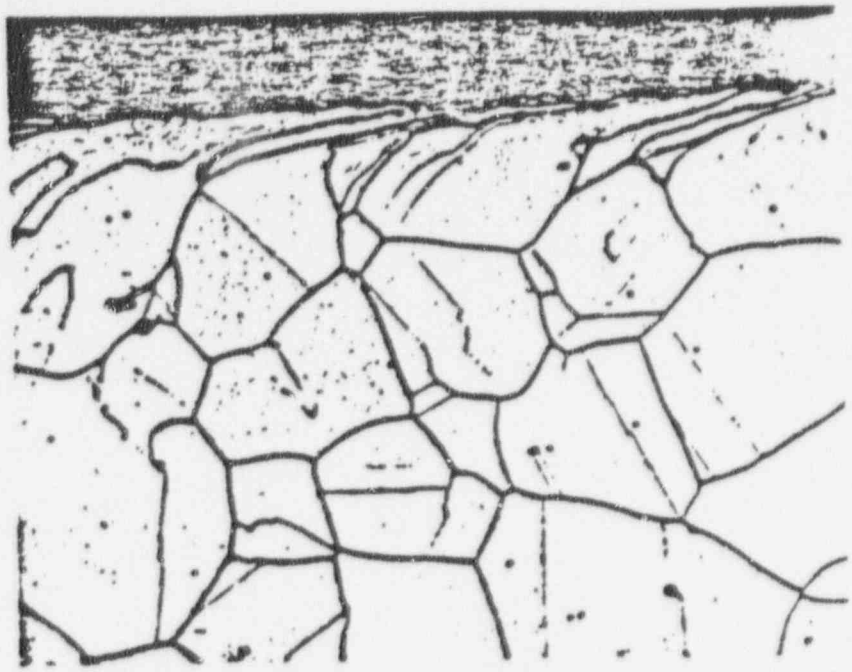

CONDITION 2: (a) GRINDING DIRECTION ←→ 400X
(b) FLAPPER WHEEL DIRECTION PERPENDICULAR TO MICROGRAPH
(c) TENSILE AXIS PERPENDICULAR TO MICROGRAPH

Figure L-6. Optical Micrograph of Specimen B1 — Typical Ground Surface Appearance

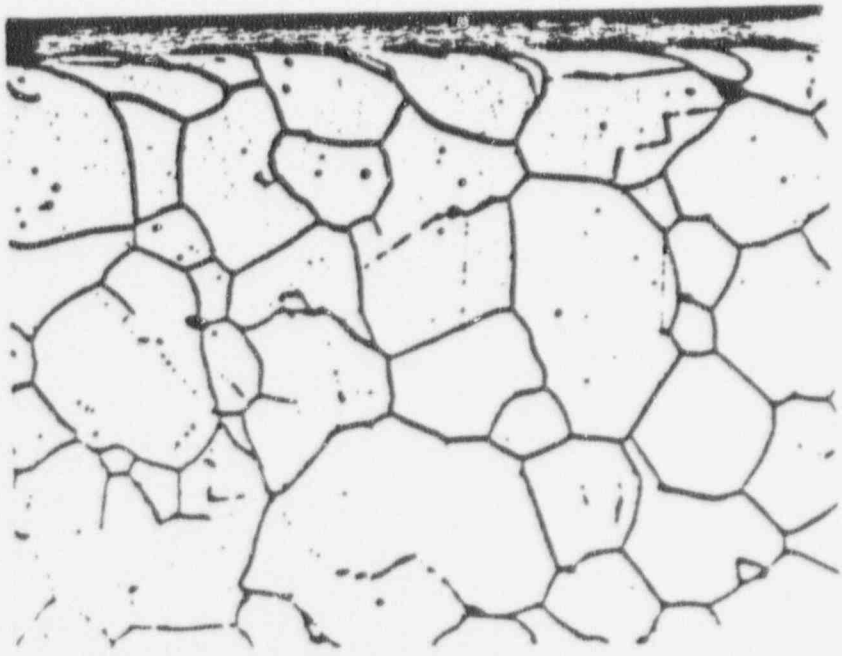

CONDITION 3: (a) GRINDING DIRECTION ←→ 400X
(b) FLAPPER WHEEL DIRECTION PERPENDICULAR TO MICROGRAPH
(c) CRATEX WHEEL DIRECTION ←→
(d) TENSILE AXIS PERPENDICULAR TO MICROGRAPH

Figure L-7. Optical Micrograph of Specimen C1 — Scattered Areas with Cold Worked Appearance

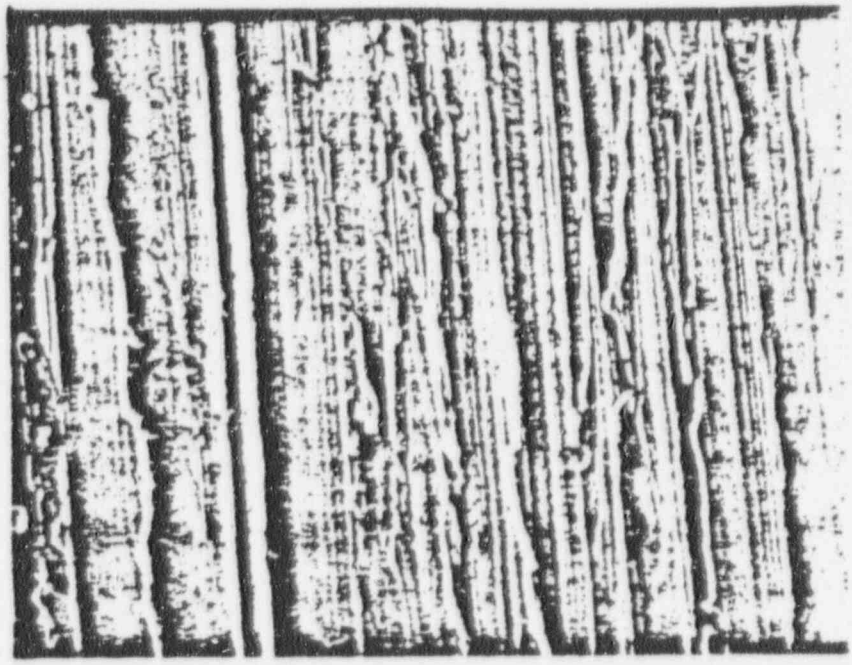

500X

Figure L-8. SEM Micrograph of As-Ground Surface — 500X of Specimen 1B, Condition 4

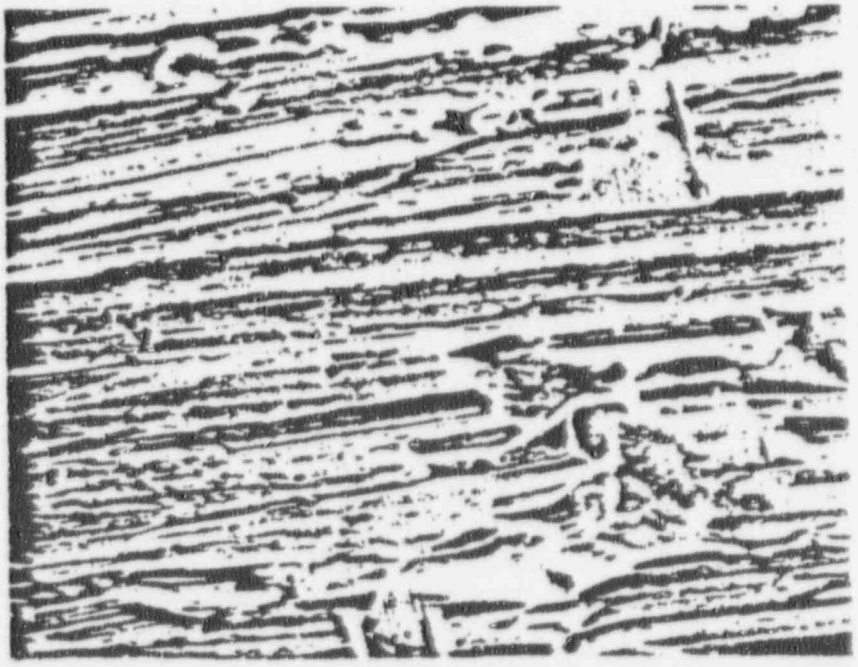

1000X

Figure L-9. SEM Micrograph of As-Ground Specimen 2B-1000X — Final Finish with Flapper Wheel, Condition 2

1000X

Figure L-10. SEM Micrograph of As-Ground Specimen 1A — Final Finish with the Cratex Polish, Condition 3

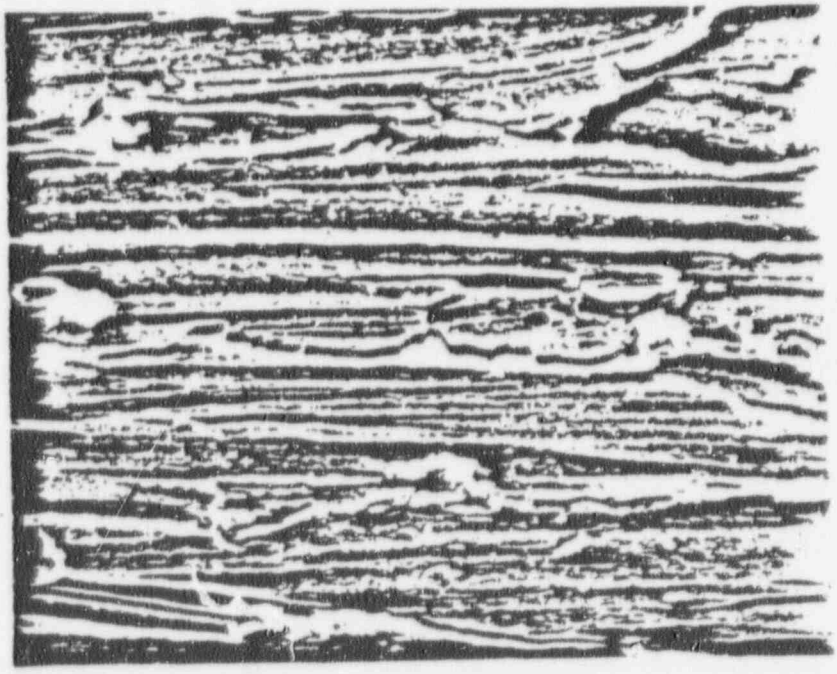

CONDITION 2: (a) GRINDING DIRECTION ←→
(b) FLAPPER WHEEL DIRECTION ←→
(c) TENSILE AXIS DIRECTION ↕

1000X

Figure L-11. SEM Micrograph of Strained Specimen A2 — Condition 2

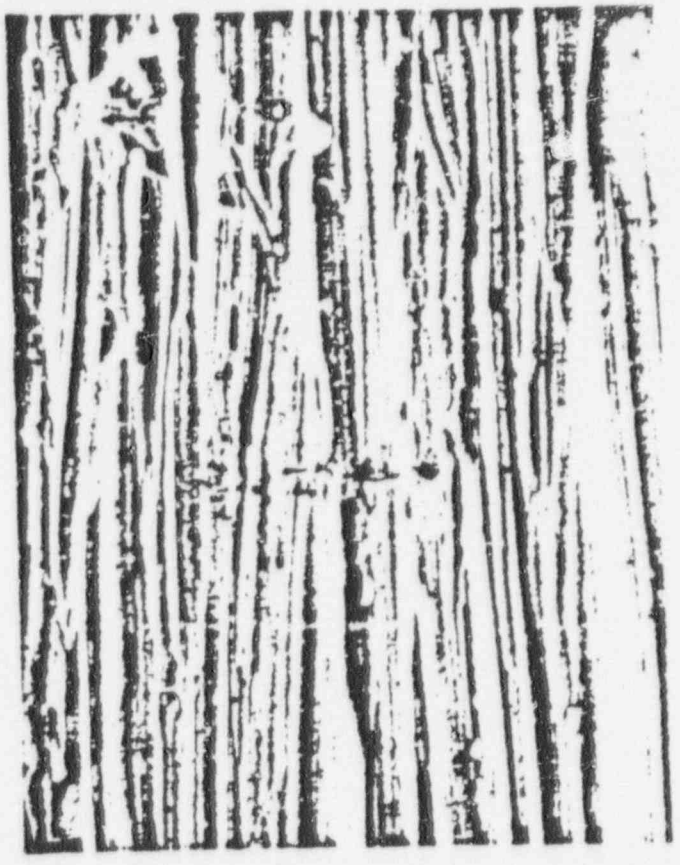

Figure L-12. SEM Micrograph of Strained Specimen B2 — Condition 2

APPENDIX M. STATISTICAL CALCULATION

M.1 INTRODUCTION

Sample calculations are presented in this Appendix to document the method of the factor of improvement calculation. These calculations are divided into two sections: the calculation of the mean and standard deviation of the reference material, and the calculation of the factor of improvement of a remedy based on the mean and standard deviation of the reference.

M.2 CALCULATION OF MEAN AND STANDARD DEVIATION

Calculation of a mean and standard deviation of test times after all samples fail is a simple procedure. Waiting for all samples to fail, however, is often a time consuming and expensive process. J. Schmee and W. Nelson[M-1] have presented a relatively simple means of estimating maximum likelihood mean and standard deviation values from data where the test is terminated before all samples fail. If the test is terminated after a fixed time it is termed singly time censored on the right, and the number of failures is random. If test is terminated after a fixed number of failures it is termed singly failure censored on the right, and the length of the test is random. In practice a combination of the above may occur. In this program the reference Type-304 statistical pipes were all run until at least three failures occurred. Some, however, were run until four failures occurred, since time permitted additional testing.

M.2.1 Symbols

- n = number of samples
- r = number of failed samples
- Y_i = failure time of ith failure
- Y_r = failure time of last failure
- $\overline{Y}$ = mean time to failure of r failures
- v = variance in failure time for r failures
- h = fraction censored (fraction still running)
- $\hat{\gamma}$ = relative variance of the r failures
- $\hat{\lambda}$ = function of h and $\hat{\gamma}$ (multiplier on time to failure)
- $\hat{\mu}$ = maximum likelihood estimate of the mean
- $\hat{\sigma}$ = maximum likelihood estimate of the standard deviation

M.2.1 Sample Calculation for Heat M0063 Pipe E11

1. The first step in calculation of a mean and standard deviation for the reference Type-304 stainless steels requires evaluation of time to failure for the failed welds. The goal here is to eliminate any bad data. For example, when the four failures in pipe E11 (M0063 reference) are plotted on normal deviate probability paper, it is noted that a straight line can easily be drawn through the first three points, but not the fourth, Figure M-1. A review of the test records showed that the pipe was overloaded briefly after the third failure. Overloads of this type are known to increase subsequent failure times. It is therefore reasonable to delete the data point for the fourth failure and make calculations based on the first three only. A similar kind of screening of data should precede calculations for other heats; for instance, for M7616 it was necessary to assign failure times since after the first failure, the pipe failed repeatedly before completing another complete cycle.

2. Take the logarithms of the failure times. For M0063 Pipe E11

Failure Times	Y_i = Log of Failure Time
1067	$Y_1 = 3.028$
1140	$Y_2 = 3.057$
1144	$Y_3 = 3.058$
2132	Eliminated for population

3. Calculate $\bar{Y}$ and v

$$\bar{y} = (y_1 + \ldots + y_r)/r,$$

$$v = \{(y_1 - \bar{y})^2 + \ldots + (y_r - \bar{y})^2\}/r;$$

for E11, r = 3

$$\bar{Y} = \frac{3.028 + 3.057 + 3.058}{3} = 3.0477$$

$$v = (3.028 - 3.0477)^2 + (3.057 - 3.0477)^2 + (3.058 - 3.047)^2/3 = 0.0002903$$

4. Calculate h and $\hat{\gamma}$

$$h = n - r/n$$

$$\hat{\gamma} = v/(Yo - \bar{Y})$$

for E11

$$h = 11 - 3/11 = 0.7273$$

$$\hat{\gamma} = 0.0002903/(3.058 - 3.047)^2 = 2.7361$$

Note $Y_o = Y_3$ for pipe E11

5. Use Table 1 from 76CRD250 to locate value of $\hat{\lambda}$.

For Pipe E11, See Page 35 of 76CRD250.

$$\hat{\lambda}(h, \hat{\gamma}) = \hat{\lambda}(0.7273, 2.7361) = 2.5772$$

Note that interpolation is required.

6. Finally calculate $\hat{y}$ and $\hat{\sigma}$

$$\hat{\mu} = \bar{y} + \hat{\lambda}(y_o - \bar{y}),$$

$$\hat{\sigma} = \{v + \hat{\lambda}(y_o - \bar{y})^2\}^{1/2}$$

for E11,

$$\hat{\mu} = 3.0477 + 2.5772\,(3.058 - 3.0477) = \underline{3.074}$$

$$\hat{\sigma} = \{0.0002903 + 2.5772\,(3.058 - 3.0477)^2\}^{1/2} = \underline{0.02374}$$

This completes the calculation of the maximum likelihood mean and standard deviation.

90015030

M.3 CALCULATION OF FACTOR OF IMPROVEMENT

The equation for calculation of the factor of improvement for a given remedy was given in Subsection 4.7.1 and is repeated here.

$$\text{Log Test Time} = F + G + \sigma\left\{-Q + U\,(1/n + r)^{1/2}\right\}$$

where
- F = mean log time to failure of reference welds
- G = log of desired improvement factor
- σ = standard deviation of log times to failure of reference welds
- Q = factor of σ for expected location of first order statistic
- U = normal distribution coefficient for 90% one-sided limit
- n = number of test welds per remedy
- r = factor of σ^2 for variance of first order statistic.

This can be rearranged to solve for G, the log of the factor of improvement.

$$G = \text{Log Test Time} - F - \sigma\left\{-Q + U\,(1/n + r)^{1/2}\right\}$$

In this equation, the value of F is the $\hat{y}$ value calculated by the Nelson and Schmee maximum likelihood method, and σ is $\hat{\sigma}$ calculated by the same method. The factors Q, U, and r are factors relating to the normal distribution and are found in Owen's handbook of statistical tables.*

M.3.1. Sample Calculation of the Factor of Improvement for M0063

1. The first step in solving for the factor of improvement is to solve the bracketed portion of the above equation.

   For all pipes tested having the same type of weld throughout, the value of n is constant. While there are 12 welds in each test pipe section, one heat-affected zone of each end weld is located in the transition piece rather than in the test pipe material. This results in 10 whole welds and 2 separate heat-affected zones in the reference material, which were added together for a total of 11.

   $$n = 11$$

   With n known, the values of Q, U, and r are derived from Owens tables as outlined below.

   $Q_1 = 1.5864$ for $n = 11$, rank $= 1$

   Owen, Page 152, Section 7.1, "Expected values of order statistics from a Normal Distribution."

   $U = 1.282$ for $\gamma = 0.90$ $\quad n = \infty$

   Owen, Page 126, Section 5.3, "One sided Tolerance limit factors for a Normal Distribution."

   $r = 0.332$ for $n = 11, i = 1, j = 1$

   Owen, Page 164, Section 7.3, "Variances and Covariance of Order Statistics in Samples up to 20 From a Normal Population."

   Therefore:

   $$\left\{-Q + U(1/n + r)^{1/2}\right\} = \left\{-1.5864 + 1.282(1/11 + 0.3332)^{1/2}\right\} = -0.752$$

90015031

2. From the above, the equation for factor of improvement can now be written as follows:

$$G = \text{Log Test Time} - F + \sigma\,(0.752)$$

It can be observed from the above result that when σ is very small the equation reduces to:

$$G = \text{Log Test Time} - F$$

or

$$\text{Factor of Improvement} = \frac{\text{Test Time}}{\text{Mean Failure Time for Reference.}}$$

Since σ was in fact very small for the three heats investigated, this approach could have been used, with little error, but was not.

3. Substitute values of F and σ into the equation.

G = Log Test Time $- F + \sigma\,(0.752)$ for M0063, E11
G = Log Test Time $- 3.074 + 0.02374\,(0.752)$
G = Log Test Time $- 3.056$

This equation will now yield G by simple substitution of the Log of Test Time for any of the remedies applied to Heat M0063.

4. Substitute Log of Test Time to Yield Factor of Improvement

Remedy	Test Time	Log Test Time	Log Test Time −3.056 G	Factor of Improvement Anti-Log G
SHT	5187	3.715	0.659	4.56
Shop CRC	6806	3.832	0.777	5.98
Field CRD	6806	3.832	0.777	5.98

The calculation of factors of improvement for other heats are performed identically.

90015032

REFERENCES

M-1. W. B. Nelson, J. Schmee, "Estimates and Approximate Confidence Limits for (log) Normal Life Distributions from Singly Censored Samples by Maximum Likelihood," Report No. 76CRD250, General Electric Company, April 1977.

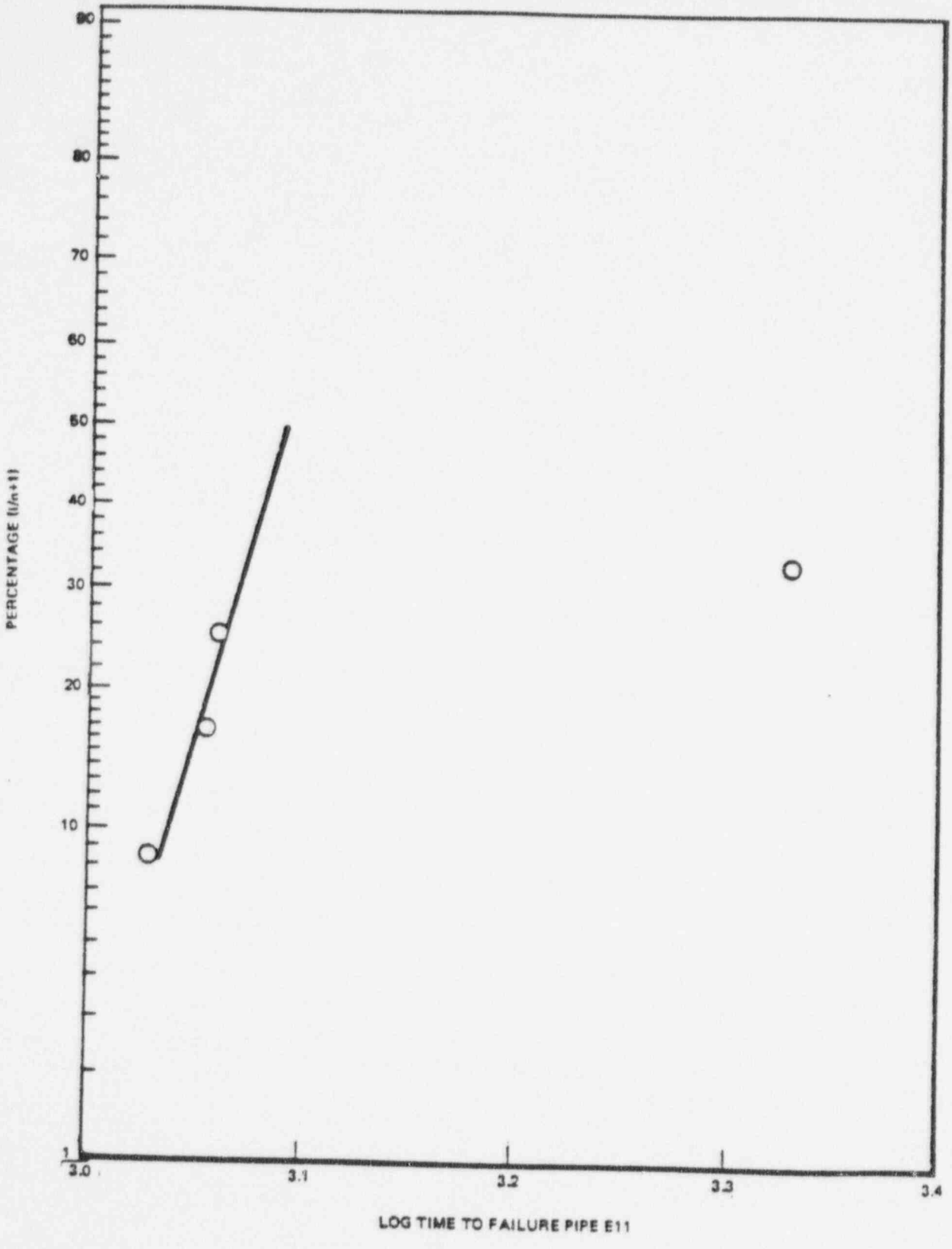

Figure M-1. Distribution of Failure Times in Pipe E11

90015034